Excited State Dynamics of Nucleobases
and
Structure and Dynamics of Melanin

A Thesis

Submitted in partial fulfillment of the requirements for

the degree of

Doctor of Philosophy

by

Sayan Mondal

20123232

IISER PUNE

Indian Institute of Science Education and Research

Pune - 411 008

2016

Certificate

Certified that the work incorporated in the thesis entitled "Excited state dynamics of nucleobases, and Structure and Kinetics of Melanin" submitted by Sayan Mondal was carried out by the candidate under my supervision. The work presented here or any part of it has not been included in any other thesis submitted previously for the award of any degree or diploma from any other University or Institution.

Date: 29/06/2016

Dr. Mrinalini Puranik

Thesis Supervisor,

Indian Institute of Science Education and

Research,

Pune, Maharashtra

Declaration

I declare that this thesis is a presentation of my original research work. Wherever contributions of others are involved, every effort is made to indicate this clearly, with due reference to the literature, and acknowledgment of collaborative research and discussions. I also declare that I have adhered to all principles of academic honesty and integrity and have not misrepresented or fabricated or falsified any idea/data/fact/source in my submission. I understand that violation of the above will be cause for disciplinary action by the Institute and can also evoke penal action from the sources which have thus not been properly cited or from whom proper permission has not been taken when needed.

Sayan mondal

Date: 29/06/2016   Roll No. 20123232

To,
bapi and mamoni

Abstract

Two of the most important classes of natural heterocycles are nitrogen containing nucleic acid bases (purines and pyrimidines), and indoles. Purines and pyrimidines are building blocks of our genetic information carrier deoxyribonucleic acid (DNA). Indole plays functionally important roles as structural units present in proteins and the biopigment melanin. This thesis presents structural and photodynamical studies on these two important macromolecules of life. DNA bases are highly photostable under ultraviolet radiation due to the ultrafast sub-picosecond (ps) lifetimes of electronic excited states associated with their absorption band centered at ~260 nm. With a combination of resonance Raman (RR) intensity analysis and quantum chemical computation, I have demonstrated that sub-100 femtosecond (fs) dynamics leads to distinct structural distortions in purines following photon absorption to two different singlet states, L_a (~260 nm) and B_b (~210 nm). These instantaneous distortions do not lie along photochemically active, lesion-forming coordinates.

Melanins are an important class of biomacromolecules that are known to have versatile functionalities, *e.g.,* acting as natural sunscreen to the entire animal kingdom, pattering and radical scavengers. They also have important technological applications. Unfortunately, the structure is not completely understood. I have obtained spectroscopic evidences that help in deriving an integrated kinetic model of enzymatic and non-enzymatic melanin formation. Using density functional theory (DFT), novel eumelanin fundamental building blocks that are inspired by experimentally detected small oligomers are proposed. Merits and demerits of these structural scaffolds in explaining several experimental observables of melanin are discussed vis-à-vis other reported models. Using a bottom-up approach and three-dimensional topographic imaging with atomic force microscopy (AFM), I have demonstrated that synthetic melanin has an organizational hierarchy that is similar to that present in natural melanin.

Acknowledgements

<div align="right">

Sayan Mondal
IISER Pune
June 2016

</div>

Contents

Ultrafast excited state dynamics of 6-chloroguanine within the B_b electronic state*

Ultrafast Nuclear Dynamics of Photoexcited Guanosine Monophosphate (GMP)

Excited state structural dynamics of Adenine in L_a and B_b Electronic States

Kinetics of Enzymatic and Non-enzymatic Melanin Formation*

Structural models of Eumelanin Protomolecules

Structural Hierarchy and Aggregation Dynamics of Self-assembled dopa-melanin

Acronyms and Abbreviations

6-ClG: 6-chloroguanine

6-ThG: 6-thioguanine

9-meA: 9-methyladenine

AFM: Atomic Force Microscopy

AP: 2-aminopurine

Ade: Adenine

AMP: Adenosine-5′-monophosphate

GMP: Guanosine-5′-monophosphate

B3LYP: Becke, three-parameter, Lee-Yang-Parr

BBO: Barium borate

Be: bending vibration involving three atoms

Breath: in-plane ring breathing vibration

CCD: Charge Couple Device

DAP: 2,6-diaminopurine

DFT: Density Functional Theory

DOS: density of electronic states

Dopa or L-dopa: 3,4-dihydroxyphenylalanine

DHI: 5,6-dihydroxyindole

DHICA: 5 6-dihydroxyindole-2-carboxylic acid

EPR: electron paramagnetic resonance

FTIR: Fourier-Transform Infrared

fs: femtosecond

FWHM: full width at half maxima or bandwidth

GS: ground state

Gua: Guanine

Guo: Guanosine

H→D: hydrogen to deuterium exchange

HB: hydrogen bonding

HF: Hartree-Fock

HOMO: highest occupied molecular orbital

HPLC: high Performance liquid chromatography

Hx: Hypoxanthine

Im: imidazole ring of purine

LBO: lithium borate

LUMO: lowest unoccupied molecular orbital

Nd-YLF: Neodymium-doped yttrium lithium fluoride

nm: nanometer

NMR: nuclear magnetic resonance

ns: nanosecond

PED: Potential Energy Distribution

PES: Potential energy surface

ps: picosecond

Pyrr: pyrrole ring of purine

Py: pyrimidine ring

QM: Quantum Mechanical

QC: Quantum Chemical

ref: reference

Sci: scissoring vibration involving three atoms

Str: bond stretching vibration involving two atoms

TD-DFT: time-dependent density functional theory

Ti-Sapph: Titanium-doped sapphire crystal (Ti^{3+}:Al_2O_3)

UVRR: ultraviolet resonance Raman spectroscopy

UV/Vis: Ultraviolet-visible

Ura: Uracil

UMP: Uridine-5′-monohosphate

Synopsis

Introduction

Unarguably, the most important classes of natural heterocycles crucial to life are nitrogen containing purines and pyrimidines, and indoles. These molecules are the building blocks of nucleic acids, and natural amino acids respectively. Adenine and guanine (purines), and thymine, cytosine, and uracil (pyrimidines) are the structural components of our genetic information carrier deoxyribonucleic acid (DNA) and Ribonucleic acid (RNA). Natural nucleobases are extraordinarily photostable molecules owing to intrinsic sub-picosecond (ps) lifetimes of their singlet excited states located in the ultraviolet (UV) region of radiation at ~260 nm.[1–6] These molecules do not spend enough time on reactive excited states for photodamage to occur because of ultrafast internal conversion (IC) to ground electronic state.[7] Apart from a few xanthine derivatives and methylated bases,[8] a majority of modified ones have longer excited state lifetimes, and exhibit fluorescence. Citing these reasons, UV-induced photostability has been argued as one of the selection pressures responsible for the natural choice of canonical nucleobases as building blocks of DNA and RNA in the prebiotic era.[9–13] All nucleobases absorb photons in the 200-230 nm wavelength region more strongly than in the 260-280 nm region. However, there are no previous reports concerning photodynamics of the electronic states lying within the 210 nm absorption band of any nucleobase system. Thus, in order to comprehend overall UV-induced photostability, photophysics on the high energy electronic states of nucleobases are to be investigated and compared with that of low-lying electronic states.

Another important class of biomaterials is melanin.[14,15] Other than DNA nucleobases, melanin is one of the abundant light-absorbing macromolecules in the animal kingdom. Apart from generally accepted three major macromolecules that are essential for life; (i) RNA and DNA, (ii) proteins and (iii) carbohydrates, melanin which is ubiquitous throughout the whole biosphere, has remained structurally and functionally less understood.[16–19] Melanins are highly cross-linked polymers made from covalent and non-covalent interactions of indolic moieties and have supramolecular structural architecture.[20–25] In mammals, melanin is present in skin, eyes, hair and also in the brain. Melanin is produced in melanosomes, vesicles localized inside melanocytes with the help of a dicopper containing oxidase known as tyrosinase.[26] Tyrosinase catalyzes the oxidation of a monophenol (i.e. tyrosine) or a diphenol (i.e. 3,4-dihydroxyphenylalanine or dopa) into dopaquinone. These quinones are very reactive and produce 5,6-dihydroxyindole (DHI) or 5,6-dihydroxyindole, 2-carboxylic acid (DHICA) depending on the presence or absence of specific enzymes.

Melanin performs biologically important functions, such as chelation of metal ions, acting as a heat sink by converting solar ultraviolet (UV) radiation into non-lethal thermal energy and acting as a reservoir of free radicals. In recent times, melanin and other similar materials, for example, polydopamine[27–29] are being explored as an active functional component in optoelectronics, biosensors, and other technological applications.[30–33] Melanin is a fundamental macromolecule of life and has potential as a next generation optoelectronic material and establishment of structure-function relationships in melanin will be of immense value to these fields.

Motivation and Specific Goals

After photoexcitation within the 260 nm absorption band, natural nucleobases relax to their electronic ground state in less than 1 ps. This ultrafast internal conversion is experimentally probed with techniques having sub-ps time resolution such as transient absorption[1] and fluorescence upconversion[34] in solution state, and with pump-probe ionization[5,35] and time-resolved photoelectron spectroscopy in gas phase.[6] As natural bases and their nucleotides are very weakly emissive (quantum yield, ϕ_F = 0.68-1.54 x 10^{-4}), fs fluorescence upconversion has been applied to measure the lifetimes of first singlet states directly. In parallel, theoretical *ab initio* calculations; computation of minimum energy paths on the excited state potential energy surface (PES) and dynamical simulations have been applied to probe early events after photoexcitation.[4,7,36–38] It has been found specific kind of out-of-plane distortions lead to the crossing of ground and excited state PES known as a conical intersection (CI) through which electronically excited population decays.

To the blue side of 260 nm absorption band, all nucleobases have $\pi\pi^*$ transitions within 210-120 nm of UV wavelength. These transitions are much stronger than those lying within ~ 260 nm band (L_a and L_b). However, there is no published literature on the effects of UV-C radiation (< 230 nm) on the photophysics of any nucleobase system. As all UV radiation and specifically those with high energy are potentially mutagenic to our gene, investigation of the high-lying electronic states are necessary to comprehend the overall effect of UV radiation on DNA bases. Furthermore, photoabsorption by these high energy states might have played important role during early biotic era when amount of UV flux on earth's surface below 240 nm of wavelength was critically high compared to today's value.[39]

Following photoexcitation, a vibronically excited nucleobase relaxes on its PES along very specific vibrational coordinates and through interaction with the surrounding solvent. Thus, time-resolved vibrational techniques such as ps infrared (ps-TRIR) spectroscopy, femtosecond (fs) transient absorption and fluorescence upconversion have been routinely applied to understand mode specific decay mechanisms.[40–42] However, these techniques are not suitable to probe the excited states

lying within UV-C region at ~ 210 nm. Another important methodology to study excited state structural dynamics of a photoexcited chromophore is through analysis of experimental resonance Raman (RR) excitation profiles.[43–45] RR intensities of a chromophore are sensitive to structural changes that happen within 100 fs of photon absorption and interaction with the local environment. Modeling of Raman excitation profiles (REP) using time-dependent formulation of RR intensities has been applied to extract ultrafast structural dynamics of all natural and several substituted nucleobases in their low energy L_a and L_b excited states.[46–53]

I have employed RR intensity analysis to extract ultrafast structural dynamics three purines, *viz.,* adenine (Ade), guanosine 5′-monophosphate (GMP) and a halogenated purine, 6-chloroguanine (6-ClG) in their high energy B_b electronic state. RR intensity analysis is unique in the sense that it can be readily applied to any electronic state of a chromophore depending on availability of laser sources. Additionally, through modeling of solute-solvent interaction within the Brownian oscillator spectral density model,[54] the time scale and amplitude of the inertial component of solvation were also extracted for all the three bases and were compared with those reported for other analogs. Specific roles of high-lying B_b (~ 210 nm) state in driving initial excited state dynamics of these purines are derived through a detailed comparison with previously published excited state dynamics on low energy L_a and L_b states. Additionally, the role of specific exocyclic substituents in tuning different spectroscopic properties of excited states of purines are derived.

Melanin has been studied extensively over the past seventy years with the help of a plethora of experimental techniques, such as nuclear magnetic resonance (NMR) in solid and solution state, electron paramagnetic resonance (EPR), UV/vis absorption,[22,55] small and wide-angle x-ray and neutron scattering,[24,56–59] vibrational spectroscopy,[60–67] mass spectrometry,[55–59] and topography imaging[20,22,23,68,74–76] and also with *ab initio* computation.[77–82] These studies have aimed at deciphering the structure of basic building unit (protomolecule) of melanin, and the structural organization from few nanometers (nm) to microns (μm) in length scale. The majority of these studies have used (i) melanin extracted from ink sack of *Sepia Officinalis* (referred as *Sepia* melanin hereafter), and (ii) melanin made through oxidation of dopa and tyrosine using tyrosinase or other oxidative agents. Comparatively, investigations on the kinetics of the melanization process itself have been limited in number.[83–88] The majority of these studies have used UV/vis absorption spectroscopy to detect evolution of structural intermediates in the tyrosinase-catalyzed oxidation of a precursor, either dopa or tyrosine. Due to the absence of narrow and well-separated absorption signatures of each of the intermediates, application of a kinetic model, such as the one proposed by Foster[89] has not been achieved. I have used UV excited RR (UVRR) vibrational signatures as chemically exclusive molecular fingerprints and determined

rates of formation and decay of reaction intermediates in a self-oxidized and enzyme assisted oxidation of dopa. Time evolution of the width of the vibrational band associated with melanin is used to quantify structural heterogeneity of formed polymers.

Over the course of the last decade, the structural models that emerged as the probable fundamental unit of melanin are (i) four to eight monomers that are connected to each other through C-C bonds, are rotated with respect to each other;[90–94] (ii) four monomers are organized in a porphyrin ring-like arrangement with a site for metal binding;[79,95] (iii) monomers are not connected via covalent bonds, instead are held together by non-covalent interactions such as, hydrogen and ionic bonds, dipole-dipole interactions.[82,96,97] Based on d'Ischia and coworkers' organosynthetic work,[92–94] I have explored novel structural models of eumelanin. Using first principle density functional theory (DFT) spectroscopic and structural properties of these small oligomers are computed and compared against available experimental data. A critical comparison of all published structural models is also presented. Furthermore, atomic force microscopy (AFM) imaging in tapping mode is applied to probe self-assembly mechanism of autoxidized dopa-melanin, the most used synthetic model for the natural pigment.

Key Findings

Vibrational Reorganizations in Substituted Purines (Chapter 3)

With the help of UVRR spectroscopy and DFT calculations, effects of exocyclic substitutions on the vibrational and electronic reorganization of five purines; Adenine (Ade), 2-aminopurine (AP), 2, 6-diaminopurine (DAP), guanosine monophosphate (GMP), and 6-chloroguanine (6-ClG) are investigated. I have established N_9H form as predominant tautomer of AP at neutral pH through isotope edited vibrational analysis. Time-dependent density functional theoretical (TD-DFT) calculations reveal unlike ordering of low energy electronic states, such as, L_a, L_b, and $^1n\pi^*$ at ~250-280 nm range, energies of the transitions located in deep UV at ~200-220 nm range are not significantly affected by substitution. Relative intensity patterns of 225 and 260 nm excited UVRR spectra reveal distinct vibronic characters of the low energy (~ 260 nm) and high energy (~ 210 nm) excited states in these purines. It is found that exocyclic heavy substitution such as chlorine (Cl) on pyrimidine moiety leads to significant amount of coupling of C-Cl vibration with modes localized on another part (imidazole) of the purine. Upon 225 nm photoexcitation, the initial excited state structural dynamics of these bases are expected to occur along the purine ring stretching coordinates associated with the observed RR bands.

Ultrafast excited state dynamics of 6-chloroguanine within the Bb electronic state (Chapter 4)

Quantitative measurements of the resonance Raman cross-section across the B_b absorption band (210-230 nm) of 6-ClG is performed and REPs of all RR active modes are constructed. I have simulated the REPs and absorption cross-section using time dependent wave packet propagation (TDWP) formalism to extract initial excited state dynamics of 6-ClG within 30-50 fs after photoexcitation. We find that imidazole and pyrimidine rings of 6-ClG undergo expansion and contraction respectively following photoexcitation to the B_b state. The amount of distortions of the excited state structure from that of the ground state is reflected in total internal reorganization energy that is determined at 112 cm^{-1}. The contribution of inertial component of solvent response towards the total reorganization energy was obtained at 1220 cm^{-1}. Additionally, our simulation also yields an instantaneous response of the first solvation shell within an ultrafast timescale, $\tau < 30$ fs, following photoexcitation. It is worthy to note here that, though theoretically predicted, the inertial component of solvation that occurs within few tens of fs has been detected in very few experimental reports.[98–101] The low internal reorganization energy of this purine is ascribed to population transfer process to other close lying electronic states, occurring in the same time scale as that of the RR process.

Ultrafast Nuclear Dynamics of Photoexcited Guanosine Monophosphate (GMP) (Chapter 5)

To understand the role of oxygen substituent (O6) at C6 site in the parent nucleobase of 6-ClG, experimental Raman excitation profiles of guanosine 5′-monophosphate (GMP) within 210-230 nm of absorption band (B_b state) is modeled. Deduced structural changes of the purine ring upon photoabsorption by the B_b state are compared with those obtained for the two lowest lying $\pi\pi^*$ (L_a and L_b at 280 and 248 nm respectively) excited states of GMP. We find that excitation to L_b state lengthens C6–N1 and C2=N3 bonds which lie along the formation coordinate of various oxidative adducts but B_b excitation does not. We also find that photoabsorption by B_b state weakens C_8–N_9 bond and thus might assist imidazole ring opening via cleavage of the same bond. Electronic excitation to different $\pi\pi^*$ states of the guanine chromophore results in contrasting structural changes; while absorption by L_a and L_b state induces expansion of pyrimidine and contraction of imidazole rings, B_b excitation results in overall shrinkage of both the rings. Computed absolute changes in internal coordinates imply that photoexcitation to none of the three singlet states of GMP does not lead to the formation of a cation radical of guanine. In comparison to 6-ClG (112 cm^{-1}), a large (980 cm^{-1}) internal reorganization contribution was determined.

Excited state structural dynamics of Adenine in La and Bb Electronic States (Chapter 6)

To have a concise understanding on photodynamics of purines on their high-lying B_b excited state, Ade is also investigated employing the same methodology. Obtained structural distortions of Ade following photoabsorption by B_b state are analyzed vis-à-vis the low energetic $\pi\pi^*$ state (L_a) that lies within the 260 nm absorption band of Ade. Electronic excitations to two different $\pi\pi^*$ states of Ade bring about distinct structural changes: while L_a excitation causes minor overall expansion of the pyrimidine ring, the B_b state induces major overall contraction of the same. We find that photoexcitation to B_b state leads to major distortions that are localized on the pyrimidine ring. On the contrary, the imidazole ring suffers maximal changes following L_a excitation. Deduced changes in internal coordinates imply that neither L_a nor B_b state absorption distort the Ade structure along the formation path of its cation. The higher value of total reorganization energy (2171 cm^{-1}) of Ade on B_b excited state in comparison with that (168 cm^{-1}) previously reported for the same chromophore on L_a state is attributed to very low total vibrational reorganization energy in case of the latter. This internal reorganization energy of 168 cm^{-1} in L_a state is credited to its intrinsic photostability, arising from ultrafast state crossing mechanisms in Ade. Detail investigation of initial photodynamics on B_b excited states shows that the properties of higher-lying electronic transitions are severely different than those on low energy (L_a and L_b) states of purines.

Kinetics of Enzymatic and Non-enzymatic Melanin Formation (Chapter 7)

I have investigated the kinetics of melanin formation from dopa in presence and absence of enzyme through electronic absorption, infrared absorption, and ultraviolet resonance Raman (UVRR) spectra at several excitation wavelengths. From these experiments, we observed kinetics of the formation of different species *en route* to melanin polymerization. Exclusive chemical signatures of monomer 3,4-dihydroxyphenylalanine (dopa), intermediate dopachrome (DC) and early time polymer are established through their vibrational bands at 1292, 1670 and 1616 cm^{-1} respectively. These Molecule-specific vibrational markers allowed us to follow the fates of intermediates that have similar absorption spectra. Direct evidence of enzymatic control of the heterogeneity of melanin oligomers by tyrosinase is provided from experimental measurements of vibrational bandwidths (full width at half maxima or FWHM). Small oligomers made with density functional theory show that the linear homopolymeric structures of DHI can account for experimentally observed wavenumbers and broad bandwidth in Raman spectra of dopa-melanin. Fitting of RR derived kinetics with first order reaction model reveals the formation of at least two

distinct intermediates preceding pigment formation. We capture RR signature of DC, the intermediate stabilized by the enzyme tyrosinase for the first time in an enzyme-assisted melanization reaction using 488 nm excitation wavelength and propose that this wavelength can be used to probe the reaction intermediates of melanin formation in solution. We explain the position (1616 cm^{-1}) and width (50-60 cm^{-1}) of experimentally observed Raman band of melanin as an outcome of intrinsic structural heterogeneity due to a distribution of tetrameric oligomers.

Structural models of eumelanin protomolecules (Chapter 8)

Starting from experimentally identified and similar covalently linked dimeric and tetrameric species of DHI; we propose and test a hierarchical assembly as the structure of possible eumelanin protomolecules. I have shown that this structural model is able to capture three crucial physical properties of melanin, *viz.*, broad optical absorption, sharp features of experimental X-ray structure factor, S(q) and radial distribution function (RDF), and most importantly position and relative intensities of experimental Raman bands. As there are multiple small oligomeric models that explain broad optical spectra, I propose and validate the use of vibrational signatures as a more rigorous constraint on any proposed structural model. I have found that in-plane benzene Dewar and C2–C3 pyrrole stretching modes are always coupled with inter-unit C–C stretching in small oligomers (up to octamer). These vibrations do not change normal mode character in the course of polymerization, but shows a saturation and later decrease in their intensities with growing chain length. The observation of saturation of width of the Raman band at 1616 cm^{-1} during the melanization reaction is explained as an intrinsic structural heterogeneity. This heterogeneity arises from chemically dissimilar coupling sites in our model. Specific types of tetrameric and octameric units have been identified to reproduce the first sharp feature in S(q) spectra and also the peak at 3 Å in experimental RDF of eumelanin.

Structural Hierarchy and Aggregation Dynamics of Self-assembled dopa-melanin (Chapter 9)

In this part of the thesis, I have investigated the self-assembled supramolecular organization of synthetic dopa-melanin using tapping mode (TM) atomic force microscopy (AFM) imaging. Dopa-melanin is prepared from oxidative polymerization of dopa in 50 mM Tris-HCl buffer (pH 7.4). A model for the self-assembled structural organization of dopa-melanin is derived based on a bottom-up synthesis approach and tapping mode (TM) atomic force microscopy (AFM) imaging. The time evolution of size distribution is found by imaging the deposited aqueous solution at different time-points of the melanin formation reaction. The dopa-melanin particles reveal intermediate structures that connect planner sheets to form both fibrillar and globular

aggregates. At an early stage of melanization, the height distribution of the disc-shaped planar structures show peak-to peak-separation of 3.66 Å, which clearly indicates characteristic π-π stacking of individual sheets of protomolecules. We determine the rate of the stacking process by monitoring decay of the populations consisting two layer thick sheets into taller structures to be k_{stack} = of 1.12 x 10^{-3} min^{-1}. Four different types of nano-aggregates are detected; (i) a few to tens of layers thick disks (D: 30-50 nm and H: 0.5-2 nm), (ii) barrel-like aggregates (D: 50-110 nm and H: 1.5-15 nm), (iii) globular agglomerates (D: 1-2 um and H: ~100 nm) and (iv) microns long parallel running stick-like structures (D: 85-180 nm and H: 10-80 nm). Based on AFM topographs we propose that the disc-shaped aggregates form barrel-like structures through π-π stacking. Further, these self-assemble in edge-to-edge fashion to form several microns long filamentous structures. While providing conclusive direct evidence for π-π stacking in eumelanin, our results also present an alternative method of analyzing formation pathway of secondary and tertiary structures in synthetic melanins and similar self-assembled systems.

Importance and Future Perspective

Following photoexcitation within the 210-230 nm (UV-C) absorption band (B_b), this thesis examines the excited state structures and solvation dynamics of purine nucleobases for the first time. The results presented show that sub-100 fs dynamics of natural purines are significantly different in low energy L_a, and high energy B_b states. The obtained structural distortions of different internal coordinates of the purine ring are analyzed in the context of lesion formation. Results presented in this thesis show that despite the significantly high absorption cross-section, B_b excited state does not directly assist photoinduced damage within hundred fs of photoabsorption. The amplitude of the inertial response of water solvation is found to be strongly dependent on instantaneous charge redistribution of the chromophore in a particular excited state. Additionally, these investigations determine the presence of a sub-50 fs response time of the fastest component of water solvation. Results presented in this thesis set the stage for further theoretical and experimental photodynamic investigations of less explored B_b and higher excited states of nucleobases. It is also established that unlike conventional transient absorption or fluorescence upconversion techniques, resonance Raman intensity analysis is readily applicable to probe deep-lying electronic states (below 230 nm) of biomolecules in solution. In addition to 260 nm absorption band, to develop a comprehensive understanding of how our genetic material responds to UV radiation, it is of paramount importance to investigate these high energy singlet states of nucleobases.

In the second part of the thesis, a kinetic model of melanin formation using absorption and vibrational spectroscopies is derived, and protomolecular structural

model of eumelanin is proposed. The work done in this thesis establishes a method of using molecule specific vibrational signatures to probe chemical kinetics of the very fundamental and yet poorly understood melanization process. The method of using 260 and 488 nm resonant excitations to probe the rates of formation and decay of kinetic intermediates can be readily applied to the case of melanins made from other precursors, such as tyrosine and DHI. Using tyrosinase from mammalian sources, it would be possible to address the definitive but yet unknown role of this enzyme in controlling heterogeneity of small oligomer populations and also in the stabilization of dopachrome. Such experiments have the potential to provide insights that would translate into a deeper understanding of the role of tyrosinase in skin disorder such as oculocutaneous albinism and hyperpigmentation and eventually in developing therapeutic strategies. Computational results presented in this thesis also point out that it is extremely important to constrain any proposed, but not experimentally verified eumelanin structural model with all available high resolution experimental data, especially, vibrational spectra and X-ray radial distribution functions. The employed bottom-up approach of probing melanin aggregation can be readily applied to a variety of melanization processes using different precursors for developing a general model of the synthetic pigments. Detection of the uniform population of ultra-thin disks in dopa-melanin nano-aggregates might guide us to a new avenue of using melanin-like materials in optoelectronics. It opens up the opportunity of examining conducting and nano-mechanical properties of these 2-dimensional (2D) structures, and their possible future technological applications.

References

1   J. M. L. Pecourt, J. Peon and B. Kohler, *J. Am. Chem. Soc.*, 2000, **122**, 9348–9349.

2   C. T. Middleton, K. de La Harpe, C. Su, Y. K. Law, C. E. Crespo-Hernández and B. Kohler, *Annu. Rev. Phys. Chem.*, 2009, **60**, 217–239.

3   C. E. Crespo-Hernández, B. Cohen, P. M. Hare and B. Kohler, *Chem. Rev.*, 2004, **104**, 1977–2020.

4   K. Kleinermanns, D. Nachtigallová and M. S. de Vries, *Int. Rev. Phys. Chem.*, 2013, **32**, 308–342.

5   H. Kang, K. T. Lee, B. Jung, Y. J. Ko and S. K. Kim, *J. Am. Chem. Soc.*, 2002, **124**, 12958–12959.

6   S. Ullrich, T. Schultz, M. Z. Zgierski and A. Stolow, *Phys. Chem. Chem. Phys.*, 2004, **6**, 2796.

7   M. Barbatti, A. J. A. Aquino, J. J. Szymczak, D. Nachtigallova, P. Hobza and H. Lischka, *Proc. Natl. Acad. Sci.*, 2010, **107**, 21453–21458.

8   J. Chen and B. Kohler, *Phys. Chem. Chem. Phys.*, 2012, **14**, 10677.

9   L. Serrano-Andrés and M. Merchán, *J. Photochem. Photobiol. C Photochem. Rev.*, 2009, **10**, 21–32.

10   S. Matsika, 2014, pp. 209–243.

11   M. Levy and S. L. Miller, *Proc. Natl. Acad. Sci. U. S. A.*, 1998, **95**, 7933–8.

12   A. L. Sobolewski and W. Domcke, *Europhys. News*, 2006, **37**, 20–23.

13   P. Ehrenfreund, S. Rasmussen, J. Cleaves and L. Chen, *Astrobiology*, 2006, **6**, 490–520.

14   G. Prota, *Melanins and Melanogenesis*, Academic Press, Inc., California, USA, 1st edn., 1992.

15   J. D. Simon and D. N. Peles, *Acc. Chem. Res.*, 2010, **43**, 1452–1460.

16   F. Solano, *New J. Sci.*, 2014, **2014**, 1–28.

17   M. d'Ischia, K. Wakamatsu, F. Cicoira, E. Di Mauro, J. C. Garcia-Borron, S. Commo, I. Galván, G. Ghanem, K. Kenzo, P. Meredith, A. Pezzella, C. Santato, T. Sarna, J. D. Simon, L. Zecca, F. A. Zucca, A. Napolitano and S. Ito, *Pigment Cell Melanoma Res.*, 2015, **28**, 520–544.

18   J. Lindgren, A. Moyer, M. H. Schweitzer, P. Sjövall, P. Uvdal, D. E. Nilsson, J. Heimdal, A. Engdahl, J. A. Gren, B. P. Schultz and B. P. Kear, *Proc. R. Soc. B Biol. Sci.*, 2015, **282**, 20150614.

19   J. Borovanský and P. A. Riley, Eds., *Melanins and Melanosomes. Biosynthesis, Biogenesis, Physiological, and Pathological Functions*, Wiley-VCH Verlag GmbH & Co. KGaA, Weinheim, Germany, 1st edn., 2011.

20   C. M. R. Clancy and J. D. Simon, *Biochemistry*, 2001, **40**, 13353–13360.

21   S. Reale, M. Crucianelli, A. Pezzella, M. D'Ischia and F. De Angelis, *J. Mass Spectrom.*, 2012, **47**, 49–53.

22   A. A. R. Watt, J. P. Bothma and P. Meredith,

Soft Matter, 2009, **5**, 3754.

23   G. W. Zajac, J. M. Gallas and A. E. Alvarado-Swaisgood, *J. Vac. Sci. Technol. B Microelectron. Nanom. Struct.*, 1994, **12**, 1512.

24   J. Cheng, S. C. Moss, M. Eisner and P. Zschak, *Pigment Cell Res.*, 1994, **7**, 255–262.

25   M. d'Ischia, A. Napolitano, V. Ball, C.-T. Chen and M. J. Buehler, *Acc. Chem. Res.*, 2014, **47**, 3541–3550.

26   J. J. Nordlund, R. E. Boissy, V. J. Hearing, R. A. King, W. S. Oetting and J.-P. Ortonne, Eds., *The Pigmentary System*, Blackwell Publishing Ltd, Oxford, UK, 2006.

27   X. Yu, H. Fan, L. Wang and Z. Jin, *Angew. Chemie Int. Ed.*, 2014, n/a–n/a.

28   M. d'Ischia, A. Napolitano, A. Pezzella, P. Meredith and T. Sarna, *Angew. Chemie Int. Ed.*, 2009, **48**, 3914–3921.

29   Y. Liu, K. Ai and L. Lu, *Chem. Rev.*, 2014, **114**, 5057–5115.

30   M. Xiao, Y. Li, M. C. Allen, D. D. Deheyn, X. Yue, J. Zhao, N. C. Gianneschi, M. D. Shawkey and A. Dhinojwala, *ACS Nano*, 2015, **9**, 5454–5460.

31   N. F. Della Vecchia, R. Avolio, M. Alfè, M. E. Errico, A. Napolitano and M. D'Ischia, *Adv. Funct. Mater.*, 2013, **23**, 1331–1340.

32   L. Panzella, G. Gentile, G. D'Errico, N. F. Della Vecchia, M. E. Errico, A. Napolitano, C. Carfagna and M. D'Ischia, *Angew. Chemie Int. Ed.*, 2013, **52**, 12684–12687.

33   M. Ambrico, N. F. Della Vecchia, P. F. Ambrico, A. Cardone, S. R. Cicco, T. Ligonzo, R. Avolio, A. Napolitano and M. D'Ischia, *Adv. Funct. Mater.*, 2014, n/a–n/a.

34   J. Peon and A. H. Zewail, *Chem. Phys. Lett.*, 2001, **348**, 255–262.

35   C. Canuel, M. Mons, F. Piuzzi, B. Tardivel, I. Dimicoli and M. Elhanine, *J. Chem. Phys.*, 2005, **122**, 074316.

36   M. Barbatti, A. C. Borin and S. Ullrich, Eds., *Photoinduced Phenomena in Nucleic Acids II*, Springer International Publishing, Cham, 2015, vol. 356.

37   M. Barbatti, A. C. Borin and S. Ullrich, Eds., *Photoinduced Phenomena in Nucleic Acids I*, Springer International Publishing, Cham, 2015, vol. 355.

38   R. Improta, F. Santoro and L. Blancafort, *Chem. Rev.*, 2016, **116**, 3540–3593.

39   C. S. Cockell, in *Ecosystems, Evolution, and Ultraviolet Radiation*, Springer New York, New York, NY, 2001, pp. 1–35.

40   J. M. L. Pecourt, J. Peon and B. Kohler, *J. Am. Chem. Soc.*, 2001, **123**, 10370–10378.

41   J. Peon and A. H. Zewail, *Chem. Phys. Lett.*, 2001, **348**, 255–262.

42   M. Towrie, G. W. Doorley, M. W. George, A. W. Parker, S. J. Quinn and J. M. Kelly, *Analyst*, 2009, **134**, 1265.

43   A. B. Myers and R. A. Mathies, in *Biological Applications of Raman Spectroscopy: Vol. 2 - Resonance Raman Spectra of Polyenes and Aromatics*, ed. T. G. Spiro, John Wiley & Sons Inc, New York, 1st edn., 1987, pp. 1–58.

44   A. B. Myers, *J. Opt. Soc. Am. B*, 1990, **7**, 1665.

45   A. B. Myers, *Acc. Chem. Res.*, 1997, **30**, 519–527.

46   A. F. El-Yazbi, A. Palech and G. R. Loppnow, *J. Phys. Chem. A*, 2011, **115**, 10445–10451.

47   S. A. Oladepo and G. R. Loppnow, *J. Phys. Chem. B*, 2011, **115**, 6149–6156.

48   B. E. Billinghurst and G. R. Loppnow, *J. Phys. Chem. A*, 2006, **110**, 2353–2359.

49   F. Teimoory and G. R. Loppnow, *J. Phys.

Chem. A, 2014, **118**, 12161–12167.

50   S. Yarasi, S. Ng and G. R. Loppnow, *J. Phys. Chem. B*, 2009, **113**, 14336–14342.

51   S. S. Ng, F. Teimoory and G. R. Loppnow, *J. Phys. Chem. Lett.*, 2011, 2362–2365.

52   B. E. Billinghurst, S. A. Oladepo and G. R. Loppnow, *J. Phys. Chem. B*, 2012, **116**, 10496–10503.

53   B. E. Billinghurst, R. Yeung and G. R. Loppnow, *J. Phys. Chem. A*, 2006, **110**, 6185–6191.

54   B. Li, A. E. Johnson, S. Mukamel and A. B. Myers, *J. Am. Chem. Soc.*, 1994, **116**, 11039–11047.

55   M. L. Tran, B. J. Powell and P. Meredith, *Biophys. J.*, 2006, **90**, 743–52.

56   Y. T. Thathachari and M. S. Blois, *Biophys. J.*, 1969, **9**, 77–89.

57   J. Cheng, S. C. Moss and M. Eisner, *Pigment Cell Res.*, 1994, **7**, 263–273.

58   J. M. Gallas, K. C. Littrell, S. Seifert, G. W. Zajac and P. Thiyagarajan, *Biophys. J.*, 1999, **77**, 1135–1142.

59   K. C. Littrell, J. M. Gallas, G. W. Zajac and P. Thiyagarajan, *Photochem. Photobiol.*, 2007, **77**, 115–120.

60   J. A. Pierce and D. M. Rast, *Phytochemistry*, 1995, **39**, 49–55.

61   M. G. Bridelli, D. Tampellini and L. Zecca, *FEBS Lett.*, 1999, **457**, 18–22.

62   V. Capozzi, G. Perna, A. Gallone, P. F. Biagi, P. Carmone, A. Fratello, G. Guida, P. Zanna and R. Cicero, *J. Mol. Struct.*, 2005, **744-747**, 717–721.

63   A. Samokhvalov, Y. Liu and J. D. Simon, *Photochem. Photobiol.*, 2007, **80**, 84–88.

64   S. A. Centeno and J. Shamir, *J. Mol. Struct.*, 2008, **873**, 149–159.

65   B. Bilińska, *Spectrochim. Acta Part A Mol. Biomol. Spectrosc.*, 2001, **57**, 2525–2533.

66   L. Sangaletti, S. Pagliara, P. Vilmercati, C. Castellarin-Cudia, P. Borghetti, P. Galinetto, R. Gebauer and A. Goldoni, *J. Phys. Chem. B*, 2007, **111**, 5372–5376.

67   L. Sangaletti, P. Borghetti, P. Ghosh, S. Pagliara, P. Vilmercati, C. Castellarin-Cudia, L. Floreano, A. Cossaro, A. Verdini, R. Gebauer and A. Goldoni, *Phys. Rev. B*, 2009, **80**, 174203.

68   G. W. Zajac, J. M. Gallas, J. Cheng, M. Eisner, S. C. Moss and A. E. Alvarado-Swaisgood, *Biochim. Biophys. Acta*, 1994, **1199**, 271–278.

69   C. Costa, A. Bertazzo, G. Allegri, G. Toffano, O. Curcuruto and P. Traldi, *Pigment Cell Res.*, 1992, **5**, 122–31.

70   A. Bertazzo, C. Costa, G. Allegri, R. Seraglia and P. Traldi, *Rapid Commun. Mass Spectrom.*, 1995, **9**, 634–640.

71   A. Napolitano, A. Pezzella, G. Prota, R. Seraglia and P. Traldi, *Rapid Commun. Mass Spectrom.*, 1996, **10**, 468–472.

72   A. Pezzella, A. Napolitano, M. D'Ischia, G. Prota, R. Seraglia and P. Traldi, *Rapid Commun. Mass Spectrom.*, 1997, **11**, 368–372.

73   A. Bertazzo, C. V. L. Costa, G. Allegri, M. Schiavolin, D. Favretto and P. Traldi, *Rapid Commun. Mass Spectrom.*, 1999, **13**, 542–547.

74   J. B. Nofsinger, S. E. Forest, L. M. Eibest, K. A. Gold and J. D. Simon, *Pigment Cell Res.*, 2000, **13**, 179–84.

75   C. M. R. Clancy, J. B. Nofsinger, R. K. Hanks and J. D. Simon, *J. Phys. Chem. B*, 2000, **104**, 7871–7873.

76   J. M. Gallas, G. W. Zajac, T. Sarna and P. L. Stotter, *Pigment Cell Res.*, 2000, **13**, 99–108.

77   D. S. Galvão and M. J. Caldas, *J. Chem. Phys.*, 1990, **92**, 2630.

78   L. E. Bolívar-Marinez, D. S. Galvão and M. J. Caldas, *J. Phys. Chem. B*, 1999, **103**, 2993–3000.

79   E. Kaxiras, A. Tsolakidis, G. Zonios and S. Meng, *Phys. Rev. Lett.*, 2006, **97**, 218102.

80   K. B. Stark, J. M. Gallas, G. W. Zajac, M. Eisner and J. T. Golab, *J. Phys. Chem. B*, 2003, **107**, 11558–11562.

81   C.-T. Chen, C. Chuang, J. Cao, V. Ball, D. Ruch and M. J. Buehler, *Nat. Commun.*, 2014, **5**.

82   G. Prampolini, I. Cacelli and A. Ferretti, *RSC Adv.*, 2015, **5**, 38513–38526.

83   E. J. Land, S. Ito, K. Wakamatsu and P. A. Riley, *Pigment Cell Res.*, 2003, **16**, 487–493.

84   E. J. Land, C. A. Ramsden and P. A. Riley, *Acc. Chem. Res.*, 2003, **36**, 300–308.

85   C. Lambert, T. G. Truscott, E. J. Land and P. A. Riley, *J. Chem. Soc. Faraday Trans.*, 1991, **87**, 2939.

86   M. R. Chedekel, E. J. Land, A. Thompson and T. G. Truscott, *J. Chem. Soc. Chem. Commun.*, 1984, 1170.

87   V. I. Stsiapura, A. A. Maskevich, V. A. Kuzmitsky, V. N. Uversky, I. M. Kuznetsova and K. K. Turoverov, *J. Phys. Chem. B*, 2008, **112**, 15893–15902.

88   V. Falguera, J. Pagán and A. Ibarz, *Food Res. Int.*, 2010, **43**, 66–69.

89   M. Foster, *Proc. Natl. Acad. Sci. U. S. A.*, 1950, **36**, 606–611.

90   M. d'Ischia, A. Napolitano, K. Tsiakas and G. Prota, *Tetrahedron*, 1990, **46**, 5789–5796.

91   A. Pezzella, A. Napolitano, M. D'Ischia and G. Prota, *Tetrahedron*, 1996, **52**, 7913–7920.

92   L. Panzella, A. Pezzella, A. Napolitano and M. D'Ischia, *Org. Lett.*, 2007, **9**, 1411–1414.

93   A. Pezzella, L. Panzella, A. Natangelo, M. Arzillo, A. Napolitano and M. D'Ischia, *J. Org. Chem.*, 2007, **72**, 9225–9230.

94   L. Capelli, P. Manini, A. Pezzella, A. Napolitano and M. D'Ischia, *J. Org. Chem.*, 2009, **74**, 7191–7194.

95   S. Meng and E. Kaxiras, *Biophys. J.*, 2008, **94**, 2095–2105.

96   D. R. Dreyer, D. J. Miller, B. D. Freeman, D. R. Paul and C. W. Bielawski, *Langmuir*, 2012, **28**, 6428–6435.

97   Y. Li, J. Liu, Y. Wang, H. W. Chan, L. Wang and W. Chan, *Anal. Chem.*, 2015, **87**, 7958–7963.

98   W. Jarzeba, G. C. Walker, A. E. Johnson, M. A. Kahlow and P. F. Barbara, *J. Phys. Chem.*, 1988, **92**, 7039–7041.

99   S. Vajda, R. Jimenez, S. J. Rosenthal, V. Fidler, G. R. Fleming and E. W. Castner, *J. Chem. Soc. Faraday Trans.*, 1995, **91**, 867.

100   S. Park and M. D. Fayer, *Proc. Natl. Acad. Sci.*, 2007, **104**, 16731–16738.

101   R. Jimenez, G. R. Fleming, P. V. Kumar and M. Maroncelli, *Nature*, 1994, **369**, 471–473.

1

Introduction

Heterocyclic compounds are ubiquitous molecules constituting almost half of the all known organic molecules. Organic molecules containing all carbon atoms in the ring, for example, benzene, are known as carbocyclic compounds. If at least one atom in the ring is not carbon, then the compound is a heterocyclic one. Amongst the two types of heterocyclic compounds, *viz.*, *aliphatic* and *aromatic*, the latter one is of particular interest, because of its wide presence in natural and synthetic systems. Among these, the most common ones are nitrogen, sulfur and oxygen containing aromatic compounds, that generally follow Hückel's 4n + 2 π electrons rule of aromaticity[1–3]. Hence, these compounds are known as heteroaromatic compounds. These nitrogen and sulfur-containing heterocycles are essential to developing antibacterial, antiviral and antifungal drugs. Large numbers of heterocyclic compounds that play crucial roles in the metabolism of living cells primarily include five of six-membered rings having one to four heteroatoms.

Unarguably, the most important classes of natural heterocycles are nitrogen containing pyrimidines and purines that are structural cores of nucleic acids,[4] and indole and imidazole groups which are building blocks of natural amino acids.[5] Pyrimidine is a six-membered ring, containing two nitrogen atoms and purine is made from a fusion of pyrimidine and another five-membered heteroring with two nitrogen atoms known as imidazole. (Fig. 1.1) Nucleobases that are derivatives of purines and pyrimidines are the structural components of our genetic information carrier deoxyribonucleic acid (DNA) and Ribonucleic acid (RNA). Imidazole ring is the core of natural amino acid histidine, neurotransmitter histamine and of many important drugs, such as antifungal agent metronidazole. Two fundamental pigments that are essential for the existence of life on earth are chlorophyll and heme. Chlorophyll is a family of green pigments present in plants and cyanobacteria, which helps plants capturing solar energy, and heme, the pigment that is responsible for red color of blood, and is a cofactor of oxygen carrying hemeproteins. Both of these are derivatives of heteroaromatic porphyrin rings, which are made from five membered nitrogen containing pyrroles. (See Fig. 1.1)
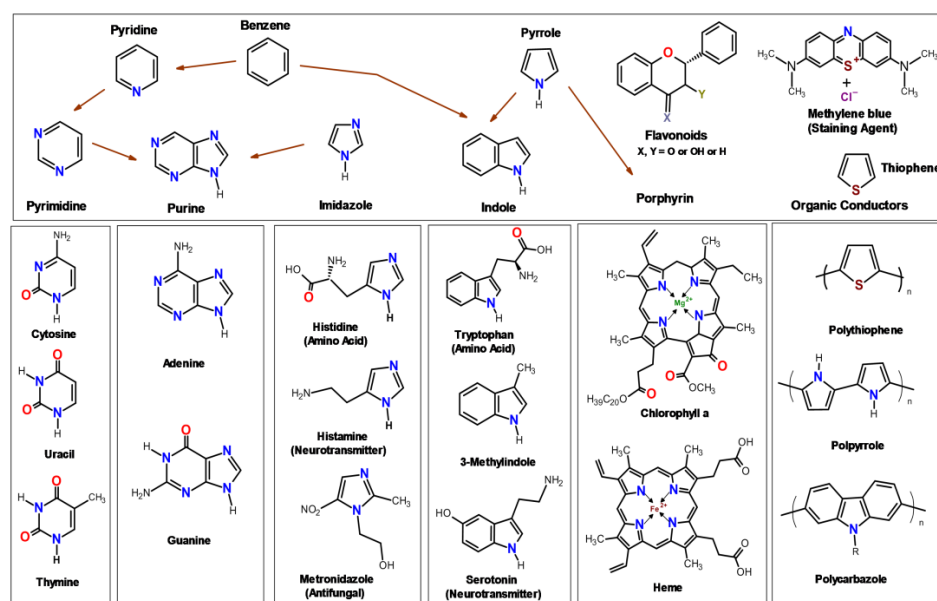
Fig. 1.1 Structure of a few naturally occurring and synthetically prepared biologically important heteroaromatic molecules.

Indole, another biologically important aromatic molecule is building unit of tryptophan, a structurally functionally important natural amino acid. Flavonoids, the most important plant pigment other than chlorophylls and an important ingredient of our everyday diet have single oxygen containing tetrahydropyran moiety.[6] (Fig. 1.1) Alkaloids, which are another important class of naturally occurring chemicals with large pharmacological applications, invariably have nitrogen, sulfur or oxygen containing heteroaromatic skeletons.[7] Conducting polymers having poly-pyrrole or poly-thiophene and many other heteroaromatic cores as structural motifs are widely used for industrial applications in optoelectronics and devices[8–11] in super capacitors,[12] designing novel biosensors[13,14] and in applications in biomedical engineering.[15] Most of the common fluorescent dyes used in tissue imaging and as photophysical probes are composed of one or more heterocycles,[16] e.g. methylene blues. (Fig. 1.1)

1.1 Importance of photophysics of heterocyclic compounds

Spectroscopic investigations of these types of heteroaromatic systems are necessary to be able to translate basic knowledge into making devices and also to understand many fundamental processes of life. For example, (i) live imaging of neurotransmitters, such as, serotonin[17] and dopamine[18] in brain tissue; (ii) probing packing interactions of proteins along folding and unfolding pathways using intrinsic amino acid probe, such as, tryptophan[19–21] and synthetically incorporated ones, such as cyanotryptophans,[22] (iii)

capturing local conformational changes and dynamics of base-pair and DNA in protein environment using location-sensitive fluorescent probes, such as 2-aminopurine (AP),[23–26] 8-vinyl adenosine,[27,28] and other designer base analogues,[29–32] (iv) understanding the origin of photostability of five natural DNA and RNA nucleobases through ultrafast photodynamical measurements on the natural and their modified forms,[33–37] (v) designing heterocyclic polymers for improved two-photon absorption (TPA) cross-section[38–40] to be used in bio-imaging and photodynamic therapies,[41–43] (vi) controlling and measuring photoinduced electronic properties of organic polymers that can be used in solar cell and as active materials in organic electronics.[44–47]

1.2 Electronic structure of heteroaromatics

At the fundamental level, optical properties of these heterocycles depend on their ground and excited state electronic structures. Comparison with the electronic structure of prototype carbocyclic molecules, benzene and naphthalene are inevitably drawn while discussing excited states of any aromatic system. Electronic excited states of these two highly symmetric aromatic systems were first studied by Platt using a linear combination of atomic orbital (LCAO) theory.[48] Platt's original nomenclature for first four $\pi\pi^*$ excited states of these two molecules involved highest occupied molecular orbital (HOMO), HOMO-1, lowest unoccupied molecular orbital (LUMO) and LUMO+1, and are designated as ^1L_b, ^1L_a, ^1B_b and ^1B_a. One single configuration, HOMO $\rightarrow$ LUMO and HOMO -1 $\rightarrow$ LUMO + 1 give rise ^1L_a and ^1B_a states respectively. On the other hand, ^1L_b and ^1B_b states are described by symmetric and antisymmetric configurational mixing of HOMO $\rightarrow$ LUMO + 1 and HOMO -1 $\rightarrow$ LUMO respectively. Use of this nomenclature in the case of heterocyclic molecules, such as indole, pyrimidines, purines and even their prototype molecule indene becomes meaningless due to their reduced symmetry. However, these symbols are useful for comparisons of equivalent electronic states across different heterocycles and those of benzene or naphthalene. Fig. 1.2 shows how the degeneracy of lowest energy π orbitals of benzene is lifted when heteroatoms are introduced (in pyrimidine and imidazole) and heteroatom containing rings are fused together (in purine and indole).
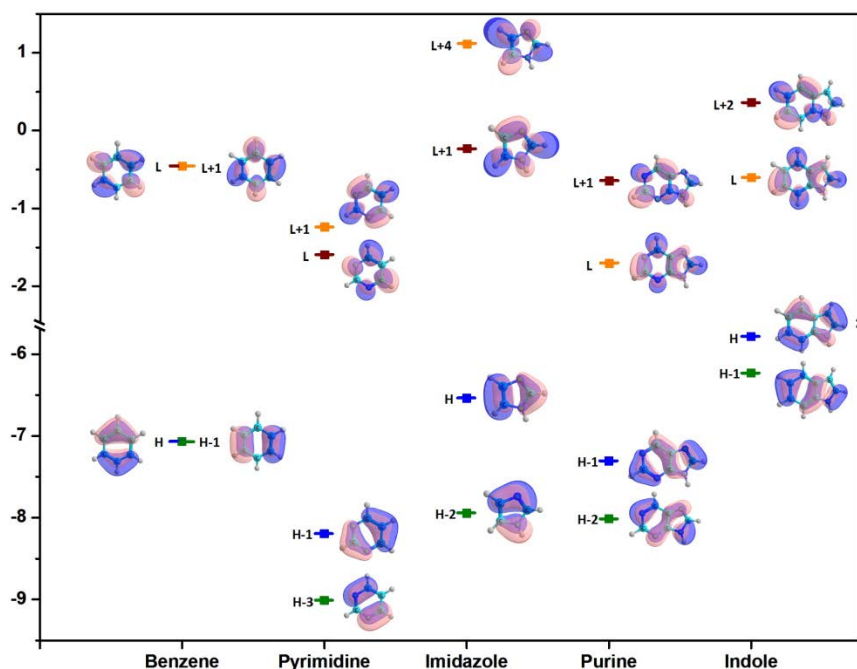
Fig. 1.2 Kohn-Sham frontier molecular orbitals (MO) of benzene, pyrimidine, imidazole, purine and indole. H and L stand for highest occupied and lowest unoccupied MO respectively. Benzene, which made from six sp^2 hybridized carbon atoms in the hexagonal arrangement is of D$_{6h}$ symmetry and has doubly degenerate highest occupied molecular orbital (HOMO or simply H) and lowest unoccupied molecular orbital (LUMO or simply L). Pyrimidine, made by substituting two carbons with two nitrogen also fulfills *aromatic sextet* rule and has six contributing π electrons to the aromatic ring. The introduction of hetero atoms breaks the symmetry of the ring and lifts the degeneracy of both HOMOs and LUMOs. Additionally, both of these four orbitals get stabilized in comparison with those in benzene. Same trend, but of different magnitudes is observed in all four nitrogen containing heteroaromatics. It is worth to note that highest occupied π orbital of purine energetically lies in between that of two component rings, pyrimidine and imidazole. Though purine and indole, two nine-membered rings have similar looking MOs, their relative ordering changes. All MOs are computed with density functional theoretical (DFT), B3LYP/6-311+G(2d,p) method in *vacuo* and are plotted with an isodensity value of 0.35 e/bohr^3.

The aromatic amino acids phenylalanine (Phe), tyrosine (Tyr), tryptophan (Trp), and histidine (His) consist of benzene, phenol, indole, and imidazole as aromatic cores respectively. They are responsible for near and far UV absorption characteristics of proteins in the region of 190-230 nm along with amide backbone and near 280 nm by tryptophan and tyrosine. Likewise, natural nucleobases; two purines adenine (Ade) and guanine (Gua) and three pyrimidines cytosine (Cyt), thymine (Thy) and uracil (Ura) are key UV absorbing chromophores in DNA and RNA in similar wavelength region as aromatic amino acids. *Ab initio* computations of excited states of benzene, phenol and imidazole,[49,50] indene[51] and indole[52] to understand photophysics of aromatic amino acids, and of purines[53,54] and pyrimidines[55,56] to unravel the mechanism of UV-induced

processes in DNA and RNA have been reported. All of these aromatic molecules have two complex band systems that are assigned to four $\pi \rightarrow \pi^*$ valence singlet excitations. The absorption band range lies between 240 and 280 nm (5.15 to 4.40 eV) contains two low-lying transitions, named ^1L_b and ^1L_a states. The other band system lies within wavelength ranging from 185 to 220 nm (6.7 to 5.4 eV) and is composed of two relatively strong transitions, ^1B_b and ^1B_a. Energetics and state configurations for electronic transitions in these aromatic compounds strongly depend on character and position of specific substitution on ring and deviates[57] from the equivalent states of benzene and naphthalene.[58]

1.3 Photophysics of nucleobases

Our genetic information carriers, DNA, and RNA are constructed using five building blocks consisting of two purines and three pyrimidine nucleobases (Fig. 1.1). All nucleic acid monomers absorb photons in blue edge of UV-B (260-350 nm) radiation in 260-280 nm range and in the red edge of UV-C (100-260 nm) radiation in 200-230 nm wavelength range. Typical average energies necessary for hemolytic cleavage of chemical bonds, such as C-C, C-H, C-O, O-H bonds in organic compounds lie within 80 to 115 kcal/mol.[59] UV photons at wavelengths within 200 to 280 nm contain enough energy (143 to 102 kcal/mol) to break these bonds in organic compounds. However, organic molecules like nucleobases do not undergo direct decomposition following absorption of UV radiation, but rather experience directional distortions in molecular structure. These distortions prepare the electronically excited molecule for photophysical events that follows in later time.

It is well established that these bases and their nucleotides exhibit quenched fluorescence in aqueous solution.[60–65] More recently, electronic spectroscopic techniques with sub-picosecond (ps) time resolution have directly detected ultrafast internal conversion (IC) through which singlet excited states ($\pi\pi^* \sim 260$ nm) of nucleic acid bases depopulate to ground state within hundreds of femtoseconds (fs).[66,67] This ultrafast IC has been established as an intrinsic mechanism, present in all nucleosides, nucleotides, nucleobase monomers in isolated gas phase,[33,68–70] aqueous solution,[34,66,67,71–74] and in base pairs.[75]

Computations of minimum energy paths (MEP) and *ab initio* photodynamical simulations on excited potential energy surfaces (PES) have characterized structural distortions that the excited base molecules undergo during ultrafast relaxation.[35,36,76–78] Decay of purines is dominated by single rate constants, and major ring-puckering motion of C_6 atom and by some extent at C_2 site are responsible for driving the system towards

conical intersections (CI) for state crossing.[79–83] On the other side, pyrimidine bases exhibit more complex deactivation pathways associated with more than one decay constant, due to the involvement of intermediate $n\pi^*$ states. As a common mechanism, all pyrimidines undergo out-of-plane distortions of C6 atom and a following twist around the C5C6 bond to hop to a lower energy surface.[70,84–86]
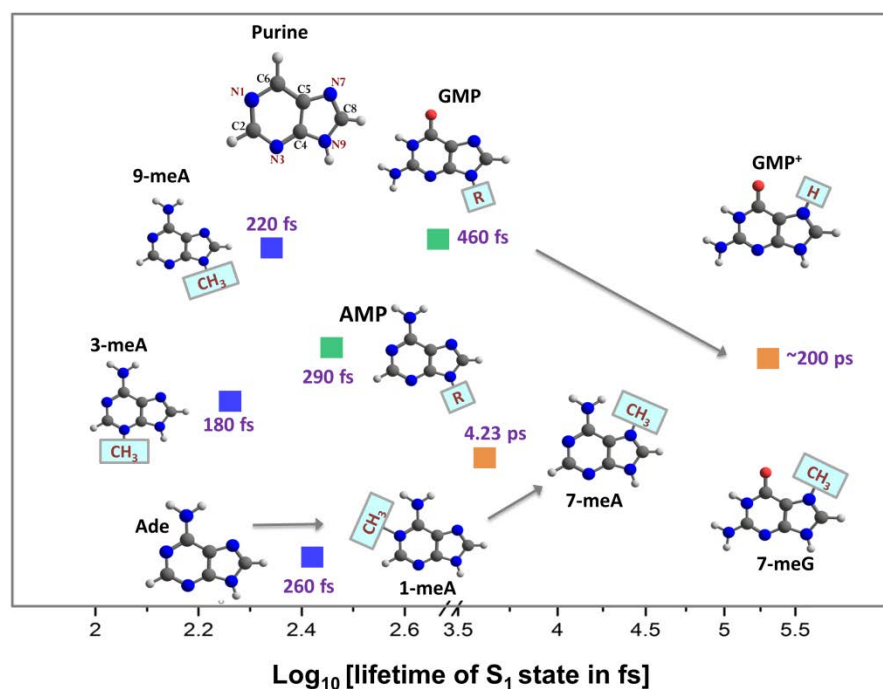
Fig. 1.3 Singlet excited state lifetimes of natural purines, Ade and Gua and their 3rd, 7th and 9th substituted forms. Ade and Gua, as well as their nucleotides, spend less than 500 fs on their first bright excited states before returning to ground state. Hydrogen or methyl substitution made at specific exocyclic sites changes lifetime of the modified bases. Methyl of hydrogen substitution at C7 position of purine ring increases lifetimes of 7-methyladenine (7-meA), 7-methylguanine (7-meG) and cation of guanosine monophosphate (GMP) by obstructing access of IC channel. On other hand, substitutions at N1, N3, and N9 position have little effect on depopulation rate of the excited state. The conventional numbering of ring atoms of purines is shown in the top left.

All natural purines, Ade, Gua, and pyrimidines Cyt, Thy and Ura, and their respective nucleotides decays to ground state in an ultrafast, sub-ps time scale (Fig. 1.3 and 1.4). Since natural nucleobases live for very short spans in the range of few tens of picoseconds (ps) in their singlet excited states, they do not get the chance to undergo photochemical transformations. This ultrafast IC to ground state decay results in the intrinsic photostability of these molecules. It is quite intuitive to think that ultrafast nonradiative decay following absorption of UV radiation might have been an evolutionary strategy, among many others, imposed by nature as a procedure to get rid of deleterious

electronic energy before harmful photoadducts can be formed. It has been suggested by several authors that apart from being able to participate in Watson–Crick base pairing, the photoresistive property could have been a key driver of their natural selection as building blocks of our genome.[87,88]

1.3.1 Why is photochemistry of nucleobases important?

The skin is the most environmentally exposed organ that absorbs a great amount of UV-A and UV-B radiation of sunlight. Despite the mentioned photoresistive properties of nucleic acid monomers, DNA of our skin, mainly in epidermal and basal layer continually gets photodamaged through direct absorption of UV light.[89] Formation of a variety of mutagenic lesions in skin DNA upon UV absorption has serious biological implications,[89–91] such as mutation and genetic instability, and subsequently development of different types of melanoma tumors[92–94] among other effects.[95,96] UV-A and UV-B can also be genotoxic, because of the activation of photosensitizing exogenous agents (drugs such as psoralens) that directly react with DNA and increase the risk of photocarcinogenesis.[97]
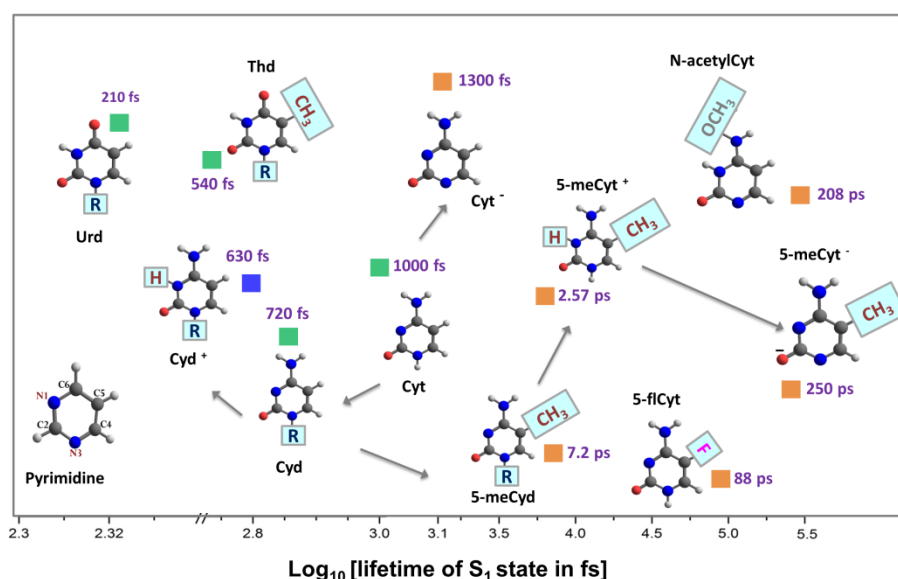
Fig. 1.4 Singlet excited state lifetimes of natural pyrimidines, Cyt, Thy and Ura and their substituted forms. Methyl or heavy Fluorine substitution at C_5 increases lifetime, and on the other side deoxyribose moiety at C_3 and hydrogen at C_1 site helps cytosine to decay faster. Methyl at 5th position on ring and substitution of one hydrogen of an amino moiety with bulky group causes two order of magnitude increase in lifetime. Like Cyt, other two natural nucleosides, uridine (Urd) and thymidine (Thd) also exhibit sub-ps decay.

Among deleterious photoinduced lesions, the most common one is the dimeric adduct between adjacent pyrimidines in single-stranded DNA. A few typical DNA photoadducts are shown in Fig. 1.5. Thy and Cyt are two pyrimidines that maximally suffer from UV-induced adduct formation such as cyclobutane pyrimidine dimer (CPD)[98] that forms via populating excited triplet state, cytosine dinucleotide (CpC) photohydrate and pyrimidine (6-4) pyrimidinone photodimer[99,100] and its Dewar valence isomers.[101] CPD and 6-4 photoproducts account for more than 95 % of the total photodamage of nucleic acids. Other rare DNA photoproducts, e.g. Thy-Ade photodimer[102–104] of adjacent ade and thy bases, and dimeric adenine photoadducts,[105,106] such as 8,8-adenine dehydrodimer[107] occur 1-10 % of the times in the CPD formation in DNA.

Ionizing radiation, such as gamma rays and UV-B light (260-350 nm) can produce a variety of radical and reactive oxygen species (ROS) in the living cell. Amongst these ROS, hydroxyl radical (OH$^\bullet$) is a major agent that oxidizes DNA bases[108] and specifically Gua to produce guanine radical cation (G$^{\bullet+}$).[109,110] Reactive G$^{\bullet+}$ leads to the formation of a variety of lesions such as 8-oxoguanine (8-oxoG) and oxazolone.[108] Formation of G$^{\bullet+}$ in DNA double strand also happens via populating a low-lying charge-transfer (CT) state upon UV irradiation.[111–113] Amongst OH$^\bullet$ induced photoadducts of Ade and Gua, 4,6-diamino-5-formamidopyrimidine (FapyAde) and 2,6-diamino-4-hydroxy-5-formamidopyrimidine (FapyGua) (Fig. 1.5 f) are major ones.[114,115]) Doetsch *et al*. have concluded that FapyAde and FapyGua are formed entirely by action of 254 nm UV radiation, and OH$^\bullet$ radical is not involved.[116] Radical cations of both, Ade and Gua lie in the pathway of forming these adducts. Whether these radical cations are formed via direct absorption of UV light is a live question in the field of DNA photodamage.
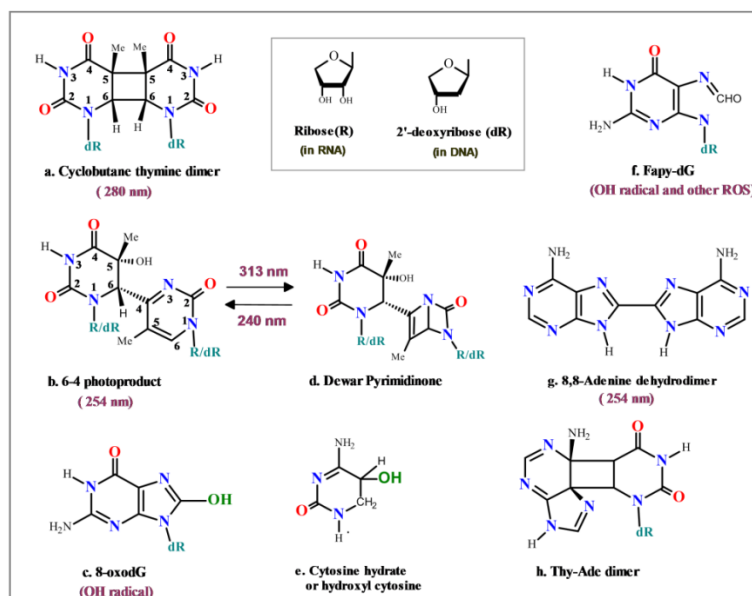
Fig. 1.5 Chemical structures of dimeric and monomeric photolesions in DNA upon UV irradiation

1.3.2 Modified nucleobases

There exist, however, a plethora of molecules that are modified versions of these natural bases, either already present in nature, such as, in viral DNA or having been synthesized in the laboratory.[117] Till date, four purines (Ade, Gua, hypoxanthine and xanthine) and one pyrimidine (Ura) have been detected in several meteorites.[118–121] Very often it has been argued that before natural selection of the modern genetic alphabet, there was a large pool of alternative molecules in the early evolutionary era.[122–125] Outcomes of synthetic experiments that simulate prebiotic environments[126–130] and the finding of traces of purine, 2,6-diaminopurine, and 6,8-diaminopurine, that are closely related to Ade and along with other hypoxanthine and xanthine in meteorites[131]; support this hypothesis. Additionally, in the pre-RNA world, apart from stability against hydrolytic deamination and cleavage of N-glycosidic bond and other factors, UV photostability is expected to be a key factor, since the influence of UV radiation of solar spectrum was several folds higher than that present today (Fig. 1.6). Consistent with this proposed hypothesis, a diverse set of modified nucleobases other than hypoxanthine are found to show significantly long (tens of ps to tens of ns) excited state lifetimes than those (sub-ps) of natural bases.[34]
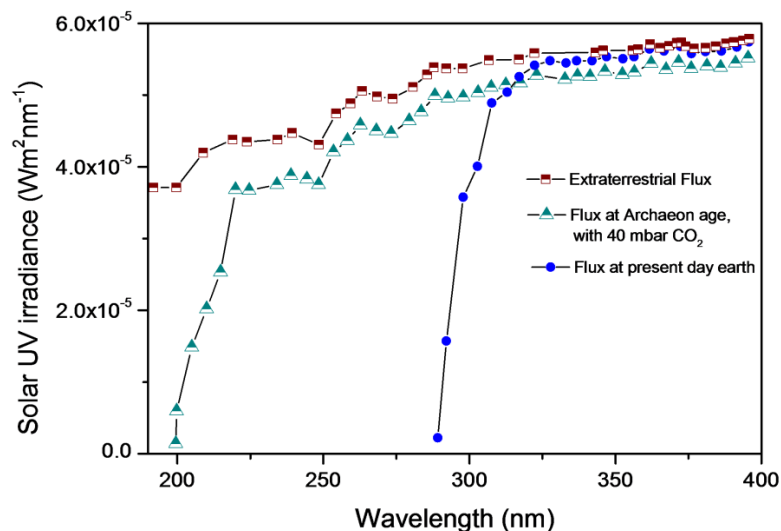
Fig. 1.6 UV irradiance of solar flux in reaching earth's surface in the prebiotic and present era. In prebiotic era due to the absence of stratospheric ozone layer, a very high flux of solar UV irradiation used to reach surface of the earth. These high energy photons are thought of key driver of prebiotic chemistry, and also believed to have been a major selection pressure behind the evolution of the photostable genetic molecules. In Archaeon era, the worst case scenario was considered by taking a lower limit of the partial pressure of CO_2 which is a major scatterers of solar UV radiation in the later stage of evolution. This figure is adapted with permission from Ref 146. Copyright (2001) Springer.

Many of these modified bases which could substitute the natural nucleobases in the nucleic acids are fluorescent, unlike natural bases. They serve as site-specific molecular beacon of DNA structure,[132] interactions in molecular recognition, (such as, DNA-protein), and dynamic processes, such as, charge-transfer dynamics in DNA,[133,134] base flipping,[23] and as selective inhibitors of specific enzymes.[135–137] These analogous molecules are designed to have 'better' spectral properties, such as, (i) high fluorescence quantum yield (Φ_F) and mono-exponential decay, (ii) having excitation wavelength significantly red-shifted from those of natural nucleobases; and structural qualities, e.g. to retain minimal perturbation of double helical structure of DNA after incorporation. While experimentalists synthesize a library of modified bases and characterize their structural and photophysical properties,[117] theoretical scientists engage in explaining and predicting light-induced processes in DNA/RNA containing these bases in comparison with natural counterparts.[138]

1.3.3 Photophysics of nucleobases

Substitutions on different exocyclic positions perturb electronic structure, and in turn, modify excited state properties of purines and pyrimidines.[88,139,140] It has been shown that it's the amino or carbonyl substitutions at C2 or C6 sites, and not the purine motif itself, which are responsible for ultrafast deactivation of UV-excited bases.[141] Substitution at the 7th position in purines and at the 5th position in pyrimidines drastically increases lifetimes of natural bases by two to three orders of magnitude, whereas N1, N3, and N9 sites are found to be relatively insensitive to substitution induced changes of lifetimes.[34] (Fig. 1.3 and 1.4)

Excited state dynamics studies have demonstrated that ring puckering modes involving N1C2H moiety and at C6 assist the fast deactivation of L_a state to ground state in Ade.[36,80] 2-aminopurine (AP), a structural isomer of Ade in which the amino group is moved from C6 to C2 site, shows strong fluorescence ($\Phi_F = 0.68$).[60,142] Unlike Ade which stays less than 200 fs, AP rests much longer (10 ns) on $^1\pi\pi^*$ singlet state.[132,133,143] Serrano-Andrés *et al.* have shown that amino moiety in AP obstructs puckering motion at the C2 site, and subsequently blocks access to a fast deactivation channel.[144] Recently, photodynamical measurements on substituted purines have established that out-of-plane motion of C2 is absolutely essential for ultrafast intersystem crossing from L_a state to $^1n\pi^*$ state that further relaxes to the ground state (S_0).[141] Therefore, systematic photodynamical studies of modified bases represent an opportunity to understand responsible structural factors governing the photostability of our genetic alphabet.

1.3.3 Relevance of photophysics of nucleobases in the deep UV

The majority of photophysical investigations have dealt with the aftermath of photoexcitation to the lowest energy, $\pi\pi^*$ electronic states (^1L_a and ^1L_b) within 260 to 280 nm of wavelengths in purines and pyrimidines. Alternatively, the understanding of photoinduced phenomena that follow absorption of red edge of UV-C spectrum in 200-240 nm wavelength range by nucleobases is limited. All nucleobases have electronic transitions (^1B_a and ^1B_b) that absorb photons in the mentioned range at the red edge of UV-C more efficiently than those lying near 260 nm. Understanding the response of nucleobases in this wavelength range is important because UV flux of solar radiation in 200-240 nm range of UV-C spectrum was several folds higher during the prebiotic era, than what is present today.[145–147] (Fig. 1.6) To understand overall UV photostability, effects of UV-C light on excited state structure and resulting photophysics have to be integrated with photodynamical results available on low energetic excited states.

In the modern era, as the stratospheric ozone layer is experiencing continuous depletion due to increase in many pollutants, the amount of UV radiation of the solar spectrum reaching the earth's surface is gradually increasing.[148,149] In this scenario, like in the prebiotic era, characterization of the response of genomic components upon mutagenic UV radiation is of relevance from the present and future perspectives too.

1.3.4 Measuring photodynamics in UV-C

To understand the effect of UV-C radiation on nucleobases, experimental measurements on these strong electronic states of $\pi\pi^*$ characters in 200-240 nm are necessary. Ultrafast electronic spectroscopic methods such as fs-transient absorption (TA) and fs-fluorescence upconversion (fs-FU) spectroscopies, and vibrational techniques, such as psUV-pump mid-IR probe have been successfully applied in investigating excited state dynamics of the nucleobases. All of these studies have probed photodynamic on lowest energy (~ 260 nm) excited states of DNA and RNA bases. However, these methods are not readily applicable to study high energetic states below 230 nm owing to intrinsic and technical limitations.

Resonance Raman (RR) spectroscopy in which Raman excitation lies within electronic absorption of the molecule, is successfully applied to characterize the manifold of electronic states of nucleobases with UV excitations.[150–154] In the RR process, the wavenumbers of bands of a molecule report structure of the S_0 state and their intensities encode information about the resonant electronic state. Observed intensity of a RR band is proportional to the square of the distortion along each FC active vibrational normal mode.

From experimentally measured RR cross-section, the structural distortions in the excited state with respect to that in the ground state molecular structure can be determined. Resonance Raman (RR) spectroscopy is the only experimental technique that can determine vibrational mode-specific instantaneous structural distortions of a molecule, subsequent to photoexcitation to an electronic state.[155–157]

Structural distortions, measured along each of the vibrational normal coordinates, are expressed as dimensionless displacements (Δ). Δs can be extracted from the analysis of excitation wavelength dependence of intensities of RR active vibrational modes, i.e. Raman excitation profiles (REP). In fact, RR intensity analyses have been successfully applied for deriving structural distortions that all natural and several modified bases undergo upon photoexcitation within low energy L_a and L_b states.[158–166] Thus derived structural distortions complement and deepen our understanding of electronic excited state PESs, which are also investigated by measuring singlet state lifetimes and computations of excited state surfaces. There are no previous experimental or theoretical investigations describing photodynamics of any nucleobase system within B_a and B_b excited states as a result of absorption of UV-C radiation.

In Chapter 3, I have investigated a series of purines using UVRR spectroscopy and quantum chemical computations to determine how exocyclic substitutions inflict structural distortions and vibrational and electronic reorganizations. With the help of multiple resonant laser excitations to different singlet excited states, Frank-Condon active modes that are expected to drive early time excited state dynamics of these bases upon photoexcitation are identified. In the following Chapters (Chapter 4, Chapter 5 and Chapter 6), I have used RR intensity analysis in conjunction with time-dependent wave packet dynamics formalism, and have determined initial excited state structural dynamics of two natural purines, adenine and guanosine monophosphate (GMP) and one modified guanine, *viz.*, 6-chloroguanine (6-ClG) in their B_b electronic state within the 210 to 230 nm wavelength range.

1.4 Structure and dynamics of the biopigment melanin

Indole is an aromatic heterocyclic compound which has a six-membered benzene ring fused to a five-membered nitrogen-containing pyrrole ring (Fig. 1.1). The indole skeleton is the primary building block of a handful of biologically important molecules[167] including (i) Tryptophan (Trp or W) which is one of the standard amino acids occurring in protein structure (Fig. 1.1); (ii) Serotonin (5-hydroxytryptamine, or 5-HT) is a monoamine neurotransmitter and its receptor agonist, tryptamine; (iii) Skatole (3-methylindole) which is found in many essential oils and is used as fragrance in perfumes, and serves as a model

of Trp;(Fig. 1.1) (iv) Melanin, the most abundant natural pigment that performs a variety of functions including very diverse skin color phenotypes.[168–170] Melanin consists of cross-linked polymers of two indole derivatives, *viz.* 5,6-dihydroxyindole (DHI) and 5,6-dihydroxyindole-2-carboxylic acid (DHICA). (Fig. 1.7)

1.4.1 Melanins: A General Introduction

Melanins are ubiquitous dark pigments found throughout the biosphere. Melanin, originally derived from Greek *melanos*, meaning 'dark', is predominantly made of heavily cross-linked organic polymers that have indole as the basic building block. Three major types of melanins, eumelanin, pheomelanin, and neuromelanin are found in skin, hair, eyes and nervous system of animals. Eumelanin and pheomelanin are black/brown and reddish/yellowish pigments that are responsible for the natural coloration of the skin, hair and eyes in the animal kingdom.[168] Eumelanin, being the primary pigment in human and all mammals, is most extensively studied, and is known to be produced via aggregation of oxidative products of DHI and DHICA. *Sepia* melanin, the natural pigment in the squid ink sack is the most studied model of eumelanin.[171–173] Pheomelanin, which is a sulfur-containing variant of melanin, is the polymerized form of benzothiazine derivatives and is responsible for the red hair of human and chicken feathers.[168,174] In other organisms such as fungus, insects (except spiders) or cephalopods, such as squid, melanin has important roles as a pigment. It is worthy to mention here that pheomelanin in reddish-brown hair is always found to be present with eumelanin.[175,176] Biopigments that are produced within neurons in different brain parts, such as, substantia nigra by the oxidation of dopamine and other catecholamine precursors are collectively known as neuromelanin.[177] Neuromelanin is also found as copolymers of multiple precursor units, such as DHI, dopamine, and cysteinyldopa.[178–180] Thus, biogenesis of melanin is a very common and omnipresent natural biochemical reaction in the living world.

1.4.2 Melanin synthesizing cells and organelles in skin

Melanogenesis is the process of producing and sequestering melanin inside membrane-bound organelles, melanosomes. These are located in specialized cells known as melanocytes. Melanocytes primarily reside in the dermal/epidermal border (basal layer between the stratum spinosum and the dermis) of human skin. They are also found in hair follicles, retinal pigment epithelium (RPE) of eyes, and in the substantia nigra region of the brain. Melanosomes, vesicle-like organelles are derived from Golgi or early endosome through the cellular surface and they encapsulate the produced melanin. Highly mobile melanosomes, controlled by hormonal signals, get transferred to other cell types such as keratinocytes in *stratum spinosum* (in the skin) or brain cells through dendritic structures

of melanocytes. Different racial skin colors are primarily determined by the difference in the number, size, and the distribution of melanosomes in keratinocytes. Production of melanin inside melanosomes depends on the genetic regulation of the enzyme, tyrosinase that catalyzes the first step of melanin synthesis. However, in the real scenario, the phenotype of skin is a complex phenomenon and is regulated via secretion of specific factors that control differentiation, proliferation and dendricity of fibroblasts and keratinocytes and also melanogenesis in melanocytes.

1.4.3 Biochemical pathway of *eu* and *pheo*-melanogenesis

Melanogenesis, the pathway of producing *eu-* and *pheo-* melanins inside melanosome are depicted in Fig. 1.7, which is reviewed in detail by Hearing VJ.[181] The key enzyme that is involved in the production of melanins in melanocytes is tyrosinase. Tyrosinases are di-copper containing oxidases that have been described in mammals and lower animals, and also in plants and fungi.[182–186] Biogenesis pathway of melanin was first elucidated by Raper[187–190] and Mason,[191] and was later modified,[192,193] and is documented in several reviews.[193–203] Tyrosinase catalyzes the first step of melanin synthesis by oxidizing a monophenol (monophenolase activity), such as L-tyrosine (would be called tyrosine hereafter) to an ortho-diphenol, 3,4-dihydroxyphelylalanine (dopa). Subsequently, tyrosinase also catalytically oxidizes (diphenolase activity) dopa which is an ortho-diphenol to its ortho-quinone, i.e. dopaquinone (DQ).[192,203–206] Though both the catalytic activities have broad substrate specificities, tyrosinase has a higher affinity for the L-isomers of the substrates than for the corresponding D-isomers.

The chemically reactive DQ undergoes spontaneous intramolecular cyclization to form cyclodopa, which then rapidly produces dopachrome (DC) by a redox reaction with DQ.[207] DC is spontaneously decomposed by decarboxylation at neutral pH to form DHI and DHICA in a 70:1 ratio.[208] However, in the presence of another enzyme, dopachrome tautomerase (DCT) (also known as Tyrosinase-related protein-2 or TYRP2), DC undergoes tautomerization and exclusively produces DHICA.[209] Both DHI and DHICA oxidize and form respective quinones that further polymerize to produce short length (6-8 units) oligomers. Thus formed oligomers further polymerize and aggregate to form a eumelanin macromolecular assembly. While DHI gets oxidized through redox exchange with DQ[210], oxidation of DHICA happens in the presence of either tyrosinase in humans[211] or tyrosinase-related protein-1 (TYRP1) in mice.[212,213] Eumelanogenesis in the presence of tyrosinase was first observed and the pathway was proposed by Raper[187–189] and later refined by Mason,[191] and thus is widely referred as the Rapar-Mason pathway.
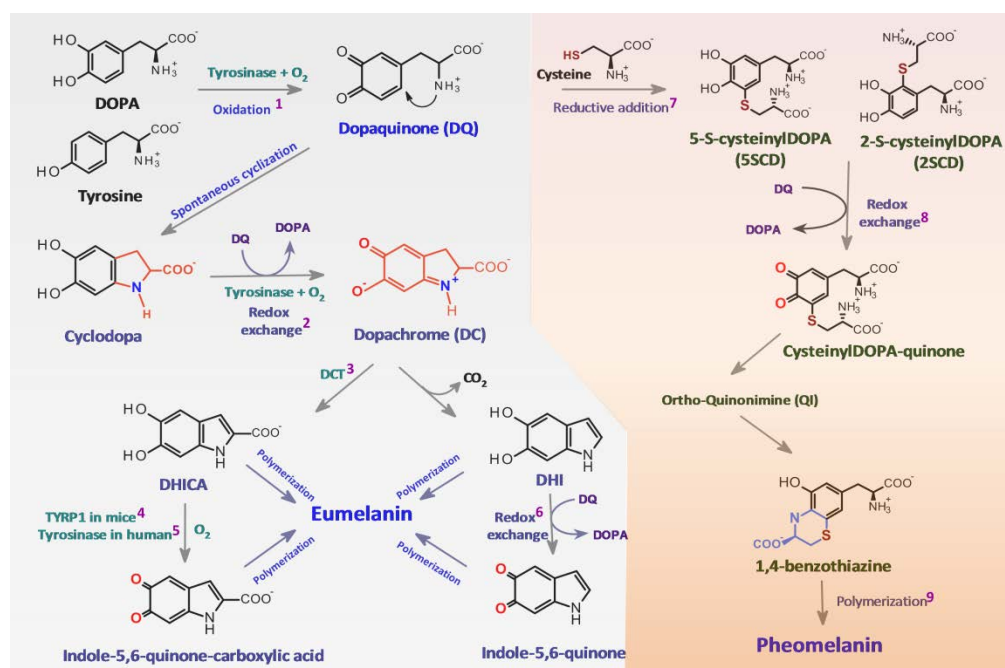
Fig. 1.7. Biosynthetic pathway of eumelanin and pheomelanin production. Dopa and tyrosinase, both gets oxidized in the presence of enzyme tyrosinase to form L-Dopaquinone (DQ) which readily undergoes spontaneous cyclization and forms orange colored intermediate L-Dopachrome (DC). 5,6-dihydroxyindole (DHI) is subsequently produced from DC via spontaneous rearrangement and decarboxylation. Alternatively, in the presence of another enzyme in melanosome, known as dopachrome tautomerase (DCT or TYRP2) 5,6-dihrdoxyindole-2-carboxylic acid (DHICA) is formed. Both, DHI and DHICA undergo oxidative polymerization to form early pigment, known as melanochrome (MC). Melanin is subsequently formed by further polymerization and aggregation of small length polymers. Pheomelanin formation commences by the reductive addition of sulfur containing amino acid cysteine to DQ to form cysteinylDOPA (CD). CD subsequently produce cysteinylDOPA-quinone and finally 1,4-benzothiazine as basic building block of pheomelanin. Abbreviations. DCT: dopachrome tautomerase or Tyrosinase-related protein-2 (TYRP2); TYRP1: Tyrosinase-related protein-1 (TYRP1) or DHICA oxidase. [1]Ref 187-191; [2]Ref 207; [3]Ref 209; [4]Ref 212,213; [5]Ref 211; [6]Ref 210; [7]Ref 194; [8]Ref 215-217; [9]Ref 218, 219.

Pheomelanin production (Fig. 1.7) initiates through the reductive addition of sulfur containing cysteine to DQ, and subsequent production of cysteinyldopa (CD).[214] CD undergoes redox exchange with DQ to produce CD-quinones.[215–217] Later, CD-quinone cyclizes to form ortho-quinonimine (QI) which is subsequently rearranged to form 1,4-benzothiazine intermediates.[218,219] These benzothiazine derivatives polymerize and produce pheomelanin.[194,216,220–222] Other than the enzyme tyrosinase, there are a number of factors such as pH, and the level of cysteine in melanosomes, presence of other proteins; that control diversity of human hair and mouse coat color pigmentation.[223,224] In human skin, complex interactions between melanocytes and surrounding keratinocytes

control *eu-/pheo*-melanin ratio.[225] In this thesis I have focused on eumelanin and the discussion on other types of melanins is limited.

1.4.4 Intermediates *en route* eumelanin

Since the original work of Raper, it had been generally believed that dopa is formed first from tyrosine on the way to DQ. However, *ortho*-quinones such as DQ were shown to be formed directly from *N*-substituted dihydric phenolic substrates in the first step of melanogenesis by Cooksey *et al.*[192] *Rate of free radical cyclization of dopa to DQ and subsequent formation of DC has been first investigated using pulse radiolysis initiated one electron oxidation.*[226,227] Further, pulse radiolysis studies have determined rates of early events in the initial phase of dopa oxidation,[210,228–231] and Ito and Wakamatsu have integrated them.[200] Though the first step of intramolecular cyclization of DQ to form cyclodopa is fairly slow,[229] formation of DC proceeds through a very fast redox reaction, with $k = 5.3 \times 10^6$ M^{-1} s^{-1}.[231] DC is an orange colored species and is generally monitored within 480-500 nm for spectrophotometric assays for determining activity and substrate specificity of tyrosinase.[191,205]

Absorption maxima (λ_{max}) of different species in the melanization pathways are depicted in Table 1.1. It is quite clear that multiple intermediates that are formed and decay dynamically on a fast time scale absorb in the same wavelength range. For example, both dopa-quinone (DQ), and quinones of DHI and DHICA absorb at ~400 nm which itself lies within the absorption band of DC. Again, the formation of melanin is generally observed at 540 nm[232–235] but cyclic ortho-quinoneimine also absorbs at the same wavelength. Moreover, absorption band (λ_{max}=480 nm) of DC, the preceding intermediate of the pigment, well extends beyond 550 nm. Thus, obtained rates of interconversions between consecutively formed species are always convoluted with multiple components.

Vibrational spectroscopies that probe the strength of each chemical bond in a molecule present an attractive alternative to detect several intermediates of similar structures. However, application of Raman and IR methods to study melanin is limited[236–240] due to its optical opaqueness and strong fluorescent background with visible to IR excitations. **I have employed resonance Raman (RR) spectroscopy with UV excitation (260 nm) to (i) get rid of the fluorescence and to (ii) probe the structural changes occurring on indolic building blocks of melanin in chapter 7. Visible excitation of 488 nm was used specifically to probe the orange color intermediate, DC produced during enzymatic oxidation of dopa. UVRR spectroscopy is an efficient tool to study the structure of biomolecules with aromatic cores, such as tryptophan, histidine and tyrosine in proteins,[241–243] nucleobases in DNA,[150,152,154] and porphyrins in heme**

proteins.[244–246] **Distinctive RR signatures of dopa, DC and melanochrome (MC) – the early pigment are established.** An integrated kinetic scheme was applied to obtain rates of formation and decay of different reactants of melanization reaction.

1.4.5 Different precursors of melanin

DHI and DHICA are the natural precursors that are produced from tyrosine and dopa in melanosome during enzymatic biosynthesis of both types of melanins (Fig. 1.7). Since pheomelanin and neuromelanin are always a mixture or a copolymer of more than one precursor, structural studies of these systems is difficult. Alternatively, there are several commercially available melanin precursors that include dopa, dopamine and other catecholamines, DHI and benzothiazine derivatives.[222,247]

Dopa and dopamine undergo self-oxidation in Tris-HCl buffer and produce an aggregated dark pigment that is structurally related to natural eumelanin and is regularly used as a synthetic model of the natural pigment.[248–254] In the absence of enzymes other than tyrosinase, both dopa and tyrosine undergo oxidation and are expected to produce melanin composed of primarily DHI units. In this thesis, I have used two types of melanins made from dopa, (i) through self-oxidation (will be called autoxidized dopa-melanin) and (ii) through oxidation with the help of mushroom tyrosinase (will be referred as dopa-melanin). In melanin research, it has been advised to mention the name of the precursor before the term 'melanin' to avoid unambiguity.[255]

1.4.6 Molecular markers of melanins

Unlike essential biopolymers of life – proteins, nucleic acids, carbohydrates and lipids, the characterization techniques to determine relative ratios of different precursors (monomer) present in melanins are not standardized yet.[255–257] One of the key methods of analyzing melanin constituents is through chemical degradation, for example, via hot oxidation with H_2O_2 or other agents in alkaline media. The key molecular markers of eumelanin and pheomelanin are established by Ito and coworkers as pyrrole-2,3,5-tricarboxylic acid (PTCA), pyrrole-2,3-dicarboxylic acid (PDCA) and 4-Amino-3-hydroxyphenylalanine (4-AHP).[258–261]These products are also obtained in oxidative degradation of commercial precursors DHI and DHICA, and the latter are accepted as basic structural building blocks of eumelanin, as originally proposed by Raper.[190]

1.4.7 Biophysical properties of melanins

1.4.7.1 Broad and featureless optical absorption

The most intriguing physical property that is believed to be a unique design to act as natural sunscreen is monotonic and featureless optical absorption of melanin solution.[262,263]Typically, the solution state absorption spectrum of synthetic dopa-melanin retains general characteristics in the case of solid state eumelanin (pellets and thin film) and aggregated state but often broadens and extends the spectra into near infrared (IR) due to pronounced Mie scattering. Disaggregated eumelanin thin films[264] and synthesized by electrospray deposition[265] show similar absorption profiles. Melanin produced from DHI, DHICA or other precursors exhibits a broad peak at ~300 nm that flattens with time as polymerization/aggregation proceeds,[266] and an intense peak at less than 250 nm that arises from residual precursor moieties. Reproduction of this dependence of absorption spectra upon wavelength has been a key determinant for constructing structural models of melanin.

1.4.7.2 Melanin has very low radiative quantum yield

Though melanin is able to absorb a maximum of encountered photons, it still has a very low radiation quantum yield ~ 10^{-4}.[267–269]. This low fluorescence quantum yield is indicative of the presence of an efficient IC mechanism in photoexcited melanin, similar to those present in natural nucleobases. Our DNA monomer components also show very low ~ (10^{-4} – 10^{-5}) fluorescence quantum yields[61,65] as a consequence of ultrashort (sub-ps) lifetimes of singlet excited states. Consistent with this, Corani *et al.* have demonstrated that DHICA derived eumelanin oligomers have sub-ps excited state decay.[270] This ultrafast relaxation has been proposed to be the collective result of intra- and inter-unit excited state proton transfer (ESPT). Photostability of DHICA derived polymers that are formed via single C-C interunit bond has important implications on the structural model of melanin, discussed in the 'Protomolecular structure of eumelanin' section. Unlike nucleobases, since the fundamental structural assembly of melanin is not unambiguously established, application of quantum chemical calculations to uncover ultrafast relaxation mechanisms in photoexcited melanin is limited.[271]

1.4.7.3 Melanin is a protonic and electronic hybrid-conductor

Eumelanin has hydration-dependent and thermally activated conductivity which has been conventionally explained within the amorphous semiconductor model for almost 50 years.[272–280] Meredith and coworkers have conclusively shown that thin film or pellets of eumelanin act as a hybrid conductor, *i.e.,* its overall conductivity derives from both

protonic and ionic current.[281,282] These authors have explicitly demonstrated that if careful equilibrium measurement is performed, then hydration dependent conductivity of melanin cannot be explained by the amorphous semiconductor model, and the current mainly derives from protons as the primary charge carrier.[282,283] Conducting protons which are generated as a result of water induced titration of comproportionation equilibrium between fully reduced and fully oxidized melanin units, flow through a hydrogen bonded water matrix.[281,284] The hybrid protonic-electronic conductivity which is dominated by ionic character is further supported through current-voltage measurements using proton-transparent electrodes.[285]

Melanin also has a hydration dependent photoconductivity which increases under UV or white light illumination.[282,286] Mostert *et al* have explained this photocurrent as a result of photoinduced oxidation of hydroxyquinone (DHI) to semiquinone (SQ) thus generating protons in the process.[281] These conductive properties are currently being harnessed and tailored to create nature inspired ionic circuitry for application in bio-compatible optoelectronic devices.[254,264,286–293] These results on hybrid conductivity have decisively disproved the amorphous semiconductor model of melanin.

1.4.7.4 Melanin scavenges free radicals

Bulk melanin contains a number of unpaired electron centers, giving a strong electron paramagnetic resonance (EPR) signal, which is one of the fundamental properties of the biopolymer that enables it to act as a free radical scavenger.[294–296] The characters and amount of free radicals present in melanin is a function of several factors including water content, pH, irradiation with UV or visible light, diamagnetic multivalent metal ions etc. In Eumelanin, the basic units are DHI, DHICA, and their fully oxidized indolequinones (IQ) and half-reduced semiquinones (SQ). Instead, their intrinsic EPR characteristic, melanins from different source are distinguished based on the response of their EPR signal to externally applied agents.[294] All of the mentioned extrinsic agents are capable of modifying the comproportionation equilibrium between DHI/DHICA and IQ, and thus alter the concentration of oxygen-centered SQ radicals. Synthetically made DHICA melanin has been found to be a better free radical scavenger than DHI melanin, attributed to a unique conformationally interrupted π-π stacking network.[297]

Mostert *et al*. have identified a carbon-centered radical other than most significant SQ radicals in solid synthetic eumelanin.[298,299] With the addition of water, while the concentration of SQ radicals increases, the carbon-centered radical is found to be destroyed. This hydration dependent destruction of carbon-centered radicals is explained by a newly proposed destacking model of melanin. The authors have proposed that in

increasing water content, the intermolecular π-π stacking arrangement of melanin protomolecules can be disrupted by the extra charge carried by SQ radicals. This procedure would expose the carbon-centered radicals to aqueous environment to be destroyed. These free radicals are implicated in the solid state charge transport in melanin. Though a number of experimental reports using EPR as the characterization tool exist, consensus on the actual structures of paramagnetic centers in melanin radicals has not been reached due to relatively less computational efforts.[300]

1.4.8 Protomolecular structure of eumelanin

Unlike the majority of biopigments, the melanin class of polymers cannot be described with a single well-defined structural model. Despite tremendous efforts from both experimentalists and theoretical scientists, we do not have a general consensus as to what the actual structures of fundamental building units in terms of inter-unit connectivity of melanin are.[201,255,301–304] The key difficulty in structural characterization of eumelanin is its insolubility in almost all known solvents over a wide range of pH and the inability to form crystals. Because of these two reasons its structure could not be deciphered at the molecular level by two classical physical methods, X-ray diffraction and nuclear magnetic resonance (NMR), both of which are very successful in the case of other macromolecules.
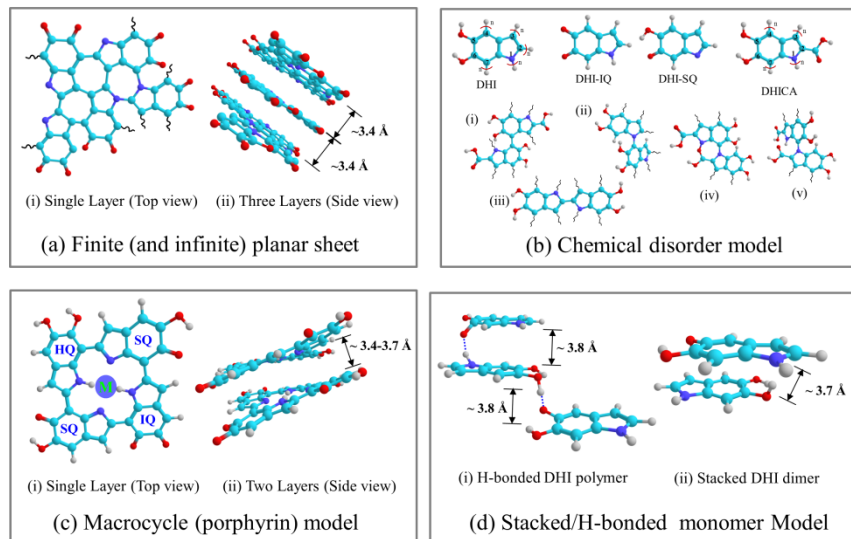
Fig. 1.8 Existing structural models of eumelanin protomolecule. (a) Finite and infinite planar sheet; (b) Chemical disorder model; (c) Macrocycle model and (d) Stacked and H-bonded monomer model. M: metal ions; HQ: hydroquinone or DHI, SQ: semiquinone which is half reduced form of DHI, IQ: indolequinone that is fully oxidized DHI. For a description of each model see text.

In 90s, based on the first x-ray crystallographic data, the basic structural architecture of eumelanin was put forward.[305–307]. According to this model, four-to-eight DHI units are covalently connected at random sites to produce planar sheet-like structures with ~ 15 Å lateral dimensions. Four to five of these planar sheets stack on top of each other along the z direction with a graphite-like interlayer spacing of ~3.4 Å. Later, high resolution TEM images[308] also supported this model, now known as the randomly linked **stacked oligomer model**. (Fig. 1.8 a) The presence of a strong peak at 1.74 Å^{-1} in structure factor data of eumelanin explained stacking planar sheets with a 3.4 Å interlayer distance.

Since at a fundamental level, cross-linking of basic building blocks (DHI and DHICA) can occur at a number of sites, melanin structure is prone to suffer from a degree of structural disorder that ultimately translates into many of its unique physical and chemical properties. To explain the broad envelope of structureless UV/Vis absorption of melanin, Meredith and coworkers argued that melanin is made of an aggregated assembly of a population of chromophoric units, each having a slightly different HOMO-LUMO gap, and thus shifted absorption maxima.[263,266,309] This simple model that is based on inherent chemical heterogeneity at molecular linkage level is known as the **chemical disorder model**. Along with broad absorption, excitation dependent shifts of the emission spectrum also suggest the possible presence of an ensemble of multiple chromophores that absorb at different wavelengths.

Using solution state NMR spectroscopy, d'Ischia and coworkers first experimentally identified modes of connections between monomers of eumelanin made from the controlled oxidation of DHI[310–314] and DHICA.[315,316] Dimers, trimers, and tetramers are formed via single C-C interunit bond. DHI has been found to polymerize at the 4th and the 7th positions, and the 2-2 dimer is the prevalent species in the presence of metal ions. In DHICA, since the 2nd position is blocked by the presence of a –COOH moiety, 4th and 7th positions take part in the polymerization. In both cases, adjacent monomer units do not reside in one plane due to steric hindrance. Though less active, the 3rd position is also found to be involved in oligomerization. Detection of a mixed population of oligomers with a variety of connection schemes introduces structural heterogeneity similar to chemical disorder, at the basic protomolecular level. However, while proposing the chemical disorder model, inactivity of N1, the oxygen atoms of carbonyl and hydroxyl moieties, and inter-monomer strain were not taken into account.[266]

Other than theoretical investigations on the stacked oligomer model, considering both infinite[317–319] and finitely extended sheets,[320–323] a unique melanin structural model

came from Kaxiras and coworkers.[324,325] Using density functional theory (DFT) these authors have refined the 'stack of finitely extended sheet' model and introduced a porphyrin-like ring containing four monomeric units (DHI and DHICA) connected in such a way that four nitrogen atoms point towards the inner core, known as the **porphyrin** or **macrocycle model.** (Fig. 1.8 c) It incorporates structural regularity and preferential connection between precursor units, unlike randomly linked extended polymers. A linear combination of energetically favorable structures can explain broad absorption spectra and a porphyrin-like core is able to accommodate a variety of metal ions. Most importantly, assembly of two to three such layers held by non-covalent π-π interactions reproduces the experimental radial distribution function[305,306] obtained by Meng *et al*. An additional simulation study has also shown that if photoexcited, these protomolecules have the ability to relax at ultrafast sub-ps time scales, a required property of melanin for performing the photoprotective role.[271] The interplanar distance, proposed by this model gained support from electron microscopy evidence of the self-assembled stacked structure of natural and synthetic melanin with an interplanar spacing of 3.7 - 4.0 Å.[303] However, despite its physically appealing and intuitive structural scaffold, this model lacks direct experimental detection.

There are a quite a few solid-state NMR reports that aimed to understand the structure of sepia and hair melanin,[326][327] synthesized melanin from multiple modified precursors in fungus,[328–331] but result in limited information on modes of interactions between monomer units. A completely **new and debatable structural architecture of a model eumelanin polymer, known as polydopamine was proposed** by Dreyer *et al* based on ^{15}N and ^{13}C solid-phase NMR evidence.[332] According to these authors, dopamine may polymerize in a way similar to those of hydroquinone (p-benzenediol) and catechol (o-benzenediol),[333–337] dictated via charge-transfer, hydrogen bonding, and stacking interactions. Recently Prampolini *et al*. have used DFT and predicted a variety of dimers that are made from DHI and it's redox forms which are non-covalently held together.[338] A mixed population of these dimers was shown to account for the broad absorption spectra of melanin.

Excitonic coupling between a variety of oligomeric structures (covalently linked oligomers, macrocycles, and non-covalently held polymers) that lie within sub-nm distances from each other has been found to be responsible for an exponential monotonic increase of absorbance with increasing photon energy.[339] In another study, using molecular dynamics simulations, these authors have also shown that eumelanin secondary structures are made from randomly oriented DHI derived macrocycles.[340] However, this apparent random orientation results in the geometric order and/or disorder at a large scale with an average interlayer distance of 3.3 Å, which is in agreement with transmission

electron microscopic (TEM) images.[340] In fact, the original chemical disorder model had implications for higher order structures in melanin. Meredith and coworkers have suggested that the degree of disorder in melanin macromolecules exists at the various levels and would vary depending on experimental conditions, such as, temperature, presence of partner molecule for π stacking, hydration state etc.[303]

The majority of theoretical studies have engaged in explaining featureless absorption spectra. Despite tremendous experimental and theoretical efforts, a consensus regarding the protomolecular structure of melanin remains at large. In this scenario, new experimental constraints are necessary to build or assess the melanin structural model. Unlike absorption, melanins (natural and synthetic) have a distinct vibrational signature.[236–238,240] Position and intensity of vibrational bands are very sensitive to any minute structural perturbations (due to covalent and non-covalent interactions). However, other than two studies,[239,341] there is no report on how vibrational signature of all the structural models compare with the experimental one. **In chapter 8, I have used observable physical properties of melanin, such as UV/Vis absorption, vibrational Raman signature, electronic density of states and radial distribution function (RDF) as constraints and employed quantum chemical methods to build structural models of early time pigments. These protomolecules are based on experimentally detected oligomeric scaffolds by d'Ischia and coworkers.**[310,313,314] Subsequently, I have also assessed merits and demerits of all proposed protomolecular models of melanin in the context of the correct reproduction of experimental spectra.

1.4.9 Secondary and tertiary assembly of melanin

Though precise atomic connections between monomeric units of any types of melanins are not unequivocally established, the macromolecular assembly is better understood.[255,257,301,302,304] The supramolecular structures of eumelanin, mainly from *sepia,* both extracted in the laboratoty and commercially available from Sigma (*Sigma*-Aldrich-M2649) and synthetically made ones have been addressed by topography imaging,[171,342,343] laser desorption mass spectroscopy,[344] x-ray and neutron scattering methods,[305,306,345] and theoretical methods.[324,325,338–340,346] The first high resolution scanning tunneling microscopic (STM) images of tyrosine melanin on Highly oriented pyrolytic graphite (HOPG) and Molybdenum disulfide (MOS_2) surfaces provided an oblong structure with dimension more than 2 nm in one direction, and < 2 nm in the perpendicular direction.[307] Less than 20 Å vertical dimension of eumelanin particles indicated the presence of stacked layer structure.

Using transmission electron microscope (TEM) and radial Fourier analysis, Meredith and coworkers have shown that both synthetic and natural melanins (from sepia and bovine epithelium) aggregate into stacked 'onion-like' layered structures, with ~3.7 Å interlayer spacing.[303] It has been further demonstrated that if the system can be disaggregated (using a base and/or a π-stack breaker), the same monotonically decreasing optical absorption of well-dispersed dilute melanin solution is observed.[264,303] This finding also reinforces the fact that the optical properties of melanins are derived from the primary protomolecular structure, and not from the aggregated state.
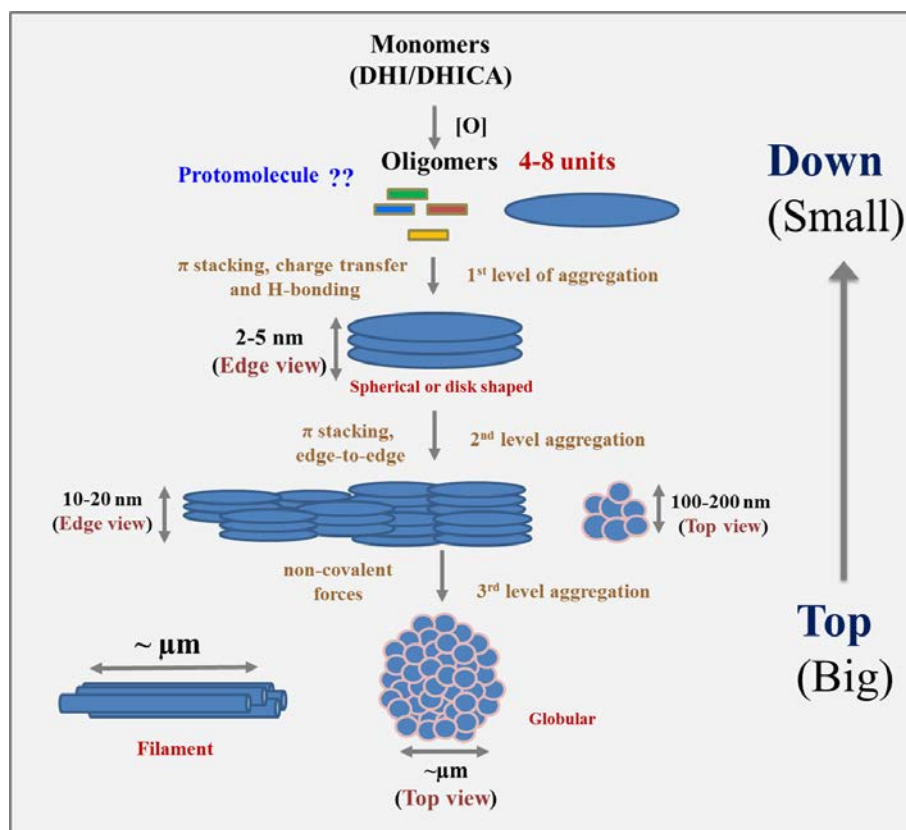
Fig. 1.9 Model of Sepia eumelanin macromolecular architecture emerged from high resolution topography imaging. (Integrated from results described in Ref 301, 304, 305, 307-309, 317 and others) Deposited melanin particles consist of a range of sizes (based on a range of molecular weight) reveals non-covalent interactions driven aggregation at different length scale, from nm to microns.

Careful analysis of several studies conducted on *Sepia* melanin provides us with size distributions that help in deriving a hierarchical scheme of the self-assembly of eumelanin. (Fig. 1.9) The majority of these studies have used top-down approaches, in which non-covalent intermolecular interactions between small assemblies of melanin are ruptured by passing the sample through a size exclusion filter or using sonication.

Deposited melanin within different molecular weight range reveals distinct sizes and shapes, starting from nanometer (nm) sized discs, spherical particles, few hundred nm sized globular aggregates and few micron (µm) long tubular structures. Several authors have tailored polydopamine (PDA) self-assembly through the use of external agents such as folic acid,[347] alcohol[348] and through carbonization.[349] However, there is no published report that has probed the aggregation dynamics of autoxidized dopa-melanin in a time-dependent manner. **In chapter 9, I have used AFM imaging in intermittent contact mode to acquire size distributions of dopa-melanin particles. The obtained size distributions along vertical dimensions give direct evidence of π-π interlayer stacking in melanin secondary structure. Our findings reveal new insights on how microns long fibrillar aggregates are assembled through association of smaller subunits.**

References

[1] E. Hückel, *Zeitschrift für Phys.* **1931**, *70*, 204.

[2] E. Hückel, *Zeitschrift für Phys.* **1931**, *72*, 310.

[3] E. Hückel, *Zeitschrift für Phys.* **1932**, *76*, 628.

[4] W. Saenger, *Principles of Nucleic Acid Structure*, Springer-Verlag, New York, NY, USA, **1984**.

[5] B. Alberts, A. Johnson, J. Lewis, M. Raff, K. Roberts, P. Walter, *Molecular Biology of the Cell, 5th Edition*, Garland Science, New York, NY, USA, **2008**.

[6] E. Grotewold, Ed., *The Science of Flavonoids*, Springer New York, New York, NY, **2006**.

[7] T. Aniszewski, *Alkaloids - Secrets of Life : Aklaloid Chemistry, Biological Significance, Applications and Ecological Role*, Elsevier B.V., Amsterdam, The Netherlands, **2007**.

[8] H. Klauk, Ed., *Organic Electronics*, Wiley-VCH Verlag GmbH & Co. KGaA, Weinheim, FRG, **2006**.

[9] A. Köhler, H. Bässler, *Electronic Processes in Organic Semiconductors*, Wiley-VCH Verlag GmbH & Co. KGaA, Weinheim, Germany, **2015**.

[10] J. Jang, **2006**, pp. 189–260.

[11] Q. Li, Ed., *Self-Organized Organic Semiconductors*, John Wiley & Sons, Inc., Hoboken, NJ, USA, **2011**.

[12] G. A. Snook, P. Kao, A. S. Best, *J. Power Sources* **2011**, *196*, 1.

[13] M. Gerard, *Biosens. Bioelectron.* **2002**, *17*, 345.

[14] T. Ahuja, I. Mir, D. Kumar, Rajesh, *Biomaterials* **2007**, *28*, 791.

[15] N. K. Guimard, N. Gomez, C. E. Schmidt, *Prog. Polym. Sci.* **2007**, *32*, 876.

[16] R. W. Sabnis, *Handbook of Fluorescent Dyes and Probes*, John Wiley & Sons, Inc, Hoboken, NJ, USA, **2015**.

[17] K. S. Hettie, T. E. Glass, *ACS Chem. Neurosci.* **2015**, acschemneuro.5b00235.

[18] B. Sarkar, A. Banerjee, A. K. Das, S. Nag, S. K. Kaushalya, U. Tripathy, M. Shameem, S. Shukla, S. Maiti, *ACS Chem. Neurosci.* **2014**, *5*, 329.

[19] D. Zhong, S. K. Pal, D. Zhang, S. I. Chan, A. H. Zewail, *Proc. Natl. Acad. Sci.* **2002**, *99*, 13.

[20] L. Zhang, Y.-T. Kao, W. Qiu, L. Wang, D. Zhong, *J. Phys. Chem. B* **2006**, *110*, 18097.

[21] L. Zhang, L. Wang, Y.-T. Kao, W. Qiu, Y. Yang, O. Okobiah, D. Zhong, *Proc. Natl. Acad. Sci.* **2007**, *104*, 18461.

[22] P. Talukder, S. Chen, B. Roy, P. Yakovchuk, M. M. Spiering, M. P. Alam, M. M. Madathil, C. Bhattacharya, S. J. Benkovic, S. M. Hecht, *Biochemistry* **2015**, *54*, 7457.

[23] B. Holz, *Nucleic Acids Res.* **1998**, *26*, 1076.

[24] J. M. Jean, K. B. Hall, *Proc. Natl. Acad. Sci.* **2001**, *98*, 37.

[25] K. B. Hall, **2009**, pp. 269–285.

[26] A. C. Jones, R. K. Neely, *Q. Rev. Biophys.* **2015**, *48*, 244.

[27] N. B. Gaied, *Nucleic Acids Res.* **2005**, *33*, 1031.

[28] C. A. Kenfack, A. Burger, Y. Mély, *J. Phys. Chem. B* **2006**, *110*, 26327.

[29] M. Rist, J. Marino, *Curr. Org. Chem.* **2002**, *6*, 775.

[30] S. G. Srivatsan, Y. Tor, *J. Am. Chem. Soc.* **2007**, *129*, 2044.

[31] R. W. Sinkeldam, N. J. Greco, Y. Tor, *Chem. Rev.* **2010**, *110*, 2579.

[32] A. Matarazzo, R. H. E. Hudson, *Tetrahedron* **2015**, *71*, 1627.

[33] S. Ullrich, T. Schultz, M. Z. Zgierski, A. Stolow, *Phys. Chem. Chem. Phys.* **2004**, *6*, 2796.

[34] C. E. Crespo-Hernández, B. Cohen, P. M. Hare, B. Kohler, *Chem. Rev.* **2004**, *104*, 1977.

[35] S. Matsika, *J. Phys. Chem. A* **2005**, *109*, 7538.

[36] M. Barbatti, A. J. A. Aquino, J. J. Szymczak, D. Nachtigallova, P. Hobza, H. Lischka, *Proc. Natl. Acad. Sci.* **2010**, *107*, 21453.

[37] M. Staniforth, V. G. Stavros, *Proc. R. Soc. A Math. Phys. Eng. Sci.* **2013**, *469*, 20130458.

[38] W. R. Zipfel, R. M. Williams, W. W. Webb, *Nat. Biotechnol.* **2003**, *21*, 1369.

[39] A. Diaspro, G. Chirico, M. Collini, *Q. Rev. Biophys.* **2005**, *38*, 97.

[40] G. S. He, L.-S. Tan, Q. Zheng, P. N. Prasad, *Chem. Rev.* **2008**, *108*, 1245.

[41] S. Brown, *Nat. Photonics* **2008**, *2*, 394.

[42] J. P. Celli, B. Q. Spring, I. Rizvi, C. L. Evans, K. S. Samkoe, S. Verma, B. W. Pogue, T. Hasan, *Chem. Rev.* **2010**, *110*, 2795.

[43] C. Zhu, L. Liu, Q. Yang, F. Lv, S. Wang, *Chem. Rev.* **2012**, *112*, 4687.

[44] P. Furuta, J. Brooks, M. E. Thompson, J. M. J. Fréchet, *J. Am. Chem. Soc.* **2003**, *125*, 13165.

[45] Y. Liang, D. Feng, Y. Wu, S.-T. Tsai, G. Li, C. Ray, L. Yu, *J. Am. Chem. Soc.* **2009**, *131*, 7792.

[46] P. M. Beaujuge, J. M. J. Fréchet, *J. Am. Chem. Soc.* **2011**, *133*, 20009.

[47] C. Wang, H. Dong, W. Hu, Y. Liu, D. Zhu, *Chem. Rev.* **2012**, *112*, 2208.

[48] J. R. Platt, *J. Chem. Phys.* **1949**, *17*, 484.

[49] B. O. Roos, M. Fülscher, P.-Å. Malmqvist, M. Merchán, L. Serrano-Andrés, in *Quantum Mech. Electron. Struct. Calc. with Chem. Accuracy*, Springer Netherlands, Dordrecht, **1995**, pp. 357–438.

[50] B. O. Roos, K. Andersson, M. P. Flscher, P. Malmqvist, L. Serrano-Andrs, K. Pierloot, M. Merchn, **n.d.**, pp. 219–331.

[51] A. C. Borin, L. Serrano-Andrés, *J. Mol. Struct. THEOCHEM* **1999**, *464*, 121.

[52] L. Serrano-Andrés, B. O. Roos, *J. Am. Chem. Soc.* **1996**, *118*, 185.

[53] M. P. Fülscher, L. Serrano-Andrés, B. O. Roos, *J. Am. Chem. Soc.* **1997**, *119*, 6168.

[54] A. C. Borin, L. Serrano-Andrés, M. P. Fülscher, B. O. Roos, *J. Phys. Chem. A* **1999**, *103*, 1838.

[55] M. P. Füelscher, B. O. Roos, *J. Am. Chem. Soc.* **1995**, *117*, 2089.

[56] J. Lorentzon, M. P. Fuelscher, B. O. Roos, *J. Am. Chem. Soc.* **1995**, *117*, 9265.

[57] M. Merchán, L. Serrano-Andrés, M. P. Fülscher, B. O. Roos, **1999**, pp. 161–195.

[58] M. Rubio, M. Merchán, E. Ortí, B. O. Roos, *Chem. Phys.* **1994**, *179*, 395.

[59] J. Kagan, *Organic Photochemistry*, Academic Press, New York, NY, USA, **1993**.

[60] D. C. Ward, E. Reich, L. Stryer, *J. Biol. Chem.* **1969**, *244*, 1228.

[61] M. Daniels, W. Hauswirth, *Science (80-.).* **1971**, *171*, 675.

[62] W. W. Hauswirth, M. Daniels, in *Photochem. Photobiol. Nucleic Acids*, Elsevier, **1976**, pp. 109–167.

[63] M. Daniels, in *Photochem. Photobiol. Nucleic Acids*, Elsevier, **1976**, pp. 23–108.

[64] P. R. Callis, *Annu. Rev. Phys. Chem.* **1983**, *34*, 329.

[65] D. Onidas, D. Markovitsi, S. Marguet, A. Sharonov, T. Gustavsson, *J. Phys. Chem. B* **2002**, *106*, 11367.

[66] J. Peon, A. H. Zewail, *Chem. Phys. Lett.* **2001**, *348*, 255.

[67] J.-M. L. Pecourt, J. Peon, B. Kohler, *J. Am. Chem. Soc.* **2001**, *123*, 10370.

[68] H. Kang, K. T. Lee, B. Jung, Y. J. Ko, S. K. Kim, *J. Am. Chem. Soc.* **2002**, *124*, 12958.

[69] C. Canuel, M. Mons, F. Piuzzi, B. Tardivel, I. Dimicoli, M. Elhanine, *J. Chem. Phys.* **2005**, *122*, 074316.

[70] H. R. Hudock, B. G. Levine, A. L. Thompson, H. Satzger, D. Townsend, N. Gador, S. Ullrich, A. Stolow, T. J. Martínez, *J. Phys. Chem. A* **2007**, *111*, 8500.

[71] C. T. Middleton, K. de La Harpe, C. Su, Y. K. Law, C. E. Crespo-Hernández, B. Kohler, *Annu. Rev. Phys. Chem.* **2009**, *60*, 217.

[72] M. K. Kuimova, J. Dyer, M. W. George, D. C. Grills, J. M. Kelly, P. Matousek, A. W. Parker, X. Z. Sun, M. Towrie, A. M. Whelan, *Chem. Commun.* **2005**, 1182.

[73] P. M. Hare, C. E. Crespo-Hernandez, B. Kohler, *Proc. Natl. Acad. Sci.* **2007**, *104*, 435.

[74] K. Kosma, C. Schröter, E. Samoylova, I. V. Hertel, T. Schultz, *J. Am. Chem. Soc.* **2009**, *131*, 16939.

[75] E. Samoylova, H. Lippert, S. Ullrich, I. V. Hertel, W. Radloff, T. Schultz, *J. Am. Chem. Soc.* **2005**, *127*, 1782.

[76] M. Z. Zgierski, S. Patchkovskii, T. Fujiwara, E. C. Lim, *J. Phys. Chem. A* **2005**, *109*, 9384.

[77] Z. Lan, E. Fabiano, W. Thiel, *J. Phys. Chem. B* **2009**, *113*, 3548.

[78] K. Kleinermanns, D. Nachtigallová, M. S. de Vries, *Int. Rev. Phys. Chem.* **2013**, *32*, 308.

[79] S. Perun, A. L. Sobolewski, W. Domcke, *J. Am. Chem. Soc.* **2005**, *127*, 6257.

[80] M. Barbatti, H. Lischka, *J. Am. Chem. Soc.* **2008**, *130*, 6831.

[81] L. Serrano-Andrés, M. Merchán, A. C. Borin, *J. Am. Chem. Soc.* **2008**, *130*, 2473.

[82] Z. Lan, E. Fabiano, W. Thiel, *ChemPhysChem* **2009**, *10*, 1225.

[83] M. Barbatti, *J. Am. Chem. Soc.* **2014**, *136*, 10246.

[84] S. Matsika, *J. Phys. Chem. A* **2004**, *108*, 7584.

[85] M.-P. Gaigeot, M. Sprik, *J. Phys. Chem. B* **2004**, *108*, 7458.

[86] H. R. Hudock, T. J. Martínez, *ChemPhysChem* **2008**, *9*, 2486.

[87] L. Serrano-Andrés, M. Merchán, *J. Photochem. Photobiol. C Photochem. Rev.* **2009**, *10*, 21.

[88] S. Matsika, **2014**, pp. 209–243.

[89] J. Cadet, E. Sage, T. Douki, *Mutat. Res. Mol. Mech. Mutagen.* **2005**, *571*, 3.

[90] Y. Matsumura, H. N. Ananthaswamy, *Toxicol. Appl. Pharmacol.* **2004**, *195*, 298.

[91] L. Marrot, J.-R. Meunier, *J. Am. Acad. Dermatol.* **2008**,

[92] F. R. de Gruijl, **2000**, pp. 359–366.

[93] G. Fabbrocini, M. Triassi, M. C. Mauriello, G. Torre, M. C. Annunziata, V. De Vita, F. Pastore, V. D'Arco, G. Monfrecola, *Cancers (Basel).* **2010**, *2*, 1980.

[94] J. C. van der Leun, F. R. de Gruijl, *Photochem. Photobiol. Sci.* **2002**, *1*, 324.

[95] N. S. Agar, G. M. Halliday, R. S. Barnetson, H. N. Ananthaswamy, M. Wheeler, A. M. Jones, *Proc. Natl. Acad. Sci. U. S. A.* **2004**, *101*, 4954.

[96] C. F. Garland, F. C. Garland, E. D. Gorham, *Ann. Epidemiol.* **2003**, *13*, 395.

[97] D. Averbeck, in *Photobiol. Med.*, Springer US, Boston, MA, **1994**, pp. 71–98.

[98] J. Cadet, L. Voituriez, F. E. Hruska, L.-S. Kan, F. A. A. M. de Leeuw, C. Altona, *Can. J. Chem.* **1985**, *63*, 2861.

[99] J. Cadet, P. Vigny, in *Bioorganic Photochem.* (Ed.: H. Morrison), Wiley-Interscience, New York, **1990**, pp. 1–272.

[100] P. H. Clingen, C. F. Arlett, L. Roza, T. Mori, O. Nikaido, M. H. Green, *Cancer Res.* **1995**, *55*, 2245.

[101] J.-L. Ravanat, T. Douki, J. Cadet, *J. Photochem. Photobiol. B Biol.* **2001**, *63*, 88.

[102] S. N. Bose, R. J. H. Davies, *Nucleic Acids Res.* **1984**, *12*, 7903.

[103] S. Bose, R. Davies, S. Sethi, J. McCloskey, *Science (80-.).* **1983**, *220*, 723.

[104] X. D. Zhao, S. Nadji, J. L. F. Kao, J. S. Taylor, *Nucleic Acids Res.* **1996**, *24*, 1554.

[105] S. Kumar, N. D. Sharma, R. J. H. Davies, D. W. Phillipson, J. A. McCloskey, *Nucleic Acids Res.* **1987**, *15*, 1199.

[106] N. D. Sharma, R. J. H. Davies, *J. Photochem. Photobiol. B Biol.* **1989**, *3*, 247.

[107] F. P. Gasparro, J. R. Fresco, *Nucleic Acids Res.* **1986**, *14*, 4239.

[108] J. Cadet, T. Delatour, T. Douki, D. Gasparutto, J.-P. Pouget, J.-L. Ravanat, S. Sauvaigo, *Mutat. Res.* **1999**, *424*, 9.

[109] S. Steenken, *Chem. Rev.* **1989**, *89*, 503.

[110] L. P. Candeias, S. Steenken, *Chem. - A Eur. J.* **2000**, *6*, 475.

[111] D. B. Hall, R. E. Holmlin, J. K. Barton, *Nature* **1996**, *382*, 731.

[112] S. O. Kelley, *Science (80-.).* **1999**, *283*, 375.

[113] N. K. Schwalb, F. Temps, *Science (80-.).* **2008**, *322*, 243.

[114] M. D. Evans, M. Dizdaroglu, M. S. Cooke, *Mutat. Res. Mutat. Res.* **2004**, *567*, 1.

[115] M. Dizdaroglu, G. Kirkali, P. Jaruga, *Free Radic. Biol. Med.* **2008**, *45*, 1610.

[116] P. W. Doetsch, T. H. Zastawny, A. M. Martin, M. Dizdaroglu, *Biochemistry* **1995**, *34*, 737.

[117] K. Nakatani, Y. Tor, *Modified Nucleic Acids*, Springer International Publishing, **2016**.

[118] W. van der Velden, A. W. Schwartz, *Geochim. Cosmochim. Acta* **1977**, *41*, 961.

[119] P. G. Stoks, A. W. Schwartz, *Nature* **1979**, *282*, 709.

[120] P. G. Stoks, A. W. Schwartz, *Geochim. Cosmochim. Acta* **1981**, *45*, 563.

[121] A. Shimoyama, S. Hagishita, K. Harada, *Orig. Life Evol. Biosph.* **1989**, *19*, 469.

[122] R. Krishnamurthy, *J. Mex. Chem. Soc.* **2009**, *53*, 23.

[123] A. C. Rios, Y. Tor, *Astrobiology* **2012**, *12*, 884.

[124] A. C. Rios, Y. Tor, *Isr. J. Chem.* **2013**, *53*, 469.

[125] N. V. Hud, B. J. Cafferty, R. Krishnamurthy, L. D. Williams, *Chem. Biol.* **2013**, *20*, 466.

[126] M. P. Robertson, M. Levy, S. L. Miller, *J. Mol. Evol.* **1996**, *43*, 543.

[127] O. Leslie E., *Crit. Rev. Biochem. Mol. Biol.* **2004**, *39*, 99.

[128] E. Borquez, H. J. Cleaves, A. Lazcano, S. L. Miller, *Orig. Life Evol. Biosph.* **2005**, *35*, 79.

[129] H. J. Cleaves II, K. E. Nelson, S. L. Miller, *Naturwissenschaften* **2006**, *93*, 228.

[130] R. Saladino, G. Botta, S. Pino, G. Costanzo, E. Di Mauro, *Chem. Soc. Rev.* **2012**, *41*, 5526.

[131] M. P. Callahan, K. E. Smith, H. J. Cleaves, J. Ruzicka, J. C. Stern, D. P. Glavin, C. H. House, J. P. Dworkin, *Proc. Natl. Acad. Sci.* **2011**, *108*, 13995.

58, S139.

[132] E. L. Rachofsky, R. Osman, J. B. A. Ross, *Biochemistry* **2001**, *40*, 946.

[133] T. Fiebig, C. Wan, A. H. Zewail, *ChemPhysChem* **2002**, *3*, 781.

[134] M. A. O'Neil, J. K. Barton, *J. Am. Chem. Soc.* **2002**, *124*, 13053.

[135] Y. HU, T. W. CONWAY, *J. Interferon Res.* **1993**, *13*, 323.

[136] K. Zinn, A. Keller, L. Whittemore, T. Maniatis, *Science (80-.).* **1988**, *240*, 210.

[137] R. K. Tiwari, J. Kusari, R. Kumar, G. C. Sen, *Mol. Cell. Biol.* **1988**, *8*, 4289.

[138] M. Barbatti, A. C. Borin, S. Ullrich, Eds. , *Photoinduced Phenomena in Nucleic Acids I*, Springer International Publishing, Cham, **2015**.

[139] J. S. Kwiatkowski, *Theor. Chim. Acta* **1969**, *13*, 149.

[140] E. Mburu, S. Matsika, *J. Phys. Chem. A* **2008**, *112*, 12485.

[141] C. E. Crespo-Hernández, L. Martínez-Fernández, C. Rauer, C. Reichardt, S. Mai, M. Pollum, P. Marquetand, L. González, I. Corral, *J. Am. Chem. Soc.* **2015**, *137*, 4368.

[142] C. Santhosh, P. C. Mishra, *Spectrochim. Acta Part A Mol. Spectrosc.* **1991**, *47*, 1685.

[143] A. Holmén, B. Nordén, B. Albinsson, *J. Am. Chem. Soc.* **1997**, *119*, 3114.

[144] L. Serrano-Andres, M. Merchan, A. C. Borin, *Proc. Natl. Acad. Sci.* **2006**, *103*, 8691.

[145] C. S. Cockell, *J. Theor. Biol.* **1998**, *193*, 717.

[146] C. S. Cockell, in *Ecosyst. Evol. Ultrav. Radiat.*, Springer New York, New York, NY, **2001**, pp. 1–35.

[147] C. S. Cockell, in *Astrobiology*, Springer Berlin Heidelberg, Berlin, Heidelberg, **2002**, pp. 219–232.

[148] J. B. Kerr, C. T. McElroy, *Science (80-.).* **1993**, *262*, 1032.

[149] D. Lubin, E. Jensen, H., *Nature* **1995**, *377*, 710.

[150] L. D. Ziegler, B. Hudson, D. P. Strommen, W. L. Peticolas, *Biopolymers* **1984**, *23*, 2067.

[151] W. L. Kubasek, B. Hudson, W. L. Peticolas, *Proc. Natl. Acad. Sci.* **1985**, *82*, 2369.

[152] S. P. A. Fodor, R. P. Rava, T. R. Hays, T. G. Spiro, *J. Am. Chem. Soc.* **1985**, *107*, 1520.

[153] S. P. A. Fodor, T. G. Spiro, *J. Am. Chem. Soc.* **1986**, *108*, 3198.

[154] J. M. Benevides, S. A. Overman, G. J. Thomas, *J. Raman Spectrosc.* **2005**, *36*, 279.

[155] A. B. Myers, *J. Raman Spectrosc.* **1997**, *28*, 389.

[156] A. B. Myers, in *Laser Tech. Chem.* (Eds.: A.B. Myers, T.R. Rizzo), Wiley-Interscience, New York, **1995**, p. 325.

[157] A. B. Myers, *Acc. Chem. Res.* **1997**, *30*, 519.

[158] B. E. Billinghurst, G. R. Loppnow, *J. Phys. Chem. A* **2006**, *110*, 2353.

[159] B. E. Billinghurst, R. Yeung, G. R. Loppnow, *J. Phys. Chem. A* **2006**, *110*, 6185.

[160] S. Yarasi, P. Brost, G. R. Loppnow, *J. Phys. Chem. A* **2007**, *111*, 5130.

[161] S. Yarasi, S. Ng, G. R. Loppnow, *J. Phys. Chem. B* **2009**, *113*, 14336.

[162] A. F. El-Yazbi, A. Palech, G. R. Loppnow, *J. Phys. Chem. A* **2011**, *115*, 10445.

[163] S. S. Ng, F. Teimoory, G. R. Loppnow, *J. Phys. Chem. Lett.* **2011**, 2362.

[164] S. A. Oladepo, G. R. Loppnow, *J. Phys. Chem. B* **2011**, *115*, 6149.

[165] B. E. Billinghurst, S. A. Oladepo, G. R. Loppnow, *J. Phys. Chem. B* **2012**, *116*, 10496.

[166] F. Teimoory, G. R. Loppnow, *J. Phys. Chem. A* **2014**, *118*, 12161.

[167] N. Kaushik, N. Kaushik, P. Attri, N. Kumar, C. Kim, A. Verma, E. Choi, *Molecules* **2013**, *18*, 6620.

[168] J. J. Nordlund, R. E. Boissy, V. J. Hearing, R. A. King, W. S. Oetting, J.-P. Ortonne, Eds. , *The Pigmentary System*, Blackwell Publishing Ltd, Oxford, UK, **2006**.

[169] J. D. Simon, D. N. Peles, *Acc. Chem. Res.* **2010**, *43*, 1452.

[170] J. Lindgren, A. Moyer, M. H. Schweitzer, P. Sjövall, P. Uvdal, D. E. Nilsson, J. Heimdal, A. Engdahl, J. A. Gren, B. P. Schultz, B. P. Kear, *Proc. R. Soc. B Biol. Sci.* **2015**, *282*, 20150614.

[171] Y. Liu, J. D. Simon, *Pigment Cell Res.* **2003**, *16*, 72.

[172] Y. Liu, J. D. Simon, *Pigment Cell Res.* **2005**, *18*, 42.

[173] J. D. Simon, L. Hong, D. N. Peles, *J. Phys. Chem. B* **2008**, *112*, 13201.

[174] K. J. McGraw, R. J. Safran, K. Wakamatsu, *Funct. Ecol.* **2005**, *19*, 816.

[175] E. J. Land, P. A. Riley, *Pigment Cell Res.* **2000**, *13*, 273.

[176] Anthony J. Thody, Elisabeth M. Higgins, Kazumasa Wakamatsu, Shosuke Ito, Susan A. Burchill, Janet M. Marks, *J. Invest. Dermatol.* **1991**, *97*, 340.

[177] W. D. Bush, J. Garguilo, F. A. Zucca, A. Albertini, L. Zecca, G. S. Edwards, R. J. Nemanich, J. D. Simon, *Proc. Natl. Acad. Sci.* **2006**, *103*, 14785.

[178] L. Zecca, F. A. Zucca, H. Wilms, D. Sulzer, *Trends Neurosci.* **2003**, *26*, 578.

[179] R. Carstam, C. Brinck, A. Hindemith-Augustsson, H. Rorsman, E. Rosengren, *Biochim. Biophys. Acta - Mol. Basis Dis.* **1991**, *1097*, 152.

[180] G. Odh, R. Carstam, J. Paulson, A. Wittbjer, E. Rosengren, H. Rorsman, *J. Neurochem.* **1994**, *62*, 2030.

[181] V. J. Hearing, *J. Invest. Dermatol.* **2011**, *131*, 8.

[182] K. Lerch, **1995**, pp. 64–80.

[183] T. Klabunde, C. Eicken, J. C. Sacchettini, B. Krebs, *Nat. Struct. Biol.* **1998**, *5*, 1084.

[184] Y. Matoba, T. Kumagai, A. Yamamoto, H. Yoshitsu, M. Sugiyama, *J. Biol. Chem.* **2006**, *281*, 8981.

[185] W. T. Ismaya, H. J. Rozeboom, A. Weijn, J. J. Mes, F. Fusetti, H. J. Wichers, B. W. Dijkstra, *Biochemistry* **2011**, *50*, 5477.

[186] H. Decker, T. Schweikardt, F. Tuczek, *Angew. Chemie Int. Ed.* **2006**, *45*, 4546.

[187] H. S. Raper, A. Wormall, *Biochem. J.* **1923**, *17*, 454.

[188] H. S. Raper, *Biochem. J.* **1926**, *20*, 735.

[189] H. S. Raper, H. B. Speakman, *Biochem. J.* **1926**, *20*, 69.

[190] H. S. Raper, *Biochem. J.* **1927**, *21*, 89.

[191] H. S. Mason, *J. Biol. Chem.* **1948**, *172*, 83.

[192] C. J. Cooksey, P. J. Garratt, E. J. Land, S. Pavel, C. A. Ramsden, P. A. Riley, N. P. M. Smit, *J. Biol. Chem.* **1997**, *272*, 26226.

[193] K. U. Schallreuter, S. Kothari, B. Chavan, J. D. Spencer, *Exp. Dermatol.* **2008**, *17*, 395.

[194] G. Prota, *J. Invest. Dermatol.* **1980**, *75*, 122.

[195] A. M. Korner, J. Pawelek, *J. Invest. Dermatol.* **1980**, *75*, 192.

[196] G. Prota, *Melanins and Melanogenesis*, Academic Press, Inc., California, USA, **1992**.

[197] G. Prota, in *Prog. Chem. Org. Nat. Prod.* (Eds.: W. Herz, G.W. Kirby, R.E. Moore, W. Steglich, C. Tamm), Springer-Verlag, Vienna, Austria, **1995**, pp. 93–148.

[198] G. Prota, *Pigment Cell Res.* **2000**, *13*, 283.

[199] S. Ito, *Pigment Cell Res.* **2003**, *16*, 230.

[200] S. Ito, K. Wakamatsu, *Photochem. Photobiol.* **2008**, *84*, 582.

[201] J. D. Simon, D. Peles, K. Wakamatsu, S. Ito, *Pigment Cell Melanoma Res.* **2009**, *22*, 563.

[202] T. Kondo, V. J. Hearing, *Expert Rev. Dermatol.* **2011**, *6*, 97.

[203] T.-S. Chang, *Int. J. Mol. Sci.* **2009**, *10*, 2440.

[204] Á. Sánchez-Ferrer, J. Neptuno Rodríguez-López, F. García-Cánovas, F. García-Carmona, *Biochim. Biophys. Acta - Protein Struct. Mol. Enzymol.* **1995**, *1247*, 1.

[205] F. García-Molina, J. L. Muñoz, R. Varón, J. N. Rodríguez-López, F. García-Cánovas, J. Tudela, *J. Agric. Food Chem.* **2007**, *55*, 9739.

[206] M. Sugumaran, *Pigment Cell Res.* **2002**, *15*, 2.

[207] E. J. Land, S. Ito, K. Wakamatsu, P. A. Riley, *Pigment Cell Res.* **2003**, *16*, 487.

[208] P. Palumbo, M. D'Ischia, G. Prota, *Tetrahedron* **1987**, *43*, 4203.

[209] A. Palumbo, F. Solano, G. Misuraca, P. Aroca, J. C. Garcia Borron, J. A. Lozano, G. Prota, *Biochim. Biophys. Acta - Gen. Subj.* **1991**, *1115*, 1.

[210] R. Edge, M. D'Ischia, E. J. Land, A. Napolitano, S. Navaratnam, L. Panzella, A. Pezzella, C. A. Ramsden, P. A. Riley, *Pigment Cell Res.* **2006**, *19*, 443.

[211] C. Olivares, C. Jimenez-Cervantes, J. A. Lozano, F. Solano, J. C. Garcia-Borron, *Biochem. J.* **2001**, *354*, 131.

[212] T. Kobayashi, K. Urabe, A. Winder, C. Jiménez-

Cervantes, G. Imokawa, T. Brewington, F. Solano, J. C. García-Borrón, V. J. Hearing, *EMBO J.* **1994**, *13*, 5818.

[213] C. Jiménez-Cervantes, F. Solano, T. Kobayashi, K. Urabe, V. J. Hearing, J. A. Lozano, J. C. García-Borrón, *J. Biol. Chem.* **1994**, *269*, 17993.

[214] J. R. Jara, P. Aroca, F. Solano, J. H. Martinez, J. A. Lozano, *Biochim. Biophys. Acta - Gen. Subj.* **1988**, *967*, 296.

[215] A. Napolitano, C. Costantini, O. Crescenzi, G. Prota, *Tetrahedron Lett.* **1994**, *35*, 6365.

[216] A. Napolitano, P. Di Donato, G. Prota, E. J. Land, *Free Radic. Biol. Med.* **1999**, *27*, 521.

[217] A. Napolitano, P. Di Donato, G. Prota, *Biochim. Biophys. Acta - Gen. Subj.* **2000**, *1475*, 47.

[218] K. Wakamatsu, K. Ohtara, S. Ito, *Pigment Cell Melanoma Res.* **2009**, *22*, 474.

[219] G. Greco, K. Wakamatsu, L. Panzella, S. Ito, A. Napolitano, M. D'Ischia, *Pigment Cell Melanoma Res.* **2009**, *22*, 319.

[220] S. Ito, K. Fujita, H. Takahashi, K. Jimbow, *J. Invest. Dermatol.* **1984**, *83*, 12.

[221] A. M. Morgan, J. Lo, D. E. Fisher, *BioEssays* **2013**, *35*, 672.

[222] A. Napolitano, S. Memoli, O. Crescenzi, G. Prota, *J. Org. Chem.* **1996**, *61*, 598.

[223] S. Ito, K. Wakamatsu, *Pigment Cell Melanoma Res.* **2011**, *24*, 63.

[224] S. Ito, K. Wakamatsu, *J. Eur. Acad. Dermatology Venereol.* **2011**, *25*, 1369.

[225] C. Duval, N. P. M. Smit, A. M. Kolb, M. Regnier, S. Pavel, R. Schmidt, *Pigment Cell Res.* **2002**, *15*, 440.

[226] M. R. Chedekel, E. J. Land, A. Thompson, T. G. Truscott, *J. Chem. Soc. Chem. Commun.* **1984**, 1170.

[227] C. Lambert, T. G. Truscott, E. J. Land, P. A. Riley, *J. Chem. Soc. Faraday Trans.* **1991**, *87*, 2939.

[228] A. Thompson, E. J. Land, M. R. Chedekel, K. V. Subbarao, T. G. Truscott, *Biochim. Biophys. Acta - Gen. Subj.* **1985**, *843*, 49.

[229] E. J. Land, P. A. Riley, *Pigment Cell Res.* **2000**, *13*, 273.

[230] E. J. Land, C. A. Ramsden, P. A. Riley, *J. Photochem. Photobiol. B Biol.* **2001**, *64*, 123.

[231] E. J. Land, S. Ito, K. Wakamatsu, P. A. Riley, *Pigment Cell Res.* **2003**, *16*, 487.

[232] A. K. Chakraborty, J. T. Platt, K. K. Kim, B. Kwon, D. C. Bennett, J. M. Pawelek, *Eur. J. Biochem.* **1996**, *236*, 180.

[233] P. Kayatz, G. Thumann, T. T. Luther, J. F. Jordan, K. U. Bartz-Schmidt, P. J. Esser, U. Schraermeyer, *Invest. Ophthalmol. Vis. Sci.* **2001**, *42*, 241.

[234] H. Ou-Yang, G. Stamatas, N. Kollias, *J. Invest. Dermatol.* **2004**, *122*, 492.

[235] G. Zonios, A. Dimou, *Opt. Express* **2008**, *16*, 8263.

[236] S. A. Centeno, J. Shamir, *J. Mol. Struct.* **2008**, *873*, 149.

[237] V. Capozzi, G. Perna, A. Gallone, P. F. Biagi, P. Carmone, A. Fratello, G. Guida, P. Zanna, R. Cicero, *J. Mol. Struct.* **2005**, *744-747*, 717.

[238] A. Samokhvalov, Y. Liu, J. D. Simon, *Photochem. Photobiol.* **2004**, *80*, 84.

[239] L. Sangaletti, P. Borghetti, P. Ghosh, S. Pagliara, P. Vilmercati, C. Castellarin-Cudia, L. Floreano, a. Cossaro, a. Verdini, R. Gebauer, a. Goldoni, *Phys. Rev. B* **2009**, *80*, 174203.

[240] I. Galván, A. Jorge, K. Ito, K. Tabuchi, F. Solano, K. Wakamatsu, *Pigment Cell Melanoma Res.* **2013**, *26*, 917.

[241] M. Nagai, H. Wajcman, A. Lahary, T. Nakatsukasa, S. Nagatomo, T. Kitagawa, *Biochemistry* **1999**, *38*, 1243.

[242] H. Takeuchi, *Biopolymers* **2003**, *72*, 305.

[243] A. R. Offenbacher, J. Chen, B. A. Barry, *J. Am. Chem. Soc.* **2011**, *133*, 6978.

[244] S. Hu, K. M. Smith, T. G. Spiro, *J. Am. Chem. Soc.* **1996**, *118*, 12638.

[245] T. G. Spiro, T. C. Strekas, *Proc. Natl. Acad. Sci.* **1972**, *69*, 2622.

[246] T. B. Freedman, J. S. Loehr, T. M. Loehr, *J. Am. Chem. Soc.* **1976**, *98*, 2809.

[247] S. J. Orlow, M. P. Osber, J. M. Pawelek, *Pigment Cell Res.* **1992**, *5*, 113.

[248] W. Korytowski, T. Sarna, *J. Biol. Chem.* **1990**, *265*, 12410.

[249] M. M. Jastrzebska, H. Isotalo, J. Paloheimo, H. Stubb, *J. Biomater. Sci. Polym. Ed.* **1995**, *7*, 577.

[250] M. Zdybel, E. Chodurek, B. Pilawa, *Appl. Magn. Reson.* **2011**, *40*, 113.

[251] H. Lee, S. M. Dellatore, W. M. Miller, P. B. Messersmith, *Science (80-.).* **2007**, *318*, 426.

[252] F. Bernsmann, A. Ponche, C. Ringwald, J. Hemmerlé, J. Raya, B. Bechinger, J.-C. Voegel, P. Schaaf, V. Ball, *J. Phys. Chem. C* **2009**, *113*, 8234.

[253] K.-Y. Ju, Y. Lee, S. Lee, S. B. Park, J.-K. Lee, *Biomacromolecules* **2011**, *12*, 625.

[254] N. F. Della Vecchia, R. Avolio, M. Alfè, M. E. Errico, A. Napolitano, M. D'Ischia, *Adv. Funct. Mater.* **2013**, *23*, 1331.

[255] M. D'Ischia, K. Wakamatsu, A. Napolitano, S. Briganti, J.-C. Garcia-Borron, D. Kovacs, P. Meredith, A. Pezzella, M. Picardo, T. Sarna, J. D. Simon, S. Ito, *Pigment Cell Melanoma Res.* **2013**, *26*, 616.

[256] J. Borovanský, P. A. Riley, Eds. , *Melanins and Melanosomes. Biosynthesis, Biogenesis, Physiological, and Pathological Functions*, Wiley-VCH Verlag GmbH & Co. KGaA, Weinheim, Germany, **2011**.

[257] F. Solano, *New J. Sci.* **2014**, *2014*, 1.

[258] S. Ito, K. Fujita, *Anal. Biochem.* **1985**, *144*, 527.

[259] S. Ito, *Biochim. Biophys. Acta - Gen. Subj.* **1986**, *883*, 155.

[260] S. Ito, K. Wakamatsu, *Pigment Cell Res.* **2003**, *16*, 523.

[261] S. Ito, K. Wakamatsu, K. Glass, J. D. Simon, *Anal. Biochem.* **2013**, *434*, 221.

[262] J. Riesz, J. Gilmore, P. Meredith, *Biophys. J.* **2006**, *90*, 4137.

[263] P. Meredith, B. J. Powell, J. Riesz, S. P. Nighswander-Rempel, M. R. Pederson, E. G. Moore, *Soft Matter* **2006**, *2*, 37.

[264] J. P. Bothma, J. de Boor, U. Divakar, P. E. Schwenn, P. Meredith, *Adv. Mater.* **2008**, *20*, 3539.

[265] M. Abbas, M. Ali, S. K. Shah, F. D'Amico, P. Postorino, S. Mangialardo, M. C. Guidi, A. Cricenti, R. Gunnella, *J. Phys. Chem. B* **2011**, *115*, 11199.

[266] M. L. Tran, B. J. Powell, P. Meredith, *Biophys. J.* **2006**, *90*, 743.

[267] J. Riesz, J. Gilmore, P. Meredith, *Spectrochim. Acta Part A Mol. Biomol. Spectrosc.* **2005**, *61*, 2153.

[268] J. Riesz, T. Sarna, P. Meredith, *J. Phys. Chem. B* **2006**, *110*, 13985.

[269] P. Meredith, J. Riesz, *Photochem. Photobiol.* **2007**, *79*, 211.

[270] A. Corani, A. Huijser, T. Gustavsson, D. Markovitsi, P.-Å. Malmqvist, A. Pezzella, M. D'Ischia, V. Sundström, *J. Am. Chem. Soc.* **2014**, *136*, 11626.

[271] S. Meng, E. Kaxiras, *Biophys. J.* **2008**, *95*, 4396.

[272] H. C. Longuet-Higgins, *Arch. Biochem. Biophys.* **1960**, *86*, 231.

[273] A. Pullman, B. Pullman, *Biochim. Biophys. Acta* **1961**, *54*, 384.

[274] B. Rosenberg, E. Postow, *Ann. N. Y. Acad. Sci.* **1969**, *158*, 161.

[275] M. R. Powell, B. Rosenberg, *J. Bioenerg.* **1970**, *1*, 493.

[276] J. E. McGinness, *Science (80-.).* **1972**, *177*, 896.

[277] J. McGinness, P. Corry, P. Proctor, *Science (80-.).* **1974**, *183*, 853.

[278] M. M. Jastrzebska, H. Isotalo, J. Paloheimo, H. Stubb, *J. Biomater. Sci. Polym. Ed.* **1996**, *7*, 577.

[279] M. Abbas, F. D'Amico, L. Morresi, N. Pinto, M. Ficcadenti, R. Natali, L. Ottaviano, M. Passacantando, M. Cuccioloni, M. Angeletti, R. Gunnella, *Eur. Phys. J. E* **2009**, *28*, 285.

[280] M. Ambrico, P. F. Ambrico, A. Cardone, T. Ligonzo, S. R. Cicco, R. Di Mundo, V. Augelli, G. M. Farinola, *Adv. Mater.* **2011**, *23*, 3332.

[281] A. Bernardus Mostert, B. J. Powell, I. R. Gentle, P. Meredith, *Appl. Phys. Lett.* **2012**, *100*, 093701.

[282] A. B. Mostert, B. J. Powell, F. L. Pratt, G. R. Hanson, T. Sarna, I. R. Gentle, P. Meredith, *Proc. Natl. Acad. Sci.* **2012**, *109*, 8943.

[283] A. B. Mostert, K. J. P. Davy, J. L. Ruggles, B. J. Powell, I. R. Gentle, P. Meredith, *Langmuir* **2010**, *26*, 412.

[284] K.-D. Kreuer, S. J. Paddison, E. Spohr, M. Schuster,

Chem. Rev. **2004**, *104*, 4637.

[285] J. Wünsche, Y. Deng, P. Kumar, E. Di Mauro, E. Josberger, J. Sayago, A. Pezzella, F. Soavi, F. Cicoira, M. Rolandi, C. Santato, *Chem. Mater.* **2015**, *27*, 436.

[286] P. Meredith, C. J. Bettinger, M. Irimia-Vladu, A. B. Mostert, P. E. Schwenn, *Reports Prog. Phys.* **2013**, *76*, 034501.

[287] Q. Fan, K. Cheng, X. Hu, X. Ma, R. Zhang, M. Yang, X. Lu, L. Xing, W. Huang, S. S. Gambhir, Z. Cheng, *J. Am. Chem. Soc.* **2014**, *136*, 15185.

[288] M. Ambrico, N. F. Della Vecchia, P. F. Ambrico, A. Cardone, S. R. Cicco, T. Ligonzo, R. Avolio, A. Napolitano, M. D'Ischia, *Adv. Funct. Mater.* **2014**, n/a.

[289] M. Ambrico, P. F. Ambrico, T. Ligonzo, A. Cardone, S. R. Cicco, M. D'Ischia, G. M. Farinola, *J. Mater. Chem. C* **2015**, *3*, 6413.

[290] M. Barra, I. Bonadies, C. Carfagna, A. Cassinese, F. Cimino, O. Crescenzi, V. Criscuolo, D. Marco, M. G. Maglione, P. Manini, L. Migliaccio, A. Musto, A. Napolitano, A. Navarra, L. Panzella, S. Parisi, A. Pezzella, C. T. Prontera, P. Tassini, *MRS Adv.* **2015**, 1.

[291] N. F. Della Vecchia, R. Marega, M. Ambrico, M. Iacomino, R. Micillo, A. Napolitano, D. Bonifazi, M. D'Ischia, *J. Mater. Chem. C* **2015**, *3*, 6525.

[292] A. Pinna, F. Simula, D. Marongiu, A. Pezzella, M. D'Ischia, G. Mula, *RSC Adv.* **2015**, *5*, 56704.

[293] T.-F. Wu, B.-H. Wee, J.-D. Hong, *Adv. Mater. Interfaces* **2015**, *2*, n/a.

[294] R. C. Sealy, J. S. Hyde, C. C. Felix, I. A. Menon, G. Prota, H. M. Swartz, S. Persad, H. F. Haberman, *Proc. Natl. Acad. Sci.* **1982**, *79*, 2885.

[295] W. S. Enochs, M. J. Nilges, H. M. Swartz, *Pigment Cell Res.* **1993**, *6*, 91.

[296] M. Różanowska, T. Sarna, E. J. Land, T. G. Truscott, *Free Radic. Biol. Med.* **1999**, *26*, 518.

[297] L. Panzella, G. Gentile, G. D'Errico, N. F. Della Vecchia, M. E. Errico, A. Napolitano, C. Carfagna, M. D'Ischia, *Angew. Chemie Int. Ed.* **2013**, *52*, 12684.

[298] A. B. Mostert, G. R. Hanson, T. Sarna, I. R. Gentle, B. J. Powell, P. Meredith, *J. Phys. Chem. B* **2013**, *117*, 4965.

[299] S. B. Rienecker, A. B. Mostert, G. Schenk, G. R. Hanson, P. Meredith, *J. Phys. Chem. B* **2015**, *119*, 14994.

[300] A. Batagin-Neto, E. S. Bronze-Uhle, C. F. de O. Graeff, *Phys. Chem. Chem. Phys.* **2015**, *17*, 7264.

[301] P. Meredith, T. Sarna, *Pigment Cell Res.* **2006**, *19*, 572.

[302] M. d'Ischia, A. Napolitano, A. Pezzella, P. Meredith, T. Sarna, *Angew. Chemie Int. Ed.* **2009**, *48*, 3914.

[303] A. A. R. Watt, J. P. Bothma, P. Meredith, *Soft Matter* **2009**, *5*, 3754.

[304] M. d'Ischia, K. Wakamatsu, F. Cicoira, E. Di Mauro, J. C. Garcia-Borron, S. Commo, I. Galván, G. Ghanem, K. Kenzo, P. Meredith, A. Pezzella, C. Santato, T. Sarna, J. D. Simon, L. Zecca, F. A. Zucca, A. Napolitano, S. Ito, *Pigment Cell Melanoma Res.* **2015**, *28*, 520.

[305] J. Cheng, S. C. Moss, M. Eisner, P. Zschak, *Pigment Cell Res.* **1994**, *7*, 255.

[306] J. Cheng, S. C. Moss, M. Eisner, *Pigment Cell Res.* **1994**, *7*, 263.

[307] G. W. Zajac, J. M. Gallas, J. Cheng, M. Eisner, S. C. Moss, A. E. Alvarado-Swaisgood, *Biochim. Biophys. Acta - Gen. Subj.* **1994**, *1199*, 271.

[308] G. W. Zajac, J. M. Gallas, A. E. Alvarado-Swaisgood, *J. Vac. Sci. Technol. B Microelectron. Nanom. Struct.* **1994**, *12*, 1512.

[309] A. Pezzella, A. Iadonisi, S. Valerio, L. Panzella, A. Napolitano, M. Adinolfi, M. D'Ischia, *J. Am. Chem. Soc.* **2009**, *131*, 15270.

[310] M. d'Ischia, A. Napolitano, K. Tsiakas, G. Prota, *Tetrahedron* **1990**, *46*, 5789.

[311] M. d'Ischia, A. Napolitano, A. Pezzella, E. J. Land, C. A. Ramsden, P. A. Riley, **2005**, pp. 1–63.

[312] A. Pezzella, L. Panzella, O. Crescenzi, A. Napolitano, S. Navaratman, R. Edge, E. J. Land, V. Barone, M. D'Ischia, *J. Am. Chem. Soc.* **2006**, *128*, 15490.

[313] L. Panzella, A. Pezzella, A. Napolitano, M. D'Ischia, *Org. Lett.* **2007**, *9*, 1411.

[314] A. Pezzella, L. Panzella, A. Natangelo, M. Arzillo, A. Napolitano, M. D'Ischia, *J. Org. Chem.* **2007**, *72*, 9225.

[315] A. Pezzella, A. Napolitano, M. D'Ischia, G. Prota, *Tetrahedron* **1996**, *52*, 7913.

[316] A. Pezzella, D. Vogna, G. Prota, *Tetrahedron* **2002**, *58*, 3681.

[317] D. S. Galvão, M. J. Caldas, *J. Chem. Phys.* **1988**, *88*, 4088.

[318] D. S. Galvão, M. J. Caldas, *J. Chem. Phys.* **1990**, *93*, 2848.

[319] D. S. Galvão, M. J. Caldas, *J. Chem. Phys.* **1990**, *92*, 2630.

[320] K. B. Stark, J. M. Gallas, G. W. Zajac, M. Eisner, J. T. Golab, *J. Phys. Chem. B* **2003**, *107*, 3061.

[321] K. B. Stark, J. M. Gallas, G. W. Zajac, M. Eisner, J. T. Golab, *J. Phys. Chem. B* **2003**, *107*, 11558.

[322] K. B. Stark, J. M. Gallas, G. W. Zajac, J. T. Golab, S. Gidanian, T. McIntire, P. J. Farmer, *J. Phys. Chem. B* **2005**, *109*, 1970.

[323] J. J. Riesz, J. B. Gilmore, R. H. McKenzie, B. J. Powell, M. R. Pederson, P. Meredith, *Phys. Rev. E* **2007**, *76*, 021915.

[324] E. Kaxiras, A. Tsolakidis, G. Zonios, S. Meng, *Phys. Rev. Lett.* **2006**, *97*, 218102.

[325] S. Meng, E. Kaxiras, *Biophys. J.* **2008**, *94*, 2095.

[326] G. A. Duff, J. E. Roberts, N. Foster, *Biochemistry* **1988**, *27*, 7112.

[327] A. R. Katritzky, N. G. Akhmedov, S. N. Denisenko, O. V. Denisko, *Pigment CELL Res.* **2002**, *15*, 93.

[328] S. Tian, J. Garcia-Rivera, B. Yan, A. Casadevall, R. E. Stark, *Biochemistry* **2003**, *42*, 8105.

[329] J. Zhong, S. Frases, H. Wang, A. Casadevall, R. E. Stark, *Biochemistry* **2008**, *47*, 4701.

[330] S. Chatterjee, R. Prados-Rosales, S. Frases, B. Itin, A. Casadevall, R. E. Stark, *Biochemistry* **2012**, *51*, 6080.

[331] S. Chatterjee, R. Prados-Rosales, S. Frases-Carvajal, S. Tan, B. Itin, H. Wang, A. Casadevall, R. E. Stark, *Biophys. J.* **2013**, *104*, 181a.

[332] D. R. Dreyer, D. J. Miller, B. D. Freeman, D. R. Paul, C. W. Bielawski, *Langmuir* **2012**, *28*, 6428.

[333] S. Senoh, C. R. Creveling, S. Udenfriend, B. Witkop, *J. Am. Chem. Soc.* **1959**, *81*, 6236.

[334] W. H. Harrison, W. W. Whisler, B. J. Hill, *Biochemistry* **1968**, *7*, 3089.

[335] D. C. S. Tse, R. L. McCreery, R. N. Adams, *J. Med. Chem.* **1976**, *19*, 37.

[336] A. O. Patil, W. T. Pennington, G. R. Desiraju, D. Y. Curtin, I. C. Paul, *Mol. Cryst. Liq. Cryst.* **1986**, *134*, 279.

[337] F. Cataldo, *Polym. Int.* **1998**, *46*, 263.

[338] G. Prampolini, I. Cacelli, A. Ferretti, *RSC Adv.* **2015**, *5*, 38513.

[339] C.-T. Chen, C. Chuang, J. Cao, V. Ball, D. Ruch, M. J. Buehler, *Nat. Commun.* **2014**, *5*, DOI 10.1038/ncomms4859.

[340] C.-T. Chen, V. Ball, J. J. de Almeida Gracio, M. K. Singh, V. Toniazzo, D. Ruch, M. J. Buehler, *ACS Nano* **2013**, *7*, 1524.

[341] S. P. Nighswander-Rempel, S. Olsen, I. B. Mahadevan, G. Netchev, B. C. Wilson, S. C. Smith, H. Rubinsztein-Dunlop, P. Meredith, *Photochem. Photobiol.* **2008**, *84*, 613.

[342] C. M. R. Clancy, J. D. Simon, *Biochemistry* **2001**, *40*, 13353.

[343] Y. Liu, J. D. Simon, *Pigment Cell Res.* **2003**, *16*, 606.

[344] S. Reale, M. Crucianelli, A. Pezzella, M. D'Ischia, F. De Angelis, *J. Mass Spectrom.* **2012**, *47*, 49.

[345] M. Arzillo, G. Mangiapia, A. Pezzella, R. K. Heenan, A. Radulescu, L. Paduano, M. D'Ischia, *Biomacromolecules* **2012**, *13*, 2379.

[346] L. Sangaletti, P. Borghetti, P. Ghosh, S. Pagliara, P. Vilmercati, C. Castellarin-Cudia, L. Floreano, A. Cossaro, A. Verdini, R. Gebauer, A. Goldoni, *Phys. Rev. B* **2009**, *80*, 174203.

[347] X. Yu, H. Fan, L. Wang, Z. Jin, *Angew. Chemie Int. Ed.* **2014**, n/a.

[348] J. Yan, L. Yang, M.-F. Lin, J. Ma, X. Lu, P. S. Lee, *Small* **2013**, *9*, 596.

[349] X. Yu, H. Fan, Y. Liu, Z. Shi, Z. Jin, *Langmuir* **2014**, *30*, 549.

2

Experimental and theoretical methods

Raman spectroscopy is a light scattering technique, which was discovered by Sir CV Raman and KS Krishnan in liquid[1–3] and by GS Landsberg and LI Mandelstam in crystal,[4–6] probes the vibrational energy levels of molecules in the ground and excited electronic state. After a photon of frequency ω_0 interacts with an atom or a molecule, apart from being elastically scattered, a small fraction (1 in 10 million) gets inelastically scattered to produce photon that is shifted to lower and higher frequency, known as Stokes and anti-stokes line respectively (Fig. 2.1). In case of Stokes scattering (Fig. 2.1, b) molecule makes a transition from a lower initial state $|i\rangle$ to a higher final vibrational state $|f\rangle$ and shifts the scattered photon (ω_{Stokes}) to red side from incident one ($\hbar\omega_{Stokes} = h\omega_0 - h\omega_v$), h and ω_v being Planck's constant and energy difference between initial and final vibrational state. Jump from an initial state of higher energy to a final state with lower energy produces scattered light that are of higher energy than incident radiation ($\hbar\omega_{anti\text{-}Stokes} = \hbar\omega_0 + \hbar\omega_v$), known as anti-stokes line that are less intense than Stokes ones (Fig. 2.1, c). By measuring the difference ($\Delta E = h\omega_0 - h\omega_S$) in incident ($\omega_0$) and scattered ($\omega_S$) photon frequencies and plotting their intensities against it, we obtain Raman spectra of a molecule. Peaks in a typical Raman spectrum of a molecule correspond to this shift in energy associated with different vibrational transition of various normal modes of the molecule, known as vibrational frequencies.

Vibrational frequencies are a measure of the strength of different chemical bonds of the molecule, and thus, can determine molecular structure. Relative intensities of different Raman active modes provide information on molecular symmetry as well. When excitation frequency does not match with any electronic transition of the molecule, the intermediate states (Fig. 2.1, b and c) are virtual states

rather than an actual excited electronic state, and thus obtained spectra is known as normal Raman spectra. All information contained in such a spectrum corresponds to the molecule in its ground electronic state (abbreviated as GS or S_0 in the remainder of this thesis).

If the virtual state in normal Raman scattering is an actual excited electronic state of the molecule, the resulting Raman process is known as the resonance Raman (RR) effect,[7,8] and is illustrated in Fig. 2.1 d. In the case of RR scattering energy of the incident radiation falls within an electronic absorption band of the molecule and cause a 10^4-10^6 times enhancement in intensity compared to that of normal Raman spectra. By tuning the excitation wavelength RR spectroscopy is suited to interrogate different chromophores selectively in an environment of a large number of different other molecules. An RR spectrum of a molecule contains information about the involved excited electronic state, which the exciting radiation is in resonance with.
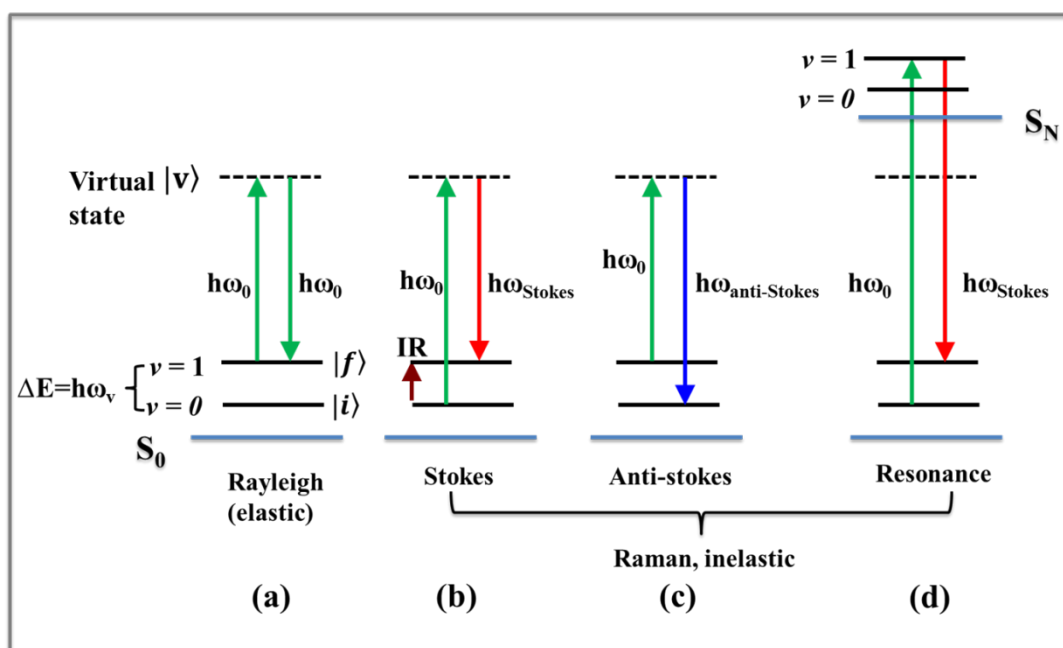
Fig. 2.1 Jablonski diagram of elastic a) Rayleigh scattering, and inelastic b) Stokes Raman, c) anti-Stokes Raman and d) resonance Raman scattering (Stokes). S_0 and S_N correspond to ground and N^{th} excited electronic states respectively. The dash lines represent virtual states. IR absorption between v=0 and v=1 state is depicted in panel (b).

Peticolas and coworkers have first reported RR spectra of purine and pyrimidine nucleotides, with pulsed excitation at 266 nm operating at a low repetition rate.[9,10] With the advent of high repetition rate solid state laser technology, Spiro and

coworkers have pioneered RR spectroscopy with ultraviolet excitation (Ultraviolet resonance Raman or UVRR) to study structure and conformations of nucleobases,[11–14] heme chromophores present in hemoglobin and cytochrome,[15–18] and aromatic amino acids.[19,20] At the same time, Asher and coworkers have also demonstrated the applicability of UVRR spectroscopy to study proteins and their constituents.[21,22] Since then, UVRR has been successfully exploited to investigate structure and hydrogen bonding strength with surrounding environment, and solution state tautomerism in nucleic acid bases,[23–33] and several other biomolecular systems.[34–51] Advancement of UVRR spectroscopy in investigating biomolecules,[52–67] specifically nucleobases[68–71] has been reviewed in several articles. Over the years, several Raman-related experimental techniques have been developed to probe structural dynamics of biomolecules, covering timescales in the range of tens of femtoseconds to several hundreds of nanoseconds.[72–83]

One of such methodologies is an analysis of modulation of resonance Raman intensity of a molecule with respect to a change in energy of resonant excitation. The plots of RR intensities of the Raman-active normal modes as a function of excitation wavelength are known as Raman excitation profiles (REP). These REPs encode information about the fate of the molecule in its excited electronic state.[10,84–90] Specifically, it can describe initial structural dynamics of a chromophore and the solvent response within a time scale of the Raman process *i.e.*, few tens of femtosecond (fs) after photoexcitation. This method has been successfully applied to several biomolecular systems including nucleobases,[91–100] aromatic amino acids,[101,102] chromophore embeded in proteins,[73,103,104] and other molecular systems.[72,105–112] RR intensities of a normal mode is very sensitive to change in a gradient along associated normal coordinate on the resonant vibronic surface, and so does the line-shape of REPs. Experimentally measured REPs can also reveal vibronic features that are not hidden under the envelope of diffuse absorption spectra and can also probe interference between close lying electronic states.[113–116]

The strong vibrational modes in a resonance Raman spectrum derive their intensities from a change in geometry of the molecule in the excited electronic state due to photoexcitation and cause a shift in the excited state potential energy surface (PES) relative to that in S_0 (Fig. 2.2). This shift is known as "dimensionless displacement", Δ_K along a normal coordinate, Q_K. The vibrational modes with maximum Δ, also known as "Franck-Condon" active modes contribute to the line shape of REP and as well as of absorption spectrum. Higher the Δ, higher is the RR

intensity of a mode and thus, RR spectra can potentially determine excited state structure of a molecule.
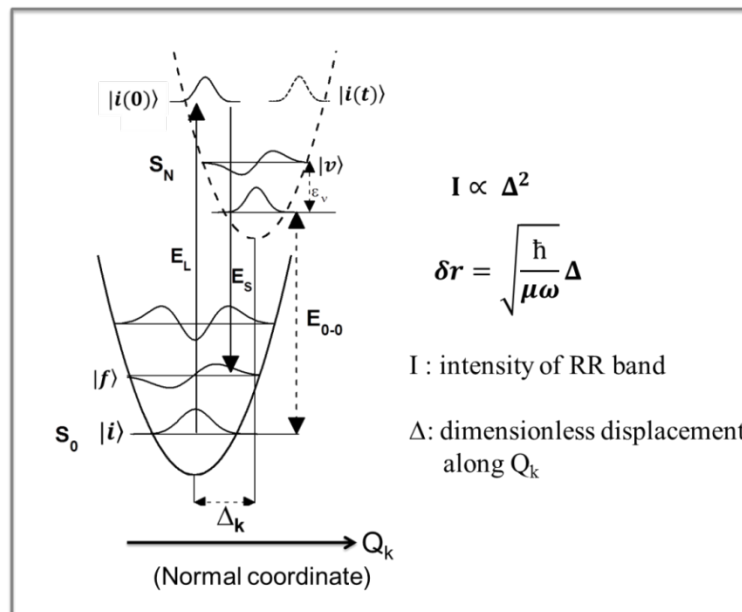
Fig. 2.2 One dimensional time-dependent picture of resonant Raman and absorption process along normal coordinate, Q_k. E_L and E_S are the incident and scattered photon energies. S_0 and S_N represent ground and resonant electronic state respectively. E_{0-0} is electronic zero-zero energy and ϵ_v is the vibrational energy of intermediate state, and Δ is the dimensionless displacement of the kth normal mode between the minima of the ground and excited state potential energy surface along Q_k.

Line-shape of REP is also affected by factors such as homogeneous and inhomogeneous broadening contributions that affect absorption line-shape also. While homogeneous broadening arises from interaction of the photo-excited molecule with surrounding solvent molecules in an ultrafast time scale (sub-ps), and slightly different micro-environment of different solute molecules gives rise to inhomogeneous broadening. Because of similar resulting effect on absorption cross-section, analysis of absorption spectra alone can not differentiate between two broadening mechanisms.[72,86,105,117] However, because of differential effects on RR line-shape, the two broadening mechanisms can be delineated by analysis REP. Quantitative estimation of the contribution of the homogeneous and inhomogeneous broadening, along with dimensionless Δ's is possible from a simultaneous analysis of absorption and REP.

A theoretical framework that can describe both the absorption and RR process in a cohesive manner within the same set of theoretical approximations and encompass parameters to capture different broadening mechanisms is necessary for the mentioned purpose. Additionally a model that describes solute-solvent interaction in an ultra-fast

time scale in the context of the response to immediate environment due to charge reorientation in the solute, upon photo-excitation has also to be applied. Theoretical background, describing absorption and Raman scattering starting form Kramer-Heisenberg-Dirac (KHD) formalism the theoretical model that has been used in this thesis for analysis of experimental REPs of various nucleobases have been described in theoretical and computational methods section.

2.1 Experimental methods

2.1.1 Ultraviolet resonance Raman spectroscopy

Experimental setup for UVRR experiments

A Ti-Sapphire oscillator is pumped by an intracavity doubled nanosecond (ns) pulsed Nd:YLF laser (527 nm) of 1 kHz repetition rate (Fig. 2.3, panel a) was also used as a 260 nm light source (Coherent Inc, Santa Clara, CA, USA). The output of Ti-Sapphire fundamental (Fig. 2.3, panel b) which is tunable from 771 nm to 840 nm is frequency doubled (385.5 nm to 420 nm) by passing through barium borate (BBO) crystal (Fig. 2.3, panel c). The third harmonic (say 260 nm) of the fundamental is generated by the mixing of the second harmonic (visible at 390 nm) and the fundamental (IR at 780 nm) of the Ti-Sapphire output and was used as RR excitation source.

Another tunable Ti:sapphire laser which is pumped by 527 nm output of a Nd:YLF diode laser (Photonics Industries, Bohemia, NY, USA) produces fundamental IR line between 840-920 nm with 25 ns pulse width and 1 kHz repetition rate. (Fig. 2.4) Intracavity frequency doubled 4th harmonic of this fundamental, generated via passing is through temperature controlled lithium borate (LBO) crystal is used as deep-UV excitation source between 210-230 nm.

The scattered light was collected through collecting lens in 135° backscattering geometry and is dispersed by a monochromator with a focal length of 1.25 m and equipped with a holographic grating with 3600 grooves/mm before detected on a 1024 x 256 pixel CCD chip (HORIBA Scientific, Edison, NJ, USA). For each excitation wavelength, the final spectrum was obtained by averaging the recorded spectra of three freshly prepared samples.
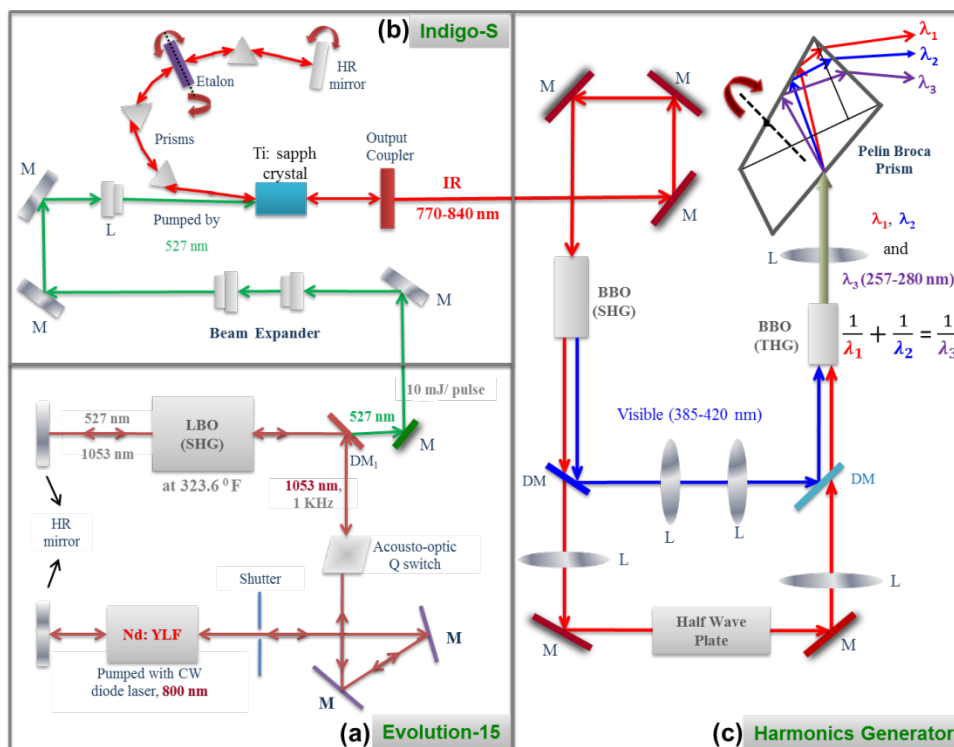
Fig. 2.3 Optical components and Ray diagram of the tunable nanosecond Ti:sapphire laser operating at 1 kHz repetition rate, and from 257 to 280 nm of 3rd harmonic (UV) output. Abbreviations, M: reflective mirror; DM: dichroic mirror; HR: high-reflection; L: lens; BBO: Beta Barium Borate; LBO: Lithium Triborate; SHG: second harmonic generator; THG: third harmonic generator

The typical laser power, incident on the sample was ~0.6 mW and an entrance slit of monochromator was set at 300 μm for optimum signal and spectral resolution. The samples were kept in a tube, made of suprasil quartz (Wilmad-Lab Glass, Vineland, NJ, USA). To reduce photodamage, the tube was made to rotate along its axis. A teflon coated magnetic bead of 2 mm in size was kept inside tube for stirring the sample. The experimental setup is described in Fig. 2.5.

All Raman spectra were fitted using Lorentzian line-shape to determine the intensity (area under the curve) and the band positions using synergy software that runs origin 5.0 (HORIBA Scientific, Edison, NJ, USA). The recorded spectra were calibrated using known band positions of organic solvents (HPLC grade) such as cyclohexane, acetonitrile, isopropyl alcohol, dimethylformamide, dimethyl sulfoxide, indene, ethyl acetate within ± 2 cm^{-1}. Typical spectral processing of a recorded Raman spectrum in described in Appendix I.
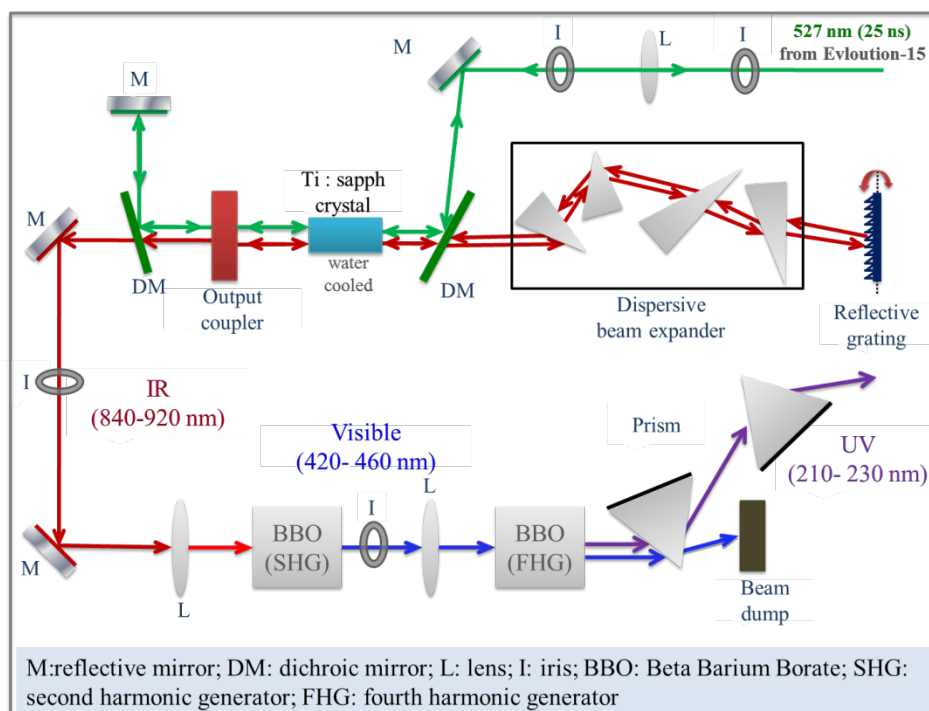
Fig. 2.4 Optical components and Ray diagram of the another tunable ns Ti:sapphire laser operating from 840 nm to 920 nm of fundamental (210 nm to 230 nm of fourth harmonic).
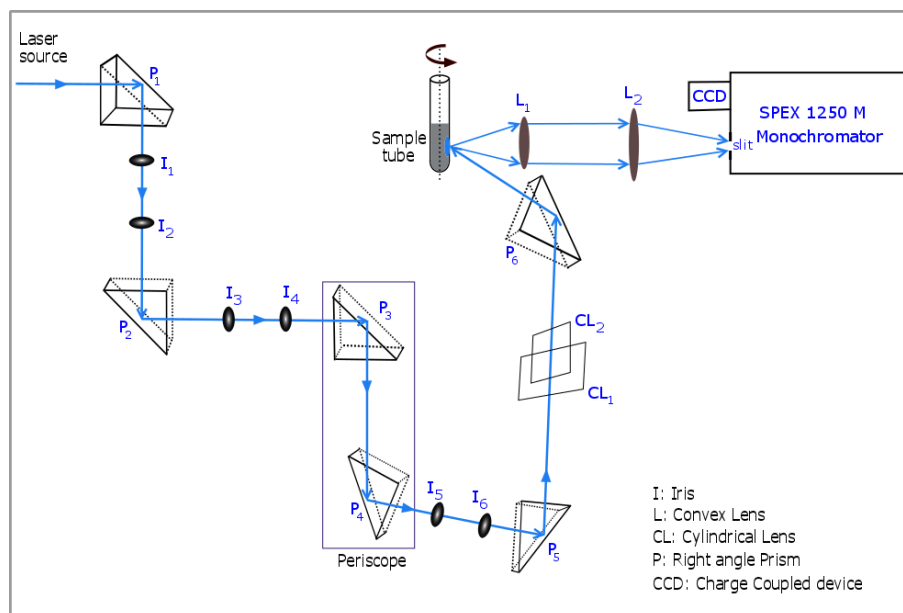
Fig. 2.5 Optical arrangement for the excitation and collection optics to record resonance Raman spectra.

Depolarization ratio measurement

Polarization characteristics of spontaneous Raman scattered radiation is physically described by Raman depolarization ratio, defined as

$$\rho = \frac{I_\perp}{I_\parallel} \qquad\qquad\qquad (2.1)$$

with $I_\perp$ and $I_\parallel$ being the intensities of Raman scattered photons having electric vector polarized in perpendicular and parallel directions respectively, to that of incident laser light. Parallel and perpendicular component of the scattered light was collected by monochromator by passing through a α-BBO Glan-laser polarizer (Thorlabs Inc., Newton, NJ, USA) placed in front of the spectrometer slit (Fig. 2.6). To get rid of the polarization dependence of the spectrometer detection a depolarizer or polarization scrambler was placed between the polarizer and the spectrometer slit. Applicability of the described method is verified by measuring depolarization ratio of acetonitrile, sodium perchlorate and sodium nitrate and comparing them with published values (Table 2.1).
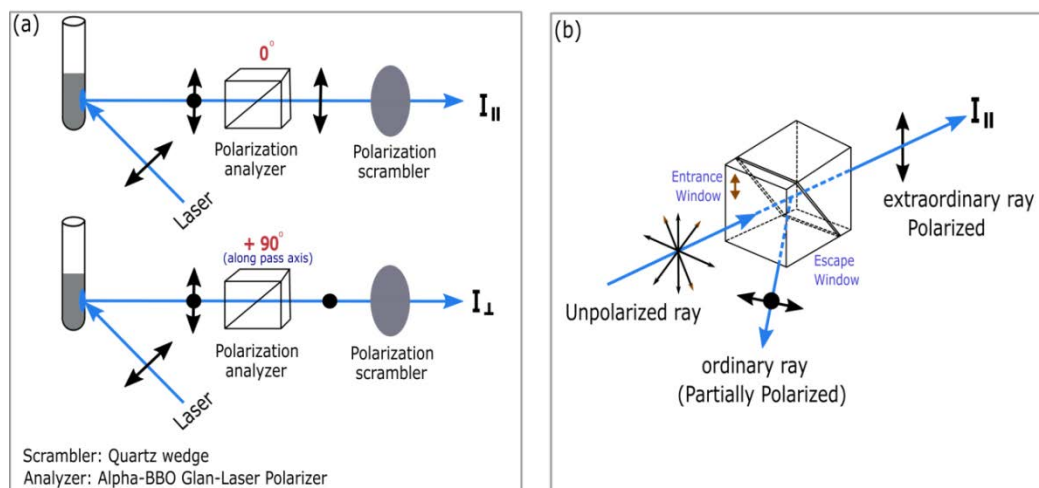
Fig. 2.6 Optical setup for measurement of the depolarization ratio. (a) The 135 ° backscattered Raman photons are filtered using a Glan-laser prism polarizer. Next, a polarization scrambler (quartz wedge) was employed before spectrometer entrance slit to eliminate polarization dependence of the spectrometer; (b) Working principal of a Glan-laser polarizer used in this study.

Spectrometer and detector efficiency

Recorded intensities of each band get altered because intensities of scattered light of different energies are detected with different efficiencies on the detector. This is because of the wavelength dependence of the throughput of the spectrometer and detection

sensitivity of the CCD detector. A recorded spectrum from sample can be corrected by measuring spectrometer efficiency, which is a function of wavelength as

$$S_\lambda = \frac{D_\lambda}{T_\lambda} \tag{2.2}$$

where D_λ is the spectrum of a NIST (National Institute of Standards and Technology, MD, USA) calibrated D_2O lamp (Ocean Optics Inc, FL, USA) recorded at a same grating position corresponding to each excitation wavelength? T_λ is the calibrated output (Cosine corrected irradiance in $\mu w/cm^2/nm$) of the same lamp. Representative example of $S_\lambda, D_\lambda, T_\lambda$ is shown in Fig. 2.7.

Corrected intensity of each Raman band ($I_{corrected}$) of sample is determined through the relation,

$$I_{corrected}(\lambda) = \left(\frac{I_N}{I_S}\right)\left(\frac{S_{\lambda_S}}{S_{\lambda_N}}\right) \tag{2.3}$$

where I_N and I_S are the intensity of Nth band of the sample and of the band of internal standard and are measured as areas under the Lorentzian curve for corresponding bands. A sample spectrum at 230 nm excitation is shown in before and after correction in Fig. 2.8. (for detailed steps see Appendix II)
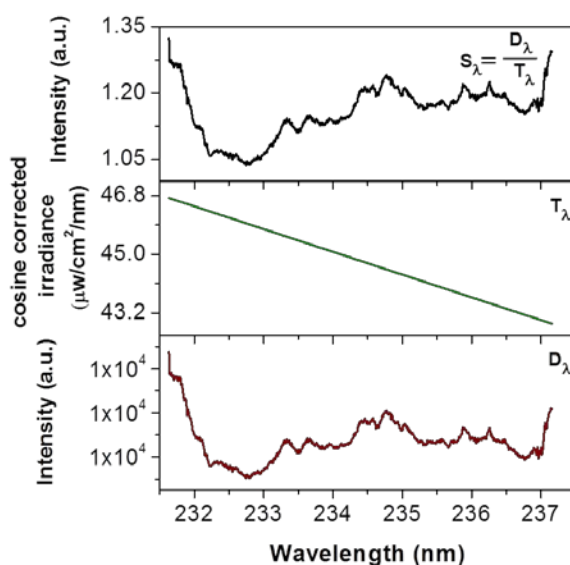
Fig. 2.7 True output of NIST calibrated standard lamp, T_λ (bottom), recorded spectrum of the same lamp, D_λ (middle) and spectrometer efficiency function, $S_\lambda = D_\lambda / T_\lambda$ (top) measured with the same monochromator grating position as that is used to record spectra of sample with 230 nm excitation wavelength.

Table 2.1 Depolarization ratio for different Raman bands of standard solvents obtained at 220 nm excitation wavelength.

Solvent	Wavenumber (cm^{-1})	Depolarization ratio, λ_{exc}=220 nm[a]	Depolarization ratio, λ_{exc}=220 nm[b]
NaNO$_3$	1045	0.21	0.19 ± 0.05
NaClO$_4$	932	0.018	0.04 ± 0.02
Acetonitrile	919	0.078	0.08 ± 0.02
	1375	0.50	0.45 ± 0.06

[a]this work; [b] values from Ref [118]
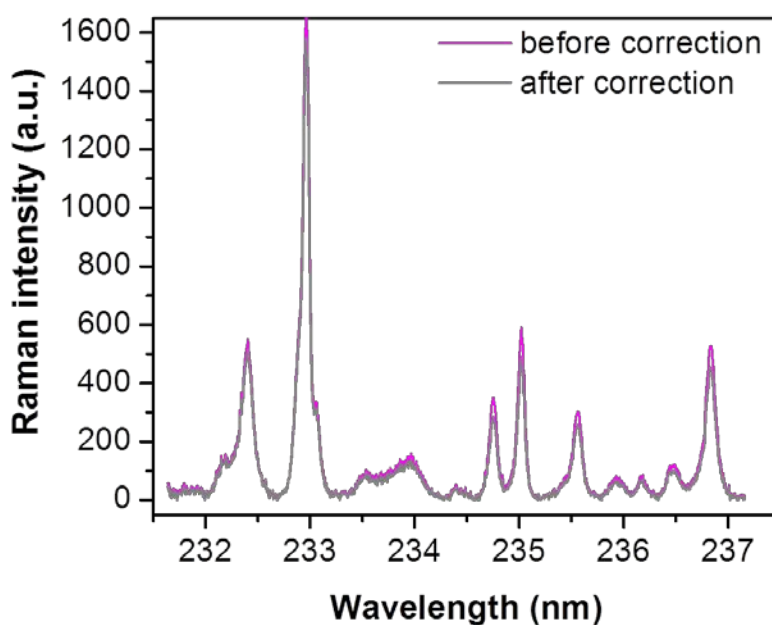
Fig. 2.8 Spectra of 6-ClGua with and without correction using function S_λ described in Fig. 2.7. Differences in relative intensities between corrected and raw spectra at both ends of the recording region point out differential wavelength-dependent response of spectrometer and CCD detector.

Self-absorption correction

Scattered resonance Raman photons of different energies get self-absorbed by the molecule itself because of the presence of significant absorption cross-section in the same energy region. The measured intensity of the RR bands has been corrected for self-absorption contribution by introducing the factors $K(\lambda_N, \lambda_S)$ [119]

$$K(\lambda_N, \lambda_S) = \frac{\varepsilon_N \chi + \varepsilon_0}{\varepsilon_S \chi + \varepsilon_0} \tag{2.4}$$

where ε_S and ε_N are the extinction coefficients at the wavelength position of the Raman band of internal standard and sample respectively. ε_0 is the extinction coefficient of sample at the excitation wavelength, and

$$\chi = sin\left(\cos^{-1}\left(\frac{n_1}{n_2}\right)\cos\varphi\right) \tag{2.5}$$

with n_1 and n_2 being the values of the refractive index of the air and the liquid sample. n_1 and n_2 are assumed here to be 1.0 and 1.33 (water) respectively. φ, the angle between the excitation light and the sample tube is $=45°$ in the case of 135° backscattering geometry. Backscattering geometry was used for collection of the Raman scattered photons to minimize loss of signal due to the self-absorption of the sample. Additionally, for every experiment care has been taken so that the excitation beam was focused near the surface of the quartz tube and thus propagation length of the Raman photons through the sample was minimized to reduce self-absorption.

Experimental resonance Raman cross-section

The absolute resonance Raman cross-sections (Å^2/molecule) of each vibrational band have been determined using known Raman cross-section of the internal standard ($NaClO_4$), using the relation, [89]

$$\sigma_N = \frac{8\pi}{3}\left(\frac{1+2\rho}{1+\rho}\right)_N\left(\frac{C_S}{C_N}\right)I_{corrected}(\lambda)\left(\frac{\partial\sigma_S}{\partial\Omega}\right)_{\|+\perp}K(\lambda_N,\lambda_S) \tag{2.6a}$$

where C_N and C_S are concentrations of the sample and internal standard respectively. $\left(\partial\sigma_S/\partial\Omega\right)_{\|+\perp}$ is the total differential cross-section of the internal standard and ρ is the depolarization ratio of the Nth Raman band of the sample. $I_{corrected}$ is described in eqn. 2.3.

Differential Raman cross-section of the internal standard

$(\partial\sigma_S/\partial\Omega)_{\|+\perp}$, the total differential cross-section of the internal standard ($NaClO_4$) is determined according to,[120]

$$\left(\frac{\partial\sigma_S}{\partial\Omega}\right)_{\|+\perp}(v_0) = K_2v_0(v_0-v_s)^3\left[\frac{v_e^2+v_0^2}{(v_e^2-v_0^2)^2}\right]^2 \tag{2.6b}$$

where ν_0 and ν_e are frequencies of the Raman excitation source and the Raman band of the internal standard respectively. For $NaClO^4$, Asher and coworkers have previously obtained the values of the parameters; $K_2 = 2.34$ x 10^{16} $\mathring{A}^2$/molecule x sr and $\nu_e = 1.28$ x 10^5 cm^{-1}.[120] These values are used to determine the total cross-section of the band at 934 cm^{-1} of $NaClO^4$ used as internal intensity standard.

Experimental absorption cross-section

The absolute absorption cross-sections ($\mathring{A}^2$/molecule) were determined using the relation,

$$\sigma_A = \frac{2.303 \times 10^{19} \times \epsilon}{N_A}$$ (2.7)

where ϵ is the extinction coefficient of the sample in cm^{-1} M^{-1} and N_A is the Avogadro's number.

2.1.2 Atomic Force Microscopy

Right after discovering scanning tunneling microscope (STM) in 1981,[121] Binnig and coworkers have also invented the atomic force microscope (AFM) in 1986.[122] AFM is a subclass of a large family of scanning probe microscopy (SPM) techniques. In all SPM enabled instruments, a tip is raster-scanned across the surface of the sample in xy plane to measure surface properties such as the electrical, magnetic or mechanical properties, and a topographical map of these measured properties are constructed to form an image.

Electron microscopes (SEM) can achieve very high (~ 1 $\mathring{A}$ or 0.1 nm) spatial resolution, but information along vertical dimension cannot be obtained. On other hand, both AFM and STM techniques are unique methods that can probe atomic, molecular and domain features in three dimensions, with resolutions reaching down similar to those in SEM. Unlike, STM that requires dry, conducting surface and high quality of vacuum for atomic resolution, AFM allows measurement of surface topography on almost all surfaces including insulating ones. Owing to its intrinsic ability to perform measurement at ambient room temperature and even in liquid, AFM became one of the most important tools in investigating structure (topography imaging), and mechanical properties, such as, local friction and stiffness (force spectroscopy) of biological samples. [123–126]

An AFM instrument consists of a cantilever and sample assembly, the laser and photodiode detector for optical detection, and the feedback and measurement electronics

(Fig. 2.9). The principle of AFM operation is measuring the force between a sharp tip and the sample surface. A typical tip is usually made of silicon (Si) or silicon nitride (Si_3N_4) with an end radius of curvature 2-20 nm and a height of 5-25 um and is mounted at the end of a cantilever (acting as a spring) with known force constant. In AFM, a laser beam is shined upon the cantilever and is reflected towards a position sensitive quadrant photodiode. The bending of the cantilever, resulting from the tip-sample interaction is measured by tracking displacement of the laser spot on the detector, and thus a height of the tip from the sample surface is probed.
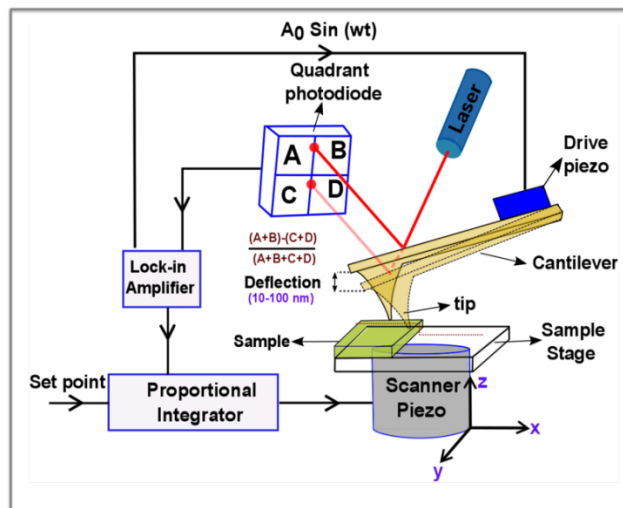
Fig. 2.9 Schematic of an atomic force microscope (AFM) operating in tapping mode.

There are two key modes of operation of an AFM: contact mode (CM) and intermittent-contact mode or tapping mode (TM). In CM, a tip is brought down onto the sample surface and topography is recorded in xy-plane through measurement of the deflection of the cantilever. As soon as the height of the first point is measured and tip approaches the second point, a feedback loop adjusts the z height of the tip relative to the probed surface. This method of tracking height features is known as constant force mode because the tip-sample distance is always maintained at a set point throughout imaging. The other mode, constant height mode in which the position of the z scanner and therefore position of the cantilever is locked at a predefined value and deflection of the cantilever is measured across xy-plane to reveal the topography of the surface. This mode has a chance of damaging the tip for the sample with protruding features and the constant force mode is preferable. In these modes operations, tip resides in a repulsive region of force curve. (Fig. 2.10)

In tapping mode (TM), the cantilever oscillates near its resonance frequency with a piezoelectric modulator and topography is measured by utilizing the attractive inter-atomic force between the tip and a sample surface. (Fig. 2.10) In this mode of operation, the tip only touches the sample at the lowest point of the oscillation cycle. As the tip approaches sample, the attractive van der Waals force (and other present interactions) between the tip and the sample affects both the amplitude and the frequency of the cantilever oscillation. These changes drive a feedback loop and control the tip-sample distance using piezo scanner mounted below sample stage. Typical cantilever used in TM has spring constant between 10-100 N/m. Lateral force exerted on sample surface during raster scanning are much lower in this mode compared to that in contact mode. Thus, tapping mode is a better choice than contact mode for imaging samples that are likely to be damaged or dislocated by dragging forces. AFM has been routinely used in investigation of soft biological samples, such as folding and unfolding,[127,128] and aggregation of individual protein molecules, nucleic acid,[129,130] mechanical properties of supported membrane and lipid bilayer,[131] and shape and plasticity of individual live cells.[132][133]
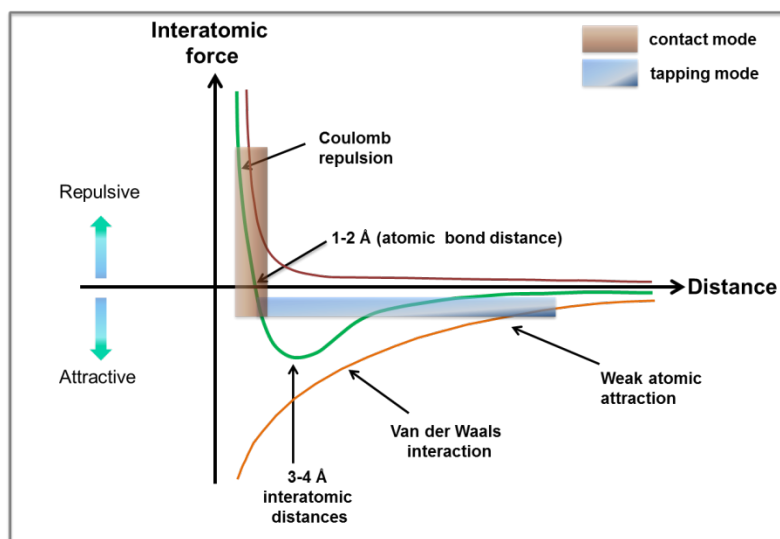
Fig. 2.10 Different regime of interatomic force curves during the tip-sample interaction.

The supramolecular assembly of the biopigment melanin is held together by a variety of non-covalent interactions including van der Walls, π-π, dipole-dipole and ionic forces. Even when deposited, melanin particles are non-covalently attached to the substrate, and can easily be dislodged by lateral force acted during imaging in CM. To avoid tip-induced damage and also contamination of tip due to sticky surface, TM-AFM has been used to study self-organization of melanin from natural and synthetic source. I

have used TM-AFM in amplitude modulation mode in a commercial AFM instrument (JPK Instruments AG, Berlin, Germany) coupled with super sharp (end radii ~ 2 nm) Si tip (Nanosensors, SSS-NCHR-50) to reveal aggregation dynamics of a model melanin polymer deposited on an atomically mica surface.

2.1.3 Confocal Raman microspectroscopy

A LabRAM HR800 confocal Raman microscope (HORIBA Jobin Yvon SAS, rue de Lille, France) equipped with an Ar^{2+} laser of 488 nm and a helium-neon diode laser operating at 785 nm was used. For typical samples, such as fixed cells, a power of 30-40 mW at the sample surface was used. A water immersion achromatic objective of 60x magnification and a numerical aperture of 1.33 was employed for excitation and maximal collection of Raman scattered photons in an 180° backscattering geometry. (Fig 2.11) Raman spectrum was recorded on a liquid nitrogen cooled CCD chip after dispersing through an 800 mm focal length spectrograph equipped with an 1800 grooves/mm grating. The recorded spectra were calibrated using 527 cm^{-1} Raman band of Si.
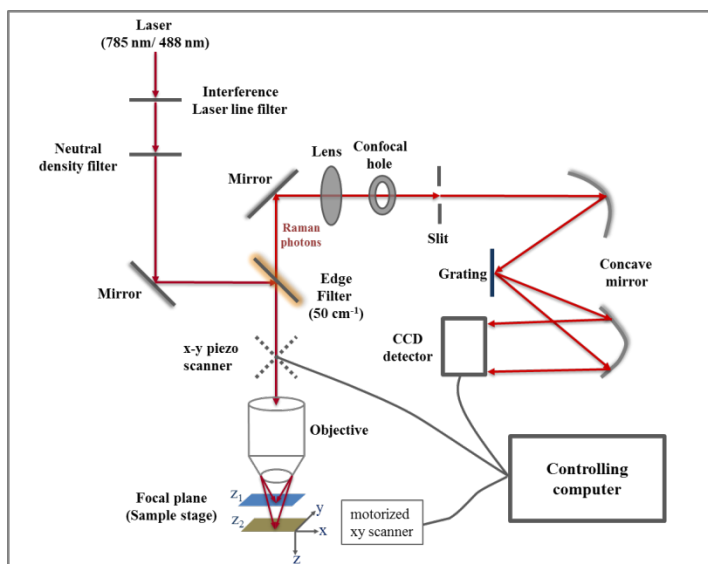
Fig. 2.11 Optical ray diagram of confocal Raman setup

2.2 Theoretical and computational methods

2.2.1 Kramer-Heisenberg-Dirac (KHD) formalism

Raman scattering can be explained by considering a two-photon process where the system reaches the final vibrational state $|f\rangle$, by emitting a photon of energy E_F from an intermediate state $|n\rangle$ which is accessed by absorbing a photon of energy E_I from an

initial vibrational state $|i\rangle$. The $\rho\sigma^{\text{th}}$ component of the general transition polarizability tensor α, as derived by Kramers and Heisenberg[134] and later modified by Dirac[135] (KHD) using second order time-dependent perturbation theory reads as,

$$(\alpha_{\rho\sigma})_{IF} = \sum_{N \neq I,F} \frac{\langle F|\vec{\mu}_\rho|V\rangle\langle V|\vec{\mu}_\sigma|I\rangle}{(E_V - E_I) - E_0 - i\Gamma_V}$$

$$+ \frac{\langle F|\vec{\mu}_\sigma|V\rangle\langle V|\vec{\mu}_\rho|I\rangle}{(E_V - E_F) + E_0 - i\Gamma_V} \tag{2.8}$$

E_0 is the energy of the incident photon and E_I, E_V, and E_F are the energy of the initial $|I\rangle$, intermediate $|V\rangle$ and final $|F\rangle$ wave functions of the vibronic states respectively. μ_ρ and μ_σ are the ρth and σ^{th} component of induced electric transition dipole moment operator in cartesian coordinate. $2\Gamma_N$ is the energy full width at half maxima of the state $|V\rangle$. It represents the homogeneous linewidth of the electronic transition due to the finite lifetime (τ_V) of the intermediate vibrational states related through uncertainty relation as, $\tau_N = 1/4\pi c\Gamma_N(\tilde{\nu})$ where Γ_N is expressed in wavenumber unit (cm^{-1}) and c is speed of light in vacuum. For initial and final sates $|I\rangle$ and $|F\rangle$, it is assumed that their lifetimes are infinite because they are real eigenstates of the system. It is worth to mention that $|I\rangle$, $|V\rangle$ and $|F\rangle$ are time-independent unperturbed wave functions of the states I, V and F. Time-dependent wave functions of these states are given by $|N(t)\rangle = |N\rangle \exp -i(\omega_N - i\Gamma_N)t$ where $\omega_N = E_N/\hbar$.

In normal Raman spectroscopy when energy of exciting radiation is much smaller than any absorption frequency of the molecule, i.e. $E_0 \ll (E_V - E_F)$, $(\alpha_{\rho\sigma})_{IF}$ will be weighted sum over the all intermediate states $|V\rangle$ of the products $\langle F|\mu_\rho|V\rangle\langle V|\mu_\sigma|I\rangle$ and the weighting factor being inversely proportional to $(E_V - E_I) - E_0 - i\Gamma_V$. Thus as natural Raman scattering is perceived as involving all possible pathways through virtual states $|V\rangle$ connecting the initial state $|I\rangle$ and the final state $|F\rangle$, it does not provide us with information about any particular intermediate state $|V\rangle$. In contrast, in case of resonance Raman only the states $|V\rangle$ for which $E_0 \approx (E_N - E_F)$ will predominate in the sum over states of eqn. 2.8, because denominator of the first term becomes very small where same of the second term cannot become smaller than the former. Practically there is limited number of intermediate $|V\rangle$ states when incident radiation energy is in resonance with a molecular electronic transition. During resonance with an electronic excited state, intermediate sates $|V\rangle$ will be vibrational levels of the excited electronic states and detailed information about these vibronic states can be obtained through analyzing resonance Raman (RR) intensities as explained in later section.

Born-Oppenhiemer approximations

KHD equation 2.8 can be simplified by physically meaningful assumptions which are justified for realistic experimental conditions to evaluate $(\alpha_{\rho\sigma})_{IF}$. First of these is Born-Oppenhiemer approximations[136] which helps us to separate fast electronic motion from relatively slow nuclear movement in a molecule. Born-Oppenhiemer approximation allows the wavefunctions of the vibronic states to be written as a product of the electronic and vibrational wavefunctions as follows,

$$|I\rangle = |gi\rangle = |g(r,Q)\rangle|i(Q)\rangle \tag{2.9a}$$

$$|F\rangle = |gf\rangle = |g(r,Q)\rangle|f(Q)\rangle \tag{2.9b}$$

$$|V\rangle = |ev\rangle = |e(r,Q)\rangle|v(Q)\rangle \tag{2.9c}$$

Here r and Q are the electronic and nuclear coordinates respectively. $|g(r,Q)\rangle|$ and $|e(r,Q)\rangle|$ are pure electronic wavefunction of ground and excited electronic states respectively. $|f(Q)\rangle$, $|i(Q)\rangle$, and $|v(Q)\rangle$ stand for the corresponding vibrational states depending parametrically on the nuclear coordinate. By using eqns. 2.9a–2.9c each of the product term of eqn. 2.8 can be written as,

$$\langle F|\vec{\mu}_\rho|V\rangle = \langle f(Q)|\langle g(r,Q)|\vec{\mu}_\rho(Q)|e(r,Q)\rangle|v(Q)\rangle\rangle \tag{2.10a}$$

$$= \langle f(Q)|\vec{\mu}_{ge}(Q)|v(Q)\rangle \tag{2.10b}$$

Where $\vec{\mu}_{ge}(Q)$ is the electronic transition dipole element operator for $g \rightarrow e$ transition. Clearly $\vec{\mu}_{ge}(Q)$ depends on the nuclear degrees of freedom through the parametric dependence of the electronic wavefunctions on coordinate Q. A Taylor series expansion of $\vec{\mu}_{ge}(Q)$ around the equilibrium geometry Q_0 of the ground state gives,

$$\vec{\mu}_{ge}(Q) = \vec{\mu}_{ge}(Q_0) + \sum_k \vec{\mu}_{ge}{}' \boldsymbol{Q_k} + \cdots = eM \tag{2.11}$$

Where $\vec{\mu}_{ge}{}' = \frac{\partial \vec{\mu}_{ge}(Q)}{\partial Q_k}$ and e is the electronic charge and M is the transition dipole length.

Condon approximation

With the application of Condon approximation,[137–139] *i.e.* magnitude of $\vec{\mu}_{ge}(Q)$ at equilibrium geometry Q_0 is much larger than the variation of the transition dipole length over the range of accessible Q, only the term linear in Q of the series is important to consider and terms containing explicit dependence on nuclear coordinate are dropped. As only one electronic state is accounted for, it is always possible to choose the coordinate system in such a way that only one component of the transition moment vector is nonzero, i.e. the operator $\vec{\mu}_{ge}(Q_0)$ becomes a scalar quantity eM, evaluated at electronic ground state minima.

Under resonance conditions, as the first term of KHD equation becomes very large compared to the second term and exploiting Born-Oppenheimer and Condon approximation as described above, eqn. 2.1 becomes,

$$\alpha_{if} = \sum_v \left[\frac{eM\langle f(Q)|v(Q)\rangle eM\langle v(Q)|i(Q)\rangle}{(E_v - E_i + E_{00} - E_L - i\Gamma_v)} \right]$$

$$= e^2 M^2 \sum_v \left[\frac{\langle f|v\rangle\langle v|i\rangle}{\varepsilon_v - \varepsilon_i + E_{00} - E_L - i\Gamma} \right] \tag{2.12}$$

where M the transition dipole moment length. E_{00} is the energy difference between the ground vibrational states of the electronic ground and excited state potential energy surface. ε_v and ε_i are the energy of the vibrational states $|v\rangle$ and $|i\rangle$ respectively. Dependence of transition dipole moment on cartesian coordinate can be eliminated conveniently by choice of direction of electric field vector of incident laser so that only $\mu_{ge}(Q_0)$ is nonzero.

Now for a randomly oriented molecule the total Raman cross-section integrated over all directions and polarization is given by sum-over-state expression,

$$\sigma_{i \to f}(E_L) = \frac{8\pi e^4 E_S^3 E_0}{9\hbar^4 c^4} \sum_{\rho\sigma} \left|(\alpha_{\rho\sigma})_{if}\right|^2$$

$$= \frac{8\pi e^4 M^4 E_S^3 E_L}{9\hbar^4 c^4} \left| \sum_v \frac{\langle f|v\rangle\langle v|i\rangle}{\varepsilon_v - \varepsilon_i + E_{00} - E_L - i\Gamma} \right|^2 \tag{2.13}$$

At the same level of approximation, the optical absorption cross-section can be expressed as sum over all vibronic transitions weighted by respective Franck-Condon factor, $|\langle v|i\rangle|^2$ as,

$$\sigma_A(E_L) = \frac{4\pi^2 e^2 M^2 E_0}{3\hbar c n_i} \sum_v \frac{\Gamma}{\pi} \frac{|\langle v|i\rangle|^2}{(\varepsilon_v - \varepsilon_i + E_{00} - E_L)^2 + \Gamma} \tag{2.14}$$

where n_i is the refractive index of the medium.

In principal, evaluation of Raman and absorption cross-section according to eqns. 2.13 and 2.14 are only possible if an infinite number of overlap integrals with all intermediate vibrational states are considered. Though the vibrational overlap decreases with higher vibronic states in case of resonance with an electronic state, for a moderate size (20–50 atoms) system tens of thousands intermediate states have to be considered for a good convergence of both the equations. An alternative approach *i.e.* time dependent wave packet (TDWP) propagation theory of RR intensities,[84] which have been introduced in next section has been used in this thesis. The theoretical formulation of TDWP is worked out in the next section starting from the sum-over-states approach.

2.2.2 Time dependent theory of resonance Raman scattering

Among two popular formalisms; transform theory[10,85,88,140–147] and TDWP method,[84,86,89,90] the latter has been employed for analyzing experimental resonance Raman excitation profile for the molecular systems studied in this thesis. After the first conception of TDWP theory by Lee and Heller,[84] this method has been first used by Myers and coworkers for determining initial structural dynamics of photoexcited polyenes and other systems.[117] Since then it has been a popular choice for investigating initial excited state dynamics of a variety of molecular system, starting from small aliphatic polyenes,[148,149] alkyl halides,[150] medium sized molecules[72,151–158] including nucleic acid bases,[91,93–99] to chromophores buried inside protein core.[73,103,104,112]

The TDWP expressions for absorption and Raman cross-section can be obtained by converting the sum-over-state formulae 2.13 and 2.14 into time domain by expressing

the denominators of the sum into a full and half-Fourier transform respectively as,[86,90,148,159–161]

$$\sigma_{i \to f}(E_L) = \frac{8\pi e^4 M^4 E_S^3 E_L}{9\hbar^6 c^4} \left| \int_0^\infty \langle f|i(t)\rangle \exp\left[\frac{i(E_L + \varepsilon_i)t}{\hbar}\right] \exp\left(-\frac{\Gamma t}{\hbar}\right) dt \right|^2 \qquad (2.15\ a)$$

and

$$\sigma_A(E_L) = \frac{4\pi e^2 M^2 E_L}{6\hbar^2 cn} \left| \int_{-\infty}^\infty \langle i|i(t)\rangle \exp\left[\frac{i(E_L + \varepsilon_i)t}{\hbar}\right] \exp\left(-\frac{\Gamma t}{\hbar}\right) dt \right| \qquad (2.15\ b)$$

where $|i(t)\rangle = e^{-iHt/\hbar} |i\rangle$ and with H being the exited state vibrational Hamiltonian.

RR and absorption process along one normal coordinate, Q_k is pictorially represented in Fig. 2.2. Upon optical excitation, the initial ground state vibrational wavefunction is found in the Frank-Condon region of the excited state potential energy surface. This wavefunction is not an eigenfunction of the excited state Hamiltonian and will start evolving in time as a wave packet in the excited state potential surface. The overlap $\langle f|i(t)\rangle$ with the final vibrational state will change in time and will also be damped by the term exp(-Γt/$\hbar$)). The square of the half-Fourier transform of the damped overlap will give the Raman cross-section.

In a similar way, the absorption cross-section is obtained by computing the damped overlap between the time evolving excite state wave packet and the initial vibrational state,$\langle i|i(t)\rangle$. Instantaneously after electronic transition (at t = 0) the Raman overlap will vanish and the absorption overlap will be maximum because the initial, $|i\rangle$ and final, $|f\rangle$ wavefunctions are orthogonal. With time, the amplitude of the time dependent overlaps would start to decrease.

For polyatomic molecules, it is difficult to compute the multidimensional overlaps, $\langle i|i(t)\rangle$ and $\langle f|i(t)\rangle$ necessary for determining the Raman and absorption cross-sections. This task is simplified by considering a few physically relevant assumptions, (i) PES of ground and excited electronic states are harmonic in nature and are only displaced with respect to each other along normal coordinates; and (ii) Duschinsky rotation, *i.e.* mixing of ground and excited state normal modes are neglected.[159] With these assumptions, the multidimensional overlaps can be expressed as products of N one-dimensional overlaps,

$$\langle f|i(t)\rangle = \langle f_1|i_1(t)\rangle\langle f_2|i_2(t)\rangle \dots \langle f_N|i_N(t)\rangle \qquad (2.16)$$

With the assumption that, only one of the modes undergoes a vibronic transition from the ground vibrational state to the first vibrational state eqn. 2.16 becomes,

$$\langle f|i(t)\rangle = \langle 1_k|0_k(t)\rangle \prod_{j \neq k} \langle 0_j|0_j(t)\rangle \tag{2.17a}$$

and

$$\langle i|i(t)\rangle = \prod_{j=1}^{N} \langle 0_j|0_j(t)\rangle \tag{2.17b}$$

Considering equalities of ground and excited states vibrational frequencies, the one-dimensional overlaps can be explicitly written as following analytic expressions,[86,148,159]

$$\langle 0_j|0_j(t)\rangle = exp\left[-\frac{\Delta_j^2}{2}\left(1 - exp^{-i\omega_j t} - \frac{i\omega_j t}{2}\right)\right] \tag{2.18a}$$

and the recursion formulae,

$$\langle 1_j|0_j(t)\rangle = \frac{\Delta_j}{\sqrt{2}}\left[exp^{-i\omega_j t} - 1\right]\langle 0_j|0_j(t)\rangle \tag{2.18b}$$

$$\langle 2_j|0_j(t)\rangle = 2^{-\frac{1}{2}}\frac{\Delta_j}{\sqrt{2}}\left[exp^{-i\omega_j t} - 1\right]^2 \langle 0_j|0_j(t)\rangle \tag{2.18c}$$

where the Δ_j is the dimensionless displacement of the jth normal mode. The time-dependent Raman overlap is linearly dependent on the dimensionless displacement Δ. Now, inserting the products of the one-dimensional overlaps into eqns. 2.15a and 2.15b, the cross-sections can be written as explicitly multidimensional forms ,

$$\sigma_{0 \to 1}(E_L) = \frac{8\pi^4 E_S^3 E_L M^4}{9\hbar^6 c^4}\left| \int_0^\infty exp\left[\frac{i(E_L - E_0)t}{\hbar} - \frac{\Gamma t}{\hbar}\right] \times \frac{\Delta_k}{\sqrt{2}}\left(exp^{-i\omega_k t} - 1\right) \right.$$

$$\left. \times \prod_{j \neq k}^{N} exp\left(-\frac{\Delta_j^2}{2}\left[1 - exp^{-i\omega_j t}\right]\right) dt \right|^2 \tag{2.19a}$$

and

$$\sigma_A(E_L) = \frac{4\pi^4 E_L M^2}{6\hbar^2 nc} \int_{-\infty}^{\infty} \exp\left[\frac{i(E_L - E_0)t}{\hbar} - \frac{\Gamma t}{\hbar}\right]$$

$$\times \prod_{j=1}^{N} \exp\left(-\frac{\Delta_j^2}{2}\left[1 - \exp^{-i\omega_j t}\right]\right) dt \qquad (2.19b)$$

Comparison of eqns. 2.18b and 2.19a, it is readily observed that, the magnitude of RR cross-section is independent of the sign of Δ, unlike the one-dimensional overlap itself.

Inhomogeneous broadening, θ primarily arises due to the slightly different local environment of each molecule in the ensemble. It might also result from solvation dynamics taking place in time scales longer than the Raman scattering processes. During, the completion of Raman process (< 50 fs), both of the mentioned phenomena would be "static" or "stationary" in nature. In this thesis, the effect of the inhomogeneous broadening on the absorption and RR cross-sections has been introduced by using a normalized Gaussian distribution of the zero-zero energies (E_0) with θ as its standard deviation or 2θ being the full line width, and the eqns. 2.19a and 2.19b become,

$$\sigma_{0\to1}(E_L) = \frac{8\pi^4 E_S^3 E_L M^4}{9\hbar^6 c^4 \theta \sqrt{2\pi}} \int_0^{\infty} dE \exp\left[-\frac{(E - E_0)^2}{2\theta^2}\right]$$

$$\times \left| \int_0^{\infty} \exp\left[\frac{i(E_L - E_0)t}{\hbar} - \frac{\Gamma t}{\hbar}\right] \times \frac{\Delta_k}{\sqrt{2}}\left(\exp^{-i\omega_k t} - 1\right) \right.$$

$$\left. \times \prod_{j\neq k}^{N} \exp\left(-\frac{\Delta_j^2}{2}\left[1 - \exp^{-i\omega_j t}\right]\right) dt \right|^2 \qquad (2.20a)$$

and

$$\sigma_A(E_L) = \frac{4\pi^4 E_L M^2}{6\hbar^2 nc\, \theta \sqrt{2\pi}} \int_0^{\infty} dE \exp\left[-\frac{(E - E_0)^2}{2\theta^2}\right] \times \int_{-\infty}^{\infty} \exp\left[\frac{i(E_L - E_0)t}{\hbar} - \frac{\Gamma t}{\hbar}\right]$$

$$\times \prod_{j=1}^{N} \exp\left(-\frac{\Delta_j^2}{2}\left[1 - \exp^{-i\omega_j t}\right]\right) dt \qquad (2.20b)$$

2.2.2.1 Homogeneous and inhomogeneous contributions to total linewidth in absorption and Raman process

The effects of the dynamics homogeneous (Γ) and static inhomogeneous (θ) broadening linewidth on the absorption and Raman overlaps and resulting cross-sections are depicted in Fig. 2.12 with the help of an example. The increase in Γ dampens both absorption and Raman overlaps with time. (Fig. 2.12, panel a and b) While transition strength determines integrated intensity of absorption spectrum, different broadening mechanisms affect the shape of the band. The lineshape due to Γ is Lorentzian, the Fourier transform of an exponential decay in the time domain. On another hand θ is described as a Gaussian distribution of transition energies. The increase in Γ or θ affects absorption spectrum by only broadening it while keeping total unchanged. (Fig. 2.12, panel c and e) However, the pure exponential damping component in the time domain (Fig. 2.12, panel a) would reflect in Lorentzian lineshape and would affect only the low energy edge of the absorption spectrum. In general, very careful examination of the absorption spectrum in the wings region away from band maxima is not performed. Absorption spectrum cannot distinguish between contributions of these two broadening mechanisms.

Resonance Raman experiment can differentiate between these two broadening mechanisms because Γ appears as damping in the amplitude level but θ which produces as a Gaussian distribution of transition energies is introduced at the probability level. Once the approximate values of displacements (Δ) are obtained from experimental relative RR intensities and transition moment (M) is evaluated from integrated absorption cross-section, the intensity of REP solely depends on the value of Γ. Change in θ affect the REP (Fig. 2.12, f) in a similar way as absorption spectrum (Fig. 2.12, e). But, an increase in Γ reduces the Raman cross-sections by an order of magnitude without making it broad, (Fig. 2.12, d) contrary to that in the absorption spectrum. (Fig. 2.12, c) The analysis of the REP is used to partition the contribution of the homogeneous and inhomogeneous broadening of the absorption spectrum in many molecular systems.
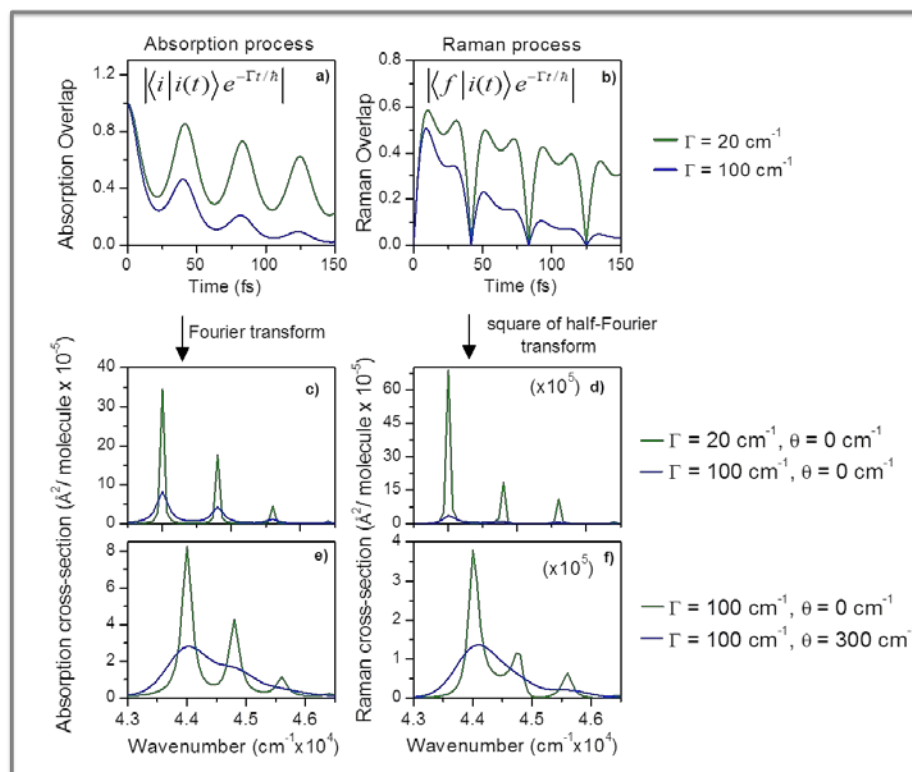
Fig. 2.12 Effect of homogeneous (Γ) and inhomogeneous (θ) linewidth on absorption and Raman process. (a) Single mode time-dependent absorption and (b) Raman overlaps for two different values of Γ: $\Gamma = 20$ cm^{-1} (green) and $\Gamma = 100$ cm^{-1} (blue). (c) Absorption spectrum and (e) Raman excitation profile with $\Gamma = 20$ cm^{-1} (green) and $\Gamma = 100$ cm^{-1} (blue) and with a fixed $\theta = 0$ cm^{-1}. (d) absorption and (f) Raman excitation profile with $\theta = 0$ cm^{-1} (green) and $\theta = 300$ cm^{-1} (blue) and with a fixed Γ of 100 cm^{-1}. Other parameters used in the calculation are: $E_0 = 44000$ cm^{-1}, M=1 Å, $\omega = 800$ cm^{-1} and $\Delta = 1$.

2.2.2.2 Model for solute-solvent bath interaction

A physically intuitive approach is to take the solute-solvent bath interaction into account and derive a more general expression for cross-sections from the time-dependent theory. It is done by introducing a line-shape function, $g_{solv}(t)$ to the damping term in eqns. 2.20a and 2.20b. As in solution, this is the dominating contributor to the line-shape function, after using them Raman and absorption cross-sections become,

$$\sigma_R(E_L) = \frac{8\pi^4 E_S^3 E_L M^4}{9\hbar^6 c^4 \theta \sqrt{2\pi}} \int_0^\infty dE \, \exp\left[-\frac{(E-E_0)^2}{2\theta^2}\right]$$

$$\times \left| \int_0^\infty \exp\left[\frac{i(E_L - E_0)t}{\hbar} - g_{solv}(t)\right] \frac{\Delta_k}{\sqrt{2}} (\exp(-i\omega_k t) - 1) \right.$$

$$\left. \times \prod_{j=1}^N \exp\left(-\frac{\Delta_j^2}{2}[1 - \exp(-i\omega_j t)]\right) dt \right|^2 \tag{2.21a}$$

and

$$\sigma_A(E_L) = \frac{4\pi^4 E_L M^2}{6\hbar^2 n \, c \, \theta \sqrt{2\pi}} \int_0^\infty dE \, \exp\left[-\frac{(E-E_0)^2}{2\theta^2}\right] \qquad \times \int_{-\infty}^\infty \exp\left[\frac{i(E_L - E_0)t}{\hbar} - g_{solv}(t)\right]$$

$$\times \prod_{j=1}^N \exp\left(-\frac{\Delta_j^2}{2}[1 - \exp(-i\omega_j t)]\right) dt \tag{2.21b}$$

There are several models to account for homogeneous broadening mechanisms resulting from solute-solvent interactions. I have used a general expression for $g_{solv}(t)$ which is developed by Mukamel and coworkers using stochastic theory and the Brownian oscillator model.[162,163] Unlike stochastic theory which only takes the effect of solvent on solute into account, a more general Brownian oscillator model considers effect of a change in solute dipole moment upon optical excitation on solvent degrees of freedoms. In the Brownian oscillator model, the solvent coordinates are considered as vibrational modes coupled to the electronic excitation of solute. If the collective movements of all the solvent molecules are considered as a single-mode strongly overdamped Brownian oscillator, the line shape function can be written as,

$$g_{solv}(t) = g'(t) + ig''(t) \tag{2.22a}$$

where,

$$g'(t) = \frac{\lambda_S}{\Lambda} \cos\left(\frac{\hbar\Lambda}{2k_B T}\right) [\exp(-\Lambda t) + \Lambda t - 1]$$

$$+ \left(\frac{4\lambda_S \Lambda k_B T}{\hbar}\right) \sum_{m=1}^\infty \frac{\exp(-\nu_m t) + \nu_m t - 1}{\nu_m(\nu_m^2 - \Lambda^2)} \tag{2.22b}$$

and

$$g''(t) = -\frac{\lambda_S}{\Lambda}[\exp(-\Lambda t) + \Lambda t - 1] \tag{2.22c}$$

and

$$\nu_m = 2\pi m k_B T/\hbar \tag{2.22d}$$

where ν_m are the Matsubara frequencies, m is a positive integer, λ_S being solvent reorganization energy and $\Lambda = 1/2\pi c\tau$ is the inverse of the solvent correlation time. The introduction of this type of line-shape function into the time-dependent expressions for the absorption and the RR cross-section provides an elegant approach to probe the solvation dynamics of the local environment within few tens of femtoseconds after photoexcitation. This method has been applied to different photoexcited chromophores in solvent and inside protein to obtain quantitative solvation information.

2.2.2.3 Total reorganization energy

The total reorganization energy (λ_{total}) of the system can be partitioned as (i) contribution from the solvent and (ii) the excess of vibrational energy of the solute immediately after upon optical excitation,

$$\lambda_{total} = \lambda_S + \lambda_{int} \tag{2.23}$$

where λ_{int} is the total internal reorganization energy of the solute summed over all vibrational degrees of freedoms. Within harmonic approximation for the PES, it can be written as,

$$\lambda_{int} = \sum_{j=1}^{3N-6} \frac{\left(\Delta_j^2 \hbar \omega_j\right)}{2} \tag{2.24}$$

with ω_j is the frequency of the jth vibrational mode in the ground and excited electronic state and Δ_j is the associated dimensionless displacement.

2.2.2.4 Changes in internal coordinates from dimensionless displacement

Changes in internal coordinates (r) of the solute upon electronic excitation can be obtained from the displacements, Δ_js which is changes in the dimensionless normal

coordinate system (q). This can be achieved through a transformation of coordinates by using the matrix, A_{ij} that project normal mode coordinates (Q) onto internal coordinate of the system using the relation,

$$r_i = \sum_j A_{ji} Q_j \tag{2.25}$$

where A is a matrix whose columns are the normal mode vectors of the solute, is obtained from the quantum chemical calculation, described in next section.

Normal mode coordinates (Q) are related to dimensionless coordinate (q) through the transformation,

$$Q_j = \left(\frac{\hbar}{\omega_j}\right)^{-\frac{1}{2}} q_j = 5.8065\, \omega_j^{-\frac{1}{2}} q_j \tag{2.26}$$

where ω_j is the frequency of the jth normal mode in cm^{-1}.

Combining eqns. 2.25 and 2.26 the internal and dimensionless coordinates can be related as,

$$r_i = 5.8065 \sum_j A_{ji}\, \omega_j^{-\frac{1}{2}} q_j \tag{2.27}$$

Eqn. 2.27 clearly shows that internal coordinate r (expressed in Å) is linearly dependent on q (dimensionless), and therefore, changes in these two coordinates can be related,

$$r_i - r_i' = \delta_i = 5.8065 \sum_j A_{ji}\, \omega_j^{-\frac{1}{2}} (q_j - q_j')$$

$$= 5.8065 \sum_j A_{ji}\, \omega_j^{-\frac{1}{2}} \Delta_j \tag{2.28}$$

2.2.3 Computation of RR spectra

2.2.3.1 RR intensities from excited state gradients

For strongly allowed electronic transitions like π–π* and charge transfer ones, for which transition dipole moment (μ_e^0) are of substantial magnitude, intensity enhancement in RR scattering primarily happens via Franck–Condon (FC) mechanism. These dipole allowed transitions which is the case for all nucleobases systems when excitation

frequency is tuned to one of the strong absorption line in UV region, produces significant magnitude of FC factors. FC factors are the overlap integral between the vibrational wavefunctions of the resonant excited state $|e^k\rangle$ with the initial $|g^i\rangle$ and final $|f^i\rangle$ wavefunctions of ground electronic states.

$$I_k \propto \Delta^2 \propto \frac{1}{\omega_k}\left(\frac{\partial E_N}{\partial Q_k}\right)^2$$

from GS - DFT

from TD-DFT and GS normal modes

I_k = RR intensity of kth fundamental

w_k = Frequency of kth fundamental
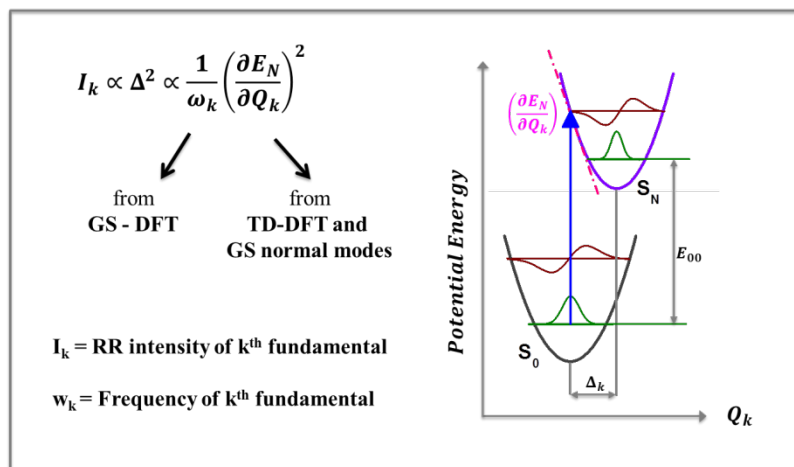
Fig. 2.13 Computation of RR intensity within short-time or gradient approximation. GS: ground electronic state; E_N: Energy of Nth electronic state; Qk : normal coordinate associated with k^{th} mode and dimensionless displacement (Δ_k) and TD-DFT stands for time dependent DFT.

The transition tensor is obtained from Kramers–Heisenberg–Dirac dispersion equation[134,135] using Born–Oppenheimer and Condon approximations,[137–139] as described in preceding section.

The demanding job of explicit computation of FC integrals is simplified using Manneback's recursion formula[164] where these are evaluated from dimensionless shift ΔQ_k, between electronic ground and excited state along vibrational normal coordinate, Qk. For a particular electronic transition, FC integrals become nonzero only if $\Delta Q_k \neq 0$ along the vibrational coordinate k. Further, application of independent mode displaced harmonic oscillator (IMDHO), *i.e.* (i) the potential of resonant electronic state is approximated by the ground state counterpart, but with a shift of their equilibrium position along Q_k; (ii) ground and excited state vibrational frequencies are unperturbed; (iii) only FC type scattering dominates and (iv) neglecting Duschinsky mixing of normal modes of ground and excited state shows that structural change along normal coordinate is proportionally related to gradient on the relevant excited state.[86,165,166] Within the

short-time approximation[167–171] for a single nondegenerate resonant state, RR intensity for k^{th} fundamental is evaluated as,[171–180] (See Ref [179] for more discussion)

$$I_k \propto \omega_0\left(\omega_0 - \omega_k^g\right)^3 \nu_0 |\mu_e^0|^4 \left(\frac{1}{\omega_k^g \mu_k^g}\right) \left|\frac{\partial E^N}{\partial Q_k}\right|_{FC}^2 \tag{2.29}$$

where $(\partial E_e/\partial Q_k)_{FC} = V_k$ is the non-mass weighted gradient on FC region of Nth excited state surface along k^{th} normal coordinate and ω_0 and ω_k being the excitation and Raman fundamental frequencies respectively. μ_e^0 and μ_k are electronic transition dipole moment of the resonant excited states and reduced mass of kth mode in ground state. The superscript 'g' stands for property of ground electronic state. Due to use of slope of excited state PES in determination of RR intensity, this method is also known as gradient approximation or IMDHO model or short-time approximation. (See Fig. 2.13)

The relative intensities for two resonant fundamentals (k and k′) within gradient approximation can be expressed as,

$$\frac{I_k}{I_{k'}} = \left(\frac{\omega_{k'}^g \mu_{k'}^g}{\omega_k^g \mu_k^g}\right)\frac{V_k'}{V_{k'}'} \tag{2.30}$$

because $\left(\omega_0 - \omega_k^g\right)^3/\left(\omega_0 - \omega_{k'}^g\right)^3$ factor becomes close to unity and thus making dependence of relative RR intensities on excitation frequencies practically negligible. V_k is computed by projecting cartesian gradients computed on the FC region of relevant electronic state along normal mode coordinates computed at GS equilibrium geometry using the following relation,

$$V_k' = \frac{1}{\sqrt{\mu_k}}\left(\frac{\partial E^N}{\partial Q_k}\right)_{Q_k=0} = \frac{1}{\sqrt{\mu_k}}\left(L^T\left(\frac{\partial E^N}{\partial x}\right)_{FC}\right) \tag{2.31}$$

where L being the orthogonal matrix obtained as solution of ground state mass weighted hessian matrix. $(\partial E^N/\partial x)_{FC}$, cartesian gradient in FC region at S_0 geometry is computed from analytical derivative of the excited state electronic energy along non-mass weighted cartesian coordinate. The term containing reduced mass, mass-weights the gradients in normal coordinate space. Excited state cartesian gradients on different model systems for relevant resonant states are computed at B3LYP/6-311+G(2d,p)//PCM or B3LYP/aug-cc-pvtz//PCM level within linear response time dependent density functional theory (LR-TD-DFT, would be called TD-DFT throughout the thesis) formalism[181,182] as implemented in G09 software suite.[183]

2.2.3.2 Dimensionless displacement (Δ_k)

The dimensionless displacement, Δ_k is the shift of S_0 and excited state minima along the normal coordinate q_k and expressed in dimensionless quantity expressed as,

$$\Delta_k \propto -\frac{1}{\omega_k}\left(\frac{\partial E^N}{\partial q_k}\right)_{FC} \tag{2.32}$$

where ω_k is the frequency of kth vibrational mode and $(\partial E^N/\partial Q_k)_{FC}$ is gradient on N^{th} excited state surface evaluated in FC region, i.e. at $Q_k=0$, and along k^{th} normal mode. Δ_k is related to mass weighted normal coordinate Q_k via the eqn. 2.26-2.28. Δ_k is expressed in terms of gradient on relevant electronic state energy along k^{th} normal mode vector which is evaluated at S_0 equilibrium geometry,

$$\Delta_k = -\left(\frac{\partial E^N}{\partial Q_k}\right)_{FC}\left(\frac{1}{\sqrt{\hbar\mu_k^g}}\right)\left(\frac{1}{\omega_k^{\frac{3}{2}}}\right) \tag{2.33}$$

All the quantities described in this equation can directly be obtained from quantum mechanical calculations. The proportionality factors are to make Δ_k dimensionless. In SI unit $\partial E_e/\partial Q_k$ is gradient in J.M^{-1}, ω_k $(= 2\pi c\nu_k)$ is in s^{-1}, $\hbar$ is reduced Planck's constant in J.S and reduced mass, μ_k is in Kg, yielding dimension of Δ_k as,

$$[\Delta_k] = \left(\frac{J}{M.}\right)\left(\frac{1}{\sqrt{J.S.Kg}}\right)\left(\frac{1}{S^{-\frac{3}{2}}}\right) = \frac{\sqrt{J}}{M.\sqrt{Kg}\,S^{-1}} = \frac{\sqrt{Kg\,M^2S^{-2}}}{M.\sqrt{Kg}\,S^{-1}.} = 1$$

2.2.3.3 Computation of ground state structure, vibrational normal modes, electronic excitation energies

Since its discovery in 1964, density functional theory (DFT) has been widely used by physicists and chemists to understand properties of isolated molecule and their clusters, solids, and mechanism of chemical reactions. Complementary and alternative to the traditional methods of quantum chemistry that are based on many-electron wavefunction $\Psi(r_1,...,r_N)$, DFT is rooted in electron density distribution n(r) .

A system containing N nonrelativistic, interacting electrons that are in a nonmagnetic state can be described with Hamiltonian $H \equiv T + V + U$, where $T =$

kinetic energy $\equiv -\frac{1}{2}\sum_j \nabla_j^2$; V = applied external potential $\equiv \sum_j v_{ext}(r_j)$ and U = electron-electron interaction energy $\equiv \frac{1}{2}\sum_{i\neq j} \frac{1}{|r_i - r_j|}$

According to Hohenberg and Kohn (HK) theorem, for a given ground state density $\rho(r)$, the external potential $V_{ext}(r)$ is uniquely determined to within an additive constant.[184] In principle, from the exact ground state density, the hamiltonian (H) can be computed and so are all the properties determined from H, such as ground state wave function $\Psi(r_1,...,r_N)$, potential energy surfaces, n^{th} excitation energy, vibrational force constants etc.

To determine this density a minimal principle for the energy is used,

$$E_{v(r)}[\rho(r)] = \int v(r)\rho(r)dr + F[\rho(r)] \tag{2.34}$$

where

$$F[\rho(r)] = (\Psi[\rho(r)], (T + U)\Psi[\rho(r)]) \tag{2.35}$$

is a functional of $\rho(r)$, because spatially dependent electron density $\rho(r)$ itself is a function of positional coordinate r(x,y,z). Hence, the name density functional theory derives from the use of functionals of $\rho(r)$. $F[n(r)]$ is expressed as summation of three terms as follows,

$$F[n(r)] = T_S[n(r)] + \frac{1}{2}\int \frac{n(r)n(r')}{|r - r'|} \, dr \, dr' + E_{xc}[n(r)] \tag{2.36}$$

with the first term being the kinetic energy of a non-interacting electronic system with density $\rho(r)$, the second term represents interaction energy and the last part is the exchange-correlation energy. $E_{xc}[\rho(r)]$ is not exactly known for any system other than for the free electron gas. Development of new functionals (exchange and correlation) with physically meaningful approximations to describe non-covalent interactions such as Van der Waals forces (in biomolecules), transition states and change transfer excitations is an active area of research. Detailed discussion and theoretical backgrounds on different type of functionals are documented in several books and reviews.[185–188]

From the early 90s, one of the most successful density functionals in predicting molecular properties (such as charge densities, atomization energies, structure and

vibrational frequencies, excited states) of small (N < 50) molecules is B3LYP. This is a hybrid functional[189] that derives from a mixture of *Becke's three parameter exchange functional (B3)[190] with* Lee-Yang-Parr's (LYP) correlation (*local and* non-local) term, and hence the name B3LYP.[191] This functional is reported to be very successful in predicting vibrational and other molecular properties for nucleobase and similar sized molecular systems.[102,192–201] In this thesis, I have used this functional as implemented in Gaussian 09 software package,[183] to obtain energy minimized ground state structures of nucleobases and melanin, structural models. Other flavors of density functionals, such as long-range corrected coulomb attenuated CAM-B3LYP[202] and functional with additional empirical dispersion correction, such as wB97xD[203] are also used to account for non-covalent interactions, i.e., due to dispersion, Van der Walls and hydrogen bonding interactions.

Extension of ground-state DFT for time dependent (TD) systems was developed by Gross and coworkers and others, popularly known as TD-DFT for computation of molecular properties (dipole moments and electric polarizability) to applied perturbation such as an electric field.[204–206] The theoretical details[207–211] and implementation of TD-DFT in Gaussian 09 package [212] are described elsewhere. TD-DFT within linear response regime (known as LR-TDDFT or simply TDDFT) has been a popular choice for computation of properties of singlet excited states, such as electronic absorption spectrum, excited state dipole moment, the gradient on excited state PES etc. This method has been a popular choice for small (N < 20) molecules, such as, aromatic amino acids[213–215], and DNA bases[216–221] to very large (N > 200-500) molecular systems, such as, chromophore embedded in a protein,[222–224] aromatic[225–227] and polymethine[228] dye and organic molecules,[229] light emitting transition metal complex,[230] quantum dots,[231] and aromatics containing dye-sensitized solar cells.[232–234] I have employed this method in conjunction with B3LYP functional to compute electronic excitation spectra and transition dipole moments of different DNA bases (Chapter 3 to chapter 6) and of melanin protomolecules (Chapter 8).

References

[1]   C. V Raman, *Indian J. Phys.* **1928**, *2*, 387.

[2]   C. V Raman, *Nature* **1928**, *121*, 619.

[3]   C. V Raman, K. S. Krishnan, *Nature* **1928**, *121*, 501.

[4]   G. S. Landsberg, L. I. Mandelstam, *Naturwissenschaften* **1928**, *16*, 557.

[5]   G. S. Landsberg, L. I. Mandelstam, *J. Russ. Physico-Chemical Soc. Phys. Sect.* **1928**, *60*, 335.

[6]   L. I. Mandelstam, G. S. Landsberg, M. Leontowitsch, *Zeitschrift fur Phys.* **1930**, *60*, 334.

[7] P. P. Shorygin, *Zhurnal Fiz. Khimii* **1947**, *21*, 1125.

[8] P. Schorygin, L. Kuzina, L. Ositjanskaja, *Mikrochim. Acta* **1955**, *43*, 630.

[9] D. C. Blazej, W. L. Peticolas, *Proc. Natl. Acad. Sci. U. S. A.* **1977**, *74*, 2639.

[10] D. C. Blazej, W. L. Peticolas, *J. Chem. Phys.* **1980**, *72*, 3134.

[11] S. P. A. Fodor, R. P. Rava, T. R. Hays, T. G. Spiro, *J. Am. Chem. Soc.* **1985**, *107*, 1520.

[12] S. P. A. Fodor, T. G. Spiro, *J. Am. Chem. Soc.* **1986**, *108*, 3198.

[13] J. R. Perno, D. Cwikel, T. G. Spiro, *Inorg. Chem.* **1987**, *26*, 400.

[14] J. R. Perno, C. A. Grygon, T. G. Spiro, *J. Phys. Chem.* **1989**, *93*, 5672.

[15] T. C. Strekas, T. G. Spiro, *Biochim. Biophys. Acta* **1972**, *278*, 188.

[16] T. C. Strekas, T. G. Spiro, *Biochim. Biophys. Acta* **1972**, *263*, 830.

[17] T. G. Spiro, T. C. Strekas, *Proc. Natl. Acad. Sci. U. S. A.* **1972**, *69*, 2622.

[18] T. G. Spiro, T. C. Strekas, *J. Am. Chem. Soc.* **1974**, *96*, 338.

[19] R. P. Rava, T. G. Spiro, *J. Am. Chem. Soc.* **1984**, *106*, 4062.

[20] D. S. Caswell, T. G. Spiro, *J. Am. Chem. Soc.* **1986**, *108*, 6470.

[21] C. R. Johnson, M. Ludwig, S. O'Donnell, S. A. Asher, *J. Am. Chem. Soc.* **1984**, *106*, 5008.

[22] C. R. Johnson, M. Ludwig, S. A. Asher, *J. Am. Chem. Soc.* **1986**, *108*, 905.

[23] L. Chinsky, B. Jollès, A. Laigle, P. Y. Turpin, *J. Raman Spectrosc.* **1987**, *18*, 195.

[24] A. Toyama, H. Takeuchi, I. Harada, *J. Mol. Struct.* **1991**, *242*, 87.

[25] Z. Dhaouadi, M. Ghomi, J. C. Austin, R. B. Girling, R. E. Hester, P. Mojzes, L. Chinsky, P. Y. Turpin, C. Coulombeau, *J. Phys. Chem.* **1993**, *97*, 1074.

[26] A. Toyama, N. Hanada, Y. Abe, H. Takeuchi, I. Harada, *J. Raman Spectrosc.* **1994**, *25*, 623.

[27] A. Toyama, N. Hanada, J. Ono, E. Yoshimitsu, H. Takeuchi, *J. Raman Spectrosc.* **1999**, *30*, 623.

[28] A. Toyama, Y. Miyagawa, A. Yoshimura, N. Fujimoto, H. Takeuchi, *J. Mol. Struct.* **2001**, *598*, 85.

[29] A. Toyama, N. Fujimoto, N. Hanada, J. Ono, E. Yoshimitsu, A. Matsubuchi, H. Takeuchi, *J. Raman Spectrosc.* **2002**, *33*, 699.

[30] N. Jayanth, S. Ramachandran, M. Puranik, *J. Phys. Chem. A* **2009**, *113*, 1459.

[31] B. E. Billinghurst, S. A. Oladepo, G. R. Loppnow, *J. Phys. Chem. B* **2009**, *113*, 7392.

[32] S. Gogia, A. Jain, M. Puranik, *J. Phys. Chem. B* **2009**, *113*, 15101.

[33] N. Jayanth, M. Puranik, *J. Phys. Chem. B* **2011**, *115*, 6234.

[34] A. Lewis, J. Spoonhower, R. A. Bogomolni, R. H. Lozier, W. Stoeckenius, *Proc. Natl. Acad. Sci.* **1974**, *71*, 4462.

[35] F. Inagaki, M. Tasumi, T. Miyazawa, *J. Mol. Spectrosc.* **1974**, *50*, 286.

[36] R. Mathies, A. R. Oseroff, L. Stryer, *Proc. Natl. Acad. Sci.* **1976**, *73*, 1.

[37] B. Aton, A. G. Doukas, R. H. Callender, B. Becher, T. G. Ebrey, *Biochemistry* **1977**, *16*, 2995.

[38] J. A. Larrabee, T. G. Spiro, *J. Am. Chem. Soc.* **1980**, *102*, 4217.

[39] M. Braiman, R. Mathies, *Proc. Natl. Acad. Sci.* **1982**, *79*, 403.

[40] D. F. Blair, G. W. Campbell, W. K. Cho, A. M. English, H. A. Fry, V. Lum, K. A. Norton, J. R. Schoonover, S. I. Chan, *J. Am. Chem. Soc.* **1985**, *107*, 5755.

[41] S. Hu, K. M. Smith, T. G. Spiro, *J. Am. Chem. Soc.* **1996**, *118*, 12638.

[42] Z. Chi, X. G. Chen, J. S. W. Holtz, S. A. Asher, *Biochemistry* **1998**, *37*, 2854.

[43] H.-J. van Manen, N. Uzunbajakava, R. van Bruggen, D. Roos, C. Otto, *J. Am. Chem. Soc.* **2003**, *125*, 12112.

[44] I. R. Rodriguez-Mendieta, G. R. Spence, C. Gell, S. E. Radford, D. A. Smith, *Biochemistry* **2005**, *44*, 3306.

[45] Z. Ahmed, I. A. Beta, A. V. Mikhonin, S. A. Asher, *J. Am. Chem. Soc.* **2005**, *127*, 10943.

[46] S. Gogia, H. Balaram, M. Puranik, *Biochemistry* **2011**, *50*, 4184.

[47] E. A. Milán-Garcés, S. Mondal, J. B. Udgaonkar, M. Puranik, *J. Raman Spectrosc.* **2014**, *45*, 814.

[48] M. Horch, J. Schoknecht, M. A. Mroginski, O. Lenz, P. Hildebrandt, I. Zebger, *J. Am. Chem. Soc.* **2014**, *136*, 9870.

[49] K. A. Okotrub, N. V. Surovtsev, *Biophys. J.* **2015**, *109*, 2227.

[50] V. Karnawat, S. Gogia, H. Balaram, M. Puranik, *ChemPhysChem* **2015**, *16*, 2172.

[51] S. Todorovic, P. Hildebrandt, L. O. Martins, *Phys. Chem. Chem. Phys.* **2015**, *17*, 11954.

[52] B. B. Johnson, W. L. Peticolas, *Annu. Rev. Phys. Chem.* **1976**, *27*, 465.

[53] A. Warshel, *Annu. Rev. Biophys. Bioeng.* **1977**, *6*, 273.

[54] R. Callender, B. Honig, *Annu. Rev. Biophys. Bioeng.* **1977**, *6*, 33.

[55] P. M. Champion, A. C. Albrecht, *Annu. Rev. Phys. Chem.* **1982**, *33*, 353.

[56] J. M. Friedman, D. L. Rousseau, M. R. Ondrias, *Annu. Rev. Phys. Chem.* **1982**, *33*, 471.

[57] R. J. H. Clark, T. J. Dines, *Angew. Chemie Int. Ed. English* **1986**, *25*, 131.

[58] S. A. Asher, *Annu. Rev. Phys. Chem.* **1988**, *39*, 537.

[59] W. H. Nelson, R. Manoharan, J. F. Sperry, *Appl. Spectrosc. Rev.* **1992**, *27*, 67.

[60] Y. Wang, H. E. Van Wart, **1993**, pp. 319–373.

[61] S. A. Asher, *Anal. Chem.* **1993**, *65*, 59A.

[62] S. A. Asher, *Anal. Chem.* **1993**, *65*, 201A.

[63] T. Kitagawa, Y. Mizutani, *Coord. Chem. Rev.* **1994**, *135-136*, 685.

[64] G. J. Thomas, *Annu. Rev. Biophys. Biomol. Struct.* **1999**, *28*, 1.

[65] H. Takeuchi, *Biopolymers* **2003**, *72*, 305.

[66] S. A. Oladepo, K. Xiong, Z. Hong, S. A. Asher, J. Handen, I. K. Lednev, *Chem. Rev.* **2012**, *112*, 2604.

[67] K. L. Gares, K. T. Hufziger, S. V. Bykov, S. A. Asher, *J. Raman Spectrosc.* **2016**, *47*, 124.

[68] P.-Y. Turpin, L. Chinsky, A. Laigle, B. Jollès, *J. Mol. Struct.* **1989**, *214*, 43.

[69] W. L. Peticolas, *Methods Enzymol.* **1995**, *246*, 389.

[70] Z. Q. Wen, G. J. Thomas, *Biopolymers* **1998**, *45*, 247.

[71] J. M. Benevides, S. A. Overman, G. J. Thomas, *J. Raman Spectrosc.* **2005**, *36*, 279.

[72] A. B. Myers, M. O. Trulson, J. A. Pardoen, C. Heeremans, J. Lugtenburg, R. A. Mathies, *J.*

Chem. Phys. **1986**, *84*, 633.

[73]   E. Fraga, M. A. Webb, G. R. Loppnow, *J. Phys. Chem.* **1996**, *100*, 3278.

[74]   K. Iwata, H. Hamaguchi, *J. Phys. Chem. A* **1997**, *101*, 632.

[75]   T. Nakabayashi, H. Okamoto, M. Tasumi, *J. Phys. Chem. A* **1998**, *102*, 9686.

[76]   I. K. Lednev, A. S. Karnoup, M. C. Sparrow, S. A. Asher, *J. Am. Chem. Soc.* **1999**, *121*, 8074.

[77]   L. Zhu, J. Kim, R. A. Mathies, *J. Raman Spectrosc.* **1999**, *30*, 777.

[78]   A. Sato, Y. Mizutani, *Biochemistry* **2005**, *44*, 14709.

[79]   C.-Y. Huang, G. Balakrishnan, T. G. Spiro, *Biochemistry* **2005**, *44*, 15734.

[80]   P. Kukura, D. W. McCamant, R. A. Mathies, *Annu. Rev. Phys. Chem.* **2007**, *58*, 461.

[81]   G. Balakrishnan, C. L. Weeks, M. Ibrahim, A. V Soldatova, T. G. Spiro, *Curr. Opin. Struct. Biol.* **2008**, *18*, 623.

[82]   M. Mizuno, M. Shibata, J. Yamada, H. Kandori, Y. Mizutani, *J. Phys. Chem. B* **2009**, *113*, 12121.

[83]   J. Dasgupta, R. R. Frontiera, C. Fang, R. A. Mathies, in *Encycl. Biophys.*, Springer Berlin Heidelberg, Berlin, Heidelberg, **2013**, pp. 745–759.

[84]   S.-Y. Lee, E. J. Heller, *J. Chem. Phys.* **1979**, *71*, 4777.

[85]   B. R. Stallard, *J. Chem. Phys.* **1983**, *78*, 712.

[86]   A. B. Myers, R. A. Mathies, in *Biol. Appl. Raman Spectrosc. Vol. 2 - Reson. Raman Spectra Polyenes Aromat.* (Ed.: T.G. Spiro), John Wiley & Sons Inc, New York, **1987**, pp. 1–58.

[87]   A. B. Myers, *J. Opt. Soc. Am. B* **1990**, *7*, 1665.

[88]   L. C. Hoskins, A. X. Pham, G. C. Rutt, *J. Raman Spectrosc.* **1990**, *21*, 543.

[89]   A. B. Myers, in *Laser Tech. Chem.* (Eds.: A.B. Myers, T.R. Rizzo), Wiley-Interscience, New York, **1995**, p. 325.

[90]   A. B. Myers, *Acc. Chem. Res.* **1997**, *30*, 519.

[91]   B. E. Billinghurst, G. R. Loppnow, *J. Phys. Chem. A* **2006**, *110*, 2353.

[92]   B. E. Billinghurst, G. R. Loppnow, *J. Phys. Chem. A* **2006**, *110*, 2353.

[93]   B. E. Billinghurst, S. A. Oladepo, G. R. Loppnow, *J. Phys. Chem. B* **2012**, *116*, 10496.

[94]   B. E. Billinghurst, R. Yeung, G. R. Loppnow, *J. Phys. Chem. A* **2006**, *110*, 6185.

[95]   A. F. El-Yazbi, A. Palech, G. R. Loppnow, *J. Phys. Chem. A* **2011**, *115*, 10445.

[96]   S. S. Ng, F. Teimoory, G. R. Loppnow, *J. Phys. Chem. Lett.* **2011**, 2362.

[97]   S. A. Oladepo, G. R. Loppnow, *J. Phys. Chem. B* **2011**, *115*, 6149.

[98]   F. Teimoory, G. R. Loppnow, *J. Phys. Chem. A* **2014**, *118*, 12161.

[99]   S. Yarasi, S. Ng, G. R. Loppnow, *J. Phys. Chem. B* **2009**, *113*, 14336.

[100] S. Yarasi, P. Brost, G. R. Loppnow, *J. Phys. Chem. A* **2007**, *111*, 5130.

[101] S. A. Asher, M. Ludwig, C. R. Johnson, *J. Am. Chem. Soc.* **1986**, *108*, 3186.

[102] E. A. Milán-Garcés, S. Kaptan, M. Puranik, *Biophys. J.* **2013**, *105*, 211.

[103] G. R. Loppnow, E. Fraga, *J. Am. Chem. Soc.* **1997**, *119*, 896.

[104] M. A. Webb, C. M. Kwong, G. R. Loppnow, *J. Phys. Chem. B* **1997**, *101*, 5062.

[105] A. B. Myers, M. O. Trulson, R. A. Mathies, *J. Chem. Phys.* **1985**, *83*, 5000.

[106] G. R. Loppnow, R. A. Mathies, *Biophys. J.* **1988**, *54*, 35.

[107] N. Biswas, S. Umapathy, *J. Chem. Phys.* **1997**, *107*, 7849.

[108] X. Cao, J. L. McHale, *J. Chem. Phys.* **1998**, *109*, 1901.

[109] M. Puranik, S. Umapathy, *Bull. Chem. Soc. Jpn.* **2002**, *75*, 1057.

[110] X. Zhao, J. A. Burt, J. L. McHale, *J. Chem. Phys.* **2004**, *121*, 11195.

[111] M. R. Waterland, S. L. Howell, K. C. Gordon, *J. Phys. Chem. A* **2007**, *111*, 4604.

[112] A. B. Myers, R. A. Harris, R. A. Mathies, *J. Chem. Phys.* **1983**, *79*, 603.

[113] D. S. Egolf, M. R. Waterland, A. M. Kelley, *J. Phys. Chem. B* **2000**, *104*, 10727.

[114] S. Luber, J. Neugebauer, M. Reiher, *J. Chem. Phys.* **2010**, *132*, 044113.

[115] K. S. K. Shin, J. I. Zink, *J. Am. Chem. Soc.* **1990**, *112*, 7148.

[116] J. L. Wootton, J. I. Zink, *J. Am. Chem. Soc.* **1997**, *119*, 1895.

[117] A. B. Myers, Excited State Structure and Dynamics of Polyenes and Bacteriorhodopsin from Resonance Raman Intensities, University of California, Berkeley, **1984**.

[118] V. L. DeVito, M. Z. Cai, S. A. Asher, L. A. Kehres, K. M. Smith, *J. Phys. Chem.* **1992**, *96*, 6917.

[119] C. Su, Y. Wang, T. G. Spiro, *J. Raman Spectrosc.* **1990**, *21*, 435.

[120] J. M. Dudik, C. R. Johnson, S. A. Asher, *J. Chem. Phys.* **1985**, *82*, 1732.

[121] G. Binnig, H. Rohrer, *Helv. Phys. Acta* **1982**, *55*, 726.

[122] G. Binnig, C. F. Quate, C. Gerber, *Phys. Rev. Lett.* **1986**, *56*, 930.

[123] K.-C. Chang, Y.-W. Chiang, C.-H. Yang, J.-W. Liou, *Tzu Chi Med. J.* **2012**, *24*, 162.

[124] S. Kasas, N. H. Thomson, B. L. Smith, P. K. Hansma, J. Miklossy, H. G. Hansma, *Int. J. Imaging Syst. Technol.* **1997**, *8*, 151.

[125] H. G. Hansma, L. Pietrasanta, *Curr. Opin. Chem. Biol.* **1998**, *2*, 579.

[126] N. E. Kurland, Z. Drira, V. K. Yadavalli, *Micron* **2012**, *43*, 116.

[127] T. Bornschlögl, M. Rief, *Methods Mol. Biol.* **2011**, *783*, 233.

[128] M. Rief, M. Gautel, F. Oesterhelt, J. M. Fernandez, H. E. Gaub, *Science (80-.).* **1997**, *276*, 1109.

[129] Y. Lyubchenko, L. Shlyakhtenko, R. Harrington, P. Oden, S. Lindsay, *Proc. Natl. Acad. Sci.* **1993**, *90*, 2137.

[130] Y. L. Lyubchenko, A. A. Gall, L. S. Shlyakhtenko, *Methods Mol. Biol.* **2014**, *1117*, 367.

[131] L. Picas, P.-E. Milhiet, J. Hernández-Borrell, *Chem. Phys. Lipids* **2012**, *165*, 845.

[132] M. P. Stewart, Y. Toyoda, A. A. Hyman, D. J. Muller, *Trends Biochem. Sci.* **2011**, *36*, 444.

[133] T. G. Kuznetsova, M. N. Starodubtseva, N. I. Yegorenkov, S. A. Chizhik, R. I. Zhdanov, *Micron* **2007**, *38*, 824.

[134] H. A. Kramers, W. Heisenberg, *Zeitschrift für Phys.* **1925**, *31*, 681.

[135] P. A. M. Dirac, *Proc. R. Soc. A Math. Phys. Eng. Sci.* **1927**, *114*, 710.

[136] M. Born, J. R. Oppenheimer, *Ann. Phys.* **1927**, *84*, 457.

[137]   E. Condon, *Phys. Rev.* **1926**, *28*, 1182.

[138]   J. Franck, E. G. Dymond, *Trans. Faraday Soc.* **1926**, *21*, 536.

[139]   E. U. Condon, *Phys. Rev.* **1928**, *32*, 858.

[140]   D. L. Tonks, J. B. Page, *Chem. Phys. Lett.* **1979**, *66*, 449.

[141]   S. Hassing, O. S. Mortensen, *J. Chem. Phys.* **1980**, *73*, 1078.

[142]   B. R. Stallard, P. R. Callis, P. M. Champion, A. C. Albrecht, *J. Chem. Phys.* **1984**, *80*, 70.

[143]   K. T. Schomacker, P. M. Champion, *J. Chem. Phys.* **1986**, *84*, 5314.

[144]   S. A. Lee, C. K. Chan, J. B. Page, C. T. Walker, *J. Chem. Phys.* **1986**, *84*, 2497.

[145]   J. R. Cable, A. C. Albrecht, *J. Chem. Phys.* **1986**, *84*, 1969.

[146]   H. M. Lu, J. B. Page, *J. Chem. Phys.* **1988**, *88*, 3508.

[147]   H. M. Lu, J. B. Page, *J. Chem. Phys.* **1989**, *90*, 5315.

[148]   A. B. Myers, *J. Chem. Phys.* **1982**, *77*, 3857.

[149]   A. B. Myers, K. S. Pranata, *J. Phys. Chem.* **1989**, *93*, 5079.

[150]   D. L. Phillips, A. B. Myers, *J. Chem. Phys.* **1991**, *95*, 226.

[151]   A. B. Myers, R. A. Mathies, *J. Chem. Phys.* **1984**, *81*, 1552.

[152]   X. Ci, A. B. Myers, *Chem. Phys. Lett.* **1989**, *158*, 263.

[153]   X. Ci, M. A. Pereira, A. B. Myers, *J. Chem. Phys.* **1990**, *92*, 4708.

[154]   F. Markel, N. S. Ferris, I. R. Gould, A. B. Myers, *J. Am. Chem. Soc.* **1992**, *114*, 6208.

[155]   M. Puranik, S. Umapathy, J. G. Snijders, J. Chandrasekhar, *J. Chem. Phys.* **2001**, *115*, 6106.

[156]   X. Zhao, J. A. Burt, J. L. McHale, *J. Chem. Phys.* **2004**, *121*, 11195.

[157]   X. Cao, J. L. McHale, *J. Chem. Phys.* **1998**, *109*, 1901.

[158]   C. M. Stuart, R. R. Frontiera, R. A. Mathies, *J. Phys. Chem. A* **2007**, *111*, 12072.

[159]   D. J. Tannor, E. J. Heller, *J. Chem. Phys.* **1982**, *77*, 202.

[160]   A. B. Myers, *J. Raman Spectrosc.* **1997**, *28*, 389.

[161]   A. M. Kelley, *J. Phys. Chem. A* **1999**, *103*, 6891.

[162]   B. Li, A. E. Johnson, S. Mukamel, A. B. Myers, *J. Am. Chem. Soc.* **1994**, *116*, 11039.

[163]   S. Mukamel, *Principles of Nonlinear Optical Spectroscopy*, Oxford University Press, New York, **1995**.

[164]   C. Manneback, *Physica* **1951**, *17*, 1001.

[165]   P. M. Champion, A. C. Albrecht, *J. Chem. Phys.* **1980**, *72*, 6498.

[166]   T. Petrenko, F. Neese, *J. Chem. Phys.* **2007**, *127*, 164319.

[167]   E. J. Heller, *Acc. Chem. Res.* **1981**, *14*, 368.

[168]   E. J. Heller, R. Sundberg, D. Tannor, *J. Phys. Chem.* **1982**, *86*, 1822.

[169]   L. Jensen, J. Autschbach, G. C. Schatz, *J. Chem. Phys.* **2005**, *122*, 224115.

[170]   L. Jensen, L. L. Zhao, J. Autschbach, G. C. Schatz, *J. Chem. Phys.* **2005**, *123*, 174110.

[171]   T. Petrenko, F. Neese, *J. Chem. Phys.* **2012**, *137*, 234107.

[172]   P. G. Szalay, G. Fogarasi, *Chem. Phys. Lett.* **1997**, *270*, 406.

[173]   A. A. Jarzęcki, T. G. Spiro, *J. Raman Spectrosc.* **2001**, *32*, 599.

[174]   J. Neugebauer, B. A. Hess, *J. Chem. Phys.* **2004**, *120*, 11564.

[175]   A. A. Jarzęcki, T. G. Spiro, *J. Phys. Chem. A* **2005**, *109*, 421.

[176]   J. Neugebauer, E. J. Baerends, E. V. Efremov, F. Ariese, C. Gooijer, *J. Phys. Chem. A* **2005**, *109*, 2100.

[177]   T. Petrenko, K. Ray, K. E. Wieghardt, F. Neese, *J. Am. Chem. Soc.* **2006**, *128*, 4422.

[178]   C. Herrmann, J. Neugebauer, M. Presselt, U. Uhlemann, M. Schmitt, S. Rau, J. Popp, M. Reiher, *J. Phys. Chem. B* **2007**, *111*, 6078.

[179]   A. A. Jarzęcki, *J. Phys. Chem. A* **2009**, *113*, 2926.

[180]   J. Guthmuller, *J. Chem. Theory Comput.* **2011**, *7*, 1082.

[181]   F. Furche, R. Ahlrichs, *J. Chem. Phys.* **2002**, *117*, 7433.

[182]   G. Scalmani, M. J. Frisch, B. Mennucci, J. Tomasi, R. Cammi, V. Barone, *J. Chem. Phys.* **2006**, *124*, 094107.

[183]   M. J. Frisch *et al. Gaussian 09, Revision D.01*, Gaussian Inc., Wallingford, **2013**.

[184]   P. Hohenberg, W. Kohn, *Phys. Rev.* **1964**, *136*, B864.

[185]   R. G. Parr, W. Yang, *Density Functional Theory of Atoms and Molecules*, Oxford University Press, New York, NY, USA, **1989**.

[186]   E. K. U. Gross, R. M. Dreizler, *Density Functional Theory: An Approximation to the Quantum Many-Body Problems*, Springer-Verlag, Berlin, **1990**.

[187]   R. G. Parr, W. Yang, *Annu. Rev. Phys. Chem.* **1995**, *46*, 701.

[188]   W. Kohn, A. D. Becke, R. G. Parr, *J. Phys. Chem.* **1996**, *100*, 12974.

[189]   A. D. Becke, *J. Chem. Phys.* **1993**, *98*, 1372.

[190]   A. D. Becke, *J. Chem. Phys.* **1993**, *98*, 5648.

[191]   C. Lee, W. Yang, R. G. Parr, *Phys. Rev. B* **1988**, *37*, 785.

[192]   A. St-Amant, in *Rev. Comput. Chem. Vol. 7*, **1996**, pp. 217–259.

[193]   N. Leulliot, M. Ghomi, H. Jobic, O. Bouloussa, V. Baumruk, C. Coulombeau, *J. Phys. Chem. B* **1999**, *103*, 10934.

[194]   B. Giese, D. McNaughton, *J. Phys. Chem. B* **2002**, *106*, 101.

[195]   B. Giese, D. McNaughton, *Phys. Chem. Chem. Phys.* **2002**, *4*, 5171.

[196]   B. Giese, D. McNaughton, *Phys. Chem. Chem. Phys.* **2002**, *4*, 5161.

[197]   S. Yarasi, B. E. Billinghurst, G. R. Loppnow, *J. Raman Spectrosc.* **2007**, *38*, 1117.

[198]   S. Gogia, A. Jain, M. Puranik, *J. Phys. Chem. B* **2009**, *113*, 15101.

[199]   N. Jayanth, S. Ramachandran, M. Puranik, *J. Phys. Chem. A* **2009**, *113*, 1459.

[200]   N. Jayanth, M. Puranik, *J. Phys. Chem. B* **2011**, *115*, 6234.

[201]   S. Mondal, M. Puranik, *Phys. Chem. Chem. Phys.* **2016**, 10.1039/C6CP01746K.

[202]   T. Yanai, D. P. Tew, N. C. Handy, *Chem. Phys. Lett.* **2004**, *393*, 51.

[203]   J.-D. Chai, M. Head-Gordon, *Phys. Chem. Chem. Phys.* **2008**, *10*, 6615.

[204]   E. Runge, E. K. U. Gross, *Phys. Rev. Lett.* **1984**, *52*, 997.

[205]   M. E. Casida, in *Recent Adv. Density Funct. Methods Part I* (Ed.: D.P. Chong), World Scientific Publishing Company, **1995**, pp. 155–189.

[206]   R. Bauernschmitt, R. Ahlrichs, *Chem. Phys. Lett.* **1996**, *256*, 454.

[207]   E. K. U. Gross, W. Kohn, in *Adv. Quantum Chem. Vol. 21*, Academic Press, Inc., **1990**, pp. 255–291.

[208]   M. E. Casida, in *Theor. Comput. Chem. Vol. 4*, **1996**, pp. 391–439.

[209]   M. E. Casida, C. Jamorski, K. C. Casida, D. R. Salahub, *J. Chem. Phys.* **1998**, *108*, 4439.

[210]   M. A. L. Marques, E. K. U. Gross, *Annu. Rev. Phys. Chem.* **2004**, *55*, 427.

[211]   M. E. Casida, *J. Mol. Struct. THEOCHEM* **2009**, *914*, 3.

[212]   R. E. Stratmann, G. E. Scuseria, M. J. Frisch, *J. Chem. Phys.* **1998**, *109*, 8218.

[213]   D. M. Rogers, N. A. Besley, P. O'Shea, J. D. Hirst, *J. Phys. Chem. B* **2005**, *109*, 23061.

[214]   C. Clavaguéra, F. Piuzzi, J.-P. Dognon, *J. Phys. Chem. B* **2009**, *113*, 16443.

[215]   P. Štěpánek, P. Bouř, *Phys. Chem. Chem. Phys.* **2014**, *16*, 20639.

[216]   A. Tsolakidis, E. Kaxiras, *J. Phys. Chem. A* **2005**, *109*, 2373.

[217]   M. K. Shukla, J. Leszczynski, *J. Phys. Chem. A* **2005**, *109*, 7775.

[218]   D. Varsano, R. Di Felice, M. A. L. Marques, A. Rubio, *J. Phys. Chem. B* **2006**, *110*, 7129.

[219]   V. Karunakaran, K. Kleinermanns, R. Improta, S. A. Kovalenko, *J. Am. Chem. Soc.* **2009**, *131*, 5839.

[220]   R. Improta, A. Lami, V. Barone, F. Santoro, *Int. J. Quantum Chem.* **2010**, *110*, 624.

[221]   Y. Zhao, Z. Cao, *J. Theor. Comput. Chem.* **2013**, *12*, 1341013.

[222]   M. A. L. Marques, X. López, D. Varsano, A. Castro, A. Rubio, *Phys. Rev. Lett.* **2003**, *90*, 258101.

[223]   X. Lopez, M. A. L. Marques, A. Castro, A. Rubio, *J. Am. Chem. Soc.* **2005**, *127*, 12329.

[224]   E. Cannuccia, O. Pulci, R. Del Sole, M. Cascella, *Chem. Phys.* **2011**, *389*, 35.

[225]   D. Jacquemin, J. Preat, V. Wathelet, M. Fontaine, E. A. Perpète, *J. Am. Chem. Soc.* **2006**, *128*, 2072.

[226]   E. A. Perpète, D. Jacquemin, *J. Mol. Struct. THEOCHEM* **2009**, *914*, 100.

[227]   J. Fabian, *Dye. Pigment.* **2010**, *84*, 36.

[228]   D. Jacquemin, Y. Zhao, R. Valero, C. Adamo, I. Ciofini, D. G. Truhlar, *J. Chem. Theory Comput.* **2012**, *8*, 1255.

[229]   D. Jacquemin, V. Wathelet, E. A. Perpète, C. Adamo, *J. Chem. Theory Comput.* **2009**, *5*, 2420.

[230]   R. D. Costa, E. Ortí, H. J. Bolink, F. Monti, G. Accorsi, N. Armaroli, *Angew. Chemie Int. Ed.* **2012**, *51*, 8178.

[231]   S. V. Kilina, D. S. Kilin, O. V. Prezhdo, *ACS Nano* **2009**, *3*, 93.

[232]   D. Rocca, R. Gebauer, F. De Angelis, M. K. Nazeeruddin, S. Baroni, *Chem. Phys. Lett.* **2009**, *475*, 49.

[233]   J. Ku, Y. Lansac, Y. H. Jang, *J. Phys. Chem. C* **2011**, *115*, 21508.

[234]   N. Santhanamoorthi, C.-M. Lo, J.-C. Jiang, *J Phys. Chem. Lett.* **2013**, *4*, 524.

3

Vibrational Reorganizations in Substituted Purines

3.1 Introduction

Natural nucleobases; adenine (Ade), guanine (Gua), thymine (Thy), cytosine (Cyt) and uracil (Ura) which are primary UV chromophores in of DNA and RNA, have extraordinary photostability under UV light within 260 nm absorption band. Experimental[1–13] and computational[14–27] results have shown that the intrinsic stability of nucleic acid bases originates due the presence of a unique manifold of electronic excited states that are exquisitely tuned to facilitate sub-picosecond (ps) de-excitation after photoabsorption. Within this manifold of states, the relative positioning of optically allowed and forbidden transitions and their respective potential energy surfaces (PES) determines the lifetime of the electronically excited state.

Photophysical investigations of systematically substituted nucleobases have been instrumental in understanding the mechanistic origin of photoresistive properties of canonical DNA and RNA bases.[8,28–51] Change and/or addition of exocyclic substitutions dramatically modulates photophysical properties in analogous base derivatives, such as orders of magnitude longer excited state lifetimes and increased fluorescence quantum yields.[35] One such example is the case of 2-aminopurine (AP) in which amino substituent is at C2 site has a strong fluorescence, unlike its nonfluorescent natural analog Ade which is 6-aminopurine.[38,39,52] *Ab initio* computation has shown that the -NH$_2$ group blocks the deactivation path associated with ring deformation at C2 site in AP, otherwise present in Ade.[40] Recently it has been shown that it is not the purine chromophore, but the specific substituent at C6 position that facilitates ultrafast internal conversion in Ade and Gua.[28]

Matsika and co-workers have examined reorganizations of electronic states in pyrimidines,[42] and several substituted purines[43] using multireference perturbation theory (MRPT) methods. They show that substitution at C6 (by amino or carbonyl group) always blueshifts the ^{1}nπ* state and redshifts the $^1\pi\pi$* state as compared to

those in the unsubstituted purines. This effect is small in C2 substituted purines and of intermediate strength in doubly substituted (at C2 and C6 site) ones. Alteration of substituent position drastically changes the structure of excited state PES and, thus influences population decay from those states. Switching of amino substituent from C6 to C2 makes AP 1000 times more fluorescent than Ade.[39,52,53] In comparison, 2,6-Diaminopurine (DAP) which is a C2 and C6 amino substituted purine, fluoresces but with a much lower quantum yield than that of AP.[52]
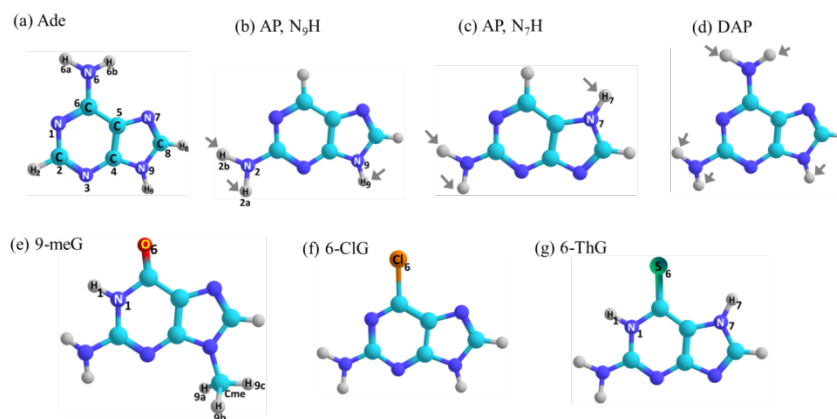
Fig. 3.1 The structure of adenine (Ade), N9H and N7H tautomer of 2-aminopurine (AP), 2,6-diaminopurine (DAP), 6-chloroguanine or 2-amino 6-chloropurine (6-ClG) and 9-methylguanine (9-meG), and 60thioguanine (6-ThG) optimized at B3LYP/6-311+G(2d,p)//PCM level of DFT. Conventional numbering scheme of ring atoms is mentioned in for Ade. The labile hydrogens that would be replaced by deuterium in a H→D exchange experiment are marked (arrow).

Other than reshuffling the ordering of energies of excited electronic states, exocyclic substitutions also modulate ground state vibrational structure. Our group has previously reported a systematic shift in vibrational wavenumbers and mode reorganizations due to exocyclic substitution by methyl (me),[54] oxo and amino moieties,[55,56] in purine and pyrimidines, and also due to the substitution of ring nitrogen atom with carbon in deazapurines.[57,58] These changes in vibrational wavenumbers report on alteration in ground state molecular geometry. Substitutions by electron donating groups, such as amino, carbonyl, and by heavy atoms such as chlorine and sulfur reorganize frontier molecular orbitals (MO) of the basic purine moiety. These substitutions can also reorganize vibrational normal modes through alteration in contributions from individual internal coordinates in potential energy distribution (PED). Results of ultrafast absorption experiments have established that substituents at C6 site play a crucial role in governing ultrafast de-excitation processes in natural purines.[28] In the current report, we derive substitution induced reorganizations in PEDs of vibrational modes of six C2 and C6 substituted purines; Ade, Gua, AP, DAP, 6-chloroguanine (6-ClG) and 6-thioguanine (6-ThG).
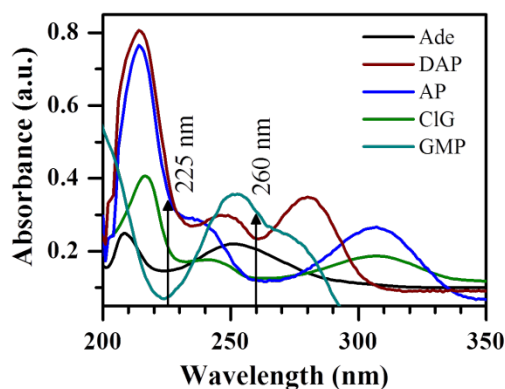
Fig. 3.2 UV-Vis absorption spectra of an aqueous solution (30 μM) of adenine, DAP, AP and GMP, and (5 μM) of 6-ClG in phosphate buffer at pH 7.0. Two excitation frequencies used for RR measurement on these nucleobases are mentioned (vertical arrow).

In the case of an electronic excitation, the vibrational modes with highest Frank-Condon (FC) activity get enhanced in a resonance Raman (RR) spectrum.[59] Within hundreds of femtoseconds (fs) of photoabsorption, distortions along these vibrational modes dictate photodynamics on excited state PES. RR spectroscopy has been routinely applied to examine the vibronic activity of nucleobases in different electronic excited states.[60–63] We employ RR spectroscopy with UV laser source tuned to be in resonance with singlet electronic excited states of the substituted purines and characterize their FC active vibrational modes. We analyze ground state structures, tautomeric equilibria, characters of electronic transitions and vibrational reorganization of the substituted purines *vis-à-vis* those of two naturally occurring DNA bases, Ade, and Gua. Two resonant excitations at 225 nm and 260 nm wavelength are used to probe distinct FC activity of these purines in two different singlet excited states. Conclusions obtained from such analyses are crucial in determining excited state dynamics of these purines. Changes in ground state vibrational coupling between different internal coordinates affect the instantaneous structural dynamics in these purines and are discussed in subsequent chapters.

3.2 Experimental and Theoretical Methods

3.2.1 Sample preparation. Ade, AP, DAP, Guanosine-5′-monophosphate (GMP), and 6-ClG free bases of HPLC grade purity were obtained from Sigma-Aldrich (St. Louis, MO, USA) and were used without further purification. As Gua is not adequately soluble ay neutral pH, its nucleotide GMP was used instead. All samples were prepared by dissolving an appropriate amount of free bases in 50 mM tris-HCl buffer at pH 7.0 and in D_2O (Sigma-Aldrich, St. Louis, MO). The tris-HCl buffer was prepared by dissolving the right amount of trizma base in miliQ purity water (Merck Millipore, Billerica, MA, USA) and pH was adjusted by addition of appropriate amount of 1 N HCl (DCl for samples in D_2O). Samples were dissolved in D_2O buffer and were left overnight before recording their spectra for complete H/D exchange. All samples for Resonance Raman experiments were 1 mM in concentration.

3.2.2 UVRR and Absorption Spectroscopy. Experimental design for UVRR spectroscopy is described in chapter 2. The resolution of the measured RR spectra is ~ 0.7 cm^{-1}/pixel and ~ 1 cm^{-1}/pixel at 260 nm and 225 nm excitation respectively. UV-Visible absorption spectra were recorded with an Evolution 300 UV-Vis spectrophotometer (Thermo Fischer Scientific, Waltham, MA, USA).

3.2.3 Computational methods. Ground state structures of all bases (Fig. 1) were energy optimized using DFT with Becke's hybrid gradient-corrected functionals (B3LYP)[64,65] and atom centered Gaussian basis set, 6-311+G(2d,p). The harmonic vibrational analysis was performed on these energy minimized structures to obtain vibrational wavenumbers. Implicit solvation employing polarization continuum model (PCM)[66,67] was used to account for the bulk dielectric effect of water on predicted geometries and vibrational wavenumbers. The hydrogen atoms that are connected to electronegative nitrogen atoms of purine ring were replaced with deuterium (D) in optimized geometry of H-species for computation of vibrational spectra of the deuterated species. The magnitude of experimentally observed shift of a band due to deuteration of labile hydrogen atoms from that in water was compared against theoretically predicted shift (to be referred as isotopic shift hereafter) for reliable vibrational assignment. PEDs of each vibrational normal mode were obtained using the Vibrational Energy Distribution Analysis (VEDA) 4.0 program.[68] Time dependent DFT (TD-DFT) within linear response regime[69,70] was applied for computation of electronic excitation energies of all nucleobases. All Single point TD-DFT calculations were performed with B3LYP functional and on ground state geometries, optimized at B3LYP/6-311+G(2d,p) level of theory in vacuo. The UV-Vis spectra were simulated with the help of the program SWizard 5.0[71] and using the Gaussian lineshape with a full width at half maxima (FWHM) of 3000 cm^{-1}. Atomic charges were calculated using Mulliken's population analysis.[72] The structures of the energy minimized molecules, normal modes of vibration and molecular orbitals were visualized using Chemcraft 1.6.[73] All DFT and TD-DFT computations were carried out using the Gaussian 09 software package.[74]

3.3 Results and Discussion

3.3.1 Ground state structures

Computed geometrical parameters for the neutral form of all the examined purines (Fig. 3.1), together with the available X-ray and NMR spectroscopy derived structures are described in Table 3.1 and Table 3.2. UV-Vis absorption spectra of these bases at pH7 are depicted in Fig. 3.2. The computed bond lengths are in good agreement with the experimental ones: the differences in the bond lengths hardly exceed 0.02 Å. Predicted structure of AP is in agreement with those computed by Broo *et al.*[75] and obtained X-ray structure.[76] Energy minimized structures of N9H species of Ade and DAP and N1H, N7H thione tautomer of 6-ThG are also in good agreement with

published crystal structure parameters of these molecules.[77–79]

GMP is modeled as 9-methylguanine (9-meG) where bulky riboside group is substituted with methyl moiety at N9 position of the purine ring for computational efficiency. Predicted bond lengths between the C6 atom and oxygen in 9-meG, chlorine in 6-ClG and sulfur (S) in 6-thioguanine (6-ThG) are in agreement with previously reported computational[80] and experimental structural parameters.[81] It is important to note here that the majority of the differences in purine ring structure of guanine (Gua) and 6-thG do not arise from the replacement of oxygen by a sulfur atom, but due to the difference in their prevalent tautomeric forms.[81]

In AP, changing electron rich -NH$_2$ group from C6 to C2 position causes an increment of electron density on N1 and N3 atoms resulting in stronger N3–C4 and N1–C6 bonds. It also makes N1–C2 and C2–N3 bonds of AP weaker than corresponding ones in Ade. The addition of another amino substitution at C6 does not significantly perturb the structure of the purine ring in DAP other than weakening C5–C6 and N$_5$–C4 bonds in comparison with those in AP. Chlorine, which has a single unpaired electron in the outer shell makes a single bond with C6 atom, whereas both, sulfur and oxygen having p^4 outer shell electron configuration make double bonds with carbon. Thus, C6–Cl6 bond of 6-ClG is longer than both C=O and C=S bonds in 9-meG and 6-thG respectively. However, the π bond between C6 and S in 6-thG is weaker than that of C=O in Gua, due to more overlap between same orbitals type (2p) of carbon and oxygen. The computed trend of these bond lengths is corroborated by X-ray crystal data. In general exocyclic substitution on pyrimidine ring has a minimal structural effect on imidazole ring, a fact predicted by DFT correctly.

While comparing between structural parameters obtained through theoretical and experimental methods, it should be noted that, structures of these bases in monocrystal, base-pair in DNA duplex or within the complex with a protein are expected to differ from those computed on isolated molecules. Structurally, a majority of changes occurs in C–N bonds of both the rings in solution phase because of the more polarizable nature of these types of bonds compared to other bonds in purine. However, bonds involving exocyclic moieties, such as C6=O6, C6–Cl6 or C6–S6 and C2–N2 undergo significant changes due to hydrogen bonding interactions with another base in mono-crystal and double-stranded DNA, and with surrounding solvent molecules.
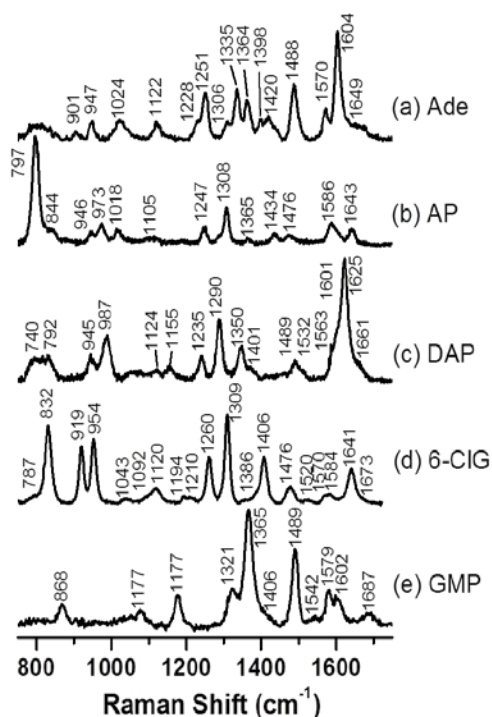
Fig. 3.3 UVRR spectra of pH 7.0 species of (a) Ade, (b) AP, (c) DAP, (d) 6-ClG and (e) GMP with 225 nm laser excitation in 750-1750 cm^{-1} Raman shift region. All bases are of 1mM concentration and used average laser power on sample was 0.6 mW.

3.3.2 Tautomerism in substituted purines at neutral pH

Identification of accurate tautomeric forms in solution state is necessary for correct assignment of vibrational modes, and subsequently to discuss their reorganizations upon substitution. Exocyclic substitutions have dramatic effects of altering Tautomeric equilibria of purines have been investigated in detail using NMR[82–85] and vibrational spectroscopic methods.[54–56,58,86–91] Due to the sensitiveness of RR spectroscopy to very small structural changes, it has been exploited for discrimination between various tautomeric states of in many substituted purines in a solution state.[54,55,58,89–91]

Table 3.1. Bond lengths (Å) of neutral Ade, AP, DAP, 6-ClG, 6-ThG and 9-meG computed at B3LYP/6-311+G(2d,p)//PCM level of theory and available experimental structural data.

Bond	Adenine		AP			DAP			6-ClG			6-ThG			9-meG	
	DFT	Exp[1]	DFT	Exp[2]	In enzyme complex[3]	DFT	Exp[4]	In enzyme complex[3]	DFT	Exp[5]	In enzyme complex[6]	DFT	Exp[7]	In double stranded DNA[8]	DFT	Exp[9]
N1–C2	1.340	1.340	1.355	1.365	1.355	1.350	1.359	1.373	1.358	1.376	1.339	1.376	1.363	1.379	1.372	1.370
C2–N3	1.332	1.330	1.343	1.343	1.363	1.340	1.396	1.343	1.340	1.357	1.367	1.314	1.327	1.330	1.314	1.323
N3–C4	1.339	1.349	1.326	1.329	1.368	1.336	1.359	1.423	1.326	1.334	1.357	1.351	1.355	1.351	1.351	1.354
C4–C5	1.395	1.381	1.407	1.400	1.372	1.394	1.333	1.385	1.409	1.396	1.470	1.401	1.395	1.374	1.392	1.374
C5–C6	1.407	1.415	1.386	1.381	1.467	1.407	1.436	1.461	1.387	1.380	1.465	1.396	1.376	1.416	1.426	1.419
C6–N1	1.345	1.351	1.332	1.332	1.329	1.339	1.319	1.359	1.311	1.313	1.345	1.386	1.411	1.386	1.415	1.390
C5–N7	1.385	1.385	1.390	1.389	1.396	1.388	1.377	1.379	1.384	1.387	1.332	1.377	1.372	1.394	1.382	1.389
N7–C8	1.311	1.308	1.306	1.318	1.372	1.308	1.351	1.381	1.307	1.310	1.348	1.352	1.344	1.300	1.309	1.300
C8–N9	1.372	1.362	1.379	1.360	1.364	1.377	1.344	1.328	1.377	1.377	1.348	1.324	1.335	1.363	1.377	1.383
N9–C4	1.372	1.374	1.369	1.368	1.396	1.371	-	1.401	1.368	1.358	1.333	1.369	1.364	1.368	1.367	1.379
C2–H2	1.085	-	-	-	-	-	-	-	-	-	-	-	-	-	-	-
C2-N2	-	-	1.369	1.353	1.400	1.375	-	1.434	1.363	1.339	1.350	1.359	1.319	1.421	1.361	1.338
N2–H2a	-	-	1.008	0.890	1.070	1.009	-	1.070	1.008	-	1.070	1.009	1.08	1.010	1.009	-
N2–H2b	-	-	1.009	0.883	1.070	1.009	-	1.070	1.008	-	1.070	1.009	0.87	1.010	1.009	-
C6–H6	-	-	1.083	0.950	1.090	-	-	-	-	-	-	-	-	-	-	-
C6–N6	1.351	1.332	-	-	-	1.355	-	1.479	-	-	-	-	-	-	-	-
N6–H6a	1.007	-	-	-	-	1.008	-	1.070	-	-	-	-	-	-	-	-
N6–H6b	1.008	-	-	-	-	1.008	-	1.070	-	-	-	-	-	-	-	-
C6–Cl	-	-	-	-	-	-	-	-	1.756	1.732	1.796	-	-	-	-	-
C6–O	-	-	-	-	-	-	-	-	-	-	-	-	-	-	1.230	1.234
C6–S	-	-	-	-	-	-	-	-	-	-	-	1.687	1.690	1.718	-	-
N7–H	-	-	-	-	-	-	-	-	-	-	-	1.010	1.10	-	-	-
N1–H	-	-	-	-	-	-	-	-	-	-	-	1.013	0.96	1.010	1.012	-
C8–H	1.079	-	1.079	0.970	1.090	1.079	-	1.090	1.079	-	-	1.079	0.94	1.091	1.079	-
N9–H	1.009	-	1.009	0.871	-	1.009	-	-	1.010	-	-	-	-	-	-	-
N9–C$_{me}$	-	1.466	-	-	-	-	-	-	-	-	-	-	-	-	1.456	-

[1]Ref [77] X-ray crystal structure of adenosine; [2]Ref [76] X-ray crystal structure of AP monohydrate; [3]Ref [92] X-ray crystal structure of Alkyltransferase of *Schizosaccharomyces pombe* (Atl1) in complex with DNA containing AP (PDB:4HDU) and DAP (PDB:4HDV); [4]Ref [78] X-ray crystal structure of a DAP derivative, 1, 2-iminomethyl-3-methyl-6-amino-methyl-9H-purine; [5]Ref [79] X-ray crystal structure 6-ClG; [6]Ref [93] X-ray crystal structure of Hexameric Purine nucleoside phosphorylases (PNP) from *B. subtilis* (BsPNP233) with 6-chloroguanosine (PDB:4DAE); [7]Ref [81] X-ray crystal structure of 6-thioguanine; [8]Ref [94] Solution state NMR structure of an 11-mer DNA containing 6-thiodeoxyguanosine opposite to cytosine (PDB: 1KB1); [9]Ref [95] X-ray structure of guanosine dihydrate.

Fig. 3.4 UVRR spectra of pH 7.0 species of (a) Ade (ade), (b) AP, (c) DAP, (d) 6-ClG, and (e) GMP with 260 nm excitation in 1110-1750 cm^{-1} Raman shift region. All bases are of 1mM concentration and incident laser power on sample was 0.6 mW.

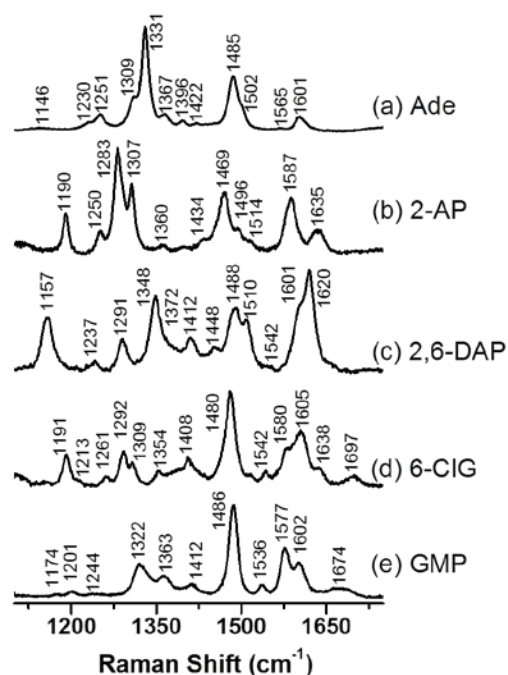The N9H tautomer has been established as the predominant form (more than 80-85 %) of Ade in solution,[85,96,97] vapor,[98] and rare-gas matrix.[99,100] The N9H tautomer of Ade has been successfully used in explaining experimental vibrational spectra of adenine in polycrystalline[101] and solution state.[102] In the current study, DFT computed wavenumbers and PEDs on N9H-Ade are in agreement with experimental band positions, (Fig. 3.3 and 3.4) and previously published assignments.[101,103,104] (Table 3.3) Correct vibrational assignment of Ade validates the use of the employed B3LYP/6-311+G(2d,p)//PCM method for computation of ground state structure and normal modes of vibrations and is used for other nucleobases throughout the rest of this thesis.

Unlike Ade, tautomeric equilibrium of AP at neutral pH is strongly debated.[76,105–109] of Fourier transformed infrared (FT-IR) spectra and resonance two-photon ionization (R2PI) spectra in the gas phase using DFT calculations concluded that N_9H tautomer is the prevalent form present in a molecular beam.[105] *Ab initio* calculations also show that the N9H form is more stable than the N7H species by 18 kJ/mol in the gas phase.[105] However, X-ray crystallographic data suggests that at least 13 % of the population of AP exists as the N7H tautomer in the crystalline state.[76] Using linear dichroism spectroscopy of AP, 2-amino-9-methylpurine (2A9MP), and the 2-aminopurine riboside (APrib) in stretched film of poly-vinyl alcohol, Holmen *et al*. have concluded the minor presence of N7H tautomer.[110] Furthermore, these authors have not found that AP has single exponential fluorescence decay with a lifetime (~ 10 ns) close to those found for 2A9MP

and 2Apr. In a later study, the presence of two fluorescence decay components (with lifetime τ_1=11.0 ns and τ_2=13.5 ns) for AP free base against only one component (τ_1=10.6 ns) for APrib was reported. This result suggested the presence of more than one tautomeric forms in aqueous solution.[106] Both N7H and N9H species of AP have been detected in supersonic jet experiments.[107,108]

Despite being subjected to a number of vibrational investigations,[105,111,112] isotope induced shifts of vibrational bands of AP has not been reported. We have obtained excellent agreement between experimental isotopic shifts of RR bands of AP and DFT computed isotope-induced shifts on the N9H-AP tautomer. (Fig. 3.3, 3.4, 3.5 and Table 3.4) We have compared experimental isotopic shifts of free AP base against the computed ones for both the N7H and N9H neutral tautomers (Table 3.5). In Table 4 it is demonstrated that the computed isotopic shifts (for N9H tautomer) of the six in-plane stretching vibrations agree reasonably well with the experimentally observed ones. The symmetric imidazole breathing vibration at 944 cm^{-1} serves as a sensitive probe for the position (N7 or N9) of the hydrogen atom. This vibration which has a significant contribution from C5–N7 stretching coordinate, is insensitive to H/D exchange, a fact also true for Ade and DAP. The predicted H→D shift (+ 15 cm^{-1}) on N7H-AP tautomer does not agree with experimental observation. The N9H form correctly predicts insensitiveness of this mode upon H/D exchange. Thus, UVRR and DFT derived isotopic shifts suggest the N9H form as the predominant tautomer of free AP at neutral pH.

Table 3.2. Mulliken charge distributions (a.u.) on atoms of neutral Ade, AP, DAP, 6-ClG, 6-ThG and 9-meG computed at B3LYP/6-311+G(2d,p)//PCM level of DFT.

	Ade	AP	DAP	6-ClG	6-ThG	9-meG
Atom	Mulliken Charges (a.u.)					
N1	-0.508	-0.466	-0.586	-0.420	-0.360	-0.453
C2	0.191	0.570	0.537	0.569	0.521	0.556
N3	-0.467	-0.525	-0.566	-0.504	-0.566	-0.595
C4	0.231	0.335	0.252	0.299	0.331	0.072
C5	0.372	0.380	0.306	-0.044	0.066	0.382
C6	0.208	-0.275	0.231	0.093	0.548	0.416
N7	-0.534	-0.509	-0.538	-0.439	-0.317	-0.544
C8	0.213	0.225	0.200	0.272	0.272	0.180
N9	-0.354	-0.356	-0.368	-0.364	-0.473	-0.077
H2	0.118					
N6	-0.477		-0.488			
H6a	0.270		0.272			
H6b	0.276		0.271			
Cl6				0.013		
S6					-0.776	
H1					0.317	0.297
N2		-0.487	-0.491	-0.478	-0.360	-0.461
H2a		0.263	0.258	0. 268	0.279	0.268
H2b		0.260	0.258	0.267	0.270	0.276
H6		0.131				
H8	0.150	0.150	0.145	0.154	0.157	0.146

H9	0.312	0.305	0.306	0.314		
H7					0.316	
Cme						-0.315
H9a						0.159
H9b						0.159
H9c						0.158

Apart from a minor presence (< 1%) of N7H species, matrix isolated FT-IR spectra of AP were also successfully assigned to DFT computed normal modes of amino-N9H tautomer only.[112] Additionally, TD-DFT computed UV-Vis absorption spectrum for N9H tautomer remarkably resembles experimental UV absorption spectrum of AP[110] in terms of peak positions and relative intensities of three bands between 200 nm and 240 nm wavelength range, (See Fig. 3.6) suggesting N9H as predominant form.
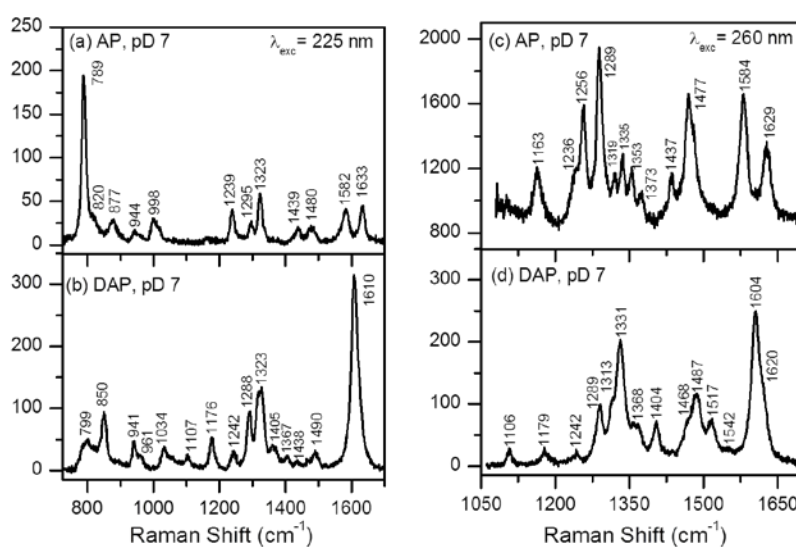
Fig. 3.5 UVRR spectra of deuterated species of AP (a and c) and DAP (b and d) pD 7.0 with 225 nm (panel a and b) and 260 nm (panel c and d) excitation. All bases are of 1mM concentration and incident laser power on the sample was 0.6 mW.

Table 3.3. Assignment of computed[a] vibrational wavenumbers on N9H form of neutral Ade to bands in experimental spectrum and computed potential energy distributions (PED)[b]

Exp. UVRR in H_2O, at 225/260 nm	Exp. UVRR of Ado in H_2O^c	Exp. Raman of Ade in solid state[d]	Comp. in vacuo[e]	Comp. in H_2O^a	PED[b] in (%)
1649/-	1650[#]	1674	1665	1636	str N6C6 (13) + be H6aN6H6b (39)
1604/1601	1603	1613	1642	1617	str N3C4 (13) + N1C6 (12) - be H6aN6H6b (12) -
-	1583	1597	1613	1604	- str N3C2 (10) + be C4N9C8 (11) - H6aN6H6b
1488/1485	1485	1483	1524	1509	str N7C8 (30) - be H8C8N7 (21)
1497/1504	1508	1463	1510	1492	str N7C8 (10) - N1C6 (21) - be H2C2N3 (24)
1440/-	1458[*]		1423	1433	- be H9N9C8 (23) + H2C2N3 (28)
-/1420	1428	1419	1440	1419	str N9C4 (27) - N9C8 (10) + be H9N9C8 (11) -

1393/1396	1386*		1373	1366	- str N1C6 (10) + N6C6 (10) - N9C8 (12) + be
1363/1367	1376	1333	1365	1348	str N1C2(29) + N7C5(21)
1328/1331	1309#	1308	1341	1319	str N3C2(40) - N1C2(16)
1249/1251	1253	1248	1272	1266	str N7C8 (23) + N1C2 (11) + be H9N9C8 (10) +
-/1230	1213#	1234	1246	1239	str N7C5 (25) + be H6bN6C6 (24) + N6C6N1 (10)
1143/1146	1176	1162	1148	1142	- str N6C6 (12) - be C2N3C4 (10) + C5N7C8 (22)
1083/-	1086*	1126	1085	1095	str N9C8 (54) + be H9N9C8 (31)
1022/-	1009	1025	1012	1013	str N1C6 (28) + be H6bN6C6 (42)
-	-	-	974	977	tors H2C2N3C4 (80) - N1C2N3C4 (16)
944/943	916#	942	942	947	- be C4N9C8 (10) + N9C8N7 (52)
902/-	899*	899	899	900	- be C6N1C2 (10) + C4N9C8 (13) + N1C2N3 (29)
840/-	851	839	849	877	tors H8C8N7C5 (84)
785/-	799*	797	805	820	tors N1C2N3C4 (13) - C6N1C2N3 (13) -
721/721	730	723	726	723	str N3C4 (23) + N9C4 (10) + be C6N1C2 (10) +
-	701*	-	685	689	- tors C4N9C8N7 (20) - out N6C5N1C6 (44) -
-	636	-	666	670	tors H9N9C8N7 (11) - H8C8N7C5 (11) -
621/623	620	623	618	619	- be C6N1C2 (12) - C4N9C8 (14) + C2N3C4 (13) -

[a]computed at B3LYP/6-311+G(2d,p)//PCM level of DFT and not scaled; [b]PEDs are computed using the VEDA 4.0 program; [c]Ref [103] 213, 266 and 515 nm excited Raman spectrum of aqueous (pH 7.0) adenosine (Ado), wavenumbers marked with * were observed with 515 nm excitation, the ones marked with # were observed with 213 nm excitation and the others were obtained with 266 nm excitation; [d]Ref [101] Normal Raman (λ_{exc} = 632 nm) of polycrystalline adenine; [e]Ref [101] computed at B3LYP/6-31++G(d,p)//vacuo; abbreviations: str, bond stretching; be, bending; out, out of plane; tors, torsion, sign indicates relative phase of movement of atoms of internal coordinates.

Unlike Ade and AP, a number of studies aimed at understanding the tautomeric composition of DAP is limited. DAP has primarily been studied using vibrational spectroscopies in the polycrystalline state,[113–115] and in a solution state.[116] Relative intensities and band positions of our 225 and 260 nm excited spectra agree with those reported by Dhaouadi *et al.* with 222 and 257 nm excitations in an aqueous solution of DAP at 4°C.[116] In agreement with these previous reports, our vibrational assignment (Table 3.6) based on a comparison of experimental and computed isotopic shifts establishes N9H tautomer as the most abundant species of DAP at neutral pH in solution. For all RR bands of DAP, other than the band at 1510 cm^{-1}, experimentally observed isotopic shifts agree with theoretical shifts that are computed on N9H–DAP.

GMP which exists as N1H, N9H and C6=O6 form in neutral pH,[56] is modeled with 9-meG. Raman wavenumbers and normal modes (Table 3.7) computed on 9-meG agree reasonably with experimental band positions in RR spectra (Fig. 3.3 and 3.4) of GMP at pH 7.0, and with previously published results.[56,117,118] DFT assisted vibrational assignment of FT-IR and 1064 nm excited FT-Raman spectra have concluded the presence of both N7H and N9H tautomers of 6-ClG in an amorphous state.[119] However,

previous investigations from our group have established that 6-ClG predominantly exists as the N9H tautomer in solution.[58,120] Vibrational assignments of 6-ClG bands are described in Table 3.8. Additionally, experimentally determined lengths of N7–C8 and C8–N9 bonds[79] that are very sensitive to the position (N7 or N9) of a hydrogen atom on imidazole ring are in agreement with the computed bond lengths on N9H tautomer.(Table 3.1)

Theoretical and experimental studies in gas and solution state have shown that 6-ThG exists as the thiol-N9H form in gas phase but as the thione-amino (N1H, N7H) form in aqueous solution and solid state.[81,121–127] Using this thione-amino tautomer, experimental FT-IR and FT-Raman spectra in a polycrystalline state,[125] and normal Raman spectra of 6-ThG[126] have been assigned. Due of unavailability of solution state Raman spectra of 6-ThG, we have used band positions in solid state spectrum[125,126] and have assigned them to normal modes computed on N1H, N7H species.(Table 3.9)
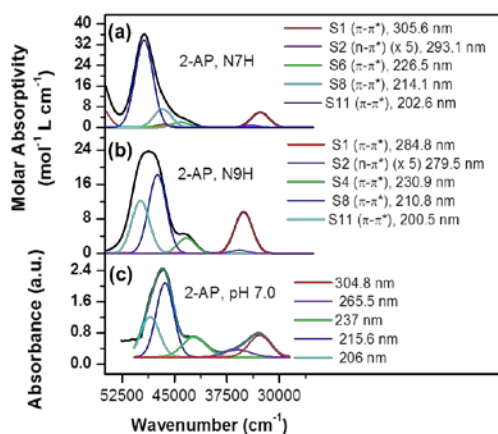
Fig. 3.6 Computed UV-Vis absorption spectra of (a) N7H and (b) N9H tautomer of 2-AP at TD-B3LYP-631G+(2d,p)//gas level of DFT and (c) experimental spectra of AP at pH 7.0. A fixed FWHM of 3000 cm^{-1} is used to simulate UV-Vis spectra from computed oscillator strength.

3.3.3 Reorganizations of electronic states upon substitutions

Computed excitation energies and oscillator strengths against available experimental λ_{max} of Ade,[128,129] AP,[110] DAP,[39,129–132] GMP,[133,134] 6-ClG[120] (see Chapter 4) and 6-ThG[125,126,135] are described in Table 3.10 a-f Several groups have computed electronic excitations lying within low-energy absorption band (~ 260 nm) of DNA and RNA bases.[43,134,136–141] Electronic structure of AP has also been investigated using theoretical and experimental methods.[39,40,109,142–147] MRPT computed trends of systematic redshift of $^1\pi\pi^*$ state upon single amino substitution (at C2 in AP), and double substitution (at C2 and C6 in DAP) compared to that in adenine agree with our TD-DFT predicted results. Positions of $^1n\pi^*$ state are also predicted in the correct order for adenine, guanine, and AP, in comparison with *ab initio* results.[43,136,137]

A striking similarity exists between frontier MOs of AP and 6-ClG (Fig. 3.7) and hence their ground state structural parameters are very similar.(Table 3.1) $^1\pi\pi^*$ state of AP, described by H→L one electron configuration (Table 3.10b) does not change either position or character upon chlorine substitution in 6-ClG (Table 3.10c). The shifts in lowest energy transition due to stabilizations and destabilizations of HOMO and LUMO orbitals in these purines are depicted pictorially in Fig. 3.7. Changing electronegative chlorine to amino group destabilizes both HOMO and LUMO by the different extent in DAP compared to that in Ade and AP. This results in a blue shift of $^1\pi\pi^*$ state of DAP from that in 6-ClG. The introduction of carbonyl moiety in place of Cl6 (in GMP) or NH_2 (in DAP) at C_6 breaks the conjugation of the pyrimidine ring and destabilizes both HOMO and LUMO in GMP compared to those in Ade, AP, DAP and 6-ClG. GMP and 6-ThG have very similar electron density in their frontier MOs, but the $^1\pi\pi^*$ state of the later lies at~340 nm,[125,126] shifted by ~65 nm from that (~ 275 nm) of the former.

Table 3.4 Assignment of computed[a,b] vibrational wavenumbers on N9H form of neutral AP to bands in experimental spectrum, isotopic shifts[c] and computed potential energy distributions (PED)[d]

Exp. UVRR in H2O, at 225/260 nm (cm⁻¹)	Exp. Gas phase FTIR[e] (cm⁻¹)	Exp. Solid state, FTIR/Raman[f] (cm⁻¹)	Comp. in H₂O[a] (cm⁻¹)	Comp. in H₂O[b] (cm⁻¹)	PED in H₂O (%)[a,c]	Exp. Shift 225/260 nm (cm⁻¹)	Comp. Shift[b] (cm⁻¹)	Comp. Shift[a] (cm⁻¹)	Exp. UVRR in D2O, at 225/260 nm (cm⁻¹)	Comp. in D₂O[a] (cm⁻¹)	Comp. in D₂O[b] (cm⁻¹)	PED in D₂O (%)[a,c]
1643/1637	1626	1618/-	1650	1683	str N3C4 (41) - C5C6 (22)	-10/-8	-7	-8	1633/1629	1642	1676	- str N3C4 (41) + C5C6 (29) + be H6C6N1 (10)
-	1594	1649/1639	1620	1644	str N2C2 (10) + be H2bN2H2a (78)	-	-475	-454	-	1166	1169	be D2aN2D2b (46)
1586/1588	1550	1582/1587	1597	1619	str C5C6 (31) - N1C2 (16)	-4/-4	-6	-6	1582/1584	1591	1613	- str C5C6 (28) + N1C2 (19)
-/1514	-	1511/1517	1528	1552	str N7C8 (39) - be H8C8N7 (21)	-	-5		-	1523	1560	str N7C8 (42) - be H8C8N7 (21)
-/1496	-	1491/1485	1481	1512	str N7C8 (16) + N1C6 (12) + be N1C2N3 (12)	-	+19	+6	-	1487	1531	- str N7C8 (17) + N3C2 (10) - N2C2 (16) - be N1C2N3 (10)
1476/1470	1467	1452/-	1435	1460	- str N2C2 (15) - be H6C6N1 (27) - C5C6N1 (11) - N1C2N3(19)	4/7	+6	+5	1480/1477	1440	1466	str N2C2 (17) + be H6C6N1 (28) + C5C6N1 (12) + N1C2N3 (18)
1434/1432	1416	1428/1425	1404	1410	- str N9C8 (17) + be H9N9C8 (36)	5/5	-		1439/1437	-	-	-
1365/-	1352	1360/1360	1369	1382	str N1C6 (14) + C5C6 (10) - N3C2 (10) - N9C4 (10) - be H2aN2C2 (13)	+11	+11	+1	1376/1373	1370	1393	str N1C6 (32) - N3C2 (11)
-	-	-	1276	1313	str N7C8 (16) - N1C6 (19) - N3C2 (10)	-13	-11	-5	1295/-	1271	1302	str N1C6 (15) + N3C2 (19) - N9C8 (15) - be H6C6N1 (11)
1307/1306	-	1310/1302	1297	1301	str N9C4 (16) + be H6C6N1 (37) - C5C6N1 (10)	15/13	+15	+9	1323/1319	1306	1316	- str C5C6 (10) + N9C4 (23) + be H6C6N1 (27)
1285/1283	1276	1284/1285	1330	1348	str N7C8 (15) + N1C6 (21) + be H8C8N7 (31)	+10/6	+1	+9	1295/1289	1339	1349	str N7C8 (14) + N1C6 (14) - be N7C8N9 (16) + H8C8N7 (37)
1247/1249	1238	1250/1255	1198	1204	- be H8C8N7 (18) + C5C6N1 (32) - C8N9C4 (11)	-8/-13	-4	0	1239/1236	1198	1200	- be H8C8N7 (21) - D2aN2D2b (23) + C5C6N1 (20)
-	-	-	975	974	tors H6C6N1C2 (60) - C5C6N1C2 (11)	-	0	0	-	974	974	tors H6C6N1C2 (79) - C5C6N1C2 (15)
946/-	955	954	945	942	be N7C8N9 (68)	-2	-2	0	944/-	942	940	str N9C8 (18) + be N7C8N9 (45)
1105/-	-	1142/-	1101	1102	- str N3C2 (28) + be H2aN2C2 (49)	-	-	-	-	-	-	-
-	-	-/1125	1080	1072	str N9C8 (54) + be		-219	-210	-	862	853	- be N7C8N9 (13) + be

					H9N9C8 (32)							D9N9C8 (55)
973/-	-	965/968	974	978	- str N1C2 (18) + N9C4 (10) + be C6N1C2 (13) - tors H6C6N1C2 (19)	-96	-100	-101	877/-	877	878	- str N1C2 (19) + be D2bN2C2 (46)
-	-	872/-	880	850	tors H8C8N7C5 (82) + N7C8N9C4 (12)		-1	0	-	880	849	tors H8C8N7C5 (83) + N7C8N9C4 (12)
844/839	-	844/840	837	837	- str N2C2 (15) - be C6N1C2 (13) + C8N9C4 (38)	-24	-20	-16	820/-	821	817	- tors C4N3C2N1 (16) + C6N1C2N3 (16) - C5C6N1C2 (16) + out N2N3N1C2 (16)
-	-	799/-	816	809	- tors C4N3C2N1 (22) + C6N1C2N3 (21) - C5C6N1C2 (20) + out N2N3N1C2 (17)	-	-3	-1	-	808	806	- str N2C2 (10) + be C8N9C4 (20)
797/797	-	787/792	805	808	str N3C2 (12) + N1C2 (19) + N9C4 (10) - be C4N3C2 (15) + C6N1C2 (10) + N1C2N3 (12)	-8/-11	-14	-13	789/786	792	794	str N3C2 (10) + N1C2 (14) + N9C4 (10) - be C4N3C2 (13) + C6N1C2 (16) + N1C2N3 (11)
-	-	744/-	744	735	- tors C6N1C2N3 (10) - C8N9C4C5 (20) - out N2N3N1C2 (41) + N9C5N3C4 (17)	-	-1	-2	-	742	734	- tors C6N1C2N3 (10) - C8N9C4C5 (19) - out N2N3N1C2 (41) + N9C5N3C4 (16)
-	-	668/-	654	655	- tors H9N9C8N7 (21) + H8C8N7C5 (14) - N7C8N9C4 (50) + C8N9C4C5 (10)	-6	-13	-13	-	641	642	tors H8C8N7C5 (15) - N7C8N9C4 (59) + C8N9C4C5 (14)
-	-	631/639	639	638	be C4N3C2 (16) + N1C2N3 (24) - N2C2N1 (17)	-5	-15	-15	-	624	623	be C4N3C2(23) + N1C2N3 (22) - N2C2N1 (10)

[a]computed at B3LYP/6-311+G(2d,p)//PCM level of DFT and not scaled; [b]computed at B3LYP/6-31G(d,p)//vacuo level of DFT and not scaled; [c]all hydrogen atoms in optimized structure of N9H (or N7H) species are replaced by deuterium (D) to make deuterated forms corresponding to species at pD 7.0 in experiment; [c]PEDs are computed using the VEDA 4.0 program; abbreviations: str, bond stretching; be, bending; out, out of plane; tors, torsion, [e] Ref [145] FTIR in gas phase; [f]Ref [111] (K.O. Evans's PhD Thesis) FT-IR and Raman (λ_{exc}= 633 nm) of polycrystalline AP.

Table 3.5 Experimental and computed[a] vibrational wavenumbers and isotopic shifts[b] with computed potential energy distribution (PED)[c] of N9H and N_7H tautomers of AP at neutral pH.

Theory, N9H-AP		Experiment		Theory, N7H-AP	
PED in H_2O (%)[c]	Comp. wavenumber, isotopic shift (cm^{-1})[b]	UVRR, wavenumber, isotopic shift (cm^{-1})[d]	FTIR, Solid state (cm^{-1})[e]	Comp. wavenumber, isotopic shift (cm^{-1})[b]	PED in H_2O (%)[c]
str N3C4 (41) - C5C6 (22)	1650, -8	1643, -10	1618	1646, -6	str N1C6 (11) - N3C2 (14) + N7C5 (27)
str N2C2 (10) + be H2bN2H2a (78)	1620, -454	1629, -466	1649	1616, -451	be H2bN2H2a (79)
str C5C6 (31) - N1C2 (16)	1597, -6	1588, -8	1582	1594, -7	- str N1C6 (11) - N3C4 (23) + be C4N9C8 (11) + C5N7C8 (16)
- str N2C2 (15) - be H6C6N1 (27) - C5C6N1 (11) - N1C2N3 (19)	1435, +5	1469, +6	1452	1452, -15	str N2C2 (17) + be H7N7C8 (12) + H6C6N1 (14)
str N1C6 (14) + C5C6 (10) - N3C2 (10) - N9C4 (10) - be H2aN2C2 (13)	1369, +1	1361, +12	1360	1371, -20	- str N2C2 (15) - N7C5 (13)
str N7C8 (15) + N1C6 (21) + be H8C8N7 (31)	1330, +9	1285, +10	1284	1319, -5	str N9C8 (14) + N1C6 (19) + N7C5 (11) + be H6C6N1 (30)
str N9C4 (16) + be H6C6N1 (37) - C5C6N1 (10)	1297, +9	1307, +15	1310	1265, -15	- str N9C8 (21) + N1C6 (12) - be H8C8N9 (15)
- be H8C8N7 (18) + C5C6N1 (32) - C8N9C4 (11)	1198, 0	1247, -8	1250	1194, +3	str N9C4 (11) - N7C5 (15) + be H8C8N9 (18) + C5N7C8 (12)
tors H6C6N1C2 (60) - C5C6N1C2 (11)	974, -101	973, -96	965	975, +35	str N1C2 (34) + N2C2 (10) - N9C4 (11) - be C6N1C2 (14) + H2aN2C2 (11)
be N7C8N9 (68)	945, 0	946, -2	954	941, +15	- be C4N9C8 (14) + N7C8N9 (56) - C5N7C8 (12)
str N3C2 (12) + N1C2 (19) + N9C4 (10) - be C4N3C2 (15) + C6N1C2 (10) + N1C2N3 (12)	805, -13	797, -8	787	802, -10	str N3C2 (10) + N1C2 (18) + be C6N1C2 (20) - C2N3C4 (10)
- str N2C2 (15) - be C6N1C2 (13) + C8N9C4 (38)	837, -16	844, -20	844	840, -15	be C4N9C8 (30)

[a] computed at B3LYP/6-311+G(2d,p)//PCM level of DFT and not scaled; [b]All hydrogen atoms in optimized structure of N_9H (or N_7H) species are replaced by deuterium (D) to make deuterated forms corresponding to species at pD 7.0 in experiment and harmonic vibrational frequencies are computed on these structure without further geometry optimization; [c]PEDs are computed using VEDA 4.0 program; [d]Experimental wavenumbers and isotopic shifts of AP free base at 225 nm excitation, described in Table 3.4; [e]Ref [111] FTIR of polycrystalline AP; abbreviations: str, bond stretching; be, bending; out, out of plane; tors, torsion; The isotopic shifts of the marker bands differentiating N9H and N7H tautomers are shown in bold.

Compared to the number of studies investigating low-lying $^1\pi\pi*$, $^2\pi\pi*$ and $^1n\pi*$ states, very few have computationally characterized electronic states below 230 nm in purines.[39,110,133,134] Within 210-220 nm region, all the purines have strong electronic transitions (B_a and B_b according to Platt's convention) that are of $\pi\pi*$ character. Low energetic L_a and L_b states at ~ 260 nm and high energetic B_a and B_b transitions at ~ 210 nm are a common feature of the class of compounds with six-membered ring fused to five-membered rings. These states are assigned to available experimental data for each purine. (Table 3.10 a-f)
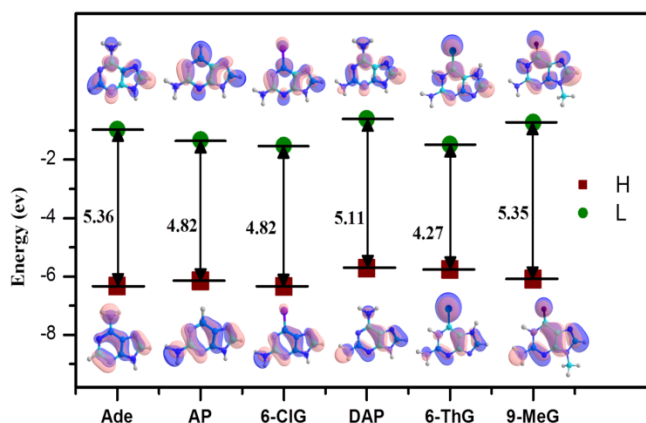
Fig. 3.7 Relative ordering of frontier molecular orbitals; highest occupied molecular orbital (HOMO or H) and lowest unoccupied molecular orbital (LUMO or L) of Ade, AP, 6-ClG, DAP, 6-ThG and 9-meG computed at B3LYP-6311+G(2d,p)//vacuo level of DFT.

Linear and magnetic dichroism measurements have resolved the B_a and B_b absorption bands of AP around ~215 nm into two components at 220.3 and 206.2 nm.[110] In agreement with experiment, TD-DFT also predicts these two states as of pure $\pi\pi*$ character at 210.7 and 200.5 nm respectively.(S_8 and S_{11} in Table 3.10a) Similar to low-lying electronic states, these two excitations also preserve their characters in 6-ClG and occur at similar positions, 217.5 and 202.2 nm respectively.[120] However, relative intensities of these two transitions differ in 6-ClG and in other purines with the occurrence of additional intermediate states. The corresponding B_b state in GMP, Ade and DAP is located at ~218 nm, ~210 nm and ~215 nm respectively. Thus, unlike L_a and L_b states, the high-lying electronic transitions of purines do not follow a substitution-dependent general trend.

3.3.4 Vibronic characters of L_a and B_b excited states

Inspection of relative intensities in UVRR spectra helps to recognize vibronic characters of the purines excited states that are in resonance with excitation lines.[60] In case of 260 nm excitation, all five bases show a distinct intensity pattern (Fig. 3.3) compared to those in their respective 225 nm excited spectra.(Fig. 3.4) Band positions and intensities of Ade and GMP spectra agree with previously published results.[56,60,61] In AP, DAP and 6-ClG, the 225 nm wavelength is in resonance

with B_b electronic state whose position and character do not get affected by substitution at C2 and C6. However, a very different experimental RR intensity pattern shows that change of -NH$_2$ substituent position from C6 (Ade) to C2 (AP) has a drastic effect on the excited state structures. Double substitutions with chlorine (in 6-ClG) or amino (in DAP) make the spectra more complex with an additional number of enhanced bands than both of single substituted Ade and AP.

Fig. 3.8 and 3.9 depict the involved molecular orbitals of five purines in each of the electronic transitions when excited with 225 and 260 nm lasers. In the case of Ade and GMP, 225 nm wavelength lies in between first allowed bright state at ~ 260 nm and B_b state at ~ 210 nm.(Fig. 3.2) In 225 nm excited spectra of Ade, the RR spectrum has a band at 1604 cm^{-1} with the largest intensity and four bands at 1488, 1354, 1335 and 1251 cm^{-1} with moderate intensities. Observed RR intensities of GMP and Ade at 225 nm are primarily derived from B_b (~210 nm) state and are discussed in detail in chapter 5 and chapter 6. The experimental[38] and computed absorption spectrum of AP (Fig. 3.6) clearly depicts a considerable amount of overlap between three close by $\pi\pi^*$ electronic states at ~ 241.7 (L_b), 220.3 (B_b) and 206.2 nm. Thus, the 225 nm excited RR spectrum of AP is expected to have contributions from these three electronic states. Enhancement and de-enhancement of vibrational bands of AP will depend on the constructive or destructive interference of the interacting electronic states along different normal mode coordinates.[148,149]

Table 3.6 Assignment of computed[a] vibrational wavenumbers on N₉H form of neutral DAP to bands in experimental spectrum, isotopic shifts[c] and computed potential energy distributions (PED)[d]

Exp. UVRR in H_2O, at 225/260 nm (cm^{-1})	Exp. UVRR in H_2O, at 280 nm (cm^{-1})[d]	Exp. Solid state, FTIR (cm^{-1})[e]	Exp. Solid state, FT-Raman[e] (cm^{-1})	Exp. Solid state, FTIR[f] (cm^{-1})	Comp. in H_2O[a] (cm^{-1})	PED in H_2O (%)	Exp. Shift 225/260 nm (cm^{-1})	Comp. Shift[a] (cm^{-1})	Exp. UVRR in D2O, at 225/260 nm (cm^{-1})	Comp. in D_2O[a] (cm^{-1})	PED in D_2O (%)
1661/-	-	1662	-	1662	1631	str N3C4 (12) - be H2bN2H2a (11) - H6bN6H6a (21)	-41	-14	-/1620	1617	str N3C4 (15) + N1C6 (15) - be N3C4C5 (14)
1622/1620	1612	1616	-	1616	1635	be H6bN6H6a (26) - N3C4C5 (10)	-12/-16	-36	1610/1604	1599	- str N3C2 (15) - be C6N1C2 (13) + C5N7C8 (16) + C4N9C8 (15)
1598/1601	-	-	-	1606	1616	be H2bN2H2a (64) - H6bN6H6a (17)	-422/-422	-425	1176/1179	1191	be D2bN2D2a (39) + D6bN6D6a (15)
-/1574	-	-	1582	1582	1596	str N3C2 (15) + be H6bN6H6a (15) - C2N3C4 (10) - C4N9C8 (12)	-	-	-	-	-
-/1542	-	1530	1530	1530	1519	- str N7C8 (38) + be H8C8N7 (22)	0	2	-/1542	1521	- str N7C8 (34) + be H8C8N7 (19)
1510/1510	1508	-	-	-	1484	- str N1C6 (33) + N6C6 (19)	7	-8	-/1517	1476	str N3C2 (12) - N1C6 (28) + N6C6 (26)
1490/1488	-	1477	1484	1477	1456	str N7C8 (10) - N1C2 (11) + N2C2 (23) + N9C4 (13)	-1	-	1490/1487	-	-
-/1412	-	-	1420	1439	1408	- str N3C4 (14) + N1C2 (13) + N9C4 (13) - be H9N9C8 (11)	-8	-11	1405/1404	1397	- str N3C4 (10) + N9C4 (23)
1401/1402	1402	1395	-	1395	1391	- str N9C8 (13) + be H9N9C8 (28)	-	-	-	-	-
-/1374	-	-	1374	-	1355	str N1C6 (11) - N1C2 (13) + be C5N7C8 (17) + H8C8N7 (13)	-43	-13	-/1331	1342	- str N1C6 (11) + N1C2 (20) - be C5N7C8 (14) - H8C8N7 (15) + N9C8N7 (11)
1348/-	1349	1335	-	-	1302	- str N7C8 (18) - N3C4 (16) + N7C5 (28) - be H8C8N7 (18)	18	19	1367/1368	1321	str N7C8 (13) + N1C2 (11) + N9C8 (20) + be H8C8N7 (18)
1290/1291	1290	-	1306	1290	1258	- str N7C8(12) + N6C6 (10) - N7C5 (21) + be H6aN6C6 (11) - H8C8N7 (17)	-2/-2	-4	1288/1289	1254	- str N7C8 (14) + N9C8 (12) - be H8C8N7 (12) + D6bN6D6a (13)
1240/1237	1237	1227	-	1227	1162	str N9C4 (14) + be C5N7C8 (14) - H8C8N7 (13)	2/5	22	1242/1242	1184	str N7C5 (18) + be H8C8N7 (11) - D2bN2D2a (15) + D6bN6D6a (17)
1155/1157	1158	1154	1158	1145	1159	str N1C2 (15) + be H2aN2C2 (23) +	-48/51	-54	1107/1106	1105	be C5N7C8 (16) + D6bN6D6a (20)

						H6aN6C6 (26)					
1124	-	1113	1116	1113	1088	str N9C8 (48) + be H9N9C8 (22)	-14	-57	1034/-	1031	- str N3C2 (10) - N1C2 (13) + N6C6 (10) - N2C2 (15) + be D2bN2D2a (10) - D6bN6D6a (14)
-	-	1145	-	-	1080	- str N3C2 (19) + be H2aN2C2 (24) - H9N9C8 (10)	-	-212	-/848	868	be D9N9C8(55) - N9C8N7 (17)
987/988	981*	984	978	984	983	str N1C6 (10) + N1C2 (18) - be C6N1C2 (11) - H6aN6C6 (26)	-26/-25	-28	961/963	955	str N9C8 (10) + be D2aN2C2 (29) + D6aN6C6 (14) - N2C2N3 (11)
945/944	948	967	946	967	948	be N9C8N7 (55)	-4	-2	941/-	946	str N9C8 (19) + be N9C8N7 (45)
831/836	831	846	-	846	833	str N3C4 (10) + be N3C4C5 (10) - C2N3C4 (10) + N1C2N3 (15) + C4N9C8 (24)	19/9	15	850/845	848	- str N1C2 (10) + be D6aN6C6 (21) - C4N9C8 (12)
-	-	891	883	883	854	tors H8C8N7C5 (84)		0	-	854	tors H8C8N7C5 (83)
795/796	-	-	817	-	809	- tors C6N1C2N3 (13) + N1C2N3C4 (22) - C5N7C8N9 (14) + out N6C5N1C6 (12) - N3N9C5C4 (24)	4/12	-1	799/798	808	- tors C6N1C2N3 (14) + N1C2N3C4 (23) - C5N7C8N9 (13) + out N6C5N1C6 (10) - N3N9C5C4 (22)
740/-	-	766	768	-	753	- tors C5N7C8N9 (11) + out N6C5N1C6 (10) - N2N1N3C2 (67)	-1	-2	739/740	751	- tors C5N7C8N9 (11) - out N2N1N3C2 (67)
723/-	-	733	-	-	686	tors C4N9C8N7 (18) + out N6C5N1C6 (51) + N3N9C5C4 (13)	17			683	tors C4N9C8N7 (16) + out N6C5N1C6 (55) + N3N9C5C4 (13)
-	-	688	-	688	660	- tors H9N9C8N7 (20) + H8C8N7C5 (12) - C4N9C8N7 (10) + C5N7C8N9 (41)		-13		647	tors H8C8N7C5 (14) - C4N9C8N7 (14) + C5N7C8N9 (53)
-/649	650	658	659	646	652	be N1C2N3 (14)	-36	-44		608	- be N3C4C5 (11) + C2N3C4 (15) + N1C2N3 (12)
-/606	-	595	-	595	636	str N6C6 (12) + N2C2 (10) + N9C4 (10) + be C6N1C2 (25)		-38		598	str N6C6 (10) + N2C2 (13) + be C6N1C2 (25)

[a]computed at B3LYP/6-311+G(2d,p)//PCM level of DFT and not scaled; [b]All hydrogen atoms in optimized structure of N9H (or N7H) species are replaced by deuterium (D) to make deuterated forms corresponding to species at pD 7.0 in experiment and harmonic vibrational frequencies are computed on these structure without further geometry optimization; [c]PEDs are computed using the VEDA 4.0 program; [d] Ref [116] UVRR of aqueous solution at 4°C with 281 nm of excitation, wavenumber marked with * was observed with 257 nm excitation; [e]Ref [115] FTIR in polycrystalline state and FT-Raman (λ_{exc}= 1064 nm); [f]Ref [114] FTIR of DAP in polycrystalline state; abbreviations: str, bond stretching; be, bending; out, out of plane; tors, torsion, sign indicates relative phase of movement of atoms of an internal coordinates
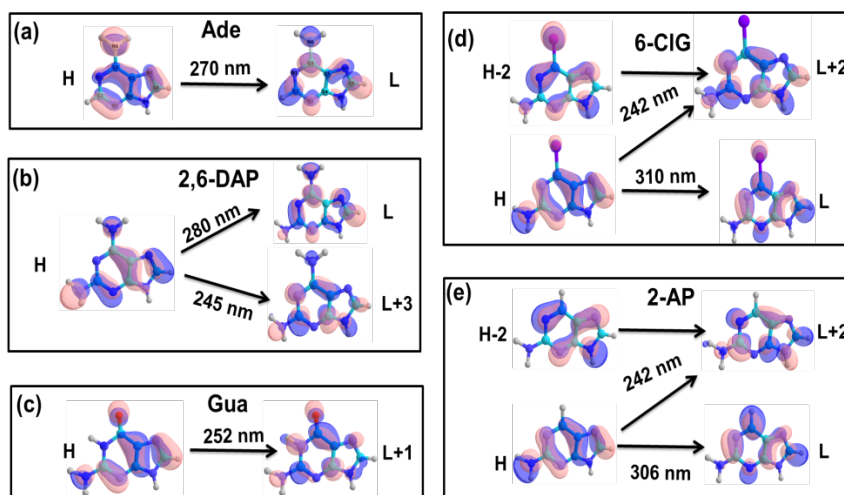
Fig. 3.8 Isodensity surfaces (0.04 *e*/bohr^3) of involved Kohn-Sham molecular orbitals in electronic transitions associated with 260 nm excited RR spectra of (a) Ade, (b) DAP (c) Gua, (d) 6-ClG and (e) AP. Experimental band maxima (in nm) corresponding to respective electronic transition are also mentioned.

Table 3.7 Assignment of experimental vibrational bands of GMP on computed[a] wavenumbers of 9-meG

Experiment		Computed			
GMP, UVRR in H$_2$O, at 225/260 nm (cm^{-1})	Gua, solid, Raman at 632.8 nm[c] (cm^{-1})	N$_9$H-Gua[c] (cm^{-1})	N$_9$H-Gua[a] (cm^{-1})	9-meG[a] (cm^{-1})	PED (%)[a,b]
1689/1681	1675	1797	1697	1696	str O6C6 (54) - be C6N1C2 (16)
1607/1602	1602	1667	1641	1642	be H2aN2H2b (75)
1580/1576	1551	1621	1592	1577	str N3C4 (27) - be C5N7C8 (11) - C4N9C8 (13)
-	-	1610	1596	1598	- str N3C2 (37) + be H1N1C2 (27)
1539/1537		1559	1550	1563	str N7C8 (15) - be N3C4C5 (12) + C4N9C8 (16)
1485/1486	1479	1517	1500	1499	be H9bCmeH9a (24)
1414/1412	1421	1441	1421	1425	str N9C4 (24) - be C5N7C8 (13)
1365/1366	1361	1365	1356	1383	str N9C8 (10) + be C5N7C8 (14)
-	1390	1390	1391	1345	- str N9C8 (16) - be H1N1C2 (13)
-	-	1337	1337	1341	str N2C2 (14) - N7C5 (13) - be H1N1C2 (25)
1249/1240	-	-	-	-	
1319/1319	1234	1310	1306	1301	- str N7C8 (15) - N3C4 (11) + N7C5 (15) - be H8C8N7 (19)
-	-	-	-		
1209/1204	1186	1176	1177	1247	str N9Cme (16) + be H8C8N7 (41) - N9C8N7 (14)
1176/1173	1159	1141	1147	1156	- str N7C5 (13) + N1C6 (33) - be C6N1C2 (10)
1121/1111	1048 #	1074	1084	1062	- str N9C8 (17) + be N9C8N7 (18) + tors H9aCmeN9C8 (17) - H9bCmeN9C8 (17)
1078/1079	1048 #	1076	1093	1112	str N3C2 (11) + N2C2 (11) + be H2bN2C2 (47)
1034/1015	1048 #	1047	1043	1074	str N1C2 (12) - N1C6 (19) + be C5N7C8 (11) - C2N3C4 (12)

-/1020	937	945	951	1027	- str N9C4(10) + str N1C2(24) - be C5N7C8(11) - be H2bN2C2(10)
866/868	848	835	835	856	str N3C4 (11) + N9C8 (11) + be N3C4C5 (12) + N1C2N3 (10) + N9C8N7 (12)
822/-	879	822	851	848	tors H8C8N7C5 (82)
794/789	775	765	798	797	- tors C5N7C8N9 (23) - out O6N1C5C6 (35) - N3N9C5C4 (21)
-/689	693	729		735	- out O6N1C5C6 (16) - N2N1N3C2 (63)
-	693 #	694		707	- tors C4N9C8N7 (14) + out O6N1C5C6 (35) - N2N1N3C2 (12) - N3N9C5C4 (16)
-	710	668		687	be O6C6N1 (20) + N2C2N3 (18)
-	-	-	-	727	str N9Cme (21) - be N1C2N3 (15) + N9C8N7 (18)
671	649	626		617	str N1C2 (14) + N1C6 (12) + be C6N1C2 (16)

[a]this study, computed at B3LYP/6-311+G(2d,p)/PCM level; [b]PEDs are computed using the VEDA 4.0 program; [c]Ref [118] Normal microRaman spectra (λ_{exc} = 632.8 nm) of polycrystalline guanine and computed on N9H-Gua at B3LYP/6-311++G(d,p)/vacuo level; [#]this band is not assigned with certainty in Ref [118]; abbreviations: str, bond stretching; be, bending; out, out of plane; tors, torsion, sign indicates relative phase of movement of atoms of internal coordinates.

The 260 nm excited UVRR spectra of GMP and 6-ClG are very similar in intensity pattern, as reported earlier,[58] however, the involved MOs in the corresponding electronic transition are quite different.(Fig. 3.8, panel c and d) While in GMP the RR intensity is primarily borrowed from a strong L_b transition at ~ 248 nm, a mixed contribution from both L_a (~ 310 nm) and B_b (~242 nm) states is expected in the enhancement of vibrations of 6-ClG. On the other hand, although the characters of involved MOs that are associated with excitation at 260 nm and 225 nm wavelengths are identical for AP and 6-ClG, their RR spectra are entirely different in terms of both band positions and relative band intensities. Especially unlike in AP, Ade, DAP and GMP three in-plane ring modes (954, 919 and 832 cm^{-1}) below 1000 cm^{-1} become RR active in 225 nm excited spectrum of 6-ClG. Thus, substitution of a Cl for O or NH$_2$ not only alters ground state structures but significantly modifies the intrinsic FC activity in the B_b electronic states. An excitation wavelength of 260 nm is located in between L_a and L_b transitions in AP, 6-ClG and DAP. Thus, RR intensities in 260 nm excited spectra of these three bases would be derived from a mixed contribution from both the electronic states.

3.3.5 Vibrational reorganization in substituted purines

3.3.5.1. Substitution effects on pyrimidine localized vibrations

Alteration of internal coordinate contributions to PEDs and shift in vibrational wavenumbers due to double substitutions at C2 and C6 position of purine is described in Table 3.11. Effects of changing C6 substituent in four purines; GMP, 6-ClG, DAP, and 6-ThG, all containing amino moiety at C2 are described in Table 3.12. Owing to positive

resonance effect, the addition of an extra NH_2 group at C2 site makes N1–C2 and C2–N3 bonds weaker in DAP compared to those in Ade. These changes are reflected in downshifting of 1649 and 1602 cm^{-1} band of Ade to 1625 and 1574 cm^{-1} in DAP respectively. Unlike in AP, in doubly substituted DAP an RR band at 1625 carries maximum intensity. These two modes get upshifted to 1585 and 1639 cm^{-1} in 6-ClG where the 6th NH_2 of DAP is substituted by a Cl atom. Such a substitution reduces π electron density of the aromatic ring through the negative inductive effect and strengthens N1–C2, C5–C6 and N3–C4 bonds. As a result, force constants of the normal modes that are composed of stretching of these bonds increases, and the corresponding Raman bands upshift.
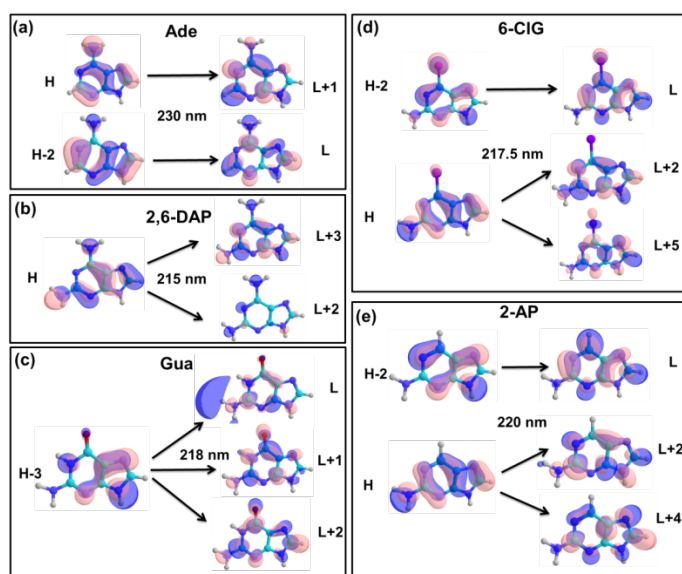
Fig. 3.9 Isodensity surfaces (0.04 *e*/bohr^3) of involved Kohn-Sham molecular orbitals in electronic transitions associated with 225 nm excited RR spectra of (a) Ade, (b) DAP (c) Gua, (d) 6-ClG and (e) AP. Experimental band maxima (in nm) corresponding to respective electronic transition are also mentioned.

The conjugation of the pyrimidine ring breaks in GMP because of oxygen substitution at C6 in place of a Cl atom (6-ClG) or an NH_2 group (DAP and Ade). C6 makes a double bond with exocyclic O6 due to a higher amount of π orbital (2p) overlap. As a consequence C6–N1, N1–C2, N3–C4 and C5–C6 bonds get weaker. A large downshift of various pyrimidine localized modes, e.g. 1407 cm^{-1}, 1469 cm^{-1} and 1585 cm^{-1} of 6-ClG to 1331 cm^{-1}, 1414 cm^{-1} and 1576 cm^{-1} in GMP, also establish the same fact. The UV-Vis absorption of 6-ThG shows a peak at ~ 340 nm, about 30 nm red-shifted from the lowest energy band (~ 310 nm) of 6-ClG and about 65 nm red-shifted from the first $\pi\pi^*$ transition of GMP (~ 275 cm^{-1}). It clearly suggests an increase in π electron conjugation of the purine ring from GMP to 6-ClG to 6-ThG. The magnitude of C6–S6 bond length (1.68 Å) lies in between that of C6=O6 (1.23 Å) in GMP and C6–Cl6 (1.75 Å) in 6-ClG.

Table 3.8 Assignment of experimental RR spectrum of 6-ClG using computation[a] on N9H tautomer and potential energy distributions (PED)[b]

Exp. UVRR in H_2O, at 225/260 nm (cm^{-1})	Computed[a] (cm^{-1})	PED (%)[b]
1641/1639	1647	str N1C6 (18) + N3C4 (16) – be N3C4C5 (14)
1602/1606	1622	str N2C2 (10) + be H2aN2H2a (76)
1585	1572	str N3C4 (12) + N3C2 (19) – be C2N3C4 (11) – C4N9C8 (13)
1520/1515	1528	str N7C8 (37) – be H8C8N7 (19)
1476/1480	1472	str N2C2 (20) + be N1C2N3 (15)
1407	1408	str N1C6 (23) – N3C4 (12) – N2C2 (12) + N9C4 (17)
1386/-	1414	- str N1C6 (10) + N9C8 (16) + be N9N9C4 (35)
-/1354	1374	- str N9C4 (10) - N7C5 (16) + be N9N9C4 (10) + H2aN2C2 (11) + C2N3C4 (15)
1309	1327	– str N7C8 (15) + N7C5 (14) – be C5N7C8 (11) – H8C8N7 (23) + N9C8N7 (12)
1260	1287	str N7C8 (16) – N1C6 (19) + N3C4 (15) + N1C2 (14) + be H8C8N7 (10)
1191/1194	1199	str N7C5 (21) – be C5N7C8 (10) + H8C8N7 (24)
1120	1103	str N3C2 (25) + be H2aN2C2 (48)
1088/1092	1086	str N9C8 (54) – be N9N9C4 (28)
1043	1037	str N1C2 (25) – be H2aN2C2 (11) – Cl6C6N1 (11)
954	953	– be C5N7C8 (12) + N9C8N7 (47)
917/919	900	str N1C2 (13) + N2C2 (10) – Cl6C6 (23) + be C6N1C2 (11) + C5N7C8 (12) – N9C8N7 (12)
831	828	str N3C4 (10) – be C2N3C4 (10) + N1C2N3 (17) + C4N9C8 (21)
800	807	tors C6N1C2N3 (14) – N1C2N3C4 (21) + C5N7C8N9 (12) – out N2N1N3C2 (10) + N3N9C5C4 (32)
787	807	tors C6N1C2N3 (14) - N1C2N3C4 (21) + C5N7C8N9 (12) - out N2N1N3C2 (10) + N3N9C5C4 (32)

[a]computed at B3LYP/6-311+G(2d,p)//PCM level of DFT and not scaled; [b]PEDs are computed using VEDA 4.0 program; abbreviations: str, bond stretching; be, bending; out, out of plane; tors, torsion, sign indicates relative phase of movement of atoms of internal coordinates.

Table 3.9 Assignment of experimental vibrational bands of 6-ThG in solid state using computation[a] on thione-amino (N_1H, N_7H) tautomer and computed potential energy distributions (PED)[b]

Experiment in polycrystalline state[c]		Experiment in solid state[d]			Computed[a]	
FTIR (cm^{-1})	FT-Raman (cm^{-1})	Raman (cm^{-1})	SERS of 6-ThG (cm^{-1})	SERS of 6-ThG + HAS (cm^{-1})	Wavenumber (cm^{-1})	PED[b] (%)
1625	1620	1667	-	-	1645	- str N3C2(11) + be H2aN2H2b(60)
1585	1590	1592	1607	1592	1625	str N3C2(20) - str N7C5(18) + be H2aN2H2b(12)
1539	1537	1543	1551	1551	1590	str N2C2(10) + be H1N1C2(42) + be N1C2N3(11)
1480	1482	1485	1499	1491	1545	str N3C4(24) + str N7C5(10) - be C4N9C8(13) - be C5N7C8(13)
1433	1439	1441	1453	1453	1493	- str N9C8(18) + be C4N9C8(10) + be H8C8N9(30)
-	-	1427	1427	1427	1450	- str N7C8(22) + be H7N7C8(35)
1370	1369	1372	1382	1375	1399	str N7C8(14) + str N2C2(16) - str N1C2(15)
1314	1326	1260	1297	1297	1372	str N3C4(15) - str N9C4(17) - str N7C5(25) + be C5N7C8(18)

1285	-	-	1271	1271	1389	- str N9C8(11) + str N9C4(11) - be H1N1C2(21)
1225	1229	1231	1247	1247	1280	str N9C8(40) + be H8C8N9(23)
1140	-	1140	1139	1145	1210	- str N7C5(19) + str N1C6(17) + be H8C8N9(18)
-	1130	-	-	1126	1199	str N1C6(45) - be H1N1C2(14)
1100	1112	-	-	-	1130	str N3C2(19) - str N9C4(13) + be H2bN2C2(36)
1078	1080	1034	1030	1030	1121	str N7C8(40) + be H7N7C8(34) - be H8C8N9(11)
-	980	992/970	990	-	1025	str N1C2(19) - be H2bN2C2(21) - be C5N7C8(12)
-	945	944	954	948	971	- str N1C2(23) + str S6C6(24) - be N7C8N9(20)
-	923	924	915	915	946	str S6C6(11) - be C4N9C8(13) + be N7C8N9(41)
812	838	839	839	839	901	tors H8C8N9C4(85) - tors C4N9C8N7(13)
	795	776	-	-	836	str N3C4(14) + be C4N9C8(29) - be C2N3C4(13) + be N1C2N3(17)
735	-	-	-	-	798	tors C2N3C4C5(23) + tors C4N9C8N7(25) - tors N1C2N3C4(13) - out N3C5N9C4(20)
693	719	714	-	-	729	out N2N1N3C2(71)
645	-	649	-	-	670	- tors H1N1C2N2(32) + tors C5N7C8N9(19) + out S6N1C5C6(24)
-	656	-	-	-	663	- tors H1N1C2N2(43) - tors H7N7C8N9(11) - tors C5N7C8N9(23)
600	-	-	-	-	647	be C2N3C4(10) - be N3C4N9(13) + be N2C2N3(11) + be N1C2N3(16) - tors H1N1C2N2(12)
565	-	562	554	561	595	tors C5N7C8N9(13) - out S6N1C5C6(40)

[a]computed at B3LYP/6-311+G(2d,p)//PCM level of DFT and not scaled; [b]PEDs are computed using the VEDA 4.0 program; [c]Ref [125] FTIR and FT-Raman (λ_{exc} = 1064 nm) of polycrystalline 6-ThG; [d]Ref [126] normal Raman of solid 6-ThG and SERS with Au nanoparticles at 632.8 nm excitation; abbreviations: str, bond stretching; be, bending; out, out of plane; tors, torsion, sign indicates relative phase of movement of atoms of an internal coordinates.

Exchanging the position of NH_2 group from C6 to C2 downshifts the pyrimidine stretching mode of Ade from 1602 cm^{-1} to 1588 cm^{-1} in AP. The introduction of another NH_2 at C2 site further downshifts this mode by 14 cm^{-1} in DAP due to an increase in π electron conjugation of the pyrimidine ring. A similar amount (10-13 cm^{-1}) of isotopic downshift of this mode in three purines (Ade, AP, and DAP) suggests a comparable amount of coupling of exocyclic NH_2 vibration with this mode. Replacing NH_2 moiety with oxygen at C6 upshifts this band back to 1602 cm^{-1} in GMP, by decreasing the π electron conjugation. Substitution of O6 by a chlorine (6-ClG) or sulfur (6-ThG) atom also upshifts of this band by 4 and 18 cm^{-1} in 6-ClG and 6-ThG respectively.(Table 3.1) Another in-plane ring distortion mode of GMP at 868 cm^{-1} undergoes a large downshift of 73 cm^{-1} in 6-ThG and of 36 cm^{-1} in 6-ClG. This trend is also in agreement with a gradual increase of π conjugation of pyrimidine ring from GMP to 6-ClG to 6-ThG.

Table 3.10 TD-DFT[a] computed vertical electronic excited state energies, oscillator strengths (f_{vac}) of the neutral forms of the studied purines; (a) Ade, (b) AP, (c) 6-ClG, (d)DAP, (e) GMP and (f) 6-ThG, and available experimental data.

a.Ade, N_9H					
This Work					Published
Singlet states	Transition type	Major orbital Contribution[b] (%)	ΔE_{vert} nm (eV)	f_{vac}	Exp. λ_{max} nm (eV)
S1	$n\pi^*$	H–1→L (90)	251.01(4.94)	0.0133	269.7 (4.60)[c]
S2, L_a	$\pi\pi^*$	H→L (83)	248.11 (5.00)	0.1916	258.5 (4.80)[c]
S3	$\pi\pi^*$	H–2→L (24) H→L+1 (63)	236.40 (5.24)	0.0346	230.0 (5.38)[d]
S4	$\pi\pi^*$	H→L+2 (84)	230.47 (5.38)	0.0071	
S5	$n\pi^*$	H–1→L+1 (85) H–1→L+2 (11)	222.54 (5.57)	0.0012	
S6	$\pi\pi^*$	H→L+3 (91)	219.48 (5.65)	0.0043	
S7	$n\pi^*$	H–3→L (95)	211.69 (5.86)	0.0006	
S8, B_b	$\pi\pi^*$	H–2→L (40) H→L+1 (12) H→L+4 (39)	200.79 (6.17)	0.1465	210.3 (5.90)[c]
S9	$\pi\pi^*$	H–2→L (15) H–1→L+2 (30) H→L+4 (26)	200.10 (6.20)	0.116	197.0 (6.30)[c]

b.AP (N_9H)							
This Work					Published		
Singlet states	Transition type	Major orbital Contribution (%)	ΔE_{vert} nm (eV)	f_{vac}	Exp.[e] λ_{max} nm (eV)	Exp.[e] ε ($M^{-1}cm^{-1}$)	ΔE_{vert}[f] nm (eV)
S1, L_a	$\pi \to \pi^*$	H→L (94)	284.78	0.1314	305.8 (4.05)	5400	295 (4.2)
S2	$n \to \pi^{*2}$	H–1→L (98)	279.49	0.0021	277.7 (4.47)	~ 140	
S4	$\pi \to \pi^*$	H–2→L (35) H→L+2 (60)	230.91	0.0498	241.7 (5.1)	4200	248 (5.0)
S8, B_b	$\pi \to \pi^*$	H–2→L (38) H→L+2 (25) H→L+4 (21)	210.76	0.2519	220.3 (5.6)	14900	
S11	$\pi \to \pi^*$	H→L+4 (47) H→L+5 (30)	200.54	0.1691	206.28 (6.0)	10900	

c.6-ClG (N_9H)					
Singlet states	Transition type	Major orbital Contribution[b] (%)	ΔE_{vert} nm (eV)	f_{vac}	Exp. λ_{max} nm (eV)
S1, L_a	$\pi\to\pi^*$	H→L(94)	284.2 (4.36)	0.1437	310.4 (3.99)
S2	$n\to\pi^*$	H–1→L(98)	264.8 (4.68)	0.0015	
S3	$n\to Ryd^*$	H→L+1(96)	235.8 (5.26)	0.0026	
S4, L_b	$\pi\to\pi^*$	H→L+2(61), H–2→L(34)	232.7 (5.33)	0.0663	241.7 (5.13)
S8, B_b	$\pi\to\pi^*$	H–2→L(+34) H→L+5(24) H→L+2(+19)	209.3 (5.92)	0.2583	217.5 (5.7)
S11	$\pi\to\pi^*$	H→L+5(+36) H–4→L(30)	201.8 (6.14)	0.1292	202.2 (6.13)

d. DAP (N_9H)						
This Work					Published	
Singlet states	Transition type	Major orbital Contribution[b] (%)	ΔE_{vert} nm (eV)	f_{vac}	Exp. λ_{max}[g] nm (eV)	ΔE_{vert}[h] nm (eV)
S1, L_a	$\pi\to \pi^*$	H→L (90%)	266.0 (4.66)	0.1658	280.0 (4.43)	269.6 (4.6)

S2, L_b	$\pi \to \pi^*$	H→L+1 (98%)	254.7 (4.87)	0.0014	253 (4.9)	
S3	$\pi \to \pi^*$	H→L+3 (80%)	240.9 (5.15)	0.0265	245 (5.06)	253 (4.9)
S4	$n \to \pi^*$	H–2→L (26%), H–1→L (62%)	239.4 (5.18)	0.0044		
S5, B_b	$n \to \pi^*$ $\pi \to \pi^*$ $\pi \to \pi^*$	H–2→L (19%), H→L+2 (13%), H→L+3 (60%)	238.3 (5.20)	0.0744	215 (5.77)	
S6	$\pi \to \pi^*$	H→L+4 (86%)	232.30 (5.34)	0.0146		
S7	$\pi \to \pi^*$	H→L+5 (83%)	210.78 (5.88)	0.0099		

e. GMP					
This Work, N_9H-Gua					Published
Singlet states	Transition type	Major orbital Contribution[b] (%)	ΔE_{vert} nm (eV)	f_{vac}	Exp. λ_{max}[i] nm (eV)
S1	$\pi \to \pi^*$	H→L (88)	264.2 (4.69)	0.0306	
S2, L_a	$\pi \to \pi^*$	H→L+1 (80)	254 (4.88)	0.1136	276 (4.47)
S3, L_b	$\pi \to \pi^*$ $\pi \to$ Ryd	H→L+2 (48) H→L+3 (40)	239.3 (5.18)	0.1276	248.2 (5.00)
S4	$\pi \to$ Ryd $\pi \to \pi^*$	H→L+3 (59) H→L+2 (36)	238.3 (5.24)	0.1124	
S18, B_b	$\pi \to \pi^*$	H–3→L (33) H–3→L+1 (23) H–3→L+2 (23)	184.6 (6.71)	0.0205	217.7 (5.7)
S19	$\pi \to \pi^*$	H–3→L (39) H–3→L+2 (36)	183.1 (6.72)	0.1411	200.1 (6.2)

f. 6-ThG (N_1H, N_7H)					
This Work					Published
Singlet states, nomenclature	Transition type	Major orbital Contribution[b] (%)	ΔE_{vert} nm (eV)	f_{vac}	Exp. λ_{max}[j] nm (eV)
S1	$n \to \pi^*$	H-1→L (99)	385.61 (3.22)	0.0000	
S2, L_a	$\pi \to \pi^*$	H→L (94)	324.97 (3.81)	0.2595	340 (3.65)
S3	$\pi \to \pi^*$	H→L+1 (94)	270.52 (4.58)	0.0123	
S4, L_b	$\pi \to \pi^*$	H→L+2 (83)	260.08 (4.76)	0.0387	256 (4.84)
S7	$n \to \pi^*$ $n \to \pi^*$	H–1→L+2 (60) H–1→L+1 (15)	251.61 (4.92)	0.0252	
S8	$\pi \to \pi^*$	H–2→L (59)	248.17 (4.99)	0.0278	
#S9	$\pi \to$ Ryd*	H–2→L +3 (97)	243.56 (5.09)	0.0159	
S11, B_b	$\pi \to \pi^*$ $\pi \to \pi^*$	H–4→L (40) H→L+4 (28)	224.47 (5.52)	0.1179	217 (5.71)
S13, B_b	$\pi \to \pi^*$ $\pi \to \pi^*$	H→L+4 (49) H–4→L (25)	215.94 (5.74)	0.0897	
#S23	$\pi \to \pi^*$	H→L+9 (88)	183.1 (6.72)	0.1411	
S25	$\pi \to \pi^*$ $^{\#}\pi \to \pi^*$	H–2→L+2 (38) H→L+8 (34)	192.15 (6.45)	0.3062	204 (6.08)

[a]computed at TD-B3LYP/6-311+G(2d,p)//vacuo level on geometry optimized at same level of ground state DFT; [b]percentages are calculated as 100 x twice the squares of the coefficients in the CI expansion of TD-DFT wave functions; [c]average experimental λ_{max} from Ref [134] and references there in; [d]Ref [128]; [e]Ref [110]; [f] Ref [43]; [g]average experimental λ_{max} from Ref [129], [130], [131], [132]; [h]From Ref [43], results are from CASSCF calculation followed by MRPT correction; [i]average experimental λ_{max} from Ref [134] and references there in; [j]average experimental transition energies from Ref [135], [126];Abbreviations: ε, molar extinction coefficient. [#]States with contributing orbitals that are not localized on the molecule.

3.3.5.2. Substitutions reorganize normal mode compositions

Exocyclic substitution not only shifts position of vibrational frequencies by modulating ground state structure but also reorganizes the PEDs associated with those vibrations. The RR band of AP at 1247 cm^{-1} that originates from bending of C5N7C8 and H8C8N7 coordinates is downshifted to 1146 cm^{-1} in Ade. This large shift is a consequence of a substantial amount of coupling of C2N3C4 and N9C8N7 bending and C6–N6 stretching, and also decoupling of stretching of N7–C5 coordinate. Switching amino group from C6 to C2 also considerably decreases the coupling of exocyclic –NH$_2$ vibration with this mode; evident from lesser isotopic shift (- 8 cm^{-1}) in AP compared to large (+ 36 cm^{-1}) shift in Ade. The introduction of a Cl or O atom in place of NH$_2$ at C6 position entirely alters PED of this mode and a direct correspondence is not found in 6-ClG and GMP respectively.
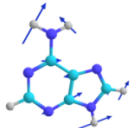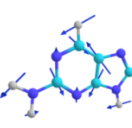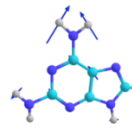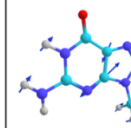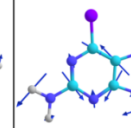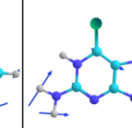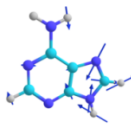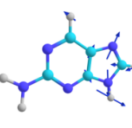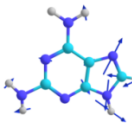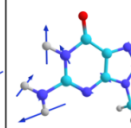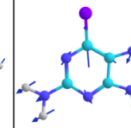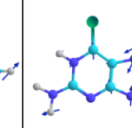
A change of substituents on the pyrimidine does not significantly distort structural parameters of the imidazole ring. (See Table 3.1) On the other hand, vibrational modes localized primarily on pyrimidine coordinates behave differently. The in-plane imidazole breathing mode which occurs at ~ 945 cm^{-1} in Ade, AP and DAP does not change its position by addition or switching of NH$_2$ moiety on pyrimidine ring. (Fig. 3.10) But, substitution of -NH$_2$ by a Cl atom at C6 causes a ~30 cm^{-1} downshift of this mode in 6-ClG. (See Table 3.12) This downshift does not result from changes in the geometry of the purine but due to the coupling of C-Cl6 stretching coordinate with imidazole breathing vibration. The heavy Cl atom increases reduced mass of this normal mode and hence decrease its frequency. Similar coupling with the exocyclic stretching coordinate is observed in 6-ClG at 919 cm^{-1}, in 6-ThG at 923 cm^{-1} and 954 cm^{-1}(Table 3.12), and in other halogenated pyrimidines also.[150] It is known that the exocyclic carbonyl (C6=O) stretching coordinate does not couple with any ring breathing vibrations of GMP. Thus, this imidazole localized mode experiences an upshift in GMP compared to the corresponding modes observed in both 6-ClG and 6-ThG. (Table 3.12) **Activation of such exocyclic stretching has unprecedented implications in initial excited state structural dynamics of these purines (GMP and 6-ClG) discussed in chapter 3 and 4.**

Table 3.11. Experimental band positions (cm^{-1}), computed[a] wavenumbers and vibrational mode descriptions for important ring modes of Ade, AP, DAP and 6-ClG.

Modes description	Ade		DAP		AP		6–ClG	
	Comp.[a] (cm^{-1})	Exp. (cm^{-1})	Comp.[a] (cm^{-1})	Exp. (cm^{-1})	Comp.[a] (cm^{-1})	Exp. (cm^{-1})	Comp.[a] (cm^{-1})	Exp. (cm^{-1})
Pyrimidine ring def.	1636	1649	1635	1620	1650	1637	1647	1639
2nd NH$_2$ sci.	-	-	1616	1601	1621	-	1622	1606

Pyrimidine def.	1617	1601	1596	1574	1597	1588	1572	1585
C8H8 be. + N7C8 str.	1509	-	1519	1542	1528	1514	1528	1515
N7C8H be. + N9C8 str. + ring def.	1366	1396	1391	1402	1369	1365	1374	1354
C5N7C8 + H8C8N7 be.	1142	1146	1162	-	1198	1249	-	-
C8N9 str. + C4N9H9 be.	1095	1083	1087	-	1080	-	1086	1092
6th NH2 rock.	1013	1022	983	988	-	-	-	-
Imidazole ring def. (C6–Cl6 str. in 6–ClG)	947	943	948	944	945	946	900	919
C8H out of plane be.	877	840	854	-	880	-	882	-
Pyrimidine tors. + C8H wagg.	820	785	809	796	805	797	807	787

[a]computed at B3LYP/6-311+G(2d,p)//PCM level of DFT on respective neutral tautomer (See text), not scaled; abbreviations: comp: computed; exp: experimental; Pu: purine ring; Pyr: pyrimidine ring; Imd: imidazole ring; Def: in-plane deformation; Breath: in-plane ring breathing mode; str: bond stretching; be: in-plane bending; Rock: in-plane rocking motion; Wag: out-of-plane wagging; Tors: out-of-plane torsional distortion. For detailed normal mode description see Table 3.3, 3.5, 3.7 and 3.9.

Fig. 3.10. Experimental (computed) vibrational frequencies and normal mode description of (a) in-plane pyrimidine stretching and (b) in-plane imidazole breathing of Ade, AP, DAP , 9-meG, 6-ClG and 6-ThG. Vibrational frequencies (not scaled) and normal modes are computed at B3LYP/6-311+G(2d,p)//PCM level. * Experimental wavenumbers correspond to those of GMP at neutral pH.

Positions of certain vibrational modes are not sensitive to the substituent present at C6 but undergo substantial rearrangement in their PEDs. One such example is the unique RR signature of GMP at 1486 cm^{-1}, that arises from stretching of the pyrimidine ring and N7–C8 bond, and also a contribution from N1–H bending. (Fig. 3.10) Upon substitution of oxygen by Cl or S, this band experiences a minimal (6 cm^{-1} and 4 cm^{-1} respectively) downshift in 6-ClG and 6-ThG. (Table 3.12) In 6-ThG, this band does not undergo major shift but the presence of hydrogen at N7 reorganizes the normal mode: N7–C8 stretching decouples and the contribution from N3–C4 and C5–N7 stretching increases compared to

those in GMP. However, according to the computed PEDs, in 6-ClG a considerable amount of NH$_2$ scissoring is coupled with this ring deformation mode. Coupling of exocyclic amino vibration with this pyrimidine stretching mode has been evident from a 18 cm^{-1} downshift of this band in inosine monophosphate (IMP) from that in GMP.[55]

In comparison, alkyl substitution at N7 or N9 does not break conjugation of the imidazole ring. Vibrational properties of such purines; 7-methylguanine (7-meG), 9-ethylguanine (9-EtG) and 7-alyl-8-oxoguanine have been studied in comparison with those of Gua by several groups.[117,151–154] Methyl substitution at N7 rearranges the bond orders of N7–C8 and C8–N9 in 7-meG compared to those in N9H-Gua or 9-meG. Such an alteration does not affect the structure of the pyrimidine ring and various exocyclic bonds involving the C2 and C6 atoms – a fact also evidenced from a similar position of vibrational frequencies in Gua and 7-meG.[117] A similar band position of the C=O stretching mode also reflects the unperturbed strength of the carbonyl bond in both N9 and N7 substituted Gua. However, the heavy –CH$_3$ moiety at N7 causes large downshift of imidazole breathing vibration; from 937 cm^{-1} in Gua to 844 cm^{-1} in 7-meG by increasing reduced mass of this normal mode.

Table 3.12. Experimental band positions (cm^{-1}), computed[a] wavenumbers and vibrational mode descriptions for important ring modes of GMP, 6-ClG and 6-ThG.

Modes description	9-meG		6-ClG		6-ThG	
	Comp.[a,b] (cm^{-1})	Exp. GMP (cm^{-1})	Comp.[a] (cm^{-1})	Exp. (cm^{-1})	Comp.[a] (cm^{-1})	Exp.[c] (cm^{-1})
NH$_2$ sci. + C2N3 str. (Triene str.)	1642	1602	1622	1606	1645	1620
Pyrimidine def.	1577	1576	1572	1585	1625	1590
N$_1$H be.+ N7C8 str.	1563	1537	1528	1515	1590	1537
Pyrimidine str. + N1H be. + N7C8 str.	1499	1486	1472	1480	1545	1482
C5C6 str. + N9H + C8H be.	1383	1366	1414	1381	-	-
C8N9 str. + N9H + N$_1$H be.	1301	1319	1327	1309	1372	1326
N$_1$H + C8H + N7H be. + C–Cl6 str. (6–ClG)	1247	1204	1198	1194	1280	1229
Pyrimidine breath. + C–Cl6, C–S6 str.	-	-	953	954	971	945
Imidazole breath. + C–Cl6 str. (6–ClG) + C–S6 (in 6-ThG)	1027	1020	900	919	946	923
In-phase pyrimidine + imidazole breath.	856	868	829	831	836	795

[a]computed at B3LYP/6-311+G(2d,p)//PCM level of DFT on respective neutral tautomer (see text), not scaled; [b]computation is performed on 9-meG; [c] Ref [125] FT-Raman of solid 6-ThG; abbreviations: comp: computed; exp: experimental; Pu: purine ring; Pyr: pyrimidine ring; Imd: imidazole ring; Def: in-plane deformation; Breath: in-plane ring breathing mode; str: bond stretching; be: in-plane bending; Rock: in-plane rocking motion; Wag: out-of-plane wagging; Tors: out-of-plane torsional distortion. For detailed mode description see Table 3.7-3.9.

3.3.5.3. Performance of DFT in predicting electronic and vibrational properties

TD-B3LYP computed excitation energies in the gas phase are within 0.2 eV of the corresponding experimental λ_{max} value. Such deviations are expected as UV-Vis absorption spectra are computed in *vacuo* and compared against solution state experimental λ_{max}. In the current study, for the purpose of comparison with published *ab initio* results, all excitation energies are computed *in vacuo*. Use of implicit, *e.g.* a continuum solvation (PCM) and explicit solvation (hydrated with hydrogen bonded water molecules)[11,109,120,141] improves prediction of (i) transition energies for both $\pi\pi^*$ and $n\pi^*$ states, and (ii) orbital description of these predicted transitions in nucleobases. Such more sophisticated and resource expensive calculations are performed for GMP, Ade and 6-ClG in preceding chapters. (See chapter 4, 5, 6) B3LYP hybrid functional is found to perform adequately in predicting vibrational properties of nucleobase systems, as previously documented by several authors.[55–57,101,117,118,155–157] The inclusion of extra diffuse and polarization functions improves predictions of vibrational wavenumbers and also reduces $\pi\rightarrow$Ryd* type contamination in configuration description of higher lying excited states below 220 nm. Although position of predicted wavenumber of a vibrational band can deviate from the experimental band position by as large as ~15 cm^{-1}, the computed isotopic shifts are found in good agreement with corresponding experimental shifts. Furthermore, it is also found that the aforementioned functional predicts isotopic shifts that are of correct magnitude and direction in comparison with experimental shifts irrespective of the size of the used Gaussian basis set. (See Table 3.4)

3.4 Conclusion

Nontrivial effects of exocyclic substitution on vibrational, geometric and electronic structures of six substituted purines are extracted by analyzing experimental resonance Raman spectra at two different excitation wavelengths, and DFT computed vibrational normal modes and excitation energies. By comparing experimental and DFT predicted isotopic shifts, **AP is established to be predominantly present as N9H tautomer at pH 7**. Gradual increase in the conjugation of the pyrimidine through substitution of O6 in GMP by NH$_2$ (in DAP), Cl (in 6-ClG) and S (in 6-ThG) moieties is explained by the systematic downshift of ring stretching vibrations. **The wavenumber associated with symmetric imidazole breathing is found to be insensitive to the position of the –NH$_2$ moiety at C2 or C6 on pyrimidine ring. However, this mode gets considerably affected with chlorine, sulfur or oxygen substitutions at C6. While Cl and S substituents at C6 cause down shift, oxygen atom at C6 position results in complete reorganization.** Unlike in all bases, the presence of N7–H in 6-thG decouples contribution of N7–C8 stretching coordinate from all in-plane ring vibrations. Independent

of the choice of basis set, DFT is shown to be extremely useful in predicting correct (in direction and magnitude) isotopic shifts rather than the absolute position of the bands themselves.

Though ground state normal modes of a molecule do not have a direct correspondence to those in its electronic excited state, they preserve their character within tens of fs after photoexcitation. Any reshuffling of these modes in the ground state would naturally hinder intramolecular energy flow through FC active vibrations and interaction of these modes with surrounding solvent bath. A **heavy substitution, such as Cl atom in place of O leads to strong coupling of imidazole localized vibrations (such as, 919 and 954 cm^{-1}) with the C6–Cl6 stretching vibration in 6-ClG. The significant intensity of these RR bands of 6-ClG at 225 nm excitation suggests a significantly different initial structural dynamics in 6-ClG than that in GMP.** In the context of the continuous search for molecular probes with better spectral properties, unique RR signatures of the non-natural nucleobases; *viz.,* AP, DAP, 6-ClG studied here have the potential be used as site-specific vibrational reporters of DNA structure and dynamics in different environments.

References

[1] J. M. L. Pecourt, J. Peon, B. Kohler, *J. Am. Chem. Soc.* **2000**, *122*, 9348.

[2] J. M. L. Pecourt, J. Peon, B. Kohler, *J. Am. Chem. Soc.* **2001**, *123*, 10370.

[3] J. Peon, A. H. Zewail, *Chem. Phys. Lett.* **2001**, *348*, 255.

[4] E. Nir, C. Plützer, K. Kleinermanns, M. de Vries, *Eur. Phys. J. D* **2002**, *20*, 317.

[5] H. Kang, K. T. Lee, B. Jung, Y. J. Ko, S. K. Kim, *J. Am. Chem. Soc.* **2002**, *124*, 12958.

[6] C. E. Crespo-Hernández, B. Cohen, P. M. Hare, B. Kohler, *Chem. Rev.* **2004**, *104*, 1977.

[7] S. Ullrich, T. Schultz, M. Z. Zgierski, A. Stolow, *Phys. Chem. Chem. Phys.* **2004**, *6*, 2796.

[8] C. Canuel, M. Mons, F. Piuzzi, B. Tardivel, I. Dimicoli, M. Elhanine, *J. Chem. Phys.* **2005**, *122*, 074316.

[9] P. M. Hare, C. E. Crespo-Hernandez, B. Kohler, *Proc. Natl. Acad. Sci.* **2007**, *104*, 435.

[10] C. T. Middleton, K. de La Harpe, C. Su, Y. K. Law, C. E. Crespo-Hernández, B. Kohler, *Annu. Rev. Phys. Chem.* **2009**, *60*, 217.

[11] V. Karunakaran, K. Kleinermanns, R. Improta, S. A. Kovalenko, *J. Am. Chem. Soc.* **2009**, *131*, 5839.

[12] M. S. de Vries, in *Photoinduced Phenom. Nucleic Acids I* (Eds.: M. Barbatti, A.C. Borin, S. Ullrich), Springer International Publishing, **2014**, pp. 33–56.

[13] M. K. Kuimova, J. Dyer, M. W. George, D. C. Grills, J. M. Kelly, P. Matousek, A. W. Parker, X. Z. Sun, M. Towrie, A. M. Whelan, *Chem. Commun.* **2005**, 1182.

[14] S. Matsika, *J. Phys. Chem. A* **2004**, *108*, 7584.

[15] L. Serrano-Andrés, M. Merchán, A. C. Borin, *Chem. - A Eur. J.* **2006**, *12*, 6559.

[16] H. R. Hudock, B. G. Levine, A. L. Thompson, H. Satzger, D. Townsend, N. Gador, S. Ullrich, A. Stolow, T. J. Martínez, *J. Phys. Chem. A* **2007**, *111*, 8500.

[17] H. R. Hudock, T. J. Martínez, *ChemPhysChem* **2008**, *9*, 2486.

[18] L. Serrano-Andrés, M. Merchán, A. C. Borin, *J. Am. Chem. Soc.* **2008**, *130*, 2473.

[19] J. J. Szymczak, M. Barbatti, J. T. Soo Hoo, J. A. Adkins, T. L. Windus, D. Nachtigallová, H. Lischka, *J. Phys. Chem. A* **2009**, *113*, 12686.

[20] R. Improta, V. Barone, A. Lami, F. Santoro, *J. Phys. Chem. B* **2009**, *113*, 14491.

[21] M. Barbatti, A. J. A. Aquino, J. J. Szymczak, D. Nachtigallova, P. Hobza, H. Lischka, *Proc. Natl. Acad. Sci.* **2010**, *107*, 21453.

[22] D. Nachtigallová, T. Zelený, M. Ruckenbauer, T. Müller, M. Barbatti, P. Hobza, H. Lischka, *J. Am. Chem. Soc.* **2010**, *132*, 8261.

[23] T. Zelený, M. Ruckenbauer, A. J. A. Aquino, T. Müller, F. Lankaš, T. Dršata, W. L. Hase, D. Nachtigallova, H. Lischka, *J. Am. Chem. Soc.* **2012**, *134*, 13662.

[24] R. Improta, V. Barone, **2014**, pp. 329–357.

[25] N. L. Doltsinis, P. R. L. Markwick, H. Nieber, H. Langer, in *Radiat. Induc. Mol. Phenom. Nucleic Acids*, Springer Netherlands, Dordrecht, **2008**, pp. 265–299.

[26] M. Barbatti, A. C. Borin, S. Ullrich, Eds. , *Photoinduced Phenomena in Nucleic Acids I*, Springer International Publishing, **2015**.

[27] R. Improta, F. Santoro, L. Blancafort, *Chem. Rev.* **2016**, *116*, 3540.

[28] C. E. Crespo-Hernández, L. Martínez-Fernández,

C. Rauer, C. Reichardt, S. Mai, M. Pollum, P. Marquetand, L. González, I. Corral, *J. Am. Chem. Soc.* **2015**, *137*, 4368.

[29] R. J. Malone, A. M. Miller, B. Kohler, *Photochem. Photobiol.* **2007**, *77*, 158.

[30] S. Yamazaki, T. Taketsugu, *J. Phys. Chem. A* **2012**, *116*, 491.

[31] M. A. Trachsel, S. Lobsiger, T. Schär, S. Leutwyler, *J. Chem. Phys.* **2014**, *140*, 044331.

[32] Á. Bányász, T. Gustavsson, E. Keszei, R. Improta, D. Markovitsi, *Photochem. Photobiol. Sci.* **2008**, *7*, 765.

[33] T. Gustavsson, Á. Bányász, E. Lazzarotto, D. Markovitsi, G. Scalmani, M. J. Frisch, V. Barone, R. Improta, *J. Am. Chem. Soc.* **2006**, *128*, 607.

[34] P. M. Hare, C. E. Crespo-Hernández, B. Kohler, *J. Phys. Chem. B* **2006**, *110*, 18641.

[35] S. Matsika, in *Photoinduced Phenom. Nucleic Acids I* (Eds.: M. Barbatti, A.C. Borin, S. Ullrich), Springer International Publishing, **2014**, pp. 209–243.

[36] M. Pollum, L. Martínez-Fernández, C. E. Crespo-Hernández, in *Photoinduced Phenom. Nucleic Acids I* (Eds.: M. Barbatti, A.C. Borin, S. Ullrich), Springer International Publishing, **2014**, pp. 245–327.

[37] L. Serrano-Andrés, M. Merchán, *J. Photochem. Photobiol. C Photochem. Rev.* **2009**, *10*, 21.

[38] A. Holmén, B. Nordén, B. Albinsson, *J. Am. Chem. Soc.* **1997**, *119*, 3114.

[39] C. Santhosh, P. C. Mishra, *Spectrochim. Acta Part A Mol. Spectrosc.* **1991**, *47*, 1685.

[40] L. Serrano-Andrés, M. Merchán, A. C. Borin, *Proc. Natl. Acad. Sci. U. S. A.* **2006**, *103*, 8691.

[41] Y. Zhang, J. Dood, A. Beckstead, J. Chen, X.-B. Li, C. J. Burrows, Z. Lu, S. Matsika, B. Kohler, *J. Phys. Chem. A* **2013**, *117*, 12851.

[42] K. A. Kistler, S. Matsika, *J. Phys. Chem. A* **2007**, *111*, 8708.

[43] E. Mburu, S. Matsika, *J. Phys. Chem. A* **2008**, *112*, 12485.

[44] S. Lobsiger, H.-M. Frey, S. Leutwyler, P. Morgan, D. Pratt, *J. Phys. Chem. A* **2011**, *115*, 13281.

[45] G. Zechmann, M. Barbatti, *Int. J. Quantum Chem.* **2008**, *108*, 1266.

[46] Y. He, C. Wu, W. Kong, *J. Phys. Chem. A* **2003**, *107*, 5145.

[47] L. Blancafort, B. Cohen, P. M. Hare, B. Kohler, M. A. Robb, *J. Phys. Chem. A* **2005**, *109*, 4431.

[48] J. Černý, V. Špirko, M. Mons, P. Hobza, D. Nachtigallová, *Phys. Chem. Chem. Phys.* **2006**, *8*, 3059.

[49] M. Barbatti, H. Lischka, *J. Phys. Chem. A* **2007**, *111*, 2852.

[50] J. Chen, B. Kohler, *Phys. Chem. Chem. Phys.* **2012**, *14*, 10677.

[51] Z. Gengeliczki, M. P. Callahan, N. Svadlenak, C. I. Pongor, B. Sztáray, L. Meerts, D. Nachtigallová, P. Hobza, M. Barbatti, H. Lischka, M. S. de Vries, *Phys. Chem. Chem. Phys.* **2010**, *12*, 5375.

[52] D. C. Ward, E. Reich, L. Stryer, *J. Biol. Chem.* **1969**, *244*, 1228.

[53] J. Drobnik, L. Augenstein, *Photochem. Photobiol.* **1966**, *5*, 83.

[54] N. Jayanth, M. Puranik, *J. Phys. Chem. B* **2011**, *115*, 6234.

[55] S. Gogia, A. Jain, M. Puranik, *J. Phys. Chem. B* **2009**, *113*, 15101.

[56] N. Jayanth, S. Ramachandran, M. Puranik, *J. Phys. Chem. A* **2009**, *113*, 1459.

[57] V. Karnawat, M. Puranik, *J. Biomol. Struct. Dyn.* **2016**, *34*, 640.

[58] S. Gogia, M. Puranik, *J. Biomol. Struct. Dyn.* **2014**, *32*, 27.

[59] R. J. H. Clark, T. J. Dines, *Angew. Chemie Int. Ed. English* **1986**, *25*, 131.

[60] S. P. A. Fodor, R. P. Rava, T. R. Hays, T. G. Spiro, *J. Am. Chem. Soc.* **1985**, *107*, 1520.

[61] Z. Q. Wen, G. J. Thomas, *Biopolymers* **1998**, *45*, 247.

[62] J. M. Benevides, S. A. Overman, G. J. Thomas, *J. Raman Spectrosc.* **2005**, *36*, 279.

[63] G. R. Loppnow, B. E. Billinghurst, S. A. Oladepo, in *Radiat. Induc. Mol. Phenom. Nucleic Acids*, Springer Netherlands, Dordrecht, **n.d.**, pp. 237–263.

[64] C. Lee, W. Yang, R. G. Parr, *Phys. Rev. B* **1988**, *37*, 785.

[65] A. D. Becke, *J. Chem. Phys.* **1993**, *98*, 5648.

[66] S. Miertuš, E. Scrocco, J. Tomasi, *Chem. Phys.* **1981**, *55*, 117.

[67] J. Tomasi, B. Mennucci, R. Cammi, *Chem. Rev.* **2005**, *105*, 2999.

[68] M. H. Jamróz, *Spectrochim. Acta Part A Mol. Biomol. Spectrosc.* **2013**, *114*, 220.

[69] R. Bauernschmitt, R. Ahlrichs, *Chem. Phys. Lett.* **1996**, *256*, 454.

[70] M. E. Casida, C. Jamorski, K. C. Casida, D. R. Salahub, *J. Chem. Phys.* **1998**, *108*, 4439.

[71] S. I. Gorelsky, *SWizard v5.0, Http://www.sg-Chem.net/, University of Ottawa, Ottawa, Canada.*, **2013**.

[72] R. S. Mulliken, *J. Chem. Phys.* **1955**, *23*, 1833.

[73] G. A. Andrienko, *Chemcraft v1.6, Http://www.chemcraftprog.com/*, **n.d.**

[74] M. J. Frisc *et al. Gaussian 09, Revision D.01*, Gaussian Inc., Wallingford, **2013**.

[75] A. Broo, A. Holmén, *Chem. Phys.* **1996**, *211*, 147.

[76] R. K. Neely, S. W. Magennis, S. Parsons, A. C. Jones, *ChemPhysChem* **2007**, *8*, 1095.

[77] T. F. Lai, R. E. Marsh, *Acta Crystallogr. Sect. B Struct. Crystallogr. Cryst. Chem.* **1972**, *28*, 1982.

[78] S. de Rosa, S. de Stefano, R. Puliti, C. A. Mattia, L. Mazzarella, *J. Nat. Prod.* **1987**, *50*, 876.

[79] D. E. Lynch, I. McClenaghan, *Acta Crystallogr. C.* **2003**, *59*, o53.

[80] J. Wang, J. Gu, J. Leszczynski, *J. Comput. Chem.* **2012**, *33*, 1587.

[81] C. E. Bugg, U. Thewalt, *J. Am. Chem. Soc.* **1970**, *92*, 7441.

[82] M. Kouchakdjian, V. Bodepudi, S. Shibutani, M. Eisenberg, F. Johnson, A. P. Grollman, D. J. Patel, *Biochemistry* **1991**, *30*, 1403.

[83] Y. Oda, S. Uesugi, M. Ikehara, S. Nishimura, Y. Kawase, H. Ishikawa, H. Inoue, E. Ohtsuka, *Nucleic Acids Res.* **1991**, *19*, 1407.

[84] S. Uesugi, M. Ikehara, *J. Am. Chem. Soc.* **1977**, *99*, 3250.

[85] M. Dreyfus, G. Dodin, O. Bensaude, J. E. Dubois, *J. Am. Chem. Soc.* **1975**, *97*, 2369.

[86] M. J. Nowak, L. Lapinski, J. S. Kwiatkowski, *Chem. Phys. Lett.* **1989**, *157*, 14.

[87] T. Stepanenko, L. Lapinski, M. J. Nowak, J. S. Kwiatkowski, J. Leszczynski, *Spectrochim. Acta Part A Mol. Biomol. Spectrosc.* **2001**, *57*, 375.

[88] M. J. Nowak, H. Rostkowska, L. Lapinski, J. S.

Kwiatkowski, J. Leszczynski, *Spectrochim. Acta Part A Mol. Spectrosc.* **1994**, *50*, 1081.

[89] T. G. Burova, V. V. Ermolenkov, G. N. Ten, R. S. Shcherbakov, V. I. Baranov, I. K. Lednev, *J. Phys. Chem. A* **2011**, *115*, 10600.

[90] G. N. Ten, T. G. Burova, V. I. Baranov, *J. Struct. Chem.* **2007**, *48*, 447.

[91] T. G. Burova, G. N. Ten, V. V. Ermolenkov, R. S. Shcherbakov, I. K. Lednev, *Opt. Spectrosc.* **2010**, *109*, 853.

[92] O. J. Wilkinson, V. Latypov, J. L. Tubbs, C. L. Millington, R. Morita, H. Blackburn, A. Marriott, G. McGown, M. Thorncroft, A. J. Watson, B. A. Connolly, J. A. Grasby, R. Masui, C. A. Hunter, J. A. Tainer, G. P. Margison, D. M. Williams, *Proc. Natl. Acad. Sci.* **2012**, *109*, 18755.

[93] P. O. de Giuseppe, N. H. Martins, A. N. Meza, C. R. dos Santos, H. D. Pereira, M. T. Murakami, *PLoS One* **2012**, 7, e44282.

[94] J. Bohon, *Nucleic Acids Res.* **2003**, *31*, 1331.

[95] U. Thewalt, C. E. Bugg, R. E. Marsh, *Acta Crystallogr. Sect. B Struct. Crystallogr. Cryst. Chem.* **1970**, *26*, 1089.

[96] M. Schumacher, H. Guenther, *J. Am. Chem. Soc.* **1982**, *104*, 4167.

[97] J. Gu, J. Leszczynski, *J. Phys. Chem. A* **1999**, *103*, 2744.

[98] R. D. Brown, P. D. Godfrey, D. McNaughton, A. P. Pierlot, *Chem. Phys. Lett.* **1989**, *156*, 61.

[99] M. J. Nowak, H. Rostkowska, L. Lapinski, J. S. Kwiatkowski, J. Leszczynski, *J. Phys. Chem.* **1994**, *98*, 2813.

[100] M. J. Nowak, L. Lapinski, J. S. Kwiatkowski, J. Leszczyński, *J. Phys. Chem.* **1996**, *100*, 3527.

[101] B. Giese, D. McNaughton, *J. Phys. Chem. B* **2002**, *106*, 101.

[102] M. Majoube, *J. Raman Spectrosc.* **1985**, *16*, 98.

[103] A. Toyama, N. Hanada, Y. Abe, H. Takeuchi, I. Harada, *J. Raman Spectrosc.* **1994**, *25*, 623.

[104] M. Shanmugasundaram, M. Puranik, *Phys. Chem. Chem. Phys.* **2011**, *13*, 3851.

[105] K. A. Seefeld, C. Plützer, D. Löwenich, T. Häber, R. Linder, K. Kleinermanns, J. Tatchen, C. M. Marian, *Phys. Chem. Chem. Phys.* **2005**, *7*, 3021.

[106] R. K. Neely, S. W. Magennis, D. T. F. Dryden, A. C. Jones, *J. Phys. Chem. B* **2004**, *108*, 17606.

[107] S. Lobsiger, R. K. Sinha, M. Trachsel, S. Leutwyler, *J. Chem. Phys.* **2011**, *134*, 114307.

[108] R. K. Sinha, S. Lobsiger, S. Leutwyler, *J. Phys. Chem. A* **2012**, *116*, 1129.

[109] A. C. Borin, L. Serrano-Andrés, V. Ludwig, K. Coutinho, S. Canuto, *Int. J. Quantum Chem.* **2006**, *106*, 2564.

[110] A. Holmén, B. Nordén, B. Albinsson, *J. Am. Chem. Soc.* **1997**, *119*, 3114.

[111] K. O. Evans, Dynamic Characterization of 2-Aminopurine in Oligonucleotides Using Fluorescence, Magnetic Resonance and Raman Spectroscopies, PhD Thesis, The University of Alabama at Birmingham, **1998**.

[112] R. Ramaekers, L. Adamowicz, G. Maes, *Eur. Phys. J. D* **2002**, *20*, 375.

[113] J. Florian, P. Mojzes, J. Stepanek, *J. Phys. Chem.* **1992**, *96*, 9278.

[114] V. Krishnakumar, R. Ramasamy, *Asian J. Chem.* **2002**.

[115] V. Krishnakumar, R. Ramasamy, *Spectrochim. Acta Part A Mol. Biomol. Spectrosc.* **2008**, *69*, 8.

[116] Z. Dhaouadi, M. Ghomi, P. Mojzes, P. Y. Turpin, L. Chinsky, *Eur. Biophys. J.* **1994**, *23*, DOI 10.1007/BF00208863.

[117] B. Giese, D. McNaughton, *Phys. Chem. Chem. Phys.* **2002**, *4*, 5171.

[118] B. Giese, D. McNaughton, *Phys. Chem. Chem. Phys.* **2002**, *4*, 5161.

[119] V. Balachandran, K. Parimala, *Spectrochim. Acta Part A Mol. Biomol. Spectrosc.* **2012**, *96*, 340.

[120] S. Mondal, M. Puranik, *Phys. Chem. Chem. Phys.* **2016**, 10.1039/C6CP01746K.

[121] C. Alhambra, F. J. Luque, J. Estelrich, M. Orozco, *J. Org. Chem.* **1995**, *60*, 969.

[122] M. J. Stewart, J. Leszczynski, Y. V. Rubin, Y. P. Blagoi, *J. Phys. Chem. A* **1997**, *101*, 4753.

[123] D. Venkateswarlu, J. Leszczynski, *J. Phys. Chem. A* **1998**, *102*, 6161.

[124] P. . Civcir, *J. Mol. Struct. THEOCHEM* **2001**, *536*, 161.

[125] S. Gunasekaran, S. Kumaresan, R. Arunbalaji, G. Anand, S. Seshadri, S. Muthu, *J. Raman Spectrosc.* **2009**, *40*, 1675.

[126] P. Li, H. Gu, J. Zhang, *Anal. Lett.* **2015**, *48*, 2063.

[127] K. Szczepaniak, W. B. Person, J. Leszczyński, J. S. Kwiatkowski, *Postepy Biochem.* **1995**, *41*, 300.

[128] C. A. Sprecher, W. C. Johnson, *Biopolymers* **1977**, *16*, 2243.

[129] L. B. Clark, I. Tinoco, *J. Am. Chem. Soc.* **1965**, *87*, 11.

[130] S. F. Mason, *J. Chem. Soc.* **1954**, 2071.

[131] J. A. Montgomery, L. B. Holum, *J. Am. Chem. Soc.* **1958**, *80*, 404.

[132] J. S. Kwiatkowski, *Theor. Chim. Acta* **1969**, *13*, 149.

[133] L. B. Clark, *J. Am. Chem. Soc.* **1994**, *116*, 5265.

[134] M. P. Fülscher, L. Serrano-Andrés, B. O. Roos, *J. Am. Chem. Soc.* **1997**, *119*, 6168.

[135] C. Santhosh, P. C. Mishra, *Spectrochim. Acta Part A Mol. Spectrosc.* **1993**, *49*, 985.

[136] A. Tsolakidis, E. Kaxiras, *J. Phys. Chem. A* **2005**, *109*, 2373.

[137] M. K. Shukla, J. Leszczynski, *J. Phys. Chem. A* **2005**, *109*, 7775.

[138] D. Varsano, R. Di Felice, M. A. L. Marques, A. Rubio, *J. Phys. Chem. B* **2006**, *110*, 7129.

[139] M. K. Shukla, J. Leszczynski, *J. Biomol. Struct. Dyn.* **2007**, *25*, 93.

[140] M. Barbatti, A. J. A. Aquino, H. Lischka, *Phys. Chem. Chem. Phys.* **2010**, *12*, 4959.

[141] Y. Zhao, Z. Cao, *J. Theor. Comput. Chem.* **2013**, *12*, 1341013.

[142] O. Gustave, L. L. Place, *Acta Phys. Pol. A* **1998**, *94*, 735.

[143] E. L. Rachofsky, J. B. A. Ross, M. Krauss, R. Osman, *J. Phys. Chem. A* **2001**, *105*, 190.

[144] J. M. Jean, K. B. Hall, *Biochemistry* **2002**, *41*, 13152.

[145] K. a Seefeld, C. Plützer, D. Löwenich, T. Häber, R. Linder, K. Kleinermanns, J. Tatchen, C. M. Marian, *Phys. Chem. Chem. Phys.* **2005**, *7*, 3021.

[146] S. Perun, A. L. Sobolewski, W. Domcke, *Mol. Phys.* **2006**, *104*, 1113.

[147] G. Kodali, K. a Kistler, S. Matsika, R. J. Stanley, *J. Phys. Chem. B* **2008**, *112*, 1789.

[148] K. S. K. Shin, J. I. Zink, *J. Am. Chem. Soc.* **1990**, *112*, 7148.

[149] S. Luber, J. Neugebauer, M. Reiher, *J. Chem. Phys.* **2010**, *132*, 044113.

[150] B. E. Billinghurst, R. Yeung, G. R. Loppnow, *J.*

Phys. Chem. A **2006**, *110*, 6185.

[151] E. Koglin, J.-M. Séquaris, P. Valenta, in (Eds.: F.R. Aussenegg, A. Leitner, M.E. Lippitsch), Springer Berlin Heidelberg, Berlin, Heidelberg, **1983**, pp. 64–71.

[152] L. E. Camafeita, S. Sánchez-Cortés, J. V. García-Ramos, in *Spectrosc. Biol. Mol.*, Springer Netherlands, Dordrecht, **1995**, pp. 307–308.

[153] L. E. Camafeita, S. Sánchez-Cortés, J. V. García-Ramos, *J. Raman Spectrosc.* **1996**, *27*, 533.

[154] O. E. Kasende, K. Szczepaniak, T. Zeegers-Huyskens, *Spectrosc. Lett.* **1997**, *30*, 415.

[155] N. Leulliot, M. Ghomi, H. Jobic, O. Bouloussa, V. Baumruk, C. Coulombeau, *J. Phys. Chem. B* **1999**, *103*, 10934.

[156] A. St-Amant, in *Rev. Comput. Chem. Vol. 7*, **1996**, pp. 217–259.

[157] S. Yarasi, B. E. Billinghurst, G. R. Loppnow, *J. Raman Spectrosc.* **2007**, *38*, 1117.

4

Ultrafast excited state dynamics of 6-chloroguanine within the B$_b$ electronic state*
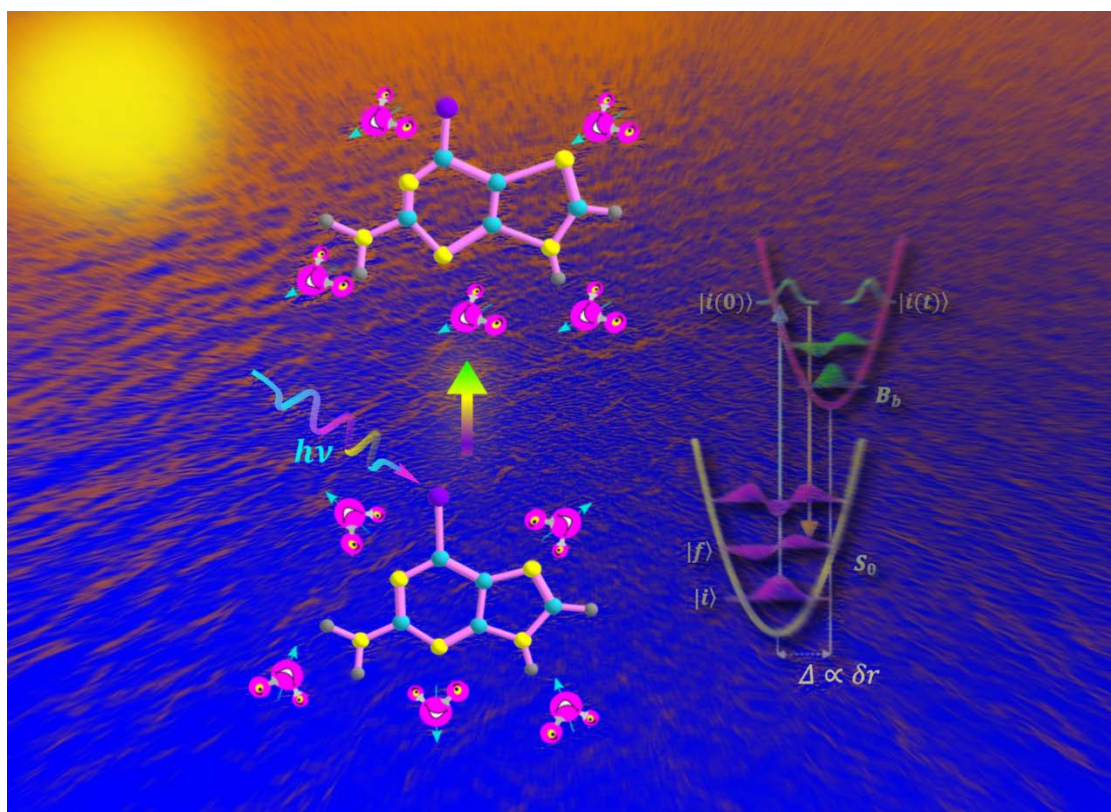
4.1 Introduction

Ultraviolet (UV) light is a ubiquitous stressor to physical, chemical and biological systems in all organisms. Although subjected to continuous cycles of photodamage and repair, deoxyribonucleic acid (DNA), our genetic information carrier, has remained structurally unaltered during a long evolutionary period. This structural robustness of DNA is ascribed to photoresistive properties of constituting nucleobases to UV radiation among other reasons. All five natural nucleic acid bases: guanine (Gua), adenine (Ade), cytosine (Cyt), thymine (Thy) in DNA, and Uracil (Ura) in RNA have substantial absorption cross-sections at UV wavelengths. These bases are shown to exhibit ultrafast relaxation from the first excited $\pi\pi^*$ state (S_1) to the ground electronic state within sub-picoseconds (ps) following photo-excitation. The underlying photophysics has been extensively studied using a variety of experimental [1–15] and theoretical methods.[16–20] These studies reveal that each natural base has a unique molecular mechanism to get rid of excess photon energy via internal conversion (IC) and vibrational relaxation. Short-lived excited states minimize the possibility of undergoing photochemical reactions leading to photoproduct formation. The absence of substituted bases with long excited state lifetimes in natural RNA and DNA suggests possible existence of UV induced photodamage as a selection pressure [21] during the prebiotic era.

UV radiation is broadly classified as UV-C (100-260 nm) and UV-B (260-350 nm) and response of nucleobases in the presence of both types of radiation is relevant to overall stability. Several studies have dealt with the effect of photoexcitation to the lowest energy, strong $\pi\pi^*$ electronic state at ~260 nm in purines and pyrimidies. Many ultrafast spectroscopic and theoretical studies of excited purines have indicated that pyramidalization initiated via torsional motions around double bonds of purine or pyrimidine rings are necessary for accessing a non-radiative path for the return to ground electronic state (S_0).[19,22–25] Resonance Raman (RR) intensity derived nuclear dynamics show that initial structural distortions in several bases may lie along photochemical reaction coordinates of various photoproducts.[7,9,11,14]

While these studies are valuable and indicate the damage UV-B may inflict, nucleobases do absorb significantly more efficiently at the red edge of UV-C region (100-260 nm) than UV-B. Since the flux of solar radiation in UV-C region was several folds higher during the early stages of evolution, than that present today, understanding the response of nucleobases to UV-C is important.[26,27] Effective dissipation of energy deposited on nucleobases following absorption of UV-C photons

would be necessary for the survival of genetic information. Our understanding of the photophysics of nucleobases in response to UV-C excitation is very poor. To our knowledge, there is no report as yet of the dynamics that a natural or analog nucleobase system undergoes upon photoexcitation in UV-C. As a part of a series of studies on purine analogues, we report here the initial excited state dynamics of 2-amino-6-chloropurine (Fig. 4.1), also known as 6-chloroguanine (6-ClG) within the B_b absorption band. In 6-ClG, the oxygen atom of Gua is replaced by a heavy and more electronegative chlorine atom. 6-ClG is used as a purine model with the specific aim of deducing the role of the carbonyl moiety in its natural counterpart Gua.
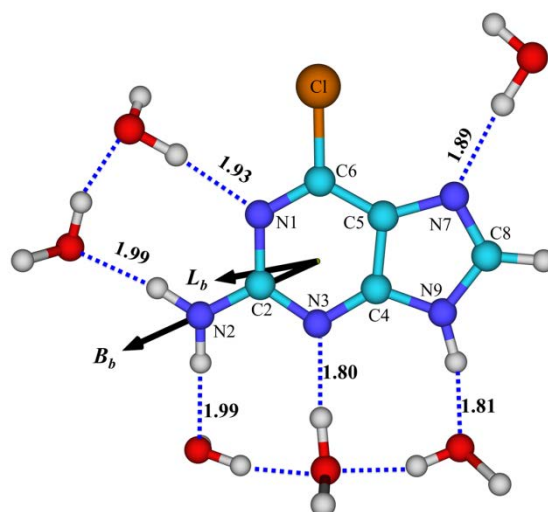
Fig. 4.1 Structure of neutral aqueous 6-ClG obtained by energy minimization at B3LYP/6-311+G(2d,p)//PCM level of theory. Aqueous 6-ClG was modeled as 6-ClG•6H$_2$O complex as shown. All H-bond distances (in Å) between water molecules and the base along are labeled. Conventional numbering of ring atoms is indicated. Directions of computed transition dipole moments for L_b and B_b states are shown with bold arrows. Indicated magnitude of the transition dipole moment vectors is magnified by a factor of two (for B_b) and three (for L_b) over the calculated value for improved visualization.

Excess vibrational energy of an electronically excited molecule is dissipated via specific vibrational modes internally and through interaction with solvent degrees of freedom. Ultrafast deactivation of natural bases in a radiationless manner contrasts with fluorescent behavior of analogous molecules which do not return to S_0 as fast as the former. In nucleobases that have sub-ps S_1 lifetime, initially populated excited state depopulates to S_0 via crossings of potential energy surfaces of close-lying electronic states, also known as conical intersection (CI). These bases can only reach a CI via out-of-plane distortion of S_0 state geometry from the Frank-Condon (FC) region of the excited electronic state. Instantaneous distortions of a nucleobase on the excited

potential energy surface (PES) are important physical quantities that determine photophysics at a later time point after photoexcitation.

RR spectroscopy is the only experimental technique that can determine vibrational mode-specific instantaneous structural distortions of a molecule following photoexcitation to an electronic state.[28–30] When Raman excitation is in resonance with a particular excited state, observed intensity of the RR band is proportional to the square of the distortion along each FC active vibrational normal mode. Conversely, if Raman intensities are measured, the distortion of the molecular structure in the excited state with respect to that in the ground state can be determined. Thus, while the wavenumbers of RR bands of a molecule report structure of the S_0 state, their intensities encode information about the resonant electronic state. Structural distortion in the excited state measured along normal coordinates is expressed as dimensionless displacements (Δ). These Δs are proportional to the slopes of the excited electronic PES along that coordinate.[31,32] Displacements taking place within tens of femtosecond (fs) after photoexcitation can be extracted from analysis of excitation wavelength dependence of intensities of RR active vibrational modes, i.e. Raman excitation profiles (REP).

We have employed Lee and Heller's time dependent wave packet (TDWP) formalism[33,34] to simulate experimental REPs and the absorption spectrum of 6-ClG in a self-consistent manner. We determined change in internal coordinates of S_0 state of 6-ClG upon photoexcitation to B_b electronic state. We find that the partitioning of internal reorganization energies among different vibrational modes is influenced by change in the charge distribution upon photoexcitation. We used a Brownian oscillator model[35] to account for homogeneous effects and a simple Gaussian broadening function to account for static, inhomogeneous broadening. Simultaneous modeling of Raman excitation profiles of multiple modes and the absorption spectrum allows us to partition the total line-width broadening contributions into two components: dynamic homogeneous, and static inhomogeneous components, contributing to both, absorption and Raman line-shapes.

4.2 Material and Methods

4.2.1 Sample Preparation and UVRR experiment

6-ClG (2–amino-6-chloropurine, 99%) was purchased from Sigma Aldrich (St. Louis, MO) and used without further purification. For UVRR measurement 6-ClG was of 1 mM in concentration in miliQ water, pH 6.8. Sodium perchlorate of 0.5 M

concentration (in milliQ water) was used as an internal standard (IS) for measured intensity of sample bands. Samples were spun in a quartz tube along its axis for reducing photodamage.

4.2.2 Raman spectral processing

The UVRR spectra of 6-ClG were obtained across a range of excitation wavelengths within 210-230 nm, following method described in Chapter 2. For every recording, integrity of sample was cross-checked by comparing the first spectrum and the last spectrum with a total accumulation of 10 min. After subtraction of buffer spectra, the Raman bands of 6-ClG were fitted using Lorentzian line-shape in Origin 7.0, and the areas under the fitted bands were taken as Raman intensity of the bands. The position and width of each RR band was kept fixed for the spectra obtained at all the excitation wavelengths.

4.2.3 Raman depolarization ratio
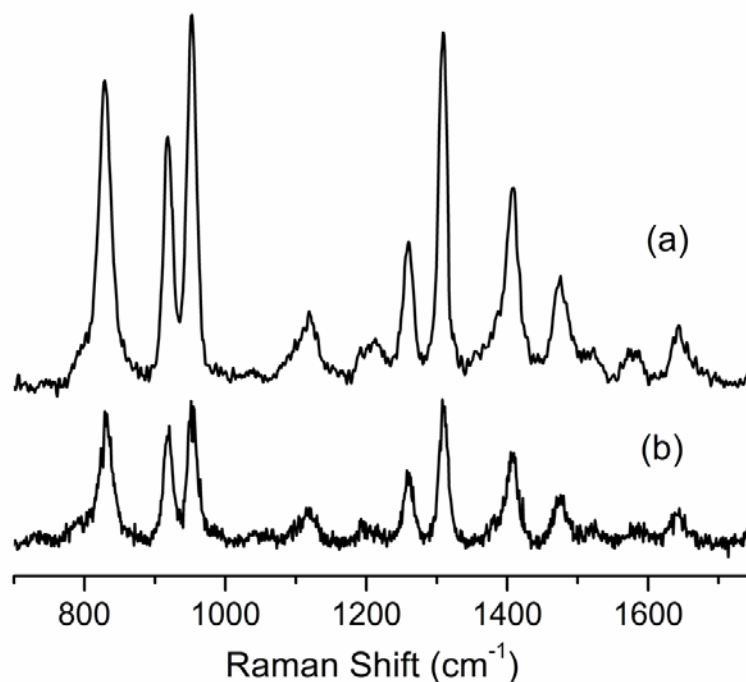
Fig. 4.2 (a) Parallel polarized and (b) depolarized spectra of 6-ClG with 220 nm laser excitation.

Raman depolarization ratios of RR bands of 6-ClG were measured by using a rotatable UV coated Glan-laser alpha-BBO polarization analyzer (Thorlabs Inc., Newton, NJ, USA), placed between collection optics and spectrometer slit, as described in chapter 2. (See Fig. 2.6 for optical setup) Fig. 4.2 shows 220 nm excited spectrum of 6-ClG in

parallel and perpendicular direction with respect to polarization of incident laser beam. The depolarization ratios of all intense bands of 6-ClG are described in Table 4.1 and are close to 0.33 except for the bands at 1641 cm^{-1}. For the low intense bands it was difficult to reliably measure intensity for the depolarized spectrum because of their inherent low intensity. Thus, a depolarization value of 0.33 is assumed for the low intensity modes.

4.2.4 UVRR cross-section and correction for spectrometer response

The absolute UVRR cross-sections of each band of 6-ClG was determined using the eqn. 2.21a and 2.21b as described in chapter 2.[29,36] Response function of the detection system, $S(\lambda) = D(\lambda)/T(\lambda)$ was measured using a calibrated D_2O lamp (Ocean Optics Inc., Dunedin, FL) and was used to correct sample band intensity for spectral sensitivity of spectrometer as described in Chapter 2 and previous publication from our lab.[37] Self-absorption of resonance Raman scattered photons lying within the absorption band of the molecule, is also corrected by the factor $K(\lambda_N, \lambda_S)$[38] described in Chapter 2.

Table 4.1. Depolarization ratio for Raman bands of 6-ClG obtained at excitation wavelength of 220 nm.

RR Band (cm^{-1})	Depolarization ratio
6-ClG, λ_{exc}=220 nm	
831	0.37 ± 0.04
919	0.38 ± 0.02
954	0.35 ± 0.05
1120	0.40 ± 0.04
1260	0.38 ± 0.01
1309	0.33 ± 0.04
1407	0.37 ± 0.04
1476	0.35 ± 0.04
1641	0.46 ± 0.16

4.2.5 Extinction coefficient and absorption cross-section

Extinction coefficient, ε (l mol^{-1} cm^{-1}) of 6-ClG was determined as slope of the linear fit of concentration against measured absorbance at eight different concentrations within 1 to 20 μM. Extinction coefficient is converted in to absorption cross-section,

σ_A (Å^2/molecule) using the relation, σ_A= 2.303 x 10^{19} ε /N_A, N_A being Avogadro's number.[37]

Absorption spectrum of 6-ClG within 190-260 nm (Fig. 4.3, panel b) region was fitted with the minimum required (four) Gaussian functions for initial fitting with no external constraints. This yielded a transition dipole length of B_b state of 1.4 Å (6th singlet state in Fig. 4.3, panel b). Since the absorption spectrum is smooth and structureless, fit to the experimental absorption spectrum does not provide unique positions and intensities to the underlying electronic bands. Several iterations of simultaneous fitting to REPs of all modes and the absorption spectrum were made to obtain a self-consistent position and width of the B_b band. This yielded a final transition dipole moment of 1.1 Å.
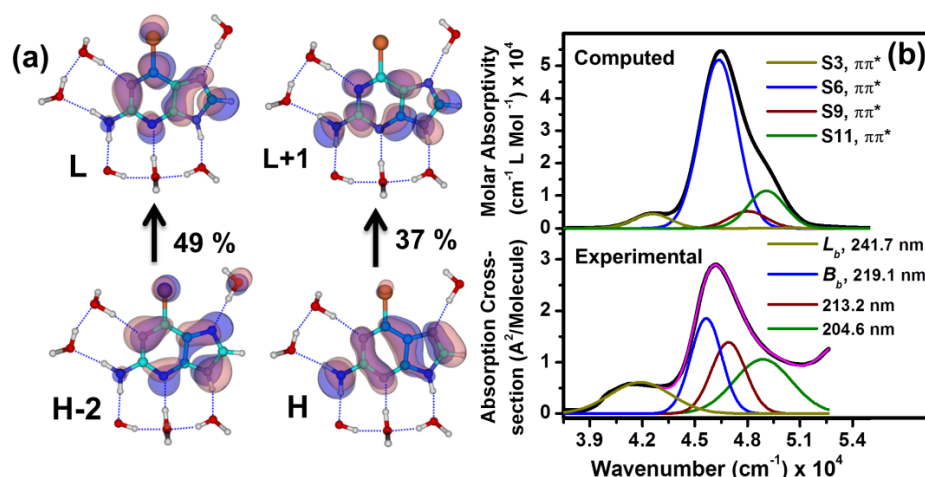
Fig. 4.3 (a) Computed molecular orbitals of 6-ClG involved in the electronic transition observed in experiments at 217.5 nm; (b) bottom: deconvolved experimental spectrum with component spectra, standard spectroscopic labels of the bands and λ_{max}; top: computed absorption spectrum, excitations and nature of the excited states of 6-ClG. Electronic absorption spectrum was computed using TD-B3LYP/6-311+G(2d,p)//PCM method on 6-ClG•6H$_2$O complex. Computed band positions are depicted with a Gaussian line shape of fixed line width (2500 cm^{-1}). H and L stand for HOMO and LUMO orbitals respectively.

4.2.6 Simulation of absorption and RR cross-section

Experimental RR excitation profiles and absorption cross-section were simulated using time dependent wave packet propagation formalism of Lee and Heller[31,33,34] through the eqns.2.21a and 2.21b, and employing Brownian oscillator spectral density model[35,39] for accounting homogeneous broadening mechanisms, described in Chapter 2.

4.2.7 Deconvolution of the absorption spectrum

The experimental transition dipole length of the B_b transition obtained from an unconstrained fit (with three Gaussians) to the experimental absorption spectrum is 1.4 Å. However, we found that the simultaneous fit to all REPs and the absorption cross-section could not be obtained with this transition dipole strength value. The best fit for all the RR active modes along with absorption spectra was obtained iteratively with a reduced transition dipole length of 1.11 Å. As no prior knowledge regarding exact location and intensity of B_b and nearby electronic states is available from experiments, such as, linear and circular dichroism spectroscopy, the experimental absorption spectrum was deconvolved with this constraint. The position of B_b state was fixed at 45641 cm^{-1} (219.1 nm) which was the peak of the simulated absorption spectra after simultaneous fit of all REPs. Next, intensity (area under Gaussian curve) of the B_b state was relaxed and those of next high lying component was manually iterated to so that the resulting area under deconvoluted B_b band yields a transition dipole length close to 1.11 Å. In this procedure TD-DFT computed results help in determining minimum number of required Gaussians to deconvolve the broad absorption spectra. (See Table 4.3)

4.2.8 Fitting of Raman excitation profiles and absorption cross-section

The initial guesses for the displacements along different normal coordinate were obtained from average intensities of the all RR bands relative to that of the band at 954 cm^{-1} in the spectrum with 216, 220 and 224 nm excitations. The transition dipole moment strength of 1.11 Å was derived from deconvolution of experimental absorption spectra as described in preceding section. Zero-zero transition energy was estimated so that the red edge of simulated absorption spectra agrees with experimental one. The solvent relaxation time less than 50 fs as obtained by Jimenez et al. from fs fluorescence up-conversion measurement on coumarin in water,[40] by Milán-Garcés *et al*. from RR intensity analysis on tryptophan in water[41] and MD simulations.[42,43] Values of the parameters were then iteratively optimized by using a self-consistent procedure to fit the REP and absorption spectrum simultaneously. The quality of the fit was determined by visual inspection and later by varying each parameter by 10 % of its best fit value. The simulation is performed with MATLAB (The MathWorks, Natick, MA)

4.2.9 Quantum chemical computation

6-ClG is modeled as N9H neutral tautomer which is most prevalent form in solution state[44]. The solvent environment around the base was mimicked by explicit water molecules whereas polarizable continuum model was employed to take into account the bulk dielectric environment. Six water molecules were strategically placed to make hydrogen bond contacts with the base (Fig. 4.1) as was done for nucleobases [45–47] previously.

Ground state structure optimization and vibrational frequency calculations were performed using B3LYP hybrid functional[48,49] and 6-311+G(2d,p) gaussian basis set. For correct description of excited states basis set was augmented with diffuse and polarization functions. Excited state energies were computed as vertical excitation on the S_0 geometry using linear response formalism of time-dependent DFT (TD-DFT)[50,51] using same basis set. Geometry optimization was performed without any symmetry constraints. Ground state equilibrium structure and excitation energies were calculated using equilibrium and non-equilibrium version of polarizable continuum model (PCM)[52,53] respectively. The matrix A_{ji} of eqn. 2.28 is obtained from normal mode computation of S_0 equilibrium structure. Signs of Δs are obtained from signs of excited state gradients along normal coordinates that were computed from analytic cartesian gradients.[54] All computations were done with Gaussian 09 software suite.[55] Vibrational normal modes and molecular orbitals are visualized using Chemcraft 1.6[56] and computed oscillator strengths are converted to extinction coefficient and stick spectra are deconvoluted with gaussian functions of fixed full width of 3500 cm^{-1}. Vibrational potential energy distribution (PED) analysis is carried out with VEDA 4.00 package.[57] Signs of these gradients are computed through eqn. 2.31 as described in chapter 2.

4.2.10 Internal reorganization energy

The total internal reorganization energy of the photo excited 6-ClG molecule is determined by the expressions 2.23 and 2.24. Δ_j's are be converted to changes in internal coordinate corresponding to jth normal mode (δ_j) using the formula 2.28.[58]

4.3 Results and Discussions

4.3.1 Electronic structure of 6-ClG

The most intense transition of GMP, B_b, is centered at 199 nm.[59] In 6-ClG, not only does this transition red-shift by 20 nm, but also becomes much narrower. The B_b state

of 6-ClG is located at 219.1 nm with a transition dipole length of 1.1 Å. Clearly, - chloro substitution affects the high lying electronic transition of 6-ClG. Dipole strength of this transition becomes considerably higher in 6-ClG as evidenced by respective experimental oscillator strengths (Table 4.2). Wavelengths corresponding to the electronic transitions observed in experimental UV-visible absorption spectra are listed in Table 4.3.

Table 4.2. Absorption cross-section of B_b electronic state of 6-ClG and GMP.

	6-ClG[a]		Guo[b]	
State	ΔE_{Exp} (nm)	f_{exp}	ΔE_{Exp} (nm)	f_{exp}
B_b	219.1	0.62	200	0.4

[a]this study; [b]Ref 59, guanosine in aqueous solution at pH 6.0, experimental oscillator strength (f_{exp}) is evaluated with the formula, $f_{exp} = 1.13 \times 10^{12} \, \eta \int \sigma(\tilde{\nu}) d\tilde{\nu}$, where η is refractive index of the medium and $\int \sigma(\tilde{\nu}) d\tilde{\nu}$ is integrated absorption cross-section in $cm^2 \, molecule^{-1}$.

To determine the nature of the molecular orbitals involved in these transitions, we computed excitation spectra using the TD-DFT formalism. Solvated 6-ClG was modeled as a complex with six water molecules, 6-ClG•$6H_2O$ (Fig 5.1). Excitation energies for electronic transitions of 6-ClG and corresponding orbital contribution were computed at TD-B3LYP/6-311+G(2d,p)//PCM level of theory and compared against experimental values (Table 4.3). Substitution at the 6th position on the purine ring with chlorine atom that is less electronegative and larger in size compared to oxygen increases π electron conjugation of purine ring. It causes a 34 nm redshift of the first bright singlet state in 6-ClG with respect to that of GMP. Similar effect is observed upon sulphur (6-thioguanine) or selenium (6-selenoguanine) substitution at this position with 55 and 85 nm redshifts relative to guanine respectively.[60] Position of the first singlet state in 6-ClG does not change with respect to that in 2-aminopurine (AP), an analogue that lacks the Cl substitution at 6th position. This fact suggests minimal contribution of valance π cloud of Cl towards conjugation in the purine ring.

Contributing orbitals for B_b transition along with experimental and computed absorption spectra are shown in Fig. 4.3, panel a. Two $\pi \rightarrow \pi^*$ excitations contribute to make this mixed transition: H–2 $\rightarrow$ L and H $\rightarrow$ L+1. We find good agreement between computed and experimental peak positions as well as relative strength (Fig. 4.3, panel b). Standard deviation of 0.05 eV obtained for computed vertical excitation energies with respect to experimental λ_{max} (Fig. 4.4) is lower than the average

accuracy achieved in computation of excitation energies using TD-DFT method (~0.2 eV or 1600 cm^{-1}).[61] Thus, a cluster-continuum model in which the solvated 6-ClG is modeled as hydrogen bonded complex with explicit water molecules and PCM solvation accounts for the bulk dielectric effect of water, is necessary for an accurate description of the excited state properties.

Table 4.3 Vertical singlet excitation energies in nm (in eV in paranthesis), oscillator strengths (f) and major orbital contribution to each transition of neutral 6-ClG by TD-B3LYP method; and comparison with published computed and experimental transition energies.

			6–ClG•6H$_2$O^a			Experimental	
	Type	Computed State order	Major orbital Contribution^b (%)	$\Delta E_{vert,PCM}$ cm^{-1} (nm)	Oscillator strength, f_{PCM}	ΔE_{Exp} cm^{-1} (nm)	ϵ (l mol^{-1} cm^{-1})
L_a	ππ*	S1	H→L (97)	32600 (307.0)	0.1562	32175 (310.8)	17589
$S_{n\pi*}$	nπ*	S2	H−1→L (95)	40100 (249.5)	0.001	-	-
L_b	ππ*	S3	H→L+1 (55)	42500 (234.8)	0.0512	41374 (241.7)	15104
	πσ*	S4	H→L+2 (93)	43400	0.0003		
	ππ*	S5	H→L+1 (86)	44600	0.0031		
B_b	ππ*	S6	H−2→L (49) H→L+1 (37)	46400 (215.6)	0.5965	45642 (219.1)	71215
	nπ*	S7	H−6→L (68)	47300	0.0022		
	#	S8	H→L+4 (85)	47500	0.0002		
	ππ*	S9	H−3→L (93)	48000 (208.4)	0.06	46905 (213.2)	64493
	ππ*	S10	H→L+5 (91)	48400 (206.7)	0.028		
	ππ*	S11	H−4→L (84)	49100 (203.6)	0.1322	48876 (204.6)	34209

^{a}TD-B3LYP method with 6-311+G(2d,p) basis set and Cluster-continuum model of solvation in which explicit water molecules from the first solvation shell are included in conjunction with non–equilibrium solvation using self consistent reaction field (SCRF-PCM or PCM) model using water as solvent. ^{b}Percentages are calculated as 100 x twice the squares of the coefficients in the CI expansion of TD-DFT wave functions. H and L stand for highest occupied molecular orbital (HOMO) and lowest unoccupied molecular orbital (LUMO) respectively. #highly delocalized state involving orbital that is not localized on the purine ring of 6-ClG.
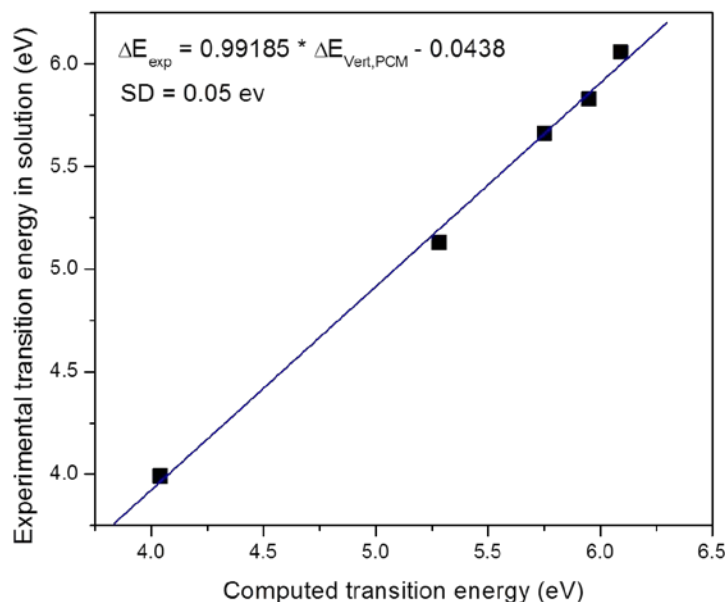
Fig. 4.4 Linear fit to experimental transition energies as a function of computed transition energies of 6-ClG•6H$_2$O complex. Computed transition energies were obtained using cluster-continuum model at TD-B3LYP/6-311+G(2d,p)//PCM level of theory and experimental values. Computed and experimental values are taken from Table 4.3.

4.3.2 RR spectra and experimental Raman excitation profiles of 6-ClG

RR spectrum of 6-ClG with laser excitation of wavelength 222 nm is shown in Fig. 4.5 Vibrational bands within 1000-1800 cm^{-1} region of 260 nm excited RR spectra of this molecule at neutral pH were previously assigned by comparison with GMP spectra and DFT calculations.[44] Normal mode assignments of all observed modes including three additional intense bands at 831 cm^{-1}, 919 cm^{-1} and 954 cm^{-1} are described in Table 4.4. Variation in intensity of different RR bands of 6-ClG as the Raman excitation wavelength is tuned across B_b absorption band from 210 to 229 nm is depicted in Fig. 4.6. The band at 932 cm^{-1} arises from sodium perchlorate used as internal intensity standard. Intensity of each band of 6-ClG in every spectrum is normalized to the intensity of the 932 cm^{-1} band. REP of each band was constructed using eqn. 2.6a. (See Chapter 2) Excluding the band at 1641 cm^{-1}, all observed bands of 6-ClG have their highest Raman cross-section between 220 and 222 nm of excitation.
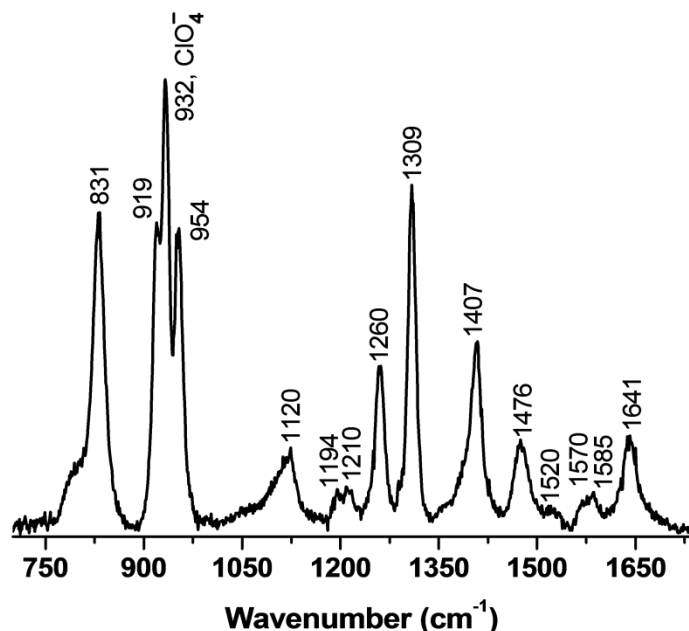
Fig. 4.5 UVRR spectrum of 6-ClG (1 mM, pH 6.8) obtained with excitation wavelength of 222 nm with incident laser power of 0.6 mW. The band at 932 cm^{-1} arises from sodium perchlorate and was used as internal intensity standard.

We observe that maxima of all experimental REPs are red shifted with respect to the absorption band maximum at 219 nm (Fig. 4.7 and 4.8). We attribute this to vibronic coupling of RR active modes with nearby electronic states. Two absorption bands are close to the band we have tuned into: one on the blue edge and another on the red edge (Fig. 4.3 and Table 4.3). REPs of 6-ClG bands at 919, 1120, 1260 and 1309 cm^{-1} have peak at 220 nm whereas maxima of REPs of bands at 954, 1407, 1476, 1520, 1585 cm^{-1} is at 218 nm. This is likely due to stronger coupling of these bands with electronic states lying on the higher energy side of B_b state compared to the first set. Such redshift in the REPs has been observed before in tryptophan within B_b absorption band.[41,62]

Depolarization ratios of all intense 6-ClG bands (except for 1120 and 1641 cm^{-1}) measured at excitation of 220 nm are close to 0.33 (Table 4.1) indicating major contribution from a single electronic state, B_a at the peak maximum. In contrast, the intensities in the wings of the REPs indicate interference from close-lying electronic states as a sudden drop in RR cross-section. This may occur if a vibrational mode is coupled with two nearby electronic states and associated Δs have opposite signs.[63–65] The resulting RR cross-section will decrease because of negation at the amplitude level ($I_{RR} \propto \Delta^2$) at regions where absorption bands corresponding to these two states

overlap. This loss of intensity is detected in experimental REPs of all RR modes at 222 nm excitation wavelength and is attributed to coupling to a lower lying state. On the red edge of the B_b state is the L_b electronic state at 241.7 nm (Fig. 4.3, panel b and Table 4.3). Destructive interference between L_b and B_b states along a vibrational mode can result in a loss or gain in RR cross-section. Presence of this feature in REPs of the bands at 1570 and 1641 cm^{-1} suggests that these modes electronically couple to the L_b state. This is expected as the directions of transition moments of both these states are nearly the same (Fig. 4.1).
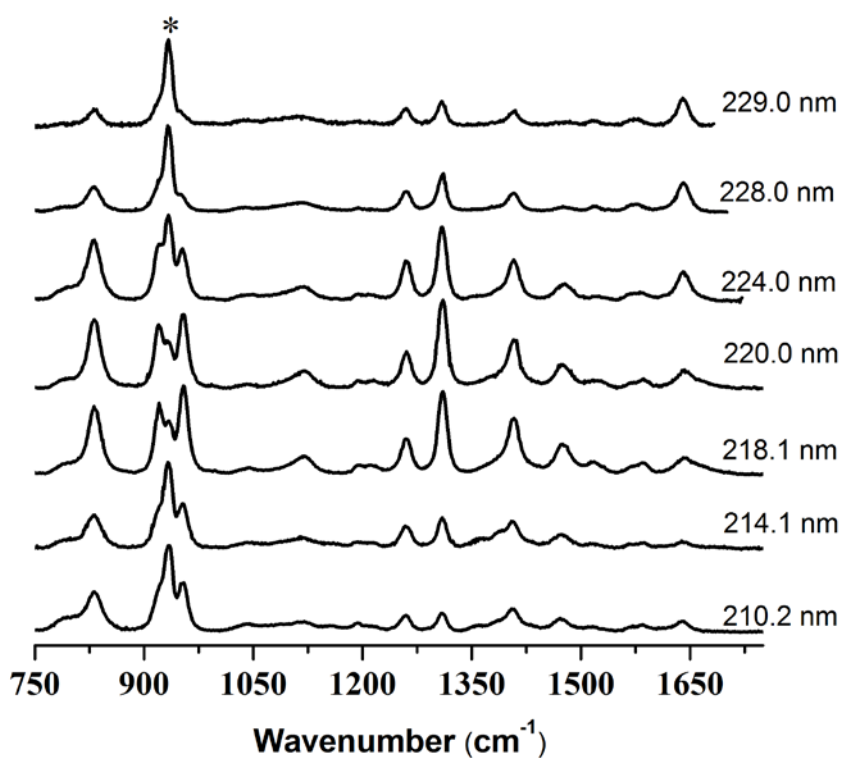
Fig. 4.6 UVRR spectra of 6-ClG (1 mM, pH 6.8) at seven different excitation wavelengths in aqueous solution. Spectra show variation in the Raman intensity of each band as the excitation wavelength is tuned across the electronic absorption band (Fig. 4.3, panel b, bottom). Spectra have been normalized to the intensity of the 932 cm^{-1} band of sodium perchlorate used as internal intensity standard (asterisk).

Table 4.4 Experimental, computed wavenumbers, potential energy distributions (PED), dimensionless displacement and estimated internal reorganization energy of all RR bands of 6–ClG. Contribution of eight modes (in bold) comprises 87% of the total internal reorganization energy.

Experimental (cm⁻¹)	Computed frequency[a] (cm⁻¹)	PED (%)[b]	$|\Delta|$[c] (Dimensionless)	Mode specific internal reorganization energy, λ_k (cm⁻¹)
800	807	tors C6N1C2N3 (14) – N1C2N3C4 (21) + C5N7C8N9 (12) – out N2N1N3C2 (10) + N3N9C5C4 (32)	-	-
831	828	str N3C4 (10) – be C2N3C4 (10) + N1C2N3 (17) + C4N9C8 (21)	0.23	**22**
919	900	str N1C2 (13) + N2C2 (10) – Cl6C6 (23) + be C6N1C2 (11) + C5N7C8 (12) – N9C8N7 (12)	0.145	**10**
954	953	– be C5N7C8 (12) + N9C8N7 (47)	0.175	15
1043	1037	str N1C2 (25) – be H2aN2C2 (11) – Cl6C6N1 (11)	-	-
1088	1086	str N9C8 (54) – be N9N9C4 (28)	-	-
1120	1103	str N3C2 (25) + be H2aN2C2 (48)	0.11	**7**
1194	1199	str N7C5 (21) – be C5N7C8 (10) + H8C8N7 (24)	0.08	4
1260	1287	str N7C8 (16) – N1C6 (19) + N3C4 (15) + N1C2 (14) + be H8C8N7 (10)	0.10	**6**
1309	1327	– str N7C8 (15) + N7C5 (14) – be C5N7C8 (11) – H8C8N7 (23) + N9C8N7 (12)	0.15	**15**
1407	1408	str N1C6 (23) – N3C4 (12) – N2C2 (12) + N9C4 (17)	0.13	**11**
1476	1472	str N2C2 (20) + be N1C2N3 (15)	0.10	**8**
1520	1528	str N7C8 (37) – be H8C8N7 (19)	0.07	4
1585	1572	str N3C4 (12) + str N3C2 (19) – be C2N3C4 (11) – C4N9C8 (13)	0.078	5
1602	1622	str N2C2 (10) + be H2aN2H2a (76)	-	-
1641	1647	str N1C6 (18) + N3C4 (16) – be N3C4C5 (14)	0.09	6
			Total	112

[a]B3LYP/6-311+G(2d,p)//PCM; [b]using VEDA 4.0, sign indicates relative phase of movement of atoms in internal coordinates; [c]obtained form best-fit parameters, described Table 4.5.

A strong interference is also observed in REPs of all the bands around 214 nm. As mentioned before, there is an overlapping $\pi\pi^*$ band on the blue edge of the B_b band in the absorption spectrum. Computational calculations of the electronic manifold of states show that there are two $\pi\pi^*$ states at 219.6 and 204.6 nm. The Raman band at 1641 cm⁻¹ arising from pyrimidine in-plane deformation is particularly strongly influenced by the presence of adjacent electronic states. Corroborating this is the depolarization ratio measurement of 0.46 for this band measured at 220 nm. REP of this mode (see Fig. 4.7) is heavily skewed towards the red edge because of stronger

coupling with the L_b electronic state than with B_b state. In Fig. 4.7 and 4.8 it is observed that though the red edge of simulated REP of all RR bands agrees well with experimentally measured values, this is not the case for 1641 cm^{-1}. Since the simulated REP is based on a single excited electronic state, it fails to reproduce the profile for this mode.

4.3.3 Simulation of experimental REP

Magnitude of Raman intensity at a particular excitation wavelength is determined by the nature of the initial displacements (Δ) on the excited state after photoexcitation. Broadening and the line shape of REPs are governed by both, homogeneous and inhomogeneous effects in distinct ways. These parameters can be extracted by quantitative modeling of the Raman intensities and the line-shape of the REP. We used time-dependent wave-packet theoretical analysis developed by Lee and Heller to model measured REPs. Dimensionless displacements were converted into internal coordinate changes with the use of force constants obtained from computational calculations. Experimental REPs and the global fits to these obtained using a common set of parameters for all 13 RR modes and the absorption spectrum are shown in Fig. 4.6 and 4.7. Overall agreement is achieved between experimental and simulated profiles for RR and absorption cross-sections. As discussed above, at the red edge of 1641 cm^{-1} mode, and to a lesser extent the low energy edge of 1260, 1570, 1585 cm^{-1} too, the simulation and experiment do not agree well. This is because the model used for simulating the REP incorporates a single excited state, (B_b), and neglects the effect of interference between electronic states. We expect that this mode would contribute significantly to assist internal conversion from B_b to L_b because of effective coupling to both states. Deviation between the experimental and computed RR cross-sections on the blue edge of B_b state is attributed to interference from higher-lying electronic states, as discussed in preceding section.

Table 4.5. Parameters used in self-consistent simulation of REP and absorption spectra

	E_0(cm^{-1})	Λ(cm^{-1})	τ(fs)	θ(cm^{-1})	M(Å)	λ_{int}(cm^{-1})	λ_S(cm^{-1})	λ(cm^{-1})
Best Fit	45700	350	15.2	360	1.11	112	1220	1332
Set 1	45720	450	11.8	420	1.11	91	1100	1191
Set 2	45690	240	22.1	220	1.11	140	1350	1490

Set 1 and Set 2 set of parameters are obtained by decreasing and increasing the best fitted Δ values by 10% and optimizing E_0, λ_S, θ and Λ iteratively.

The solvent relaxation time is constrained by the width of the experimental REPs while the absorption spectrum is not sensitive to change in the same. Parameters were chosen so that fits to the red edges of both absorption and RR cross-sections were good. This is because two interfering electronic states contribute to the blue side of all REPs. Robustness of fit on variation of estimated parameters is discussed in later section.
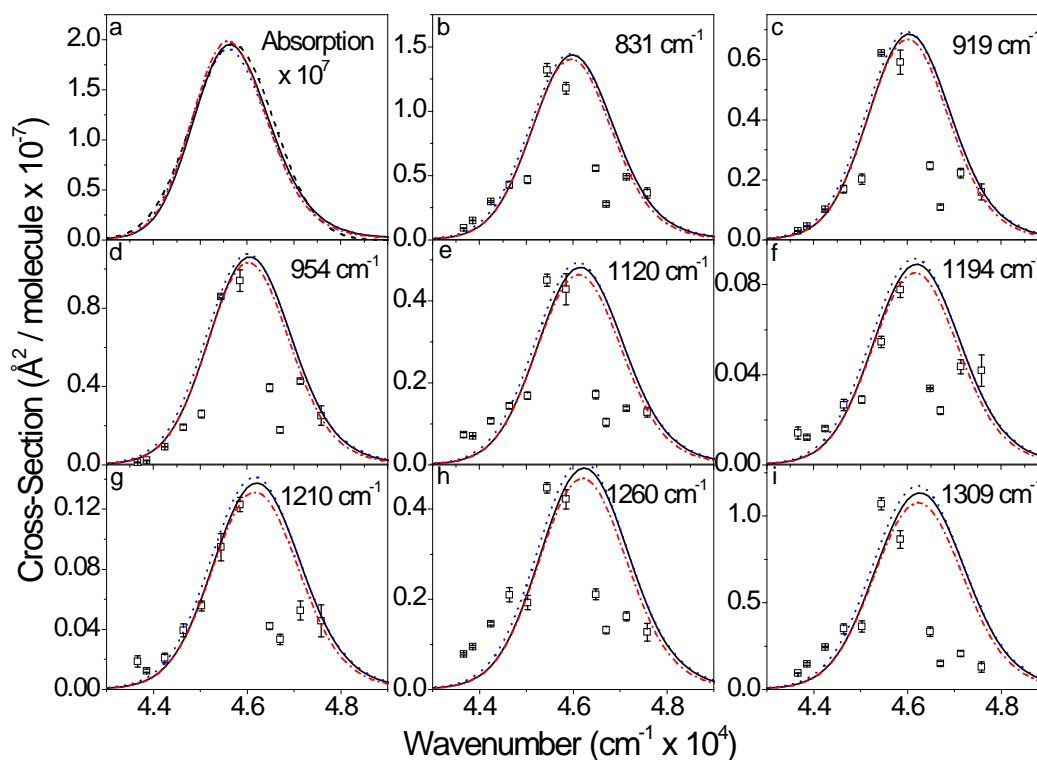
Fig 4.7 Experimental and simulated Raman excitation profiles and absorption cross-sections of 6-ClG in the 210-230 nm region. (a) Experimental (*black dashed*) and simulated (*black solid*) absorption spectrum. (b–i) Experimental (*open square*) and simulated (*black solid*) Raman excitation profiles for eight resonant modes of 6-ClG. The simulated absorption and Raman excitation profiles were obtained by using the parameters in Table 4.5. Set 1 (*red dash dot*) and Set 2 (*blue dot*) were obtained with two sets of deltas obtained by decreasing and increasing 10% those values in the best fit respectively.

4.3.4 Internal reorganization energy and mode-specific reorganization

The internal reorganization (λ_{int}) energy of the solute influences relative intensities of RR modes. Total internal reorganization (λ_{int}) energy of 6-ClG along all 13 RR active modes was determined at 112 cm^{-1}. Six modes corresponding to bands at 831 cm^{-1}, 919 cm^{-1}, 954 cm^{-1}, 1309 cm^{-1}, 1407 cm^{-1} and 1476 cm^{-1} account for 75 % of the total internal reorganization energy. Mode compositions determined from potential energy

distribution (PED) (Table 4.4) indicate that maximum distortion occurs in ring stretching coordinates localized on both pyrimidine and imidazole rings. Similar value of λ_{int} (168 cm^{-1}) is estimated in a closely related purine base, *viz.* 9-methyladenine (9–meA) following excitation within its L_a band at ~ 260 nm. Relatively high values of internal reorganization energies (~1000–1500 cm^{-1}) were found for various pyrimidine systems in their first bright state[6–8,11,12] indicating their high degree of structural flexibility following UV excitation. Relatively low value λ_{int} suggests that despite efficient absorption of UV-C photons in the B_b absorption band, the ground state structure of 6-ClG does not undergo major distortion as compared to other pyrimidine bases.
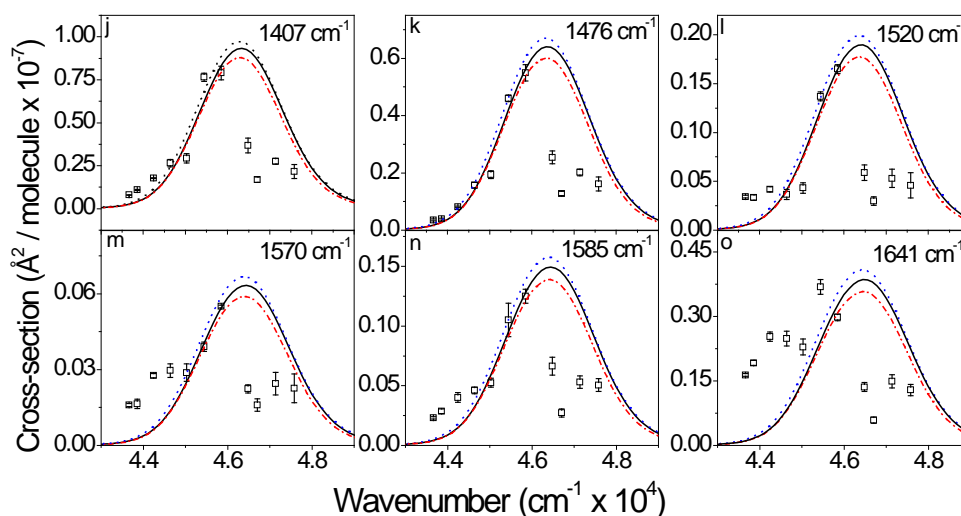
Fig. 4.8 Experimental and simulated Raman excitation profiles of the other five resonant modes of 6–ClG. The simulated Raman excitation profiles were obtained by using the same sets of parameters as in Fig. 4.7.

In the simulation (Fig 4.7 and 4.8), values of Δs which determine mode specific λ_{int} depend on both, breadth of the absorption band of the resonant electronic state and intensity of RR bands. Relatively low value of λ_{int} is consistent with a narrow B_b absorption band in 6-ClG (FWHM of 2000 cm^{-1}) in comparison with those (~ 3500-4000 cm^{-1}) in other nucleobases in the same wavelength region. In 6-ClG, overall internal reorganization energy (112 cm^{-1}) is small compared to those of similar molecules. While rare, this is not unprecedented and a similar situation has been reported before by Loppnow and coworkers who determined total internal reorganization energy of 9-methyladenine (9-meA) at 168 cm^{-1} within lowest L_a electronic state at ~ 260 nm.[9] Dynamical simulation has shown that N$_9$H-adenine (N$_9$H-Ade) undergoes state crossing starting within 30 fs of photoexcitation to L_a state.[66] Thus ultrafast population transfer to nearby $\pi\pi^*$ and $n\pi^*$ states via conical

intersection happens within time scale of the resonance Raman process itself. This dephasing mechanism would lead to significantly low RR cross-section and as a result, low internal reorganization energy of N9H tautomer of Ade was observed in comparison to those of all other nucleobases.[7,8,11–14] In 6-ClG, there are four closely spaced electronic states (Fig. 2b) within 190-230 nm and their interference is also probed in all measured REPs (Fig. 4 and 5). Thus, we suspect ultrafast state crossing similar to that present in N9H-Ade to be active in 6-ClG also, and hence has a low internal reorganization energy. This ultrafast state crossing to close by electronic states is further supported by the fact that 6-ClG does not show appreciable fluorescence at 220 nm excitation.

4.3.5 Structural distortions of 6-ClG upon photoexcitation

The dimensionless displacements, Δ, obtained from the simulation were converted into geometrical changes in internal coordinates (Table 4.6) using normal mode descriptions of 6-ClG computed at B3LYP/6-311+G(2d,p)//PCM level of theory using eqn. 2.28. Internal coordinates undergoing major distortion are also described in Table 4.6. Major changes are found along stretching coordinates of both rings as expected in case of a $\pi\pi^*$ transition. Specifically, imidazole ring is found to be expanded through C5–N7, N7=C8 and N9–C4 bonds (by 0.019, 0.008 and 0.03 Å respectively). Pyrimidine ring primarily undergoes contraction through N1–C2 and C6–N1 bonds by 0.04 and 0.014 Å respectively. It is important to note that photochemically relevant coordinates that can favor the production of various oxidative adducts of 2′-dG are reported to lie along imidazole ring stretching coordinates such as $C_8–N_9$ bond upon 260 nm excitation.[14] Unlike 2′-dG in L_a state, photoexcitation of 6-ClG to B_b state does not induce elongation of C8–N9 bond. Thus excitation to B_b does not favor cleavage of this bond and subsequent formation of oxidative lesions like formamidopyrimidine in 6-ClG.

Though the transition dipole of B_b state is aligned along $C_2–N_2$ bond, there is negligible distortion (-0.007 Å) along this bond. Consistent with this is the absence of RR enhancement of NH_2 scissoring mode at 1671 cm^{-1}. In contrast, another exocyclic bond C6–Cl6 is found to contract by a major amount, 0.056 Å, the highest among all internal coordinates. Strong distortion of this bond is due to considerable amount of mixing of imidazole in-plane vibrational mode (919 cm^{-1}) with the C6–Cl6 stretching coordinate and supported by PED computed with DFT. This type of coupling is not seen in Gua where carbonyl stretching does not strongly couple with any of the in-plane imidazole distortion modes. Similar effect of normal mode mixing of Carbon–Fluorine (F) stretching coordinate with ring stretching vibration is found in another

halogen substituted pyrimidine base, 5-Fluorouracil as well[6]. It is worth noting that the π cloud of C6–Cl6 bond does not take part in electronic excitation of the purine ring.

Table 4.6 Internal coordinates and displacements for the modes that undergo the largest distortion following photoexcitation of 6-ClG into the B_b state

Internal coordinates (Bond length)	Internal coordinates in ground state (Å)	Change in internal coordinates (Å)
N1=C2	1.3582	-0.041
C6–N1	1.3111	-0.014
N3=C4	1.3257	0.02
C4–C5	1.4093	-0.001
C5=C6	1.387	-0.001
C4–N9	1.3675	0.032
C5–N7	1.3842	0.019
N7–C8	1.3067	0.008
C6–Cl6	1.7560	-0.056

Fluctuation in electronic transition frequencies of solute due to thermal motions of solvent is partitioned into ultrafast homogeneous and slower inhomogeneous components. At ambient temperature, it is sufficient to consider a single solvent coordinate interacting with the solute to model the homogeneous part. Among several models describing this component, we employed Brownian oscillator spectral density model of Mukamel and coworkers.[35,39] This model includes physical parameters such as coupling strength between solute electronic transition and solvent bath coordinate via solvent reorganization energy (λ_s) and dynamic relaxation time of solvent oscillator (τ). As the Raman process completes within tens of fs, both λ_s and τ represent ultrafast dynamics of water molecules in first solvation shell around the solute. With this model, our simulation yields solvent reorganization energy of 1220 cm^{-1} with a relaxation time of 15 fs for 6-ClG in B_b state. Comparable values of solvent reorganization energies are obtained in other purines, such as in 9-meA and 2′-dG at 1050 and 1200 cm^{-1} respectively following excitation to L_a state.[9,14] A value of 1230 cm^{-1} was reported for tryptophan when excited within B_b state.[41]

Solvent reorganization energy of 6-ClG in B_b state obtained here is in the same range (185-1650 cm^{-1}), as that for eight natural and substituted purine and pyrimidine bases[6–14] in their first singlet states. Amplitude of solvent response depends on the magnitude of change in the instantaneous, induced dipole moment of the solute upon photoexcitation and is expected to be an intrinsic property of the resonant excited state. Thus, in 6-ClG maximum contribution (92%) towards total reorganization

energy (1332 cm^{-1}) estimated from our simulation originates from inertial response of water.

In response to instantaneous charge reorientation of a solute induced by an electronic excitation, the fastest component of water solvation dynamics is found to be less than 50 fs from molecular dynamics simulations,[42,43,67,68] time dependent stokes shift,[69,70] 2-dimensional IR echo[71] and fluorescence up-conversion[40] experiments using different probe molecules. Time-resolved Stokes shift (TRSS) experiments on tryptophan and organic dyes reveal that a substantial amount of the total Stokes shift always occurs within tens of femtosecond that is beyond the temporal resolution of the typical fluorescence experiments. The relaxation time obtained from intensity analysis of RR bands represents pure inertial component of solvent response. This response time is expected to be a characteristic of the molecule itself rather than that of the investigated resonant electronic state. We have found an ultrafast component of water response with a ~15 fs dynamics correlation time, which is on the same order as that (~8 fs) measured using tryptophan as probe.[41]

In several reports Loppnow and coworkers have estimated this ultrafast component of water dynamics using solvent reorganization energy as parameter for a number of purine and pyrimidine bases following photo-excitation to the first $\pi\pi^*$ state.[6–14] These authors have used Brownian oscillator model in a high temperature limit assuming $\Lambda/D = 0.1$ where D is the coupling strength between solvent bath coordinate and transition dipole of solute ($D^2 = 2\lambda_S k_B T$) and Λ is inverse of solvent relaxation time, τ. This choice would constrain the inertial relaxation component to a lower value within 63.3–192 fs. In the current model, we vary τ as an independent parameter over a range to reproduce width of measured REPs. We believe that since we have 13 independent modes, and the parameters are being determined with a simultaneous fit to all REPs, the data will allow independent determination of Λ and τ. Although it has been reported that computed REPs are not responsive to change in Λ by ~50 cm^{-1},[41,72] in our simulations, we find that to reproduce the width of the measured REPs a Λ value of 350 cm^{-1} corresponding to 15 fs relaxation time is required. If Λ is decreased by 50 %, (175 cm^{-1} corresponding to $\tau = 30.4$ fs) while the simulated absorption spectrum agrees better with experimental absorption lineshape, all the computed REPs are much broader than measured values (Fig. 4.9 and 4.10). On the other hand if Λ is increased to 550 cm^{-1} ($\tau = 9.7$ fs) width of all REPs decrease by small amount compared to optimum values while simulated absorption spectra remains practically unchanged. Thus, for best agreement between measured and

simulated REPs a dynamic solvent response time < 30 fs is necessary and 15 fs provides the best fit.
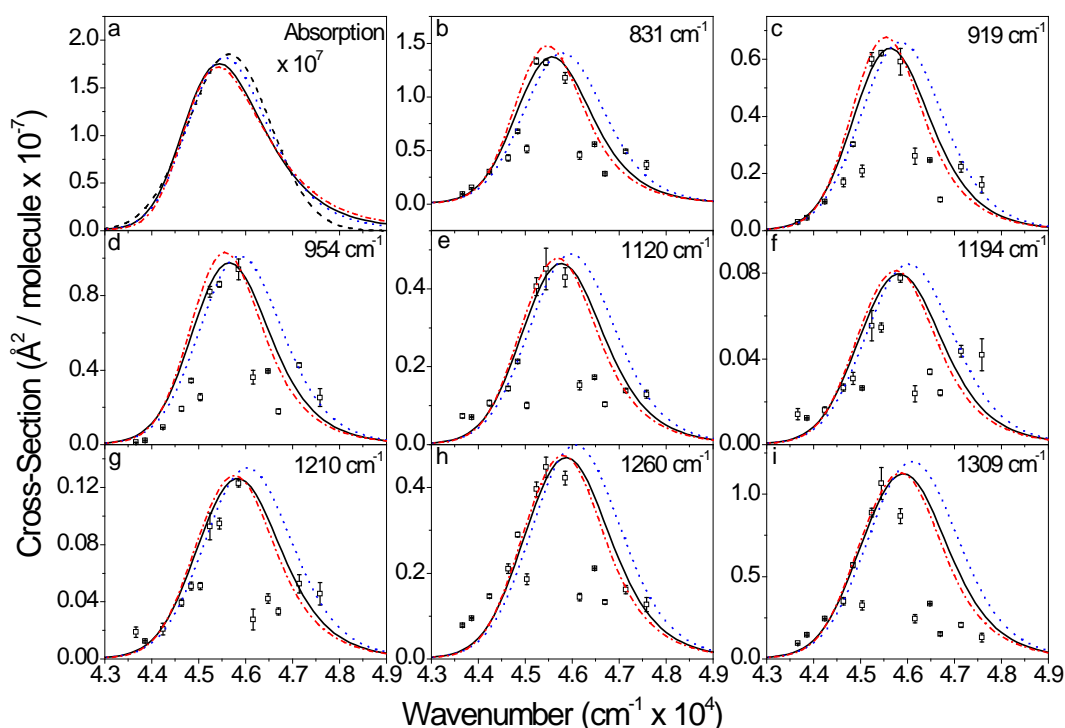
Fig. 4.9 Dependence of the simulated absorption and Raman excitation profiles on Λ. Panel (a) the experimental (*black dashed*) and simulated (*black solid*) absorption spectrum. Panel (b-i) The experimental (*open square*) and simulated (*black solid*) Raman excitation profiles for eight resonant modes of 6-ClG. The simulated absorption and Raman excitation profiles were obtained by using the best fitted parameters in Table 4.5 while varying Λ and adjusting E_0. Set 1 (*red dash dot*) and set 2 (*blue dot*) were obtained with values of Λ of 550 cm^{-1} and 175 cm^{-1} respectively with adjusted E_0 values to 45820 cm^{-1} and 45680 cm^{-1} respectively while all other parameters remained the same.

Partitioning of homogeneous (λ_S) and inhomogeneous (θ) components is possible in our simulation because both of them affect simulated absorption and RR cross-section in distinct ways. Inhomogeneous broadening, θ, arises due to site effect of slightly different micro-solvated structures of solute leading to a distribution of electronic transition energies. The θ value of 360 cm^{-1} resulting from these simulations is ascribed to these micro-configurations that remain practically immobile on the time scale of the Raman process. For a variety of purine and pyrimidine bases, contribution of θ to total line-width broadening is found to be 900-1300 cm^{-1}. [6–14] All of these nucleobases have either amino (9-meA) or carbonyl (Ura, Thy) moiety or both of them (2′-dG and Cyt) present as strong hydrogen bonding partners for surrounding water

molecules and thus favor formation of a number of static, micro-solvated structures. DFT calculation on uracil, thymine and cytosine interacting with explicit water molecules also predicts extensive nucleobase-water interaction.[73–76] Apart from these static structures any other slower (>100 fs) component of solvation will also contribute to the inhomogeneous broadening component obtained from our simulation.
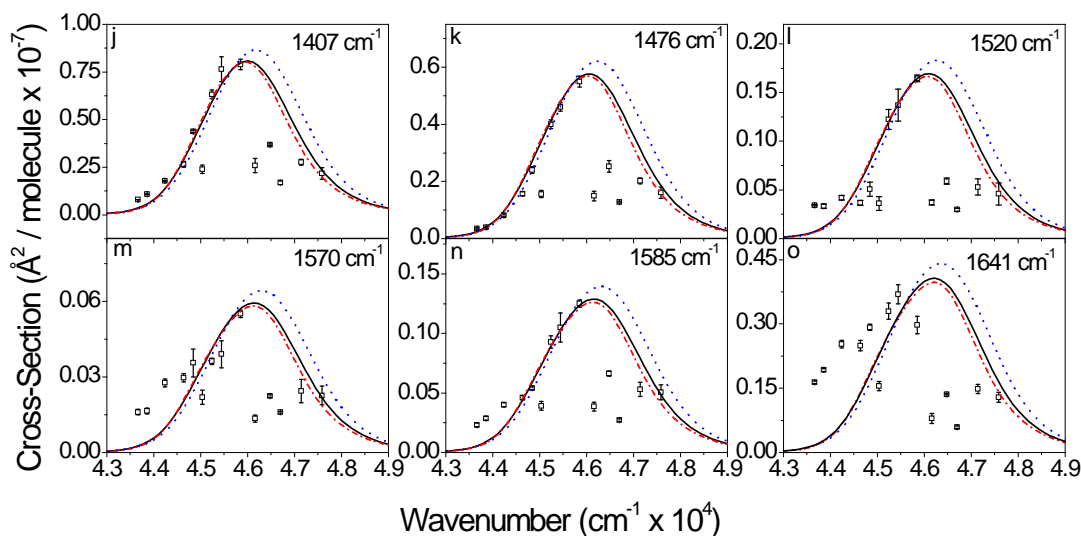
Fig. 4.10 Dependence of the simulated absorption and Raman excitation profiles on the amplitude of homogeneous broadening parameter, Λ. Panels (j)-(o): experimental (*open square*) and simulated (*black solid*) Raman excitation profiles for five resonant modes of 6-ClG. The absorption and Raman excitation profiles were obtained with the same set of parameters as in Fig. 4.9.

Among several nucleobases, 5-FlUra has the largest inhomogeneous line-width (1300 cm^{-1}), determined from RR intensity analysis within 260 nm absorption band.[6] An increase in θ value by 300 cm^{-1} over that of Ura[8] was accounted for by greater amount of dipolar interaction between the hydrophilic -fluoro group and water. In 6-ClG, the presence of a relatively hydrophobic -chloro group reduces interaction with water at the 6th position on purine ring. In computational modeling of solvated 6-ClG we placed six explicit water molecules within hydrogen bonding distances in the initial starting configuration. As the energy was minimized, the water molecules moved away from the chlorine and the final lowest energy configuration of this system does not have explicit hydrogen bonds with chlorine. The loss of a hydrogen bonding partner at the 6th position can thus decrease possible number of hydrated static micro-structures which is reflected in the low value of the inhomogeneous contribution to the overall spectral broadening.

6-ClG (λ_{abs} = 311 nm) has a feeble fluorescence with maximum emission at ~380 nm producing a large Stokes shift of 5900 cm^{-1} (Fig. 4.11). An analogue of 6-ClG, aminopurine (2-AP) shows a similar lower energy emission but with a large quantum yield of 0.66.[77] The large Stokes shift[78] of 2-AP in protic solvents such as water is attributed to the formation of close hydrogen bonded network between several water molecules and the donor/acceptor site of the base, and thus inhibition of free rotation of -NH$_2$ group.[79,80] With a very similar electronic structure, large portion of total reorganization energy (2950 cm^{-1}) of 6-ClG is also expected to derive from similar solvation structure as in 2-AP. In our calculation, we also find that formation of hydrogen bonded complex between 6-ClG and six explicit water molecules is necessary for correct reproduction excitation energies.
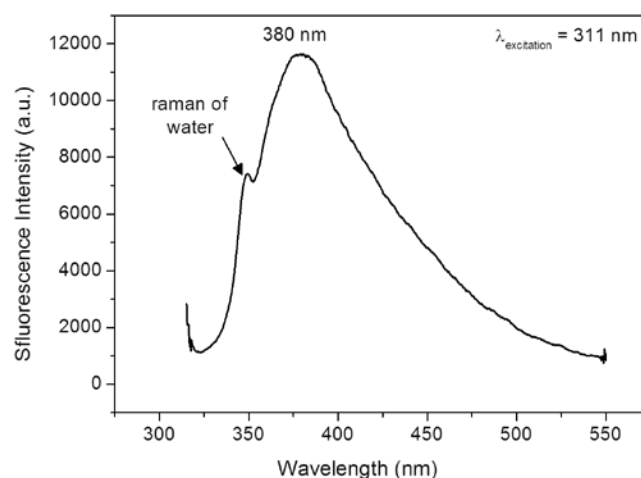
Fig. 4.11 Steady state fluorescence spectra of 6-ClG (2.5 mM in Phosphate buffer, pH 7.0, 20 mM) with 311 nm excitation wavelength. Emission spectra was recorded with Fluorolog spectrophotometer (FluoroMax 4, Horiba Scientific, USA).

4.3.6 Caveats and future prospect

The semi-empirical approach for simulation of Raman intensities[29,37,41,58,72,81–86] that combines the Lee and Heller formalism with additional inputs from TD-DFT and DFT computational parameters has limitations. The sub-50 fs dynamics derived from the resonance Raman intensity analysis depend on several important elements that are not determined with complete certainty in this approach. Simulations of RR intensity analysis employed here are based on the assumptions that the B_b excited state is mainly a single, non-degenerate state and that the potential energy surface is harmonic. Although measured depolarization ratios of most RR active modes are close to 0.33, vibronic coupling with high and low lying electronic states is evident in all measured REPs. A thorough description should take into account these close-lying

135

states for the RR intensity analysis to account for all interacting electronic states. However, this would be a considerably more complex approach with several additional parameters. In the current we have not accounted for these states because of lack of information regarding these crucial physical parameters, such as, zero-zero energies, strengths and directions of transition dipoles of all interfering electronic states. Moreover the uncertainties (~ 15 %) of the integrated peak area of the RR bands might counteract the iterative optimization process that will involve three times the number of parameters used in our current model. Nevertheless, these first measurements of REPs of a higher-lying excited state reveal the mode-specific influence of coupling between electronic states.

We have shown the computed spectra from TD-DFT obtained gradient and compared it with experimental spectrum at 220 nm. (Fig. 4.12) The computed RR spectrum does not agree well with experimental one. We note that, RR cross-sections are proportional to the square of the dimensionless displacements. Correct prediction of their signs through computation of gradient within TD-DFT approach does not necessarily ensure equally correct prediction of RR intensities themselves. However, the obtained signs of all Δs with three different functionals, *viz.* B3LYP, PBE0 and wB97xD are identical. (Table 4.7) This method is well documented and has been used by several groups Guthmuller and coworkers,[87,88] Franzen and coworkers,[89] Jensen and coworkers,[90,91] Barone and coworkers,[92] Brown and coworkers[93,94] and others.
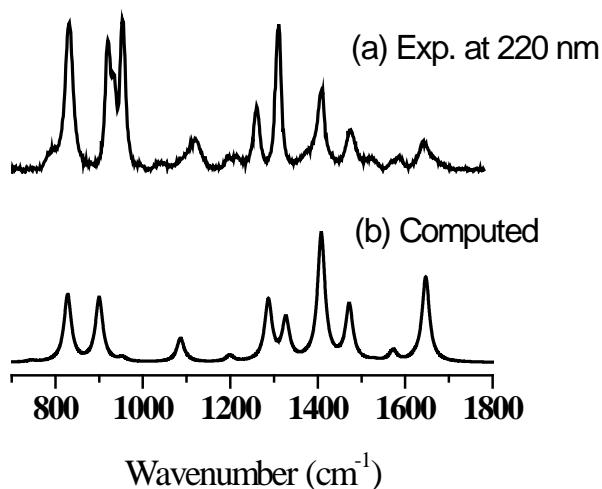
Fig. 4.12 (a) Experimental RR spectrum of 6-ClG at 220 nm and (b) computed spectrum with excited state (B_b) gradient computed at TD-B3LYP level of theory with 6-311+G(2d,p) basis set. This spectrum is computed using equation 2.30 and method described in chapter 2.

Determining the signs of the dimensionless normal coordinates relies on the accuracy of the excited-state calculations. In the current study we have used TD-DFT with B3LYP functional to obtain these signs. In principal more advanced quantum chemical calculations, such as, complete active space self-consistent field (CASSCF)

approach can be employed to obtain these signs of the excited state gradients. However, application of this type of resource intensive methods for deep-lying excited states is challenging. The normal mode compositions which tend to vary depending upon chosen theoretical method and the model complex itself would also impact the extracted structural distortions.

Table 4.7 Sign of dimensionless displacements (Δ) on resonant B_b electronic state obtained with three different functionals at B3LYP optimized geometry on isolated 6-ClG.

Experimental wavenumber (cm^{-1})	Computed wavenumber[a] (cm^{-1})	TD-B3LYP on S6	TD-PBE0 on S7	TD-wB97xD on S6
800	807	-1	-1	-1
831	828	-1	-1	-1
919	900	1	1	1
954	953	-1	-1	-1
1043	1037	-1	-1	-1
1088	1086	-1	-1	-1
1120	1103	-1	-1	-1
1194	1199	-1	-1	-1
1260	1287	-1	-1	-1
1309	1327	-1	-1	-1
1407	1408	-1	-1	-1
1476	1472	1	1	1
1520	1528	1	1	1
1585	1572	-1	-1	-1
1602	1622	-1	-1	-1
1641	1647	1	1	1

[a]at B3LYP/6-311+G(2d,p)//PCM; All calculations are performed with 6-311+G(2d,p) basis set and PCM solvation. All single point TD-DFT calculations are performed on equilibrium geometry of isolated 6-ClG, optimized with B3LYP functional. Signs of Δs (with three functional mentioned) are obtained with ground state normal modes computed with B3LYP functional using eqn. 2.31. B_b state of 6-ClG corresponds to the computed 6th (S6), 7th (S7) and 6th (S6) singlet state with B3LYP, PBE0 and wB97xD functional respectively.

The uncertainties in the accuracy of the TD-DFT calculations due to the vibronic interferences from multiple states, the signs of the dimensionless displacements and the neglected non-adiabatic state crossing effects warrant more experimental and theoretical investigation. Experimental methods, such as femtosecond stimulated resonance Raman spectroscopy and other time-resolved pump-probe experiments with sub-ps time resolutions would be useful to

independently probe the short-time dynamics in FC region of 6-ClG. These experiments in conjunction with relevant theoretical studies would be able to provide a general methodology to study deep-lying interfering electronic states in purines and other important biomolecules.

4.4 Conclusion

Upon photoexcitation within B_b absorption band located within UV-C region, 6-ClG undergoes distortion via expansion of imidazole ring and concomitant contraction of pyrimidine ring. This is accompanied by shortening of C_6–Cl bond. We determine an ultrafast (< 30 fs) inertial response of surrounding water molecules. This inertial response accounts for more than 77 % of the total line-width contribution due to solvent response (1220 cm^{-1}) of water. Relatively low internal reorganization energy indicates that 6-ClG does not undergo significant structural distortions when excited to the B_b electronic state in comparison to other nucleobases that were examined in the lower energy states. Despite the significantly high absorption cross-section 6-ClG is a more stable nucleobase. The directions of dimensionless displacements indicate that photoexcitation of this purine base does not directly assist cleavage of imidazole ring, as speculated for 2′-dG when excited to L_a and L_b states.[14]

Initial excited state parameters determined in the current investigation lay down the foundation for future studies to reveal properties of absorbing singlet states of natural nucleobases in 210-230 nm region of UV-C radiation. Use of a suitable spectroscopic probe in the field of photodynamics of DNA is ever growing through use of environment sensitive fluorescence of 2-AP as a site-specific reporter. Efforts have been made towards synthesis of new nucleobase analogues such as 8–vinyl adenosine[95] with better fluorescent properties in recent times. The high absorption cross-section in deep UV and distinct vibrational spectra of 6-ClG mean that it has the potential to be incorporated into small oligomers as a site-specific interrogator of events like base stacking and base pairing in DNA.

References

[1] J. M. L. Pecourt, J. Peon, B. Kohler, *J. Am. Chem. Soc.* **2000**, *122*, 9348.

[2] J. Peon, A. H. Zewail, *Chem. Phys. Lett.* **2001**, *348*, 255.

[3] Y. Zhang, R. Improta, B. Kohler, *Phys. Chem. Chem. Phys.* **2014**, *16*, 1487.

[4] C. E. Crespo-Hernández, B. Cohen, P. M. Hare, B. Kohler, *Chem. Rev.* **2004**, *104*, 1977.

[5] M. Towrie, G. W. Doorley, M. W. George, A. W. Parker, S. J. Quinn, J. M. Kelly, *Analyst* **2009**, *134*, 1265.

[6] B. E. Billinghurst, R. Yeung, G. R. Loppnow, *J. Phys. Chem. A* **2006**, *110*, 6185.

[7] S. Yarasi, P. Brost, G. R. Loppnow, *J. Phys. Chem. A* **2007**, *111*, 5130.

[8] S. Yarasi, S. Ng, G. R. Loppnow, *J. Phys. Chem. B* **2009**, *113*, 14336.

[9] S. A. Oladepo, G. R. Loppnow, *J. Phys. Chem. B* **2011**, *115*, 6149.

[10] S. S. Ng, F. Teimoory, G. R. Loppnow, *J. Phys. Chem. Lett.* **2011**, 2362.

[11] B. E. Billinghurst, G. R. Loppnow, *J. Phys. Chem. A* **2006**, *110*, 2353.

[12] B. E. Billinghurst, S. A. Oladepo, G. R. Loppnow, *J. Phys. Chem. B* **2012**, *116*, 10496.

[13] F. Teimoory, G. R. Loppnow, *J. Phys. Chem. A* **2014**, *118*, 12161.

[14] A. F. El-Yazbi, A. Palech, G. R. Loppnow, *J. Phys. Chem. A* **2011**, *115*, 10445.

[15] S. Ullrich, T. Schultz, M. Z. Zgierski, A. Stolow, *Phys. Chem.*

Chem. Phys. **2004**, *6*, 2796.

[16] M. Barbatti, A. J. A. Aquino, J. J. Szymczak, D. Nachtigallova, P. Hobza, H. Lischka, *Proc. Natl. Acad. Sci.* **2010**, *107*, 21453.

[17] M. Barbatti, Z. Lan, R. Crespo-Otero, J. J. Szymczak, H. Lischka, W. Thiel, *J. Chem. Phys.* **2012**, *137*, 22A503.

[18] T. Zelený, P. Hobza, D. Nachtigallová, M. Ruckenbauer, H. Lischka, *Collect. Czechoslov. Chem. Commun.* **2011**, *76*, 631.

[19] L. Serrano-Andres, M. Merchan, A. C. Borin, *Proc. Natl. Acad. Sci.* **2006**, *103*, 8691.

[20] D. Nachtigallová, T. Zelený, M. Ruckenbauer, T. Müller, M. Barbatti, P. Hobza, H. Lischka, *J. Am. Chem. Soc.* **2010**, *132*, 8261.

[21] C. S. Cockell, *Planet. Space Sci.* **2000**, *48*, 203.

[22] I. Conti, M. Garavelli, G. Orlandi, *J. Am. Chem. Soc.* **2009**, *131*, 16108.

[23] M. Barbatti, *J. Am. Chem. Soc.* **2014**, *136*, 10246.

[24] M. Barbatti, H. Lischka, *J. Phys. Chem. A* **2007**, *111*, 2852.

[25] C. E. Crespo-Hernández, L. Martínez-Fernández, C. Rauer, C. Reichardt, S. Mai, P. Pollum, P. Marquetand, L. González, I. Corral, *J. Am. Chem. Soc.* **2015**, *137*, 4368.

[26] C. S. Cockell, in *Ecosyst. Evol. Ultrav. Radiat.* (Eds.: C.S. Cockell, A.R. Blaustein), Springer New York, New York, NY, **2001**, pp. 1–35.

[27] C. S. Cockell, in *Astrobiology* (Eds.: G. Horneck, C. Baumstark-Khan), Springer Berlin Heidelberg, Berlin, Heidelberg, **2002**, pp. 219–232.

[28] A. B. Myers, *J. Raman Spectrosc.* **1997**, *28*, 389.

[29] A. B. Myers, in *Laser Tech. Chem.* (Eds.: A.B. Myers, T.R. Rizzo), Wiley-Interscience, New York, **1995**, p. 325.

[30] A. B. Myers, *Acc. Chem. Res.* **1997**, *30*, 519.

[31] E. J. Heller, R. Sundberg, D. Tannor, *J. Phys. Chem.* **1982**, *86*, 1822.

[32] E. J. Heller, *Acc. Chem. Res.* **1981**, *14*, 368.

[33] S.-Y. Lee, E. J. Heller, *J. Chem. Phys.* **1979**, *71*, 4777.

[34] D. J. Tannor, E. J. Heller, *J. Chem. Phys.* **1982**, *77*, 202.

[35] B. Li, A. E. Johnson, S. Mukamel, A. B. Myers, *J. Am. Chem. Soc.* **1994**, *116*, 11039.

[36] S. P. A. Fodor, R. A. Copeland, C. A. Grygon, T. G. Spiro, *J. Am. Chem. Soc.* **1989**, *111*, 5509.

[37] A. B. Myers, Excited State Structure and Dynamics of Polyenes and Bacteriorhodopsin from Resonance Raman Intensities, University of California, Berkeley, **1984**.

[38] C. Su, Y. Wang, T. G. Spiro, *J. Raman Spectrosc.* **1990**, *21*, 435.

[39] S. Mukamel, *Principles of Nonlinear Optical Spectroscopy*, Oxford University Press, New York, **1995**.

[40] R. Jimenez, G. R. Fleming, P. V. Kumar, M. Maroncelli, *Nature* **1994**, *369*, 471.

[41] E. A. Milán-Garcés, S. Kaptan, M. Puranik, *Biophys. J.* **2013**, *105*, 211.

[42] R. B. Barnett, U. Landman, A. Nitzan, *J. Chem. Phys.* **1989**, *90*, 4413.

[43] M. Maroncelli, G. R. Fleming, *J. Chem. Phys.* **1988**, *89*, 5044.

[44] S. Gogia, M. Puranik, *J. Biomol. Struct. Dyn.* **2014**, *32*, 27.

[45] V. Karunakaran, K. Kleinermanns, R. Improta, S. A. Kovalenko, *J. Am. Chem. Soc.* **2009**, *131*, 5839.

[46] M. Barbatti, *J. Am. Chem. Soc.* **2014**, *136*, 10246.

[47] M. Shanmugasundaram, M. Puranik, *Phys. Chem. Chem. Phys.* **2011**, *13*, 3851.

[48] C. Lee, W. Yang, R. G. Parr, *Phys. Rev. B* **1988**, *37*, 785.

[49] A. D. Becke, *J. Chem. Phys.* **1993**, *98*, 5648.

[50] R. Bauernschmitt, R. Ahlrichs, *Chem. Phys. Lett.* **1996**, *256*, 454.

[51] M. E. Casida, C. Jamorski, K. C. Casida, D. R. Salahub, *J. Chem. Phys.* **1998**, *108*, 4439.

[52] S. Miertuš, E. Scrocco, J. Tomasi, *Chem. Phys.* **1981**, *55*, 117.

[53] G. Scalmani, M. J. Frisch, *J. Chem. Phys.* **2010**, *132*, 114110.

[54] G. Scalmani, M. J. Frisch, B. Mennucci, J. Tomasi, R. Cammi, V. Barone, *J. Chem. Phys.* **2006**, *124*, 094107.

[55] M. J. Frisch *et al. Gaussian 09, Revision D.01*, Gaussian Inc., Wallingford, **2013**.

[56] S. I. Gorelsky, *SWizard v5.0, Http://www.sg-Chem.net/, University of Ottawa, Ottawa, Canada.*, **2013**.

[57] M. H. Jamróz, *Spectrochim. Acta Part A Mol. Biomol. Spectrosc.* **2013**, *114*, 220.

[58] A. M. Moran, A. M. Kelley, *J. Chem. Phys.* **2001**, *115*, 912.

[59] L. B. Clark, *J. Am. Chem. Soc.* **1994**, *116*, 5265.

[60] J. Wang, J. Gu, J. Leszczynski, *J. Comput. Chem.* **2012**, *33*, 1587.

[61] A. D. Laurent, D. Jacquemin, *Int. J. Quantum Chem.* **2013**, *113*, 2019.

[62] J. A. Sweeney, S. A. Asher, *J. Phys. Chem.* **1990**, *94*, 4784.

[63] K. S. K. Shin, J. I. Zink, *J. Am. Chem. Soc.* **1990**, *112*, 7148.

[64] J. L. Wootton, J. I. Zink, *J. Am. Chem. Soc.* **1997**, *119*, 1895.

[65] D. S. Egolf, M. R. Waterland, A. M. Kelley, *J. Phys. Chem. B* **2000**, *104*, 10727.

[66] M. Barbatti, H. Lischka, *J. Am. Chem. Soc.* **2008**, *130*, 6831.

[67] J. S. Bader, D. Chandler, *Chem. Phys. Lett.* **1989**, *157*, 501.

[68] R. W. Impey, P. A. Madden, I. R. McDonald, *Mol. Phys.* **982**, *46*, 513.

[69] W. Jarzeba, G. C. Walker, A. E. Johnson, M. A. Kahlow, P. F. Barbara, *J. Phys. Chem.* **1988**, *92*, 7039.

[70] S. Vajda, R. Jimenez, S. J. Rosenthal, V. Fidler, G. R. Fleming, E. W. Castner, *J. Chem. Soc. Faraday Trans.* **1995**, *91*, 867.

[71] S. Park, M. D. Fayer, *Proc. Natl. Acad. Sci.* **2007**, *104*, 16731.

[72] X. Cao, J. L. McHale, *J. Chem. Phys.* **1998**, *109*, 1901.

[73] O. V. Shishkin, L. Gorb, J. Leszczynski, *J. Phys. Chem. B* **2000**, *104*, 5357.

[74] O. Shishkin, L. Gorb, J. Leszczynski, *Int. J. Mol. Sci.* **2000**, *1*, 17.

[75] M.-P. Gaigeot, M. Ghomi, *J. Phys. Chem. B* **2001**, *105*, 5007.

[76] M. K. Shukla, J. Leszczynski, *J. Phys. Chem. A* **2002**, *106*, 11338.

[77] C. Santhosh, P. C. Mishra, *Spectrochim. Acta Part A Mol. Spectrosc.* **1991**, *47*, 1685.

[78] D. C. Ward, E. Reich, L. Stryer, *J. Biol. Chem.* **1969**, *244*, 1228.

[79] J. Smagowicz, K. L. Wierzchowski, *J. Lumin.* **1974**, *8*, 210.

[80] O. K. Abou-Zied, *J. Photochem. Photobiol. A Chem.* **2013**, *261*, 1.

[81] A. B. Myers, R. A. Mathies, in *Biol. Appl. Raman Spectrosc. Vol. 2 - Reson. Raman Spectra Polyenes Aromat.* (Ed.: T.G. Spiro), John Wiley & Sons Inc, New York, **1987**, pp. 1–58.

[82] X. Zhao, J. A. Burt, J. L. McHale, *J. Chem. Phys.* **2004**, *121*, 11195.

[83] C. M. Stuart, R. R. Frontiera, R. A. Mathies, *J. Phys. Chem. A* **2007**, *111*, 12072.

[84] M. R. Waterland, S. L. Howell, K. C. Gordon, *J. Phys. Chem. A* **2007**, *111*, 4604.

[85] G. R. Loppnow, B. E. Billinghurst, S. A. Oladepo, in *Radiat. Induc. Mol. Phenom. Nucleic Acids*, Springer Netherlands, Dordrecht, **2008**, pp. 237–263.

[86] A. M. Kelley, *J. Phys. Chem. A* **1999**, *103*, 6891.

[87] J. Guthmuller, *J. Chem. Theory Comput.* **2011**, *7*, 1082.

[88] J. Guthmuller, L. González, *Phys. Chem. Chem. Phys.* **2010**, *12*, 14812.

[89] J. F. Gaff, S. Franzen, B. Delley, *J. Phys. Chem. A* **2010**, *114*, 11681.

[90] D. W. Silverstein, N. Govind, H. J. J. van Dam, L. Jensen, *J. Chem. Theory Comput.* **2013**, *9*, 5490.

[91] K. A. Kane, L. Jensen, *J. Phys. Chem. C* **2010**, *114*, 5540.

[92] A. Baiardi, J. Bloino, V. Barone, *J. Chem. Phys.* **2014**, *141*, 114108.

[93] S. Sun, A. Brown, *J. Phys. Chem. A* **2015**, *119*, 3961.

[94] S. Sun, A. Brown, *J. Phys. Chem. A* **2014**, *118*, 9228.

[95] N. B. Gaied, *Nucleic Acids Res.* **2005**, *33*, 1031.

5

# Ultrafast Nuclear Dynamics of Photoexcited Guanosine Monophosphate (GMP)
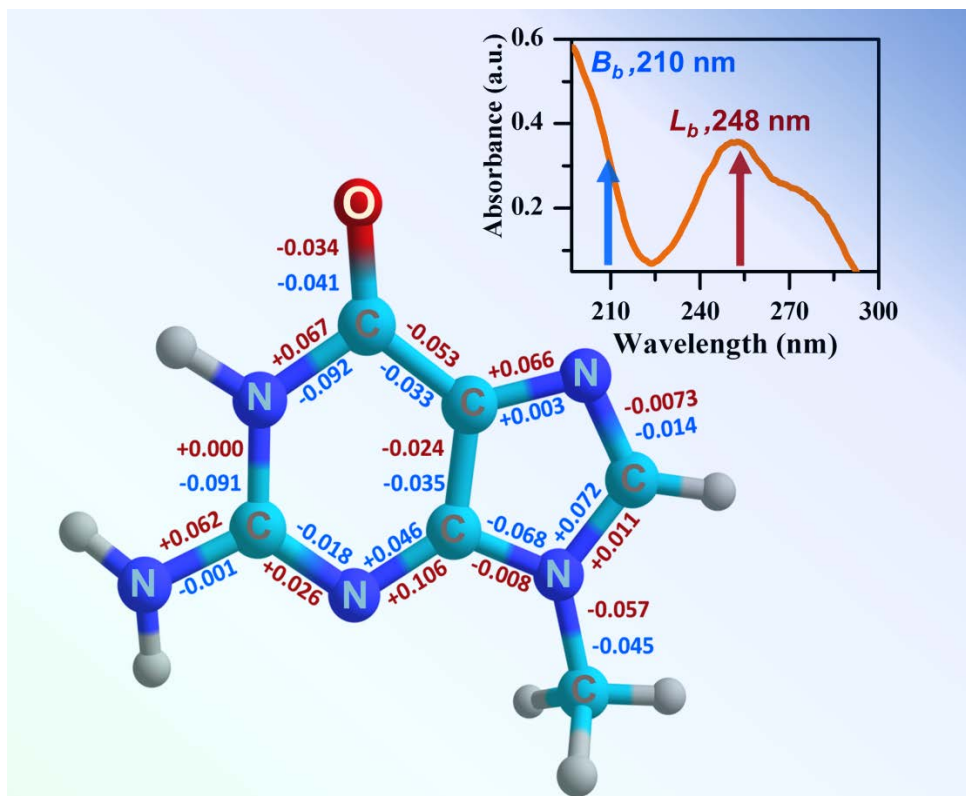
5.1 Introduction

Following photoexcitation, ultrafast nonradiative relaxation minimizes lesion formation in purine and pyrimidines.[1] It is often argued that this intrinsic resistance against photodamage makes these bases natural candidate as building blocks of our genetic code.[2] Despite their exceptional photoresistivity, canonical nucleobases are damaged by UV radiation. Among all bases, guanosine-5′-monophosphate (GMP), (Fig. 5.1) the nucleoside of Gua is particularly important because of its ability to form lesion through one electron oxidation, which leads to a mutation in the gene. Photochemical damages occur following events on excited state PES after absorption of photons. To understand photoreactivity of GMP under UV radiation, photophysics on first two singlet states (L_a and L_b in Fig. 5.2) have been extensively studied using femtosecond transient absorption (fsTA) [3,4], UV pump mid-IR probe[5,6], picosecond time resolved IR (psTRIR)[7], fs time resolved fluorescence,[8–10] resonance Raman (RR) spectroscopy[11] and photo-dynamical simulations.[12–14]
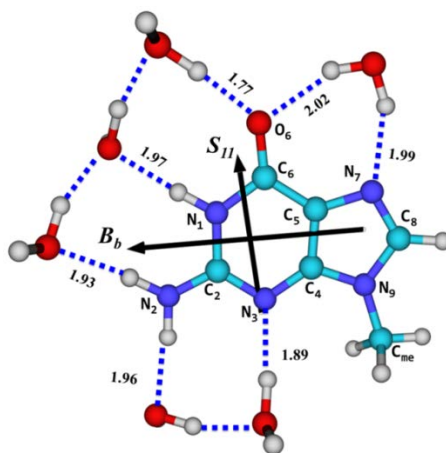
Fig. 5.1. The structure of neutral aqueous GMP obtained by energy minimization at B3LYP/6-311+G(2d,p)//PCM level of theory. Aqueous GMP was modeled as 9-meG•6H$_2$O complex as shown above. All hydrogen bonds (H-bond) distances (in Å) between water molecules and the base are labeled. The conventional numbering of ring atoms is indicated. Directions of computed transition dipole moments ($\vec{\mu}$) for B_b and S_{11} states are shown with bold arrows. Indicated magnitude of the transition dipole moment vectors is magnified by a factor of two (for B_b) and three (for S_{11}) over the calculated value for improved visualization. Computed $\vec{\mu}$ of B_b and S_{11} state are oriented at 86.1° and 8.4° with respect to $\overrightarrow{C_6 - N_3}$ and have magnitude of 2.38 and 1.07 Au respectively.

GMP excited to L_a (280 nm) state returns to S_0 via ultrafast IC within one ps. On the other hand, when excited to the next bright state, L_b, at 252 nm, ultrafast IC from L_b to L_a takes place within 100 fs before returning to S_0. RR spectroscopy on 2′-

deoxyguanosine (2′-dG) has revealed that three in-plane ring stretching vibrational modes at 1366, 1490 and 1573 cm^{-1} couple these two close-lying electronic states.[11] This study also reports that the internal coordinates that suffer maximum distortions are coincident with the formation coordinate of various oxidative products of Gua. However, the absolute value of dimensionless displacements (Δ) along each normal mode alone cannot determine the direction of distortions (shortening or lengthening) of all internal coordinates.
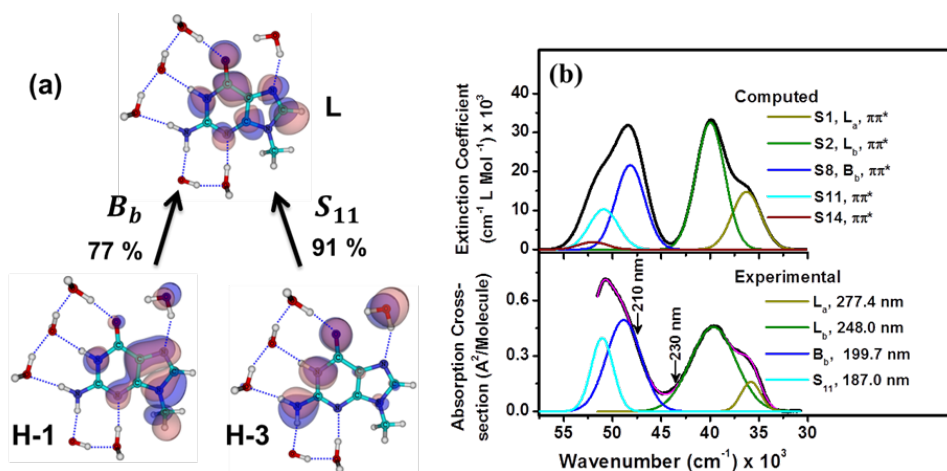
Fig. 5.2 (a) Computed molecular orbitals of GMP involved in the electronic transition observed in experiments at 210 nm; (b) bottom: deconvolved experimental spectra with standard spectroscopic labels of the bands and λ_{max}; top: computed absorption spectra, excitations, and nature of the lower and higher excited states of GMP. The electronic absorption spectrum was computed using TD-B3LYP/6-311+G(2d,p)//PCM method on 9-meG•6H$_2$O complex. Computed band positions are depicted with a Gaussian line shape of fixed line width (3500 cm^{-1}). H and L stand for highest occupied molecular orbital or HOMO and lowest unoccupied molecular orbital or LUMO orbitals respectively. Absorption cross-section was determined following the procedure described in the experimental method section. Computed states of GMP are described in Table 5.1. The region of absorption spectra (210 – 230 nm) covered in measuring REPs of resonant modes of GMP is marked with arrows in the bottom panel of b.

GMP has two other strong ππ* transitions, (Fig. 5.2) which are located in the UVC region at 200 nm (will be called B_b hereafter) and 187 nm respectively.[15] Because of more efficient photoabsorption in this region, it is expected that higher singlet states must play an important role in photoresistivity of GMP and in general of other bases also. Experimental measurements on these high-lying ππ* electronic states are necessary to determine the effect of more energetic UV light on the structure and the resulting photophysics of Gua chromophore. Ultrafast spectroscopic techniques such as fsTA and fs fluorescence techniques are routinely applied to investigate photodynamics occurring on

singlet excited states that lie within 260 nm absorption band of DNA and RNA bases. However, these methods are not readily applicable to studies involving high energetic electronic states owing to inherent and technical limitations.

To obtain photodynamical information of B_b electronic state of GMP, resonance Raman intensity analysis is employed.[16] The intensity of a RR bands is proportional to the square of the slope along different vibrational coordinates in the Franck-Condon (FC) region of the resonant vibronic state. RR spectroscopy has been previously applied to deduce photo-induced instantaneous structural dynamics in several nucleobases.[11,17–24] Strong resonance enhancement of in-plane vibrational modes makes this technique suitable for interrogating nucleobases including GMP in different $\pi\pi^*$ states.[11,25–31]

Experimental REPs of RR bands of GMP throughout red edge of B_b absorption band are constructed. We simulate these REPs using time-dependent wave packet propagation (TDWP) formalism[32] (See Chapter 2 for technical details) of RR intensity and derive parameters describing nuclear dynamics of GMP within 50 fs of photoexcitation. We obtain dimensionless displacements (Δ) along each of the FC active vibrational coordinates and obtain structural distortions of the purine ring therefrom. Additionally, we also determine amplitude and time scale of an inertial component of solvation shell surrounding GMP employing Brownian oscillator model.[33] Total linewidth broadening that contributes to both REPs and diffuse absorption spectra are partitioned into fast and dynamics homogeneous, and slow and static inhomogeneous components.

Changing the exocyclic substituent at various sites on purine and pyrimidine rings perturbs their ground state structure. It also affects their electronic structure and therefore the resulting photophysics on excited state PES. Both effects lead to a change in the excited state lifetime through modulation of different pathways on PES.[1,2,34–36] In general, it is shown that S_1 lifetime undergoes 1000 fold increase in guanine with a methyl or hydrogen substitution[37–39] and 40 fold increase in adenine with hydrogen substitution[40] at N7 site. In the previous chapter, early time structural and solvation dynamics of a purine, 6-chloroguanine (6-ClG) subsequent to photoexcitation within 210-230 nm wavelength range has been determined.[41] 6-ClG is a substituted purine in which oxygen of Gua is substituted with the heavier and less electronegative chlorine atom. Effect of substitution on nuclear dynamics of a series of pyrimidines in their lowest energy $\pi\pi^*$ excited states has been investigated by Loppnow and co-workers using RR intensity analysis.[18–21,23,24] They have found that substitutions such by -fluoro (Fl) or methyl (-CH$_3$) moieties at the C5 site results in a significant increase in internal

reorganization energies along photochemically relevant coordinates in 5-fluorouracil and thymine (5-methyluracil) respectively as compared to that in uracil.[18]

With a direct comparison of excited state dynamical parameters in case of GMP and 6-ClG, we determine the role of substitution at the C6 site governing structural dynamics and photoreactivity of guanine chromophore. In this report, we have measured resonance Raman spectra GMP at excitation wavelengths throughout the B_b absorption band within the 210-230 nm wavelength range to reveal the nature and mode of coupling of this state with the low and the high-lying electronic states also.

5.2 Material and Methods

5.2.1 Sample Preparation and UVRR experiment

GMP (Guanosine-5'-monophosphate, 99%) was purchased from Sigma Aldrich (St. Louis, MO) and used without further purification. For UVRR measurement, GMP was dissolved in phosphate buffer 1 mM in concentration, pH 6.8. Sodium perchlorate of 0.5 M concentration (in milliQ water) was used as an internal standard (IS) for measured intensity of sample bands. (See Chapter 2 for experimental setup)

5.2.2 Measurement of Raman depolarization ratio

Measurement of Raman depolarization ratios of RR bands of GMP was carried out using method described in chapter 2. Fig. 5.3 shows 210 nm excited spectrum of GMP in parallel and perpendicular direction with respect to the polarization of the incident beam. The depolarization ratios of intense bands of GMP are described in Table 5.1. For the bands that are of low intensity in perpendicular polarization, a value of 0.33 was assumed.

5.2.3 Determination of RR cross-section

Measured intensity of each RR band of GMP was corrected for the spectral response of the spectrometer using eqn. 2.2 and 2.3 and was converted to cross-sections using the eqn. 2.6a. (See Chapter 2)

5.2.4 Extinction coefficient and absorption cross-section

The extinction coefficient, ε (l mol^{-1} cm^{-1}) of GMP was determined as slope of the linear fit of concentration against measured absorbance at eight different concentrations within 10 to 100 μM. Obtained value of ε (Table 5.1) agrees with published results.[42] The

extinction coefficient is converted into absorption cross-section, σ_A (Å^2/molecule) using the relation, $\sigma_A = 2.303 \times 10^{19} \varepsilon /N_A$, N_A being Avogadro's number.
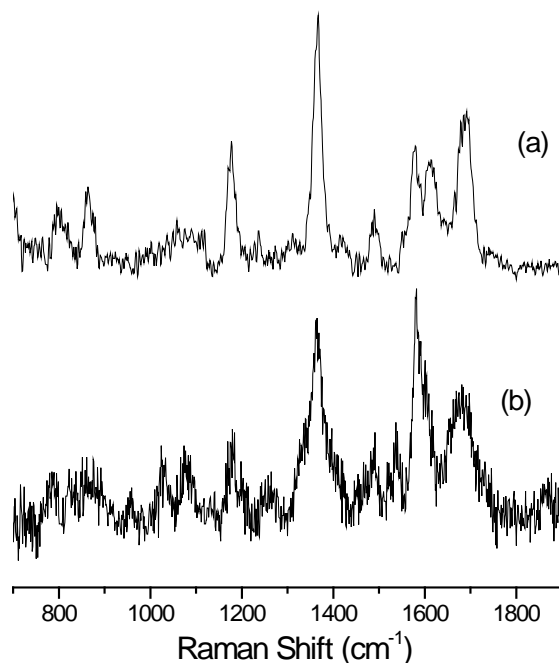
Fig. 5.3 (a) Polarized and (b) depolarized spectra of 1 mM GMP with 210 nm laser excitation. Incident laser power was 0.6 mW.

5.2.5 Simulation of RR and absorption cross-section

The resonance Raman excitation profile and absorption spectra of GMP within the B_b absorption band are simulated using self-consistent time-dependent wave packet (TDWP) formalism[32,43] through the eqns. 2.21a and 2.21b. The solvent induced homogeneous broadening that arises from instantaneous solute-solvent interactions upon photoabsorption by the solute is modeled according to the Mukamel and Myers Brownian oscillator model,[33,44] described with expressions 2.22 a-d.(Chapter 2)

Initial guesses for the Δ's along different normal coordinates were obtained from relative intensities of all the twelve RR bands with respect to the band at 1365 cm^{-1} at 210 nm excitation wavelength. The transition dipole moment strength of 0.96 Å was derived from deconvolution of the experimental absorption spectra by Gaussian line shape (Fig. 5.2, Panel b, bottom). Initially, zero-zero transition energy was estimated such that the red edge of simulated absorption and REPs of all modes agreed with experimental values. Values of the parameters were then iteratively optimized by using a self-consistent procedure to fit the REP and absorption spectrum simultaneously with experimentally measured spectra.[45] The quality of the fit was determined by visual inspection and later

by varying each parameter by 20 % of its best fit value. The simulation is performed using a commercial MATLAB package (The MathWorks, Natick, MA)

5.2.6 Determination of reorganization energy

The total internal reorganization energy of the photoexcited GMP is determined by the expression, $\lambda_{int} = \sum_{j=1}^{3N-6}(\Delta_j^2 \hbar \omega_j)/2$. (Eqn. 2.24) These Δ_j's are converted to changes in internal coordinate corresponding to the jth normal mode (δ_j) using eqn. 2.28

Table 5.1 Vertical singlet excitation energies ($\Delta E_{vert,PCM}$) in cm^{-1} (nm and eV in parenthesis), oscillator strengths (f_{PCM}) and major orbital contribution to each transition of neutral GMP and comparison with published experimental and computed transition energies.

		Computed				Experimental		
Type, Nomenclature	State order	Major orbital Cont.[b] (%)	$\Delta E_{vert,PCM}$[a,c] nm/eV	f_{PCM}[a,c]	Published ΔE_{vert} (eV)	ΔE_{Exp}[c] nm/eV	ΔE_{Exp}[g] nm/eV	ε[c] (L mol^{-1} cm^{-1})
$\pi\pi^*$, L_a	S1	H→L (95)	275.7/4.50	0.238	4.65[d], 4.73[e], 4.46[f]	277.4/4.47	275.5/4.50	7063.8
$\pi\pi^*$, L_b	S2	H→L+1 (95)	250.1/4.96	0.524	5.10[d], 5.11[e], 4.71[f]	248.0/5.00	248.0/5.00	12083 12080[h]
-	S3	H→L+2 (95)	238/5.21	0.0003				
$n\pi^*$, $S_{n\pi^*}$	S4	H−2→L (81)	220.7/5.62	0.0005	5.53[d], 5.98[e], 5.64[f]	222.2/5.58	217.5/5.70	
#	S5	H→L+3(98)	219.0/5.66	0.0004				
#	S6	H→L+4(95)	213.6/5.80	0.008				
$\pi\pi^*$	S7	H→L+5(85)	209.1/5.93	0.080				
$\pi\pi^*$, B_b	S8	H−1→L (77) H→L+5 (9)	207.5/5.98	0.348	6.49[e], 6.23[f]	199.7/6.21	200.0/6.20	17250
$n\pi^*$	S9	H−5→L (68)	206.9/5.99	0.038				
$\pi\pi^*$	S10	H→L+6 (86)	197.9/6.27	0.006	6.59[e]			
$\pi\pi^*$	S11	H−3→L (91)	196.4/6.31	0.166	6.72[e], 6.53[f]	187.0/6.63	187.8/6.60	

[a]computed on 9-meG•6H$_2$O complex at TD-B3LYP method with 6-311+G(2d,p) basis set and cluster-continuum model as described in the computational method. Six explicit water molecules from first solvation shell are included and non–equilibrium solvation using self-consistent reaction field (SCRF-PCM or PCM) model using water as solvent is employed; [b]Percentages are calculated as 100 x twice the squares of the coefficients in the CI expansion of TD-DFT wave functions; [c] Extinction coefficient, this work; [d]Ref [48], in solution with cluster-continuum method and TD-X3LYP method; [e]Ref [49], in gas phase with CASSCF method on N9H-Gua; [f]Ref [50], in gas phase with real-time TD-DFT implemented in time domain and on N$_9$H-Gua; [g]collected form Ref [49], experimental λ_{max} were determined from UV-Vis absorption in liquid, linear dichroism, circular dichroism, magnetic circular dichroism and polarized absorption spectroscopy in crystalline state on guanosine, gunanine and 9-ethylguanine. [h]Ref [42]; #electronic states with orbital contributions that are not localized on the purine.

5.2.7 Quantum chemical calculations

All computations were performed with Gaussian 09 software suite. GMP in aqueous solution is modeled as 9-methylguanine (9-meG) in complex with six explicit water molecules, 9-meG•6H$_2$O. A polarizable continuum model of solvation was employed to take into account the bulk dielectric environment of water. Six water molecules were strategically placed around isolated 9-meG within hydrogen bond contacts.[3] (See Fig. 5.1) Energy minimized molecular structure on S_0 state, harmonic vibrational frequencies and associated normal mode vectors, and excited state transition dipole moments are computed using B3LYP hybrid functional. Geometry optimization of S_0 state was performed without any symmetry constraints. Pople type basis sets that are augmented with diffuse and polarization functions, 6-311+G(2d,p) was used for the reliable description of electronic excited states. Excited state energies were computed as vertical transitions on the S_0 geometry using linear response formalism of time-dependent DFT (TD-DFT) method. Coordinates of the optimized structure of 9-meG•6H$_2$O complex are described in Table 5.2. The signs of Δs, therefore of gradients on B_b state is computed with eqn. 2.31. (See Chapter 2)

5.3. Results and Discussions

UVRR spectra of the Gua chromophore have been reported by several groups with Raman excitations lying within B_b, L_a and L_b absorption bands of GMP and 2′-deoxy GMP (dGMP) and different N9 substituted forms.[11,25–31,51,52] Peticolas and co-workers have identified differential enhancement patterns of RR bands of Gua, 9-methylGua and 9-ethylGua across the whole absorption spectrum between 200 to 295 nm[27,51,52] Relative enhancements factors for each band of dGMP with four excitation wavelengths *viz.* 200, 218, 240 and 266 nm were reported by Spiro and co-workers.[26] Resonance enhanced modes in each of the three electronic states are primarily in-plane ring stretching vibrations due to their strong ππ* character. Fig.5.4 depicts the 212 nm excited spectra of GMP showing maximum enhancement of triene modes at 1365 and 1580 cm^{-1} and of the carbonyl stretching mode at 1689 cm^{-1}, agrees with previous measurements.[26,27]

Semi-empirically derived transition monopoles for ππ* transitions of Gua have suggested that excitation to B_b state would result in electron delocalization over both rings of Gua,[53] later confirmed by complete active space self-consistent field (CASSCF) calculation.[49] Our TD-DFT computation also describes this state of pure ππ* character, is associated with a 77% of H–1→L, one electron configuration (Table 5.1) and is delocalized over both the rings (Fig. 5.2, panel a). This description agrees with CASSCF computed configuration, H–1→L (51%) for B_b state of N9H-Gua.[49] Singlet excitation energies of Gua, investigated by several authors in the gas phase,[50,53–55] and in solution.[3,48,49,56–59] Comparison with published excitation energies shows that magnitudes

of computed vertical excitation energies of Gua vary depending on the level of used theory and basis set, and employed solvation model.[60] (Table 5.1) Using TD-B3LYP method on 9-meG•6H$_2$O complex, we have obtained good agreement between computed vertical transition energies of four $\pi\pi^*$ electronic states of GMP and corresponding experimental λ_{max}.

Fig. 5.5 demonstrates intensity variation of RR active modes of GMP within B_b absorption band within 210-230 nm as a function of excitation wavelengths. Experimental REPs show that while all modes loose intensity, the band at 1486 cm^{-1} shows opposite trend from 210 nm towards 230 nm of excitation. This intensity loss indicates coupling of this mode with low lying L_b state instead of currently investigated B_b state. Loppnow and co-worker have reported REP of 2′-deoxyguanosine (2′-dG) throughout L_a and L_b bands within 244-290 nm of absorption spectra.[11] They have found that initial nuclear dynamics of photoexcited 2′-dG lie along the modes at 1490, 1580, and 1689 cm^{-1} in L_a excited state, and 1321,1490, 1580, and 1607 cm^{-1} in L_b excited state. Maximum contribution in structural dynamics within B_b absorption band of GMP is expected to occur along vibrational modes bearing most intensity at 1177, 1365, 1580 and 1689 cm^{-1}.
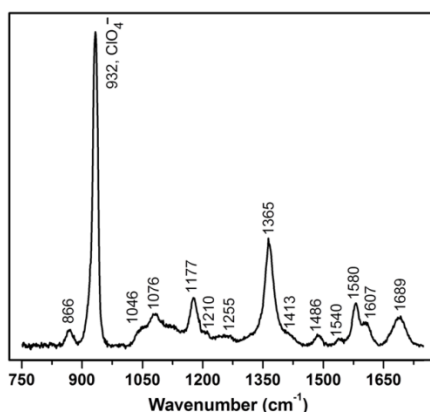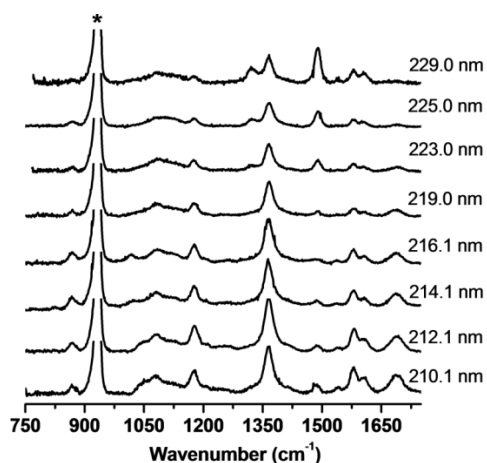

Fig. 5.4 UVRR spectrum of GMP (1 mM, pH 6.8 in miliQ water) obtained with excitation wavelength of 212 nm with incident laser power of 0.6 mW. The band at 932 cm^{-1} corresponds to sodium perchlorate that was used as internal intensity standard

Table 5.2 Coordinates (Å) of optimized ground state structure of 9-meG•6H$_2$O complex[a].

Atom Name		X	Y	Z	Atom Name		X	Y	Z
1	N	0.712208018	0.682435976	-0.156261808	20	H	3.381012929	2.529011099	-0.184898764
2	C	-0.652624776	0.870915154	-0.183151950	21	H	2.850177768	3.131274077	-1.528405185
3	N	-1.508827744	-0.146214849	-0.142579930	22	O	0.538421976	4.521891032	0.320417883
4	C	-0.914953814	-1.356807821	-0.098488882	23	H	1.409115933	4.133178062	0.100886055
5	C	0.448117878	-1.634668210	-0.038583901	24	H	0.592208080	4.785818185	1.246368000
6	C	1.362829858	-0.550108855	-0.058176159	25	O	-3.961255254	2.912637088	-0.194092161
7	N	-1.539953950	-2.574571144	-0.089572245	26	H	-4.428581736	3.044200077	-1.027182783
8	C	-0.541730921	-3.519600746	-0.022066162	27	H	-4.244304756	2.031574960	0.136308122
9	N	0.658108111	-3.001801867	0.011646133	28	O	-4.213443138	0.334350061	0.708300044
10	N	-1.091206880	2.133085974	-0.273376142	29	H	-3.289481140	0.110451992	0.447501916
11	H	-0.771700241	-4.573677905	-0.003856115	30	H	-4.245593831	0.242546805	1.668142905
12	H	-0.481209977	2.925839002	-0.072842836	31	O	3.529223835	-3.372441845	0.055895934
13	H	-2.093317774	2.317067144	-0.287010923	32	H	3.529098949	-2.400952851	0.030846800
14	O	2.606274153	-0.599091089	-0.011765198	33	H	2.568172862	-3.548547800	0.052286946

15	H	1.320046935	1.497412861	-0.287684036	34	C	-2.972594987	-2.833825133	-0.158579075
16	O	4.456368834	1.359281195	0.517533762	35	H	-3.401564057	-2.322929899	-1.019187973
17	H	4.626107199	1.440787192	1.463576210	36	H	-3.122948002	-3.905212208	-0.267436127
18	H	3.830931068	0.606656736	0.413763162	37	H	-3.468236157	-2.490964843	0.748403741
19	O	2.601097741	2.960937741	-0.611827856					

[a]computed at B3LYP/6-311+G(2d,p)//PCM level

Fig. 5.5 Resonance Raman spectra of GMP (1 mM, pH 6.8 in miliQ water) at eight different excitation wavelengths. Spectra have been normalized to the intensity of the 932 cm^{-1} band of sodium perchlorate used as internal intensity standard (asterisk).

## 5.3.1 Characterization of B_b state of GMP from RR intensity

Absorption cross-section and constructed REPs of RR bands of GMP are depicted in Fig. 5.6 and 5.7. Intensities of six resonant modes at 1076, 1177, 1210, 1255, 1365, 1413, 1540 and 1689 cm^{-1} of GMP follow the red edge of the B_b state without any gain in the RR cross-section after 223 nm towards resonance with the L_b state. As the region of absorption spectra within 223-230 nm falls at the blue edge of the L_b band, measurement of REPs in this region reveal those vibrational coordinates that connect both the electronic states. Four modes at 867, 1046, 1580 and 1607 cm^{-1} start gaining intensity with the excitation wavelength entering into the L_b state after 222 nm. Thus, these four modes are FC active in both B_b and L_b electronic states. A similar phenomenon was reported for 2′-deoxyguanosine (dGuo) where three modes at 1490, 1573 and 1600 cm^{-1} couple the lowest singlet L_a and the next high-lying L_b state.[11] Interference between these two states cannot be anticipated from apparently well-separated bands in absorption spectra.

Change in delocalized π electron density (Fig. 5.2, panel a) over the whole purine ring permits enhancement of ring modes at 1076, 1177 and 1365 cm^{-1} arising from stretching (str.) of pyrimidine, imidazole bonds and of triene coordinates (along N3–C4–C5–N7) respectively. Normal mode description predicts that significant amount of NH$_2$ rocking motion is involved in two in-plane ring modes at 1076 and 1177 cm^{-1}. Amino scissoring vibration appearing at 1607 cm^{-1} has moderate intensity at 212 nm with excitation wavelength. The involved molecular orbitals show that the π electrons,

localized on –NH$_2$ moiety do not take part in B_b transition, but are involved in another dipole-allowed $\pi\pi^*$ transition (state S_{11} in Table 5.1). Thus, enhancement of this vibration is expected to originate from the contribution of the later electronic state via Albrecht's B term.[61]
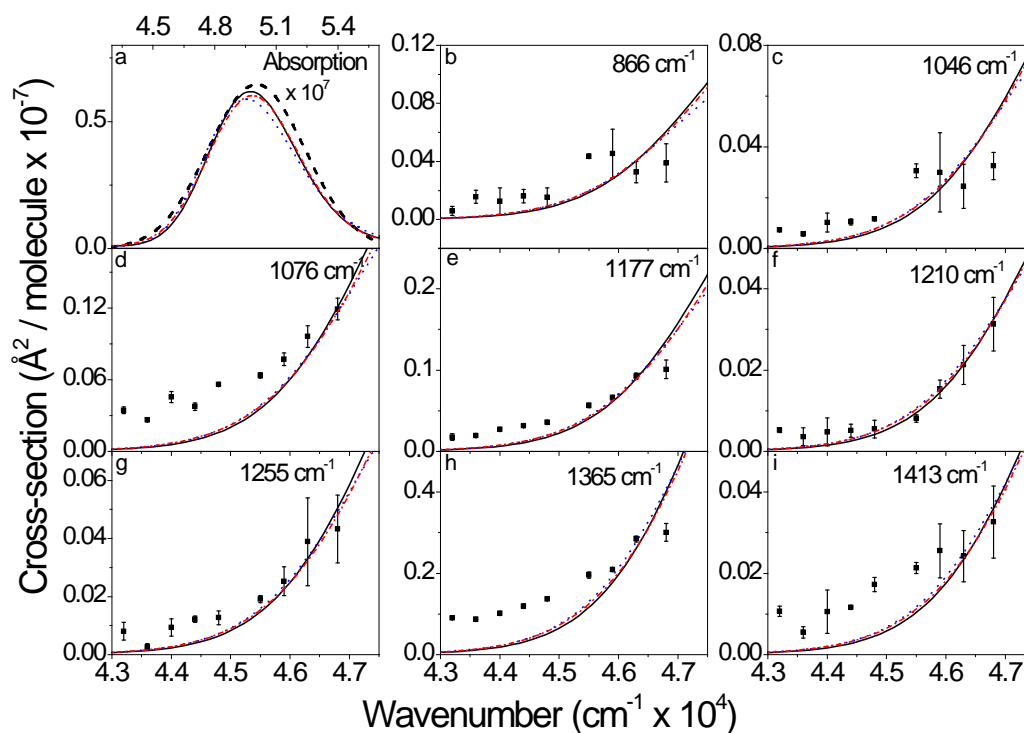
Fig. 5.6 Experimental and simulated Raman excitation profiles and absorption cross-sections of GMP in the 210-230 nm region. (a) Experimental (*black dashed*) and simulated (*black solid*) absorption spectrum. (b–i) experimental (points) and simulated (solid) Raman excitation profiles for eight resonant modes of GMP. The simulated absorption and Raman excitation profiles were obtained by using the parameters in Table 5.3. Set 1 (*red dash dot*) and Set 2 (*blue dot*) were obtained with two sets of deltas obtained by decreasing and increasing 20% those values in the best fit respectively, and varying E_0, Γ, θ and Λ iteratively.
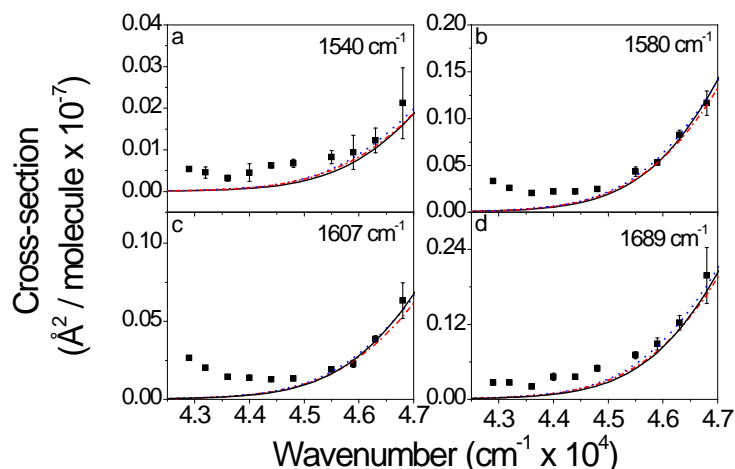
Fig. 5.7 Experimental and simulated Raman excitation profiles of the other four resonant modes of GMP. The simulated Raman excitation profiles were obtained by using the same sets of parameters as Fig. 5.6

Vibronic coupling of two modes at 1580 and 1607 cm^{-1} with L_b state is also supported from enhancement in RR cross-section as the laser wavelength is tuned towards this electronic transition, is also found by another group.[11] The fundamental mode responsible for the band at 1580 cm^{-1} originate from NH$_2$ scissoring (sci.) and C–N str. (C2–N3 + C4–C5 and N7–C8 str.) while the band at 1607 cm^{-1} is ascribed to pure exocyclic NH$_2$ sci. motion. From REPs of 2′-dG measured within L_a and L_b absorption bands[11] it is evident that though both of these RR modes gain intensity in L_b state, amino sci. vibration at 1607 cm^{-1} gradually decouples from L_a state.

Table 5.3 Parameters used in self-consistent simulation of REPs and absorption spectra

Molecule	Excited State		E_0 (cm^{-1})	Λ (cm^{-1})	T (fs)	θ (cm^{-1})	M (Å)	λ_{int} (cm^{-1})	λ_S (cm^{-1})	λ (cm^{-1})
6-ClG[a]	B_b	Best fit	45700	350	15.2	360	1.11	112	1220	1332
2′-dG[b]	L_a	Best fit	35750	65.9^3	80.5^3	900	0.56	153	1050	1203
	L_b	Best fit	37600	82.7^3	64.2^3	900	0.83	904	1650	2554
GMP	B_b	Best fit	49100	250	21.2	1350	0.96	995	2550	3545
		Set 1	48600	320	16.6	1020	0.96	1433	3250	4683
		Set 2	49360	220	24.1	1680	0.96	637	2200	2837

[a]Ref [41] (also See Chapter 4); [b]The reported slopes (from Ref [11]) (β/ℏ) along normal modes of vibrations for 2′-dG are converted to dimensionless displacement, Δ via the equation, $\Delta_k = -(\beta_k/\omega_k)$, k being the normal mode coordinate. Mode-specific reorganization energy (λ_k) is computed using the relation, $\lambda_k = (\Delta_k^2 \hbar\omega_k)/2$. ℏ is unity in atomic unit. Total internal reorganization energy is computed by summing over all such λ_k's. The inverse of solvent relaxation time (Λ) is calculated from the relation between solvent reorganization energy (homogeneous linewidth) and coupling strength (D) between

solvent coordinate and electronic transition, $D^2 = 2\ \lambda_s k_B T$ and the assumption of $\Lambda/D=0.1$ in high temperature limit. Then solvent correlation time τ is estimated from the relation, $\Lambda = 1/2\pi c\tau$ where c is the speed of light. Set 1 and Set 2 were obtained with two sets of deltas obtained by decreasing and increasing 20% those values in the best fit (see Table 5.8) and optimizing E_0, λ_S, θ and Λ iteratively.

Measured depolarization (dp) ratios (ρ) of RR bands of GMP at 210 nm excitation wavelength are tabulated in Table 5.4, and depolarized and polarized spectra are shown in Fig. 5.3. A value of $\rho=0.18$ for the band at 1607 cm^{-1} with 210 nm excitation indicates interference from the red edge of the S_{11} transition. Thus, the effective cross-section of this mode must result from interference between B_b and next in energy allowed transition. The shape of the REP of the band at 1365 cm^{-1} suggests plausible coupling with both of the L_b and S_{11} states. This mode is delocalized on several purine N–C internal coordinates that suffer changes in bond order during photoexcitation to any these states. A ρ value of 0.17 for this band at 210 nm excitation implies interference from B_b band, located on the blue side of our probe wavelengths. Our TD-DFT computation also predicts a bright state (S_{11}) on the blue side of the B_b band. As we have measured the dp ratio at 210 nm excitation which is near the maxima of B_b band (Fig. 5.2), a value of ρ close to 0.33 for the two modes 1486 and 1689 cm^{-1} suggests that their RR enhancement is due to the sole contribution from B_b state.

Table 5.4 Depolarization ratios for Raman bands of GMP obtained at an excitation wavelength of 210 nm.

RR Band (cm^{-1})	Depolarization ratio with $\lambda_{exc}= 210$ nm
1177	0.22 ± 0.02
1365	0.17 ± 0.02
1486	0.36 ± 0.04
1540	0.29 ± 0.04
1580	0.26 ± 0.02
1607	0.18 ± 0.03
1689	0.30 ± 0.03

The REP of the carbonyl stretching vibration at 1689 cm^{-1} follows the red edge of the B_b absorption band and does not get enhanced with excitation wavelength greater than 223 nm. It indicates decoupling of this mode from the L_b electronic state; a fact also supported by the very low intensity of this mode compared to other ring str. ones at excitation wavelength within the L_b absorption band at 244 and 257 nm.[11] The carbonyl stretching coordinate couples with the lowest singlet excited state L_a as expected from the

direction of the transition dipole moment and reported RR enhancement of this mode at 290 nm Raman excitation. Tinoco and co-workers have suggested that the enhancement of the carbonyl str. mode at 1689 cm^{-1} with 200 nm excitation is probably originating from the high-lying S_{11} transition at ~190 nm because B_b monopole contribution is not localized on this part of the molecule.[53] Nevertheless, the measured dp ratio of 0.30 with 210 nm excitation indicates a major contribution from a single excited state.

5.3.2 Geometrical changes upon photo-excitation

The simulated absorption and REPs for twelve resonant modes of GMP are shown in Fig. 5.5 and 5.6, and the best-fitted parameters are depicted in Table 5.5. Parameters corresponding to L_a and L_b excited states of 2′-dG[11] and the B_b excited state of 6-chloroguanine (6-ClG)[41] are also tabulated for comparison. A value of depolarization ratio close to 0.33 for intense bands of GMP at 210 nm excitation indicates that the B_b state is primarily responsible for the FC activity of these RR active modes. Additionally, the acceptable agreement between simulated RR intensities obtained using short-time dynamics approach with TD-DFT computed gradient[62] and those obtained in 210 nm excited spectra of GMP also suggests the involvement of a single excited state (data not shown). Thus, apart from a low-intensity mode at 679 cm^{-1}, measured REP of all 12 RR active modes of GMP have been modeled using a single excited state using the time-dependent theory of RR scattering. Although we have obtained a good fit between experimental and simulated cross-sections, deviations at places clearly suggest the presence of interference from high and low lying S_{11} and L_b states respectively.

The breadth of the diffuse absorption band shape is determined by the relative contribution of Δs of all RR modes. Thus, though measured REPs are on the red edge of the B_b absorption band and do not cover both sides of the B_b absorption band, a correctly deconvoluted absorption spectrum guarantees reliable estimation of Δs. The inverse of solvent correlation time, (Λ=1/2πcτ) is insensitive to RR cross-section and absorption spectra but depends on the overall shape of the REP. As complete REP is not available on both sides of the absorption peak, Λ is fixed at 250 cm^{-1}, a value close to what is estimated for similar sized molecules as 6-ClG (See Chapter 4) in B_b and tryptophan[63] in B_b electronic states. In the current study, the effect of this parameter is not tested on simulated RR cross-section.

Table 5.5 Internal coordinates and displacements for the modes that undergo largest distortions following photoexcitation of GMP^a to L_a, L_b and B_b states.

Internal coordinates description	Value in ground state	Changes in L_a state	Changes in L_b state	Changes in B_b state

Bond length	(Å)	(Å)	(Å)	(Å)
N1–C2	1.3781	0.004	0.000	-0.091
C2=N3	1.3301	-0.003	0.026	-0.018
C2–N2	1.3392	0.011	0.062	-0.001
N3–C4	1.3491	0.017	0.106	0.046
C4=C5	1.3924	-0.007	-0.024	-0.035
C5–C6	1.4189	-0.037	-0.053	-0.033
C6–N1	1.3972	0.013	0.067	-0.092
C5–N7	1.3841	0.007	0.066	0.003
N7=C8	1.3072	-0.025	-0.073	-0.014
C8–N9	1.3763	0.023	0.011	0.072
N9–C4	1.3688	-0.035	-0.008	-0.068
C6=O	1.2453	-0.017	-0.034	-0.041
N9– C$_{methyl}$	1.4575	-0.017	-0.057	-0.045

[a]GMP in solution is modeled as 9-meG•6H$_2$O.

Structural distortions along different internal coordinates following photoexcitation to all three singlet excited states of GMP are described in Table 5.5 using the best fit Δs. Following photoexcitation to the L_a state, both the imidazole and the pyrimidine rings undergo similar amounts of absolute distortion (0.09 and 0.08 Å respectively) with respect to their ground state structures. However, after taking into account the sign of these distortions, **it is found that the imidazole ring decreases in size through a major decrease in N7=C8 and N9–C4 bond lengths while in pyrimidine, the C$_5$–C$_6$ bond suffers maximum distortion (– 0.037 Å). Because of comparatively high transition strength, photoexcitation into the L_b state leads to the more absolute amount of distortions in both the rings than those corresponding to the L_a state. The pyrimidine ring experiences more distortion than imidazole and expands through N3–C4, C6–N1, and C2=N3 bonds.**

Photoabsorption by the B_b state of GMP produces contrasting effects from those of the L_b state; inducing an overall contraction of both the pyrimidine and the imidazole rings by 0.223 and 0.042 Å respectively. Imidazole distortion occurs through weakening and strengthening of the C$_8$–N$_9$ and the N$_9$–C$_4$ bonds by 0.072 and 0.068 Å respectively. The L_b transition couples with the imidazole ring via C5–N7 and N7=C8 internal coordinates and the B_b state does it via C8–N9 and N$_9$–C$_4$ ones. The pyrimidine ring specifically couples with the B_b state via the N1–C2 str. coordinate and not with any of the other two electronic states. For both B_b and L_b photoexcitation, atomic bonds

localized on the triene coordinate and the C6–N1 bond undergo primary distortions. **Photoexcitation to L_b state results in a lengthening of the C2–N2 bond by maximum amount (0.06 Å) among all electronic states. It implies the presence of strong coupling of this transition with the exocyclic amino group; in agreement with an enhancement of the –NH$_2$ scissoring mode at the 1607 cm^{-1} band at excitation within the L_b band.**

Two exocyclic bonds on pyrimidine and imidazole ring *i.e.,* C6=O and N9–C$_{methyl}$ bonds are found to be strengthened due to charge redistribution after photoexcitation to all three singlet states. Their magnitudes in L_a state are the lowest owing to comparatively low transition strengths of this state among all three. This finding indicates that UV excitation of GMP does not induce geometrical changes that coincide with the photo-dissociation coordinate of either oxo or methyl (ribophosphate) groups. Chloro substitution at the place of oxygen in the Gua chromophore causes dramatic changes in terms of distortion of both the rings; imidazole gets expanded with a concurrent contraction of the pyrimidine ring in 6-chloroguanine (6–ClG). **Two component bonds of the triene coordinate, C5=C6 and C4–C5, do not couple with the B_b state of 6–ClG as in GMP.** Though the overall magnitude of distortion is much less in 6-ClG than in GMP due to absorption by B_b state, the C6–Cl bond is found to be shortened by 0.056 Å: a value similar to that of the C6=O bond in GMP.

5.3.3 Implications on photoinduced adduct formation

For Gua residues in DNA, two major types of damage occurs, (i) photochemical damage leading to formation of apurinic or abasic (AP) sites through cleavage of the glycosidic bond at N$_9$ and (ii) oxidative damages mainly leading to the formation of formamidopyrimidine and 8-oxo-7,8-dihydro-2′-deoxyguanosine (8–oxodG) via cleavage of the C$_8$–N$_9$ bond, and oxidation at C$_8$ by a hydroxyl radical respectively.[64] In addition, oxazolone and its precursor imidazolone[65,66] are also oxidation products of dG. 8-oxodG is 1000 times more reactive than dG[67] and forms oxazolone[68] as a secondary product upon oxidation by various oxidizing agents. However, it is important to note that none of these adducts are results of direct irradiation of Gua by UV light. These adducts form through oxidation of dG and 8–oxodG by oxidants such as peroxynitrite[69] and various reactive oxygen species (ROS). The amount and the direction of instantaneous structural

changes that follows photoexcitation can point out if the primary reaction coordinate of formation of any of the mentioned adducts coincides with initial structural dynamics of GMP.

Photoabsorption by all three dipole-allowed states triggers weakening of the C8–N9 bond, specifically by 0.07 Å in the case of B_b. This indicates initial structural dynamics of GMP lie along the formation coordinate of the formamidopyrimidine adduct as predicted by Yazbi *et al.*[11] In the case of all three electronic transitions, the N9–C$_{methyl}$ bond gets strengthened, e.g. by 0.057 Å in L_b excitation. This fact indicates that photoexcitation of isolated GMP does not induce instantaneous distortions that lead to direct cleavage of the glycosidic bond.

Decomposition of the pyrimidine ring at C$_6$ site through cleavage of the C6–N1 bond can lead to the formation of another lesion, oxazolone. Cleavage of C2=N3 with a following breakage of the C6–N1 bond leads to the formation of a carbodiimide (HNCNH) fragment in collision-induced dissociation (CID) of Gua in the gas phase.[70] Loss of an NH$_3$ group as the dissociation product of guanine also happens via cleavage of the C6–N1 bond.[71,72] We find that photoexcitation within the L_b absorption band weakens both of C2=N3 and C6–N1 bonds which are the primary steps for formation of mentioned lesions. On the contrary, excitation to the higher energetic B_b state does not cause any of these structural distortions and thus does not directly assist the decomposition of the pyrimidine ring at the C6 site.

Quantum chemical calculation shows that during formation of a cation radical of 9-meG (9-meG$^{+\bullet}$) by an electron loss, the purine ring suffers maximum distortion along the hexatriene alike sequence along N2–C2=N3–C4=C5–N7=C8–N9 bonds. Our computed structure of radical of 9-meG (Fig 5.8 and Table 5.6) and distortions of bonds with respect to neutral species are in agreement with previously reported results on N$_9$H-Gua and its cation radical species.[70,73] (Table 5.7) 9-meG$^{+\bullet}$ forms by removal of an electron from the aforementioned bond sequence in the neutral molecule. As the lone pair of the amino group at the C$_2$ site contributes significantly in conjugation with the aforementioned hexatriene sequence, the C2–N2 bond gets shortened by 0.05 Å along with a partial planarization of the amino group. All these bonds experience 0.03–0.05 Å change in length with alternating directions, starting with the lengthening of C2=N3 bond (Table 5.7).
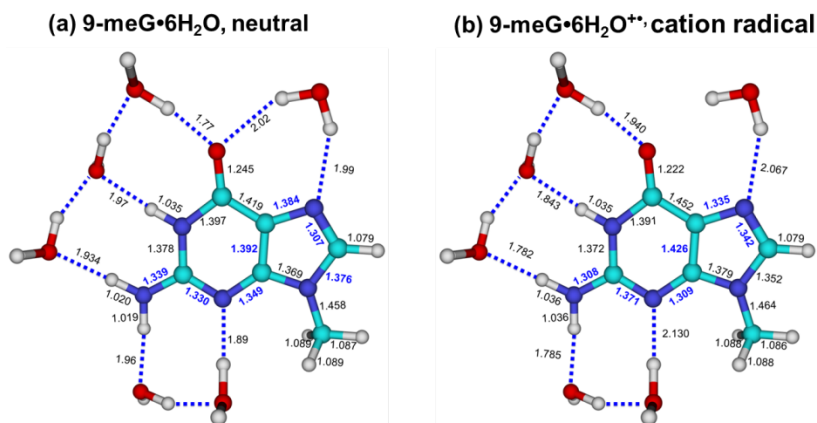
Fig. 5.8 Energy optimized bond lengths of (a) neutral 9-meG•6H$_2$O (corresponding to Fig. 1) and its (b) cation radical, 9-meG•6H$_2$O$^{+•}$, computed with restricted and unrestricted version of B3LYP/6-311+G(2d,p)//PCM method respectively. The conventional numbering of atoms is same as described in in Fig. 5.1. The bond sequence, N2–C2=N3–C4=C5–N7=C8 that undergoes maximal distortion from the neutral ground state is shown in blue and described in Table 5.7.

Deduced initial structural changes following photoexcitation to none of the GMP excited states leads to a decrease in the C2–N2 bond length, but instead cause an increase by 0.01 and 0.06 Å in L_a and L_b respectively, whereas B_b excitation does not perturb this exocyclic bond at all. In fact **in L_a and B_b state, distortions in all these bonds lie in exactly opposite direction compared to the structural changes that occurs to form Gua$^{+•}$ from neutral Gua. Thus, photoexcitation to none of the three singlet electronic states of GMP causes distortions that assist in the formation of cation radical within first 50 fs of photoabsorption.**

Table 5.6 Coordinates (Å) of optimized ground state structure of radical cation of 9-meG•6H$_2$O complex[a].

Atom Name		X	Y	Z	Atom Name		X	Y	Z
1	N	0.735802	0.734309	-0.129937	20	H	3.361309	2.564684	-0.116256
2	C	-0.626165	0.903245	-0.140767	21	H	2.787092	3.045392	-1.488686
3	N	-1.502392	-0.151459	-0.126532	22	O	0.396133	4.469773	0.123306
4	C	-0.928307	-1.327233	-0.110898	23	H	1.312192	4.145921	0.012339
5	C	0.470062	-1.604564	-0.061551	24	H	0.357396	4.878715	0.996381
6	C	1.397214	-0.487463	-0.054766	25	O	-3.854585	2.768633	-0.237649
7	N	-1.532917	-2.566295	-0.119558	26	H	-4.254953	2.920328	-1.102302
8	C	-0.529418	-3.470756	-0.074004	27	H	-4.280111	1.961093	0.122605
9	N	0.69362	-2.920892	-0.03355	28	O	-4.412926	0.287605	0.800741
10	N	-1.119147	2.114052	-0.165633	29	H	-3.49114	0.041466	0.611842
11	H	-0.718654	-4.533025	-0.074595	30	H	-4.504857	0.237952	1.760548
12	H	-0.524369	2.958145	-0.083479	31	O	3.627555	-3.490408	0.05762
13	H	-2.142317	2.262849	-0.225777	32	H	3.762306	-2.533071	0.040649
14	O	2.615866	-0.566302	-0.001732	33	H	2.657933	-3.561078	0.033884
15	H	1.343811	1.564141	-0.247675	34	C	-2.967859	-2.84767	-0.190334
16	O	4.539778	1.494374	0.588633	35	H	-3.396101	-2.319796	-1.039474
17	H	4.743614	1.604045	1.52558	36	H	-3.098035	-3.917932	-0.323302

| 18 | H | 4.005221 | 0.682694 | 0.522056 | 37 | H | -3.453048 | -2.531581 | 0.730611 |
| 19 | O | 2.552526 | 2.919788 | -0.560237 | | | | | |

[a] computed at unrestricted B3LYP/6-311+G(2d,p)//PCM level. To obtain cation radical from the neutral species, charge and spin multiplicity is set to 1 and 2 respectively. A stationary point is confirmed by the absence of imaginary eigenvalues in solution of the force constant matrix.

Table 5.7 Changes in the internal coordinates for those undergo major distortion during cation radical formation of Gua and the corresponding distortions that follow photoexcitation of GMP to L_a, L_b and B_b electronic state.

Internal Coordinate	Change in internal coordinate form neutral ground state structure				
	In Cation Radical		Following photoexcitation to[c]		
Bond	9-meG•6H$_2$O$^{+•}$ [a]	N$_9$H-Gua$^{+•}$ [b]	L_a	L_b	B_b
N2–C2	-0.031	-0.046	0.011	0.062	-0.001
C2=N3	0.041	0.048	-0.003	0.026	-0.018
N3–C4	-0.040	-0.045	0.017	0.106	0.046
C4=C5	0.034	0.044	-0.007	-0.024	-0.035
C5–N7	-0.049	-0.045	0.007	0.066	0.003
N7=C8	0.035	0.031	-0.025	-0.013	-0.014
C8–N9	-0.024	-0.018	0.023	0.011	0.073
N9–C4	0.010	0.004	-0.035	-0.008	-0.068
C6=O6	-0.023	-0.014	-0.017	-0.034	-0.041
C5–C6	0.033	0.021	-0.037	-0.053	-0.033
C6–N1	-0.006	0.001	0.013	0.067	-0.092
N1–C2	-0.010	-0.012	0.004	0.000	-0.091
C$_9$-C$_{methyl}$	0.006	-	-0.017	-0.057	-0.045

[a]Differences in internal coordinates of optimized structures of neutral and cation radical of 9-meG•6H$_2$O complex (described in Table 5.2 and 5.6 respectively); [b]Ref 94, structures of neutral and cation radical of isolated N$_9$H-Gua are computed at restricted and unrestricted B3LYP/6-31+G(d,p)//vacuo level of DFT respectively; [c]distortions of internal coordinates of 9-meG•6H$_2$O following photoexcitation (also described in Table 5.5).

5.3.4 Internal reorganization, solvation and linewidth broadening mechanisms

Experimental and computed wavenumbers, vibrational mode assignment, potential energy distribution (PED), and estimated mode-specific internal reorganization energies for RR active modes of GMP are described in Table 5.8. Total internal reorganization energy (λ_{int}) of GMP determined from best-fitted Δs is 995 cm^{-1} comprises of 28% of the total reorganization energy, 3545 cm^{-1}. A similar value of λ_{int} (904 cm^{-1}) has been obtained in the case of 2′-dG in L_b state. As ribophosphate or ribose sugar do not electronically couple with the purine π electron system, comparable values of λ_{int} indicate

similar magnitudes of absolute distortions in both L_b and B_b states. Though total reorganization energies are of comparable magnitudes, their mode specific contributions result in different amounts of changes in internal coordinates as discussed in preceding sections. Unlike in GMP, a relatively low value of λ_{int}, 112 cm^{-1} has been obtained for 6-ClG in the case of B_b state excitation. The chlorine atom at the 6th position of purine not only restores conjugation of the pyrimidine ring of GMP, and causes a ~ 30 nm red shift of the L_a state but also alters overall electronic structure. The introduction of multiple close-lying states near intense B_b band (~220 nm) on 6-ClG eventually results in structural distortions that are minor compared to those GMP.

Steady state fluorescence quantum yield of natural nucleobases, their nucleotides, and nucleosides at room temperature are within 0.68−1.54 x 10^{-4} and have λ_{max} in the 305−335 nm range.[74,75] Average stokes shifts measured for 2′-dG and dGMP are ~9632 and ~10092 cm^{-1} respectively. Thus, reorganization energy of dGMP estimated from the Stokes shift is ~ 5000 cm^{-1}, which is higher than those estimated for any of the other purine bases. Several nucleobases, such as, 2'-deoxyadenosine-5'-monophosphate (dAMP), 2-aminopurine (2-AP), 2′-deoxycytidine-5′-monophosphate (dCMP) and , 2'-deoxythymidine-5'-monophosphate (dTMP) have Stokes shift at 3070, 2950, 3040, 3500 cm^{-1} respectively. This large red shift derives from a greater amount of stabilization of first singlet state of dGMP due to directional dipolar interaction with surrounding water molecules.

The amplitude of the inertial component of solvation dynamics constituting the homogeneous part of the total linewidth broadening contribution was reported at 1050 and 1650 cm^{-1} following photoexcitation of 2′-dG in L_a and L_b state respectively.[11] We determine this component at 2550 cm^{-1} for GMP when excited within B_b absorption band. **A significantly higher value of solvent reorganization energy in this electronic state as compared to those for the same chromophore in L_a and L_b states is attributed to a larger change in dipole moment of guanine in B_b state from that of the ground state. This interpretation is in agreement with *ab initio* computed dipole moment (10.17 Debye) of B_b state, which is 3 D more than that of the ground state value,** while dipole moments of L_a and L_b states do not differ by more than 1 D from that of the ground state.[49] A higher transition dipole length (0.96 Å) of the B_b state compared to that of the L_b state (0.83 Å) is expected to polarize the instantaneous charge distribution, leading to more interaction with a polar solvent.

The simulation also provides with a 21.2 fs solvent correlation time associated with 2550 cm^{-1} of reorganization energy. Following photoexcitation, such an ultrafast response of water has been reported from the time dependent stokes shift,[76,77] IR two-

dimensional echo,[78] three-pulse photon echo,[79] fluorescence up-conversion[80] measurements on several chromophores. The presence of a sub-50 fs inertial response primarily owing to inertial motions of the solvent molecules has been predicted from molecular dynamics simulations also.[81–84] Using RR intensity analysis, a < 30 fs component of water dynamics for similar sized molecule, e.g. 6-ClG (Chapter 04) and tryptophan[63] has been reported. It has been reported that computed REPs are not responsive to change in Λ by ~50 cm^{-1}.[63,85] The widths rather than the intensities of REPs are sensitive to change in τ (=$1/2\pi\Lambda$). As the REPs reported in this study do not have experimental points on both sides of absorption maxima, it is difficult to put a certain limit on changes of this parameter.

Apart from the absolute magnitude of the transition dipole, the overall charge redistribution on the purine ring might play an important role in instantaneous alteration of local solvation structure. Exocyclic substitution can also affect the inertial component by modulating the ability of the base to interact with water molecule. **Despite similar transition dipole strength compared to that of GMP, a twofold decrease in the magnitude of the fastest component of water response is observed in 6-ClG.** (Table 5.3 and See chapter 4) Hydrophobic chlorine atom at 6th position in place of oxygen reduces the number of possible interactions with solvent molecules significantly. A similar effect is observed in the case of introduction of exocyclic hydrophobic substituents such as methyl (5-methyluracil or thymine) of fluorine (5-fluorouracil) moiety to cause a sharp reduction in the homogeneous linewidth component to 355 and 655 cm^{-1} respectively from that (1450 cm^{-1}) obtained in uracil.[18–20]

The presence of hydrophilic groups (-oxo and -ribophosphate) on GMP can effectively increase the inhomogeneous linewidth (θ) in comparison to that of 6-ClG or 2'-dG. This effect results from the formation of slightly different micro-solvated environments of solute. These static structures modulate zero-zero transition energies a little for each of such configurations and this phenomenon is known as 'site broadening'. Almost a fourfold increase of this component is seen in GMP (1350 cm^{-1}) than that (350 cm^{-1}) found in 6-ClG. The hydrophobic -chloro group in place of oxygen decreases overall interaction of 6-ClG with surrounding solvent and potentially reduces the number of formed micro-solvated clusters. Inhomogeneous linewidth (1350 cm^{-1}) of GMP measured with photoexcitation within B_b band is a little higher than that estimated (900 cm^{-1}) 2'-dG within L_a and L_b bands.[11] This increase in inhomogeneous linewidth might also result due to the presence of an extra phosphate group connected to the ribose sugar and a hydroxyl moiety at the 4th position of the ribose in GMP as compared to 2'-dG. These

hydrophilic moieties would tend to increase hydrogen bonding with surrounding water, and thus can contribute in increasing the number of static micro-configurations.

5.4 Caveats

In our simulation, we did not take into account a low-intensity band of GMP at 679 cm^{-1}. Because this band bears no more than 5% of total integrated intensities al all RR active modes, exclusion of this mode won't have a drastic effect on outcomes of our simulation. Fig 5.6 and 5.7 also describes the effect of change of best-fitted Δs on absorption and RR cross-sections. We that, the overall fit of REPs would be better constrained is experimental points on other sides of the B_b absorption band are provided. However, experimental RR spectra with excitations below 210 nm were not available due limited laser resources presently available in our laboratory. Even though RR spectra with more high energy excitation were available, we suspect the increase in interference from high-lying electronic states too. In that scenario, it would be more appropriate to use a more sophisticated two-state model, as employed for two lowest L_a and L_b excited states of 2′-dG[11] for the resonance Raman intensity analysis to obtain the squares of the dimensionless displacements. However, for such treatment, the relative orientation of transition dipoles of such interfering states of GMP below 230 nm would also be necessary.

Another important factor that is critical for determination of instantaneous distortions of different bonds of GMP is signs of the dimensionless Δs, and therefore of the gradients along each normal coordinate in FC region of the B_b excited state. We found that the obtained signs of the gradients are not sensitive to the choice of functionals. However, the ground state normal mode vectors (matrix 'A$_{ij}$' in eqn. 2.28) that are also necessary to project the dimensionless displacements onto changes in internal coordinates can vary with the number of explicit water molecules included in the solvated model complex. Simulation of RR spectra of nucleobases on B_b and higher electronic states is not very common,[86] as for the low energy L_a and L_b electronic states.[87–92] The uncertainties in TD-DFT obtained signs of excited-state gradients warrant more theoretical studies on these electronic states of GMP and of other nucleobases also. Measurement of experimental RR cross-sections with excitation lines on the blue side of 210 nm would be helpful to provide a better understanding of the short-time structural dynamics of GMP under UV-C radiation. More challenging measurement of Raman depolarization ratios across the 190 nm to 230 nm region would certainly reveal nature of coupling of the close-lying electronic states.

5.5 Conclusion

Experimentally measured resonance REP of GMP within the B_b absorption band reveals that different sets of vibrational degrees of freedom are responsible for coupling of L_b state with high lying B_b and low-lying L_a states. Two ring stretching modes appearing at 1580 and 1607 cm^{-1} and in-plane ring deformation modes at 866 and 1020 cm^{-1} are recognized to vibronically couple the B_b state with L_b state and can assist internal conversion between the mentioned states. Determination of magnitude and direction of distortion of each bond of the purine ring of GMP reveals coupling of specific internal coordinates with three different singlet states in a quantitative manner. **Excitation to none of the three singlet states of Gua is found to directly assist the formation of the guanine cation radical. Other than a weakening of the C8–N9 bond, photoexcitation to B_b state does not cause any distortion of the purine ring that lies along the photochemical reaction coordinate of various lesion formations.** B_b excitation causes overall shrinkage of both the rings of Gua, in contrast to an expansion and contraction of pyrimidine and imidazole rings respectively in case of excitation to either of L_a and L_b states respectively.

Large (72 %) contribution of the ultrafast inertial component of solvation towards total reorganization energy (3545 cm^{-1}) of GMP is attributed to the presence of the hydrophilic ribophosphate group that takes part in directional dipolar interaction with surrounding water molecules. The presence of strong hydrogen bond accepting moieties on GMP results in a high value of inhomogeneous broadening linewidth of 1350 cm^{-1}. Correct orbital description and good agreement between computed and experimental excitation energies of GMP, computed on 9-meG•H_2O model complex also indicate that non-covalent interactions are important to consider in describing excited states of nucleobases. **Our experimentally determined distortions would be of importance for assessing the performance of different theoretical methods and more precisely in developing accurate physical models for the reliable description of high energetic singlet states in GMP and in other nucleobases.**
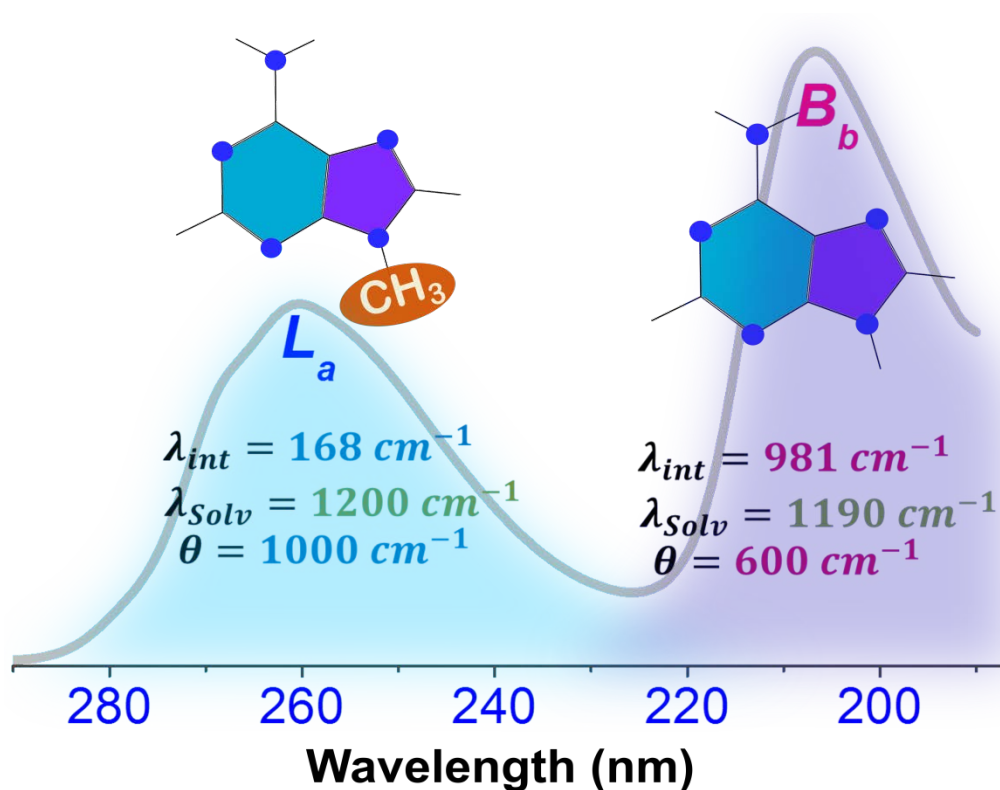
References

[1] C. E. Crespo-Hernández, B. Cohen, P. M. Hare, B. Kohler, *Chem. Rev.* **2004**, *104*, 1977.

[2] L. Serrano-Andrés, M. Merchán, *J. Photochem. Photobiol. C Photochem. Rev.* **2009**, *10*, 21.

[3] V. Karunakaran, K. Kleinermanns, R. Improta, S. A. Kovalenko, *J. Am. Chem. Soc.* **2009**, *131*, 5839.

[4] J. M. L. Pecourt, J. Peon, B. Kohler, *J. Am. Chem. Soc.* **2000**, *122*, 9348.

[5] J. B. Nielsen, J. Thøgersen, S. K. Jensen, S. B. Nielsen, S. R. Keiding, *Phys. Chem. Chem. Phys.* **2011**, *13*, 13821.

[6] Y. Zhang, R. Improta, B. Kohler, *Phys. Chem. Chem. Phys.* **2014**, *16*, 1487.

[7] M. Towrie, G. W. Doorley, M. W. George, A. W. Parker, S. J. Quinn, J. M. Kelly, *Analyst* **2009**, *134*, 1265.

[8] J. Peon, A. H. Zewail, *Chem. Phys. Lett.* **2001**, *348*, 255.

[9] C. C.-W. Cheng, C. Ma, C. T.-L. Chan, K. Y.-F. Ho, W.-M. Kwok, *Photochem. Photobiol. Sci.* **2013**, *12*, 1351.

[10] F.-A. Miannay, T. Gustavsson, A. Banyasz, D. Markovitsi, *J. Phys. Chem. A* **2010**, *114*, 3256.

[11] A. F. El-Yazbi, A. Palech, G. R. Loppnow, *J. Phys. Chem. A* **2011**, *115*, 10445.

[12] Z. Lan, E. Fabiano, W. Thiel, *ChemPhysChem* **2009**, *10*, 1225.

[13] M. Barbatti, J. J. Szymczak, A. J. A. Aquino, D. Nachtigallová, H. Lischka, *J. Chem. Phys.* **2011**, *134*, 014304.

[14] B. Heggen, Z. Lan, W. Thiel, *Phys. Chem. Chem. Phys.* **2012**, *14*, 8137.

[15] L. B. Clark, *J. Am. Chem. Soc.* **1994**, *116*, 5265.

[16] A. B. Myers, Excited State Structure and Dynamics of Polyenes and Bacteriorhodopsin from Resonance Raman Intensities, University of California, Berkeley, **1984**.

[17] B. E. Billinghurst, G. R. Loppnow, *J. Phys. Chem. A* **2006**, *110*, 2353.

[18] B. E. Billinghurst, R. Yeung, G. R. Loppnow, *J. Phys. Chem. A* **2006**, *110*, 6185.

[19] S. Yarasi, P. Brost, G. R. Loppnow, *J. Phys. Chem. A* **2007**, *111*, 5130.

[20] S. Yarasi, S. Ng, G. R. Loppnow, *J. Phys. Chem. B* **2009**, *113*, 14336.

[21] S. S. Ng, F. Teimoory, G. R. Loppnow, *J. Phys. Chem. Lett.* **2011**, 2362.

[22] S. A. Oladepo, G. R. Loppnow, *J. Phys. Chem. B* **2011**, *115*, 6149.

[23] B. E. Billinghurst, S. A. Oladepo, G. R. Loppnow, *J. Phys. Chem. B* **2012**, *116*, 10496.

[24] F. Teimoory, G. R. Loppnow, *J. Phys. Chem. A* **2014**, *118*, 12161.

[25] L. D. Ziegler, B. Hudson, D. P. Strommen, W. L. Peticolas, *Biopolymers* **1984**, *23*, 2067.

[26] S. P. A. Fodor, R. P. Rava, T. R. Hays, T. G. Spiro, *J. Am. Chem. Soc.* **1985**, *107*, 1520.

[27] W. L. Kubasek, B. Hudson, W. L. Peticolas, *Proc. Natl. Acad. Sci.* **1985**, *82*, 2369.

[28] L. Chinsky, B. Jollès, A. Laigle, P. Y. Turpin, *J. Raman Spectrosc.* **1987**, *18*, 195.

[29] J. R. Perno, D. Cwikel, T. G. Spiro, *Inorg. Chem.* **1987**, *26*, 400.

[30] A. Toyama, N. Hanada, J. Ono, E. Yoshimitsu, H. Takeuchi, *J. Raman Spectrosc.* **1999**, *30*, 623.

[31] N. Jayanth, S. Ramachandran, M. Puranik, *J. Phys. Chem. A* **2009**, *113*, 1459.

[32] S.-Y. Lee, E. J. Heller, *J. Chem. Phys.* **1979**, *71*, 4777.

[33] B. Li, A. E. Johnson, S. Mukamel, A. B. Myers, *J. Am. Chem. Soc.* **1994**, *116*, 11039.

[34] M. Barbatti, A. J. A. Aquino, J. J. Szymczak, D. Nachtigallova, P. Hobza, H. Lischka, *Proc. Natl. Acad. Sci.* **2010**, *107*, 21453.

[35] G. R. Loppnow, B. E. Billinghurst, S. A. Oladepo, in *Radiat. Induc. Mol. Phenom. Nucleic Acids*, Springer Netherlands, Dordrecht, **n.d.**, pp. 237–263.

[36] T. Gustavsson, R. Improta, D. Markovitsi, *J. Phys. Chem. Lett.* **2010**, *1*, 2025.

[37] J. M. L. Pecourt, J. Peon, B. Kohler, *J. Am. Chem. Soc.* **2001**, *123*, 10370.

[38] S. Georghiou, T. M. Nordlund, A. M. Saim, *Photochem. Photobiol.* **1985**, *41*, 209.

[39] T. Fujiwara, Y. Kamoshida, R. Morita, M. Yamashita, *J. Photochem. Photobiol. B Biol.* **1997**, *41*, 114.

[40] B. Cohen, P. M. Hare, B. Kohler, *J. Am. Chem. Soc.* **2003**, *125*, 13594.

[41] S. Mondal, M. Puranik, *Phys. Chem. Chem. Phys.* **2016**, *18*, 13874.

[42] M. J. Cavaluzzi, *Nucleic Acids Res.* **2004**, *32*, 13e.

[43] A. B. Myers, R. A. Mathies, E. J. Tannor, David J.Heller, *J. Chem. Phys.* **1982**, *77*, 3857.

[44] S. Mukamel, *Principles of Nonlinear Optical Spectroscopy*, Oxford University Press, New York, **1995**.

[45] A. B. Myers, *J. Raman Spectrosc.* **1997**, *28*, 389.

[46] R. Bauernschmitt, R. Ahlrichs, *Chem. Phys. Lett.* **1996**, *256*, 454.

[47] M. E. Casida, C. Jamorski, K. C. Casida, D. R. Salahub, *J. Chem. Phys.* **1998**, *108*, 4439.

[48] Y. Zhao, Z. Cao, *J. Theor. Comput. Chem.* **2013**, *12*, 1341013.

[49] M. P. Fülscher, L. Serrano-Andrés, B. O. Roos, *J. Am. Chem. Soc.* **1997**, *119*, 6168.

[50] A. Tsolakidis, E. Kaxiras, *J. Phys. Chem. A* **2005**, *109*, 2373.

[51] Y. Nishimura, M. Tsuboi, W. L. Kubasek, K. Bajdor, W. L. Peticolas, *J. Raman Spectrosc.* **1987**, *18*, 221.

[52] P. Lagant, G. Vergoten, W. L. Peticolas, *J. Raman Spectrosc.* **1999**, *30*, 1001.

[53] W. Hug, I. Tinoco, *J. Am. Chem. Soc.* **1973**, *95*, 2803.

[54] L. Serrano-Andrés, M. Merchán, A. C. Borin, *J. Am. Chem. Soc.* **2008**, *130*, 2473.

[55] P. G. Szalay, T. Watson, A. Perera, V. F. Lotrich, R. J. Bartlett, *J. Phys. Chem. A* **2012**, *116*, 6702.

[56] B. Mennucci, A. Toniolo, J. Tomasi, *J. Phys. Chem. A* **2001**, *105*, 7126.

[57] M. Parac, M. Doerr, C. M. Marian, W. Thiel, *J. Comput. Chem.* **2010**, *31*, 90.

[58] P. G. Szalay, T. Watson, A. Perera, V. Lotrich, G. Fogarasi, R. J. Bartlett, *J. Phys. Chem. A* **2012**, *116*, 8851.

[59] K. Hunger, L. Buschhaus, L. Biemann, M. Braun, S. Kovalenko, R. Improta, K. Kleinermanns, *Chem. - A Eur. J.* **2013**, *19*, 5425.

[60] R. Improta, V. Barone, **2014**, pp. 329–357.

[61] A. C. Albrecht, *J. Chem. Phys.* **1961**, *34*, 1476.

[62] J. Guthmuller, *J. Chem. Theory Comput.* **2011**, *7*, 1082.

[63] E. A. Milán-Garcés, S. Kaptan, M. Puranik, *Biophys. J.* **2013**, *105*, 211.

[64] R. Shimoda, M. Nagashima, M. Sakamoto, N. Yamaguchi, S. Hirohashi, J. Yokota, H. Kasai, *Cancer Res.* **1994**, *54*, 3171.

[65] J. Cadet, M. Berger, G. W. Buchko, P. C. Joshi, S. Raoul, J.-L. Ravanat, *J. Am. Chem. Soc.* **1994**, *116*, 7403.

[66] S. Raoul, M. Berger, G. W. Buchko, P. C. Joshi, B. Morin, M. Weinfeld, J. Cadet, *J. Chem. Soc. Perkin Trans. 2* **1996**, 371.

[67] R. M. Uppu, R. Cueto, G. L. Squadrito, M. G. Salgo, W. A. Pryor, *Free Radic. Biol. Med.* **1996**, *21*, 407.

[68] N. Y. Tretyakova, J. C. Niles, S. Burney, J. S. Wishnok, S. R. Tannenbaum, *Chem. Res. Toxicol.* **1999**, *12*, 459.

[69] C. Szabó, B. Zingarelli, M. O'Connor, A. L. Salzman, *Proc. Natl. Acad. Sci. U. S. A.* **1996**, *93*, 1753.

[70] P. Cheng, Y. Li, S. Li, M. Zhang, Z. Zhou, *Phys. Chem. Chem. Phys.* **2010**, *12*, 4667.

[71] J. M. Rice, G. O. Dudek, *J. Am. Chem. Soc.* **1967**, *89*, 2719.

[72] J. Sultan, *Int. J. Mass Spectrom.* **2008**, *273*, 58.

[73] R. Improta, G. Scalmani, V. Barone, *Int. J. Mass Spectrom.* **2000**, *201*, 321.

[74] P. R. Callis, *Annu. Rev. Phys. Chem.* **1983**, *34*,

329.

[75]   D. Onidas, D. Markovitsi, S. Marguet, A. Sharonov, T. Gustavsson, *J. Phys. Chem. B* **2002**, *106*, 11367.

[76]   W. Jarzeba, G. C. Walker, A. E. Johnson, M. A. Kahlow, P. F. Barbara, *J. Phys. Chem.* **1988**, *92*, 7039.

[77]   S. Vajda, R. Jimenez, S. J. Rosenthal, V. Fidler, G. R. Fleming, E. W. Castner, *J. Chem. Soc. Faraday Trans.* **1995**, *91*, 867.

[78]   S. Park, M. D. Fayer, *Proc. Natl. Acad. Sci.* **2007**, *104*, 16731.

[79]   R. Jimenez, D. A. Case, F. E. Romesberg, *J. Phys. Chem. B* **2002**, *106*, 1090.

[80]   R. Jimenez, G. R. Fleming, P. V. Kumar, M. Maroncelli, *Nature* **1994**, *369*, 471.

[81]   R. W. Impey, P. A. Madden, I. R. McDonald, *Mol. Phys.* **1982**, *46*, 513.

[82]   M. Maroncelli, G. R. Fleming, *J. Chem. Phys.* **1988**, *89*, 5044.

[83]   R. B. Barnett, U. Landman, A. Nitzan, *J. Chem. Phys.* **1989**, *90*, 4413.

[84]   J. S. Bader, D. Chandler, *Chem. Phys. Lett.* **1989**, *157*, 501.

[85]   X. Cao, J. L. McHale, *J. Chem. Phys.* **1998**, *109*, 1901.

[86]   D. Rappoport, S. Shim, A. Aspuru-Guzik, *J. Phys. Chem. Lett.* **2011**, *2*, 1254.

[87]   D. C. Blazej, W. L. Peticolas, *J. Chem. Phys.* **1980**, *72*, 3134.

[88]   W. L. Peticolas, T. Rush, *J. Comput. Chem.* **1995**, *16*, 1261.

[89]   T. I. Rush, W. L. Peticolas, *J. Phys. Chem.* **1995**, *99*, 14647.

[90]   J. Neugebauer, B. A. Hess, *J. Chem. Phys.* **2004**, *120*, 11564.

[91]   S. Sun, A. Brown, *J. Phys. Chem. A* **2014**, *118*, 9228.

[92]   S. Sun, A. Brown, *J. Phys. Chem. A* **2015**, *119*, 3961.

6

Excited state structural dynamics of Adenine in L_a and B_b Electronic States

$$\lambda_{int} = 168 \; cm^{-1}$$
$$\lambda_{Solv} = 1200 \; cm^{-1}$$
$$\theta = 1000 \; cm^{-1}$$

$$\lambda_{int} = 981 \; cm^{-1}$$
$$\lambda_{Solv} = 1190 \; cm^{-1}$$
$$\theta = 600 \; cm^{-1}$$

6.1 Introduction

UV induced photodynamics of adenine (Ade) which is the other natural purine nucleic acid apart from Guanine (Chapter 05) is the focus of this chapter. Ade has a distinct excited state dynamics compared to Gua owing to the presence of a different manifold of electronic states that result from a change in the exocyclic substituent. Several spectroscopic studies with sub-ps time resolution have investigated relaxation of electronically excited Ade (Fig. 6.1) following photoexcitation within the 260 nm absorption band.[1–13] In general, it has been found that photoexcited Ade exhibits biexponential decay behavior with an ultrafast component ($\tau_1 \sim 0.1$ ps) and a slower one ($\tau_2 \sim 0.75–1$ ps) Several computational studies have identified different possible relaxation pathways involving multiple states between S_0 and the initially populated excited state.[2,14–25] However, it is agreed that CI between lowest energetic excited states and S_0 are of two types: (i) puckered ring structure at C2 and (ii) C6 site.[2,17,18,26] In solution phase, the majority (90%) of electronically excited population decays through the first mechanism while a minor population fraction (4 %) relaxes through the latter. However association of these two CIs with a particular singlet excited state (L_a or L_b or $S_{n\pi*}$) is not clearly resolved yet. While τ_1 is attributed to direct depopulation from L_a to S_0[17] or to an underlying state ($L_a{\rightarrow}S_{n\pi*}$ or $L_a{\rightarrow}L_b$),[25] and the slower component is assigned to repopulation of S_0 state from the latter states. Furthermore, for higher excitation energy a deactivation channel is accessed through an intermediate Rydberg state ($\pi\sigma*$) via cleavage of the N9–H bond.[19]

All of the experimental reports discussed in the preceding section have measured sub-ps decay rates of electronically excited populations but do not provide structural information during relaxation. Instantaneous nuclear dynamics following photoexcitation of 9-methylAde (9-meA, hereafter) have been investigated by Loppnow and coworkers.[27] Excited state dynamics derived from resonance Raman (RR) intensity analysis throughout the L_a absorption band (~260 nm) reveals that major structural dynamics happens along three vibrational modes at 1343, 1437 and 1537 cm^{-1}. These modes are associated with internal coordinates of the imidazole ring and vibrations of the exocyclic $–CH_3$ and $–NH_2$ moieties.[27–30] Relatively low values of internal reorganization energy and hence minor structural distortions of the purine ring of 9-meA were ascribed to the inherent photoresistive property of the Ade chromophore.

Apart from L_a and L_b singlet states in the UV-B region (260-320 nm), Ade has strong $\pi\pi*$ transitions, located in the red edge of the UV-C region (100-260 nm). These electronic states absorb UV photons much more efficiently than those located within the 260 nm band due to a higher absorption cross-section. More photoabsorption in the UV-C region would naturally deposit more electronic energy

that needs to be dissipated for Ade to be photostable. As solar flux below 240 nm wavelength was considerably higher in the prebiotic era than today,[31,32] these high-lying excited states might have played an important role in the evolved photoresistive properties of Ade and in general of all nucleobases. Along with already photodynamic properties in UV-B region described in preceding sections, experimental measurements on the excited states in UV-C region is also necessary to determine overall UV photostability of Ade.
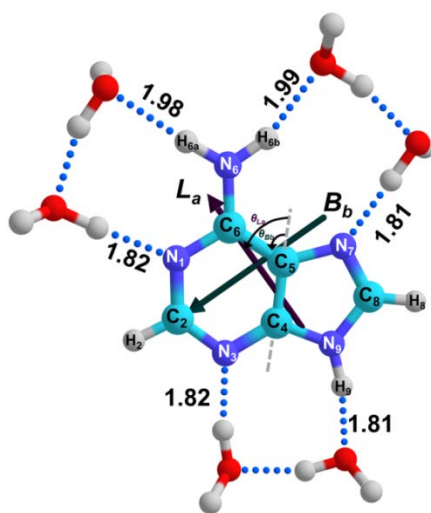
Fig. 6.1 Aqueous adenine was modeled as N9H-Ade•6H$_2$O complex as shown above. Conventional numbering of ring atoms is indicated. All H-bond distances (in Å) between water molecules and the base along are labeled. Directions of computed transition dipole moments ($\vec{\mu}$) for L$_a$ and B$_b$ states at TD-CAMB3LYP/6-311+G(2d,p)//PCM level are shown with bold arrows. Computed $\vec{\mu}$ of L$_a$ and B$_b$ state are oriented at 41° (θ_{La})and 130.4° (θ_{Bb}) with respect to $\overrightarrow{C_4 - C_5}$ and have magnitude of 1.76 and 1.79 Au respectively.

Resonance Raman (RR) spectroscopy is a powerful probe of molecular structure and structural dynamics on the electronic excited state.[33–36] Resonant enhancement of vibrational modes, coupled to an electronic excited state occurs when the exciting laser is tuned to lie within the corresponding absorption band of the molecule. The intensity of RR bands contains information of the resonant electronic state. RR spectroscopy has been successfully applied in characterizing manifold of electronic excited states and vibrational properties in nucleobases[35,37–49]and Ade systems.[27,50–55] We have characterized the high-lying B_b electronic state (~ 200 nm) of Ade by measuring excitation wavelength dependent intensity modulation of RR bands i.e. Raman excitation profiles (REP) within 210-230 nm wavelength range.

In case of resonant excitation, the intensity of an RR band is proportional to the square of the slope along associated vibrational normal coordinates in the FC region of the resonant vibronic state. Excitation wavelength dependence of cross-sections of RR modes encodes for events that occur on FC region on resonant vibronic potential energy surface (PES) within tens of femtoseconds (fs) of photoexcitation. Resonance enhancement of several vibrational modes makes RR spectroscopy suitable for characterization of Ade in different excited states.[38,39,51,52,56] Simulation of experimentally measured REPs and absorption spectra according to time-dependent wave packet propagation (TDWP) formalism allows us to obtain excited state

parameters such as instantaneous structural distortions of the chromophore.[33–36] This method has been successfully applied to a variety of molecular systems[57–62] and for several nucleobases.[27,43–46,63–65]

In this chapter, we simulate experimentally measured REPs of Ade throughout the red edge of B_b absorption band (210-230 nm) using TDWP formalism. From the simulation, we determine the excited state structure of Ade on B_b electronic state through conversion of dimensionless displacements (Δ) along each of the FC active modes into changes in internal coordinates. Using a self-consistent approach, we partition static inhomogeneous and dynamics homogeneous broadening contributions because unlike absorption, absolute RR cross-section depends on the two line-broadening mechanisms in a distinct manner. We describe the ultra-fast electronic dephasing due to instantaneous solute-solvent bath interaction according to the Brownian oscillator model.[66] We obtain the amplitude and time scale of this inertial component of solvation as solvent reorganization energy (λ_{solv}) and the solvent correlation time (τ). Thus obtained excited state structure, reorganization energy and solvation parameters of Ade in B_b electronic state are compared with those previously reported in L_a state of the same chromophore (9-meA)[27] and other nucleobases.

## 6.2. Material and Methods

6.2.1 Experimental method

Ade of 1 mM concentration in miliQ water of pH 6.8 was used for RR measurement using optical setup described in chapter 02. Sodium perchlorate was used as internal intensity standard (IS). Typical incident laser power on the sample was less than ~ 0.6 mW. Ade (HPLC, 99%) and sodium perchlorate were purchased from Sigma-Aldrich and were used without further purification.

Absolute RR cross-section of each Ade band was determined using eqn. 2.6a. Correction for spectral sensitivity of spectrometer and self-absorption of Raman scattered photons by the sample itself was done following methods described in chapter 2. Depolarization ratios of Ade bands are also measured using optical arrangement described in Fig.2.6

6.2.2 Simulation of RR and absorption cross-section

RR excitation profiles and absorption spectra of Ade within the B_b absorption band are modeled according to Lee and Heller's self-consistent time-dependent wave packet (TDWP) formalism with eqn. 2.21a and 2.21b. Solvent induced dephasing in sub-100 fs time scale was simulated according to oscillator

model. (See eqns. 2.22a-d in Chapter 2). Static inhomogeneous broadening (θ) is introduced in both Raman and absorption processes as a phenomenological parameter in the form of normalized Gaussian distributions of transition energies. From best-fit Δ, changes in the internal coordinate (δ_j) that are associated to a normal mode are computed from using eqn. 2.28
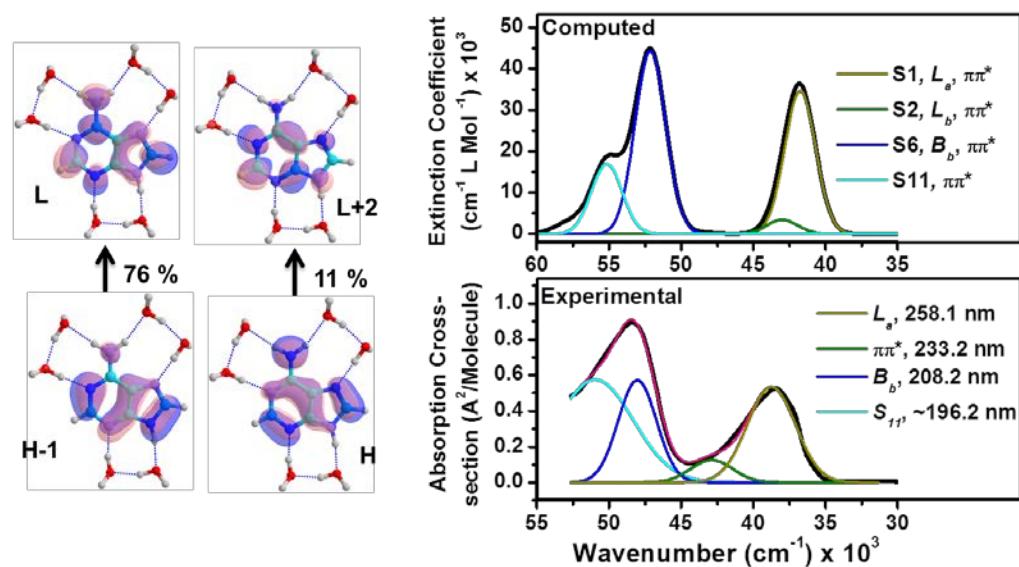
Fig. 6.2 (a) Computed molecular orbitals of adenine involved in the B_b electronic transition observed in experiments at 210 nm; (b) bottom: deconvolved experimental spectra with standard spectroscopic labels of the bands and λ_{max}; top: computed absorption spectra, excitations and nature of the lower and higher excited states of adenine. The electronic absorption spectrum was computed using TD-CAMB3LYP/6-311+G(2d,p)//PCM method on N9H-Ade•6H$_2$O complex as shown in a. Computed band positions are described with a Gaussian line shape of fixed line width (2500 cm^{-1}). H and L stand for HOMO and LUMO orbitals respectively. Absorption cross-section was determined following the procedure described in the experimental method section. Computed states of Ade are described in Table 6.2.

Relative intensities of the all 17 RR bands of Ade with respect to that of the band at 725 cm^{-1} at 220 nm excitation wavelength are used as initial guesses for the Δs along different normal coordinates, assuming a short-time approximation, i.e. intensity of fundamental vibration is proportional to the square of Δs.[35,67,68] Transition strength of B_b electronic state is derived (0.75 Å) from the deconvoluted absorption band by a Gaussian line-shape (Fig. 6.2b, bottom). In the first step, a value of zero-zero transition energy was used such that the red edge of simulated absorption and REPs of all RR modes showed good agreement with experimental values. All parameters were then iteratively optimized using a self-consistent approach[34–36,69] to obtain a good fit between simulated and experimental REPs and the absorption spectrum. Robustness of

the obtained fit was tested by varying Δs by 20 % of their best-fitted values and obtaining the best possible fit iteratively.

6.2.3 Quantum mechanical calculations

All quantum mechanical (QM) computations were performed with Gaussian 09 software suite. The N9–H tautomer, which is the prevalent species of Ade at neutral pH[70–74] is modeled as Ade•6H$_2$O, a complex with six strategically placed explicit water molecules.[26] (See Fig. 6.1) PCM solvation was used to account for the bulk dielectric property of water.[75,76] Optimization of the S_0 structure, computation of vibrational frequencies and normal modes are performed within density functional theory (DFT) using B3LYP hybrid functional and atom centered 6-311+G(2d,p) Gaussian basis set, augmented with diffuse and polarization functions. Geometry optimization was performed without any symmetry constraints and an absence of any imaginary eigenvalue of force constant matrix ensures local minima on PES of S_0. Vertical excitation energies, transition dipole moments and analytic gradients on singlet excited states were computed within linear response formalism of time-dependent DFT (hereafter referred to as TD-DFT) method on B3LYP/6-31+G(2d,p)//PCM optimized geometry.

### 6.3. Results and Discussions

6.3.1 REPs of Ade within B_b absorption band

Ade and its N9 substituted forms have been previously investigated with ultraviolet excited RR (UVRR) spectroscopy in solution.[27,37,38,51–53,77–80] UVRR spectrum of Ade with 210 nm excitation wavelength is shown in Fig. 6.3. Between 500 to 1900 cm^{-1} wavenumbers, seventeen RR active modes of Ade are observed, as reported by several authors, using different excitation wavelengths within B_b absorption band.[38,56,77,78] Earlier experimental studies have shown that REPs of all Ade RR modes have a peak ~260 nm corresponding to the strong ππ* (L_a) state, and a peak ~ 210 nm corresponding to B_b state which is also of ππ* character.[38,78] A report of RR enhancement pattern in UV-C region has indicated presence of two electronic transitions at ~185 and at 210 nm.[38] Presence of an electronic transition (B_b) at 210 nm was established by the presence of a maximum in measured REPs of two RR bands at 730 and 1581 cm^{-1} at the same place. With 210 nm excitation, five vibrational modes located at 725, 1120, 1251, 1333 and 1602 cm^{-1} bear maximum intensity and are different than those enhanced at excitations within the 260 nm absorption band.[37,78] Due to the difference in FC activity, initial structural dynamics of Ade is expected to differ significantly when excited within 210 nm absorption band compared to reported dynamics[27] following excitation within 260 nm absorption band.
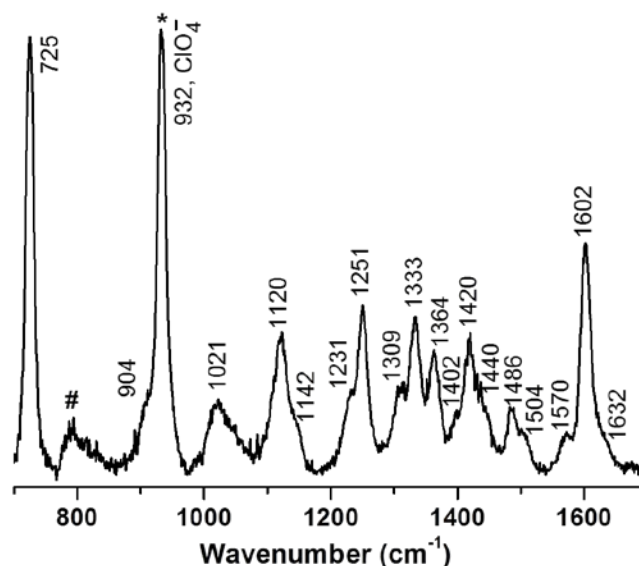
Fig. 6.3 UVRR spectrum of Ade obtained with excitation wavelength of 210 nm. The band (*) at 932 cm^{-1} corresponds to sodium perchlorate, used as internal intensity standard. The band marked by '#' does not correspond to sample and is a contribution from quartz tube.

The intensity variation of Ade RR bands as a function of excitation wavelengths within B_b absorption band is shown in Fig. 6.4. This intensity modulation is quantitatively expressed as the RR cross-sections using eqn. 2.6 and is plotted as REPs (Fig. 6.5 and 6.6). A continuous decrease in the RR cross-section, observed for all seventeen RR modes of Ade with excitation wavelengths from 210 nm to 225 nm (Fig. 6.5 and 6.6) is in agreement with previously reported trends of four RR bands.[38] Increase in RR cross-sections of all except four bands at 725, 904 and 1021 and 1420 cm^{-1} in the red edge (> 225 nm) of the REPs indicates possible decoupling of these modes with the low-lying excited state. In agreement with this claim, REPs of 9-meA within 260 nm absorption band do not show significant enhancement of these bands.[27] Unlike two previous studies reporting low-resolution REPs,[38,56] we have measured REPs of Ade within the red edge of the B_b absorption band with 12 excitation lines between 210 and 230 nm. No excitation wavelength dependent shift in the position of Ade RR bands is observed.
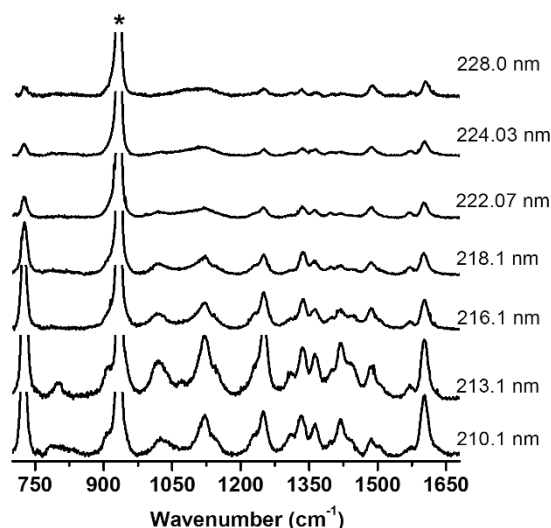
Fig. 6.4 Resonance Raman spectra of adenine at seven different excitation wavelengths in an aqueous solution of pH 7.0. Variation in intensity of each band in the Raman spectrum is visible as the excitation wavelength is tuned across the electronic absorption band (Fig. 2, panel B, bottom). The spectra have been normalized to the intensity of the 932 cm^{-1} band of sodium perchlorate, used as internal intensity standard (asterisk).

6.3.2 Computation of excitation energies, vibrational wavenumbers, and normal mode vectors

In several computational investigations on nucleobases explicit water molecules were introduced to account for non-covalent interactions along with continuum type bulk solvation, known as a cluster-continuum model.[81] Such applications include *ab initio* simulation of decay of photoexcited Ade,[4,26] computation of pKa values of nucleobases,[82] prediction of vibrational frequencies[83] and others.[82,84–86] Citing these results, Ade in solution is modeled as Ade•6H$_2$O complex for reliable computation of electronic excitation energies, vibrational wavenumbers and associated ground state normal mode vectors. Optimized geometry of Ade•6H$_2$O complex at B3LYP/6-311+G(2d,p)//PCM level of theory is described in Fig. 6.1. (xyz coordinates are described in Table 6.1)

UV-vis spectra of Ade has been studied using a variety of electronic spectroscopic techniques in solution,[87–91] in stretched PVA film[92]and in the vapor phase.[93–98] Apart from wavefunction based methods,[2,16–18,99–102] linear response TD-DFT has been a popular choice for computation of excited state properties of nucleobases including Ade.[103–110]

Table 6.1 XYZ Coordinates (Å) of energy optimized ground state structure of Ade•6H$_2$O complex[a]

Atom No		X	Y	Z	Atom No.		X	Y	Z
1	N	-0.639046	-1.670515	-0.028895	18	O	-1.51648	4.184113	-0.011133
2	C	0.643912	-2.044287	-0.038467	19	H	-0.909061	3.401079	-0.030373
3	N	1.720960	-1.267509	-0.027117	20	H	-1.360799	4.660795	-0.835009
4	C	1.404043	0.039761	-0.006069	21	O	5.052399	0.678353	-0.041101
5	C	0.115325	0.569346	0.001485	22	H	5.561808	0.94127	0.734648
6	C	-0.960949	-0.350377	-0.008857	23	H	4.996826	-0.205518	-0.009236
7	N	2.252202	1.112815	0.008926	24	N	-2.248265	0.000281	-0.000447
8	C	1.467365	2.225899	0.023605	25	H	-2.977289	-0.711913	-0.018078
9	N	0.180502	1.953702	0.019247	26	H	-2.553445	0.970446	0.029622
10	H	1.888174	3.219130	0.036620	27	H	0.822323	-2.114267	-0.057106
11	H	3.283446	1.075320	0.012256	28	O	-2.440652	-2.824415	-0.014541
12	O	-4.487561	-1.998646	0.011294	29	H	-2.303579	-4.231115	0.794588
13	H	-5.017496	-2.047503	-0.792780	30	H	-1.778292	-2.085120	0.009512
14	H	-3.892883	-2.781623	-0.011981	31	O	-3.728827	2.577174	0.039222
15	O	4.433529	-1.994984	-0.106901	32	H	-4.226702	2.709583	0.854177
16	H	3.455115	-1.846561	-0.049710	33	H	-3.034166	3.274145	0.03431
17	H	4.664097	-2.544370	0.651641					

[a]computed at B3LYP/6-311+G(2d,p)//PCM level

In agreement with published results, L_a state (HOMO → LUMO) which bears most of the oscillator strength of the 260 nm absorption band is found to be most stabilized in polar solvents. (Table 6.2) $S_{n\pi^*}$ which is the lowest in energy in the gas phase gets destabilized in a polar solvent like water and shifts to a higher energy than both of L_a and L_b states.[98,102,106,110,111] In comparison with the published solution phase results, an identical trend of relative energies for three lowest states: $L_a < L_b < S_{n\pi^*}$ was obtained from our calculation on Ade•6H$_2$O complex.

The mentioned energy ordering is obtained with TD-DFT calculations using B3LYP functional and with Coulomb-attenuated long-range corrected CAM-B3LYP[112] functional. The same trend is observed with additional dispersion corrected wB97xD[113] functionals also. (data not shown) However, while computing the B_b excited state corresponding to 210 nm absorption band, B3LYP is found to predict spurious state. It predicts three closely spaced states with low oscillator strength (0.1). These states are predicated to be heavily contaminated and involve contributions from MOs that are not localized on the purine ring, but on surrounding water molecules. This problem was not found in the case of CAM-B3LYP or wB97xD functionals. Thus, we have computed all excited states at CAM-B3LYP/6-31G+(2d,p)//PCM level on Ade•6H$_2$O complex, (Table 6.2) and the involved MOs and deconvoluted experimental and theoretical absorption spectra are shown in Fig. 6.2**.**

Table 6.2 Vertical singlet excitation energies in nm (in eV in parenthesis), oscillator strengths (f) and major orbital contribution to each transition of neutral adenine by TD-CAMB3LYP method; and comparison with published computed and experimental transition energies.

		Ade•6H$_2$O[a]			Experimental			Computed[f]	
State	Type	Major orbital Contribution[b] (%)	$\Delta E_{vert,PCM}$ cm^{-1} (nm/ eV)	f_{PCM}	ΔE_{Exp} cm^{-1} (nm/ eV)[c]	ε (l mol^{-1} cm^{-1})[c]	ΔE_{Exp} cm^{-1} (nm/ eV)	ΔE_{gas} cm^{-1} (nm/ eV)	f_{gas}
S1 (L$_a$)	$\pi\pi^*$	H→L (94)	41780 (239.5/ 5.18)	0.40	38744 (258.1/ 4.8)	13361	38715 (258.5/ 4.80)[d]	41941 (238.46/ 5.20)	0.370
S2 (L$_b$)	$\pi\pi^*$	H→L+1 (18) H−1→L (15) H→L+2 (63)	42990 (232.6/ 5.33)	0.04			43393 (230.0/ 5.38)[e]	41377 (241.7/ 5.13)	0.070
S3	nπ^*	H−2→L (85)	47426 (210.7/ 5.88)	0.0003	-		37102 (269.7/ 4.60)[d]		
S4	$\pi\pi^*$	H→L+1 (63) H→L+2 (18)	48717 (205.1/ 6.04)	0.004					
S5	nπ^*	H−2→L+2 (68)	51378 (194.4/ 6.37)	0.001					
S6 (B$_b$)	$\pi\pi^*$	H−1→L (76), H→L+1 (11)	52104 (191.8/ 6.46)	0.51	480741 (208.2/ 5.96)	22969	47587 (210.3/ 5.90)[d]	50330 (198.7/ 6.24)	0.851
S7	$\pi\pi^*$	H→L+5 (58) H→L+9 (18)	53879 (185.4/ 6.68)	0.011				54201 (184.52/ 6.72)	0.159
S11	$\pi\pi^*$	H−3→L(53) H−1→L+2(26)	55169 (181.3/ 6.84)	0.19	50975 (196.2/ 6.32)	16447	50814 (197.0/ 6.30)[d]	56379 (177.39/ 6.99)	0.565

[a]Excited states are computed with TD-CAM-B3LYP/6-311+G(2d,p)//PCM on Ade•6H$_2$O complex optimized at B3LYP/6-311+G(2d,p)//PCM level; [b]Percentages are calculated as 100 x twice the squares of the coefficients in the CI expansion of TDDFT wave functions; [c]this work; [d]average experimental value from Ref [99] and references therein; [e]Ref [90]; [f] Ref [99] with complete active space multiconfigurational second-order perturbation theory (CASPT2) method on N9H-Ade in gas phase.

In contrast to the large number of studies dealing with low energy excited states, experimental and theoretical investigations of the electronic states of Ade below 230 nm has been limited in number. The position of the strongest electronic transition in this region, 210 nm (B_b) has been identified in independent experimental measurements using magnetic circular dichroism (MCD)[88] and linear dichroism (LD)[92] spectroscopies on several Ade systems, and has also been characterized through RR measurements.[56] In agreement with previous *ab initio* results,[99,100] our TD-DFT calculation (Fig. 6.2 and Table 6.2) also predicts this state as a $\pi\pi^*$ transition (at 191.8 nm) and has a mixed orbital contributions: HOMO − 1 → LUMO (76 %) and HOMO → LUMO + 1 (11 %). Involved molecular orbitals (MO) (Fig. 6.2, Panel a) show that B_b excitation perturbs delocalized π electron density over pyrimidine and imidazole rings, therefore changing the associated bond orders. This suggests RR

enhancement of vibrational modes that are associated with in-plane stretching of aromatic bonds in case of a resonant excitation. A high value of experimentally obtained transition dipole strength, 0.75 Å of this state is also supported by the large value of predicted oscillator strength (0.51).

On the blue side of B_b state, another electronic state (S_{11}, hereafter) is predicted at 181.3 nm (Fig. 6.2 and Table 6.2) with moderate oscillator strength of 0.19 with a HOMO − 3 → LUMO (53 %) and HOMO − 1 → LUMO + 2 (26 %) orbital contribution. (Table 6.2) This state is assigned to the experimental band located at ~196 nm in circular dichroism (CD),[89,90] MCD[88] and polarized absorption spectroscopy.[114] The position of this state helped in deconvolution of the absorption spectrum within 190-230 nm (52500-43500 cm^{-1}).

Fundamental Ade vibrations have been assigned by several groups with semiempirical[51,115–119] and *ab initio* calculations.[29,83,120–128] Among the latter type of calculations, McNaughton and coworkers have published the most comprehensive report and assigned SERS spectra of Ade using DFT.[128] Vibrational assignment and potential energy distribution (PED) of all seventeen RR active modes at B3LYP/6-311+G(2d,p)//PCM level of DFT is described in Table 6.3. B3LYP functional has been extensively used for computation of vibrational frequencies of nucleobase systems.[61,83,129–132] Without using any scaling factors, we obtained good agreement between computed and experimental wavenumbers. Though the normal modes computed on Ade•6H$_2$O complex are similar to those calculated on isolated N$_9$H-Ade by McNaughton and coworkers[128] there are subtle differences in the composition of PEDs. These differences originate from site-directed H-bonding interactions at N$_1$, N$_3$, N$_7$, N$_9$-H sites and of the–NH$_2$ moiety with explicit water molecules. These interactions do not drastically alter the composition of PEDs, but changes contribution of individual internal coordinates. After establishing Ade•6H$_2$O as an adequate model for Ade in water, excited state gradient on B_b state complex

6.3.3 Raman depolarization ratios in B_b state

Depolarized and polarized RR spectra of Ade at 215 nm excitation wavelength are depicted in Fig. 6.7, and resulting depolarization ratios (ρ) are described in Table 6.4. Apart from two bands at 1486 and 1602 cm^{-1} all RR active modes of Ade at 215 nm excitation have a ρ value close to 0.33, suggesting a major contribution from a single B_b electronic state. Two aforesaid bands, assigned to the in-plane breathing of pyrimidine and stretching of imidazole rings are perhaps vibronically coupling B_b state with one of the close-lying transitions, thus producing a higher value of the depolarization ratio. As the majority of bands have depolarization ratio 0.33, neglecting vibronic coupling with other electronic states, we consider 'A' term enhancement[133] through FC coupling with B_b electronic state only.

6.3.4 Ultrafast structural dynamics of photoexcited Ade

Simulated absorption and REPs for seventeen resonant modes of Ade at excitations within the B_b absorption band are depicted in Fig. 6.5 and 6.6, and the corresponding parameters are described in Table 6.5. We have obtained a good fit between experimental and simulated cross-sections of both absorption spectra and RR bands of Ade. Though we have obtained ρ value higher than 0.33 for bands at 1486 and 1602 cm^{-1}, simulated REPs of both bands agree reasonably well with experimental values in the rising edge of the spectra. The increase in RR cross-section for all bands other than two bands at 725 and 904 cm^{-1} with Raman excitation below 225 nm indicates a contribution from low-lying excited states, located within the blue edge of the diffuse absorption band at 260 nm. Increase in cross-section at the red edge of REPs of three bands at 1304, 1486 and 1504 cm^{-1} shows strong coupling from lower excited states. It is important to note that though the depolarization ratio of the band at 1402 cm^{-1} is found to be 0.33 at 215 nm excitation, measured REP of this band throughout the 210-230 nm region reveal vibronic coupling contribution from other electronic state.

Table 6.3 Experimental and computed vibrational wavenumbers, PED, normal mode description, dimensionless displacements and internal reorganization energies for all RR modes of adenine.

Exp. wavenum. (cm^{-1})	Comp[a] wavenum. (cm^{-1})	PED[b] (%)	Mode description	$\|\Delta\|$[c]	λ_{int}[d] (cm^{-1})
1602	1624	str N3C4 (12) - be C5N7C8 (11) - H9N9C8 (14) - C4N9C8 (13)	Pyr str	0.32	81.3
1486	1527	- str N7C8 (14) + N6C6 (24) + be C8H (13)	Pyr breath + Imid str	0.221	36.4
1440	1499	- str N7C8 (17) - N3C2 (10) + N1C6 (11) - be C2H (10) - C4N9C8 (10)	In-plane purine def	0.220	34.8
1420	1438	- str N6C6 (11) - N9C4 (26) + be C5N7C8 (22)	In-plane purine def	0.31	68.1
1402	1381	be C2H (20)	Pyr breath	0.11	8.8
1364	1485	- str N9C8 (12) + be H9N9C8 (39) + C2H (21)	CH and NH be	0.27	49.1
1333	1358	str N1C2 (39) + N7C5 (11)	Pyr def	0.30	60.9
1309	1337	str N3C2 (37) + N7C5 (13) - be N1C2N3 (15)	Pyr def	0.20	25.6
1251	1284	str N7C8 (27) + N1C2 (10) + be C8H (29)	Imid def	0.37	83.7
1231	1243	str N7C5 (32) - be N6C6C5 (10) + C6N6H6a (12)	Rock NH$_2$	0.19	21.3
1142	1143	str N9C8 (13) + be C5N7C8 (21) - C8H (24)	Pyr breath	0.17	16.5
1120	1176	str N9C8 (39) - be N7C8N9 (11)	Imid def	0.51	145.9
1021	1029	str N1C6 (32) + rock NH$_2$ (16)	Rock NH$_2$	0.39	76.2
904	923	- be C6N1C2 (10) + N1C2N3 (20) + C4N9C8 (13)	In-plane pyr def	0.31	42.5
725	742	- str N3C4 (12)	In-phase pyr + imid breath	0.80	230.0
				Total	981

[a]without scaling and computed at B3LYP/6-311+G(2d,p) level on N9H-Ade•6H$_2$O complex with PCM solvation; [b]Potential energy distributions (PEDs) of each normal mode computed using

VEDA4.0 program, sign indicates relative phase of movement of internal coordinates; [c]best-fitted dimensionless Δ's for all RR active modes of adenine with parameters described in Table 6.5; [d]mode specific internal reorganization energies calculated using the relation, $\lambda_k = (\Delta_k^2 \omega_k)/2$; Abbreviations, str, bond stretching; be, angle bending; out, out of plane motion; tors, torsional vibration and rock, rocking motion of exocyclic amino group; def, in-plane ring deformation; breath, ring breathing; rock, rocking motion; Pyr, pyrimidine ring; Imid, imidazole ring.

Table 6.4 Depolarization ratios for Raman bands of adenine obtained at an excitation wavelength of 215 nm.

| RR Band (cm-1)	Depolarization ratio (ρ)
725	0.33
1021	0.34
1120	0.28
1142	0.38
1231	0.33
1251	0.37
1309	0.31
1333	0.49
1364	0.18
1402	0.33
1420	0.31
1486	0.60
1602	0.51

Table 6.5 Parameters used in the self-consistent simulation of REPs and absorption spectra of adenine in L_a and B_a electronic states, and comparison with GMP.

	Molecule	Excited State	E_0 (cm^{-1})	Λ (cm^{-1})	τ (fs)	θ (cm^{-1})	M (Å)	λ_{int} (cm^{-1})	λ_S (cm^{-1})	λ_{total} (cm^{-1})
Best-Fit	Ade	B_b	47250	200	26.5	600	0.75	981	1190	2171
Set 1			46900	150	35.4	550	0.75	1413	975	2417
Set 2			47575	300	17.7	675	0.75	628	1325	1966
	9-meA[a]	L_a	37200	70.5	75.3	1000	0.87	168	1200	1368
Best-Fit	GMP	B_b	49100	250	21.2	1350	0.96	995	2550	3545

[a]from Ref [27], For 9-meA; solvent correlation time, τ ($= 1/2\pi c\Lambda$) is calculated from reported solvent reorganization energy, λ_s = of 1200 cm^{-1} and its relation with coupling strength (D): $D^2 = 2\lambda_s k_B T$ with the high-temperature limit assumption, Λ/D=0.1; where c is speed of light, k_B is Boltzmann constant and T is temperature in K. In this published work, RR intensity analysis was performed on 9-meA throughout its first singlet excited state (L_a) centered at ~ 260 nm. Set 1 and Set 2 set of parameters are obtained by decreasing and increasing the best fitted Δ values by 20 % and adjusting E_0, λ_S, θ, and Λ iteratively.

Structural distortions of different internal coordinates that contribute in PED of each of the RR active modes of Ade in B_b electronic state are deduced from best-fitted Δ's using eqn. 2.28 and are presented in Table 6.6. The breadth of

the diffuse absorption band shape is primarily determined by the relative contribution of Δs of all FC active vibrational modes. Thus, though measured REPs lie on the red edge of the B_b absorption band and do not cover both sides of the spectrum, a correctly deconvoluted absorption spectrum guarantees reliable estimation of the Δs. A correct deconvolution (Fig. 6.2, b) is possible because the position of B_b state is already determined in previously published reports.
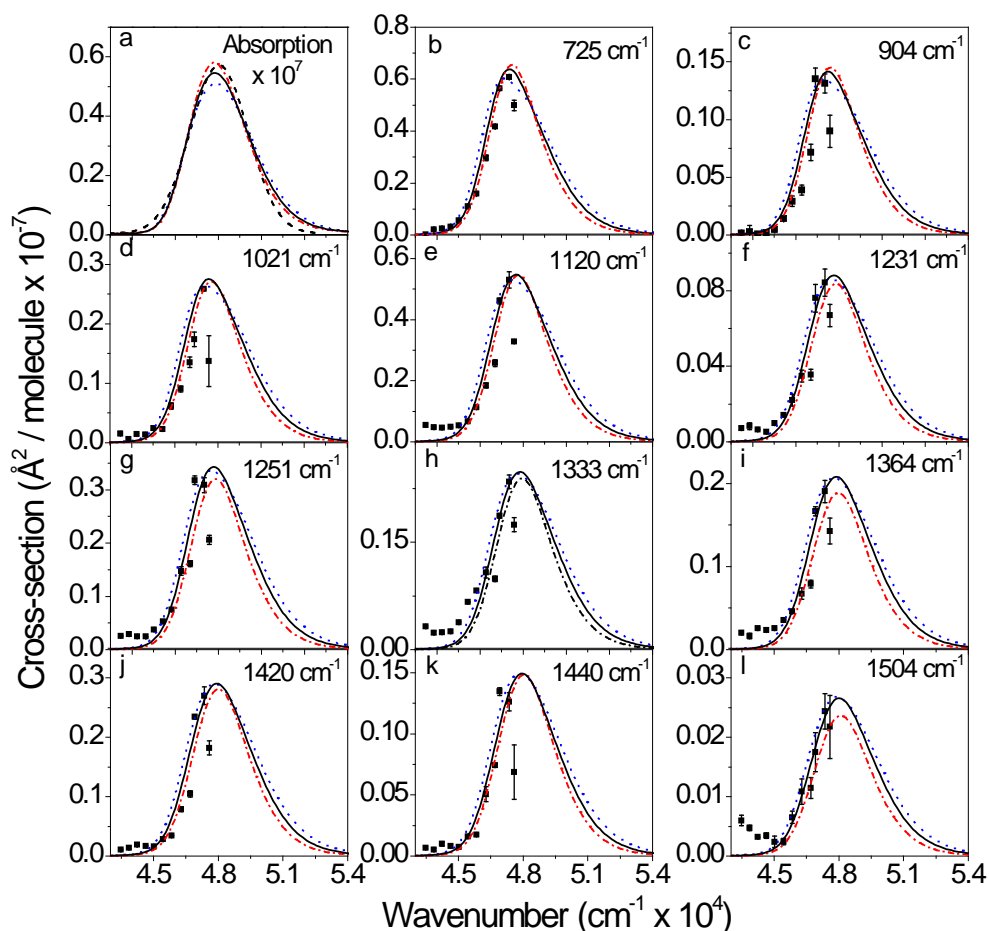

Fig. 6.5 Experimental and simulated Raman excitation profiles and absorption cross-section in the 210-230 nm absorption band of adenine. (a) Experimental (dashed) and simulated (solid) absorption spectrum. (b–l) Experimental (points) and simulated (solid) Raman excitation profiles for eleven resonant modes of adenine. The simulated absorption and Raman excitation profiles were obtained by using the parameters in Table 6.5. Set 1 (*red dash dot*) and Set 2 (*blue dot*) were obtained with two sets of deltas obtained by decreasing and increasing 20% those values in the best fit respectively.

In a previous study, nuclear dynamics of 9-meA following photoexcitation within the 260 nm absorption band is reported.[27] Both, Ade and 9-meA have the same UV chromophore, differing with respect to the N9 substituent, which is a methyl moiety in the latter in place of a hydrogen atom in the former. Despite the difference in

the details of deactivation pathways, non-radiative relaxation of 9-meA and Ade following 267 nm excitation are found to be very similar with sub-ps decay constants.[4,9]
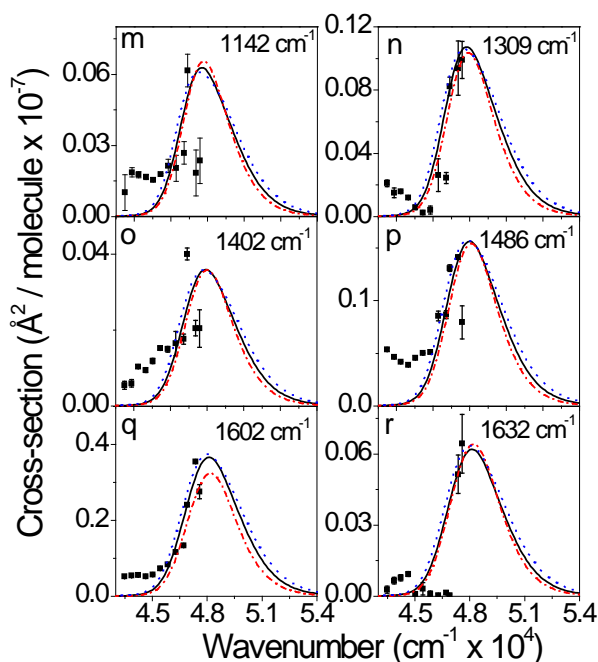
Fig. 6.6 Experimental and simulated Raman excitation profiles of the other five resonant modes of adenine. The simulated Raman excitation profiles were obtained by using the same sets of parameters as in Fig. 6.5.
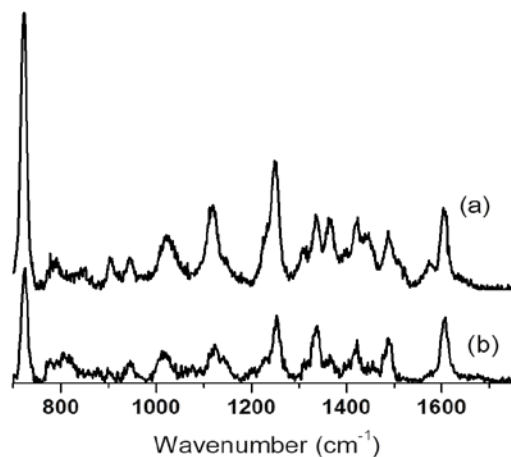
Fig. 6.7 (a) Parallel polarized and (b) depolarized RR spectra of aqueous adenine with 215 nm laser excitation. Incident laser power on sample was was 0.6 mw and sample concentration was 2 mM in miliQ water.

Due to heavy substitution at the N9 site, the positions of fundamental vibrations of Ade differ a little from those reported for 2′-deoxyadenosine (Ado),[80] adenosine-5′-monophosphate (AMP),[52] 2′-deoxyadenosine 5′-monophosphate (dAMP) and 9-meA.[27,116,117,134] Additionally, a methyl group which is heavier than hydrogen alters PED of modes that are mainly localized on the imidazole part of Ade. For a direct comparison between structural distortions following photoexcitation to either L_a or B_b states, changes in internal coordinates of 9-meA need to be determined separately. For this purpose, 9-meA in solution was modeled as 9-meA•5H$_2$O (Fig. 6.8 and Table 6.7) and vibrational normal modes were computed (Table 6.8). Calculated PEDs are in agreement with previously published results.[30] These ground

state normal modes were used to convert published Δs[27] into changes in internal coordinates (Table 6.6) according to eqn. 2.28.

Table 6.6 Internal coordinates that undergo the largest distortion following photoexcitation into B_b and L_a states, and during cation formation in Ade.

Internal coordinates description	Ade•6H$_2$O[a]		9-meA•5H$_2$O[b]		Adenine Cation[c]
	Value in ground state	Changes in B_b state	Value in ground state	Changes in L_a state[b]	Changes in adenine cation from ground state structure
Bond length	(Å)	(Å)	(Å)	(Å)	(Å)
N1–C2	1.3363	-0.045	1.3364	-0.048	-0.02
C2=N3	1.3280	0.016	1.3289	0.022	0.04
C2–H2	1.0849	0.000	1.085	0.000	-
N3–C4	1.3453	0.021	1.3431	0.034	-0.03
C4=C5	1.3933	-0.007	1.3933	-0.004	0.03
C5–C6	1.4158	-0.014	1.4158	0.020	0.02
C6=N1	1.3590	-0.077	1.3586	-0.015	0.01
C5–N7	1.3860	-0.020	1.3842	-0.016	-0.04
N7=C8	1.3153	-0.013	1.3140	0.014	0.04
C8–N9	1.3620	0.015	1.3656	0.032	-0.03
N9–C4	1.3679	0.021	1.3718	0.055	0.01
C6–N6	1.2453	-0.041	1.3341	-0.004	-0.03
N9– H	1.4575	-0.001	-	-	-
N9– C$_{me}$	1.4577	-	1.4577	0.025	-
C8– H	1.0788	-0.001	1.0792	0.003	-

[a]Best-fit Δs for Ade in B_b electronic state are converted into changes into internal coordinates using eqn. 2.28. To do so, gradient on B_b (state S6 in Table 6.2) excited state using TD-CAM-B3LYP methos was determined using eqn. 2.31 (See Chapter 2); [b]Reported best-fit Δs for 9-meA in L_a state are taken form Ref [27] and converted into changes into internal coordinates using the same method. For both complex (Ade•6H$_2$O and 9-meA•5H$_2$O) ground state normal mode vectors are evaluated at B3LYP/6-311+G(2d,p)//PCM level; (see Table 6.3 and 6.8 respectively) [c]computed change in bond lengths of adenine cation from those of neutral molecule at PBE/TZP level of DFT from Ref [135].

Instantaneous charge redistribution that follows photoexcitation to B_b state brings about major changes in internal coordinates of pyrimidine and imidazole rings (Table 6.6). In general, bond order of all the double bonds increases and those of the single bonds decreases. Specifically, N1–C2 and C6=N1 bonds of pyrimidine, and C5–N7 and N9–C4 bonds of imidazole ring suffer maximal distortions. Purine ring of 9-meA experiences major distortions in the bonds of imidazole ring subsequent to L_a excitation. We find that photoabsorption by two $\pi\pi^*$ states (L_a and B_b) of Ade have contrasting effect on the geometry of pyrimidine ring; while excitation to B_b state

leads to overall contraction, L_a state does no induce overall distortion of the same. Photoabsorption by B_b state causes major distortion (-0.077 Å) of the C6=N1 bond; a fact also observed in two other purine systems studied in this thesis, namely, guanosine-5′-monophosphate (GMP) and 6-chloroguanine in case of B_b photoexcitation. (See Chapter 04 and Chapter 05).
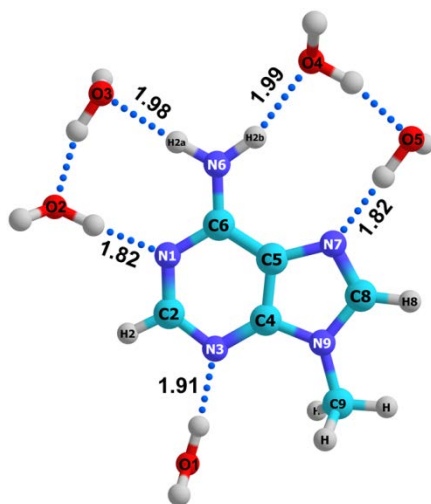
Fig. 6.8 Energy optimized structure of neutral 9-meA in solution as 9-meA•5H$_2$O complex at B3LYP/6-311+G(2d,p)//PCM level of theory used for computation of excited states. All H bond distances (in Å) between water molecules and base along with conventional numbering of ring atoms are mentioned.

Excitation into both of the electronic states distorts internal geometry of the imidazole ring, C4–C5, C5–N7, C8–N9 and N9–C4 bonds in same direction and N7=C8 in opposite direction. Taking into account the directions of the changes in each internal coordinate, we further find that B_b excitation does not cause overall distortion of the imidazole ring, whereas L_a excitation results in expansion of the same. Covalent bonds involving exocyclic hydrogen atoms and either C or N atoms do not get affected significantly due to excitation to either of the ππ* states. This is supported by excited state dynamics simulation[19] which show that no dissociative state of πσ* character associated with the abstraction of exocyclic hydrogens forms within tens of fs of photoexcitation to L_a state.

Computed transition dipole of L_a excited state of Ade is aligned along the center of the short molecular axis (C4–C5) and the C_6 atom, and that of B_b states is directed from C_5 towards C_2 (Fig. 6.1). This opposite orientation with respect to the exocyclic amino moiety suggests a difference in alteration of electron density on the C6–N6 bond upon photoexcitation to two different states. The amino scissoring mode at 1680 cm^{-1} does not couple with B_b electronic state and therefore does not show RR enhancement. However, we find that the C6–N6 bond instantaneously shortens by 0.041 Å from ground state value after B_b photoexcitation. This effect is due to mixing of the C6–N6 stretching coordinate with intense ring stretching modes rather than direct FC coupling of the mentioned coordinate with the excited electronic state. The

latter type of coupling is also found in the case of guanine chromophore, where excitation to L_b (252 nm) state electronically enhance exocyclic NH_2 (at C2 position) scissoring vibration at 1607 cm^{-1} and subsequently weakens the C2–N2 bond. (Chapter 05) Excitation to L_a state does not cause any major distortion of the C6–N6 bond, but affects the other exocyclic bond *viz.*, the N9–C9 one. Though the $-CH_3$ moiety does not actively participate in electronic excitation, the N9–methyl bond is found to weaken following photoabsorption.

The magnitude of distortions are obtained with the help of sign of Δs computed from TD-DFT gradients evaluated on B_b state at ground state geometry and ground state normal mode vectors and wavenumbers. The ground state normal modes that converts the Δs to changes in internal coordinates is expected to vary a little with change in choice of functional or the explicitly solvated complex. In chapter 04, it has been shown that the computed signs of Δs do not depend on the choice of the used density functionals.

6.3.5 Implications for photoproduct formation

Ionizing radiation and UV excitation interact with the electrons of the π conjugated purine ring and may induce selective bond cleavage. Ionization and dissociation experiments, supported by *ab initio* calculations have concluded that primary fragmentation of neutral Ade initiates through cleavage of one of the C2=N3, C5–C6 or N7–C8 bonds.[135–141] Among these three bonds, while only the C2=N3 bond of the pyrimidine ring weakens by 0.016 Å following B_b excitation, all of them experience lengthening in the case of L_a excitation. (Table 6.6). Thus, UV-B and UV-C excitation may assist fragmentation of Ade. Photoabsorption by either L_a or B_b state weakens the C8–N9 bond of the imidazole ring, and therefore may favor cleavage of the same during FaPyA production. None of the RR intensity derived distortions (Table 6.6) subsequent to photoabsorption are found to lie along any dehydrogenation coordinate of Ade.

DFT calculations at PBE/TZP level have deduced the structure of the Ade cation, produced via abstraction of one electron from the neutral molecule.[135] In ionized Ade, the C8 atom has the highest positive charge; which is in agreement with the fact that this site undergoes $^\bullet$OH radical attack.[142] An electron is withdrawn from the N1=C6–C5=C4–N9 bond sequence and from the π cloud localized around C2=N3 and N7=C8 bonds. As a result, all the double bonds of purine ring *i.e.*, N1=C6, C5=C4, C2=N3 and N7=C8, along with two single bonds C6–C5 and C4–N9 weaken (by 0.01, 0.03, 0.04, 0.04, 0.02 and 0.01 Å respectively). At the same time the remaining bonds *i.e.*, N3–C4, C5–N7, N1–C2, C8–N9 and C6–N6 become stronger (by 0.03, 0.04, 0.02, 0.03, 0.03 Å respectively).

Table 6.7 XYZ Coordinates (Å) of energy optimized ground state structure of 9-meA•$5H_2O$ complex[a]

Atom No.		X	Y	Z	Atom No.		X	Y	Z
1	N	-0.297237	-1.678546	-0.028057	18	H	-1.094161	3.341764	-0.04686
2	C	1.017778	-1.916379	-0.033895	19	H	-1.680875	4.532127	-0.868388
3	N	2.010277	-1.032835	-0.019907	20	N	-2.071295	-0.183694	-0.000767
4	C	1.557242	0.23146	-0.001269	21	H	-2.722508	-0.96788	-0.01598
5	C	0.221103	0.62628	0.003181	22	H	-2.475492	0.749395	0.036502
6	C	-0.754734	-0.399443	-0.007994	23	H	1.305373	-2.962441	-0.05133
7	N	2.295054	1.387902	0.014014	24	O	-1.863913	-4.009425	-0.044403
8	C	1.391994	2.412204	0.025601	25	H	-1.67103	-4.512285	0.755704
9	N	0.141651	2.008117	0.019105	26	H	-1.282154	-3.205633	-0.009704
10	H	1.71047	3.443287	0.037533	27	O	-3.807268	2.225476	0.065999
11	O	-4.086714	-2.405311	0.012249	28	H	-4.301717	2.310282	0.889373
12	H	-4.615343	-2.50244	-0.788278	29	H	-3.191787	2.99278	0.043861
13	H	-3.414365	-3.12232	-0.02206	30	C	3.748583	1.498618	0.018956
14	O	4.634442	-2.219435	-0.090229	31	H	4.156946	1.024316	0.910247
15	H	3.762502	-1.769361	-0.038669	32	H	4.162392	1.020695	-0.867659
16	H	4.909785	-2.339418	0.825531	33	H	4.015414	2.552482	0.017802
17	O	-1.778346	4.057646	-0.034344					

[a]computed at B3LYP/6-311+G(2d,p)//PCM level.

Directions of instantaneous distortions along N1–C2, C2=N3, C5–N7 and C6–N6 bonds upon B_b excitation and along N1–C2, C2=N3, C5–C6, C5–N7, N7–C8 and N9–C4 bonds after L_a excitation are in agreement with structural changes associated with a cation formation. However, the magnitude and direction of concomitant changes in all involved bonds do not lie along the cation formation coordinate in either excited states. (Table 6.6)

6.3.6 Linewidth broadening and ultrafast solvation

The linewidth of electronic absorption spectrum and REPs of vibrational modes can be partitioned into two components: (i) homogeneous broadening, originating from the dynamic fluctuation of transition energies due to solvent-induced dephasing, and (ii) inhomogeneous broadening, arising due of spectroscopically distinct solutes in different local solvation environments. The homogeneous component is associated with the interaction between solute transition dipole and a set of low frequency solvent vibrations that is collectively described by a single mode. Within the Brownian oscillator model,[66,143] this is described as solvent reorganization energy (λ_{solv}), obtained at 1190 cm^{-1} for Ade in B_b electronic state. Owing to an instantaneous change in charge distribution of the solute, the solvent (water) molecules undergo reorientation. Because FC states are generated within tens of fs of photoabsorption, and Raman, being a scattering phenomenon also takes place simultaneously; this dynamical component of solvation represents the inertial response of the first solvation shell. We also determine a solvent correlation time (τ) of 26.5 fs corresponding to this ultrafast inertial dynamics of water., and also found for other chromophores using RR intensity analysis.[61]

A similar magnitude of homogeneous linewidth (1200 cm^{-1}) was obtained for 9-meA in L_a excited state[27] (Table 6.5). In spite of the difference in strengths and directions of L_a and B_b state transition dipoles, a comparable magnitude of solvent reorganization energy indicates similar overall coupling strength between the solvent bath and both the electronic states. The reported value of λ_{Solv} =1200 cm^{-1} for 9-meA in L_a state corresponds to a solvent correlation time of 75.3 fs[27] which is ~ 3 times larger than that estimated (26.5 fs) (Table 6.5) for Ade in B_b state in the current study. I have obtained a similar < 30 fs solvent relaxation time for another purine, GMP and 6-ClG in its B_b excited state. (Chapter 04 and Chapter 05) The obtained solvent correlation time of 26.5 fs is also in agreement with reported experimental measurements[61,144–148] and molecular dynamics simulations[149–152] detecting the presence of an ultrafast component of water response following photoexcitation. Instead of using λ_{Solv} as a parameter to estimate an inverse of solvent correlation time (Λ) within the high-temperature limit[27] (see description in Table 6.5) we obtain it through independent iterations of both, λ_{Solv} and τ. We note that simulated REPs are not very sensitive to change in the inverse of relaxation time, Λ (= $1/2\pi c\tau$) and we estimate a lower (17.7 fs) and higher (35.4 fs) limit of τ by varying Δs by 20 % from best-fitted values.

Solvation processes that occur at much longer time scales as compared to the RR process are contained in static inhomogeneous broadening (θ) which is determined at 600 cm^{-1} for Ade. Formation of optically distinct species of a solute in water does not depend on the probe wavelength. Thus, the inhomogeneous broadening parameter is an intrinsic characteristic of the chromophore itself rather than of the investigated excited state. A larger value (1000 cm^{-1}) of this parameter was obtained for 9-meA,[27] suggesting a higher number of solvated micro-configurations compared to Ade. Nucleobases with the carbonyl group as an exocyclic substituent, such as 2′-deoxyguanosine (2′-dG), uracil, thymidine and their derivatives are found to have inhomogeneous linewidth lying within 900 cm^{-1} to 1320 cm^{-1} that is higher than that of Ade. Addition of a hydrophilic phosphate moiety (in GMP) is also found to increase the value of θ significantly to 1350 cm^{-1} from its corresponding value (900 cm^{-1}) in 2′-dG[46] (see Table 5.3, Chapter 05)

In general, the –CH$_3$ substituent, being a hydrophobic moiety, would tend to decrease interaction of 9-meA with surrounding water molecules, but necessarily would not cause a decrease in the number of micro-solvated clusters. Several studies report on the effect of micro-solvation on pairing and stacking properties of nucleobases,[153–159] but none of them compares solvation structure of Ade with that of 9-MeA on equal footing. Theoretical studies by Hobza and co-workers have found that methylation at N$_9$ site of Ade leads to stacked conformation in comparison to the preferred H-bonded structure in case of canonical bases.[155,156] In agreement with our

finding, the $-CH_3$ moiety was found to increase inhomogeneous broadening contribution in thymine (5-methyluracil) by 200 cm^{-1} from that of uracil.[44,45] Like in thymine, methyl at N$_9$ position in 9-meA is expected to affect the local solvation structure at nearby sites, and therefore might result in the formation of more distinct solvated structures.

6.3.7 Mode specific internal reorganization energy and photostability

Experimental and computed wavenumbers, potential energy distribution (PED), and associated mode-specific internal reorganization energies for intense RR modes of Ade are described in Table 6.3. Seven modes at 725 cm^{-1}, 1021 cm^{-1}, 1120 cm^{-1}, 1251 cm^{-1}, 1333 cm^{-1}, 1420 cm^{-1} and 1602 cm^{-1} contribute to 76 % of the total internal reorganization energy, λ_{int} = 981 cm^{-1}. A similar value of λ_{int} (995 cm^{-1}) obtained for GMP (Table 6.5) indicates a similar amount of absolute magnitude of structural distortions in both cases. Comparable values of total vibrational reorganization energies were obtained for several pyrimidines[43–45,63–65,160] and a purine, 2′-dG[46] in their first bright state. A significantly low value of λ_{int} that was obtained for 9-meA at 168 cm^{-1} (Table 6.5) in the low energetic L_a state,[27] suggesting minimal distortion of the purine ring. Loppnow and co-workers have attributed this to the intrinsic photostability of Ade.[27]

A mixed quantum-classical dynamical simulation of N9H–Ade shows that excitation within the 260 nm band initially populates both L_a and L_b states.[19] Practically, the full population (98.3%) of these two states decays to intermediate $S_{n\pi*}$ state within 60 fs of excitation and exponentially relaxes to S_0 subsequently. This simulation also shows that population transfer between close-lying electronic states starts within 25 fs which is the time scale of RR process also. Thus, the initially prepared vibrational wave-packet hops on to the PES of other electronic states in sub-50 fs time scale instead of decaying on the initially prepared excited state surface. This mechanism would decrease RR cross-section of all FC active modes that are in resonance with L_a excited state. Thus, decreased RR cross-section would naturally lead to the lesser amount of distortions and gets reflected in the low value of λ_{int}.

Comparatively, large internal reorganization energies have been found in guanine in B_b (See Chapter 5) and L_b state[46] and in several natural and substituted pyrimidines in their lowest energy L_a state.[43–45,63–65,160] Surprisingly, the natural pyrimidine bases that also exhibit ~ 1 ps excited state lifetime, but do not have internal reorganization energy as low as that of Ade in L_a state. A 153 cm^{-1} of internal reorganization energy for 2′-dG in L_a state[46] can result from two reasons: (i) a considerably lower transition dipole strength (0.56 Å) of this state and/or (ii) possible sate crossing occurring in the same time scale of the resonance Raman process.

Table 6.8 Experimental and computed wavenumbers, and potential energy distributions (PED) of vibrational modes of 9-meA.

RR, Solution, 257 nm [a]	Raman, Solid [b]	IR, Ar matrix [c]	SERS [d]	Comp. Freq [e]	IR-UV ion-dip, Freq [f]	Comp. Freq [f], Scaled (0.983)	Comp. Freq, 9-meA [g]	Comp. Freq, 9-meA + $5H_2O$ [h]	PED [i]	Assignment
cm^{-1}	cm^{-1}	cm^{-1}	cm^{-1}	cm^{-1}	cm^{-1}	cm^{-1}	cm^{-1}	cm^{-1}	(%)	
1680	1680	1632	-	1630	1632	1627	1636	1694	be $H_{6b}N_6H_{6a}$ (80)	δ_{Sciss} NH_2
1603	1573	1596	1597	1592	1599	1593	1596	1595	str N_3C_4 (24) - N_9C_4 (10)	ν (N_3-C_4) + ν (N_7-C_8) + δ_{Rock} NH_2
1537	1526	-	1568	1575	-	1579	1610	1622	- str N_3C_2 (17) - be $C_6N_1C_2$ (15) + $C_4N_9C_8$ (11) - $N_3C_4C_5$ (10) + $C_5N_7C_8$ (10)	-
-	-	1511	1524	1513	1515	1507	1533	1547	str N_7C_8 (10) - N_6C_6 (13) + be $C_4N_9C_8$ (13) - $H_8C_8N_7$ (13)	ν (N_7-C_8) + ν (N_9-C_9)
1498	1517	1483	-	1494		1489	1506	1506	be $HC_{me}H$ (23)	δ C_2H + CH_3 def + Pyr def
-	-	1449	-	1486	1450	1456	1475	1478	- be $HC_{me}H$ (38) + $HC_{me}H$ (39) + tor $HC_{me}N_9C_8$ (15)	CH_3 def
-	-	1476	1460	-	1470	1473	1492	1505	be $H_2C_2N_1$ (18) + $HC_{me}H$ (34)	δ C_2H + CH_3 def + ν (C_6-N_1) + ν (C_2-N_3)
1437	-	1435	-	1437	1429	1439	1458	1460	- be $HC_{me}H$ (38) + $HC_{me}H$ (39) + tor $HC_{me}N_9C_8$ (15)	CH_3 def + ν (N_7-C_8)
-	-	1411	1406	-	1414	1415	1429	1441	str N_6C_6 (10) - N_9C_4 (18) - be C_2H_2 (12) + $C_5N_7C_8$ (16)	-
-	-	1370	-	-	1369	1369	1390	1398	- str N_9C_4 (11) + be C_2H_2 (28)	-
1343	-	1328	1329	1338	1327	1336	1351	1360	str N_1C_2 (30) + N_7C_5 (11) - be $C_5N_7C_8$ (11)	-
-	-	1344	-	-	1345	1341	1361	1377	str N_9C_8 (28)	Ring Def + ν (C_8-N_9)
-	-	1295	-	-	1292	1307	1323	1335	str N_3C_2 (31) - N_3C_4 (10) + N_7C_5 (13)	-
1254	1256	1254	1242	1257	1256	1254	1274	1280	str N_1C_2 (10) - N_7C_5 (11) + be $H_8C_8N_7$ (31)	-
1208	1230	1234	-	1230	1232	1241	1262	1264	str N_7C_8 (12)	-

									PED	
-	-	-	-	-	1199	1199	1216	1218	str N_7C_5 (22) + be $H_8C_8N_7$ (14)	-
-	-	-	1113	-	1136	1131	1151	1153	be $HC_{me}H$ (17) - $HC_{me}H$ (17) - tor $HC_{me}N_9C_8$ (54)	CH_3 def
-	-	-	-	-	1067	1055	1077	1092	str N_9C_8 (12) + be $C_2N_3C_4$ (12)	δ_{rock} NH_2 + CH_3 def
1010	1047	1044	-	1043	1036	1041	1061	1073	be $N_9C_8N_7$ (23) + tor $HC_{me}N_9C_8$ (13) - $HC_{me}N_9C_8$ (13)	δ_{rock} NH_2 + Imd def + CH_3 def + ν (C_8-N_9)
-	-	-	1015	-	1000	984	1004	1017	str N_1C_6 (32) + be $H_{2b}N_2O_3$ (11)	-
-	-	944	958	-	958	961	975	980	tor $H_2C_2HN_3$ (77) - $N_1C_2N_3C_4$ (10)	γ C_2H
-	-	894	-	-	895	892	908	935	be $N_1C_2N_3$ (22)	Ring def
-	-	843	-	-	841	838	873	877	- tor $H_8C_8HO_5$ (71) - $C_4N_9C_8N_7$ (13)	γ C_8H
-	-	800	-	-	800	796	820	824	tor $N_1C_2N_3C_4$ (17) - $C_6N_1C_2N_3$ (15) - $C_5N_7C_8N_9$ (18) - out $N_3N_9C_5C_4$ (23)	τ_{def} (Pyr + Imd)
728	-	-	735	731	730	734	745	758	str N_9C_8 (13) + N_9C_{me} (19) + be $N_9C_8N_7$ (11)	τ_{def} (Pyr + Imd) + ν (N_9-C_9)
-	-	-	-	714	715	718	726	723	be O1HN3 (12)	-
-	-	681	-	-	673	679	691	700	- tor $H_{6a}N_6C_6C_5$ (12) - $H_{6b}N_6H_{6a}O_3$ (11) - $C_2N_3C_4N_9$ (10) - $N_1C_2N_3C_4$ (13) - $C_6N_1C_2N_3$ (11) + out $N_3N_9C_5C_4$ (17)	τ Ring
601	-	645	620	645	640	650	658	655	tor $C_5N_7C_8N_9$ (46)	τ Ring
-	-	581	-	588	577	578	590	606	be $N_6C_6C_5$ (13) + $H_{2b}N_2O_3$ (13)	τ NH_2
-	-	575	-	563	553	558	570	569	- tor $N_1C_2N_3C_4$ (16) + $C_6N_1C_2N_3$ (19) - $C_4N_9C_8N_7$ (19) - out $N_6N_1C_5C_6$ (14)	τ Ring
535	542	-	536	552	-	532	544	552	str N_9C_4 (11) + N_9C_{me} (14) - be $C_4N_9C_8$ (11) + $C_2N_3C_4$ (21) - $C_{me}N_9C_4$ (13)	Ring def
-	-	-	-	529	-	523	531	542	be $C_6N_1C_2$ (16) - $C_2N_3C_4$ (12) + $N_1C_2N_3$ (10)	τ Ring

[a] Ref [27] RR with 257 nm excitation of aqueous solution at pH 7; [b] Ref [28] FT-IR and Raman with xx nm of polycrystalline state; [c] Ref [117] FT-IR spectra in Ar gas matrix; [d] Ref [134] Surface enhanced Raman scattering (SERS) on adsorbed 9-meA on Ag electrode and with 514.5 nm excitation; [e] Ref [30] Computed at B3LY/6-31G(d)//gas level and scaled according to scaled quantum mechanical (SQM) method described there in; [f] Ref [29] Computed at B3LY/6-311++G(df, pd)//gas level and scaled by 0.983; [g, h] this work. Computed on isolated 9-meA (g) and 9-meA•$5H_2O$ (h) at B3LYP/6-311+G(2d,p)//PCM level and vibrational frequencies are not scaled. [I] normal modes and PEDs are computed on 9-meA•$5H_2O$ complex using VEDA 4.0; Abbreviations: PED: = Potential Energy Distribution; ν = bond stretching; δ and be : in-plane bending, γ and out: out of plane bending; τ and tors: out of plane torsion; sciss: scissoring; rock: rocking

motion; Pyr: pyrrole ring; Imd: imidazole ring; def: ring deformation; twist: twisting motion. Negative sign in front of a contribution in PED indicate out of phase vibration with respect to that with positive sign.

A low internal reorganization energy, 112 cm^{-1} of 6-ClG after excitation within very strong B_b band (dipole strength = 1.11 Å) has been attributed to possible ultrafast population transfer within nearby electronic states. (See Chapter 4) 6-ClG is the first purine that has been found to have such a less value of λ_{int} in higher electronic states below 230 nm. Both Ade and GMP (or Gua) do not possess this characteristic in their respective B_b state.

6.4 Conclusion

A self-consistent analysis of REPs and absorption spectra combined with *ab initio* DFT calculations unveil ultrafast structural dynamics of photoexcited Ade on B_b electronic state. Initial photodynamics is found to be dominated by seven FC active modes at 725 cm^{-1}, 1021 cm^{-1}, 1120 cm^{-1}, 1251 cm^{-1}, 1333 cm^{-1}, 1420 cm^{-1} and 1602 cm^{-1}. Together these modes constitute 76 % of the total vibrational reorganization following photoexcitation. Derived dimensionless Δs give excited state structure in terms of distortions from that in the ground electronic state. We also combine and compare the outcome of a previously published paper reporting RR intensity derived distortions of the same chromophore on L_a excited state. We find that the overall structure of the pyrimidine ring gets majorly distorted following excitation to B_b state and the imidazole ring undergoes maximum changes subsequent to L_a excitation.

We obtain an < 50 fs component of solvation associated with the inertial response of the first solvation shell of Ade. This is in agreement with the previously reported fastest component of water response using a variety of chromophores as probes and using a plethora of techniques including RR intensity analysis. Similar solvation time scales are obtained in the case of two other purines studied in this thesis. (Chapter 4 and 5) Though photoexcitation into L_a and B_b singlet states of Ade results in significantly different charge redistribution, and therefore distinctive distortions of the purine ring, it produces almost identical solvent reorganization energy in both states. On B_b singlet state about half (55 %) of total RR intensity derived reorganization energy originates from the inertial response of water, but in case of L_a excitation it is dominated (88 %) by ultrafast solvation only. Apart from the weakening of the C8–N9 bond of the imidazole ring, none of the two singlet excited states, L_a and B_b induces any distortions that lie along the formation coordinate of the Ade cation or other major ring-cleaving lesions. These findings support the hypothesis that photostability in UV-C region might have played a key role behind the natural selection of Ade as one of the ingredients for our gene.

6.5 Future outlook on photodynamics of nucleobases in deep-UV

Using RR intensity analysis, characteristics of π-π* electronic states within 210-230 nm of purines are uncovered. Interactions between several close-lying electronic states are found to play a crucial role in driving the initial dynamics following photoabsorption. RR intensity analysis is shown to be a unique method to derive initial dynamics of purines upon excitation within high energy electronic excited states that are not possible to be investigated using traditional ultrafast spectroscopies such as fs transient absorption and fs fluorescence up-conversion techniques. Herein reported results on three purines; 6-ClG, GMP, and Ade (Chapter 4, 5 and 6) warrant future experimental and theoretical efforts to obtain the general attribute of the high-lying excited states of purines, and in general the broad family of nucleic acid bases. These investigations, if performed on several nucleobases and their analogs, can potentially unravel new insights on photo-reaction dynamics of our genetic alphabets upon irradiation of deep-UV. Investigating nucleobases with UV-C photon below 230 nm of wavelength presents with an opportunity to understand possible photo-reactions during the prebiotic era when solar flux in deep-UV was considerably higher (Fig 1.6) than today's value. Herein reported experimental RR cross-sections of nucleobases within B_b absorption band would also serve as a stringent parameter for validation and future improvement of application of time-dependent DFT for high-lying valence excited states.

References

[1]   B. Cohen, P. M. Hare, B. Kohler, *J. Am. Chem. Soc.* **2003**, *125*, 13594.

[2]   I. Conti, M. Garavelli, G. Orlandi, *J. Am. Chem. Soc.* **2009**, *131*, 16108.

[3]   C. E. Crespo-Hernández, L. Martínez-Fernández, C. Rauer, C. Reichardt, S. Mai, M. Pollum, P. Marquetand, L. González, I. Corral, *J. Am. Chem. Soc.* **2015**, *137*, 4368.

[4]   T. Gustavsson, N. Sarkar, I. Vayá, M. C. Jiménez, D. Markovitsi, R. Improta, *Photochem. Photobiol. Sci.* **2013**, *12*, 1375.

[5]   H. Kang, K. T. Lee, B. Jung, Y. J. Ko, S. K. Kim, *J. Am. Chem. Soc.* **2002**, *124*, 12958.

[6]   H. Kang, B. Jung, S. K. Kim, *J. Chem. Phys.* **2003**, *118*, 6717.

[7]   S. Ullrich, T. Schultz, M. Z. Zgierski, A. Stolow, *Phys. Chem. Chem. Phys.* **2004**, *6*, 2796.

[8]   S. Ullrich, T. Schultz, M. Z. Zgierski, A. Stolow, *J. Am. Chem. Soc.* **2004**, *126*, 2262.

[9]   C. Canuel, M. Mons, F. Piuzzi, B. Tardivel, I. Dimicoli, M. Elhanine, *J. Chem. Phys.* **2005**, *122*, 074316.

[10] H.-H. Ritze, H. Lippert, E. Samoylova, V. R. Smith, I. V Hertel, W. Radloff, T. Schultz, *J. Chem. Phys.* **2005**, *122*, 224320.

[11] C. Canuel, M. Elhanine, M. Mons, F. Piuzzi, B. Tardivel, I. Dimicoli, *Phys. Chem. Chem. Phys.* **2006**, *8*, 3978.

[12] H. Satzger, D. Townsend, M. Z. Zgierski, S. Patchkovskii, S. Ullrich, A. Stolow, *Proc. Natl. Acad. Sci.* **2006**, *103*, 10196.

[13] C. Z. Bisgaard, H. Satzger, S. Ullrich, A. Stolow, *ChemPhysChem* **2009**, *10*, 101.

[14] A. L. Sobolewski, W. Domcke, *Eur. Phys. J. D* **2002**, *20*, 369.

[15] C. M. Marian, *J. Chem. Phys.* **2005**, *122*, 104314.

[16] S. Perun, A. L. Sobolewski, W. Domcke, *J. Am. Chem. Soc.* **2005**, *127*, 6257.

[17] L. Serrano-Andres, M. Merchan, A. C. Borin, *Proc. Natl. Acad. Sci.* **2006**, *103*, 8691.

[18] L. Serrano-Andrés, M. Merchán, A. C. Borin, *Chem. - A Eur. J.* **2006**, *12*, 6559.

[19] M. Barbatti, H. Lischka, *J. Am. Chem. Soc.* **2008**, *130*, 6831.

[20] Y. Lei, S. Yuan, Y. Dou, Y. Wang, Z. Wen, *J. Phys. Chem. A* **2008**, *112*, 8497.

[21] E. Fabiano, W. Thiel, *J. Phys. Chem. A* **2008**, *112*, 6859.

[22] R. Mitrić, U. Werner, M. Wohlgemuth, G. Seifert, V. Bonačić-Koutecký, *J. Phys. Chem. A* **2009**, *113*, 12700.

[23] M. Barbatti, A. J. A. Aquino, J. J. Szymczak, D. Nachtigallova, P. Hobza, H. Lischka, *Proc. Natl. Acad. Sci.* **2010**, *107*, 21453.

[24] A. N. Alexandrova, J. C. Tully, G. Granucci, *J. Phys. Chem. B* **2010**, *114*, 12116.

[25] M. Barbatti, Z. Lan, R. Crespo-Otero, J. J. Szymczak, H. Lischka, W. Thiel, *J. Chem. Phys.* **2012**, *137*, 22A503.

[26] M. Barbatti, *J. Am. Chem. Soc.* **2014**, *136*, 10246.

[27] S. A. Oladepo, G. R. Loppnow, *J. Phys. Chem. B* **2011**, *115*, 6149.

[28] R. Savoie, D. Poirier, L. Prizant, A. L. Beauchamp, *J. Raman Spectrosc.* **1981**, *11*, 481.

[29] G. C. P. van Zundert, S. Jaeqx, G. Berden, J. M. Bakker, K. Kleinermanns, J. Oomens, A. M. Rijs, *ChemPhysChem* **2011**, *12*, 1921.

[30] Y. Xue, D. Xie, G. Yan, *Int. J. Quantum Chem.* **2000**, *76*, 686.

[31] C. S. Cockell, J. A. Raven, *Philos. Trans. R. Soc. A Math. Phys. Eng. Sci.* **2007**, *365*, 1889.

[32] C. S. Cockell, in *Ecosyst. Evol. Ultrav. Radiat.*, Springer New

York, New York, NY, **2001**, pp. 1–35.

[33] S.-Y. Lee, E. J. Heller, *J. Chem. Phys.* **1979**, *71*, 4777.

[34] A. B. Myers, Excited State Structure and Dynamics of Polyenes and Bacteriorhodopsin from Resonance Raman Intensities, University of California, Berkeley, **1984**.

[35] A. B. Myers, R. A. Mathies, in *Biol. Appl. Raman Spectrosc. Vol. 2 - Reson. Raman Spectra Polyenes Aromat.* (Ed.: T.G. Spiro), John Wiley & Sons Inc, New York, **1987**, pp. 1–58.

[36] A. B. Myers, in *Laser Tech. Chem.* (Eds.: A.B. Myers, T.R. Rizzo), Wiley-Interscience, New York, **1995**, p. 325.

[37] L. D. Ziegler, B. Hudson, D. P. Strommen, W. L. Peticolas, *Biopolymers* **1984**, *23*, 2067.

[38] W. L. Kubasek, B. Hudson, W. L. Peticolas, *Proc. Natl. Acad. Sci.* **1985**, *82*, 2369.

[39] S. P. A. Fodor, R. P. Rava, T. R. Hays, T. G. Spiro, *J. Am. Chem. Soc.* **1985**, *107*, 1520.

[40] S. P. A. Fodor, T. G. Spiro, *J. Am. Chem. Soc.* **1986**, *108*, 3198.

[41] A. Toyama, H. Takeuchi, I. Harada, *J. Mol. Struct.* **1991**, *242*, 87.

[42] A. Toyama, Y. Takino, H. Takeuchi, I. Harada, *J. Am. Chem. Soc.* **1993**, *115*, 11092.

[43] B. E. Billinghurst, G. R. Loppnow, *J. Phys. Chem. A* **2006**, *110*, 2353.

[44] S. Yarasi, P. Brost, G. R. Loppnow, *J. Phys. Chem. A* **2007**, *111*, 5130.

[45] S. Yarasi, S. Ng, G. R. Loppnow, *J. Phys. Chem. B* **2009**, *113*, 14336.

[46] A. F. El-Yazbi, A. Palech, G. R. Loppnow, *J. Phys. Chem. A* **2011**, *115*, 10445.

[47] G. J. J. Thomas, M. Tsuboi, *Adv. Biophys. Chem* **1993**, *3*, 1.

[48] Z. Q. Wen, G. J. Thomas, *Biopolymers* **1998**, *45*, 247.

[49] N. Jayanth, S. Ramachandran, M. Puranik, *J. Phys. Chem. A* **2009**, *113*, 1459.

[50] Y. Nishimura, M. Tsuboi, W. L. Kubasek, K. Bajdor, W. L. Peticolas, *J. Raman Spectrosc.* **1987**, *18*, 221.

[51] Z. Dhaouadi, M. Ghomi, J. C. Austin, R. B. Girling, R. E. Hester, P. Mojzes, L. Chinsky, P. Y. Turpin, C. Coulombeau, *J. Phys. Chem.* **1993**, *97*, 1074.

[52] A. Toyama, N. Hanada, Y. Abe, H. Takeuchi, I. Harada, *J. Raman Spectrosc.* **1994**, *25*, 623.

[53] N. Fujimoto, A. Toyama, H. Takeuchi, *J. Mol. Struct.* **1998**, *447*, 61.

[54] A. Toyama, Y. Miyagawa, A. Yoshimura, N. Fujimoto, H. Takeuchi, *J. Mol. Struct.* **2001**, *598*, 85.

[55] N. Jayanth, M. Puranik, *J. Phys. Chem. B* **2011**, *115*, 6234.

[56] J. R. Perno, C. A. Grygon, T. G. Spiro, *J. Phys. Chem.* **1989**, *93*, 5672.

[57] X. Zhao, J. A. Burt, J. L. McHale, *J. Chem. Phys.* **2004**, *121*, 11195.

[58] A. M. Moran, A. M. Kelley, *J. Chem. Phys.* **2001**, *115*, 912.

[59] X. Cao, J. L. McHale, *J. Chem. Phys.* **1998**, *109*, 1901.

[60] M. R. Waterland, S. L. Howell, K. C. Gordon, *J. Phys. Chem. A* **2007**, *111*, 4604.

[61] E. A. Milán-Garcés, S. Kaptan, M. Puranik, *Biophys. J.* **2013**, *105*, 211.

[62] C. M. Stuart, R. R. Frontiera, R. A. Mathies, *J. Phys. Chem. A* **2007**, *111*, 12072.

[63] B. E. Billinghurst, R. Yeung, G. R. Loppnow, *J. Phys. Chem. A* **2006**, *110*, 6185.

[64] S. S. Ng, F. Teimoory, G. R. Loppnow, *J. Phys. Chem. Lett.* **2011**, 2362.

[65] B. E. Billinghurst, S. A. Oladepo, G. R. Loppnow, *J. Phys. Chem. B* **2012**, *116*, 10496.

[66] B. Li, A. E. Johnson, S. Mukamel, A. B. Myers, *J. Am. Chem. Soc.* **1994**, *116*, 11039.

[67] D. J. Tannor, E. J. Heller, *J. Chem. Phys.* **1982**, *77*, 202.

[68] G. R. Loppnow, R. A. Mathies, *Biophys. J.* **1988**, *54*, 35.

[69] A. B. Myers, *Acc. Chem. Res.* **1997**, *30*, 519.

[70] M. T. Chenon, R. J. Pugmire, D. M. Grant, R. P. Panzica, L. B. Townsend, *J. Am. Chem. Soc.* **1975**, *97*, 4636.

[71] M. Dreyfus, G. Dodin, O. Bensaude, J. E. Dubois, *J. Am. Chem. Soc.* **1975**, *97*, 2369.

[72] N. C. Gonnella, H. Nakanishi, J. B. Holtwick, D. S. Horowitz, K. Kanamori, N. J. Leonard, J. D. Roberts, *J. Am. Chem. Soc.* **1983**, *105*, 2050.

[73] B. Cohen, P. M. Hare, B. Kohler, *J. Am. Chem. Soc.* **2003**, *125*, 13594.

[74] T. G. Burova, V. V Ermolenkov, G. N. Ten, R. S. Shcherbakov, V. I. Baranov, I. K. Lednev, *J. Phys. Chem. A* **2011**, *115*, 10600.

[75] S. Miertuš, E. Scrocco, J. Tomasi, *Chem. Phys.* **1981**, *55*, 117.

[76] J. Tomasi, B. Mennucci, R. Cammi, *Chem. Rev.* **2005**, *105*, 2999.

[77] D. C. Blazej, W. L. Peticolas, *Proc. Natl. Acad. Sci. U. S. A.* **1977**, *74*, 2639.

[78] S. P. A. Fodor, R. P. Rava, T. R. Hays, T. G. Spiro, *J. Am. Chem. Soc.* **1985**, *107*, 1520.

[79] C. A. Grygon, T. G. Spiro, *Biopolymers* **1990**, *29*, 707.

[80] A. Toyama, H. Takeuchi, I. Harada, *J. Mol. Struct.* **1991**, *242*, 87.

[81] R. Improta, V. Barone, **2014**, pp. 329–357.

[82] V. Karunakaran, K. Kleinermanns, R. Improta, S. A. Kovalenko, *J. Am. Chem. Soc.* **2009**, *131*, 5839.

[83] M. Shanmugasundaram, M. Puranik, *Phys. Chem. Chem. Phys.* **2011**, *13*, 3851.

[84] Y. Zhao, Z. Cao, *J. Theor. Comput. Chem.* **2013**, *12*, 1341013.

[85] N. Kungwan, K. Kerdpol, R. Daengngern, S. Hannongbua, M. Barbatti, *Theor. Chem. Acc.* **2014**, *133*, 1480.

[86] X. Liu, A. L. Sobolewski, R. Borrelli, W. Domcke, *Phys. Chem. Chem. Phys.* **2013**, *15*, 5957.

[87] L. B. Clark, I. Tinoco, *J. Am. Chem. Soc.* **1965**, *87*, 11.

[88] W. Voelter, R. Records, E. Bunnenberg, C. Djerassi, *J. Am. Chem. Soc.* **1968**, *90*, 6163.

[89] W. C. Brunner, M. F. Maestre, *Biopolymers* **1975**, *14*, 555.

[90] C. A. Sprecher, W. C. Johnson, *Biopolymers* **1977**, *16*, 2243.

[91] P. R. Callis, *Annu. Rev. Phys. Chem.* **1983**, *34*, 329.

[92] A. Holmén, A. Broo, B. Albinsson, B. Nordén, *J. Am. Chem. Soc.* **1997**, *119*, 12240.

[93] L. B. Clark, G. G. Peschel, I. Tinoco, *J. Phys. Chem.* **1965**, *69*, 3615.

[94] E. Nir, K. Kleinermanns, L. Grace, M. S. de Vries, *J. Phys. Chem. A* **2001**, *105*, 5106.

[95] C. Plützer, E. Nir, M. S. de Vries, K. Kleinermanns, *Phys. Chem. Phys.* **2001**, *3*, 5466.

[96] C. Plützer, K. Kleinermanns, *Phys. Chem. Chem. Phys.* **2002**, *4*, 4877.

[97] E. Nir, C. Plützer, K. Kleinermanns, M. de Vries, *Eur. Phys. J. D* **2002**, *20*, 317.

[98] Z. Lan, Y. Lu, E. Fabiano, W. Thiel, *ChemPhysChem* **2011**, *12*, 1989.

[99] M. P. Fülscher, L. Serrano-Andrés, B. O. Roos, *J. Am. Chem. Soc.* **1997**, *119*, 6168.

[100] M. Merchán, L. Serrano-Andrés, M. P. Fulscher, B. O. Roos, **1999**, pp. 161–195.

[101] E. Mburu, S. Matsika, *J. Phys. Chem. A* **2008**, *112*, 12485.

[102] V. Ludwig, Z. M. da Costa, M. S. do Amaral, A. C. Borin, S. Canuto, L. Serrano-Andrés, *Chem. Phys. Lett.* **2010**, *492*, 164.

[103] M. K. Shukla, J. Leszczynski, *J. Comput. Chem.* **2004**, *25*, 768.

[104] A. Tsolakidis, E. Kaxiras, *J. Phys. Chem. A* **2005**, *109*, 2373.

[105] D. Varsano, R. Di Felice, M. A. L. Marques, A. Rubio, *J. Phys. Chem. B* **2006**, *110*, 7129.

[106] R. Improta, V. Barone, *Theor. Chem. Acc.* **2008**, *120*, 491.

[107] Y. Zhao, Z. Cao, *J. Theor. Comput. Chem.* **2013**, *12*, 1341013.

[108] T. Fahleson, J. Kauczor, P. Norman, F. Santoro, R. Improta, S. Coriani, *J. Phys. Chem. A* **2015**, *119*, 5476.

[109] F. Santoro, R. Improta, T. Fahleson, J. Kauczor, P. Norman, S. Coriani, *J. Phys. Chem. Lett.* **2014**, *5*, 1806.

[110] B. Mennucci, A. Toniolo, J. Tomasi, *J. Phys. Chem. A* **2001**, *105*, 4749.

[111] S. Yamazaki, S. Kato, *J. Am. Chem. Soc.* **2007**, *129*, 2901.

[112] T. Yanai, D. P. Tew, N. C. Handy, *Chem. Phys. Lett.* **2004**, *393*, 51.

[113] J.-D. Chai, M. Head-Gordon, *Phys. Chem. Chem. Phys.* **2008**, *10*, 6615.

[114] H. H. Chen, *J. Chem. Phys.* **1973**, *58*, 2593.

[115] M. Majoube, *J. Raman Spectrosc.* **1985**, *16*, 98.

[116] M. Majoube, *J. Mol. Struct.* **1986**, *143*, 427.

[117] S. G. Stepanian, G. G. Sheina, E. D. Radchenko, Y. P. Blagoi, *J. Mol. Struct.* **1985**, *131*, 333.

[118] V. Hrouda, J. Florian, P. Hobza, *J. Phys. Chem.* **1993**, *97*, 1542.

[119] R. Letellier, M. Ghomi, E. Taillandier, *Eur. Biophys. J.* **1987**, *14*, 243.

[120] J. Florián, *J. Mol. Struct. THEOCHEM* **1992**, *253*, 83.

[121] J. Wiorkiewicz-Kuczera, M. Karplus, *J. Am. Chem. Soc.* **1990**, *112*, 5324.

[122] M. J. Nowak, L. Lapinski, J. S. Kwiatkowski, J. Leszczynski, *Spectrochim. Acta Part A Mol. Spectrosc.* **1991**, *47*, 87.

[123] M. J. Nowak, H. Rostkowska, L. Lapinski, J. S. Kwiatkowski, J. Leszczynski, *J. Phys. Chem.* **1994**, *98*, 2813.

[124] M. J. Nowak, H. Rostkowska, L. Lapinski, J. S. Kwiatkowski, J. Leszczynski, *Spectrochim. Acta Part A Mol. Spectrosc.* **1994**, *50*, 1081.

[125]   M. Majoube, P. Millié, P. Lagant, G. Vergoten, *J. Raman Spectrosc.* **1994**, *25*, 821.

[126]   M. J. Nowak, L. Lapinski, J. S. Kwiatkowski, J. Leszczyński, *J. Phys. Chem.* **1996**, *100*, 3527.

[127]   R. Santamaria, E. Charro, A. Zacarias, M. Castro, *J. Comput. Chem.* **1999**, *20*, 511.

[128]   B. Giese, D. McNaughton, *J. Phys. Chem. B* **2002**, *106*, 101.

[129]   S. Gogia, A. Jain, M. Puranik, *J. Phys. Chem. B* **2009**, *113*, 15101.

[130]   N. Jayanth, S. Ramachandran, M. Puranik, *J. Phys. Chem. A* **2009**, *113*, 1459.

[131]   N. Jayanth, M. Puranik, *J. Phys. Chem. B* **2011**, *115*, 6234.

[132]   S. Gogia, M. Puranik, *J. Biomol. Struct. Dyn.* **2014**, *32*, 27.

[133]   A. C. Albrecht, *J. Chem. Phys.* **1961**, *34*, 1476.

[134]   K. Itoh, K. Minami, T. Tsujino, M. Kim, *J. Phys. Chem.* **1991**, *95*, 1339.

[135]   L. Sadr-Arani, P. Mignon, H. Chermette, H. Abdoul-Carime, B. Farizon, M. Farizon, *Phys. Chem. Chem. Phys.* **2015**, *17*, 11813.

[136]   R. Brédy, J. Bernard, L. Chen, B. Wei, A. Salmoun, T. Bouchama, M. C. Buchet-Poulizac, S. Martin, *Nucl. Instruments Methods Phys. Res. Sect. B Beam Interact. with Mater. Atoms* **2005**, *235*, 392.

[137]   L. Chen, R. Brédy, J. Bernard, G. Montagne, A. R. Allouche, S. Martin, *J. Chem. Phys.* **2011**, *135*, 114309.

[138]   M. M. Dawley, K. Tanzer, W. A. Cantrell, P. Plattner, N. R. Brinkmann, P. Scheier, S. Denifl, S. Ptasińska, *Phys. Chem. Chem. Phys.* **2014**, *16*, 25039.

[139]   B. F. Minaev, M. I. Shafranyosh, Y. Y. Svida, M. I. Sukhoviya, I. I. Shafranyosh, G. V Baryshnikov, V. A. Minaeva, *J. Chem. Phys.* **2014**, *140*, 175101.

[140]   T. Schlathölter, F. Alvarado, S. Bari, A. Lecointre, R. Hoekstra, V. Bernigaud, B. Manil, J. Rangama, B. Huber, *ChemPhysChem* **2006**, *7*, 2339.

[141]   J. Tabet, S. Eden, S. Feil, H. Abdoul-Carime, B. Farizon, M. Farizon, S. Ouaskit, T. D. Märk, *Phys. Rev. A* **2010**, *82*, 22703.

[142]   J. Cadet, T. Douki, J.-L. Ravanat, *Free Radic. Biol. Med.* **2010**, *49*, 9.

[143]   S. Mukamel, *Principles of Nonlinear Optical Spectroscopy*, Oxford University Press, New York, **1995**.

[144]   W. Jarzeba, G. C. Walker, A. E. Johnson, M. A. Kahlow, P. F. Barbara, *J. Phys. Chem.* **1988**, *92*, 7039.

[145]   R. Jimenez, G. R. Fleming, P. V. Kumar, M. Maroncelli, *Nature* **1994**, *369*, 471.

[146]   S. Vajda, R. Jimenez, S. J. Rosenthal, V. Fidler, G. R. Fleming, E. W. Castner, *J. Chem. Soc. Faraday Trans.* **1995**, *91*, 867.

[147]   R. Jimenez, D. A. Case, F. E. Romesberg, *J. Phys. Chem. B* **2002**, *106*, 1090.

[148]   S. Park, M. D. Fayer, *Proc. Natl. Acad. Sci.* **2007**, *104*, 16731.

[149]   R. W. Impey, P. A. Madden, I. R. McDonald, *Mol. Phys.* **1982**, *46*, 513.

[150]   M. Maroncelli, G. R. Fleming, *J. Chem. Phys.* **1988**, *89*, 5044.

[151]   R. B. Barnett, U. Landman, A. Nitzan, *J. Chem. Phys.* **1989**, *90*, 4413.

[152]   J. S. Bader, D. Chandler, *Chem. Phys. Lett.* **1989**, *157*, 501.

[153]   M. Hanus, M. Kabeláč, J. Rejnek, F. Ryjáček, P. Hobza, *J. Phys. Chem. B* **2004**, *108*, 2087.

[154]   V. R. Smith, E. Samoylova, H.-H. Ritze, W. Radloff, T. Schultz, *Phys. Chem. Chem. Phys.* **2010**, *12*, 9632.

[155]   M. Kabeláč, P. Hobza, *Chem. - Eur. J.* **2001**, *7*, 2067.

[156]   M. Kabeláč, L. Zendlová, D. Řeha, P. Hobza, *J. Phys. Chem. B* **2005**, *109*, 12206.

[157]   L. Belau, K. R. Wilson, S. R. Leone, M. Ahmed, *J. Phys. Chem. A* **2007**, *111*, 7562.

[158]   D. M. Close, C. E. Crespo-Hernández, L. Gorb, J. Leszczynski, *J. Phys. Chem. A* **2008**, *112*, 12702.

[159]   R. F. Ribeiro, A. V Marenich, C. J. Cramer, D. G. Truhlar, *Phys. Chem. Chem. Phys.* **2011**, *13*, 10908.

[160]   F. Teimoory, G. R. Loppnow, *J. Phys. Chem. A* **2014**, *118*, 12161.

7

Kinetics of Enzymatic and Non-enzymatic Melanin Formation*
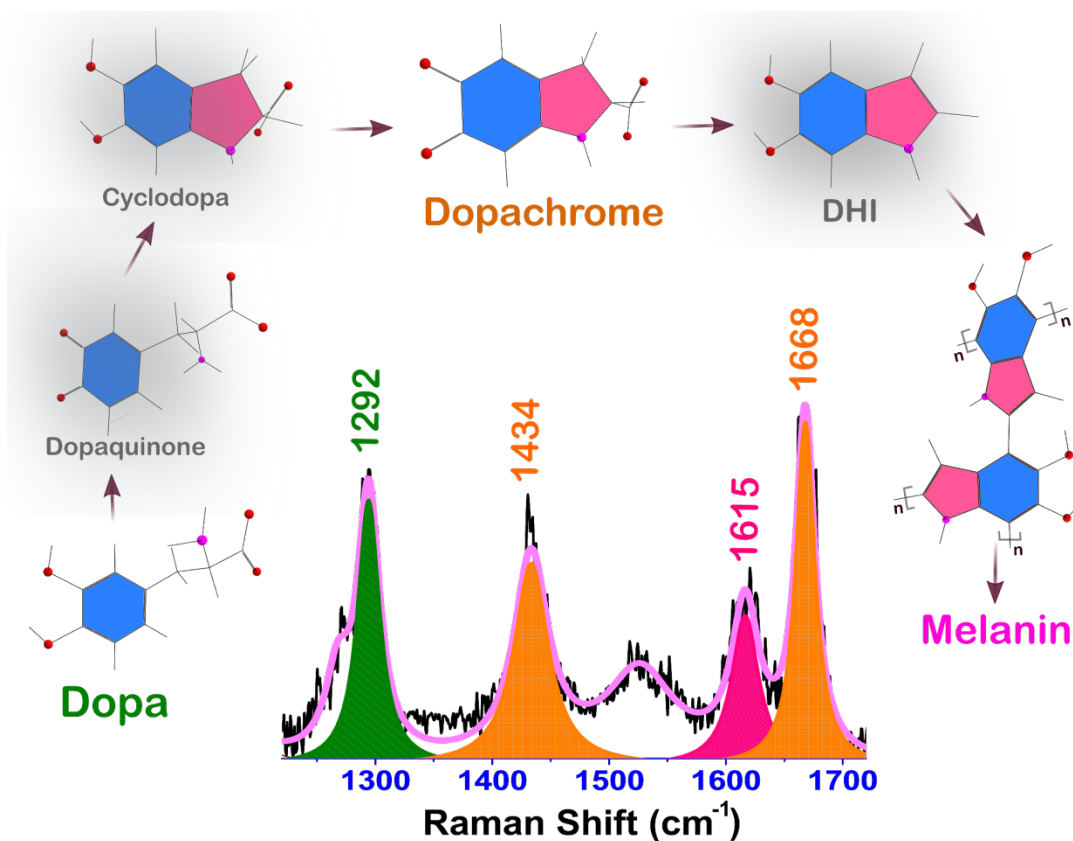
*Results presented in this chapter are in collaboration with Arya Thampi, a masters student of IISER Pune.

7.1. Introduction

Structure and self-assembled organization of melanin have been studied at different levels of structural hierarchy using both, the top-down and bottom-up approaches from macro (microns) to nano (nanometer) length scales and is documented in many excellent reviews.[1–11] Fundamental building blocks of eumelanins are 5,6-dihydroxyindole (DHI) and 5,6-dihydroxyindole-2-carboxylic acid (DHICA). McGinness *et al.* have shown that synthetic and natural eumelanins have amorphous semiconductor-like properties.[12–15] It has been established that melanin is not a semiconductor, but a hydration state dependent protonic-electronic conductor.[16,17] Broad UV-visible absorbance and conductive behavior of melanin have been traditionally explained with an extended heteropolymer model.[18–21] The model proposes that melanin is a polymer formed via bonding between monomers. Covalent linking is proposed to occur randomly between monomers at any two of available sites. The model ignores further specific details of monomeric coupling. These studies used π-Huckel theory to show that the linear homopolymer of 5 to 6 monomer units leads to a highly delocalized band structure that in turn produces the broadband absorption of eumelanin. Subsequently, the broadband absorption has been explained as a superposition of a large number of Gaussian bands, each associated with a slightly different heteropolymer (5-6 monomer units that arrange in a sheet-like structure) by Stark *et al.*[22–24] and Meredith and coworkers.[25] The latter group has termed it the chemical disorder model.[4,25,26]

The finite sized stacked sheet model emerged from X-ray diffraction experiments,[27–30] scanning tunneling microscopy (STM)[31–33] and atomic force microscopy (AFM) imaging[34–36] by several groups on synthetic and sepia melanin. These experiments suggest that protomolecules of 15-20 Å lateral dimensions are made from covalent bonding between 5-6 monomeric units (DHI or DHICA and their redox forms) with an average interatomic distance of ~ 1.42 Å. In later stages of aggregation, 3-4 such protomolecules stack on each other in a planar arrangement to form an aggregate of 10-12 Å vertical dimension with a 3.3-3.5 Å interlayer distance. AFM images of sepia melanin on mica[34] obtained in the tapping mode reveal 100-200 nm granules and 35 nm filamentous structures. Questions that remain unanswered are: what is the chemical structure of the protomolecule and how are these protomolecules assembled into larger species?

Structural constraints from above experiments have led to the development of a macrocycle-based model of melanin structure.[37–39] In this model, tetrameric macrocyclic structures consisting of 4 monomers (DHICA, DHI, and their redox forms) form the protomolecule. These protomolecules further stack (laterally and/or vertically) and are

stabilized by non-covalent interactions to produce the melanin aggregate. Using density functional theory (DFT) and the superposition principle, this model explains the broad optical absorption spectra of melanin, experimental X-ray parameters such as the structure factor and its natural capacity to bind metal ions. Recently, Chen *et al.* used this model of protomolecules and derived mass density (1.55 g/cm^3) and Young's modulus (~5 GPA) of eumelanin that is in excellent agreement with experimental data.[40]

Although successful in explaining the aforementioned experimental data, the caveat of the macrocycle model is that there is no direct, structural evidence for the formation of macrocyclic protomolecules on the path to melanin formation. On the other hand, linear protomolecules of melanin have been observed in experiments by Prota, d'Ischia and co-workers.[41–47] In bottom-up approaches, they used DHI and DHICA to make melanin under conditions of controlled oxidation and employed 2-dimensional solution NMR and mass spectroscopy for analysis. These showed that initial polymeric species are small linear oligomers up to tetramers made from monomers units that are intertwisted with respect to each other. Early oligomerization primarily occurs through covalent bonding at 2, 4 and 7 positions in DHI[42,45] (Fig. 7.1) and 4 and 7 positions in DHICA[44] (Fig. 7.1). An important aspect of melanin that remains to be satisfactorily explained by the linear model is the nature of interaction with metal ions that allows reversible binding.[48,49] The third and most recent model of a synthetic melanin, poly-dopamine (PDA or dopamine-melanin) put forward by Dreyer *et al.* propose that the pigment is not a covalently linked polymer but a supramolecular structure assembled by aggregation of monomers through charge transfer, π-stacking, and hydrogen bonding interactions.[50,51]

Optical experiments and calculations indicate that structures of protomolecules influence photochemical properties of melanin aggregates and are critical to the understanding of the function. Linear oligomers (dimers and trimers) of DHICA exhibit 1000 times more efficient deactivation of their excited states than the monomers and DHI-derived oligomers. This has been attributed to intra- and inter-unit excited state proton transfer (ESPT) on the sub-picosecond time scale.[52,53] Semiempirical and DFT calculations on a variety of protomolecules including macrocycles, finitely extended sheet, and linear oligomers show that the enhanced UV-visible absorption at high energy (<250 nm) end of the absorption spectrum can only be accounted for by consideration of excitonic coupling between protomolecules.[54]

Thus, because the molecular structure of protomolecules and parameters governing the subsequent polymerization and aggregation processes are not unequivocally known, a comprehensive model of melanin formation is still not available. Critical

requirements are high-resolution experiments at a molecular level that contain chemical information integrated with characterization at larger spatial scales. While several methods can be used for characterization of the aggregation process, chemical identity can be reliably obtained from NMR and vibrational spectra. Vibrational spectra are sensitive to small changes in molecular structure and are expected to allow differentiation between macrocyclic and linear models.
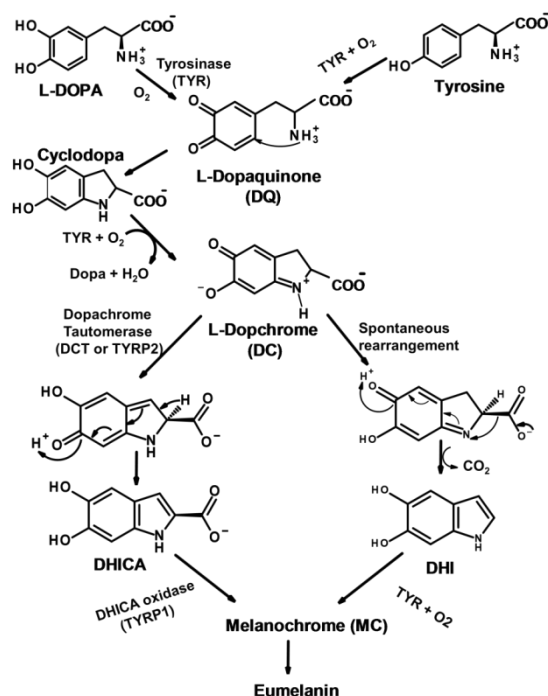
Fig. 7.1. Raper-Mason scheme of eumelanin production pathway using both tyrosine and L-Dopa (dopa) as a precursor. In the current study, we are investigating the pathway of DHI melanin formation from dopa via autoxidation and tyrosinase assisted oxidation of dopa.

We have used a combination of UV-visible microscopy, vibrational spectroscopy, quantum chemical modeling to delineate the polymerization and aggregation kinetics of melanin formation. Together these studies allowed us to propose a kinetic and structural model for melanin. We compare enzymatic and non-enzymatic synthesis and demonstrate the role of the enzyme in limiting heterogeneity of melanin pigment as compared to production through free oxidation. Analysis of vibrational bandwidths is used to quantitate heterogeneity of melanin.

7.2. Experimental and computational methods

7.2.1 Sample Preparation for RR and absorption spectroscopy

3,4-dihydroxyphenylalanine (dopa), sodium phosphate dibasic, monosodium phosphate, 2-Amino-2-(hydroxymethyl)-1,3-propanediol (Tris) and mushroom tyrosinase (tyrosinase) in the form of lyophilized powder were purchased from Sigma-Aldrich (St. Louis, MO, USA) and used without further purification. For autoxidized melanin formation 5 mM dopa was made in 50 mM Tris-HCl buffer of pH 7.4 in an eppendorf that was kept open in the ambient environment (22 °C and ~ 50 % relative humidity) but covered with aluminum foil for protection from light. Tyrosinase assisted melanin was made in a quartz tube (Wilmad Lab Glass, New Jersey, USA) which was purged with argon to reduce the rate of oxidation so that reaction can be monitored spectroscopically. Tyrosinase was freshly prepared of 20 µg/ml concentration from a stock of 1 mg/ml in 40 mM phosphate buffer (PB) of pH 6.8. An aliquot of 200 µl from a stock of dopa (4 mM), prepared in a gas-tight environment was transferred to an argon purged quartz tube using a gas-tight syringe (Hamilton Robotics, Bonaduz, Switzerland). Tubes are sealed with rubber septa and parafilm after purging with argon. Next, freshly prepared tyrosinase was transferred to the tube containing pre-purged dopa in same stoichiometric ratio to commence the reaction. For self-oxidized melanin, multiple reactions were started in appropriate time intervals and samples of desired time points (within 0-192 hr) is recorded on the same day. Melanization during enzymatically catalyzed reaction was followed in an appropriate time interval immediately after starting the reaction.

7.2.2 RR spectroscopy with 260 nm excitation

RR measurement was performed in a 135° backscattering geometry with 260 nm excitation, generated as the third harmonic of 780 nm fundamental wavelength of a tunable Ti-sapphire oscillator of 25 ns pulse width and 1 kHz repetition rate (Indigo Coherent Inc., California, USA) as described previously,[55,56] and in chapter 2. RR spectra of both the self- and enzymatic oxidation reaction were measured without any dilution as it is described in preceding section. Each spectrum in both cases is acquired for 1 min exposure time with a 15 min total accumulation period.

7.2.3 RR spectroscopy with 488 nm excitation

Tyrosinase assisted oxidation reaction was started in an eppendorf by mixing freshly prepared dopa and tyrosinase in the same stoichiometric ratio as described in preceding section, in aerobic conditions. After five minutes of mixing, 50 µL of this mixture was kept on a quartz slide. RR spectra from the reaction mixture were obtained using an upright confocal LabRAM HR 800 Raman microscope (HORIBA Jobin Yvon SAS, rue de Lille, France) equipped with an achromatic water immersion objective of 60x magnification and 1.2 numerical aparture. A continuous wave Argon ion laser of 488 nm wavelength (Spectra-Physics, Santa Clara, CA, USA) was used as excitation source.

Spectra were acquired on a liquid nitrogen cooled CCD detector after dispersing through a 800 mm focal length spectrometer equipped with 600 gr/mm grating. Incident power on the sample was < 10 mW. A confocal pinhole of 400 µm was used to maximize collected signal, and a slit width of 200 µm was used to achieve good spectral resolution (1.8 cm^{-1}/pixel). Each spectrum is recorded with a 4 s exposure and 40 s of total accumulation time. Multiple spectra recorded within a time interval of 5 to 15th min, 30 to 60th min and 82 to 92nd min from initiation of the reaction are averaged to obtain spectra at 10th, 45th and 87th min respectively.

7.2.4 Absorption spectroscopy

Self-oxidized melanin samples were diluted 50 times for recording of consecutive absorption spectra in a quartz cuvette within 205-800 nm with a double beam Evolution 300 UV-Vis Spectrophotometer (Thermo Fisher Scientific, Inc., Waltham, MA, USA). Each spectrum was average of three cycles, and each cycle was recorded with 0.5 nm data interval, and with a 120 nm/min scan speed. The enzymatic reaction was made in an argon purged glass tube (542-PP, Wilmad-Lab Glass, Vineland, NJ, USA) and consecutive absorption spectra were recorded with a double beam spectrophotometer (Shimadzu UV-Vis 2600, Shimadzu Deutschland GmbH-Duisburg, Germany). Each spectrum was accumulated for 3 min and 0.5 nm data interval at a 120 nm/min scan speed.

7.2.5 Fourier Transformed Infra-Red (FTIR) spectroscopy

Self-oxidized melanin at certain time points was precipitated by incubation with chilled (-20°C) methanol of HPLC grade in 1:25 stoichiometry. After decantation, the settled melanin was further washed three times with methanol and was vacuum dried afterward in a desiccator for more than twelve hours. This powder sample was mixed with potassium bromide (KBr) in 1:10 ratio to make a thin palette for measurement of IR absorption in Nicolet 6700 FT-IR spectrophotometer (Thermo Fisher Scientific, Inc., Waltham, MA, USA). Reported spectra are average of three spectra from three palettes, each from an independently set reaction.

7.2.6 Raman Data Analysis

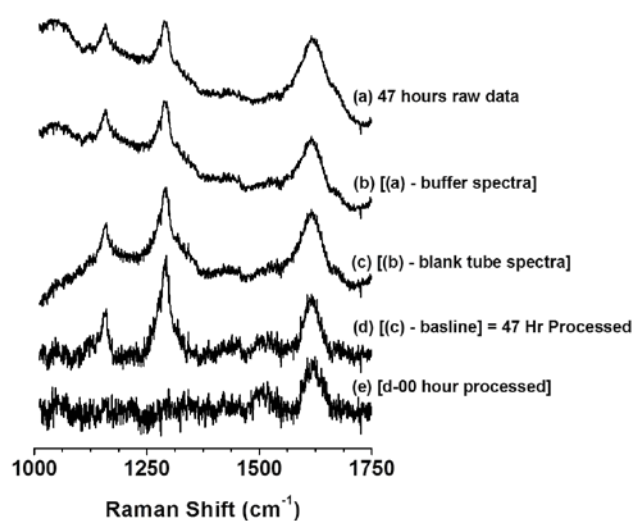A spectrum of buffer was subtracted from that of each time point to remove the broad contribution of water near 1650 cm^{-1} followed by removal of the spectrum of a blank quartz tube. As low and high wavenumber region of the spectrum is of different slope in case of autoxidation reaction, a baseline created by joining 6 – 7 points is subtracted to make two regions (1150-1400 cm^{-1} and 1550-1700 cm^{-1}) of Raman spectrum flat (Fig. 7.2) . No shift in band position was observed due to this correction.

The spectrum of dopa recorded at 0th hour (within 0-15 min) was subtracted from each spectrum at every consecutive time points to remove monomer contribution. A fraction of

dopa spectrum was subtracted till disappearance of the band at 1292 cm^{-1}. Lorentzian functions were used to determine band position and area under the curve was treated as intensity. Because, the addition of traditional internal intensity standard such as Na_2SO_4 leads to aggregation of formed melanin, the intensity of freshly taken DMF acquired before and after each 15 min of data accumulation was used as an external intensity standard. The average integrated intensity of 1092 cm^{-1} band of DMF recorded intermittently is used for intensity normalization for spectrum at each time point. Absorption spectra were used for analysis as recorded without any post processing. Normalized intensities and absorbance values from Raman and UV-Vis spectra respectively at different time points were used to determine the kinetics of both the reactions. All data fitting and kinetic analysis are done using Synergy software (Horiba Jobin-Yvon, Kyoto, Japan).

7.2.7 Quantum Mechanical Modeling

Vibrational spectra of different intermediates *en route* melanin were computed with DFT using hybrid B3LYP functional.[57,58] Ground state structure of dopa was optimized at B3LYP/6-31G(d,p) level of theory in gas phase, and subsequently, the harmonic vibrational analysis was performed at the same level of theory. For a *vis-à-vis* comparison of normal modes of vibration, various small oligomeric species of DHI were also analyzed at same theoretical level. After geometry optimization at the mentioned level, single point energy of these polymers are computed with a bigger basis set 6–311+G(2d,p) using the same functional in vacuo. Use of B3LYP/6–311+G(2d,p) method for determining relative stability of DHI oligomers is validated by comparing relative energies of multiple species from the lowest energetic one with increasing size of the basis set (Fig. 7.3)

Fig. 7.2 Processing protocol of RR data for autoxidized melanization reaction of dopa in 50 mM Tris-HCl buffer at pH 7.4. At first, a spectrum of buffer is subtracted form that of reaction mixture (b) to remove mainly contribution of water Raman band. Next spectrum of a blank quartz tube is subtracted (c) to remove increasing scattering component at low energy end of the spectra. Thus obtained spectrum is subjected to a manual baseline subtraction (d) for spectral deconvolution purpose. At the end, spectrum of pure dopa is subtracted from that obtained in previous step to obtain pure melanin signature at each time point (e).
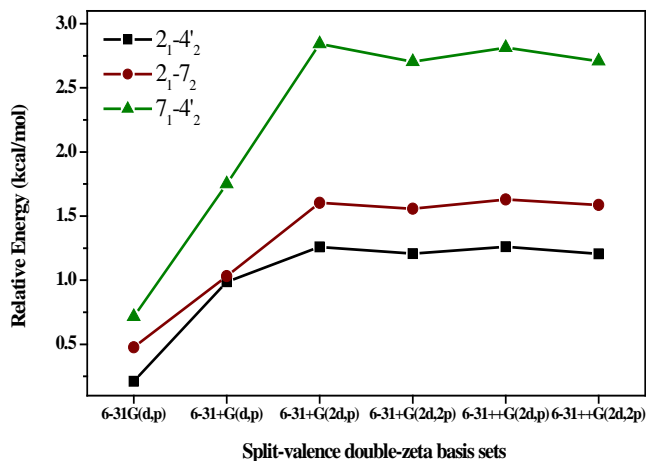
Fig. 7.3 Relative single point (SP) energies of three DHI tetramers (in legend) from 2-4 dimer, computed on B3LYP/6-31G(d,p)//gas optimized geometry with basis sets that have increasing order of polarization and diffuse functions (mentioned on abscissa).

For all three species, it is seen that after 6-31(G) split valence basis set is augmented with a 'p' type diffuse function along with 2 sets of 'd' and one set of 'p' polarized functions on heavy and hydrogen atom respectively, accuracy of relative energetics do not change. Thus to have a time efficient scheme without losing quality of relative energies between similar sized DHI tetramers, 6-31+G(2d,p) basis set have been used throughout this study.

Vibrational spectra of DC was computed on energy minimized ground state structure at B3LYP/6-311+G(2d,p) level of DFT.[57,58] For a reliable description of the solvated chromophore, an explicit water molecule is added near carbonyl moiety at 5th and 6th position, and polarizable continuum method (PCM) was also employed to account for bulk solvation.[59–61] (Fig. 7.4) UV-Vis absorption spectra and RR spectra of DC was computed using time-dependent formulation of DFT in linear regime.[62,63] (See Supplementary Information for method of computing RR spectra) A more expensive model with bigger basis set and explicit solvation was employed in the case of DC for accurate assignment of RR spectra and electronic transitions. We note that use of different theoretical models for obtaining vibrational spectra of DC and dopa is justified as we do not compare spectroscopic properties of melanin protomolecules (small polymers of DHI) and DC. In all ground state geometry optimizations, the stationary point is ensured by the absence of any imaginary frequency in the harmonic vibrational analysis. All quantum chemical calculations are performed with Gaussian 09 suite of programs.[64]

7.3. Results

Fig. 7.1 shows the Raper-Mason pathway of eumelanin formation.[65–70] The eumelanogenesis pathway has been investigated at different levels by several groups; the initial kinetic steps of formation of dopaquinone (DQ),[71–73] redox exchange reaction DQ with following intermediates[73–76] and specific role of the key enzyme tyrosinase[77–79] and several other regulatory enzymes[80–84] involved, and the steps following dopachrome (DC) formation.[85,86] Due to complex dynamics of different interconverting chemical species, and not-completely-understood role of different enzymes in catalyzing the specific intermediary reaction, construction of a unified kinetic scheme[75,79,87–89] describing the entire melanization reaction remains at large. We have followed the early steps of melanin formation with vibrational spectra that contain molecular fingerprints. A potential challenge in obtaining vibrational fingerprints of melanin is its intrinsic fluorescence. We minimized the interference from fluorescence by using UV excitation of 260 nm. This selection ensures that the Raman spectrum is well removed from the luminescence. Since 260 nm falls within the π-π* excitation located on the indolic conjugated ring, vibrational modes corresponding to this moiety are resonance enhanced. The use of this resonance condition considerably simplifies the spectrum.
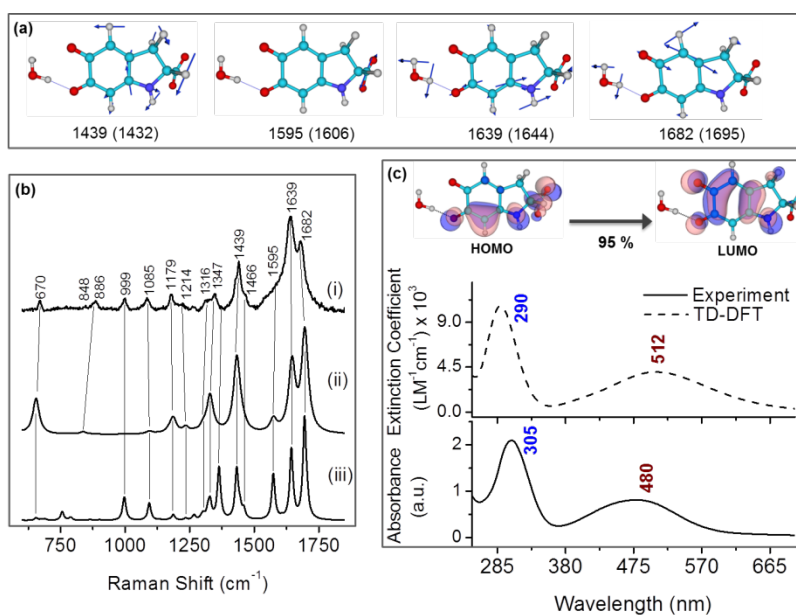
Fig. 7.4 (a) Description of normal modes of four intense RR bands of dopachrome (DC), with experimental and (computed) wavenumbers; (b) Experimental 488 nm excited (i) and computed RR (ii), and normal Raman spectrum (iii) of DC. Computation is performed on DC+ H_2O as a model. RR spectra is simulated within excited state gradient method (See Section 2.2.3.1 in Chapter 2) using wB97xD functional[90] at ground state geometry, optimized with B3LYP functional. Raman bands are broadened with Lorentzian lineshape having a FWHM of 15 cm^{-1}. (c) HOMO and LUMO orbitals (top) that take part in 480 nm excitation corresponding to S_1 state, predicted at 512 nm in DC. Absorption spectrum is computed on

same optimized structure DC+H$_2$O complex at TD-B3LYP formalism. Computed oscillator strengths are broadened with 2800 cm^{-1} Gaussian linewidth to obtain the simulated absorption spectrum. All computations on DC are performed with 6-311+G(2d,p) basis set and employing PCM solvation.

We monitored reaction kinetics of melanin formation from precursor dopa with the aid of tyrosinase using absorption and resonance Raman (RR) spectroscopy. Vibrational bands associated with catecholic C–OH group of dopa (1292 cm^{-1}), aromatic C–C stretch (1616 cm^{-1}) and carbonyl stretching (1670 cm^{-1}) are identified as probes of dopa, melanin/melanochrome and dopachrome respectively. In agreement with previous reports,[91–93] a comprehensive assignment of vibrational bands of dopa is described in Table 7.1. A new absorption band at 363 nm is used to probe melanochrome/melanin more reliably than commonly used 540 nm. A minimal model of reaction kinetics is proposed and rates of formation are obtained from evolution of intensities of these bands with time.

Table 7.1 Assignment of vibrational modes of L-dopa from experiment and B3LYP/6-31G(d,p)//gas level of DFT calculation.

Raman, 735 nm [2]	IR[3]	FT-Raman[3]	Raman, 514.5 nm[4]	Raman 260 nm[5]	DFT [5,6]	Assignment
-	-	1100	-	-	1110	Ring breath. + CH$_2$ twist. + CH be.
-	1122	1124	-	1111	1094	Ring breath. + CH$_2$ twist. + CH be.
1143	1145	1142	-	-	1140	C$_5$-OH + C-C str. + CH be.
-	1160	1165	-	1157	1155	CH + COH be.
-	-	-	-	-	1200	C$_6$OH + CH be.
1203	1203	-	-	1211	1228	Ring str.
	1230	-	-	-	1251	C$_6$-OH str. + CH be.
1267	1255	1265	-	1264	1279	CH$_2$ + NH$_2$ rock.
-	1285		-	-	1284	CH be. + Ring str.
1297	1300	1300	1290, m	1292	1299	C$_5$–OH str. + Ring breath.
1328	-	-	-	1327	1333	Ring dist.+ CH$_2$ be.
1343	1352	1350	-	1354	1385	C$_6$-OH be. + Ring str.
1427	1405	1407	-	-	1454	Ring breath. + COH be.
-	1460	1445	-	1444	1469	Ring breath.
-	1595	-	-	-	1643	Ring dist.
1611	1605	1610	1627, s	1616	1628	Aromatic C=C str.
-	-	-	-	-	1647	NH$_2$ sci.
-	-	-	1680, s	-	1712	C=O str.

[2]Ref [91]; [3]Ref [92]; [4]Ref [93]; [5,6]this work; [6]vibrational wavenumbers are scaled with a factor of 0.98; abbreviations; str, bond stretching; be, bending; dist, distortion; breath, breathing; wag, wagging; twist, twisting; sci, scissoring.

Additionally for a parallel comparison, formation of melanin via a non-enzymatic auto-oxidation of dopa is also followed. We have captured RR signature of dopachrome, the enzymatically stabilized intermediate *en route* melanin for the first time. Linear homopolymer of DHI is revisited and DFT (in Ground state and time dependent) is applied to show that eight tetrameric species can capture the feature of experiential Raman spectra of dopa-melanin.

7.3.1. Dopachrome is stabilized in enzyme assisted formation of melanin

Fig. 7.5, panel (a) show time evolution of absorption spectra of dopa as oxidative polymerization proceeds in the presence of mushroom phenol oxidase, commonly known as mushroom tyrosinase (EC 1.14.18.1). As enzymatic oxidation proceeds, absorption in the visible region increases. The reaction is initiated by adding tyrosinase to a solution of dopa (see method section). An orange-colored species is formed within 2 min. This new species is marked by two characteristic bands at 305 and 480 nm in the absorption spectrum that persist for two hours. The intermediate is identified as dopachrome (DC) from its characteristic absorption band[94,95], at 480 nm and by its vibrational signature discussed in the following section.

As DC decays, a new species is formed that has a broad absorption extending from 300 nm to near IR. This species is identified as melanochrome (MC) that subsequently aggregates into melanin. In previous studies, formation of melanin and MC has been monitored through change in the absorbance at 540 nm.[96–99] We note however, that due to the broad band at 480 nm (FWHM ~100 nm) arising from DC that also extends well into the red region of the spectrum, kinetic rates derived from absorbance at 540 nm would contain contribution from multiple absorbing species. We propose the use of 363 nm as a wavelength of less interference to monitor MC formation as discussed below.

Fig. 7.5, panel (c) shows absorption spectra of dopa, DC, MC and a species formed within 20-30 min of initiation of the reaction. We obtained the spectrum of DC by subtracting the spectrum of dopa ('0' min) from that at 60th min of a tyrosinase assisted oxidation reaction. Similarly, the spectrum of MC was obtained by subtracting the spectrum of the reaction mixture at 60th min (corresponding to maximum DC concentration) from the spectrum at 200th min (corresponding to maximum MC concentration). We find a novel, exclusive spectroscopic signature of soluble melanochrome pigment at 363 nm that is formed *en route* formation of melanin. This provides a probe to monitor formation of MC that is more specific and contains a minimum contribution from DC absorption. We note that like dopa, all intermediate species on the melanin formation pathway have the characteristic ππ* transition ~280 nm originating from transitions centered on the benzene ring structure. Therefore, measurement of decay kinetics of dopa by monitoring absorbance within the ππ* band would lead to complex kinetics.

Formation of DHI from DC is a spontaneous and fast process that has not yet been captured in any spectroscopic studies. We did find a weak band at 298 nm in the difference spectra between the 30th and 20th min of reaction during enzymatic oxidation that is characteristic of DHI.[100] Nevertheless, this band could not be used to monitor DHI because of interference from intense bands on either side at 280 and 305 nm from dopa and DC respectively.

In the enzyme-assisted reaction, the formation of MC is marked by the appearance of a broad band centered at ~570 nm. The intensity of this band increases concurrently with decrease in absorbance at 480 nm (indicating decay of DC) (Fig. 7.5, panel b). A gradual red-shift of the overall absorption envelope, from 480 nm to 570 nm, indicates the formation of short oligomers. Oligomerization is expected to lead to delocalization of electron density that in turn leads to lowering of the HOMO-LUMO separation. HOMO and LUMO stand for highest occupied and lowest unoccupied molecular orbital respectively. The lowering of HOMO-LUMO separation manifests as a red shift in the absorption spectrum. Increasing spectral width of this band indicates rising heterogeneity in the polymer population. Spectral broadening is further analyzed quantitatively in a later section below.
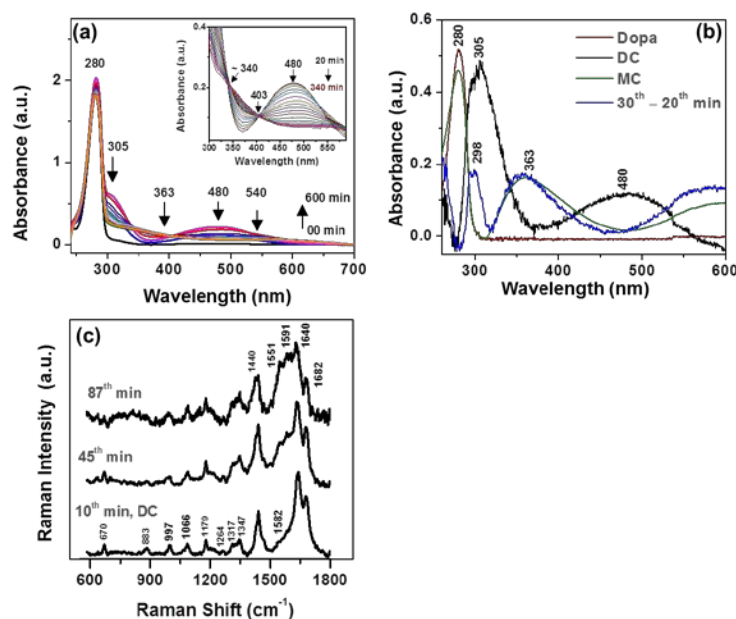
Fig. 7.5 (a) Consecutively measured absorption spectra of tyrosinase assisted polymerization of dopa from 0 to 600 min; (b) UV-Vis absorption spectra of dopa, DC, MC, and species that forms between 20th and 30th min reaction. (c) RR spectra of species that forms during tyrosinase assisted polymerization of dopa from 5th to 15th min (10th min), from 30th to 60th min (45th min) and 82nd to 92nd min (87th min) with 488 nm laser excitation. In panel a, each spectrum is recorded in an interval of 10 min and accumulated for 3 min. Absorption maxima corresponding to different reactants are mentioned: dopa (at 280 nm), DC (at 305 and 480 nm) and MC (at 363 and 540 nm). Inset shows enlarged version of the same in mentioned region of wavelengths and depict two isosbestic points at 340 and 403 nm; In panel b, Spectra of MC is obtained by subtracting spectrum at 60th min (corresponding to maximum concentration of DC) from that at 200th min. Species formed between 20th to 30th min of reaction is obtained by subtracting the spectrum recorded at 20th min from that recorded at 30th min. This spectrum is magnified eleven times for visual comparison with spectra of other species. Spectral signature

of DC is obtained by subtracting spectrum of dopa from that of the reaction at 60th min. Spectra of dopa is scaled by a factor of four; In panel c, consecutively recorded spectra within mentioned time interval are averaged to obtain the spectrum at 10th , 45th and 87th min.

Early on, in 1950, Foster proposed the first simple kinetic model of enzymatic and non-enzymatic oxidation of tyrosine. He proposed that DQ was the early, key intermediate prior to melanin formation.[101] Other studies have reported that cyclodopa rapidly converts to DQ ($5.3 \times 10^6\,M^{-1}s^{-1}$) and that DQ in turn converts to dopachrome at a fast rate $3.8\ s^{-1}$ from pulse radiolysis experiments.[71–73,102] In the present experiments, we did not detect any DQ (λ_{max}=400 nm).[72] This implies that DQ converts to DC within the dead-time of our experiment. DC was detected as mentioned above and was sufficiently stable to allow us to determine kinetics of its formation and decay.

## 7.3.2 Molecular fingerprints allow delineation of kinetic steps

Dopa converts to melanin via several intermediates that have similar spectral characteristics. As a consequence, while the absorption spectra discussed above provide information on the overall kinetics of melanin formation, they do not yield unequivocal chemical identity of the intermediate molecules being observed. Their identities can be established through vibrational spectra. We obtained resonance Raman signatures of precursor dopa, intermediate species and products. These spectral signatures are chemical fingerprints and allowed us identify the intermediates as DC and melanochrome as discussed below. Further, we were able to use these vibrational spectral fingerprints to follow the kinetics of decay and formation of each intermediate.

The resonance Raman spectrum of dopa obtained with Raman excitation with laser light at 260 nm is shown in Fig. 7.6, panel (a). A prominent band is observed at 1292 cm^{-1} and two low intensity bands are observed at 1158 cm^{-1} and 1616 cm^{-1}. As autoxidative polymerization proceeds, intensity of the 1292 cm^{-1} band of dopa decreases and that of 1616 cm^{-1} band increases (Fig. 7.7, panel c). Thus the species formed from dopa oxidation has a vibrational signature at 1616 cm^{-1} as well. We also followed the kinetics with FTIR spectroscopy to obtain complementary information. Sample preparation and procedure of FTIR measurement of precipitated melanin is described in method section above**.** Fourier transformed infrared absorption spectrum (FTIR) of monomeric dopa is shown in Fig. 7.6, panel (c), bottom row.
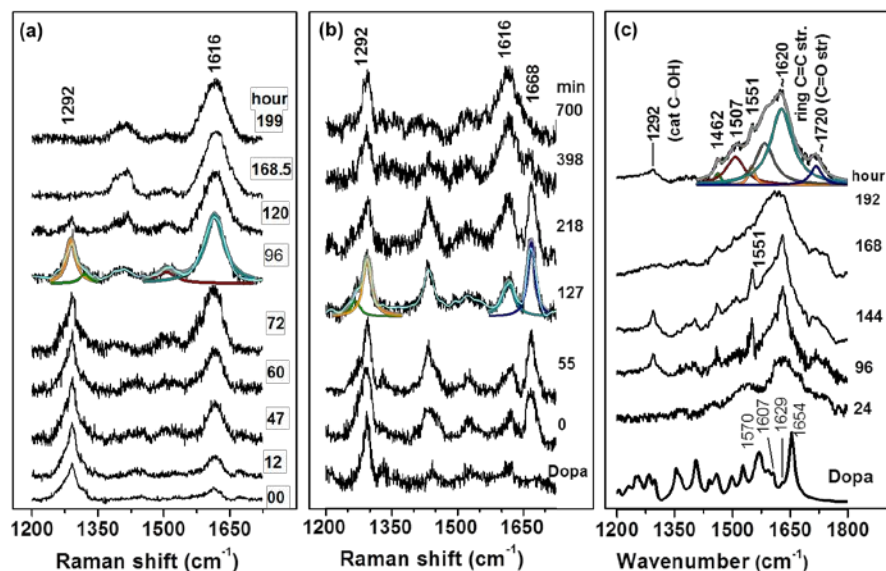
Fig. 7.6 Raman spectra of reaction of (a) autoxidized and (b) tyrosinase assisted dopa-melanin formation with 260 nm laser excitation and (c) FTIR absorption spectra of precipitated melanin formed via autoxidation of dopa. Every spectrum is labeled with respective time point. See Method section for details of reaction. Representative deconvolution of RR bands is shown in (a) and (b) for spectra of 96 hr and 127 min respectively.
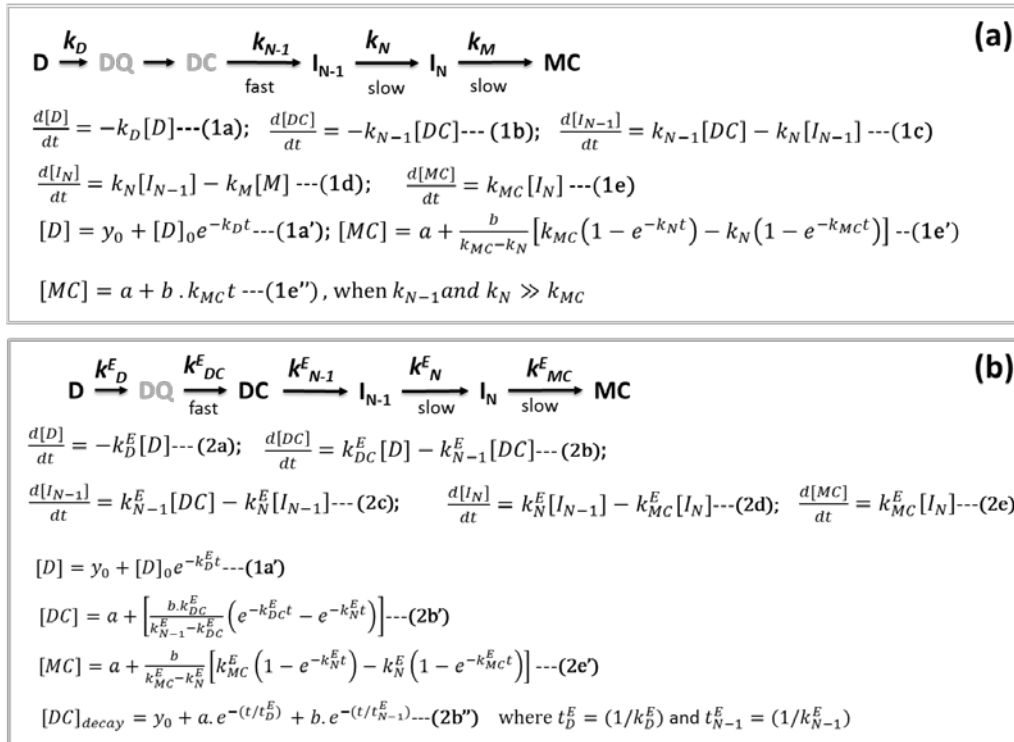
Rate of decay of dopa in the presence and absence of the enzyme was measured from change in intensity of the Raman band at 1292 cm^{-1} (Fig. 7.7, panel a). This band is assigned to catecholic C–OH stretching (str.) at 5 and 6 positions of the benzene ring in dopa (Fig. 7.11, panel a). The band at 1616 cm^{-1} arises from aromatic C–C str. of benzene ring (Fig. 7.11, panel a), (See Table 7.1 for complete assignment) grows during polymerization and saturates (Fig. 7.7, panel c). In the non-enzymatic reaction, this is the only intense band present in the spectrum at the final time point observed. At this point, the solution achieves a characteristic dark color of melanin pigment. Thus, we identify this band as a spectral signature of MC and melanin. This 1616 cm^{-1} band allowed us to make a direct measurement of the formation rate of MC without interfering signals from other intermediates.
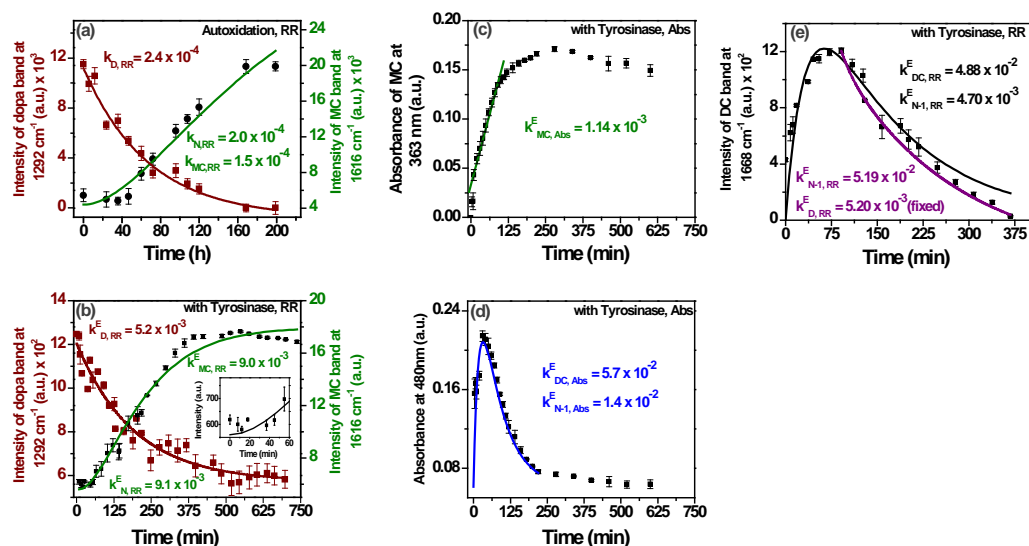
Fig. 7.7 Kinetics of decay of dopa (maroon) and formation of MC (green) in self-oxidation (panel a, from RR intensity) and in tyrosinase assisted oxidation (panel b, From RR intensity; panel d, from absorbance). Dopa and MC have been monitored using their RR signature at 1292 and 1616 cm^{-1} (panel a and c), and MC is also probed using absorbance at 363 nm (panel c); Formation and decay kinetics of DC using (d) absorbance at 480 nm and (e) RR band at 1668 cm^{-1} during tyrosinase assisted oxidation. In panel (e), biexponential decay of DC using intensity of 1668 cm^{-1} band is depicted in purple. For detail see text. Abbreviations, E as superscript denotes enzymatic reaction; Rates without E as superscript represents those in autoxidation reaction. D, DC and MC stands for dopa, dopachrome and melanochrome respectively; Abs and RR indicates rates obtained from absorbance and RR intensity respectively; N and N-1 as subscripts stand for Nth and N-1th intermediates respectively.

During enzymatic oxidation, immediately upon addition of the enzyme, two prominent bands appear at 1670 cm^{-1} and 1439 cm^{-1} see Fig. 7.6, panel (b). The intensity of these bands initially increases up to 60 min and then decreases, Fig. 7.7, panel (f). As the intensity of these bands decreases, another band appears at 1616 cm^{-1} that steadily increases in intensity until it saturates at ~400 min, Fig. 7.7, panel (f). From the non-enzymatic reaction discussed earlier, we can immediately identify the species responsible for this band as MC.

(a)

$$D \xrightarrow{k_D} DQ \longrightarrow DC \xrightarrow[\text{fast}]{k_{N-1}} I_{N-1} \xrightarrow[\text{slow}]{k_N} I_N \xrightarrow[\text{slow}]{k_M} MC$$

$$\frac{d[D]}{dt} = -k_D[D] \text{---(1a)}; \quad \frac{d[DC]}{dt} = -k_{N-1}[DC] \text{--- (1b)}; \quad \frac{d[I_{N-1}]}{dt} = k_{N-1}[DC] - k_N[I_{N-1}] \text{---(1c)}$$

$$\frac{d[I_N]}{dt} = k_N[I_{N-1}] - k_M[M] \text{---(1d)}; \quad \frac{d[MC]}{dt} = k_{MC}[I_N] \text{---(1e)}$$

$$[D] = y_0 + [D]_0 e^{-k_D t} \text{---(1a')}; \quad [MC] = a + \frac{b}{k_{MC}-k_N}\left[k_{MC}(1-e^{-k_N t}) - k_N(1-e^{-k_{MC}t})\right] \text{--(1e')}$$

$$[MC] = a + b \cdot k_{MC}t \text{ ---(1e'')}, \text{ when } k_{N-1} \text{ and } k_N \gg k_{MC}$$

(b)

$$D \xrightarrow{k^E_D} DQ \xrightarrow[\text{fast}]{k^E_{DC}} DC \xrightarrow{k^E_{N-1}} I_{N-1} \xrightarrow[\text{slow}]{k^E_N} I_N \xrightarrow[\text{slow}]{k^E_{MC}} MC$$

$$\frac{d[D]}{dt} = -k^E_D[D] \text{--- (2a)}; \quad \frac{d[DC]}{dt} = k^E_{DC}[D] - k^E_{N-1}[DC] \text{--- (2b)};$$

$$\frac{d[I_{N-1}]}{dt} = k^E_{N-1}[DC] - k^E_N[I_{N-1}] \text{--- (2c)}; \quad \frac{d[I_N]}{dt} = k^E_N[I_{N-1}] - k^E_{MC}[I_N] \text{---(2d)}; \quad \frac{d[MC]}{dt} = k^E_{MC}[I_N] \text{---(2e)}$$

$$[D] = y_0 + [D]_0 e^{-k^E_D t} \text{---(1a')}$$

$$[DC] = a + \left[\frac{b.k^E_{DC}}{k^E_{N-1}-k^E_{DC}}\left(e^{-k^E_{DC}t} - e^{-k^E_N t}\right)\right] \text{---(2b')}$$

$$[MC] = a + \frac{b}{k^E_{MC}-k^E_N}\left[k^E_{MC}\left(1-e^{-k^E_N t}\right) - k^E_N\left(1-e^{-k^E_{MC}t}\right)\right] \text{---(2e')}$$

$$[DC]_{decay} = y_0 + a.e^{-(t/t^E_D)} + b.e^{-(t/t^E_{N-1})} \text{---(2b'')} \quad \text{where } t^E_D = (1/k^E_D) \text{ and } t^E_{N-1} = (1/k^E_{N-1})$$

Equations. Reduced model of melanization kinetics during (a) non-enzymatic and (b) enzymatic oxidation of Dopa (D). DQ, DC, MC stands for dopaquinone, dopachrome and melanochrome respectively. I_N and I_{N-1} are two preceding intermediates of MC. k_D is decay rate of dopa and k_{DC}, k_{N-1}, k_N, k_{MC} are first order rate of formation of DC, I_{N-1}, I_N^{th} intermediate and MC respectively. Superscript E in panel (b) represents rates in presence of tyrosinase. Equations (a'-e') are the solution for first order rates of different reactants, describe through equations (a-e). The grayed out species (DQ and DC in panel a, and DQ in panel b) are not detected in our experiment.

Vibrations at ~1670 cm^{-1} are typical markers of the exocyclic carbonyl modes of ortho-, meta- and para-quinones and analogous molecules.[103] The most likely species with a carbonyl group on the pathway to melanization is DC. This is consistent with the observation from absorption spectra (Fig. 7.5, panel a) that show an intermediate with lambda max at 480 nm. To unequivocally identify the intermediate responsible for this band at 1668 cm^{-1}, we carried out computational calculations with DFT method to obtain ground state structure and vibrational spectra of DC. The structure of DC in the ground state was obtained by energy minimization at B3LYP/6-311+G(2d,p)//PCM level. Vibrational normal mode analysis was carried out on this structure at the same level. Computational normal mode analysis indeed predicts that the origin of this band is the stretching of carbonyl (C=O) moiety present on the 5th and 6th position of indole ring of DC. Further evidence that the bands at 1670 cm^{-1} and 1439 cm^{-1} arise from DC is obtained through resonance Raman spectra obtained with 488 nm excitation (*vide infra*) (Fig. 7.5, panel d and Fig. 7.3). Since DC has a large absorption cross section at 488 nm, this leads to selective resonance enhancement of its vibrational signature in a complex mix of

various other reactants, products and intermediates. This is the first report of an experimental RR signature of DC during an enzymatic reaction. Having established the origin of the 1670 cm^{-1} band, we used it to follow the formation and decay of DC.

During the auto-oxidation of dopa (Fig. 7.6, panel a), the signature of DC is not observed either at 1670 or at 1439 cm^{-1}. This is consistent with the absence of the 480 nm peak, assigned to DC, in time-dependent UV-visible absorption spectra (Fig. 7.6, panel b). The signature of DC is only observed in the presence of tyrosinase. Thus, during autoxidation, DC rapidly converts to DHI and further downstream species on a timescale much faster than that of the Raman measurement (~5 min). The presence of tyrosinase stabilizes the DC intermediate and extends its lifetime allowing us to capture its Raman signature. While on the one hand the enzyme tyrosinase accelerates the overall melanization reaction, it slows down intermediate step(s) involving conversion of DC into further intermediates. In contrast, complete consumption of monomeric dopa through polymerization and aggregation in a self-oxidized reaction requires ~8 days. It is pertinent to note that several studies have used melanin produced through autoxidation of dopa within 2-3 days as a model for physical studies.[104–107] It would be interesting to check if these physical techniques find any differences between the melanin formed after 2-3 days and at the completion of the reaction at 8 days.

7.3.3. Formation and decay kinetics of reactants on melanin pathway

7.3.3.1 Kinetics of dopa consumption

Single exponential fit to the Raman intensity of the dopa marker band, 1292 cm^{-1}, shows that during autoxidation it decays with a rate constant (k_D) of 2.4 x 10^{-4} min^{-1} (Fig. 7.7, panel a) while the rate constant for dopa decay during enzymatic oxidation (k^E_D) is 5.2 x 10^{-3} min^{-1} (Fig. 7.7, panel b). Thus, dopa is consumed more slowly in the autoxidation reaction and the 1292 cm^{-1} band is absent in the last spectrum recorded (Fig. 7.6, panel a). We note however, that since the enzymatic reaction is carried out under conditions of limited oxygen, the reaction does not reach completion under these experimental conditions and all of the dopa is not consumed as seen from the residual 1292 cm^{-1} band (Fig. 7.6, panel b, top spectrum). Nevertheless, thus obtained decay rate of dopa is in agreement with the consumption rate (~ 1.29 - 4.57 x 10^{-3} min$^-$) of another melanin precursor (tyrosine) during tyrosinase assisted oxidation in aerobic atmosphere.[79]

7.3.3.2 Kinetics of dopachrome formation and decay

The change in absorbance at 480 nm with time as the catalyzed reaction proceeds is shown in Fig. 7.7, panel (d). The absorbance increases as DC is formed, reaches maximum absorption at 60th min and decays due to conversion of DC to melanochrome. To extract the rates of DC formation and decay, we fitted the observed data with Eq 2b′. The rate of DC formation obtained from increase of absorbance (at 480 nm) is k^E_{DC} = 5.7 x 10^{-2} min^{-1} while that of DC decay is k^E_{N-1}=1.4 x 10^{-2} min^{-1}. Since melanin and its

intermediates have overlapping absorbance spectra, it is possible that these rates contain contribution from other intermediates besides DC as well. Hence, we also followed the formation and decay of DC with its molecule specific signature, the vibrational band at 1668 cm^{-1} (Fig. 7.7, panel e). We observed an initial rise in DC concentration followed by a decrease after maximum concentration was reached at 60 min. The rise and fall were modeled with Eq. 2b′ that was also used to model absorbance. The rate of DC formation k^E_{DC} (Raman) is found to be 4.9 x 10^{-2} min^{-1} in agreement with that obtained from absorbance. On the other hand, rate of loss of intensity of the 1668 cm^{-1} band was found to be k^E_{N-1} = 4.7 x 10^{-3} min^{-1} (Fig. 7.7, panel e) that is 4 times slower than that obtained from absorbance. This discrepancy is addressed below.

RR intensity reports on species with C=O at 5th and 6th position of the indolic block. We found that the decay of the 1668 cm^{-1} band follows biexponential kinetics: one of the rates corresponds to decay of DC and a minor amount is the contribution from the precursor dopa (Fig. 7.6, panel a, 0th hr spectrum) itself. Dopa has a low intensity vibrational band at this position. Dopa oxidizes to form indolequinone species (<10 %) that has a carbonyl moiety on benzene ring similar to DC. Thus Raman decay profile of DC within 90-400 min was fitted with two exponential time constants (Eq. 2b″) k^E_D (loss of monomeric dopa) and k^E_{N-1} (loss of pure DC). We have an independent measurement for decay of dopa, k^E_D = 5.2 x 10^{-3} min^{-1}, derived from decay of the 1292 cm^{-1} band. Thus the decay rate of DC is obtained as k^E_{N-1} = 5.8 x 10^{-2} min^{-1} comparable to that obtained from absorbance (1.4 x 10^{-2} min^{-1}). This decay rate of agrees well with that (4.0 x 10^{-4} sec^{-1} = 2.4 x 10^{-2} min^{-1}) obtained for DC, formed via oxidation of dopa by Ag$_2$O at pH 6.8.[85]

7.3.3.3 Kinetics of melanochrome and preceding intermediates

During enzymatic oxidation (Fig. 7.7, Panel c) following an initial rise the MC concentration remains constant after 120 min. Soon after the maximum concentration of DC is achieved, a precipitate of melanin starts building up in the sample tube. The apparent saturation after the 100th min is due to precipitation of the heavier polymers that are formed. A fit to the linear part of the absorbance yields a rate of MC formation as k^E_{MC} = 1.1 x 10^{-3} min^{-1}.

We monitored the Raman signature of MC at 1616 cm^{-1} in these reactions. Kinetics of MC formation is found to be distinct in the autoxidation (Fig. 7.7, panel a) and enzymatic reactions (Fig. 7.7, panel b). In contrast with the immediate increase in MC observed in the absorbance kinetics, Raman data reveal a lag phase in both reactions. The absorption and Raman spectra report on different populations because of the origin of the spectra. While the electronic absorption band at 363 nm contains contributions from different intermediates, the vibrational band at 1616 cm^{-1} is an intrinsic and specific signature of aromatic C=C str. of polymers of DHI formed during melanization. Since the rate of DC decay does not match that of MC formation, kinetics measured with RR imply that DC does not directly convert to MC. There must be at least one intermediate between

the decay of DC and formation of MC. Since we do not have the identity of this intermediate, as the most general case we assume that DC converts to an intermediate, I_{N-1} and the precursor to MC is a distinct, unknown molecule, I_N.

The absorption and Raman signatures of MC report on not just one distinct molecule but all initial soluble melanin precursors with similar skeletal ring structures. These polymers grow by addition of monomers to existing short polymers. It is reasonable to assume that after the formation of the first monomeric precursor of MC, likely DHI, the rate for subsequent dimerization and further addition of monomers to the polymers should be similar. If MC and its precursor I_N form at similar rates ($k_N \approx k_{MC}$) in consecutive reactions, the observed rate of the reaction can be represented by Eq. 1e′. Modeling the experimental data with this equation yields $k_{MC} = 1.5 \times 10^{-4}$ min^{-1} and $k_N = 2.0 \times 10^{-4}$ min^{-1} (Fig. 7.7, panel a). The enzymatic process is modeled by Eq. 2e′ that yields the two rates as $k^E_{MC} = 9.0 \times 10^{-3}$ min^{-1} and $k^E_N = 9.1 \times 10^{-3}$ min^{-1} that are an order of magnitude faster than the uncatalyzed reaction (Fig. 7.7, panel b).

7.3.4 Raman and IR vibrational bandwidths provide a quantitative measure of melanin heterogeneity

Melanin produced through either method has a symmetric, broad RR band centered at 1616 cm^{-1}. This broad band consists of several closely spaced Raman bands of slightly different wavenumbers. Corroborating this is the FTIR spectrum shown in Fig. 7.6, panel (c). FTIR spectra were obtained in the absence of bulk water and have less broadening for the monomer resulting in higher resolution. Spectra of melanin recorded at different times after reaction initiation are shown in Fig. 7.6, panel (c). As soon as polymerization starts, spectral signature of dopa that has many sharp bands is lost and a broad band appears ~1620 cm^{-1} instead. Unlike in RR spectra, where the central position of observed C=C str. (1616 cm^{-1}) does not change, distinct shoulders are seen in FTIR spectra owing to differential absorption by closely spaced vibrational modes. Though spectra of melanin at the 96th and 144th h contain a sharp band at 1551 cm^{-1} that appears like a monomer feature, dopa does not have a band at this position. This band must arise from one of the monomeric intermediates *en route* to melanin polymerization. Additionally while the broad band spans from 1420 to 1780 cm^{-1}, shoulders are observed at 1462, 1507, 1551, 1584, 1627 and 1717 cm^{-1}. Collectively these bands indicate the presence of several distinct species in the reaction mixture. The band at 1717 cm^{-1}, a marker of C=O str. is weak and indicates presence of very low amounts of carbonyl moiety in melanin, the other bands below 1630 cm^{-1} likely arise from ring str. modes of different reaction intermediates.

For a quantitative assessment of presence of different type of polymers from vibrational spectroscopic data, theoretical simulation of Raman spectra of different type of melanin models was necessary. FTIR spectra contain IR active modes from all polymeric species unlike RR measurement where a particular mode from all species is enhanced. It is

important to note that, while FTIR spectroscopy was performed on a dry, solid sample made into a pellet, RR spectra were recorded in solution. Thus it is also possible that in IR measurements, macromolecular assembly of melanin that is known to be held together via non-covalent interaction between proto-molecules was disrupted during sample preparation.
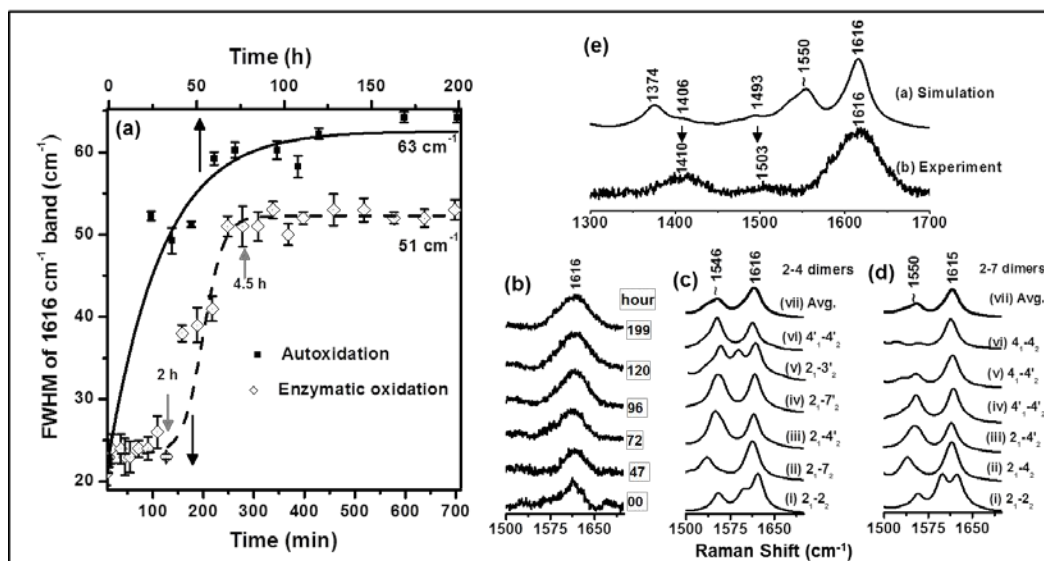
Fig. 7.8 (a) Time evolution of full width at half maxima (FWHM) of melanochrome RR signature at 1616 cm^{-1} in the tyrosinase-assisted (dotted) and self-oxidation of dopa to form melanin. Enzymatic and auto-oxidation data are fitted with exponential and sigmoidal function respectively to for a visual comparison only; (b) RR spectra of auto-oxidized reaction within melanin band region at various time points mentioned; computed Raman spectra of lowest energy tetramers of (c) 2-4 and (d) 2-7 dimers of DHI; and (e) average Raman spectra of 20 energetically most favorable DHI tetramers (top) along with 260 nm excited Raman spectra of dopa melanin in tris-HCl buffer (bottom). A fixed Lorentzian line width of 25 cm^{-1} and a scaling factor of 0.98 for computed vibrational wavenumbers are used for simulation of all spectra. In panel d, out of fourteen lowest energy species (See Fig. 7.9), spectra of six tetramers are shown. The spectrum displayed in top row (vii of panel d) is average of all fourteen spectra.

In Fig. 7.8, panel (a), we show time evolution of the full-width at half maximum (FWHM) of the band centered at 1616 cm^{-1} during both enzymatic and non-enzymatic oxidation. As small, soluble oligomeric species of melanin polymers are made from structurally analogous monomers, their aromatic stretching vibrations are expected to have similar but slightly different positions. We use the FWHM of the overall band as a measure of heterogeneity of the pigment formed.

Upon autoxidation, the FWHM of the 1616 cm^{-1} band immediately begins to increase and continues to grow monotonically until it reaches saturation at 200 h (FWHM = 63 cm^{-1}). Presence of the enzyme restricts the FWHM and introduces a distinct lag phase of 2 h in the growth of the FWHM. After the lag phase is completed, there is a quadratic rise in heterogeneity followed by prolonged saturation period. The maximum FWHM achieved in the presence of the enzyme is smaller (51 cm^{-1}) than that in the autoxidation reaction. Thus, enzymatic control of melanization appears to limit heterogeneity of population of early polymeric species during melanin formation.
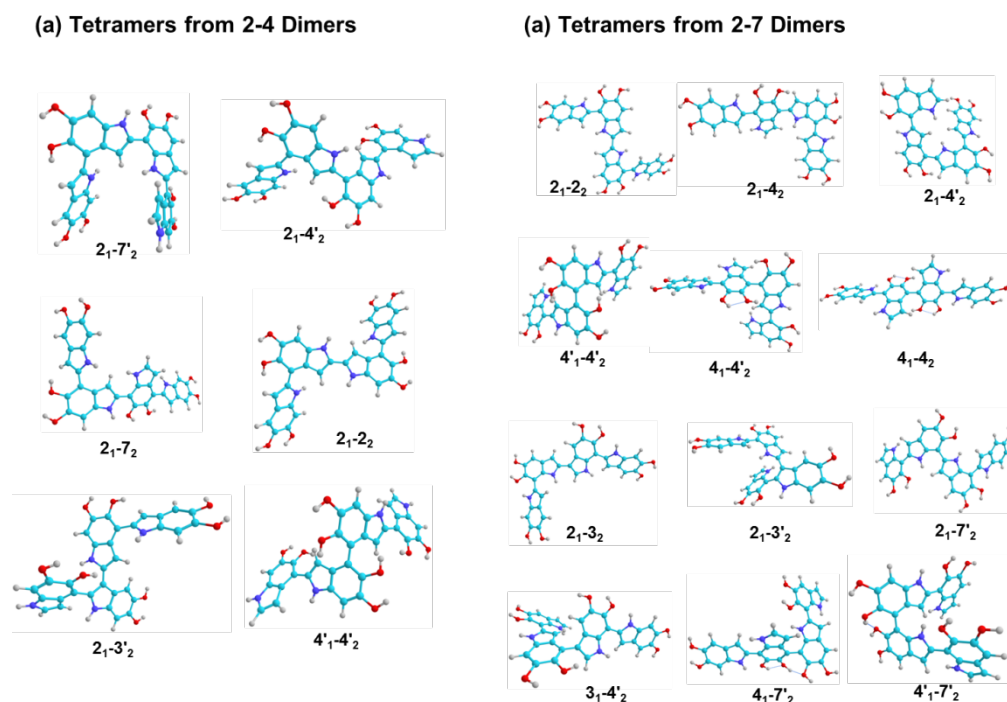
Fig. 7.**9** Lowest energy DHI tetramers made from (a) 2-4 dimers and (b) 2-7 dimers. Relative energies of these oligomers are described in Table 7.4.

The duration of this lag phase is longer than the time it takes to achieve the maximum concentration of DC ~ 60 min. Thus formation of DC is required for the next step and accumulation of a threshold quantity of DC accelerates the formation of MC. Since free DC is unstable in the autoxidation reaction, these data suggest that presence of tyrosinase stabilizes DC. Additionally, tyrosinase also plays a regulatory role in limiting the heterogeneity of melanin. The mechanism through which this is accomplished warrants deeper investigation. The fact that despite the differences in bandwidth, the central wavenumber of the broad melanin band is similar in both reactions implies that the skeletal structures of the initial polymers formed with and without the enzyme are similar.

7.3.5. Species responsible for the 480 nm absorption is dopachrome

To establish the identity of the intermediate that absorbs at 480 nm in the enzyme induced melanization reaction, we used visible resonance Raman spectroscopy in conjunction with computational modeling of DC structure and spectra. The strong and broad 480 nm absorption band of DC originates from a localized HOMO→LUMO (95%) transition involving π electrons of the indole ring and both carbonyls at 5th and 6th position (Fig. 7.4, panel c, top row). Thus, Raman excitation at 488 nm is expected to preferentially enhance vibrational signature of DC over other molecules in solution. Fig. 7.5, panel (b) shows average of Raman spectra (λ_{exc}=488 nm) of species formed from 5th to 15th min, 30th to 60th min and 82nd to 92nd min of polymerization by tyrosinase in open air. Several bands are observed in the 550-1900 cm^{-1} region. The computed spectrum of DC is in complete agreement with the experimental bands confirming the identity of the species being observed. (Fig. 7.4, panel b)

Description of vibrational modes (See Table 7.2) of DC shows that the ring stretching vibrations coupled with catecholic C=O stretching are RR enhanced with 488 nm excitation. Two important bands of DC at 1640 and 1682 cm^{-1} are assigned to carbonyl group vibrations coupled with ring stretching from DFT calculations (See Fig. 7.4, panel a). A Raman band around 1680 cm^{-1} was also observed during Mn(III)$^+$ assisted oxidation reaction of a series of catecholamines and was assigned to ν(C=O) vibration.[93] Loss of intensity of two bands at 1640 and 1682 cm^{-1} indicates decay of DC and appearance of new bands at 1551 cm^{-1} and 1591 cm^{-1} is sign of formation of new species. These bands may mark signatures of soluble polymers that are formed during early polymerization. The position of these bands suggests their origin as aromatic ring str. with slightly differing in force constants.[108–110]

To further establish the structure of DC, we modeled the 488 nm excited resonance Raman intensities. RR spectra in resonance with the first excited state (S_1) were computed (Fig. 7.4, panel b). RR spectrum was computed from gradients along each normal mode evaluated with time-dependent DFT (TD-DFT) on potential energy surface of S_1 state of DC. Vertical excited states are computed at ground state geometry optimized with B3LYP/6-311+G(2d,p)//PCM level of theory. Details of the method of computing RR spectra are described in supporting information. Overall, trends in the enhancement patterns of other modes are correctly predicted. Two discrepancies are noted in the relative intensities of 1682 and 1639 cm^{-1} bands. We note that these two modes have a significant contribution of the stretching mode of the carbonyl bond. Thus, local solvation structure around C=O moiety at 5th and 6th positions is expected to affect the computed RR intensity through modulation of normal modes.

Table 7.2 Experimental[a] and computed[b] vibrational wavenumbers of dopachrome.

RR 488 nm	DFT	Assignment
670	653	Ben. breath.
-	676	In-plane rock.
-	688	Ben. tors.
-	756	Ben. + Pyr. symm. breath.
-	776	C_4H+C_7H wag.
-	781	Ring str.
848	837	Pyr. def.
-	865	C_4H+C_7H wag.
886	901	C_4H wag.
999	996	Pyr, breath.
-	999	Pyr, breath. + CH_2 be.
1085	1094	N_1-C_2 str.
1179	1186	C_4-C_5 + CH be.
1214	1235	CH + NH be.
1266	1267/1297	CH be.
1316	1303	$C_4-C_5 + C_5-C_6$ str.
1347	1329	$C_5-C_6 + C_2-C_3$ str.
-	1364	C_2-COO^- str. + COO^- symm. Str.
1439	1432	C_8-C_9 str.
1466	1445	$N_1H + C_7H$ be.
-	1460	CH_2 sci.
1595	1574	$C_6=O + C_7=C_8$ str. + C_7H be.
-	1606	COO^- asymm. str
1639	1644	$C_6=O + C_7=C_8 + C_8-N_1$
1682	1695	$C_9=C_4 + C_5=O$ str.

[a]RR with 488 nm excitation, recorded with LabRam HR 800 confocal Raman microscope, equipped with 60 x water emersion objective and 1800 gr/mm grating; [b]computed at B3LYP/6-311+GF(2d,p)//PCM level of DFT and not scaled; abbreviations, Ben., benzene ring; Pyr., pyrrole ring; symm., symmetric; asymm., asymmetric; breath., breathing motion; wag., wagging; def., in-plane ring deformation; be., bending; str., bong stretching.

7.3.6 Simulation of melanin vibrational signature

Attempts have been made to explain experimental Raman spectra[111–118] of synthetic and natural eumelanin using macrocyclic protomolecules[119,120] and individual isolated monomers as models with the help of first principals DFT.[108,121] Centeno and coworkers have assigned surface enhanced Raman bands of sepia melanin using fundamental vibrations of indole and various substituted pyrroles.[118] The reported FTIR spectrum of *sepia* melanin[118] and 633 nm excited micro-Raman spectrum[116] of eumelanin from another source shows a broad band at ~1600 cm^{-1} with a shoulder at ~1400 cm^{-1}. (For microRaman signature of melanin containing skin cells, see Appendix V) With the help of vibrational signature of different monomers and their redox forms, both these studies have assigned the broad band at ~1600 cm^{-1} to C=C aromatic stretching. None of these studies have explained the origin of >80 cm^{-1} bandwidth, in contrast to that of 15-18 cm^{-1} in indolic monomers.

In our model, we computed structures and energies of homodimers of DHI made through covalent coupling at 2, 3, 4 or 7 sites. The 2-2, 2-4 and 2-7 dimers are energetically most stable (See Table 7.3), consistent with experimental findings on structures of small length polymers formed during oxidative polymerization of DHI.[42,43,45,46] It is known that the 2-2 dimer is in highest abundance only in presence of metal ions. Since metal ions were not present in our experiments we restrict further analysis to 2-4 and 2-7 dimers only. In the next step, tetramers were formed by covalent linking of two DHI dimers (Fig. 7.10, panel a and b). The most stable tetrameric species were selected based on their relative single point energies. (Table 7.4 and see Fig. 7.9 for optimized structures) Average of such fifteen spectrum were used to simulate experimental Raman spectra (Fig. 7.8, panel c-e) at B3LYP/6-31G(d,p) level of DFT. Optimized structures and corresponding vibrational spectra in 200-2000 cm^{-1} Raman shift region of all such tetramers are shown in Fig. 7.9.

Table 7.3 Relative energies in kcal/mol for 10 homo-dimers of DHI computed at [a]B3LYP/6-31G(d,p) and [b]B3LYP/6-31+G(2d,p) level of DFT. 2_1–2_2 (2–2), 2_1–4_2 (2–4) and 2_1–7_2 (2–7) are the most stable dimers of DHI when compared at both the methods mentioned.

DHI–DHI dimer			
Unit 2→ Unit 1 ↓	2_2	3_2	4_2	7_2
2_1	0.09^a,**0.00** ^{b}	2.21^a, 2.14^b	0.00^a,**1.01** ^{b}	0.53 ^{a},**1.48** ^{b}
3_1		4.66^a, 4.65^b	5.07^a, 5.09^b	5.07^a, 5.09^b
4_1			1.26^a, 2.31^b	0.61^a, 2.35^b
7_1				5.12^a, 6.47^b

Most stable species are marked in bold. Subscript 1 and 2 stand for first and second unit of a dimer respectively. All single point energies are computed on geometry optimized at B3LYP/6-31G(d,p) level of DFT.

Fig. 7.8, panel c and d show computed component and average (top row) Raman spectra of six most stable tetramers, made from 2-4 dimer (Fig. 7.8, panel c) and fourteen most stable tetramers, made from 2-7 dimers (Fig. 7.8, panel d). Computed average Raman spectra of all twenty tetramers are shown in Fig. 7.8, panel (e) (top) with experimental spectrum (bottom). As the oxidation reaction progresses, experimental Raman spectra (Fig. 7.8, panel a and b) show that the melanochrome band at 1616 cm^{-1} not only gains intensity but becomes broad as well during course of the reaction. We hypothesize that number of distinct species of small chain polymers increases with time, and results in chemical heterogeneity. In all computed spectra of tetramers, the in-plane benzene stretching vibration (~1616 cm^{-1}) has the highest intrinsic Raman activity. This mode preserves its normal mode character in dopa (Fig. 11, panel a, 1628 cm^{-1}) and in and DHI, (Fig. 7.11, panel b, 1616 cm^{-1}).

Table 7.4 Relative energies in kcal/mol for homo-tetramers of DHI (from 2-4 and 2-7 dimers, for optimized structures see Fig. 7.9) computed at [a]B3LYP/6-31G(d,p) and [b]B3LYP/6-31+G(2d,p) level of DFT.

| Tetramers from 2-4 dimers						
Unit 2→ Unit 1↓	2_2	3_2	7_2	$3'_2$	$4'_2$	$7'_2$
2_1	0.00 [a], **0.00** [b]	2.77 [a], 3.21 [b]	0.48 [a], **1.60** [b]	2.06 [a], **2.08** [b]	0.21 [a] **1.26** [b]	1.17 [a] **1.82** [b]
3_1		9.69 [a], 9.94 [b]	6.69 [a], 7.32 [b]	4.82 [a],5.72 [b]	5.64 [a],5.95 [b]	8.56 [a],8.63 [b]
7_1			6.65 [a],6.28 [b]	7.12 [a],6.93 [b]	0.71 [a],2.84 [b]	4.97 [a],6.63 [b]
$3'_1$				5.93 [a], 5.46 [b]	3.47 [a], 3.67 [b]	5.11 [a], 5.20 [b]
$4'_1$					1.61 [a], **2.88** [b]	2.76 [a], 5.69 [b]
$7'_1$						4.86 [a], 6.32 [b]
Tetramers from 2-7 dimers						
Unit 2→ Unit 1↓	2_2	3_2	4_2	$3'_2$	$4'_2$	$7'_2$
2_1	0.31 [a], **0.00** [b]	2.62 [a], **2.15** [b]	0.00 [a], **0.80** [b]	2.67 [a], **2.15** [b, #]	0.04 [a], **1.13** [b]	1.37 [a], **2.30** [b]
3_1		4.78 [a], 4.16 [b]	3.10 [a],3.32[b]	5.57 [a],4.93[b]	2.62 [a],**2.57** [b]	5.52 [a],5.26 [b]
4_1			0.87 [a],**1.87**[b, #]	2.95 [a],2.86 [b]	0.63 [a],**1.51**[b]	0.87 [a],**2.73** [b]
$3'_1$				6.75 [a],**6.68**[b, #]	2.87 [a],**2.67** [b]	7.99 [a],7.23 [b]
$4'_1$					0.50 [a],**1.22** [b]	1.66 [a],**2.82** [b]
$7'_1$						7.51 [a],8.13 [b]

2_1–2_2 (2–2), 2_1–4_2 (2–4) and 2_1–7_2 (2–7) are the most stable dimers of DHI when compared at both the methods mentioned. Most stable species are marked in bold. Subscript 1 and 2 stand for first and second unit respectively. All single point energies are computed on geometry optimized at B3LYP/6-31G(d,p) level of DFT. [#] 2_1-$3'_2$, 4_1-4_2, $3'_1$-$3'_2$ tetramers are experimentally detected.
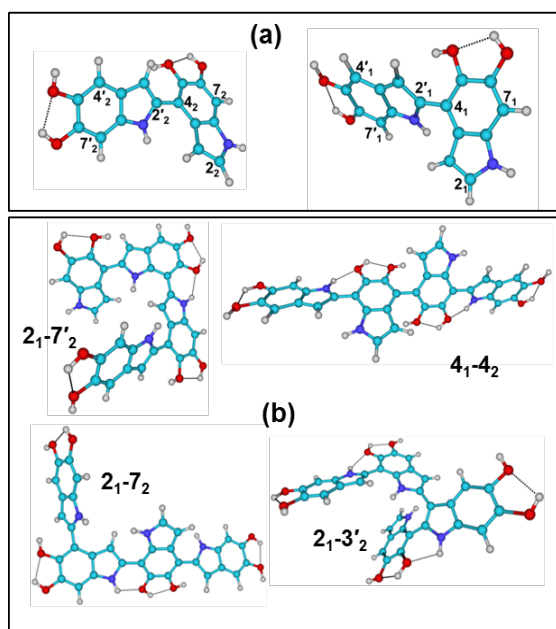
Fig. 7.10 (a) Numbering scheme for two DHI dimers (2-4) that are covalently linked to form tetramers and (b) energy optimized structures of four representative DHI tetramers; 2₁-7′₂ and 2₁-7₂ from 2-4 dimer and 4₁-4₂ and 2₁-3′₂ from 2-7 dimers. Optimized structures of 2₁-7′₂ and 2₁-3′₂ tetramers indicate that both of them have potential to form stacked structures with similar species.

Benzene dewar vibration as the origin of this band in melanin is also supported by presence of identical vibrational normal mode that are observed within 1616-1657 cm^{-1} wavenumber in a series of substituted indoles.[108–110] (Table 7.5) Furthermore, oligomerization at 2, 4 and 7th site increases electronic conjugation between rings and enhances intensity of these modes in tetramers also, Fig. 7.11, panel (c) (1618 cm^{-1}) and panel (d) (1613 cm^{-1}). We also note that the normal mode composition of this mode remains unaltered in higher order oligomers. Thus, linear combination of Raman spectra of these tetramers reproduces the broad band at 1616 cm^{-1} in the experimental spectrum (Fig. 7.8, panel e).

The width of the melanin band at 1616 cm^{-1} in the computed spectra (Fig. 7.8, panel e, top) is less than that of the experimental band (Fig. 7.8, panel e, bottom). Thus, experimental data would be consistent with the presence of a large number of close lying vibrations that would result from oligomers (tetramers and there of higher order oligomers) of similar chain length, but with different connectivity between monomers. We did not take into account oligomers of different length and those made from hetero-species. The other intense band in computed spectra within 1550-1580 cm^{-1} region arises from strong electronic coupling between adjacent rings through the connecting bond. Presence of this band at different positions in various tetramers also contributes to the broadening of the 1616 cm^{-1} band. However, the mode corresponding to the band at ~1550 cm^{-1} does not get resonance enhanced at 260 nm excitation. In addition to accounting for the position and enhancement of the benzene C=C str. mode, our model explains the natural width (FWHM >80 cm^{-1}). Thus, these small oligomers are the fundamental structural unit. A comprehensive model based on this protomolecular model described here is currently being developed.
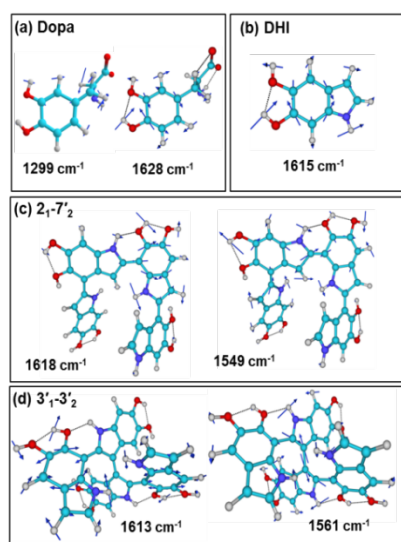
Fig. 7.11 Computed normal modes of (a) dopa, (b) DHI, (c) 21-7′2 tetramer of 2-4 dimer and (d) 3′1-3′2 tetramer of 2-7 dimer of DHI at B3LYP/6-31G(d,p) level of theory. The aromatic ring stretching mode of dopa (1628 cm^{-1}) preserves its composition in DHI (1616 cm^{-1}) and in tetramers (1618 and 1613 cm^{-1} in c and d respectively) also. The other intense mode of these tetrameric species is a ring stretching vibration that couples with inter-unit C-C stretching (1549 and 1561 cm^{-1} in (c) and (d) respectively). All computed wavenumbers are scaled by a factor 0.98.

Table 7.5 Experimental vibrational wavenumbers corresponding to aromatic ring stretching in substituted indoles[108–110] within 1550-1630 cm^{-1} of wavenumber region.

Substituted Indoles	Wavenumber	
	Aromatic ring str.	
Indole	1616 [3]	1577 [3]
3-formylindole	1612 [3]	1576 [3]
1-methyl-3-formylindole	1611 [3]	1576 [3]
1-ethyl-3-formylindole	1610 [3]	1575 [3]
3-acetylindole	1612 [3]	1579 [3]
1-methyl-3-acetylindole	1633 [3]	1574 [3]
1,3-diacetylindole	1607 [3]	1584 [3]
5,6-dihydroxyindole-2-carboxylic acid	1649 [2], 1657 [1]	1600 [1]
Indole-2-carboxylic acid	1627 [2]	1582 [2]

[1]Raman, λ_{exc} = 1064 nm, Ref [108]; [2]Raman, λ_{exc} = 785 nm, Ref [109]; [3]FT-IR, Ref [110]; As the exocyclic substituent changes, the π electron densities of the indole ring changes, therefore, strengths of the aromatic bonds also.

7.4. Discussion

Combined kinetic scheme with obtained rate constants of formation and decay of reactants and intermediates on melanin synthesis pathway is presented in Fig. 7.12. Consumption of precursor, dopa, is found to be exponential, with a rate of 5.2 x 10^{-3} min^{-1} in presence of tyrosinase (k^E_D). Using absorbance at 480 nm and fingerprint vibrational signature at 1668 cm^{-1} as probe, the next intermediate DC is found to form with a slower rate, k^E_{DC} = 4.9-5.7 x 10^{-2} min^{-1}. DC forms at a rate that is an order of magnitude faster than decay rate of dopa, and thus suggests presence of intermediates. These intermediates are known as DQ and cyclodopa. (Fig. 7.12) In fact, the spontaneous decay of unstable DQ to cyclodopa has been previously probed by pulse radiolysis technique. It has been shown that, in neutral conditions, after reaching a critical concentration, the reductive cyclization of DQ is very fast with a rate constant, k_{DQ} of 3–7 s^{-1} (or 1.8–4.2 x 10^2 min^{-1}).[71–73] Additionally, it is also known that the redox generation of DC form DQ is exceptionally fast, with a rate constant of 10^9 M^{-1} s^{-1}.[102]
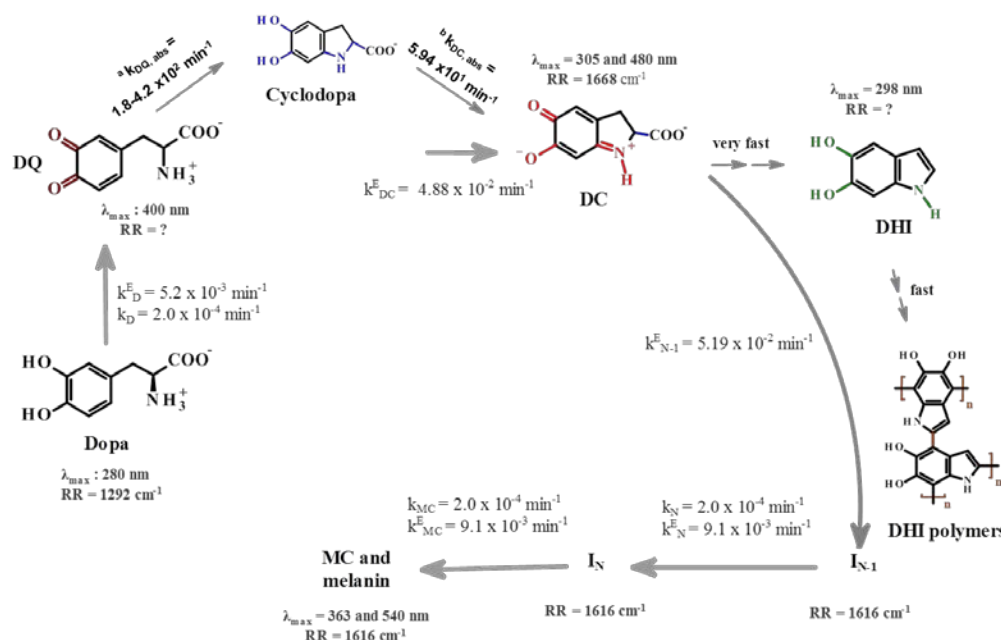
Fig. 7.12 Integrated scheme with kinetics rates of melanin formation. Rate constants of different reactants are summarized from the current study and previously published results. k^E_D and k_D are consumption rate of dopa in presence of tyrosinase and in autoxidation reaction respectively. k_{DQ} is the cyclization rate of DQ obtained from pulse radiolysis experiments. k^E_{DC} and k^E_{N-1} are formation rate of DC and I_{N-1} respectively. k^E_{N-1} is also the decay rate of DC. $^a k_{DQ}$ is from Ref [71–73,76] and Ref [102].

Thus the initial steps in dopa oxidation generally proceed rapidly, beyond time resolution of our experiment. Conversion of DQ to cyclodopa and successively to DC is known to be spontaneous, but exact role of tyrosinase in the process is not specifically known. The aforementioned pulse radiolysis experiments do not probe natural enzyme assisted reaction. Experiment, such as stopped-flow technique coupled with Raman spectroscopy with milliseconds time resolution would be suitable to probe the initial redox exchange steps in eumelanization. Our DFT calculations show that DQ and the intermediate cyclodopa preceding DC has unique vibrational signature that can be used to probe their kinetics. (Fig. 7.13) It is known that dopa inactivates tyrosinase in anaerobic condition.[122,123] At the end anaerobic oxidation (> 600 min), monomer signature (1292 cm^{-1}) is still observed as a result of remaining unused dopa. This can be either a result of depleted oxygen in the reaction tube or due to the absence of active enzyme. Recently the use of excess amount of tyrosinase has been suggested during production of enzyme assisted melanin.[8] Moreover, once DC is formed with the help of amount of oxygen present initially, the consecutive downstream reactions get spontaneously triggered and the role of tyrosinase during these steps is not conclusively known. Deciphering role of

stoichiometry of tyrosinase and the precursor, and dissolved oxygen on observed reaction rates needs further investigations. The remaining dopa can also result during redox generation of one molecule of DC and dopa from two molecules of DQ. To delineate these steps conclusively, rapid-mixing experiments that can simultaneously probe these interconverting species is necessary.
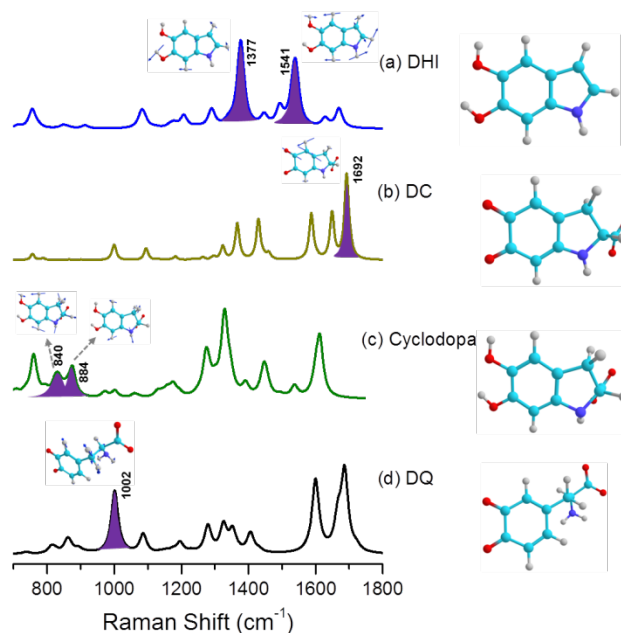
Fig. 7.**13** Optimized structures and computed Raman spectrum of (a) DHI, (b) DC, (c) cyclodopa and (d) DQ at pH 7 with B3LYP/6-311+G(2d,p)//PCM level of DFT. All four species has unique vibrational spectra due to their distinct chemical structure. The distinct vibrational bands representing DQ, cyclodopa and DHI are marked (filled with violet) in their respective spectrum. The associated normal modes are also depicted. Computed spectra are not scaled.

DC decays to DHI via spontaneous decarboxylation and subsequently forms a precursor of pigment, MC. Absence of spectroscopic signature of DHI in any of our measurement implies a faster formation and decay rate than that could be detected in our experiment. Decay of DC and formation of MC is explained by considering, at least, two intermediates, I_{N-1} and I_N. DC decays and $I_{N-1}{}^{th}$ intermediate forms with rate 5.18×10^{-2} min^{-1} and 1.4×10^{-2} min^{-1} respectively. Consecutively $I_{N-1}{}^{th}$ intermediate converts to I_N that subsequently produces MC with slower rate $\sim 9.1 \times 10^{-3}$ min^{-1}. Overall, in presence of enzyme, formation and decay rates of DC are found to be one order of magnitude faster than consumption rate of dopa, and formation rates of I_n and MC. In autoxidation, DC is not stable enough to be detected and the overall kinetics follows the rates that are slower than those in tyrosinase-catalyzed reaction.

Falguera *et al.* have noted an interesting fact; a gradual decrease of extinction coefficient (ε) of DC at 480 nm with the increase in the initial concentration of the precursor.[79] This is a consequence of the fact that, in their kinetic model, ε is kept a free parameter. Extinction coefficient is an intrinsic property of a molecule. These authors rationalize their observation as; "melanin formation is a complex reaction in which a group of heterogeneous length chain pigments are formed. In this way, chains with different composition will affect differently to the global coefficient." Our data clearly demonstrates that absorbance at 480 nm has a significant amount of contribution from early time pigment and melanin itself. Thus, for the successful development of a reliable kinetic model of melanin formation, DC and melanin have to be probed with non-interfering spectroscopic probes, such as distinct RR signature.

Sutter *et al.* have used fluorescence of thioflavin T (ThT) to analyze the kinetics autoxidized of dopa-melanin formation in solution phase.[124] ThT is a molecular rotor which has weakly emissive state in solution but fluoresces once inter-unit rotation is constrained.[125] They have observed an initial time-lag, then rise and finally saturation of ThT fluorescence during the course of melanization reaction. From this observation it was inferred that as melanin starts aggregating, ThT gets intercalated between sheet-like structures, resulting in an increase in fluorescence. These authors have argued, the presence of the time-lag indicates dopa-melanin is not formed by monomer addition; instead, it involves formation of protomolecular seed first. Similar lag-period in our time evolution of RR bandwidth support commencement of production of protomolecular structure after small length polymers reach a critical concentration. Our kinetic data shows that MC and the preceding intermediate, I_{N-1} form at similar rate in both enzymatic and non-enzymatic reactions. We rationalize this finding by arguing that after a critical chain length, subsequent addition of monomer would proceed with a similar rate.

7.5. Conclusion

We have examined the initial polymerization process of melanin with multiple probes, Raman, infrared, UV-visible absorption, and computational models. We have used vibrational spectroscopy to obtain chemical identity of the intermediates of melanin and used these to follow the kinetics of the reaction. Using a kinetic model, we report the rates of consumption of the monomeric melanin precursor, dopa, rates of formation and decay of the key intermediate dopachrome and formation of melanochrome. Exclusive chemical signatures of dopa, intermediate DC and early time polymer are established through their vibrational bands at 1292, 1670 and 1616 cm^{-1} respectively. These Molecule-specific vibrational markers allowed us to follow the fates of intermediates that have similar absorption spectra.

Melanin produced in enzyme-assisted and autoxidation reactions are turned out to have vibrational fingerprint at the same 1616 cm^{-1} wavenumber position. However, we find that, tyrosinase not only accelerates rates of consumption of dopa and formation of melanin by an order of magnitude compared to those in an autoxidation reaction, but also

drives the eumelanization through distinct pathway. The role of the enzyme is better understood and shows that the enzyme stabilizes selective intermediates to control the heterogeneity of melanin. Preceding the pigment formation, distinct population of short length DHI polymers, implicated in several reports are found to have smaller Raman bandwidth compared to their aggregated product, melanin. We explain the position and width of experimentally observed Raman band of melanin as an outcome of intrinsic structural heterogeneity due to a distribution of tetrameric oligomers. Our computational results show that the experimentally detected oligomeric scaffolds[41–47] that are relatively unexplored as natural structural model of melanin need further investigations.

References

[1]   P. Meredith, T. Sarna, *Pigment Cell Res.* **2006**, *19*, 572.
[2]   S. Ito, *Biochim. Biophys. Acta - Gen. Subj.* **1986**, *883*, 155.
[3]   P. A. Riley, *Int. J. Biochem. Cell Biol.* **1997**, *29*, 1235.
[4]   P. Meredith, B. J. Powell, J. Riesz, S. P. Nighswander-Rempel, M. R. Pederson, E. G. Moore, *Soft Matter* **2006**, *2*, 37.
[5]   J. D. Simon, D. Peles, K. Wakamatsu, S. Ito, *Pigment Cell Melanoma Res.* **2009**, *22*, 563.
[6]   M. d'Ischia, A. Napolitano, A. Pezzella, P. Meredith, T. Sarna, *Angew. Chemie Int. Ed.* **2009**, *48*, 3914.
[7]   S. Ito, K. Wakamatsu, M. D'ischia, A. Napolitano, A. Pezzella, in *Melanins and Melanosomes* (Eds.: J. Borovanský, P.A. Riley), Wiley-VCH Verlag GmbH & Co. KGaA, Weinheim, Germany, **2011**, pp. 167–185.
[8]   M. d'Ischia, K. Wakamatsu, A. Napolitano, S. Briganti, J.-C. Garcia-Borron, D. Kovacs, P. Meredith, A. Pezzella, M. Picardo, T. Sarna, J. D. Simon, S. Ito, *Pigment Cell Melanoma Res.* **2013**, *26*, 616.
[9]   F. Solano, *New J. Sci.* **2014**, *2014*, 1.
[10]   M. d'Ischia, A. Napolitano, V. Ball, C.-T. Chen, M. J. Buehler, *Acc. Chem. Res.* **2014**, *47*, 3541.
[11]   M. d'Ischia, K. Wakamatsu, F. Cicoira, E. Di Mauro, J. C. Garcia-Borron, S. Commo, I. Galván, G. Ghanem, K. Kenzo, P. Meredith, A. Pezzella, C. Santato, T. Sarna, J. D. Simon, L. Zecca, F. A. Zucca, A. Napolitano, S. Ito, *Pigment Cell Melanoma Res.* **2015**, *28*, 520.
[12]   H. C. Longuet-Higgins, *Arch. Biochem. Biophys.* **1960**, *86*, 231.
[13]   A. Pullman, B. Pullman, *Biochim. Biophys. Acta* **1961**, *54*, 384.
[14]   J. E. McGinness, *Science (80-.).* **1972**, *177*, 896.
[15]   J. McGinness, P. Corry, P. Proctor, *Science (80-.).* **1974**, *183*, 853.
[16]   A. B. Mostert, B. J. Powell, F. L. Pratt, G. R. Hanson, T. Sarna, I. R. Gentle, P. Meredith, *Proc. Natl. Acad. Sci.* **2012**, *109*, 8943.
[17]   J. Wünsche, Y. Deng, P. Kumar, E. Di Mauro, E. Josberger, J. Sayago, A. Pezzella, F. Soavi, F. Cicoira, M. Rolandi, C. Santato, *Chem. Mater.* **2015**, *27*, 436.
[18]   D. S. Galvão, M. J. Caldas, *J. Chem. Phys.* **1988**, *88*, 4088.
[19]   D. S. Galvão, M. J. Caldas, *J. Chem. Phys.* **1990**, *93*, 2848.
[20]   D. S. Galvão, M. J. Caldas, *J. Chem. Phys.* **1990**, *92*, 2630.
[21]   L. E. Bolívar-Marinez, D. S. Galvão, M. J. Caldas, *J. Phys. Chem. B* **1999**, *103*, 2993.
[22]   K. B. Stark, J. M. Gallas, G. W. Zajac, M. Eisner, J. T. Golab, *J. Phys. Chem. B* **2003**, *107*, 3061.
[23]   K. B. Stark, J. M. Gallas, G. W. Zajac, M. Eisner, J. T. Golab, *J. Phys. Chem. B* **2003**, *107*, 11558.
[24]   K. B. Stark, J. M. Gallas, G. W. Zajac, J. T. Golab, S. Gidanian, T. McIntire, P. J. Farmer, *J. Phys. Chem. B* **2005**, *109*, 1970.
[25]   J. J. Riesz, J. B. Gilmore, R. H. McKenzie, B. J. Powell, M. R. Pederson, P. Meredith, *Phys. Rev. E* **2007**, *76*, 021915.
[26]   M. L. Tran, B. J. Powell, P. Meredith, *Biophys. J.* **2006**, *90*, 743.
[27]   J. Cheng, S. C. Moss, M. Eisner, *Pigment Cell Res.* **1994**, *7*, 263.
[28]   J. Cheng, S. C. Moss, M. Eisner, P. Zschak, *Pigment Cell Res.* **1994**, *7*, 255.
[29]   J. M. Gallas, K. C. Littrell, S. Seifert, G. W. Zajac, P. Thiyagarajan, *Biophys. J.* **1999**, *77*, 1135.
[30]   Y. T. Thathachari, M. S. Blois, *Biophys. J.* **1969**, *9*, 77.
[31]   P. Díaz, Y. Gimeno, P. Carro, S. González, P. L. Schilardi, G. Benítez, R. C. Salvarezza, A. H. Creus, *Langmuir* **2005**, *21*, 5924.
[32]   G. W. Zajac, J. M. Gallas, A. E. Alvarado-Swaisgood, *J. Vac. Sci. Technol. B Microelectron. Nanom. Struct.* **1994**, *12*, 1512.
[33]   G. W. Zajac, J. M. Gallas, J. Cheng, M. Eisner, S. C. Moss, A. E. Alvarado-Swaisgood, *Biochim. Biophys. Acta - Gen. Subj.* **1994**, *1199*, 271.
[34]   C. M. R. Clancy, J. D. Simon, *Biochemistry* **2001**, *40*, 13353.
[35]   Y. Liu, J. D. Simon, *Pigment Cell Res.* **2003**, *16*, 72.
[36]   Y. Liu, J. D. Simon, *Pigment Cell Res.* **2003**, *16*, 606.
[37]   E. Kaxiras, A. Tsolakidis, G. Zonios, S. Meng, *Phys. Rev. Lett.* **2006**, *97*, 218102.
[38]   S. Meng, E. Kaxiras, *Biophys. J.* **2008**, *94*, 2095.
[39]   S. Meng, E. Kaxiras, *Biophys. J.* **2008**, *95*, 4396.
[40]   C.-T. Chen, V. Ball, J. J. de Almeida Gracio, M. K. Singh, V. Toniazzo, D. Ruch, M. J. Buehler, *ACS Nano* **2013**, *7*, 1524.
[41]   M. d'Ischia, A. Napolitano, A. Pezzella, E. J. Land, C. A. Ramsden, P. A. Riley, **2005**, pp. 1–63.
[42]   M. d'Ischia, A. Napolitano, K. Tsiakas, G. Prota, *Tetrahedron* **1990**, *46*, 5789.
[43]   L. Panzella, A. Pezzella, A. Napolitano, M. D'Ischia, *Org. Lett.* **2007**, *9*, 1411.
[44]   A. Pezzella, A. Napolitano, M. D'Ischia, G. Prota, *Tetrahedron* **1996**, *52*, 7913.
[45]   A. Pezzella, L. Panzella, O. Crescenzi, A. Napolitano, S. Navaratman, R. Edge, E. J. Land, V. Barone, M. D'Ischia, *J. Am. Chem. Soc.* **2006**, *128*, 15490.
[46]   A. Pezzella, L. Panzella, A. Natangelo, M. Arzillo, A. Napolitano, M. D'Ischia, *J. Org. Chem.* **2007**, *72*, 9225.
[47]   A. Pezzella, D. Vogna, G. Prota, *Tetrahedron* **2002**, *58*, 3681.
[48]   L. Hong, J. D. Simon, *J. Phys. Chem. B* **2007**, *111*, 7938.
[49]   Y. Liu, J. D. Simon, *Pigment Cell Res.* **2005**, *18*, 42.
[50]   D. R. Dreyer, D. J. Miller, B. D. Freeman, D. R. Paul, C. W. Bielawski, *Langmuir* **2012**, *28*, 6428.
[51]   Y. Li, J. Liu, Y. Wang, H. W. Chan, L. Wang, W. Chan, *Anal. Chem.* **2015**, *87*, 7958.
[52]   A. Corani, A. Huijser, T. Gustavsson, D. Markovitsi, P.-Å. Malmqvist, A. Pezzella, M. D'Ischia, V. Sundström, *J. Am. Chem. Soc.* **2014**, *136*, 11626.
[53]   M. Gauden, A. Pezzella, L. Panzella, M. T. Neves-Petersen, E. Skovsen, S. B. Petersen, K. M. Mullen, A. Napolitano, M. D'Ischia, V. Sundström, *J. Am. Chem. Soc.* **2008**, *130*, 17038.
[54]   C.-T. Chen, C. Chuang, J. Cao, V. Ball, D. Ruch, M. J. Buehler, *Nat. Commun.* **2014**, *5*, DOI

10.1038/ncomms4859.

[55]   S. Gogia, A. Jain, M. Puranik, *J. Phys. Chem. B* **2009**, *113*, 15101.

[56]   N. Jayanth, M. Puranik, *J. Phys. Chem. B* **2011**, *115*, 6234.

[57]   C. Lee, W. Yang, R. G. Parr, *Phys. Rev. B* **1988**, *37*, 785.

[58]   A. D. Becke, *J. Chem. Phys.* **1993**, *98*, 5648.

[59]   S. Miertuš, E. Scrocco, J. Tomasi, *Chem. Phys.* **1981**, *55*, 117.

[60]   G. Scalmani, M. J. Frisch, *J. Chem. Phys.* **2010**, *132*, 114110.

[61]   J. Tomasi, B. Mennucci, R. Cammi, *Chem. Rev.* **2005**, *105*, 2999.

[62]   R. Bauernschmitt, R. Ahlrichs, *Chem. Phys. Lett.* **1996**, *256*, 454.

[63]   M. E. Casida, C. Jamorski, K. C. Casida, D. R. Salahub, *J. Chem. Phys.* **1998**, *108*, 4439.

[64]   M. J. Frisch *et al. Gaussian 09, Revision D.01*, Gaussian Inc., Wallingford, **2013**.

[65]   H. S. Raper, *Biochem. J.* **1926**, *20*, 735.

[66]   H. S. Raper, *Biochem. J.* **1927**, *21*, 89.

[67]   H. S. Raper, H. B. Speakman, *Biochem. J.* **1926**, *20*, 69.

[68]   H. S. Raper, A. Wormall, *Biochem. J.* **1923**, *17*, 454.

[69]   H. S. Mason, *J. Biol. Chem.* **1948**, *172*, 83.

[70]   C. J. Cooksey, P. J. Garratt, E. J. Land, S. Pavel, C. A. Ramsden, P. A. Riley, N. P. M. Smit, *J. Biol. Chem.* **1997**, *272*, 26226.

[71]   C. Lambert, T. G. Truscott, E. J. Land, P. A. Riley, *J. Chem. Soc. Faraday Trans.* **1991**, *87*, 2939.

[72]   E. J. Land, S. Ito, K. Wakamatsu, P. A. Riley, *Pigment Cell Res.* **2003**, *16*, 487.

[73]   E. J. Land, C. A. Ramsden, P. A. Riley, *Acc. Chem. Res.* **2003**, *36*, 300.

[74]   R. Edge, M. D'Ischia, E. J. Land, A. Napolitano, S. Navaratnam, L. Panzella, A. Pezzella, C. A. Ramsden, P. A. Riley, *Pigment Cell Res.* **2006**, *19*, 443.

[75]   S. Ito, K. Wakamatsu, *Photochem. Photobiol.* **2008**, *84*, 582.

[76]   E. J. Land, P. A. Riley, *Pigment Cell Res.* **2000**, *13*, 273.

[77]   P. Palumbo, M. D'Ischia, G. Prota, *Tetrahedron* **1987**, *43*, 4203.

[78]   C. Olivares, F. Solano, *Pigment Cell Melanoma Res.* **2009**, *22*, 750.

[79]   V. Falguera, J. Pagán, A. Ibarz, *Food Res. Int.* **2010**, *43*, 66.

[80]   A. Palumbo, F. Solano, G. Misuraca, P. Aroca, J. C. Garcia Borron, J. A. Lozano, G. Prota, *Biochim. Biophys. Acta - Gen. Subj.* **1991**, *1115*, 1.

[81]   K. Tsukamoto, I. J. Jackson, K. Urabe, P. M. Montague, V. J. Hearing, *EMBO J.* **1992**, *11*, 519.

[82]   C. Jiménez-Cervantes, F. Solano, T. Kobayashi, K. Urabe, V. J. Hearing, J. A. Lozano, J. C. García-Borrón, *J. Biol. Chem.* **1994**, *269*, 17993.

[83]   R. E. Boissy, C. Sakai, H. Zhao, T. Kobayashi, V. J. Hearing, *Exp. Dermatol.* **1998**, *7*, 198.

[84]   C. Olivares, C. Jimenez-Cervantes, J. A. Lozano, F. Solano, J. C. Garcia-Borror, *Biochem. J.* **2001**, *354*, 131.

[85]   A. Palumbo, M. D'Ischia, G. Misuraca, G. Prota, *Biochim. Biophys. Acta - Gen. Subj.* **1987**, *925*, 203.

[86]   J. M. Pawelek, *Pigment Cell Res.* **1991**, *4*, 53.

[87]   V. J. Hearing, *J. Invest. Dermatol.* **2011**, *131*, E8.

[88]   S. Ito, K. Wakamatsu, in *Pigment. Syst.*, Blackwell Publishing Ltd, Oxford, UK, **n.d.**, pp. 282–310.

[89]   T. Kondo, V. J. Hearing, *Expert Rev. Dermatol.* **2011**, *6*, 97.

[90]   J.-D. Chai, M. Head-Gordon, *Phys. Chem. Chem. Phys.* **2008**, *10*, 6615.

[91]   A. Akemi Ooka, R. L. Garrell, *Biopolymers* **2000**, *57*, 92.

[92]   S. A. Siddiqui, A. K. Pandey, A. Dwivedi, S. Jain, N. Misra, *J. Chem. Pharm. Res.* **2010**, *2*, 835.

[93]   W. J. Barreto, S. Ponzoni, P. Sassi, *Spectrochim. Acta Part A Mol. Biomol. Spectrosc.* **1998**, *55*, 65.

[94]   H. W. Duckworth, J. E. Coleman, *J. Biol. Chem.* **1970**, *245*, 1613.

[95]   I. Behbahani, S. A. Miller, D. H. Okeeffe, *Microchem. J.* **1993**, *47*, 251.

[96]   J. Pawelek, A. Körner, A. Bergstrom, J. Bologna, *Nature* **1980**, *286*, 617.

[97]   J. M. Pawelek, M. Murray, *Cancer Res.* **1986**, *46*, 493.

[98]   A. K. Chakraborty, J. T. Platt, K. K. Kim, B. Kwon, D. C. Bennett, J. M. Pawelek, *Eur. J. Biochem.* **1996**, *236*, 180.

[99]   K. Nagasaki, M. Kumazawa, S. Murakami, S. Takenaka, K. Koike, K. Aoki, *Appl. Environ. Microbiol.* **2008**, *74*, 5106.

[100] M. Gauden, A. Pezzella, L. Panzella, A. Napolitano, M. D'Ischia, V. Sundström, *J. Phys. Chem. B* **2009**, *113*, 12575.

[101] M. Foster, *Proc. Natl. Acad. Sci. U. S. A.* **1950**, *36*, 606.

[102] M. R. Chedekel, E. J. Land, A. Thompson, T. G. Truscott, *J. Chem. Soc. Chem. Commun.* **1984**, 1170.

[103] R. T. Packard, R. L. McCreery, *J. Phys. Chem.* **1988**, *92*, 6345.

[104] F. Binns, R. F. Chapman, N. C. Robson, G. A. Swan, A. Waggott, *J. Chem. Soc. C Org.* **1970**, 1128.

[105] E. Buszman, B. Pilawa, M. Zdybel, D. Wrześniok, A. Grzegorczyk, T. Wilczok, *Chem. Phys. Lett.* **2005**, *403*, 22.

[106] M. Zdybel, E. Chodurek, B. Pilawa, *Appl. Magn. Reson.* **2011**, *40*, 113.

[107] A. Beberok, M. Zdybel, B. Pilawa, E. Buszman, D. Wrześniok, *Chem. Phys. Lett.* **2014**, *592*, 41.

[108] H. Okuda, A. Nakamura, K. Wakamatsu, S. Ito, T. Sota, *Chem. Phys. Lett.* **2007**, *433*, 355.

[109] S. P. Nighswander-Rempel, S. Olsen, I. B. Mahadevan, G. Netchev, B. C. Wilson, S. C. Smith, H. Rubinsztein-Dunlop, P. Meredith, *Photochem. Photobiol.* **2008**, *84*, 613.

[110] F. Billes, P. V. Podea, I. Mohammed-Ziegler, M. Toşa, H. Mikosch, D.-F. Irimie, *Spectrochim. Acta Part A Mol. Biomol. Spectrosc.* **2009**, *74*, 1031.

[111] J. A. Pierce, D. M. Rast, *Phytochemistry* **1995**, *39*, 49.

[112] E. Harki, T. Talou, R. Dargent, *Food Chem.* **1997**, *58*, 69.

[113] M. G. Bridelli, D. Tampellini, L. Zecca, *FEBS Lett.* **1999**, *457*, 18.

[114] B. Bilińska, *Spectrochim. Acta Part A Mol. Biomol. Spectrosc.* **2001**, *57*, 2525.

[115] Z. Huang, H. Lui, X. K. Chen, A. Alajlan, D. I. McLean, H. Zeng, *J. Biomed. Opt.* **2004**, *9*, 1198.

[116] V. Capozzi, G. Perna, A. Gallone, P. F. Biagi, P. Carmone, A. Fratello, G. Guida, P. Zanna, R. Cicero, *J. Mol. Struct.* **2005**, *744-747*, 717.

[117] A. Samokhvalov, Y. Liu, J. D. Simon, *Photochem. Photobiol.* **2007**, *80*, 84.

[118] S. A. Centeno, J. Shamir, *J. Mol. Struct.* **2008**, *873*, 149.

[119] L. Sangaletti, S. Pagliara, P. Vilmercati, C. Castellarin-Cudia, P. Borghetti, P. Galinetto, R. Gebauer, A. Goldoni, *J. Phys. Chem. B* **2007**, *111*, 5372.

[120] L. Sangaletti, P. Borghetti, P. Ghosh, S. Pagliara, P. Vilmercati, C. Castellarin-Cudia, L. Floreano, A. Cossaro, A. Verdini, R. Gebauer, A. Goldoni, *Phys. Rev. B* **2009**, *80*, 174203.

[121] B. J. Powell, T. Baruah, N. Bernstein, K. Brake, R. H. McKenzie, P. Meredith, M. R. Pederson, *J. Chem. Phys.* **2004**, *120*, 8608.

[122] J. L. Muñoz-Muñoz, J. R. Acosta-Motos, F. Garcia-Molina, R. Varon, P. A. Garcia-Ruíz, J. Tudela, F. Garcia-Cánovas, J. N. Rodríguez-López, *Biochim. Biophys. Acta - Proteins Proteomics* **2010**, *1804*, 1467.

[123] Y. Tomita, A. Hariu, C. Mizuno, M. Seiji, *J. Invest. Dermatol.* **1980**, *75*, 379.

[124] J. U. Sutter, J. Bidláková, J. Karolin, D. J. S. Birch, *Appl. Phys. Lett.* **2012**, *100*, 113701.

[125] V. I. Stsiapura, A. A. Maskevich, V. A. Kuzmitsky, V. N. Uversky, I. M. Kuznetsova, K. K. Turoverov, *J. Phys. Chem. B* **2008**, *112*, 15893.

8

Structural models of Eumelanin Protomolecules

UV-Vis
Absorption

Vibrational
Raman

X-ray
Structure Factor

Electronic
Density of States

Macrocycle

Non-covalently bonded

Covalently linked twisted

Extended heteropolymer

IQ : z=H and x,y=O
DHI/HQ : z=H and x,y=OH
SQ: x (or y)=OH and y (or x)=O
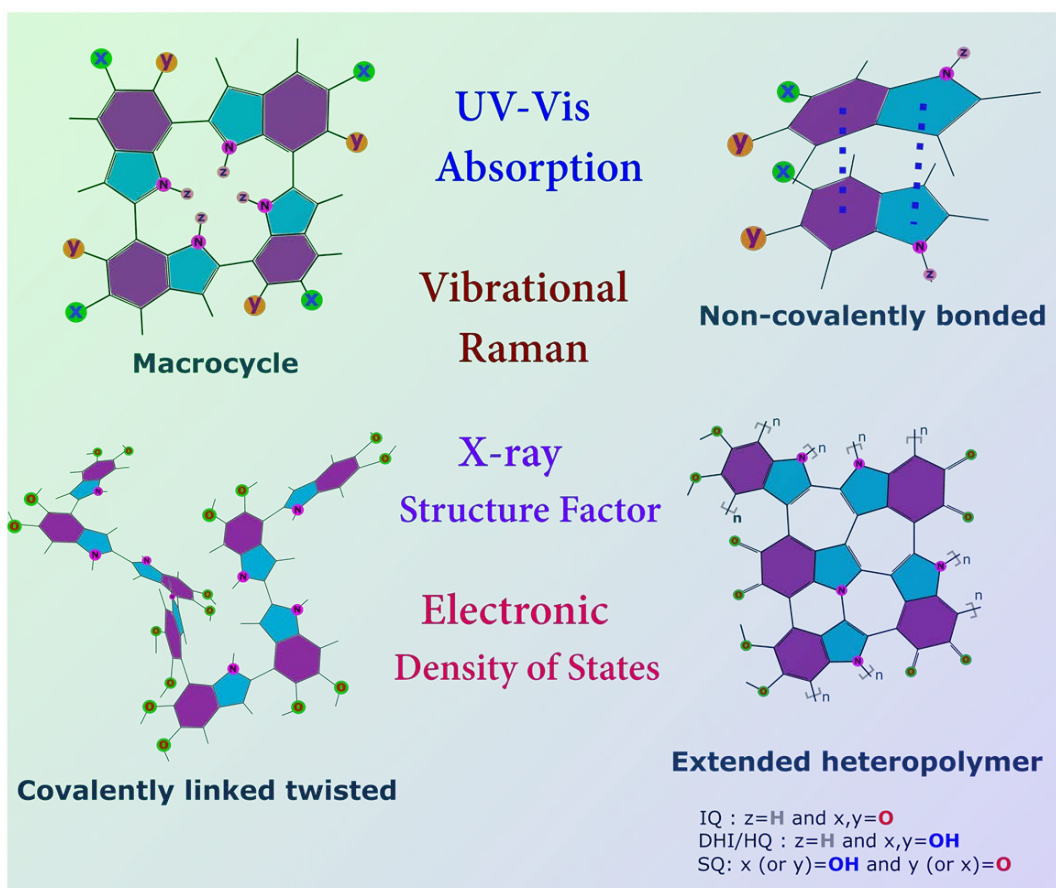
8.1 Introduction

The accurate microscopic structure of the melanin classes of macromolecules has eluded scientists for more than half a century.[1–10] In recent times, because of its ability to convert optical energy into electrical and heat energy, these synthetic melanins have garnered the considerable attention of material scientists to exploit it as multi-functional soft material in technological applications.[11–14] Apart from the quest for structural elucidation of an omnipresent natural pigment, melanin has engaged scientists by its multifaceted properties as an advanced functional biomaterial in recent times.[7,11–18] After several experimental studies including X-ray and inelastic neutron scattering,[19–23] mass spectroscopy,[24–33] high resolution topography imaging,[34–41] vibrational spectroscopy,[42–50] and theoretical modeling,[51–69] the structure-property relationship behind versatile functionalities of this macromolecule remains at large.

There are three naturally occurring melanins; (i) gray to black colored eumelanin, (ii) reddish pheomelanin and (ii) neuromelanin which is present in dopaminergic neurons in the substantia nigra. Other than these three, all chemically prepared pigments via oxidation of 3,4-dihydroxyphenylalanine (DOPA) and dopamine (DA) are referred as synthetic eumelanins. Chemical degradation studies have shown that at the primary level it is accepted that natural and synthetic eumelanins are made from 5,6-dihydroxyindole-2-carboxylic acid (DHICA) and 5,6-dihydroxy-indole (DHI) and their various oxidative states.[70–76] But the primary level of structural organization which consists of the fundamental building unit, referred as protomolecule is highly debatable. The current state of understanding of the organization of this complex macromolecule at fundamental level includes several competing structural models.

The broad UV/Vis absorption characteristic of eumelanin is equally well explained by different structural models starting from (i) finite and infinitely extended heteropolymer,[54,55,57,59,69] (ii) stacked macrocycle,[61,63,64] (iii) non-covalently held monomers,[33,68,77,78] and recently proposed (iv) geometric order/disorder model.[66,67] There exist an intrinsic heterogeneity in the chemical nature of the coupling sites of the monomers and all types of small oligomers. This effect leads to size distributions of melanin protomolecules in a mass spectrum of eumelanin. Meredith and coworkers have termed this intrinsic size distribution as chemical disorder model.[60] Heterogeneous populations of the protomolecules with differing structures exist in all the proposed models. This disorder emerges through (i) random site polymerization (in extended heteropolymer model); (ii) changes in stoichiometry of the different monomeric units to form a porphyrin-like structure (in stacked macrocycle model);[61] (iii) a heterogeneous distribution of non-covalently held homo- and hetero-dimers of the monomers (in non-

covalently held monomers model)[68] and due to presence of unique (iv) structural ordering of different protomolecules, including linear, macrocycle and non-covalently bound monomers.[67] All of these four models except the last one show that linear superposition of computed absorption spectra from a finite number of oligomeric motifs can explain the broad featureless absorbance of eumelanin within UV to near-IR wavelength range. The fourth model demonstrates that excitonic coupling between different types of the protomolecules arises from certain geometric ordering and is the reason behind the monotonic upsurge in absorption spectra in the high energy range.[67]

X-ray derived structural parameters[20,21] and several high resolution scanning probe microscopic studies[34,36,40] of eumelanins from different sources have suggested a layered sheet structure, commonly referred as stacked oligomer model. Using density functional theory (DFT) Kaxiras and co-workers have proposed an inner porphyrin-like tetrameric structure made from covalent linking of four units of DHICA, DHI, and their redox forms.[61,64] In this model, the fundamental aggregate is made from 4-5 such layers with an interplanar distance of 3.3–3.6 Å, thus making its vertical dimension 14–17Å. Within this model the broad peak ~0.45Å^{-1} in experimental X-ray derived structure factor, S(q) spectra[20] have been interpreted as an inherent structural order *i.e.*, the longest dimension of the fundamental unit is of the order 15–20 Å. Although, this computationally predicted model explains (i) optical absorption, (ii) binding and releasing property of metal ions and (iii) the stacked structure model, a direct experimental detection of such protomolecules is far-fetched.
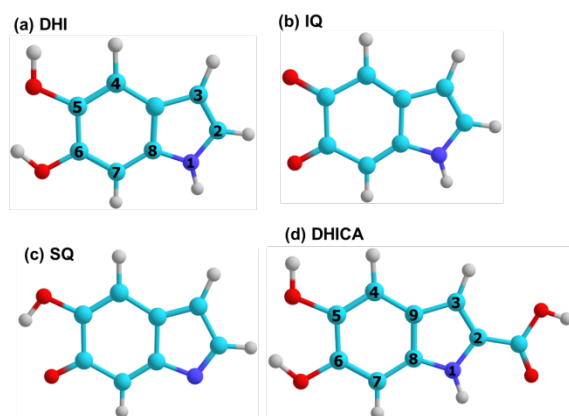
Fig. 8.1 Optimized structure of four melanin building units (a) DHI or HQ, (b) indolequinone or IQ (c) semiquinone or SQ and (d) DHICA at B3LYP/6-31G(d,p)//*vacuo* level. The conventional numbering of ring atoms is shown for DHI (a) and DHICA (d).

D'Ischia, Prota and colleagues have isolated small polymeric species of model eumelanin from controlled oxidation of both DHI and DHICA.[79–86] Structures of these oligomers are established through solution state nuclear magnetic resonance (NMR) spectroscopy. These studies have shown that oligomerization proceeds through 2nd, 3rd, 4th or 7th sites in DHI polymers and through 4th and 7th position in DHICA oligomers. (Fig. 8.1) These small length oligomers are formed via single interunit covalent bonds. In

solution, two dimers of DHICA shows sub-picoseconds excited state decay compared to that of DHICA[87,88] and DHI.[89] This finding is in line with the photoprotective role of eumelanin in our skin. Apart from a few initial reports,[55,58,69] this types of oligomeric scaffolds have not been explored in detail as potential eumelanin protomolecules.

Experimental and computational investigations on eumelanin look-alike dopamine-melanin (also known as poly-dopamine) have indicated the presence of significant amount of non-covalent interactions in the supramolecular assembly.[33,68,73,77,78,90] This melanin, prepared through oxidative aggregation of dopamine, has emerged as a universal biocompatible coating material and many other potential applications in bio-organic devices. Nuclear magnetic resonance (NMR) and electrospray ionization mass spectrometry (ESI-MS) evidences led to the conclusion that aggregate of dopamine-melanin consists of non-covalently bound (hydrogen bonds, π-stacking and ionic interactions) monomers, [33,77,78] and covalently connected units.[33,78] *Ab initio* computations have also predicted non-covalently stabilized dimers of DHI and its different redox forms; indolequinone (IQ), and semiquinone (SQ) with average interplanar distance of 2.7–3.2 Å.[68] A heterogeneous population of these dimers also explains the broad eumelanin absorption spectra. Thus, there exists a severe disagreement about the structures of the fundamental melanin building blocks.

Apart from Kaxiras and co-workers[61] no other authors who have proposed alternative models have taken into account X-ray derived structural parameters. Moreover, other than two reports[47,50] none of the proposed models have been tested to reproduce the experimental vibrational signature of melanin. Normal Raman spectra of sepia melanin feature a band around ~1615 cm^{-1} with a shoulder ~1380 cm^{-1}.[42–44,46–49] Compared to spectra of small molecules, these two eumelanin bands are broad with a full width at half maxima (FWHM) of 50-80 cm^{-1}. In chapter 7, it has been shown that 260 nm excited resonance Raman (RR) spectra of synthetic and enzymatically prepared melanin have a band 1615 cm^{-1} with an FWHM of ~70 cm^{-1}. As the reported vibrational signature is not as heterogeneously broadened as the UV/Vis absorption spectra, we envisage that it would naturally impose a structural constraint on any proposed model.

Our proposed model is inspired from previously reported structures of DHI and DHICA oligomers. In the present scenario where no consensus has been reached on the protomolecular structure of melanin, it is important to explore the viability of a model whose smallest structural components are taken from experimentally detected oligomers. The most important feature of these small oligomeric chains is their self-packing ability which is naturally induced by steric interactions among exocyclic hydroxyl and hydrogen atoms. In this study, we propose and capture essential physical, structural and electronic

properties of this twisted linear chain model vis-à-vis other proposed models via first principle density functional theoretical calculations.

8.2 Computational Methods

Geometry optimization without any symmetry constraint on all dimers, tetramers and octamers are performed using Becke three-parameter hybrid functional with non-local exchange-correlation of Lee-Young-Parr, known as B3LYP functional.[91,92] Harmonic vibrational frequencies are computed with the same functional in conjunction with Pople's split–valence Gaussian basis set 6-31G supplemented with one set of the d functions on heavy atoms and one set of p functions on hydrogen atoms. The computed wavenumbers are scaled by a factor 0.98 to obtain the least deviation from experimental wavenumbers for benzene Dewar ring stretching vibration (1615 cm^{-1}). Hexadecamers that are made from selected octamers pairs are optimized by keeping the internal geometry of the constituting parts fixed while relaxing the inter-unit bond and related dihedral angle. Kohn-Sham molecular orbitals are computed for all oligomeric species with same functional as used for band gap estimation of many organic conductors.

Single point (SP) potential energies at a higher level of theory, *viz.* B3LYP/6-31+G(2d,p)//*vacuo* level are computed on B3LYP/6-31G(d,p)//*vacuo* optimized structures. To avoid dealing with large numbers of oligomers, an energy cut-off of $5K_BT$ (~3 kcal/mol at 300 K) from the lowest energetic species is used for the dimers and tetramers. (See text in Chapter 7 and Fig. 7.3 for validity of the used method for relative SP energy calculation) The computed energies of 2-4 and 2-7 DHI dimers lie within 3 kcal/mol of energy from that of the most stable 2-2 dimer, and these three DHI dimers are also experimentally reported previously. Absorption spectra are computed with same B3LYP functional with 6–31+G(d) basis set in gas phase within linear response regime of time dependent DFT (TD-DFT).[93,94] Use of this method to predict absorption spectrum is validated by comparing computed and experimental spectra of DHI.(Fig. 8.3) The predicted position of $^1\pi\pi^*$ state of DHI is blue shifted with respect to experimental value. This is expected because the TD-DFT computation is performed in vacuo. However, relative position and intensities of two low energy transitions of DHI are correctly predicted. Basis set which is minimally augmented with diffuse function is used because for higher order oligomer TD-DFT computations become resource expensive. All quantum chemical computations are performed with Gaussian 09 software package.[95] Absorption and vibrational spectra, and molecular orbitals (MO) are visualized with ChemCraft v1.6.[96]

X-ray scattering properties, such as Radial distribution functions (RDF) and S(q) of the energy optimized DHI octamers are computed with the program, Interactive Structure Analysis of Amorphous and Crystalline Systems (I.S.A.A.C.S) v2.8.[97,98] RDF and S(q) are computed after each oligomer is placed is a cubic box whose dimension is

adjusted so that resulting mass density is close to 1.3 g/cm^3, obtained experimentally.[20] These computed properties on predicted protomolecules are compared with experimentally reported spectra. Electronic densities of states (DOS) spectra are computed using GaussSum v3.0,[99,100] using an FWHM value of 0.5 eV. Computed DOS spectrum is compared with band position in X-ray photoemission spectra of melanin film.
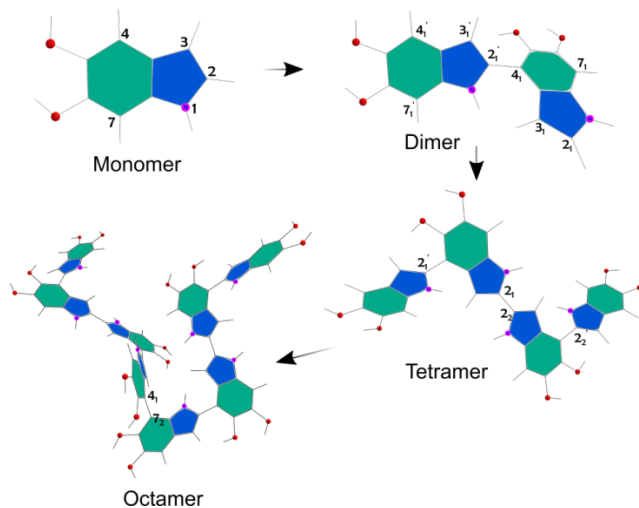
Fig. 8.2 Representative scheme of polymerization of DHI monomers into the formation of higher order scaffolds; dimer (2-4) and tetramer (2_1-2_2) and octamer (4_1-7_2). Oxygen and nitrogen atom is depicted in red and pink respectively. Oxygen and nitrogen atoms are represented by red and pink circle respectively.
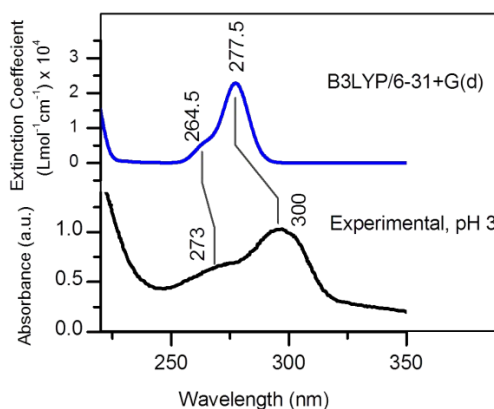
Fig. 8.3 Computed (top) and experimental (bottom) absorption spectra of DHI. The. The spectrum is computed with TD-B3LYP/6-31+G(d)//*vacuo* method on B3LYp/6-31G(d,p)//*vacuo* optimized geometry, and is deconvoluted with a Gaussian line shape having FWHM value of 2000 cm^{-1}. Experimental spectrum is of fully protonated species (i.e. neutral DHI) in aqueous solution at pH 3.0 and is adapted with permission Ref 98, Copyright (2009) American Chemical Society.

8.3 Results and Discussions

8.3.1 DHI oligomers are self-packing in nature

We have found among all 10 possible dimers, three *viz.*2–2, 2–4 and 2–7 are the most energetically favorable dimeric species of DHI in the gas phase. (Fig. 8.4 and Table 7.3) It has been established through controlled polymerization of DHI moiety that 2–4 and 2–7 are the prevalent dimers in the absence of metal ions[80,83–86]and 2–2 is the most abundant one in the presence of divalent metal ions.[79,83,85] In the absence of metal ions, 2–4 and 2–7 dimers are used to make higher order polymeric scaffolds as described in Chapter 7. We find that the tetramers falling within 5 k_BT (= 3 kcal/mol at 300 K) of energy from lowest energetic species naturally include the ones that are detected experimentally. (See Table 7.3) In accord with experimental findings, our computed structures show that these oligomers are not planar due to steric hindrance by neighboring sites. We find that 2–2 coupling results in lowest strain with an interplanar angle of 19.2º ± 5º, and 4–4 and 3–3 coupling leads to maximally nonplanar structure with inter-unit angle of 58º ± 3º and 51º ± 8º respectively. As the bulkier acetyl group might impose more structural constraint in controlled oxidation experiments, the presence of other low energy tetrameric structures (within 3 kcal/mol) cannot be ruled out. Most energetically stable dimers and tetramers of DHICA are also depicted in Fig. 8.4.

It is accepted that the protomolecular assemblies are affected by heterogeneity originating at different levels, (i) size distribution of smaller oligomers, (ii) diversity in molecular scaffold and positional isomerism due to multiple coupling sites, and (iii) redox states of the participating monomeric units.[10] Nonplanarity of small oligomers has a decisive role on the resulting π-electron delocalization during further polymerization and thus has control on the optical band gap of these species. Fig. 8.2 describes the polymerization scheme from the 2–4 dimer of DHI and depicts the intertwined nature of the formed polymers. The DHI octamers can be classified into three distinct classes of oligomeric populations. (Fig. 8.5) Interaction from neighboring indole ring through H-bonding and steric constraint imposed by overlapping of π–electron cloud decide the structural characters. The most abundant classes are partially helical in nature (Fig. 8.5, b) and random coil type (Fig. 8.5, a). The self-packing nature imposes a constraint on the attainable size of the latter types. The longest dimension of these octamers in this model are found to lie within 1.7 to 2.0 nm, (see Fig. 8.20) which is in very good agreement with mass spectroscopic and scanning tunneling microscopic (STM) evidence of ~ 20 Å lateral dimension of the fundamental protomolecules. The third class of semi-planar structures (Fig. 8.5, c) have the potential to form secondary structural scaffold via non-covalent interactions such as π-π, H-bonding, and van der Walls interactions.

8.3.2 Linear intertwined oligomers explain broad UV/Vis absorption

Explanation of broad absorption characteristics has always been the primary aim to validate any eumelanin structural models. TD-DFT computed absorption spectra of three representative oligomers of 2–4 DHI dimers is shown in Fig. 8.6, a. It clearly depicts a gradual redshift of the first absorption band, which is associated to mainly HOMO→LUMO type transition with an increase in chain length (n) of the polymer. This decrease in band gap due to increases in π-electron delocalization is linear in nature with the number of aromatic units added (Fig. 8.6, b), is well documented for organic conducting polymers.
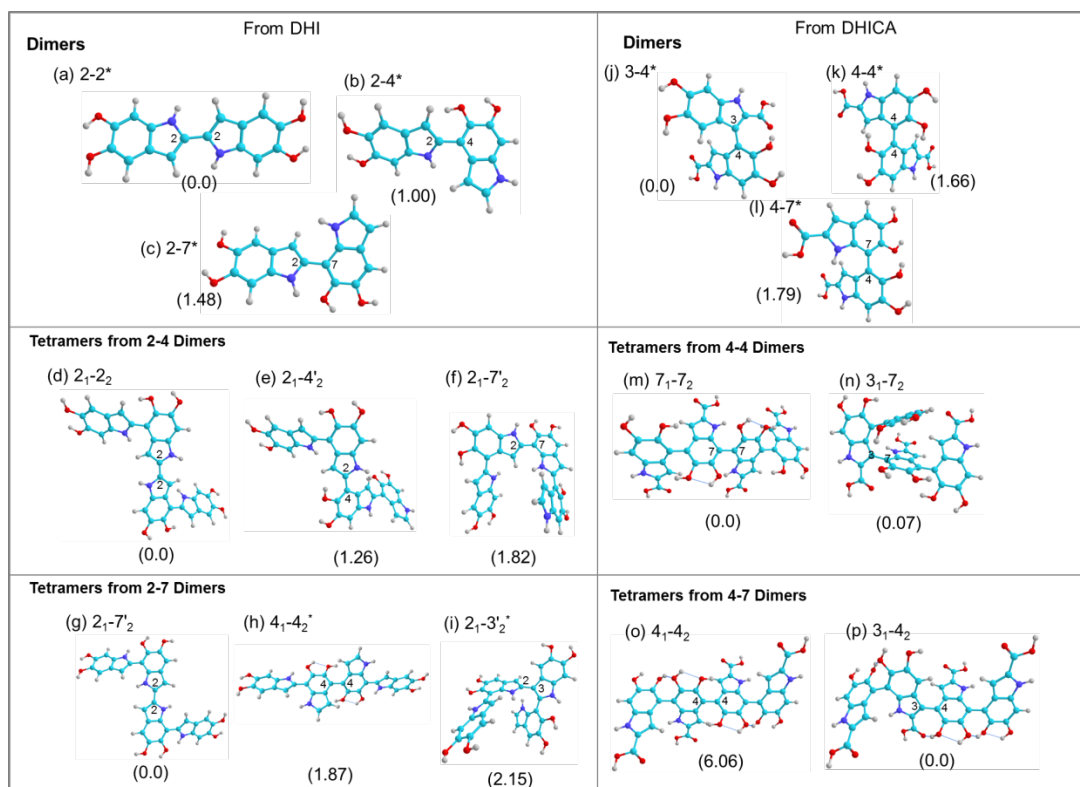
Fig. 8.4. Energy optimized structure of most stable dimers and tetramers of DHI (a-i) and DHICA (j-p). The species that are marked by an asterisk are detected in solution state experiments. (Ref 88-95) The quantities described inside parenthesis for each structure is relative energy (kcal/mol) with respect to lowest energetic species in each category. '1' and '2' as subscript depict the first and second unit of a homopolymer. '′' as superscript represents one of the two same numbered sites in one unit of a homopolymer.

The difference between highest occupied MO and lowest unoccupied MO, HOMO–LUMO gap (HLG) tends to converge to band gap for conducting polymers with n ≥ 10.[101] This saturation effect of HLG is observed for DHI polymers with n ≤ 16 and agrees with the trend of vertical transition energies of first singlet (S_1) state for same. The

S_1 state energies are computed for a lesser number of polymers with n ≤ 8. (Fig. 8.6, b) The offsets in absolute energies among both trends are expected because S_1 energies are computed with the TD-B3LYP method using extra diffusion function augmented basis set compared to the one used for HLG calculations. However, linear extrapolation of these trends does not give a band gap estimate because melanin is not a pure organic conductor, but a hybrid ionic-electronic one.[102] The conductivity of eumelanin film is more of ionic (proton) character[103] unlike conventional organic conductors and also shows a strong dependence of its hydration state.

Computed UV/Vis absorption spectra of all tetramers and octamers (of both DHI and DHICA) show significant absorption in 250-500 nm (Fig. 8.6) range which is the most absorbed region of optical spectra by all types of melanins. These oligomers of different chain length, if placed in proximity, are expected to form secondary and tertiary aggregates. As a result of short-range dipole-dipole interactions between these aggregates, a monotonically increasing band shape of absorption in the high energy range is expected to be reproduced. The origin of excitonic coupling as a result of closely (few nanometers) placed eumelanin protomolecules is recently explained by Buehler and coworkers.[67]
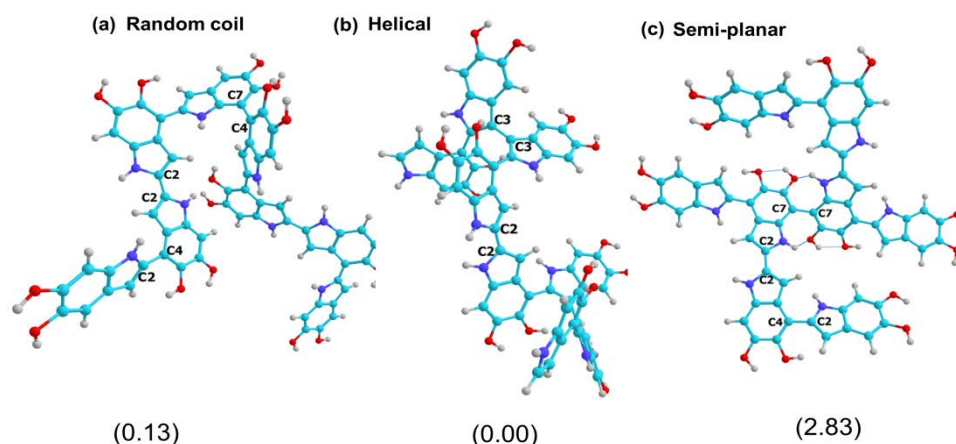
Fig. 8.5. Optimized structures of three representative classes of DHI octamers (a) random coil $(4'_1-7'_2$ from 2_1-2_2 tetramer), (b) partial helical $(2_1-2_2$ from $3'_1-3'_2$ tetramer) and (c) semi-planar types $(7_1-7_2$ from 2_1-2_2 tetramer) made from 2-4 DHI dimers. All geometries are energy minimized at B3LYP/6-31G(d,p) level of DFT in *vacuo*. The relative single point (SP) energies (in kcal/mol) of the three representative octamers are shown in parenthesis (bottom row). SP energies are computed at B3LYP/6-311+G(2d,p)//*vacuo* level of DFT.

Inspection of frontier molecular orbitals of the DHI oligomers reveals certain features of electronic structure that can be related to experimental optical and electron transport properties of eumelanin (Fig. 8.7). The introduction of continuous helicity in the chain through inter-unit twist between adjacent rings interrupts π-electron conjugation between farthest parts of the oligomer. This would affect in electronic

233

conductivity along these protomolecular chains. (ii) a negligible amount of spatial overlap of HOMO (electronic ground state) and LUMO (excited configuration following vertical transition) in the majority of protomolecules suggest very low fluorescence quantum yield, well observed phenomena in eumelanin.[104,105] However, these bulk properties of melanin would strongly depend on its aggregated structure in the presence of environment.
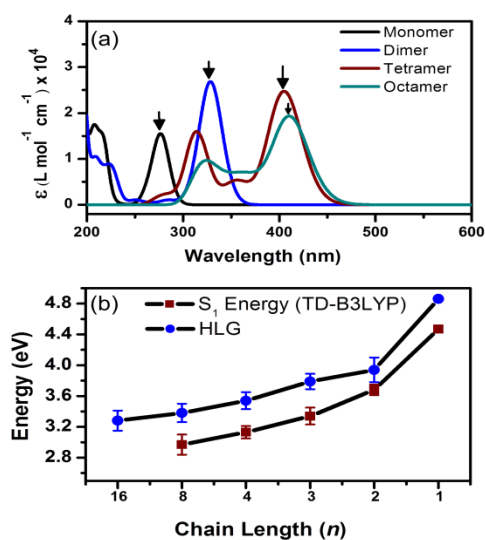
Fig. 8.6 (a) TD-DFT computed absorption spectrum of DHI monomer, 2-4 dimer, 2_1-2_2 tetramer from 2-4 dimer and $4'_1$-$7'_2$ octamer from 2_1-2_2 tetramer and (b) evolution of S_1 state energy and HOMO-LUMO gap (HLG) averaged over all studied oligomers with an increase in chain length. The S_1 transition is marked by the a vertical arrow for each species in (a). HLG are computed at B3LYP/6-31G(d,p) level of DFT while vertical excitation energies for S1 state are calculated at TD-B3LYP/6-31+G(d) level on B3LYP/6-31G(d,p) optimized geometry. A gaussian line width (FWHM) of 2500 cm^{-1} has been used to simulate absorption spectra.
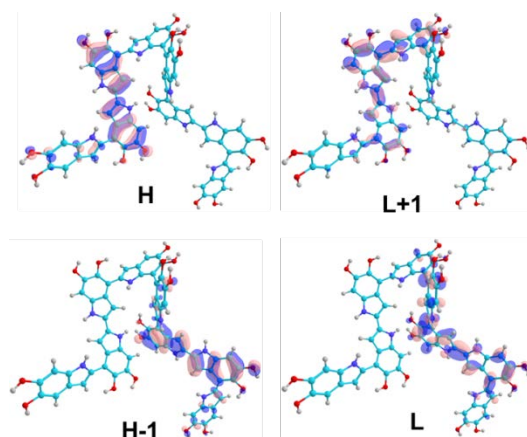
Fig. 8.7 Kohn-Sham frontier molecular orbitals HOMO (H), LUMO (L), and H-1 and L+1 for $4'_1$-$7'_2$ octamer from 2_1-2_2 tetramer of 2-4 dimer, computed at B3LYP/6-31G(d,p) level of DFT.

8.3.3 Vibrational signature of the DHI oligomers explains experimental spectra

Fig. 8.8 describes the effect of increased polymer chain length on Raman spectra of DHI oligomers. Extension of chain through monomer addition has definitive effects on normal mode description as well as the positions of the bands. Pyrrole distortion consisting of stretching of the C2–C3 bond coupled to inter-unit C–C stretching (C$_{2-4}$ str. in 2-4 dimer)

at 1557 cm^{-1} has the highest intensity in the 2–4 dimer. Upon tetramerization (in 2_1-2_2 tetramer from 2-4 dimer) the in-phase benzene and pyrrole breathing coupled with bridging C_{2-2} bond stretching has the maximum intensity owing to increase in one symmetric component (α_{xx}) of the polarizability tensor. This mode splits into four modes upon octamer formation with the intensity of same order of magnitude (Table 8.1 and Fig. 8.9) and appears at nearby positions ~ 1555 cm^{-1}.

This anomalous increase in Raman activity can be anticipated from inspection of HOMOs and LUMOs of the octamers. In general, the HOMOs of octamers (Fig. 8.7), $C_2=C_3$, $C_5-C_6=C_7$, $C_8=C_9-C_4$ moieties are of π type and have antibonding character. But in LUMO, the inter-unit C-C bonds are of π type bonding character, and conjugate either with the $C_4=C_5$ segment of the benzene ring or the C_9-C_3 bond of the pyrrole ring. This unique delocalization character of π electrons along the selective inter-unit C–C bond is expected to be manifested in modulating component of polarizability tensor along specific vibrational modes, described in preceding section.
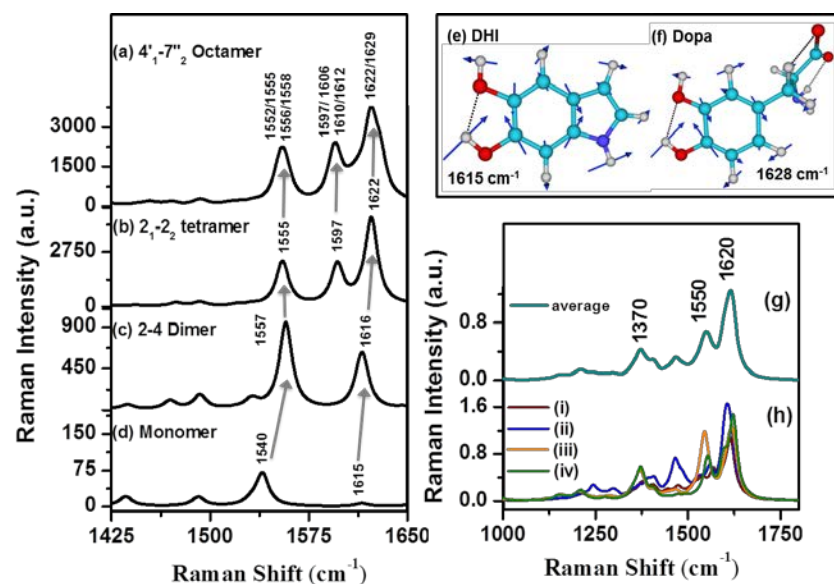
Fig. 8.8 Computed Raman spectrum (a – d) of DHI monomer, 2-4 dimer, 2_1-2_2 tetramer and $4'_1$-$7''_2$ octamer form mentioned dimer; normal modes description of benzene dewar mode corresponding to experimental 1620 cm^{-1} Raman band of melanin in (e) DHI and (f) DOPA; (g)average and (h) individual Raman spectra of fourteen octamers from four types of tetramers, (i) $3'_1$-$3'_2$, (iii) $4'_1$-$7'_2$ and (iv) 2_1-2_2 tetramer from 2-4 and (ii) $3'_1$-$3'_2$ tetramer from 2-7 dimers. Computed Raman wavenumbers are scaled by a factor of 0.98 and a Lorentzian line shape with 25 cm^{-1} FWHM is used generate the spectra from computed Raman activity.

Table 8.1. Frequency, intrinsic Raman activity and normal mode description (major contribution) of most intense in-plane ring modes in DHI monomer, dimer (2–4), tetramer (2_1–2_2) and octamer ($4'1$–$7''2$)

	Raman Shift (cm^{-1})	Assignment	Raman Activity (Å^4/amu)
		Monomer	
DHI	1377	benzene breath. + 6–OH be.	94
DHI	1540	Pyrrole breath. (C_2–C_3 str.)	68
DHI	1615	benzene dewar	6
		Dimer	
2–2	1596	in–phase benzene dewar + C_{2-2} str.	6017
2–2	1625	Pyrrole breath. (C_2–C_3 str.) + C_{2-2} str.	6565
2–2	1612	Out–of–phase benzene dewar	1.1
2–4	1557	Pyrrole breath. (C_2–C_3 str.) + $\mathbf{C_{2-4}}$ str.	1878
2–4	1616	in–phase benzene dewar + $\mathbf{C_{2-2}}$ str.	958
2–4	1615	Out–of–phase benzene dewar	312
2–7	1557	Pyrrole breath. (C_2–C_3 str.) + $\mathbf{C_{2-4}}$ str.	1900
2–7	1618	In–phase benzene dewar + $\mathbf{C_{2-7}}$ str.	2197
2–7	1613	Out–of–phase benzene dewar	13
		Tetramers from 2–4 dimer	
2_1–2_2	1555	Pyrrole breath. (C_2–C_3 str.) + benzene breath. (along 4–7 axis) + $\mathbf{C_{2-4}}$ str.	8388
2_1–2_2	1597	In–phase benzene dewar + Pyrrole breath (C_2–C_3 str.) + $\mathbf{C_{2-2}}$ str.	7914
2_1–2_2	1615	Out–of–phase benzene dewar	61
2_1–2_2	1622	In–phase benzene breath. (C5–C7 str.) + C_2–C_3 str. + $\mathbf{C_{2-2}}$ str.	17309

	Raman Shift (cm^{-1})	Assignment	Raman Activity (Å^4/amu)
		Octamer from 2_1–2_2 tetramer of 2–4 dimer	
$4'_1$–$7''_2$	1552	benzene dewar + pyrrole dist. (C_2–C_3 str.) + $\mathbf{C_{2-2}}$ str.	7117
	1555	benzene dewar + pyrrole dist. (C_2–C_3 str.) + $\mathbf{C_{2-4}}$ str.	6095
	1556	benzene dewar + pyrrole dist. (C_2–C_3 str.) + $\mathbf{C_{2-4}}$ str.	1857
	1558	benzene dewar + pyrrole dist. (C_2–C_3 str.) + C_4–C_5 + C_6–C_7 str. + $\mathbf{C_{2-4}}$ str.	4329
	1594	benzene dewar + C_4–C_5 + C_7–C_8 str. + $\mathbf{C_{2-2}}$ str. + C_6O–H + C_5O–H be.	9697
	1597	benzene dewar + $\mathbf{C_{2-2}}$ str.+ C_6O–H be.	7909
	1606	C_4–C_5 + C_6–C_7 + C_8–N_1 + C_9–C_4 str. (one ring) + benzene dewar (one ring) + C_6O–H be.	2187
	1610	benzene dewar (three rings) + C_6O–H be.	1149
	1612	benzene dewar + $\mathbf{C_{2-2}}$ str. + C_6O–H be.	1907
	1622	In–phase benzene dewar + C_6–C_7 str. + Pyrrole dist. (C_2–C_3 str.) + $\mathbf{C_{2-2}}$ str.	22653
	1629		11108

abbreviations, benzene dewar, breathing of benzene ring along C4-C7 axis; be., bending; str., stretching; breath., breathing of ring; In normal mode description number following atom name depicts position on the indole ring as described in Fig. 8.1 and C_{2-2} and C_{2-4} represents inter-unit C–C bond between two monomers connected at C_2 and C_2 site, and C_2 and C_4 site. Vibrational frequencies are computed at B3LYP/6-31G(d,p) level of DFT and scaled by 0.98.

1555 cm^{-1} (**8388**)
in-phase C$_2$–C$_3$ str. + C$_{2-4}$ str.

1597 cm^{-1} (**7914**)
in-phase benzene dewar + C$_{2-2}$ str.

1612 cm^{-1} (**234**)
Out-of-phase benzene dewar

1558 cm^{-1} (**478**)
out-of-phase pyrrole breath.

1622 cm^{-1} (**17309**)
in-phase C$_2$–C$_3$ + C$_6$–C$_7$ str. + C$_{2-2}$ str.

1615 cm^{-1} (**289**)
in-phase benzene dewar

Fig. 8.9 Normal mode description of 2_1-2_2 tetramer of 2-4 DHI dimers at B3LYP/6-31G(d,p) level of DFT. With each normal mode representation computed vibrational wavenumber (scaled by 0.98) and Raman activity (in parenthesis) in $\mathring{A}^4$/molecule is mentioned. It is important to note that in-phase breathing modes (1555, 1597 and 1622) which have a significant amount of interunit coupling (C$_{2-2}$ or C$_{2-4}$) has the highest intrinsic Raman activity. The in-phase and out-of-phase ring breathing (1615 and 1612 respectively) without inter-unit coupling has low intensity.

In-phase benzene Dewar vibration coupled with C$_{2–2}$ str. at 1622 cm^{-1} in tetramer splits into two intense modes with conserved normal mode character in octamer (Fig. 8.8 and Table 8.1) at 1622 and 1629 cm^{-1}. The other ring breathing mode, mainly localized on C2–C3 str. and the benzene Dewar vibration at 1597 cm^{-1} in the tetramer give rise to five similar modes at 1594, 1597, 1606, 1610 and 1612 cm^{-1} with Raman activity of comparable order of magnitude (Table 8.1). This is the general trend for all oligomers made from different tetramers of 2–4, 2–7, and 2–2 dimers. This splitting of modes into multiple numbers of nearly situated bands due to inter-unit coupling via π electron delocalization introduces a substantial amount of broadening, which increases but eventually saturates with a more combinatorial choice of smaller building units.

The intensity of benzene Dewar mode at ~1615 cm^{-1} which is of lowest value in 3,4-dihydroxyphenylalanine or dopa, preserves its normal mode character in DHI (Fig. 8.8, e and f), and gradually grows during oligomerization. This band also becomes broader due to the presence of closely spaced (in wavenumber) similar modes with comparable intensities, arising solely due to strong vibrational coupling between in-plane ring vibrations. This coupling between indolic monomer units results from π electron delocalization along the inter-unit C–C bond. All individual spectra from a heterogeneous

population of octamers from four different tetrameric species (Fig. 8.8, h) and their averaged behavior (Fig. 8.8, g) show that two major bands ~ 1615 and ~ 1380 cm^{-1} dominate the whole Raman spectra. Out of these, the one at 1615 cm^{-1} is of highest intensity as seen in experimental normal Raman spectra[46,48] and in resonance Raman spectra. (See Chapter 7) The peaks near 1370, 1465 and 1550 cm^{-1} can account for the presence of multiple underlying bands that result from unconstrained deconvolution of 633 nm excited Raman spectra of eumelanin by Capozi, V. *et al.*[46] The assignment of the experimental band ~1615 cm^{-1} as benzene in-plane distortion is further supported by the occurrence of the same in 260 nm excited spectra without enhancement of other modes. (See Chapter 7) Vibrational assignment of several eumelanin bands including the benzene Dewar mode (~ 1615 cm^{-1}) is also performed via systematic comparison with spectra of substituted indoles.[49]

Enhancement in Raman activity of in-plane benzene modes does not merely originate from the additive effect of two component spectra of the constituting species. (Fig. 8.10) Extension of conjugation between two tetrameric units occurs via overlapping of π cloud along inter-unit C-C bond and leads to a six-fold increase of normalized Raman activity of the most intense mode. It is important to note that coupling at the 2–2 site changes the position of the 1570 cm^{-1} (in tetramer) band to 1618 cm^{-1} (in octamer) without modifying its normal mode, *viz.*C_2–C_3 and C_8–C_9 str. with a minor contribution from benzene str. On the contrary, in the case of 2–4, 2–7, 4–4 or 4–7 coupling it is the benzene Dewar mode that gets enhanced. Interestingly, both C_2–C_3 pyrrole str. and benzene Dewar modes occur at ~1615 cm^{-1} when they get enhanced due to oligomerization, and thus explain the experimental broad Raman band around the similar position.

In a study by Meredith and co-workers, the effect of dimerization on a substituted model monomer, *viz.,* N-methyl-5-hydroxy-6-methoxy-indole (MHMI) to form specifically the 4–4 dimer has been previously reported.[106] Though we are dealing with oligomers from experimentally observed DHI dimeric species, we note here an important result from the mentioned report which is of direct relevance to the current study. They have found that positions of bands in 785 nm excited Raman spectra are similar for the MHMI monomer and its dimer. However, a close inspection of experimental and computed spectra reveals a huge increase in relative intensity and simultaneous broadening of the band at ~ 1620 cm^{-1} which are ascribed to the Dewar benzene mode coupled with the vibration of other units. In our calculations we observe the same effect for all three types of DHI dimers (Fig. 8.11) and in the 4–4 dimer (Fig. 8.12) also. Contradictory to claims by previous authors that vibrations of each monomer are unperturbed due to inter-unit dihedral angle, we find strong inter-

unit coupling modifying intrinsic Raman activity of the fundamental ring modes. Specifically, this coupling is found to be responsible for the manifold enhancement of benzene Dewar mode intensity ~ 1620 cm^{-1} which are evidenced in experimental Raman spectra.
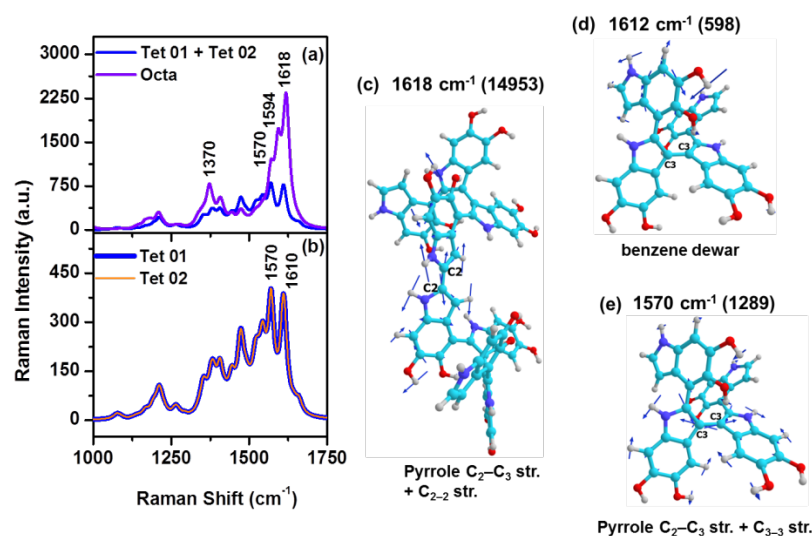

Fig. 8.10. Computed Raman spectra of (a) 2_1-2_2 octamer and addition of individual component spectra, (b) spectra of each component tetramer connected at C_2 site, and normal modes of (c) most intense band at 1618 cm^{-1} in octamer and (d-e) of two most intense bands at 1570 and 1612 cm^{-1} in component tetramers at B3LYP/6-31G(d,p) level of DFT. Intrinsic Raman activities (Å^4/amu) are mentioned in parenthesis. Each spectrum is normalized by the number of monomer units and vibrational wavenumbers are scaled by 0.98. It is to note that six-fold increase in the integrated intensity of band near 1615 cm^{-1} in octamer than that in tetramers is caused by the coupling of interunit C_{2-2} bond str. with pyrrole breathing. Panel (a) shows that this enhancement is not mere an additive effect of two tetramers but an electronic effect that led to increasing in the symmetric element of polarizability tensor.
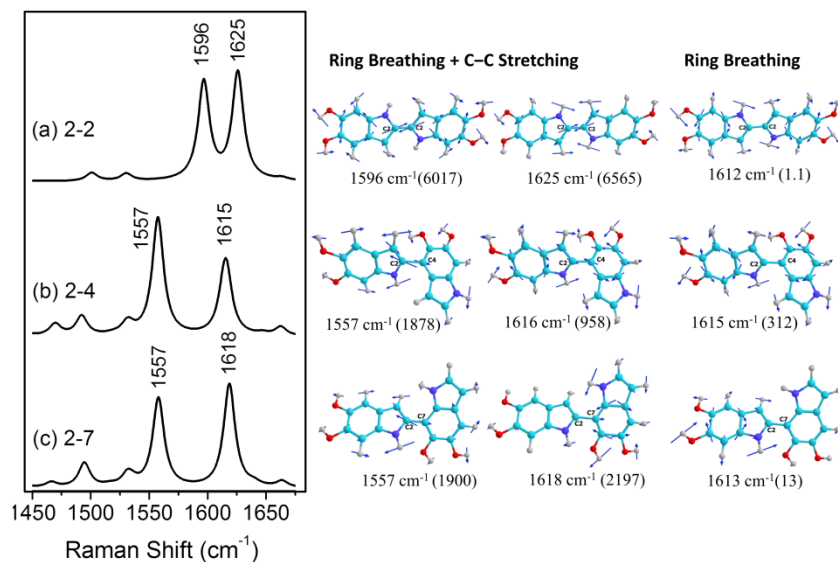
Fig. 8.11. Computed normal Raman spectrum of DHI (a) 2-2, (b) 2-4 and (c) 2-7 dimers and normal modes of intense ring modes. With each normal mode description computed vibrational wavenumber and Raman activity (in parenthesis) in Å^4/molecule is mentioned. In each dimer, two intense modes, among which the ones (1625, 1616 and 1618 cm^{-1}) at higher frequency region is originated from in-phase ring breathing of both the rings coupled with the moderate amount of inter-unit C-C stretching, are identified. The other intense modes (1596, 1557, 1557 cm^{-1}) at lower wavenumber region is ascribed to in-plane pyrrole (in 2-4 and 2-7) or pyrrole and benzene (in 2-2) distortion which is strongly coupled with stretching vibrations of bridging C-C bond. All vibrational wavenumbers are computed at B3LYP/6-31G(d,p) level of DFT and scaled by a factor of 0.98.

Evolution of computed Raman activity of two most intense modes during polymerization is depicted in Fig. 8.13. We find that normalized Raman activity for intense modes like those ~1615 cm^{-1} and 1570 cm^{-1}, ascribed to benzene Dewar (breathing along C_4-C_7 axis) and pyrrole C_2–C_3 bond str. respectively reaches a maximum and then falls with increasing chain length. It turns out that after a certain length (n=8) further addition of monomer unit is neither able to enhance the intensity of the inter-unit bond str. mode nor modulate their position. Thus, analysis of computed Raman intensity imposes a limit on the protomolecular size that is not to be exceeded after octamer for a description of other molecular properties.
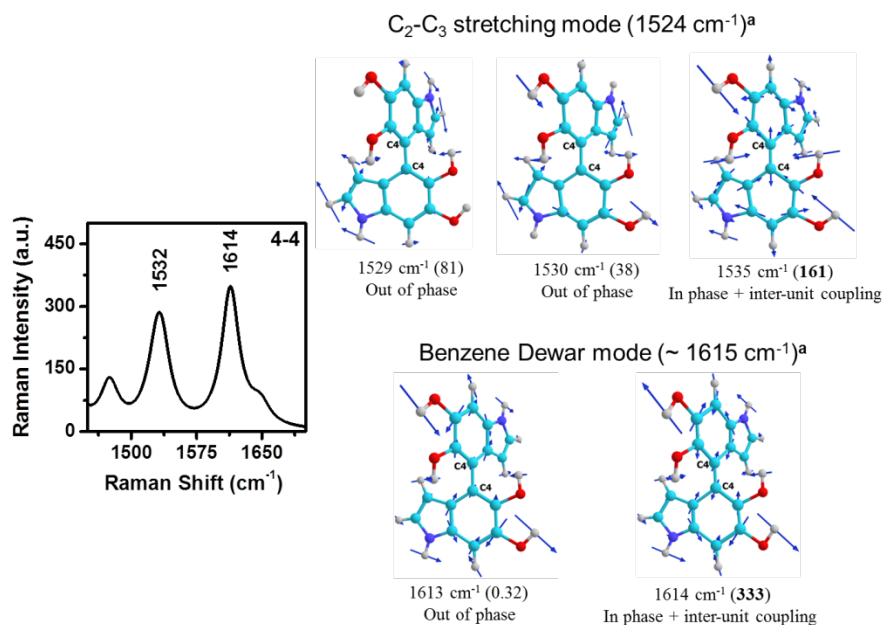
Fig. 8.12. Computed normal Raman spectrum (on left) of 4-4 DHI dimers along with normal modes (on right) of intense ring modes. Raman activity (in parenthesis) in $Å^4$/molecule is mentioned corresponding to each predicted vibrational wavenumber. It is clearly seen that for the benzene breathing (Dewar) mode (bottom row), out of two the one (1614 cm^{-1}) which is made off in phase vibration of both the rings and coupled with inter-unit C-C stretching is of three order of magnitude than the other out of phase mode. Note that inter-unit dihedral angle for this dimer is 60$^°$ which is less than reported value (72$^°$) in N-methyl-5-hydroxy-6-methoxy-indole (MHMI) dimer due to the presence of bulky methyl and methoxy moieties as a peripheral substitution. The Same effect is seen for C_2-C_3 stretching of pyrrole ring also (top row). The mode (1535 cm^{-1}) with in-phase pyrrole breathing and strong interunit C-C stretching has the highest intensity of all three vibrations. All vibrational wavenumbers are computed at B3LYP/6-31G(d,p) level of DFT and scaled by a factor of 0.98. ^{a}Experimental band position of MHMI dimer is taken from Ref [106].

8.3.4 Macrocycle and non-covalently held monomer models do not explain melanin vibrational spectra

In the macrocycle model, eumelanin protomolecules comprise of semi or full planar structures that are made from mixing DHI (H), SQ or MQ (M) and IQ (I) in different stoichiometry through covalent linkage.[61,64] Heterogeneous populations of 16 most stable tetramers have explained the broad absorption spectra by superposition principle with two shoulders at 240 and 350 nm.[61] Sangaletti, L. *et al.* have concluded IHHH to be the abundant species based on a comparison of computed Raman and electronic density of states (DOS) spectra of two such tetramers (IHHH and QIQI) with experimentally measured Raman and photoemission spectra.[50] In this report, the presence of low intensity vibrational modes near most intense bands at ~ 1600 and 1400 cm^{-1} got masked due to the use of Lorentzian lineshape with an FWHM of ~ 100 cm^{-1}. Such large

bandwidth is at least four times than typically experimentally observed value (25 cm^{-1}) for the 1615 cm^{-1} band in dopa. (See Chapter 7) Though the measurement is performed on same commercial synthetic melanin, the reported Raman peaks (~1370 and ~1600 cm^{-1}) in one study[47] differ from those (~1490 and ~1570) in another study.[50] Positions and intensities reported in the previous study show good agreement with results obtained by other groups[45,46,48] and with our RR spectra, described in Chapter 7. These band positions are referred whenever a comparison of computed spectra with experimental spectra in drawn hereafter. In the current study, we have performed detailed vibrational analysis on the effect of cyclic tetramer formation on resulting Raman spectra for five such tetramers, *viz.* IHHH, HHH, IMIM, HMIM and HMHM.
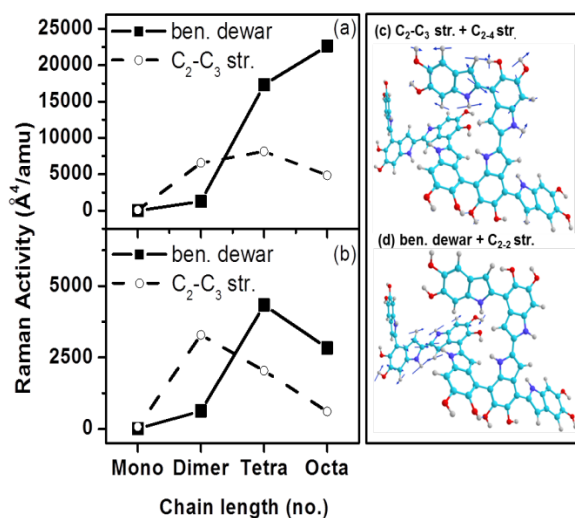
Fig. 8.13. Evolution of (a) intrinsic and (b) normalized Raman activities of benzene (ben.) dewar (breathing along C_4-C_7 axis) and pyrrole C_2-C_3 bond stretching (str.) mode with increase of polymer chain length, (c-d) normal mode description of these two modes for the same octamer as in Fig. 8.8. Raman activities are normalized by the number of monomer units in each oligomer.

Apart from HHHH tetramer, these proposed but experimentally not yet observed macrocyclic species give rise to vibrational characteristics (Fig. 8.14) that do not encompass the features of experimental spectra. Unlike optical spectra, normal Raman signatures of three types of tetramers, *viz.* HMIM, IMIM and HMHM (Fig. 8.14, bottom row) are found to vary in terms of both position and intensities, depending on the identity of covalently linked neighbors among three monomer types (Fig. 8.14, middle row).

In three tetramers, a different type of ring stretching (str.) (Fig. 8.14, top row) including C_2–C_3 str., C_7–C_8str. with a minor contribution from str. of inter-unit $C_{2–7}$ bond is observed. Additionally, calculation of the IHHH tetramer also produces similar results showing modes near 1500 cm^{-1} with highest intensity and benzene Dewar modes having an order of less activity (Fig. S7, panel c and d). In any of the cases neither symmetric in-phase benzene stretching gain activity ~1615 cm^{-1} where the most intense band lie in experimental spectrum nor modes < 1380 cm^{-1} lose intensity. The HHHH macrocycle is found to be the only one, formation of which leads to activation of in-phase benzene dewar mode coupled with inter-unit stretching at 1619 cm^{-1} and pyrrole C_2–C_3 stretching near 1580 cm^{-1} (Fig. 8.15, panel a and b).

These two modes are uniquely present only in the HHHH tetramer and are identical to the most intense modes of intertwined linear polymers.
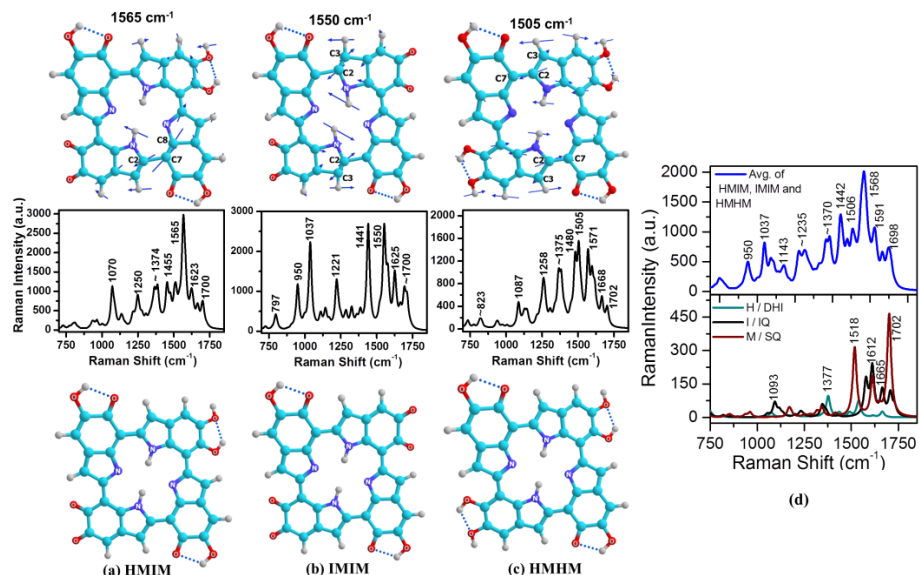
Fig. 8.14. Structure and computed Raman spectra of three tetramers (reported in Ref [61,64]) made up by mixing of DHI (H) and semiquinone or quinone methide (M) (a) HMIM, (b) IMIM and (c) HMHM. Computed Raman spectra for these species are shown above each structure (middle row) and normal mode descriptions for the most intense band for each tetramer are also shown (top row), (d) average Raman spectra of three tetramers (top) and those of individual monomer (bottom). A Lorentzian line-shape with FWHM value of 25 cm^{-1} is used for generating all spectra and Raman activities of tetramers are normalized by a number of monomer units.
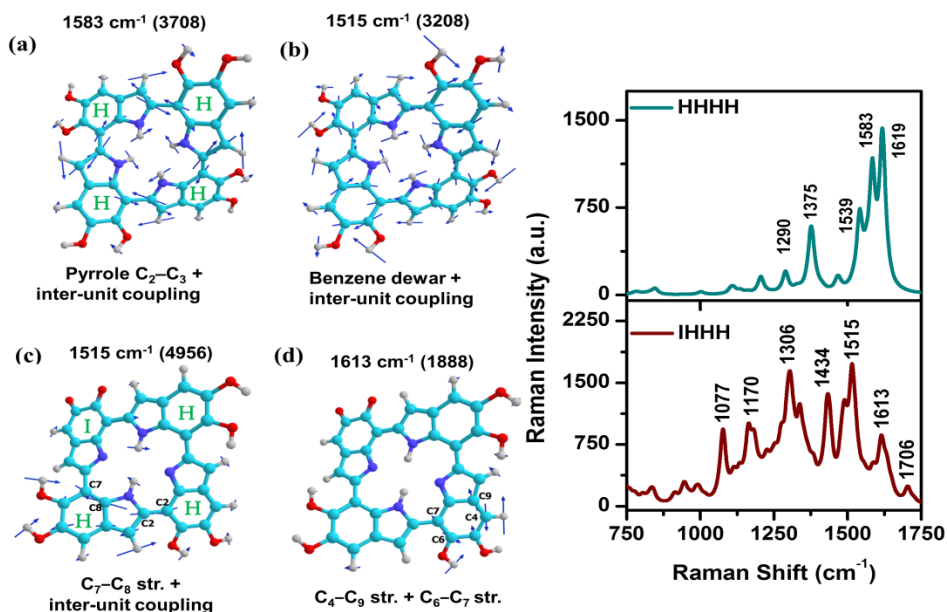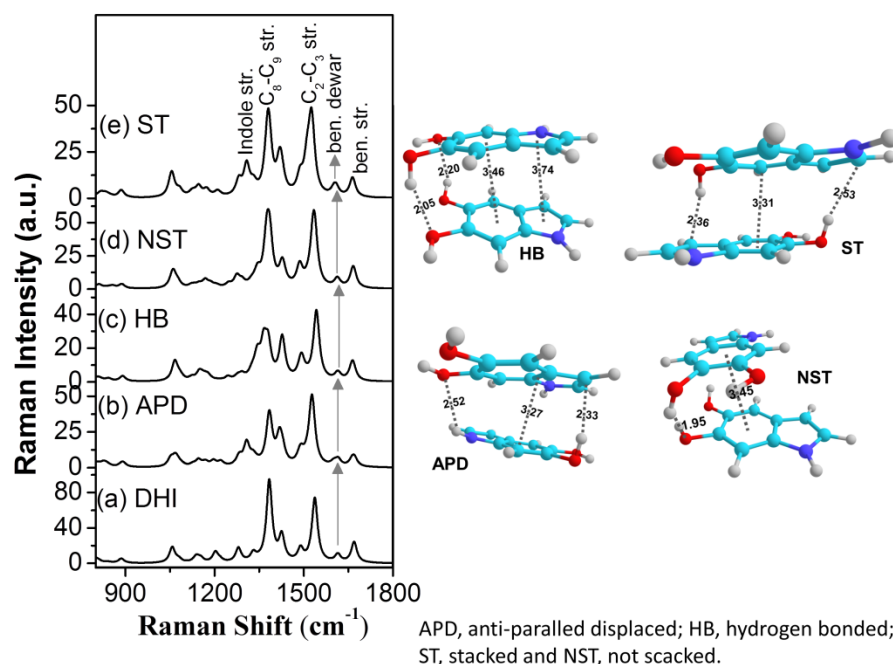
Fig. 8.15. Computed Raman spectra, (on the right column) and vibrational normal modes of HHHH (a-b) and IHHH (c-d) porphyrin-like tetramer. Intrinsic Raman activity (Å^4/amu) of each mode is mentioned in parenthesis. Normal mode descriptions of corresponding vibrations are also mentioned. Vibrational wavenumbers are scaled by 0.98. Benzene Dewar mode at ~ 1620 cm^{-1} gets activated in only HHHH tetramer among all five studied ones (HHHH, IHHH, IMIM, HMIM, and HMHM). In none of the other macrocyclic tetramer, coupling of in-phase symmetric benzene str. vibration with inter-unit (C-C) bond str. is observed.
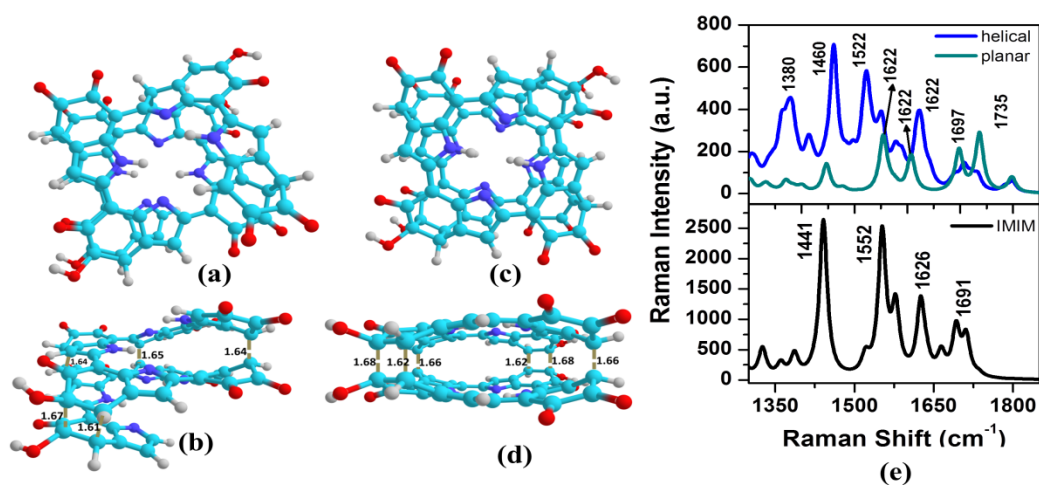
Fig. 8.16. Optimized structure of IMIM octamer through helical (a) top and (b) side view and planar stacking (c) top and (d) side view of two tetrameric units. (e) Computed Raman spectra for IMIM tetramer (bottom) and octamer made from planar and helical stacking (top). For assessment of the effect of stacking on relative intensities, Raman activity of each tetramer is normalized by the number of monomer units present. Helical stacking of IMIM tetramer gives rises to the intense band at 1380, 1460, 1522 and 1622 cm^{-1}. Out of these, benzene Dewar mode of a single ring, coupled to inter-unit C_{2-7} str. ~ 1622 cm^{-1} loses its intensity by three fold due to helical stacking. At the same time three other modes, though losing Raman activity, becomes more intense within 1350-1550 cm^{-1} region than the one at 1622 cm^{-1}. The bands below 1550 cm^{-1} region are always less intense than that ~ 1620 cm^{-1} in experimental Raman spectra of melanin. Planar stacking leads to significant intensity gain of the carbonyl stretching mode, pyrrole str. coupled to interunit C_{2-7} str. and in-phase C_9-C_3 str. at 1735, 1554 and 1607 cm^{-1} respectively, without activating Dewar mode near 1620 cm^{-1}. Contrary to absorption spectra where both types of stacking lead to a mere broadening of the electronic band near 400 nm, result in a sharp decrease in Raman activity and severe intensity redistribution among coupled modes.

Furthermore, stacking (helical and planar) of these macrocyclic units via interplanar covalent bonds leads to a several fold decrease of Raman activity of the ring modes near the 1620 cm^{-1} region. (Fig. 8.16) At the same time, these type of stacking activates other modes below the 1500 cm^{-1} region, which is not in accord with experimental normal Raman spectra. Furthermore by using dispersion and long-range

corrected hybrid density functional wB97xD,[107] we have shown that in none of the four types of non-covalently held DHI-DHI dimers which are proposed recently,[68] intrinsic Raman activity of benzene Dewar mode at ~ 1615 cm^{-1} gets enhanced as compared to that of the monomer (Fig. 8.17).


APD, anti-paralled displaced; HB, hydrogen bonded; ST, stacked and NST, not scacked.

Fig. 8.17. Optimized structure (on right panel) and computed Raman spectra (on left panel) of DHI (a) monomer, and (b) APD, (c) HB, (d) NST and (e) ST dimers at wB97xD/6-31G(d,p) level of DFT. Computed wavenumbers are scaled by a factor of 0.96. Interatomic distances between atoms in two monomer units are given in Å in each structure. Each monomer unit is optimized at wB97xD/6-31G(d,p) level of DFT, before creating the dimers with inter-layer distances as described in Ref 77. Following this, a constrained geometry optimization (freezing internal coordinates of both rings and coordinate of one ring with respect to another) and then a completely relaxed geometry optimization is performed at the same level of theory. Note that interlayer and hydrogen bond distances differ from that published in mentioned paper due to the use of dispersion-corrected DFT in the current study against MP2 method in the previous one.

Although these twenty different dimeric species have been able to explain broad UV-Vis absorption spectra of eumelanin just like other proposed models did, our data points out their inability to explain the most intense feature of experimental Raman spectra. We note that though consideration of non-covalent interactions between various oligomers of different lengths and shape is of utmost importance to form supramolecular structures in eumelanin; those interactions probably happen after formation of a finite population of protomolecules.

8.3.5 DHI oligomers explain X-ray derived structural parameters of eumelanin

The calculated s(q) and RDF of four DHI octamers and monomer are shown in Fig. 8.18. Kaxiras and co-workers have shown that a 3.1 Å shift in both lateral dimensions and 3.3 Å inter-layer spacing between three macrocycles which are rotated by 30° between adjacent layers can reproduce the very first peak in S(q) spectra.[61]
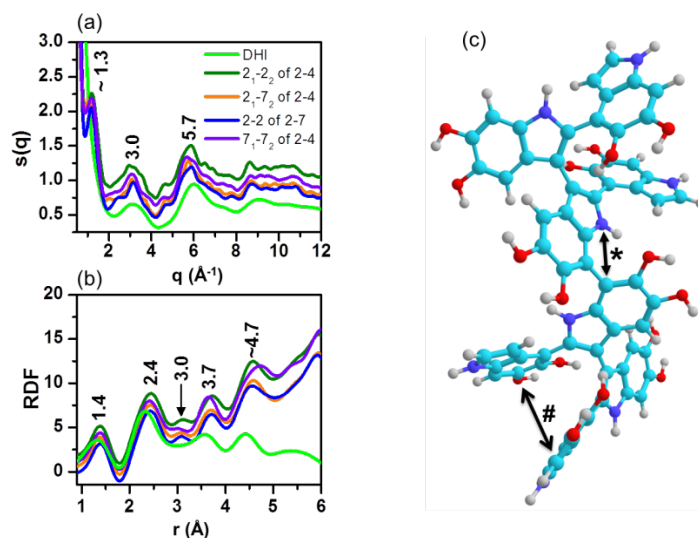
Fig. 8.18. Computed (a) structure factors S(q) and (b) radial distribution functions (RDF) for four DHI octamers made from 2-4 and 2-7 dimers and (c) a representative DHI octamer. S(q) and RDF are computed using I.S.A.A.C.S v 2.8 software on optimized structures at B3LYP/6-31G(d,p)//vacuo level of DFT. In both the Fig.s, abscissas are vertically displaced for a clear visualization. It is evident that the shoulder at 3 Å in RDF spectra and the first peak in S(q) spectra is absent in monomer and only appear in oligomers. The Distance marked by asterisk corresponds to ~ 3.0 Å peak in RDF and that marked by '#' depicts partial stacking.

In our model, the first peak in S(q) ~ 1.3 Å^{-1} originates without any enforced three-dimensional (3D) stacking arrangement. Additionally, these linear but inter-twisted protomolecules reproduce a shoulder at ~ 3 Å in RDF in agreement with experimental data.[20] This peak is explained as distances between the N of indole and the third C of the next adjacent monomers. In macrocycle model, it was ascribed to distances between N and C_2 or C_8 atoms of adjacent neighbors of the inner porphyrin-like ring.[61]

The first peak in RDF at 1.38 Å that originates from average distance between C, N, and O with other C atoms is also clearly reproduced by the current structural

model. We emphasize that the first peak in S(q) appears to be sharp for tetrameric species that are specifically formed via 3–3 coupling between dimers (2–4 or 2–7) while appearing as shoulder in other species. One of the key outcomes of this model is its ability to give a natural explanation of the first peak in S(q) as an intrinsic structural order, compared to a necessary stacking arrangement of the protomolecules in the macrocycle model. Unlike the stacked macrocycle model, higher-order structural organization in our model would not specifically need a 3.4–3.6 Å interlayer distances.

8.3.6 Electronic density of states (DOS) and X-ray photoelectron spectra

Sangaletti, L. *et al*. have explained x-ray absorption and photoemission spectra of synthetic melanin thin films using DFT derived density of electronic states (DOS) of constituting monomers[47] and two macrocyclic protomolecules, namely, IHHH and QIQI.[50] Surprisingly DHI (HQ or H) alone seems to capture the experimental feature in the valence band region, and by the IHHH tetramer. Fig. 8.19 depicts computed DOS spectra of four different octamers of our protomolecular model along with tentative assignment of reported binding energy (BE) peaks.
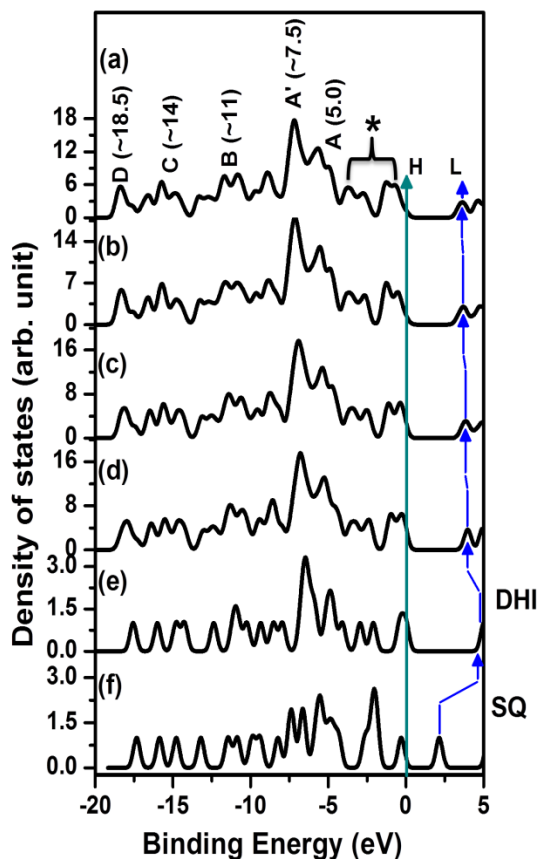
Fig. 8.19. Calculated density of states of the (a) 2_1-7_1, (b) 2_1-2_2, (c) 2_1-7_2 and (d) 7-7 octamers from $3'_1$-$3'_2$ tetramer of 2-4 DHI dimers, and of (d) DHI and (f) SQ. For each calculated spectrum, the HOMO and LUMO energies are indicated by arrow. The calculated spectra have been aligned to have the HOMO level of each molecule at the same energy value that has been set to zero. HOMO energy shifts are + 4.48, + 4.52, + 4.65 and + 4.72 eV respectively for these mentioned octamers respectively and + 5.0 and + 6.09 eV for DHI and SQ respectively. These DOS spectra are obtained from the B3LYP/6-31G(d,p) computed Kohn-Sham energy levels and convoluted with gaussian functions of 0.5 eV FWHM in GaussSum 3.0. The nomenclature and binding energy (BE) values in eV (in parenthesis) are from Ref 56. The computed LUMO energy for DHI falls at 4.96 eV above that of HOMO and falls out of BE scale. Additional electronic state contribution below peak A is marked by asterisk in panel (a).

These bands are observed in valence band photoemission spectra and obtained with X-ray sources of different energies.[47,50] It is evident that these octameric species are able to explain the position of experimental BE peaks,(in parenthesis in Fig. 8.19) as good as by IHIH macrocycle reported earlier.[50] The contribution of additional electronic states to the photoemission spectrum in the low BE side of peak A is detected in experiment[47] and is consistently found in DOS spectra of all octamers (Fig. 8.19 a-d), as in the case of the IHHH tetramer too.[50] Similarity among DOS spectra of several octamers also supports the well-accepted fact about eumelanin structure that, it is not made of a single type of protomolecular structure but are composed of a complex hierarchical assembly of a variety of protomolecules.

8.3.7 Metal ion binding

A metal ion can be captured in a catecholic or quinone-imine configuration of the DHI unit, and by a –COOH moiety in the case of DHICA derived melanin. Binding of transition metal cations like Zn^{2+} and Ni^{2+} at the catecholic moiety is implicated in the dimerization step of DHI, to form symmetric units via 2–2 coupling by increasing nucleophilic reactivity of the C_2 site more than that of C_4 or C_7 sites.[79,85] Catecholic mode of Fe(III) chelation at neutral pH is supported by IR spectroscopic and DFT studies on hair melanin[108] and melanin prepared from both, DHI and DHICA as precursors.[48,109–111] Though the macrocycle model proposes an attractive way of incorporating metals into melanin in a metal–porphyrin-like coordination, recent experimental and theoretical results suggest otherwise. It has been reported that the experimental shift in IR active modes of eumelanin due to binding with Fe(III) is well explained by DFT computed shift on the model of Fe(III) bound at catechol and quinone-imine site of DHI.[108]

8.4 Future Perspective

Molecular dynamics (MD) simulation study has shown that protomolecules including both macrocyclic and linear get arranged into secondary structures, that in turn form tertiary structures upon non-covalent association.[66] This finding supports supramolecular onion-like layered assembly, observed in high resolution electron microscopic images of eumelanin.[40] The random-coil and partially helical octamers whose maximum attainable length is constrained in our model can also form partially stacked structure. (Fig. 8.20) A large number of similar structural motifs would also result from the polymerization of DHICA, and different redox forms. Our results warrant MD simulations with a finite population of these DHI oligomers and similar DHICA polymers to find out what hierarchical assembly they form upon non-covalent

association. Such large-scale simulation would also predict Young's modulus and mass density that can be compared with available experimental values.

In a natural system DHI, DHICA and their redox species coexist. The comproportionation equilibrium between these redox states controls electrical conductivity of eumelanin. Hydration state severely affects this equilibrium and solvation would also have a decisive effect on the relative stability of different monomeric species. All DFT computations performed in this study is *in vacuo* and the predicted small oligomers are in accord with experimental data. Nonetheless, for a comprehensive understanding of the photodynamical events in individual tetramers and octamers, solvation would play an important role. Other than homopolymeric species, heteropolymers of DHI, DHICA, IQ and SQ with different stoichiometry should also be considered for computing spectroscopic observables. The inclusion of different redox forms into our model would also cause significant visible absorption due to the presence of carbonyl moiety, as well as would increase structural heterogeneity.
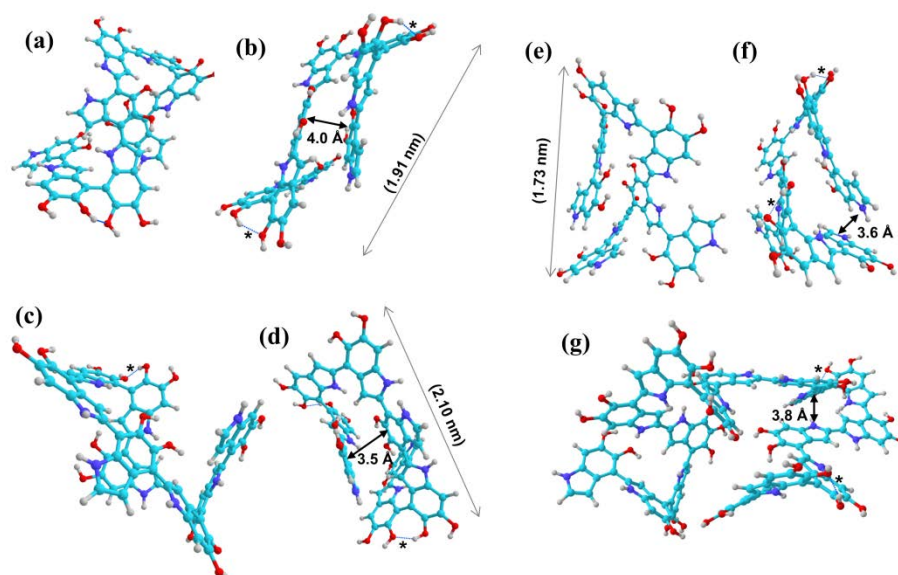
Fig. 8.20. Examples of a few DHI octamers that are self-packing and, have inherent stacking interactions. (a) front and (b) side view of 2_1-7_2 octamer form $4'_1$-$7'_2$ tetramer; (c) front and (d) side view of 2_1-$7'_2$ octamer form $4'_1$-$7'_2$ tetramer; (e) front and (f) side view of 2_1-$4'_1$ octamer form $4'_1$-$7'_2$ tetramer and (g) 2-2 hexadecamer made from 2_1-2_2 octamer of $4'_1$-$7'_2$ tetramer from of 2-4 dimers. In all of these protomolecules stabilizing hydrogen-bonding interactions between monomeric units are perceived (asterisk). The largest dimension of the octamers is also mentioned (double sided arrow and value in parenthesis)

8.5 Conclusions

The results presented in this chapter unravel a physical model for basic building blocks of one of the most functionally versatile, yet structurally less understood eumelanin pigment. We have found that experimental Raman band positions and their relative intensities, in conjunction with electronic absorption and x-ray derived parameters are able to put structural constraint for building models of eumelanin protomolecules. Our computational results specifically show that the character of electronic coupling, necessary to be present between covalently linked monomeric units of melanin to give rise to an enhanced Raman band at ~1615 and ~1400 cm^{-1}, as observed in experimental Raman spectra. **A major success of our model is its ability to explain key physical and spectroscopic properties of melanin by considering a population of structures that are inspired from experimentally detected small oligomers. To the best of our knowledge, this is the only structural model of eumelanin that can explain position and intensity of experimental vibrational spectra along with UV-Vis absorption characteristics, XPS spectral features and X-ray derived RDF.**

In our model, all three classes, namely semi-planar, random coil and partially helical protomolecules show similar vibrational behavior leading to the successful explanation of experimental Raman spectra of melanin. Our finding supports the general idea, as recently documented by d'Ischia *et al*., that eumelanin class of macromolecules cannot be solved as a unique structure, but can only be described as a statistical ensemble of a plethora of different but distinct structures, which are capable of making tertiary structures via non-covalent interactions. **While supporting this general idea, our results also provide a unified strategy to test merits of different eumelanin structural models.**

References

[1]   S. Ito, *Biochim. Biophys. Acta - Gen. Subj.* **1986**, *883*, 155.

[2]   Y. Liu, J. D. Simon, *Pigment Cell Res.* **2003**, *16*, 606.

[3]   P. Meredith, T. Sarna, *Pigment Cell Res.* **2006**, *19*, 572.

[4]   P. Meredith, B. J. Powell, J. Riesz, S. P. Nighswander-Rempel, M. R. Pederson, E. G. Moore, *Soft Matter* **2006**, *2*, 37.

[5]   J. D. Simon, L. Hong, D. N. Peles, *J. Phys. Chem. B* **2008**, *112*, 13201.

[6]   J. D. Simon, D. Peles, K. Wakamatsu, S. Ito, *Pigment Cell Melanoma Res.* **2009**, *22*, 563.

[7]   M. d'Ischia, A. Napolitano, A. Pezzella, P. Meredith, T. Sarna, *Angew. Chemie Int. Ed.* **2009**, *48*, 3914.

[8]   S. Ito, K. Wakamatsu, M. D'ischia, A. Napolitano, A. Pezzella, in *Melanins and Melanosomes* (Eds.: J. Borovanský, P.A. Riley), Wiley-VCH Verlag GmbH & Co. KGaA, Weinheim, Germany, **2011**, pp. 167–185.

[9]   F. Solano, *New J. Sci.* **2014**, *2014*, 1.

[10]   M. d'Ischia, A. Napolitano, V. Ball, C.-T. Chen, M. J. Buehler, *Acc. Chem. Res.* **2014**, *47*, 3541.

[11]   M. Ambrico, N. F. Della Vecchia, P. F. Ambrico, A. Cardone, S. R. Cicco, T. Ligonzo, R. Avolio, A. Napolitano, M. D'Ischia, *Adv. Funct. Mater.* **2014**, n/a.

[12]   T.-F. Wu, B.-H. Wee, J.-D. Hong, *Adv. Mater. Interfaces* **2015**, *2*, n/a.

[13]   T.-F. Wu, J.-D. Hong, *Biomacromolecules* **2015**, *16*, 660.

[14]   N. F. Della Vecchia, R. Avolio, M. Alfè, M. E. Errico, A. Napolitano, M. D'Ischia, *Adv. Funct. Mater.* **2013**, *23*, 1331.

[15]   P. Meredith, C. J. Bettinger, M. Irimia-Vladu, A. B. Mostert, P. E. Schwenn, *Reports Prog. Phys.* **2013**, *76*, 034501.

[16] Q. Fan, K. Cheng, X. Hu, X. Ma, R. Zhang, M. Yang, X. Lu, L. Xing, W. Huang, S. S. Gambhir, Z. Cheng, *J. Am. Chem. Soc.* **2014**, *136*, 15185.

[17] V. Gargiulo, M. Alfè, R. Di Capua, A. R. Togna, V. Cammisotto, S. Fiorito, A. Musto, A. Navarra, S. Parisi, A. Pezzella, *J. Mater. Chem. B* **2015**, *3*, 5070.

[18] M. Xiao, Y. Li, M. C. Allen, D. D. Deheyn, X. Yue, J. Zhao, N. C. Gianneschi, M. D. Shawkey, A. Dhinojwala, *ACS Nano* **2015**, *9*, 5454.

[19] Y. T. Thathachari, M. S. Blois, *Biophys. J.* **1969**, *9*, 77.

[20] J. Cheng, S. C. Moss, M. Eisner, *Pigment Cell Res.* **1994**, *7*, 263.

[21] J. Cheng, S. C. Moss, M. Eisner, P. Zschak, *Pigment Cell Res.* **1994**, *7*, 255.

[22] J. M. Gallas, K. C. Littrell, S. Seifert, G. W. Zajac, P. Thiyagarajan, *Biophys. J.* **1999**, *77*, 1135.

[23] M. Arzillo, G. Mangiapia, A. Pezzella, R. K. Heenan, A. Radulescu, L. Paduano, M. d'Ischia, *Biomacromolecules* **2012**, *13*, 2379.

[24] A. Napolitano, A. Pezzella, G. Prota, R. Seraglia, P. Traldi, *Rapid Commun. Mass Spectrom.* **1996**, *10*, 468.

[25] C. Kroesche, M. G. Peter, *Tetrahedron* **1996**, *52*, 3947.

[26] A. Napolitano, A. Pezzella, G. Prota, R. Seraglia, P. Traldi, *Rapid Commun. Mass Spectrom.* **1996**, *10*, 204.

[27] A. Pezzella, A. Napolitano, M. D'Ischia, G. Prota, R. Seraglia, P. Traldi, *Rapid Commun. Mass Spectrom.* **1997**, *11*, 368.

[28] A. Pezzella, M. D'Ischia, A. Napolitano, A. Palumbo, G. Prota, *Tetrahedron* **1997**, *53*, 8281.

[29] A. Bertazzo, C. V. L. Costa, G. Allegri, M. Schiavolin, D. Favretto, P. Traldi, *Rapid Commun. Mass Spectrom.* **1999**, *13*, 542.

[30] K. Stępień, A. Dzierżęga-Lęcznar, S. Kurkiewicz, I. Tam, *J. Am. Soc. Mass Spectrom.* **2009**, *20*, 464.

[31] S. Reale, M. Crucianelli, A. Pezzella, M. D'Ischia, F. De Angelis, *J. Mass Spectrom.* **2012**, *47*, 49.

[32] J. Liebscher, R. Mrówczyński, H. A. Scheidt, C. Filip, N. D. Hădade, R. Turcu, A. Bende, S. Beck, *Langmuir* **2013**, *29*, 10539.

[33] Y. Li, J. Liu, Y. Wang, H. W. Chan, L. Wang, W. Chan, *Anal. Chem.* **2015**, *87*, 7958.

[34] G. W. Zajac, J. M. Gallas, A. E. Alvarado-Swaisgood, *J. Vac. Sci. Technol. B Microelectron. Nanom. Struct.* **1994**, *12*, 1512.

[35] G. W. Zajac, J. M. Gallas, J. Cheng, M. Eisner, S. C. Moss, A. E. Alvarado-Swaisgood, *Biochim. Biophys. Acta - Gen. Subj.* **1994**, *1199*, 271.

[36] C. M. R. Clancy, J. D. Simon, *Biochemistry* **2001**, *40*, 13353.

[37] Y. Liu, J. D. Simon, *Pigment Cell Res.* **2003**, *16*, 606.

[38] Y. Liu, J. D. Simon, *Pigment Cell Res.* **2003**, *16*, 72.

[39] P. Díaz, Y. Gimeno, P. Carro, S. González, P. L. Schilardi, G. Benítez, R. C. Salvarezza, A. H. Creus, *Langmuir* **2005**, *21*, 5924.

[40] A. A. R. Watt, J. P. Bothma, P. Meredith, *Soft Matter* **2009**, *5*, 3754.

[41] M. Jastrzebska, I. Mróz, B. Barwiński, R. Wrzalik, S. Boryczka, *J. Mater. Sci.* **2010**, *45*, 5302.

[42] J. A. Pierce, D. M. Rast, *Phytochemistry* **1995**, *39*, 49.

[43] M. G. Bridelli, D. Tampellini, L. Zecca, *FEBS Lett.* **1999**, *457*, 18.

[44] B. Bilińska, *Spectrochim. Acta Part A Mol. Biomol. Spectrosc.* **2001**, *57*, 2525.

[45] Z. Huang, H. Lui, X. K. Chen, A. Alajlan, D. I. McLean, H. Zeng, *J. Biomed. Opt.* **2004**, *9*, 1198.

[46] V. Capozzi, G. Perna, A. Gallone, P. F. Biagi, P. Carmone, A. Fratello, G. Guida, P. Zanna, R. Cicero, *J. Mol. Struct.* **2005**, *744-747*, 717.

[47] L. Sangaletti, S. Pagliara, P. Vilmercati, C. Castellarin-Cudia, P. Borghetti, P. Galinetto, R. Gebauer, a Goldoni, *J. Phys. Chem. B* **2007**, *111*, 5372.

[48] A. Samokhvalov, Y. Liu, J. D. Simon, *Photochem. Photobiol.* **2007**, *80*, 84.

[49] S. A. Centeno, J. Shamir, *J. Mol. Struct.* **2008**, *873*, 149.

[50] L. Sangaletti, P. Borghetti, P. Ghosh, S. Pagliara, P. Vilmercati, C. Castellarin-Cudia, L. Floreano, a. Cossaro, a. Verdini, R. Gebauer, a. Goldoni, *Phys. Rev. B* **2009**, *80*, 174203.

[51] H. C. Longuet-Higgins, *Arch. Biochem. Biophys.* **1960**, *86*, 231.

[52] A. Pullman, B. Pullman, *Biochim. Biophys. Acta* **1961**, *54*, 384.

[53] J. McGinness, P. Corry, P. Proctor, *Science (80-.).* **1974**, *183*, 853.

[54] D. S. Galvão, M. J. Caldas, *J. Chem. Phys.* **1988**, *88*, 4088.

[55] D. S. Galvão, M. J. Caldas, *J. Chem. Phys.* **1990**, *92*, 2630.

[56] D. S. Galvão, M. J. Caldas, *J. Chem. Phys.* **1990**, *93*, 2848.

[57] K. B. Stark, J. M. Gallas, G. W. Zajac, M. Eisner, J. T. Golab, *J. Phys. Chem. B* **2003**, *107*, 11558.

[58] K. B. Stark, J. M. Gallas, G. W. Zajac, M. Eisner, J. T. Golab, *J. Phys. Chem. B* **2003**, *107*, 3061.

[59] K. B. Stark, J. M. Gallas, G. W. Zajac, J. T. Golab, S. Gidanian, T. McIntire, P. J. Farmer, *J. Phys. Chem. B* **2005**, *109*, 1970.

[60] M. L. Tran, B. J. Powell, P. Meredith, *Biophys. J.* **2006**, *90*, 743.

[61] E. Kaxiras, A. Tsolakidis, G. Zonios, S. Meng, *Phys. Rev. Lett.* **2006**, *97*, 218102.

[62] J. J. Riesz, J. B. Gilmore, R. H. McKenzie, B. J. Powell, M. R. Pederson, P. Meredith, *Phys. Rev. E* **2007**, *76*, 021915.

[63] S. Meng, E. Kaxiras, *Biophys. J.* **2008**, *95*, 4396.

[64] S. Meng, E. Kaxiras, *Biophys. J.* **2008**, *94*, 2095.

[65] A. Pezzella, A. Iadonisi, S. Valerio, L. Panzella, A. Napolitano, M. Adinolfi, M. D'Ischia, *J. Am. Chem. Soc.* **2009**, *131*, 15270.

[66] C.-T. Chen, V. Ball, J. J. de Almeida Gracio, M. K. Singh, V. Toniazzo, D. Ruch, M. J. Buehler, *ACS Nano* **2013**, *7*, 1524.

[67] C.-T. Chen, C. Chuang, J. Cao, V. Ball, D. Ruch, M. J. Buehler, *Nat. Commun.* **2014**, *5*, DOI 10.1038/ncomms4859.

[68] G. Prampolini, I. Cacelli, A. Ferretti, *RSC Adv.* **2015**, *5*, 38513.

[69] L. E. Bolívar-Marinez, D. S. Galvão, M. J. Caldas, *J. Phys. Chem. B* **1999**, *103*, 2993.

[70] S. Ito, K. Jimbow, *J. Invest. Dermatol.* **1983**, *80*, 268.

[71] T. Morishima, E. Fukuda, *Arch. Dermatol. Res.* **1985**, *277*, 248.

[72] H. Okuda, K. Yoshino, K. Wakamatsu, S. Ito, T. Sota, *Pigment Cell Melanoma Res.* **2014**, *27*, 664.

[73] S. Ito, K. Wakamatsu, *Pigment Cell Res.* **1998**, *11*, 120.

[74] S. Ito, Y. Nakanishi, R. K. Valenzuela, M. H. Brilliant, L. Kolbe, K. Wakamatsu, *Pigment Cell Melanoma Res.* **2011**, *24*, 605.

[75] M. d'Ischia, K. Wakamatsu, A. Napolitano, S. Briganti, J.-C. Garcia-Borron, D. Kovacs, P. Meredith, A. Pezzella, M. Picardo, T. Sarna, J. D. Simon, S. Ito, *Pigment Cell Melanoma Res.* **2013**, *26*, 616.

[76] M. d'Ischia, A. Napolitano, A. Pezzella, *European J. Org. Chem.* **2011**, *2011*, 5501.

[77] D. R. Dreyer, D. J. Miller, B. D. Freeman, D. R. Paul, C. W. Bielawski, *Langmuir* **2012**, *28*, 6428.

[78] S. Hong, Y. S. Na, S. Choi, I. T. Song, W. Y. Kim, H. Lee, *Adv. Funct. Mater.* **2012**, *22*, 4711.

[79] A. Napolitano, M. G. Corradini, G. Prota, *Tetrahedron Lett.* **1985**, *26*, 2805.

[80] M. d'Ischia, A. Napolitano, K. Tsiakas, G. Prota, *Tetrahedron* **1990**, *46*, 5789.

[81] A. Pezzella, A. Napolitano, M. D'Ischia, G. Prota, *Tetrahedron* **1996**, *52*, 7913.

[82] A. Pezzella, D. Vogna, G. Prota, *Tetrahedron* **2002**, *58*, 3681.

[83] M. d'Ischia, A. Napolitano, A. Pezzella, E. J. Land, C. A. Ramsden, P. A. Riley, **2005**, pp. 1–63.

[84] A. Pezzella, L. Panzella, O. Crescenzi, A. Napolitano, S. Navaratman, R. Edge, E. J. Land, V. Barone, M. D'Ischia, *J. Am. Chem. Soc.* **2006**, *128*, 15490.

[85] L. Panzella, A. Pezzella, A. Napolitano, M. D'Ischia, *Org. Lett.* **2007**, *9*, 1411.

[86] A. Pezzella, L. Panzella, A. Natangelo, M. Arzillo, A. Napolitano, M. D'Ischia, *J. Org. Chem.* **2007**, *72*, 9225.

[87] M. Gauden, A. Pezzella, L. Panzella, M. T. Neves-Petersen, E. Skovsen, S. B. Petersen, K. M. Mullen, A. Napolitano, M. D'Ischia, V. Sundström, *J. Am. Chem. Soc.* **2008**, *130*, 17038.

[88] A. Corani, A. Huijser, T. Gustavsson, D. Markovitsi, P.-Å. Malmqvist, A. Pezzella, M. D'Ischia, V. Sundström, *J. Am. Chem. Soc.* **2014**, *136*, 11626.

[89] M. Gauden, A. Pezzella, L. Panzella, A. Napolitano, M. D'Ischia, V. Sundström, *J. Phys. Chem. B* **2009**, *113*, 12575.

[90] F. Bernsmann, A. Ponche, C. Ringwald, J. Hemmerlé, J. Raya, B. Bechinger, J.-C. Voegel, P. Schaaf, V. Ball, *J. Phys. Chem. C* **2009**, *113*, 8234.

[91] C. Lee, W. Yang, R. G. Parr, *Phys. Rev. B* **1988**, *37*, 785.

[92] A. D. Becke, *J. Chem. Phys.* **1993**, *98*, 5648.

[93] R. Bauernschmitt, R. Ahlrichs, *Chem. Phys. Lett.* **1996**, *256*, 454.

[94] M. E. Casida, C. Jamorski, K. C. Casida, D. R. Salahub, *J. Chem. Phys.* **1998**, *108*, 4439.

[95] M. J. Frisch *et al. Gaussian 09, Revision D.01*, Gaussian Inc., Wallingford, **2013**.

[96] G. A. Andrienko, *Chemcraft v1.6, Http://www.chemcraftprog.com/*, **n.d.**

[97] S. Le Roux, V. Petkov, *J. Appl. Crystallogr.* **2010**, *43*, 181.

[98] *I.S.A.A.C.S v2.8, Http://isaacs.sourceforge.net/*, **n.d.**

[99] N. M. O'boyle, A. L. Tenderholt, K. M. Langner, *J. Comput. Chem.* **2008**, *29*, 839.

[100] *GaussSum v3.0, Http://gausssum.sourceforge.net*, **n.d.**

[101] S. S. Zade, M. Bendikov, *Org. Lett.* **2006**, *8*, 5243.

[102] A. B. Mostert, B. J. Powell, F. L. Pratt, G. R. Hanson, T. Sarna, I. R. Gentle, P. Meredith, *Proc. Natl. Acad. Sci.* **2012**, *109*, 8943.

[103] J. Wünsche, Y. Deng, P. Kumar, E. Di Mauro, E. Josberger, J. Sayago, A. Pezzella, F. Soavi, F. Cicoira, M. Rolandi, C. Santato, *Chem. Mater.* **2015**, *27*, 436.

[104] J. Riesz, T. Sarna, P. Meredith, *J. Phys. Chem. B* **2006**, *110*, 13985.

[105] P. Meredith, J. Riesz, *Photochem. Photobiol.* **2007**, *79*, 211.

[106] S. P. Nighswander-Rempel, S. Olsen, I. B. Mahadevan, G. Netchev, B. C. Wilson, S. C. Smith, H. Rubinsztein-Dunlop, P. Meredith, *Photochem. Photobiol.* **2008**, *84*, 613.

[107] J.-D. Chai, M. Head-Gordon, *Phys. Chem. Chem. Phys.* **2008**, *10*, 6615.

[108] T. G. Costa, B. Szpoganicz, G. F. Caramori, V. R. de Almeida, A. S. Mangrich, A. P. Mangoni, *J. Coord. Chem.* **2014**, *67*, 986.

[109] L. Hong, J. D. Simon, *J. Phys. Chem. B* **2007**, *111*, 7938.

[110] Y. Liu, L. Hong, V. R. Kempf, K. Wakamatsu, S. Ito, J. D. Simon, *Pigment Cell Res.* **2004**, *17*, 262.

[111] L. K. Charkoudian, K. J. Franz, *Inorg. Chem.* **2006**, *45*, 3657.

9

Structural Hierarchy and Aggregation Dynamics of Self-assembled dopa-melanin
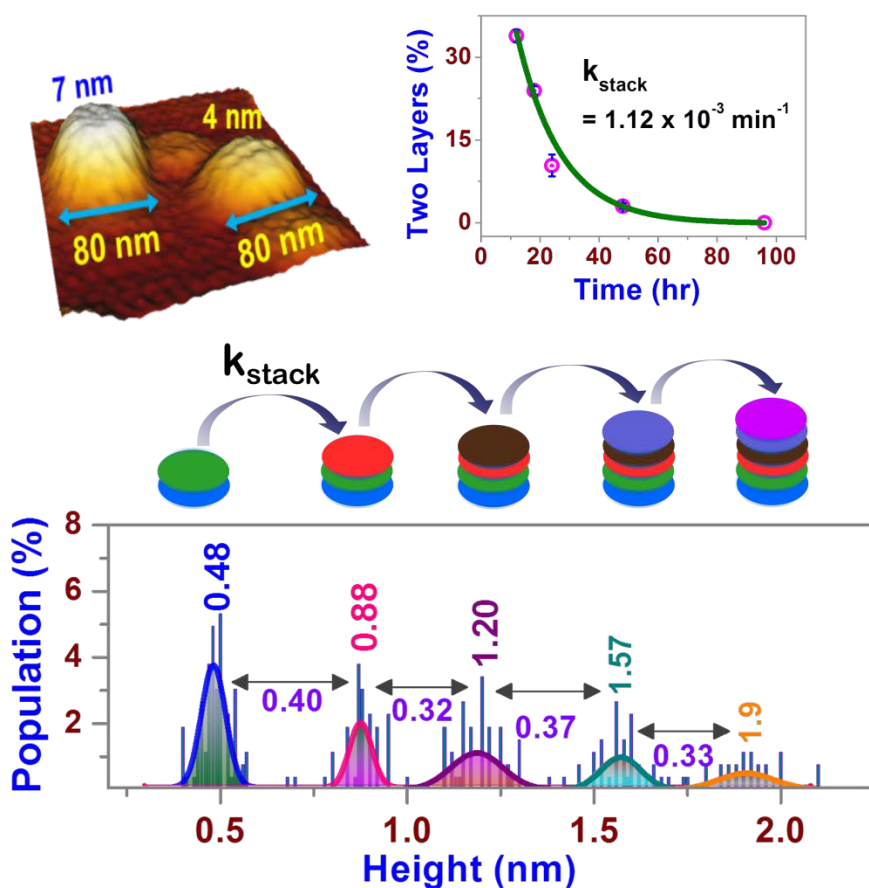
9.1 Introduction

In the last century, the primary, secondary and thereof tertiary structure of essential macromolecules in living organism; proteins, lipids, carbohydrates and DNA are precisely determined. Other that these four molecules of life, melanins, an important class of functional biopigment that is not yet structurally and functionally understood.[1–3] Other than being a natural sunscreen[4] owing to its broad UV/Vis absorption[5] and exceptionally low radiative quantum yield,[6] melanin shows humidity dependent ionic-electronic conductivity,[7,8] extreme affinity towards metal ions,[9] and free radical scavenging ability.[10] Due to its unique conducting and charge transportation properties, melanin has found itself as an active ingredient in variety of optoelectronic and photonic,[11–19] chemical sensing,[16] and biocompatible platforms.[20–22] A melanin-like material, *viz.* polydopamine (PDA) emerged as a universal versatile coating for organic and inorganic surfaces.[23] Primary, self-assembled secondary and higher order structures of melanin classes of macromolecules are closely related to its versatile functionalities. Comprehension of the self-driven ordering mechanisms of melanin at different length scale is important from both fundamental as well as technological perspective.

Among the two most abundant forms of melanins; brown to black eumelanin and red to yellow pheomelanin, the former is predominant in the human and animal kingdom. The eumelanins comprise of protomolecules (primary structure) which are derived from the oxidative coupling of 5,6-dihydroxyindole (DHI) and 5,6-dihydroxyindole-2-carboxilic acid (DHICA). These fundamental units form secondary structures through self-association driven by a variety of non-covalent forces. Although the structures of the protomolecules themselves are strongly debated, the secondary and higher order organization of eumelanin are better understood,[24–28] at length scales from tens of nanometers to several microns.[24,29–59] (See Table 9.1 for extensive review of all imaging experiments on melanin and related material) Several of these studies have employed a top-down approach that involves separation of a different mass fraction of the purified natural pigment by chemical and/or mechanical means and subsequently use of surface imaging and/or mass spectrometric method for structural characterization. *Sepia* melanin (melanin from ink sack of *Sepia Officinalis*) and synthetic tyrosine-derived ones are investigated using combination of topography imaging[30–32,35,39] such as scanning and Transmission electron microscopy (SEM and TEM), scanning tunnelling microscopy (STM), atomic force microscopy (AFM) and matrix-assisted laser desorption ionization (MALDI) mass spectrometry.[55–59] The results derived from these studies led to the development of hierarchical structural models of *Sepia* melanin formation.[24,27,40,41,44]

Synthetically prepared melanin by self-oxidation of 3,4-dihydroxyphenylalanine (dopa) and dopamine, known as dopa-melanin and polydopamine respectively serve as a model for natural eumelanins.[28,65–69] Though thin films made from these model melanins[46,57,58,70] and other similar polymers[19,71] are investigated for possible optoelectronic applications, the number of reports investigating their aggregated secondary structure is limited.[50,58] Using AFM imaging, Jastrzebska *et al*.[50] have observed microns long fibrous structures (~ 250 nm in width and ~ 50 nm in height). Synthetically prepared dopa-melanin contains DHI as a structural unit,[72] but natural eumelanin, such as *Sepia* melanin is a copolymer of both DHI and DHICA. Thus, initially formed protomolecules and aggregated secondary structures of this model melanin might be distinct from those of the natural polymer. It is recently shown that, when chemically induced, aggregation of a polydopamine leads to the formation of unique nanostructures that are not observed in the natural system.[73,74]

In this chapter, I have investigated the self-aggregation process of dopa-melanin in the absence of any external chemical agent through surface imaging technique. Instead of disassembling the larger aggregates from the end product, we employ a bottom-up approach for this purpose. The time course of the self-oxidized melanization process is followed in deposited state with tapping mode AFM (TM-AFM) imaging on atomically flat mica and statistical analysis is performed on acquired three-dimensional (3D) topographies. AFM has been routinely used for structural investigations of biological materials and molecules,[75–78] and different types of melanins. Unlike a synthetic model like dopa-melanin, the aggregation dynamics can't be studied in a time-dependent manner for naturally occurring melanin. The height analyses, as well as the lateral size distribution of features evident in TM-AFM imaging provide definitive evidence of structural hierarchies in dopa-melanin. The observed evolution of the particle sizes in AFM images is used to develop aggregation model which is compared vis-à-vis with that of natural *Sepia* melanin.

An important aspect of melanin's self-organization is the experimentally observed stacked, graphite-like sub-structure in its nano-aggregates. Several x-ray and neutron diffraction experiments of *Sepia* and tyrosine-melanins gave evidence of the presence of stacked structures with a 3.3-4 Å inter-sheet distance.[29,32,33,35,36,49,56] AFM images of synthetic melanin particles in dopa-melanin thin film also suggested the presence of stacking interactions.[57,58] Intermolecular distances of 3-4 Å are characteristic of interacting π electron rich systems, such as porphyrin, DNA, grapheme, aromatic amino acids.[79,80] Meredith and coworkers presented transmission electron microscopy (TEM) evidence for sheet structures with a regular spatial period of ~3.7-4 Å in different types of eumelanins,[47] The presence of stacked protomolecules in melanins has theoretical support too.[81,82] In this work, we exploit

the intrinsic vertical resolution (< 0.3 nm, see Fig. 9.2) of TM-AFM to measure heights of the secondary structures of dopa-melanin. The statistical analysis of the particle height distributions directly probes the ~ 3.66 Å interlayer distances typical of π-π stacking. Additionally, a kinetic rate of conversion of a few layers thick aggregates to taller structures is also determined.

9.2 Experimental Methods

9.2.1 Sample preparation

Dopa-melanin was made via auto-oxidative polymerization of 5mM DOPA in 50 mM Tris-HCl buffer at pH 7.4, as used in many previous studies.[68,69] The reaction mixture was kept in an eppendorf, open to air oxidation in the ambient environment and covered with aluminum foil. 10-15 μl of melanin from an ongoing reaction mixture is seeded on a freshly cleaved mica plate (Electron Microscopy Sciences, Hatfield, PA, USA) and was dried at room temperature in dark for 2 days, and stored in a vacuum desiccator. Water evaporates within 10-15 minutes and thus the polymerization/aggregation process freezes. During plating the sample on mica, no pipetting was done as pipetting was found to form large aggregates of melanin particles.(Fig. 9.1) The three-dimensional (3D) topography of self-assembled aggregates at time points starting from 12 hours (hr) throughout 120 hr were imaged from two independently started oxidation reactions.

9.2.2 AFM measurement

Imaging of melanin particles was performed in intermittent-contact also known as tapping mode (TM) using an AFM. (JPK Instruments AG, Berlin, Germany) For highest spatial resolution cantilever having Super Sharp Silicon tip (Nanosensors, SSS-NCHR-50, S/N-66441F11L654) with ~2 nm radius of curvature was employed. To avoid tip-induced damage of melanin soft cantilever with a nominal force constant of ~42 N/m was used. Clancy *et al* have also used Si cantilever with a force constant of 30 N/m in TM-AFM imaging of *Sepia* melanin.[41] Particles are located on mica region by imaging a bigger area (15-50 μm^2) with low resolution (on 256x256 or 512x512 pixel). Later high resolution (HR) images of the smaller region (2-10 μm^2) were acquired on 1024x1024 or 2048x2048 pixels. HR images are recorded with a lateral resolution $\sim$ 5-20 nm/pixel. Smallest lateral dimension of detected melanin particles (at 12-18th hr) is $\sim$ 25 nm and since a super sharp tip with an average radius of $\sim$ 2 nm was used, minimal tip-convolution effect is expected in the obtained topography. Resolution of acquired images along vertical directions is better than 0.3 nm (3 Å) owing to atomically flat surface of freshly cleaved mica. (Fig. 9.2) Non-destructive nature of the TM-

AFM allowed detection of extremely thin (0.5-2 nm) melanin particles at room temperature. A raster scan speed of 06-0.8 Hz was used for imaging, as higher scan speed are found to displace top layer or cut through the sample.
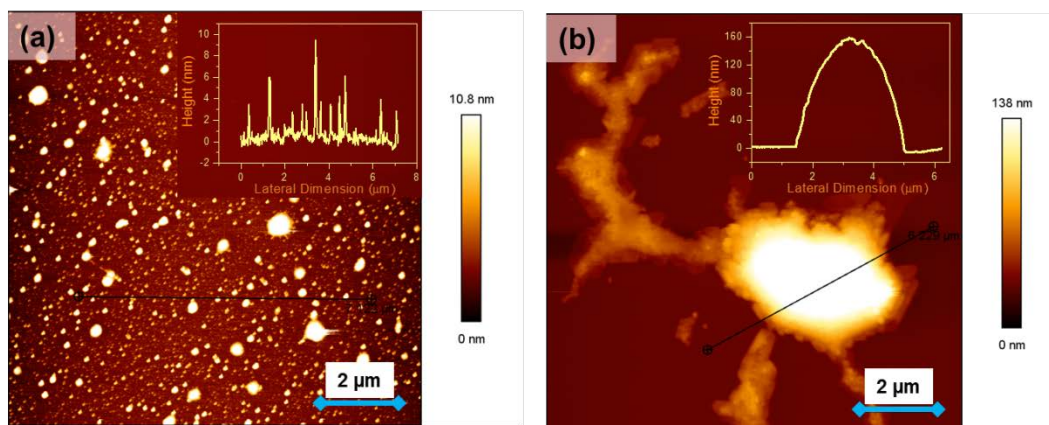
Fig. 9.1. Mechanical agitation leads to aggregation of dopa-melanin. Height images of dopa-melanin particles deposited on mica (in 10 x 10 μm^2 area) (a) without pipetting and (b) with pipetting. In (a) well-separated dopa-melanin particles are visible, whereas in (b) large micron-sized aggregate of ~ 160 nm height is observed. This is evident from the height cross-section along a line (in black) in each case shown as an inset. The color coded intensities are shown as scale bar with height (in nm) of the particles.

9.2.3 Image analysis

Data acquired in height channel was imported in JPKSPM v5.18 (JPK Instruments AG, Berlin, Germany) image analysis software. After image baseline is flattened with default polynomial subtraction algorithm implemented in this software, diameter, and height of each particle were measured manually by cross-section measurement tool. The maximum value of valley to peak height was taken as measured height and the lateral difference between two edges of the Gaussian profile is used as measured diameter. Lateral (D) and vertical (H) size distributions (normalized population in %) are obtained from measurement on 280 to 1400 individual melanin granules from acquired images of a particular time point. Size distribution of tubular aggregates (at 120th hr) was obtained from measurement on ~ 300 individual fibrillar structures.

Table 1. Review of key results on structural hierarchy present in melanin and melanin-like synthetic materials using topography imaging techniques.

| Melanin samples	Imaging technique	Detected particle size distributions	Ref
(1) Extracted and purified from ink sacs of *Sepia Officinalis*, (2) Mushroom tyrosinase oxidized tyrosine-enzymatic melanin, (3) Persulphate oxidized tyrosine-chemical melanin (from Sigma, Cat. M8631) All three types were in potassium (K^+) saturated form i.e. equilibrated in KCl.	SEM of sieve separated (through square opening with dimension varying from 25 to 125 µm) melanin particles	(1) Aggregates of *sepia* melanin-K^+ form are made of spherical particles with diameter ranging from 105 nm to 225 nm (2) Discrete *sepia* melanin particles are of 150 ±34 nm average diameter (3) Both, chemically and enzymatically prepared tyrosine melanins were not found to be composed of similar discrete particles.	Zeise, L. et al. Pig. Cell Res. **1992**, 5, 132-142
Extracted and purified from ink sacs of *Sepia Officinalis* in its K^+ form (*Sepia* melanin-K^+)	SEM of sieve separated (through square opening with dimension varying from 25 to 125 µm) melanin particles with	(1) Aggregates composed of smaller spherical assemblies with diameter ranging from 70 nm - 460 nm. (2) Discrete spherical particles are of ~ 159.5 ±29.7 nm in diameter.	Zeise, L. et al. Pig. Cell Res. **1993**, 3, 48-53
Persulphate oxidized tyrosine-melanin , deposited through micro-pipetting and galvanostatic deposition on highly oriented pyrolytic graphite (HOPG) and Molybdenum disulfide (MoS2).	STM	(1) STM images on MoS_2 show average lateral width of ~ 20 Å (2 nm) and height of ~ 10 ± 1.5 Å. The detected longitudinal structures correspond to 2-3 layer of planar sheet with ~3.5 Å interplanar distance along with 3-4 Å separation between first layer and substrate. (2) Stacking of planar sheets with a characteristic ~3.5 Å interlayer distance was proposed. It accounts for the stacking feature found as a peak at ~ 1.74 Å^{-1} in x-ray derived structure factor spectra.	Zajac, G. W. et al. J. Vac. Sci. Technol. **199**4; Zajac, G. W. et al. Biochimica et Biophysica Acta **1994**
Sepia melanin (from sigma) and synthetic melanin made form oxidation of dopa by tyrosinase, and filtered through size exclusion filters	SEM of melanin dried on conductive carbon tabs that were sputter coated with Au/Pd	(1) Sepia melanin and dopa-melanin (tyrosinase assisted oxidation) is structurally dissimilar. (2) Images of mass fraction of 1000 < MW <3000 of *sepia* eumelanin reveals a structural order with subunits having ~ 15 ± 1 nm of lateral dimension.	Nofsinger, J. B. et al. Pig. Cell Res. **2000**, 13, 179-184

Bleached (with hydrogen peroxide)and un-bleached tyrosine-derived melanin (from Genzyme Corporation)	(1) STM of melanin deposited from diluted tetrahydrofuran (THF) solution on highly oriented pyrolitic graphite (HOPG) (2) TM-AFM of melanin deposited on Mg^{2+} doped glass cover slip from methanol/THF (99:1) solution	(1) STM images show deposition with average lateral dimension of 2.3 nm for bleached and un-bleached melanin. TM-AFM detects relatively bigger structures of 6-30 nm in size. (2) Both, TM-AFM and STM detect ~ 1.5 nm as average height of smallest melanin particles. (3) Bleaching causes a decrease of ~ 1 nm in height of these particles. STM shows a decrease from 15 ± 5 Å to 5 ± 1.3 Å and TM-AFM yields similar results (from 14 ± 5 Å to 6 ± 2 Å). These bleached structures are expected to be single or at most two layers thick (4) Decrease in height is explained as breaking of π-π stacking interactions between different sheet structures due to bleaching via oxidation by H_2O_2 or air/light combination.	Gallas, J. M. et al. Pig.Cell Res. **2000**, 13, 99–108

Sepia melanin (from sigma) was sonicated, centrifuged and then filtered through ultrafiltration membrane having specific molecular weight cut-off.	CM- and TM-AFM imaging of drop casted melanin on mica.	(1) Aggregated structures seen through optical microscope are of 1 µm in size, and AFM reveals these are composed of granular substructures of 100-200 nm size. (2) CM-AFM images reveals three types of structural assemblies in *Sepia* melanin deposits,		Clancy, C. M. R. et al. Biochemistry **2001**, 40, 13353-13360
		Type	D (nm)	H (nm)
		Small particles	> 20	4-15
		Isolated particles	~ 150	-
		Microns long Filaments	15-50	3-6

Melanin was extracted from ink sac of *sepia Officinalis* and was ultra-centrifuged. The pellet was resuspended in double distilled water after washing six times.	UHR-SEM and AFM of *sepia* melanin deposited with different techniques. For AFM measurements, mass-selected fractions of *Sepia* melanin was	(1) Size and shape of micron-sized globular aggregates of *Sepia* eumelanin strongly depend upon the isolation, purification, storage and deposition procedures. (2)UHR-SEM images of (i) *Sepia* melanin (from sigma), and melanin (ii) freeze-dried with liquid N_2 and (iii) supercritically dried with CO_2 from ink sac of *Sepia* reveal granular structures diameter of ~150 nm. (3) Unlike air-dried sample that shows thin layers of uniformly distributed granules, freeze-died melanin exhibits shell-like and rod-like aggregates. Supercritically dried melanin shows highly disperse porous aerogel like structures that are also made of similar granules.	Liu, Y. et al. Pig. Cell Res. **2003**, 16, 72-80.

	obtained by passing through ultrafiltration disk membrane having a ranges of molecular weight cut-off.	(4) AFM images of *Sepia* melanin having molecular weight < 1000 amu and deposited on mica reveal filament-like aggregates. These fibrillar structures are several microns in length, ~15-50 nm in width or diameter and ~3-5 nm in height. (5) UHR-SEM and AFM also detects a ~ 10 nm fundamental constituents that aggregate into ~ 150 nm globular granules.	
Sepia melanin from sigma and extracted from ink sac of *sepia officinalis* with different metal ion content. *Sepia* melanin was sonicated and passed through amicon ultrafiltration disk membrane before deposition for AFM.	UHR-SEM of melanin, after deposition and air-drying on mica or silicon and sputter coated with Au/Pd. TM-AFM of size-selected melanin particles deposited and air-dried on mica.	(1) Irrespective of metal ion content, *Sepia* melanin maintain granular secondary structures ~ 10-20 nm lateral dimension. In all four types of metal (Fe, Zn, Cu, Ca) ion saturated melanin, these substructure are found to form tertiary structures of ~150 nm. (2) Repetitive washing with ethylenediaminetetraacetic acid (EDTA) tend to decrease average diameter of ~150 nm sized aggregates by ~ 5 nm. (3) For EDTA washed samples, AFM images of MW < 100 kDa fraction reveals into island-type lateral aggregations about 8–50 nm in diameter and 1–1.5 nm in thickness. These structures are preferably single-layered lateral assemblies of the fundamental aggregates of ~ 2 nm size.	Liu, Y. et al. Pig. Cell Res. **2005**, 18, 42-48.
Electrochemically deposited synthetic tyrosine-eumelanin (from Sigma, Cat. M8631) on silver surface.	STM and AFM	(1) HR-STM images of the early stages of film growing on Au (111) surface show small particles of 5−8 nm in size and 0.3−0.4 nm in height, arranged in ordered arrays. (2) Three-dimensional (3D) globular aggregates of 150−200 nm in diameter form after 16 hr. These structures resemble closely those found in eumelanin films prepared by solvent evaporation.	Diaz, P. et al. Langmuir **2005**, 21, 5924-5930.
Melanin extracted form bovine retinal pigment epithelium (RPE) and *Sepia* melanin, and (from Sigma) air oxidized dopa-melanin	TEM on amorphous carbon (grapheme). SEM on mica after sputter coating with Platinum (Pt).	(1) HR-electron micrographs of synthetic and natural melanins reveal onion-like structure made of stacked plane which are arranged in concentric rings. (2) The fundamental aggregates seem to be curved planar sheets with sub-10 nm lateral dimension. (3) 2D-fourier analysis of TEM images yields peak in radial power spectrum at a spatial period ~ 3.7-4.0 Å. (4) Additional peak ~ 7 Å and ~ 13 Å are also observed. While the second peak probably corresponds to dimension of the indolic protomolecular structure, and the partially de-stacked structures of the aggregates give rise the peak at 7 Å.	Watt, A. A. R. et al. Soft Matter 2009, 5, 3754-3760.
Self-oxidized dopa-melanin in double distilled water	TM-AFM on mica, gold and glass substrate	(1) Self-assembled dopa-melanin form microns long tubular aggregates on all three surfaces. (2) These stick-like structures are of 200-250 nm in width (diameter) and of 30-50 nm in height. (3) Formed melanin aggregates are well separated on mica compared to other two	Jastrzebska, M. et al. J. Mater. Sci. 2010, 45, 5302–5308.

		surfaces.	
Oxidation of DHI and its 2-7′-biindole dimer by horseradish peroxidase (HRP) and H_2O_2	DLS and small angel neutron scattering (SANS)	(1) Fundamental unit of this melanin is two dimensional (2D) planar sheets of ~55 nm thickness (2) DHI and 2-7′-biindole derivatives are constantly absorbed by already formed DHI eumelanin	Arzillo, M. et al. Biomacromolecules **2012**, 13, 2379 −2390.
Polydopamine (PDA) made via self-oxidation of dopamine hydrochloride in basic pH 8.8 at room temperature and carbonized at 800 °C	SEM and HR-TEM	(1) SEM images show PDA nanoparticles are of ~100 nm in diameter. (2) Carbonization at slow rate (5°C/min) prevents rupture of nanoparticle compared to faster one (10°C/min) (3) Carbonized PDA nanostructures are similar to amorphous carbon. HR-TEM images reveal graphite like structures which contain several tens (~40) of stacked layers of total ~15 nm of thickness, with a ~ 0.34 nm (3.4 Å) interlayer distance. (4) These PDA nanogranules have structural similarity with melanin supramolecular assembly measured by various techniques.	Yu, X. et al. Langmuir **2014**, 30, 5497 −5505
Polydopamine (PDA) made via self-oxidation of dopamine hydrochloride in acidic pH ()	SEM and HR-TEM	Gaphite like stacked structure as observed in PDA nanostructures made in basic pH.	Zheng, W. et al. Langmuir **2015**, 31, 11671 −11677.
Polydopamine (PDA) made from self-assembly of dopamine hydrochloride (0.3 mg/ml) in presence of folic acid (0.15 mg/ml) in tris-HCL buffer at pH 8.8	SEM, TEM and AFM	(1) SEM images show formation of nanobelts and nanofibers that are several hundred nm to tens of μm in length. (2) HR-TEM imaging reveals structures of different contrast within one belt: fibers are formed by curling of nanobelts or nanosheets. (3) Height of these nanobelts are determined ~ 30 nm from AFM measurements.	Yu, X et al. Angew. Chem. Int. Ed. **2014**, 53, 12600 −12604.
Tyrosinase assisted oxidation of L-dopa solution (containing 5 μM CuSO4 for activating tyrosinase) and deposited on glass slide at 40 °C.	SEM and AFM	(1) Enzymatically synthesized spherical eumelanin particles of 30-60 nm diameters. (2) Distributions of different types of aggregates are present: (i) randomly distributed partially coalesced structures; (ii) linearly associated chain like structures and (iii) isolated particles.	Strube, O. I. et al. Biomacromolecules **2015**, 16, 1608 −1613.

Abbreviations – SEM, scanning electron microscopy; AFM, atomic force microscopy; HR, high resolution; UHR, ultra high resolution; TM-AFM, tapping or intermittent contact mode AFM; CM-AFM, contact mode AFM; STM, scanning tunneling microscopy; TEM, tunneling electron microscopy; PDA, polydopamine; DHI, 5,6-dihydroxyindole; DHICA, 5,6-dihydroxyindole-2-carboxylic acid; PTCA, pyrrole-2,3,5-tricarboxylic acid; PDCA, pyrrole-2,3-dicarboxylic acid
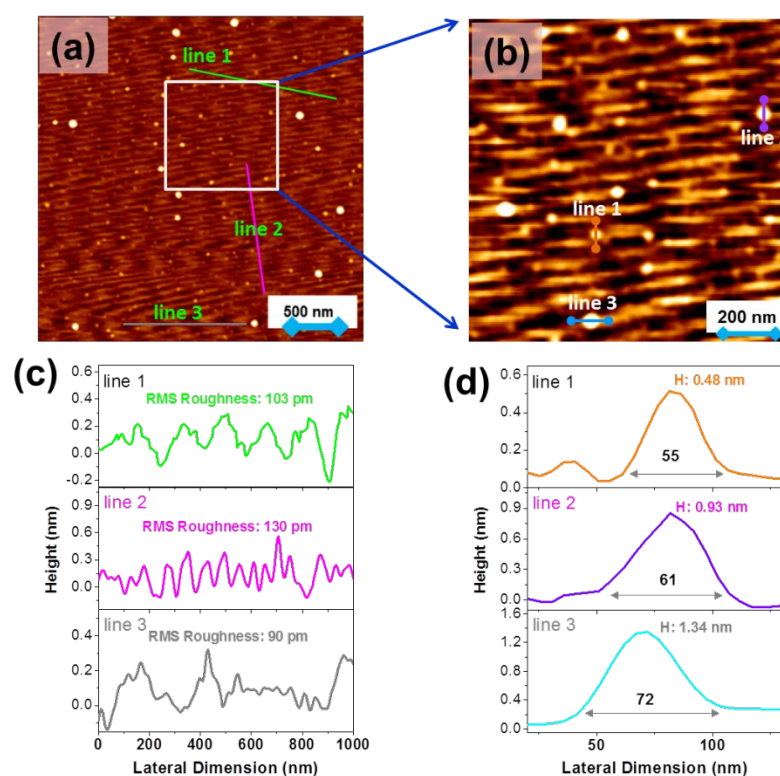
Fig. 9.2. The vertical resolution of the measured particle heights in TM-AFM images. (a) An image acquired at 48th hr and (b) magnified version of the 1 x 1 um² area marked by white square; Height cross-section (c) along line 1, line 2 and line 3 on mica surface shown in panel a, and (d) of three particles along line 1, line 2 and line 3 in panel b. Panel c shows RMS roughness of the mica surface (there is no melanin particle along the three lines in a) is ~ 90-130 picometer (pm); Panel d demonstrates detection of three particles that are ~ 0.5- 1.3 nm in height.

9.3 Results and Discussions

9.3.1 Dopa-melanin has disk-shaped secondary structure

TM-AFM topography images of the deposited dopa-melanin nanostructures on freshly cleaved mica at different time are shown in Fig.9.3, panel (a-f). The gradual increase of particle sizes in lateral and vertical dimension is observed with time from 12th to 96th hr. At the initial time (12 and 18 hr), structures of lateral dimension (D) = 30-60 nm and of 0.5-2 nm in thickness or height (H) was observed. (See Fig. 9.4, panel a and b) The high aspect ratio along two perpendicular directions suggests a disk-shaped structure. The larger dimension (~ 40-50 nm) of the initially formed disk-shaped granules agrees with that of *Sepia* melanin aggregate detected in previous TM-AFM and SEM investigations[41,42] and are also in accord with the average size (30-60 nm) of tyrosinase oxidized dopa-melanin.[83] With time, these disks grow in lateral and vertical direction and form fibrillar aggregates at 120th hr. These secondary structures are possibly made from

the association of smaller (< 5 nm) fundamental structures, detected in other melanins.[39–41,56,60–64]
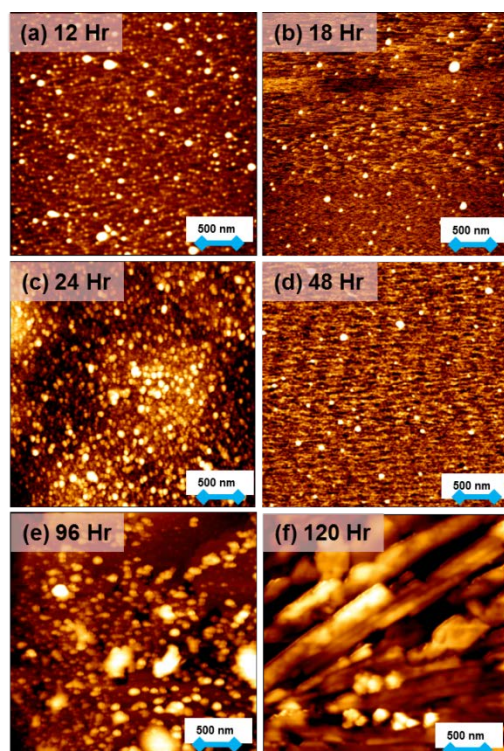
Fig. 9.3. TM-AFM topography images of dopa-melanin particles deposited on mica at (a) 12th, (b) 18th, (c) 24th, (d) 48th, (e) 96th and (f) 120th hr of self-oxidation reaction. Each image represents a 3 x 3 um^2 area.

Melanin granules with a smaller size (D ~ 15-20 nm) have been observed in SEM and AFM images of a mass-selected fraction of *Sepia* melanin.[39–41] The pore size (~ 3-4 nm) of the membrane filters used to separate this mass-fractions put a higher limit on the size of the fundamental aggregates. Consistent with this results from several MALDI investigations suggesting that the fundamental aggregates of eumelanin have a molecular weight of 500 to 1500 amu.[60–64] Small angle scattering experiments have also determined lateral extent of tyrosine-derived melanin to be ~5.4 nm.[56] These smaller units non-covalently self-assemble into tens of nm sized granules which upon further aggregation produce the hundreds of nm sized secondary structures, typically observed in the majority of imaging experiments,[38–44,47,49] such as ours. Thus, the disk-shaped granules observed at the earliest time in our study are also expected to be formed through association of these sub-5 nm units similar to those present in *Sepia* melanin. The presence of such inter-unit non-covalent interactions is inferred from results of electrospray ionization mass spectrometry (ESI-MS) and solid state nuclear magnetic resonance (NMR) spectroscopy.[53,55]

### 9.3.2 TM-AFM detects stacking off in dopa-melanin nano-aggregates

Size distribution at 12th and 48th hr show that the lateral sizes and heights of nano-aggregates lie within 30-60 nm (Fig. 9.4, panel a) and within 0.5 to 4 nm (Fig. 9.4, panel b) respectively. Particle heights within similar range are previously reported

for different eumelanins including dopa-melanin.[32,35,58] To distinguish the discrete population of disk-shaped aggregates we perform statistical analysis on a large number of particles from three images corresponding to each time point. The resulting continuous distributions, depicted in Fig.9.5 readily show a number of well-resolved peaks at an initial time (12, 18 and 24th hr), suggesting the presence of a distinct population with different heights. The intensity of each peak relative to another indicates relative concentration of granules with a particular height at a given time.

The distributions at 12th, 18th, 24th and 48th hr clearly show distinguishable height population of dopa-melanin particles with an average peak-to-peak interval of ~ 0.366 ± 0.02 nm (~ 3.66 Å). This is a direct evidence of fundamental π-π stacking during the early stage of melanization and in several other supramolecular systems. The water-insoluble 'primary' protomolecules come together to form a sheet-like 'secondary' aggregate. These sheets self-assemble into 'tertiary' structure through interlayer π-π and van der Walls forces, in order to minimize solvophobic interaction.[80] Depending on the synthetic environment, these tertiary aggregates form further higher order structures. The use of the terminologies 'primary', 'secondary' and 'tertiary' in melanin self-assembly is borrowed in analogy with protein structure. To the best of our knowledge, this is the first direct measurement of heterogeneously distributed stacked tertiary structures of eumelanin nano-aggregates detected through topography imaging experiments. This has been achieved through (i) synthesis and arresting of early-time secondary structures and (ii) using the intrinsic ability of TM-AFM to detect these particles with very high (better than 0.3 nm) vertical resolution.[84]

The distribution at 12th hr shows that majority of the disk-like (D ~ 30-40 nm) aggregates has a height ~ 0.5 nm (0.4 < H < 0.68). The next consecutively occurring peaks lie at ~0.88 nm, ~1.20 nm, ~1.57 nm and ~1.9 nm. According to Kaxiras's theoretically proposed model, the majority of fundamental protomolecules are either planar or partially helical, and their thickness is < 0.5 Å.[81,85,86] Thus after arranging two disks on top of each other with a ~ 3.66 Å separation, the distance between mica and the first layer is ~ 1.3 Å (inset of Fig. 9.5, 12 hr). With time, the heterogeneity in height distribution increases as evidenced by the presence of an additional number of peaks at a later time (Fig. 9.5, 24 and 48 hr) and formation of much taller (tens of nm) aggregates at 96th hr. (Fig. 9.4, panel b). The relative intensity of first two peaks decreases from 12th to 24th hr, indicating an association of disks to form taller barrel-like structures. At 48th hr the height of majority of these disks are clustered around ~ 0.9 nm (0.65 < H < 1.07 nm) and ~ 1.26 nm (1.1 < H < 1.35 nm) representing stack of 3 and 4 layers respectively.
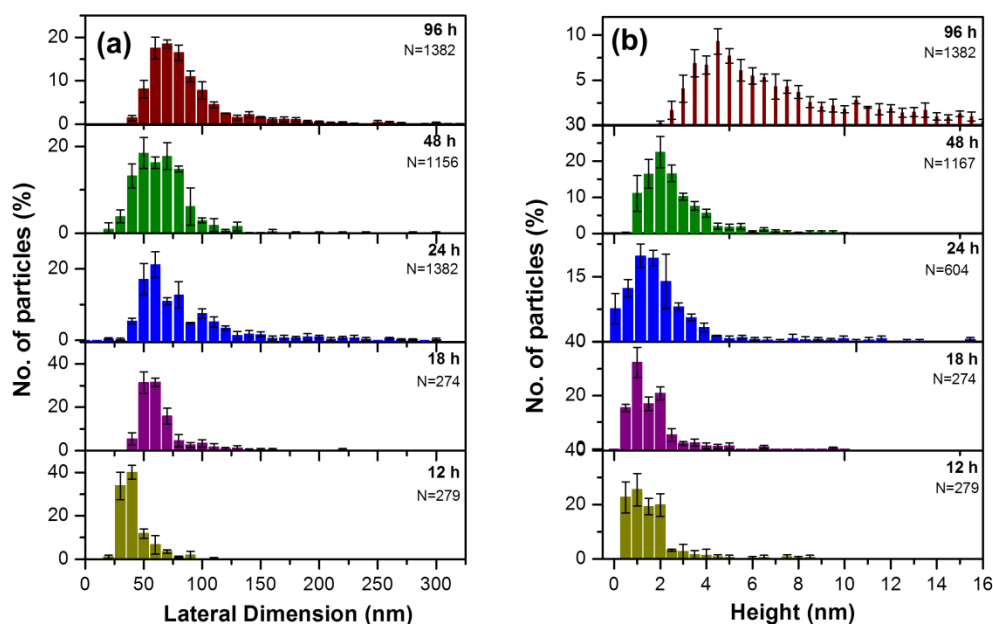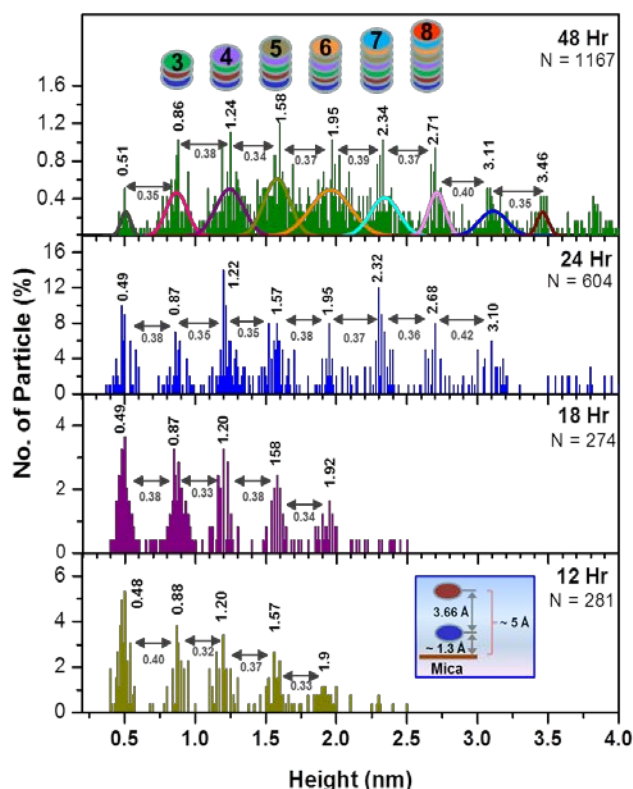
Fig. 4 Size distribution of the dopa-melanin particles measured along (a) lateral and (b) vertical dimension. Each panel is labeled with a respective time point in hr and the total number of particles (N) counted from three images to obtain the statistics. The bin size in the histograms described in (a) is 10 nm in (b) is 0.5 nm. The continuous distribution corresponding to (b) is depicted in Fig. 5.

Using AFM and STM imaging, Gallas *et al*. have reported that bleaching with light/air combination or oxidation with H_2O_2 reduces heights of the tyrosine-melanin particles.[38] Non-covalent interactions such as π-stacking, van der Walls forces and hydrogen bonding that hold eumelanin layers together break during treatment with the bleaching agent, thus causes a decrease in particle heights. Physically disruptive processes such as; sonication and ultrafiltration are also prone to disrupt these non-covalent contacts. Our bottom-up approach is a straightforward process: drop casting the sample from an ongoing autoxidation reaction on cleaved mica and drying it instantly before imaging. While our findings support commonly accepted stacked oligomer model of eumelanin, it also gives a unique analysis procedure to investigate the kinetics of such aggregation process on surface.

At a particular time when an aliquot of sample is seeded and instantly dried on mica, the arrested population represents the concentration of dopa-melanin particles synthesized in a solution state. The time-evolution of the integrated population that have a height within 0.3 to 0.7 nm (first peak in Fig.9.5) is found to follow first order exponential decay with a time constant 1.12×10^{-3} min^{-1}. (Fig. 9.6) This is the conversion rate of all two-layer thick disks into taller structures. It would also be the rate of association of further layers assuming the forward rates are many times larger than reverse rates. In fact, this is the case in the current scenario; melanin production via self-oxidation of dopa is a continuous forward

reaction. Melanin aggregation is a situation similar to irreversible formation of fibrils during aggregation reaction of proteins.

Fig. 9.5 Continuous height distribution of the dopa-melanin particles measured along vertical dimension. Each panel is labeled with respective time point in hr and the total number of particles (N) counted to obtain the statistics. Inset shows first two layers on mica (in panel 12 hr) and pictorial depiction of gradual increase in height through stacking of layers (in 48 hr).
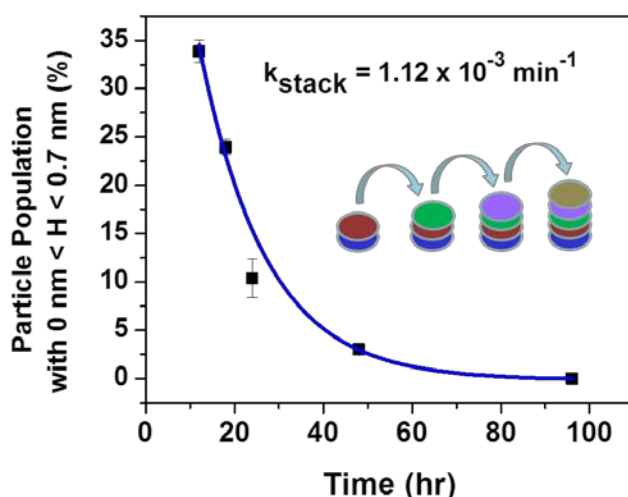
Fig. 9.6 Exponential decay kinetics of population of dopa-melanin particles whose height lie within 0.3 nm to 0.7 nm. This population represents the integrated intensity if the peak in Fig. 9.5. The inset pictorially describes conversion of two layer thick disks into barrel-like aggregates that are made from continuous addition of consecutive layer.

Using TEM Meredith and coworkers have shown that when dispersed in a solvent constrained environment, both natural (from *Sepia* and bovine RPE) and synthetically prepared melanins form curly onion-like tertiary structures.[47] On the contrary, drop-casting from water-based reaction leads to the formation of the barrel like nano-aggregates that undergo further aggregation. Fourier transform of

the TEM images reveals a sharp spatial period at ~ 3.7-4 Å, corresponding to inter-layer π-π stacking. The additional broad peaks at 7 Å in bovine RPE melanin and at 13 Å in the case of synthetic melanin were hypothesized to represent the fundamental length scale of the protomolecules and the partially destacked aggregates respectively. These features are not observed in our study, as TM-AFM only detects heterogeneity in the vertical dimension of consecutively added layers in melanin secondary structures.

The distributions of Fig. 9.4 indicate continuous growth in both dimensions with time. The lateral dimension of early time aggregates increases from ~ 40 nm at 12th hr to an average value of ~ 80 nm at 96th hr. The increase in the breadth of the distributions (Fig. 9.4, panel a) implies the formation of disk-shaped particles differing in lateral sizes. Up to 96th hr the increase in D result from continuous growth of initially (before 12th hr) started nucleation process (from the coalescence of a few ~ 5 nm sized particles), instead of the association of tens of nm sized aggregates. The particles synthesized after 96th hr lies within 100-200 nm of lateral dimension. The height distribution at 96th hr (Fig. 9.4, panel b, 96th hr) demonstrates a sudden increase in particle height heterogeneity, that result into formation of much taller aggregates with 2 nm < H < 15 nm. The lateral sizes of these particles are still ~ 80-90 nm which is a marginal increase from that at (~ 70 nm) 48th hr. These two facts together indicate that after initial aggregate reach a critical lateral size, they tend to grow vertically instead of expanding horizontally.

Initially, the poor solubility of the heteroaromatic protomolecules leads to the formation of disk-shaped structures that simultaneously grow laterally and stack on top of each other. The surface area to volume ratio of a cylinder (= 2/radius+2/height) minimizes rapidly when the relative increase in height is much more than that of lateral dimension. Thus, these barrel-like structures tend to stabilize by reducing surface energy by growing in the vertical direction from few nm to tens of nm while keeping a relatively narrow (D = 100-200) lateral size distributions. Therefore, non-covalent van der Walls forces and π-π interaction, and probably a predicted interlayer covalent bonding[85,86] between sheets play a dominant role in the synthesis of these barrel-shaped aggregates.

9.3.3 Edge-to-edge self-assembly leads to formation of fibrillar structure

At 120th hr formation of fibrillar aggregates are observed. (Fig. 9.3, panel f and Fig. 9.7) The presence of filamentous assemblies has previously been reported in both auto-oxidized dopa-melanin[50] and in *Sepia* melanin.[41] These stick-like aggregates are structurally heterogeneous and are found to be composed of four distinct populations with 80 nm < D < 180 nm and 10 nm < H < 80 nm.(Table 2). The large variation in vertical dimensions of these fibrils originates from the heterogeneity in heights of barrel-like aggregates synthesized at preceding time point.(*vide supra*) Similar structures of comparable dimension (D: 200-250 nm and

H: 30-50 nm) are reported in dopa-melanin aggregates on different substrates including on mica.[50] Comparatively, more homogeneous structural distributions may arise due to the use of pH 8.5 which is slightly more basic than that (pH 7.4) used in this study, and can maintain melanin in the more water miscible state.[87] The filaments observed in *Sepia* melanin, however, are a much smaller dimension, 15-50 nm in diameter and 3-6 nm in height.[41]
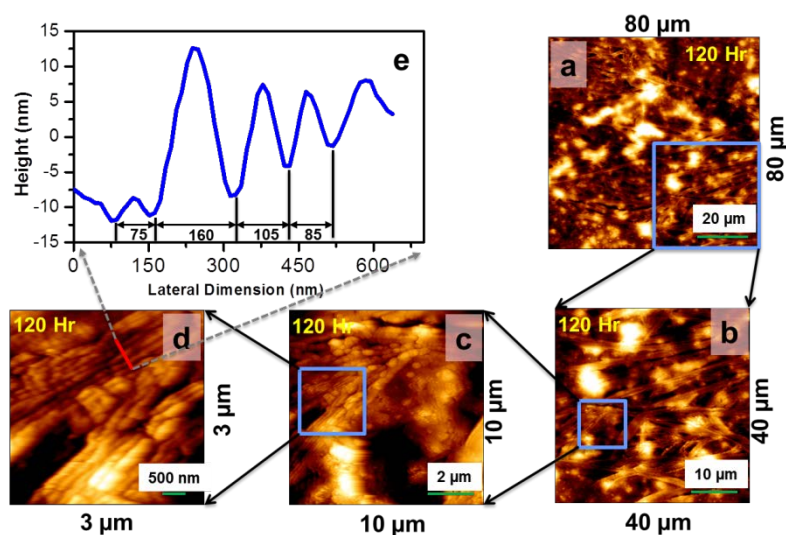

Fig. 9.7 TM-AFM images (height channel) of dopa-melanin fibrils at 120th hour of self-oxidation reaction. Height images of (a) 80 x 80 um^2 , (b) 40 x 40 um^2 , (c) 10 x 10 um^2 , (d) 3 x 3 um^2 region on mica and (e) height cross-section of individual tubules measured across a straight line (marked in red) in panel (d). The lateral resolution of images in (b), (c) and (d) is 9.8 nm/pixel.

The formation process of filamentous assemblies, along with the dimension of the component aggregates is depicted in Fig.9.8, panel a. At 10-20 µm scale (Fig. 9.7, panel a and b) these aggregates seem to form a web-like mesh through cross-linking on top of each other. Further, high resolution imaging of smaller areas (Fig. 9.7, panel c and d) reveals that these fibrils run parallel for 2 to 10 microns, in agreement with the previous report.[50] A height cross-section across the width (marked in red, Fig. 9.7, panel d) of a series of such structures reveals the presence of fibrils with varying lateral and longitudinal dimension. (Fig. 9.7, panel d and Table 2)

Although, these filaments seem to run continuously for tens of microns, are in fact formed via lateral association of similar sized aggregates.(See Fig. 9.8, panel a and Fig. 9.10, panel b) The height cross-section (Fig. 9.3, panel c) along two such assemblies clearly reveals that barrel-like structures with hundreds of nm in lateral dimensions and tens of nm in height align laterally through edge-to-edge interactions. The fact that, the lower limit (~80 nm) of the width of these fibrils is the same as the average lateral dimension of the barrel like aggregates formed at

96th hr, strengthens the same. These fibrils elongate through continual association of similar sized aggregates without preferential orientation.(Fig. 9.9)
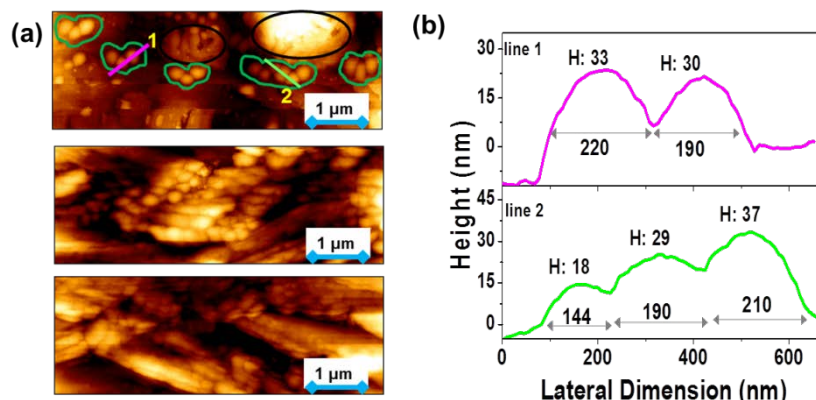

Fig. 9.8. Intermediates en route fibrillar aggregates. (a) TM-AFM images revealing the lateral association of hundreds on nm sized granules (H ~ 10-30 nm). These images are acquired at 120hr of reaction. Linear arrangement of these granules is depicted in top panel (encircled in green); (b) height cross-section of the granules along line 1 and line 2 (marked in magenta and green). Alternatively, globular structures (> 1 um in lateral dimension) that also result from the association of hundreds of nm sized sub-units (shown in black circle and see Fig. 9.11 for more detail).

In addition to fibrillar structures, micron-sized agglomerates are also formed. (encircled in black in Fig. 9.8, panel a; Fig. 9.10, panel b and Fig.9.11) Similar sized primary aggregate with tens of nm in height was reported in previous AFM measurements of the dopa-melanin film deposited from organic solvents[57,58] and for *Sepia* melanin.[41] We observe the fibrillar aggregates are predominant compared to agglomerates in dopa-melanin. Two types of competing interactions lead to two distinct types of tertiary structures. Solvophobic effect[80] due to water insolubility of the eumelanin aggregates drives its self-assembling process at the primary level and form agglomerates. However, whence stabilized by further attractive electrostatic interactions between adjacent nano-aggregates, they tend to align linearly and form filamentous structures. In 100 nm thick dopa-melanin film deposited from DMF or DMSO fibrillar structures were not detected.[58] This could be due to the facts that, (i) DMF and DMSO de-stack melanin structure,[47] and (ii) an absence of solvophobic effect as synthetic melanins are soluble in these organic solvents.

Table 2. Size distribution of dopa-melanin fibrillar structures formed at 120th hr of self-aggregation reaction on mica. The obtained statistics is from measurement on ~300 individual fibrillar structures.

| Height	Diameter
(nm)	
10 – 18	85 ± 16
15 – 30	110 ± 30
30 – 45	144 ± 30
30 – 80	180 ± 40
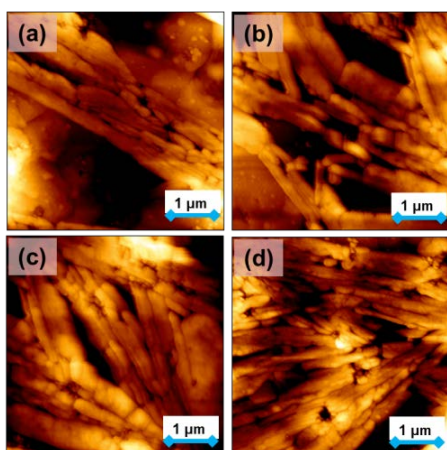
Fig. 9.9. Absence of preferential orientation of dopa-melanin fibrils. TM-AFM height images of filamentous aggregates from different regions (5 um x 5 um) of same sample on mica. Lateral resolution of these images is 7.3 nm/pixel

9.3.4 Role of substrate on formed melanin aggregates

Using contact mode (CM) AFM, Jastrzebska *et al*. have imaged dopa-melanin on different substrates (mica, glass, and gold) with varying hydrophilicity.[50] Their results show that melanin nano-granules have a tendency to be joined after drop drying on all three mentioned surfaces and self-organize into stick-like structures. Interactions of the dopa-melanin suspension with the substrate impact the shape of a droplet, thus the drying process also. However, on all three surfaces formation of a fibrillar structure with variable dimensions was observed. We have used mica as substrate as better separated melanin nan-aggregates were found to form on a mica surface in comparison to others.
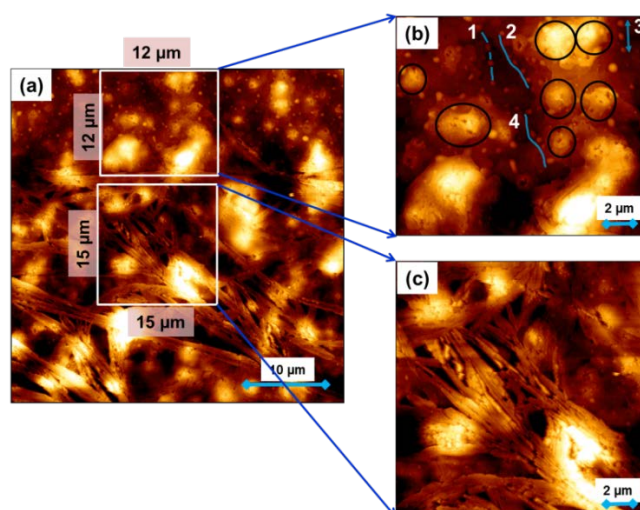
Fig. 9.10. (a) Coexistence of fibrillar and globular aggregates at 120th hr; (b) agglomerate which are of 2-4 um in lateral dimension (D) and 100-200 nm in height (H) and smaller ones with D ~ 300-500 nm and H ~ 30-80 nm; (c) tubular structure which are produced via association of smaller particles in panel b (marked as 1, 2, 3 and 4) and are of tens of um in lateral dimension. Lateral resolution of this image (42 x 42 um) is ~ 20.5 nm/pixel. A magnified version of globular agglomerates (panel b) is shown in Fig. 9.11.
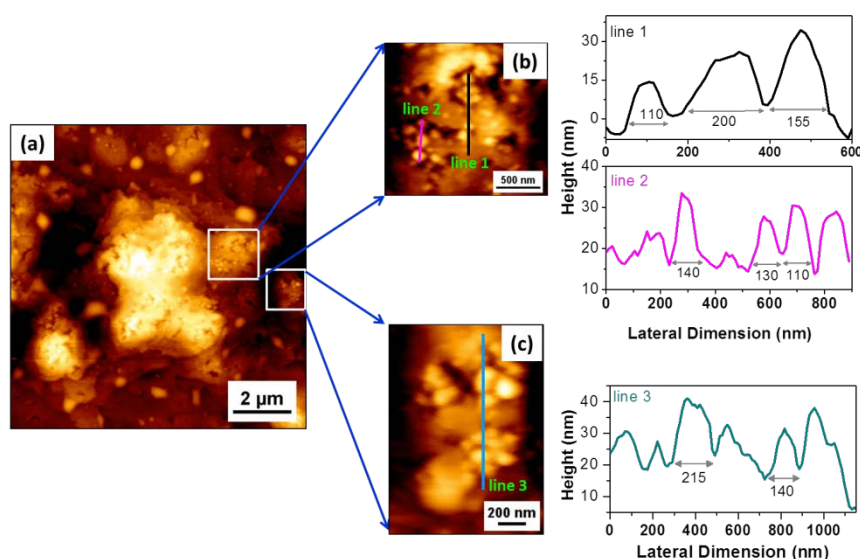

Fig. 9.11. (a) TM-AFM height image of micron-sized aggregates of dopa-melanin at 120th hr of oxidation reaction on mica. (b-c) association of hundreds on nm sized granules leads to the formation of these larger aggregates. (d-e) Cross-sections along line 1, line 2 and line 3 reveal a dimension of these smaller granules: D ~ 80-200 nm and H: 10-30 nm. Lateral resolution of this image (42 x 42 um) is ~ 12 nm/pixel.

Mica does not influence the structural association of eumelanin because the herein obtained structural features are consistent with previously published results using SEM, STM and TEM images of different melanins on various conducting surfaces[30–32,35,38,39,42–44,47,48] and also with AFM images acquired by other groups.[40,41,43,44,46,49,50] We have used mica as a substrate on which dopa-melanin aggregates, formed at a different time was dried and were imaged. We have purposefully avoided CM-AFM imaging because melanin is a soft material that is easily distorted by the tip of a cantilever while imaging.

9.3.5 Effect of Tris on self-assembly

Vecchia *et al* have given NMR evidence that indicates the possibility of the presence of Tris moiety in PDA during self-aggregation of dopamine in Tris buffer.[88] In a later study, folic acid-induced aggregation of PDA, a possibility of hybrid Yu *et al* also suggested the formation of hybrid material containing dopamine, folic acid and Tris itself.[74] Tris buffer alone aggregates on mica and form globular structures that are hundreds of nanometer in length and ~ 10 nm in height. (Fig. 9.12)
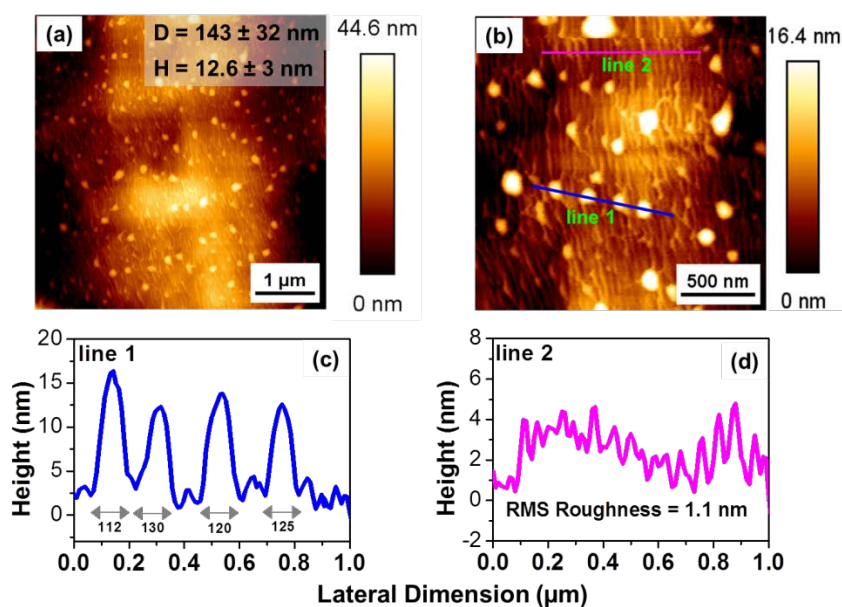
Fig. 9.12. (a) and (b) TM-AFM topography image of aggregated buffer (Tris-HCl, pH 7.4, 50 mM) on mica. Height cross-section of aggregated buffer along (a) line 1 (four aggregates) and (b) line 2 (no particles). Sizes of the aggregates of dried buffer; D = 143 ± 32 nm and H = 12.6 ± 3 nm are much bigger in both lateral and vertical dimensions than those of dopa-melanin granules observed at the initial time. The lateral resolution of the images is 10 nm/pixel. The average roughness of the buffer deposited surface is > 1 nm which is much more than that (< 0.3 pm) of the mica surface (see Fig. 9.2). The obtained statistics is for 100 aggregates of panel (a).

However, detected melanin particles at earliest (12th hr) have vertical dimension ~0.5-2 nm and a lateral dimension of tens of nm, both of which are smaller than those of Tris aggregates. Additionally, our AFM images of self-oxidized dopa-melanin in Tris-HCl buffer shows remarkable structural similarities with those of dopa-melanin made in aerated double distilled water.[50] Thus, Tris is not expected to have a significant effect in the self-aggregation mechanism of dopa-melanin.

9.3.6 Model for hierarchical structural organization of dopa-melanin

The hierarchical aggregation model that emerges from our analysis of the evolution of particle size distributions is described in Fig. 9.13. First, tens of nm sized disk-shaped aggregates that are few layers thick are synthesized. These flat sheet-like structures grow in lateral dimension through continuous addition of fundamental aggregates (sub-5 nm in size) and also in the vertical direction via interlayer attractive interactions. After reaching D ~ 100 nm, barrel-like structures are formed with tens of nm heights. These nano-aggregates either form microns long (L) stick-like structures or micron sized (D) agglomerates. This model can directly be compared with the aggregation model of natural *Sepia* eumelanin.[24,27,40,41,44] By comparing Scheme 1 and that described in Ref 24 it is readily seen that dopa-melanin shares a striking structural resemblance with that of *Sepia* melanin. The chemical environments under which the primary protomolecules are synthesized and undergo self-organization are very different for synthetic dopa-melanin in an eppendorf and natural melanin in the ink gland of *Sepia officinalis*. The pigment purified following standard procedure[30] contain 6-8 % protein by mass in *Sepia* melanin[42,89,90] and a variety of metal ions depending on the source.[91–93] The dopa-melanin prepared in the current study does not contain any metal or cross-linking protein molecules. Though the fibrils in *Sepia* sample seem to be continuous[41] unlike those in dopa-melanin, the intermediary steps of formation of higher order structure is very similar in both the cases. Despite being assembled in the presence of very different chemical ingredients both the synthetic and natural melanins have similar structural features.

It seems structural hierarchy in dopa-melanin derived in this work is not an effect induced by the chemical preparation and drying procedure but indeed is a common feature for both types of eumelanins; *Sepia* as well as synthetic. Our findings also strengthen conclusion of previous TEM measurements showing the very similar tertiary structure in several eumelanins.[47] There are several reports regarding the impact of chemical agent and synthetic environment on hierarchical structures of melanin-inspired materials for technological applications.[28,73,74,88,94–96] In principal the bottom-up approach together with AFM imaging described here can be extended to investigate the enzymatic reaction

of melanin formation, and the role of varying pH and concentration of different metal ion on secondary structural scaffolds.
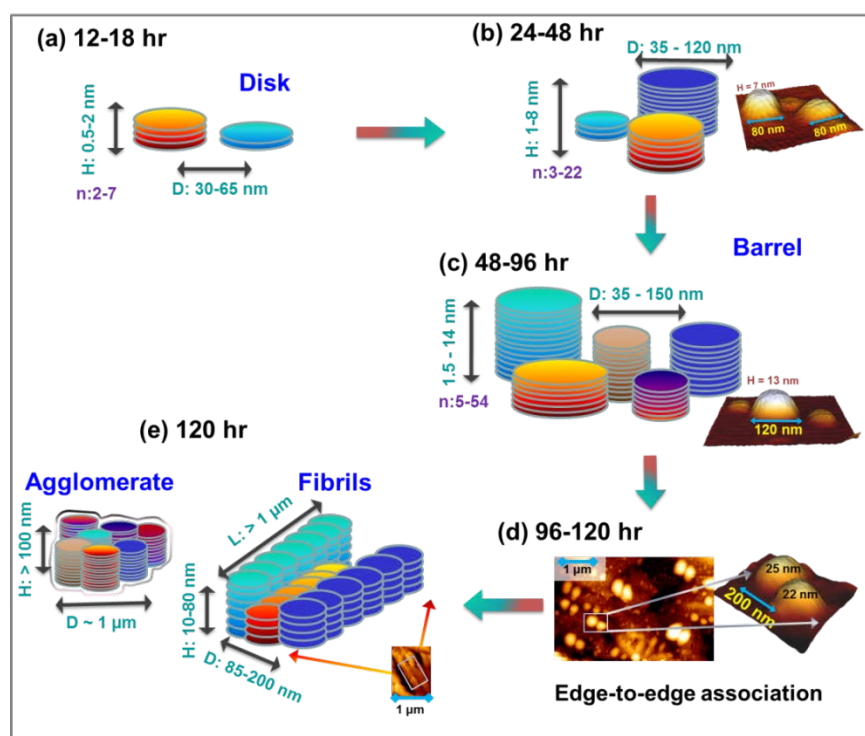
Fig. 9.13. Derived aggregation pathway and intermediate structures of dopa-melanin. The different color of the disk and barrel-shaped structures represent heterogeneity in height of melanin particles. As soon as aggregation starts, (12th hr) a few layers (2-7) thick and tens of nm in size disk-shaped secondary structures are synthesized. With time, these aggregates continually grow in lateral dimension, and also increase along vertical dimension. As soon as (48th -96th hr) the melanin particles reach a lateral size ~ 80-100 nm, a large number of barrel-like structures which are heterogeneously distributed in heights (1.5-14 nm) are synthesized via interlayer Van der Walls interaction. Between 96th to 120th hr, non-covalent interactions dominated by edge-to-edge association of the previously synthesized barrel-like aggregates leads to the array-like arrangement. Thus, fibrillar structures with hundreds of nm in diameter and tens of nanometers in height are formed. Abbreviations. n: number of stacked layers; D: largest lateral dimension and H: vertical dimension or height.

9.4 Conclusion

In this chapter, a hierarchical aggregation model of a synthetic eumelanin system, namely dopa-melanin is derived. We present direct TM-AFM evidence for planar sheet structure with varying lateral dimensions which stack with a ~ 3.66 Å interlayer separations, a characteristic of π-π stacking in graphene and other heteroaromatic systems. Our data reveals the presence of a *Sepia* melanin-like but distinct aggregation pathway in synthetic dopa-melanin formation. The detected lateral and longitudinal sizes of various aggregates of dopa-melanin are consistent with previously reported structural characteristics of several eumelanins. The detected structural organizations of dopa-

melanin are; (i) a few to tens of layers thick disks (D:30-50 nm and H:0.5-2 nm), (ii) barrel-like structures (D: 50-110 nm and H: 1.5-14 nm), (iii) globular (D ~ 1-2 um and H: 10-30 nm) aggregates and (iv) microns long fibrils (D: 85-180 nm and H: 10-80 nm). While providing conclusive evidence for the commonly accepted stacked oligomer model that stems from results of X-ray and neutron scattering and imaging experiments, our results present an alternative approach of analyzing secondary and tertiary structure formation pathway in melanins. We demonstrate that imaging with TM-AFM can not only unravel structural intermediates but when coupled with statistical analysis it can determine rates of layer formation in self-organized systems, such as melanin aggregation.

Melanin-like materials hold promise for coming age bio-optoelectronics[16,97] and related applications. For such applications need tailoring of conducting and structural properties of the functional film. Melanin in the solid state shows very intriguing humidity dependent hybrid conductivity.[8,98–100] AFM imaging in conducting mode can be combined with our bottom-up approach to understanding structure-dependent conductivities and also local mechanical properties of the nano-aggregates of dopa-melanin and related polymers.

References

[1] G. Prota, *Melanins and Melanogenesis*, Academic Press, Inc., California, USA, **1992**.

[2] J. D. Simon, *Acc. Chem. Res.* **2000**, *33*, 307.

[3] S. Roy, in *Prog. Chem. Org. Nat. Prod.*, Springer Vienna, Vienna, **2007**, pp. 131–185.

[4] N. Kollias, R. M. Sayre, L. Zeise, M. R. Chedekel, *J. Photochem. Photobiol. B Biol.* **1991**, *9*, 135.

[5] J. Riesz, J. Gilmore, P. Meredith, *Biophys. J.* **2006**, *90*, 4137.

[6] P. Meredith, J. Riesz, *Photochem. Photobiol.* **2007**, *79*, 211.

[7] A. B. Mostert, B. J. Powell, F. L. Pratt, G. R. Hanson, T. Sarna, I. R. Gentle, P. Meredith, *Proc. Natl. Acad. Sci. U. S. A.* **2012**, *109*, 8943.

[8] J. Wünsche, Y. Deng, P. Kumar, E. Di Mauro, E. Josberger, J. Sayago, A. Pezzella, F. Soavi, F. Cicoira, M. Rolandi, C. Santato, *Chem. Mater.* **2015**, *27*, 436.

[9] L. Hong, J. D. Simon, *J. Phys. Chem. B* **2007**, *111*, 7938.

[10] L. Panzella, G. Gentile, G. D'Errico, N. F. Della Vecchia, M. E. Errico, A. Napolitano, C. Carfagna, M. D'Ischia, *Angew. Chemie Int. Ed.* **2013**, *52*, 12684.

[11] M. A. Rosei, L. Mosca, F. Galluzzi, *Synth. Met.* **1996**, *76*, 331.

[12] J. B. Nofsinger, S. E. Forest, J. D. Simon, *J. Phys. Chem. B* **1999**, *103*, 11428.

[13] P. Meredith, *Components Based on Melanin and Melanin-like Bio-Molecules and Processes for Their Production*, **2007**, US20040231719.

[14] J. P. Bothma, J. de Boor, U. Divakar, P. E. Schwenn, P. Meredith, *Adv. Mater.* **2008**, *20*, 3539.

[15] M. Ambrico, N. F. Della Vecchia, P. F. Ambrico, A. Cardone, S. R. Cicco, T. Ligonzo, R. Avolio, A. Napolitano, M. D'Ischia, *Adv. Funct. Mater.* **2014**, n/a.

[16] T.-F. Wu, B.-H. Wee, J.-D. Hong, *Adv. Mater. Interfaces* **2015**, *2*, n/a.

[17] M. Xiao, Y. Li, M. C. Allen, D. D. Deheyn, X. Yue, J. Zhao, N. C. Gianneschi, M. D. Shawkey, A. Dhinojwala, *ACS Nano* **2015**, *9*, 5454.

[18] M. Barra, I. Bonadies, C. Carfagna, A. Cassinese, F. Cimino, O. Crescenzi, V. Criscuolo, D. Marco, M. G. Maglione, P. Manini, L. Migliaccio, A. Musto, A. Napolitano, A. Navarra, L. Panzella, S. Parisi, A. Pezzella, C. T. Prontera, P. Tassini, *MRS Adv.* **2015**, 1.

[19] J. Wünsche, L. Cardenas, F. Rosei, F. Cicoira, R. Gauvin, C. F. O. Graeff, S. Poulin, A. Pezzella, C. Santato, *Adv. Funct. Mater.* **2013**, *23*, 5591.

[20] Y. Liu, K. Ai, J. Liu, M. Deng, Y. He, L. Lu, *Adv. Mater.* **2013**, *25*, 1353.

[21] Q. Fan, K. Cheng, X. Hu, X. Ma, R. Zhang, M. Yang, X. Lu, L. Xing, W. Huang, S. S. Gambhir, Z. Cheng, *J. Am. Chem. Soc.* **2014**, *136*, 15185.

[22] V. Gargiulo, M. Alfè, R. Di Capua, A. R. Togna, V. Cammisotto, S. Fiorito, A. Musto, A. Navarra, S. Parisi, A. Pezzella, *J. Mater. Chem. B* **2015**, *3*, 5070.

[23] H. Lee, S. M. Dellatore, W. M. Miller, P. B. Messersmith, *Science (80-.).* **2007**, *318*, 426.

[24] Y. Liu, J. D. Simon, *Pigment Cell Res.* **2003**, *16*, 606.

[25] P. Meredith, B. J. Powell, J. Riesz, S. P. Nighswander-Rempel, M. R. Pederson, E. G. Moore, *Soft Matter* **2006**, *2*, 37.

[26] P. Meredith, T. Sarna, *Pigment Cell Res.* **2006**, *19*, 572.

[27] M. d'Ischia, A. Napolitano, A. Pezzella, P. Meredith, T. Sarna, *Angew. Chemie Int. Ed.* **2009**, *48*, 3914.

[28] M. d'Ischia, A. Napolitano, V. Ball, C.-T. Chen, M. J. Buehler, *Acc. Chem. Res.* **2014**, *47*, 3541.

[29] Y. T. Thathachari, M. S. Blois, *Biophys. J.* **1969**, *9*, 77.

[30] L. Zeise, B. L. Murr, M. R. Chedekel, *Pigment Cell Res.* **1992**, *5*, 132.

[31] L. Zeise, R. B. Addison, M. R. Chedekel, *Pigment Cell Res.* **1993**, *3*, 48.

[32] G. W. Zajac, J. M. Gallas, J. Cheng, M. Eisner, S. C. Moss, A. E. Alvarado-Swaisgood, *Biochim. Biophys. Acta* **1994**, *1199*, 271.

[33] J. Cheng, S. C. Moss, M. Eisner, P. Zschak, *Pigment Cell Res.* **1994**, *7*, 255.

[34] G. W. Zajac, J. M. Gallas, J. Cheng, M. Eisner, S. C. Moss, A. E. Alvarado-Swaisgood, *Biochim. Biophys. Acta - Gen. Subj.* **1994**, *1199*, 271.

[35] G. W. Zajac, J. M. Gallas, A. E. Alvarado-Swaisgood, *J. Vac. Sci. Technol. B Microelectron. Nanom. Struct.* **1994**, *12*, 1512.

[36] J. Cheng, S. C. Moss, M. Eisner, *Pigment Cell Res.* **1994**, *7*, 263.

[37] J. M. Gallas, K. C. Littrell, S. Seifert, G. W. Zajac, P. Thiyagarajan, *Biophys. J.* **1999**, *77*, 1135.

[38] J. M. Gallas, G. W. Zajac, T. Sarna, P. L. Stotter, *Pigment Cell Res.* **2000**, *13*, 99.

[39] J. B. Nofsinger, S. E. Forest, L. M. Eibest, K. A. Gold, J. D. Simon, *Pigment Cell Res.* **2000**, *13*, 179.

[40] C. M. R. Clancy, J. B. Nofsinger, R. K. Hanks, J. D. Simon, *J. Phys. Chem. B* **2000**, *104*, 7871.

[41] C. M. R. Clancy, J. D. Simon, *Biochemistry* **2001**, *40*, 13353.

[42] Y. Liu, J. D. Simon, *Pigment Cell Res.* **2003**, *16*, 72.

[43] P. Díaz, Y. Gimeno, P. Carro, S. González, P. L. Schilardi, G. Benítez, R. C. Salvarezza, A. H. Creus, *Langmuir* **2005**, *21*, 5924.

[44] Y. Liu, J. D. Simon, *Pigment Cell Res.* **2005**, *18*, 42.

[45] M. L. Tran, B. J. Powell, P. Meredith, *Biophys. J.* **2006**, *90*, 743.

[46] J. P. Bothma, J. de Boor, U. Divakar, P. E. Schwenn, P. Meredith, *Adv. Mater.* **2008**, *20*, 3539.

[47] A. A. R. Watt, J. P. Bothma, P. Meredith, *Soft Matter* **2009**, *5*, 3754.

[48] M. Abbas, F. D'Amico, L. Morresi, N. Pinto, M. Ficcadenti, R. Natali, L. Ottaviano, M. Passacantando, M. Cuccioloni, M. Angeletti, R. Gunnella, *Eur. Phys. J. E* **2009**, *28*, 285.

[49] P. Borghetti, A. Goldoni, C. Castellarin-Cudia, L. Casalis, F. Herberg, L. Floreano, A. Cossaro, A. Verdini, R. Gebauer, P. Ghosh, L. Sangaletti, *Langmuir* **2010**, *26*, 19007.

[50] M. Jastrzebska, I. Mróz, B. Barwiński, R. Wrzalik, S. Boryczka, *J. Mater. Sci.* **2010**, *45*, 5302.

[51] M. Abbas, M. Ali, S. K. Shah, F. D'Amico, P. Postorino, S. Mangialardo, M. C. Guidi, A. Cricenti, R. Gunnella, *J. Phys. Chem. B* **2011**, *115*, 11199.

[52] S. Reale, M. Crucianelli, A. Pezzella, M. D'Ischia, F. De Angelis, *J. Mass Spectrom.* **2012**, *47*, 49.

[53] D. R. Dreyer, D. J. Miller, B. D. Freeman, D. R. Paul, C. W. Bielawski, *Langmuir* **2012**, *28*, 6428.

[54] M. Arzillo, G. Mangiapia, A. Pezzella, R. K. Heenan, A. Radulescu, L. Paduano, M. D'Ischia, *Biomacromolecules* **2012**, *13*, 2379.

[55] Y. Li, J. Liu, Y. Wang, H. W. Chan, L. Wang, W. Chan, *Anal. Chem.* **2015**, *87*, 7958.

[56] J. M. Gallas, K. C. Littrell, S. Seifert, G. W. Zajac, P. Thiyagarajan, *Biophys. J.* **1999**, *77*, 1135.

[57] M. I. N. da Silva, S. N. Dezidério, J. C. Gonzalez, C. F. O. Graeff, M. A. Cotta, *J. Appl. Phys.* **2004**, *96*, 5803.

[58] S. N. Dezidério, C. A. Brunello, M. I. N. da Silva, M. A. Cotta, C. F. O. Graeff, *J. Non. Cryst. Solids* **2004**, *338-340*, 634.

[59] K. C. Littrell, J. M. Gallas, G. W. Zajac, P. Thiyagarajan, *Photochem. Photobiol.* **2007**, *77*, 115.

[60] C. Costa, A. Bertazzo, G. Allegri, G. Toffano, O. Curcuruto, P. Traldi, *Pigment Cell Res.* **1992**, *5*, 122.

[61] A. Bertazzo, C. Costa, G. Allegri, R. Seraglia, P. Traldi, *Rapid Commun. Mass Spectrom.* **1995**, *9*, 634.

[62] A. Napolitano, A. Pezzella, G. Prota, R. Seraglia, P. Traldi, *Rapid Commun. Mass Spectrom.* **1996**, *10*, 468.

[63] A. Pezzella, A. Napolitano, M. D'Ischia, G. Prota, R. Seraglia, P. Traldi, *Rapid Commun. Mass Spectrom.* **1997**, *11*, 368.

[64] A. Bertazzo, C. V. L. Costa, G. Allegri, M. Schiavolin, D. Favretto, P. Traldi, *Rapid Commun. Mass Spectrom.* **1999**, *13*, 542.

[65] W. Korytowski, T. Sarna, *J. Biol. Chem.* **1990**, *265*, 12410.

[66] M. M. Jastrzebska, H. Isotalo, J. Paloheimo, H. Stubb, *J. Biomater. Sci. Polym. Ed.* **1995**, *7*, 577.

[67] M. M. Jastrzebska, S. Jussila, H. Isotalo, *J. Mater. Sci.* **1998**, *33*, 4023.

[68] M. Jastrzebska, A. Kocot, L. Tajber, *J. Photochem. Photobiol. B Biol.* **2002**, *66*, 201.

[69] M. Zdybel, E. Chodurek, B. Pilawa, *Appl. Magn. Reson.* **2011**, *40*, 113.

[70] F. Bernsmann, A. Ponche, C. Ringwald, J. Hemmerlé, J. Raya, B. Bechinger, J.-C. Voegel, P. Schaaf, V. Ball, *J. Phys. Chem. C* **2009**, *113*, 8234.

[71] M. Abbas, F. D'Amico, L. Morresi, N. Pinto, M. Ficcadenti, R. Natali, L. Ottaviano, M. Passacantando, M. Cuccioloni, M. Angeletti, R. Gunnella, *Eur. Phys. J. E* **2009**, *28*, 285.

[72] S. Ito, *Biochim. Biophys. Acta - Gen. Subj.* **1986**, *883*, 155.

[73] J. Yan, L. Yang, M.-F. Lin, J. Ma, X. Lu, P. S. Lee, *Small* **2013**, *9*, 596.

[74] X. Yu, H. Fan, L. Wang, Z. Jin, *Angew. Chemie Int. Ed.* **2014**, n/a.

[75] C. S. Goldsbury, S. Scheuring, L. Kreplak, in *Curr. Protoc. Protein Sci.*, John Wiley & Sons, Inc., Hoboken, NJ, USA, **2009**, pp. 17.7.1–17.7.19.

[76] P. Hansma, V. Elings, O. Marti, C. Bracker, *Science (80-.).* **1988**, *242*, 209.

[77] T. Ando, T. Uchihashi, T. Fukuma, *Prog. Surf. Sci.* **2008**, *83*, 337.

[78] V. J. Morris, A. R. Kirby, A. P. Gunning, *Atomic Force Microscopy for Biologists*, PUBLISHED BY IMPERIAL COLLEGE PRESS AND DISTRIBUTED BY WORLD SCIENTIFIC PUBLISHING CO., **1999**.

[79] S. Tsuzuki, T. Uchimaru, *Curr. Org. Chem.* **2006**, *10*, 745.

[80] C. A. Hunter, J. K. M. Sanders, *J. Am. Chem. Soc.* **1990**, *112*, 5525.

[81]   C.-T. Chen, V. Ball, J. J. de Almeida Gracio, M. K. Singh, V. Toniazzo, D. Ruch, M. J. Buehler, *ACS Nano* **2013**, *7*, 1524.

[82]   C.-T. Chen, C. Chuang, J. Cao, V. Ball, D. Ruch, M. J. Buehler, *Nat. Commun.* **2014**, *5*, DOI 10.1038/ncomms4859.

[83]   O. I. Strube, A. Büngeler, W. Bremser, *Biomacromolecules* **2015**, *16*, 1608.

[84]   C. Möller, M. Allen, V. Elings, A. Engel, D. J. Müller, *Biophys. J.* **1999**, *77*, 1150.

[85]   E. Kaxiras, A. Tsolakidis, G. Zonios, S. Meng, *Phys. Rev. Lett.* **2006**, *97*, 218102.

[86]   S. Meng, E. Kaxiras, *Biophys. J.* **2008**, *94*, 2095.

[87]   R. Crippa, V. Horak, G. Prota, P. Svoronos, L. Wolfram, **1990**, pp. 253–323.

[88]   N. F. Della Vecchia, R. Avolio, M. Alfè, M. E. Errico, A. Napolitano, M. D'Ischia, *Adv. Funct. Mater.* **2013**, *23*, 1331.

[89]   M. R. Chedekel, B. L. Murr, L. Zeise, *Pigment Cell Res.* **1992**, *5*, 143.

[90]   E. Vedralová, B. Jan, D. Jiři, *J. Biochem. Biophys. Methods* **1987**, *14*, 343.

[91]   L. Zecca, M. Gallorini, V. Schünemann, A. X. Trautwein, M. Gerlach, P. Riederer, P. Vezzoni, D. Tampellini, *J. Neurochem.* **2001**, *76*, 1766.

[92]   Y. Liu, V. R. Kempf, J. Brian Nofsinger, E. E. Weinert, M. Rudnicki, K. Wakamatsu, S. Ito, J. D. Simon, *Pigment Cell Res.* **2003**, *16*, 355.

[93]   Y. Liu, L. Hong, V. R. Kempf, K. Wakamatsu, S. Ito, J. D. Simon, *Pigment Cell Res.* **2004**, *17*, 262.

[94]   X. Yu, H. Fan, Y. Liu, Z. Shi, Z. Jin, *Langmuir* **2014**, *30*, 5497.

[95]   Y. Liu, K. Ai, L. Lu, *Chem. Rev.* **2014**, *114*, 5057.

[96]   K.-Y. Ju, Y. Lee, S. Lee, S. B. Park, J.-K. Lee, *Biomacromolecules* **2011**, *12*, 625.

[97]   N. F. Della Vecchia, R. Marega, M. Ambrico, M. Iacomino, R. Micillo, A. Napolitano, D. Bonifazi, M. D'Ischia, *J. Mater. Chem. C* **2015**, *3*, 6525.

[98]   A. B. Mostert, K. J. P. Davy, J. L. Ruggles, B. J. Powell, I. R. Gentle, P. Meredith, *Langmuir* **2010**, *26*, 412.

[99]   A. B. Mostert, B. J. Powell, F. L. Pratt, G. R. Hanson, T. Sarna, I. R. Gentle, P. Meredith, *Proc. Natl. Acad. Sci.* **2012**, *109*, 8943.

[100]   A. Bernardus Mostert, B. J. Powell, I. R. Gentle, P. Meredith, *Appl. Phys. Lett.* **2012**, *100*, 093701.

Appendix I

Spectral Processing of Resonance Raman Data

A.I.1 Raman data acquisition

The reported RR spectrum of a molecule at a particular excitation wavelength is average of three spectra which are recorded from three freshly prepared samples. Every one of these three spectra is average of ten consecutively collected spectra, each of which is recorded with an acquisition time of one minute. Thus, each final Raman spectrum was acquired for a total 10 min of accumulation time. The spectrum of buffer (Fig. A.I.1, b) and quartz tube (Fig. AI.1, c) is sequentially subtracted from the averaged spectrum (Fig. A.I.1, a), to obtain a pure spectrum (Fig. A.I.1, d) of the molecule.
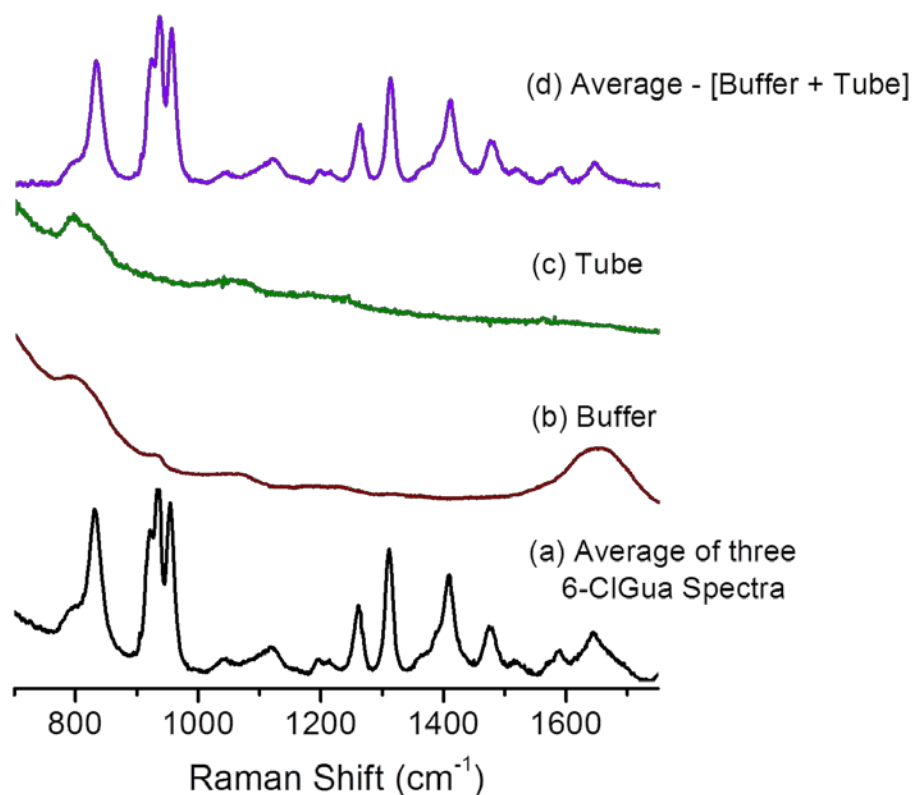
Fig. A.I.1 Typical subtraction and processing protocol of a RR spectrum

A.I.2 Spectral processing and used line-shape

The final spectrum (Fig. A.I.1, d) is deconvoluted with Lorentzian lineshape functions as shown in Fig. A.I.2. At each excitation wavelength, a preliminary fit with no constraints on line-width, band position and their integrated intensities is performed. Later, for each sample band, an average line width and position is determined from data recorded at several excitation wavelengths. At final fitting procedure, these bandwidths and positions are used to determine the relative intensities of all bands observed in a single spectrum.
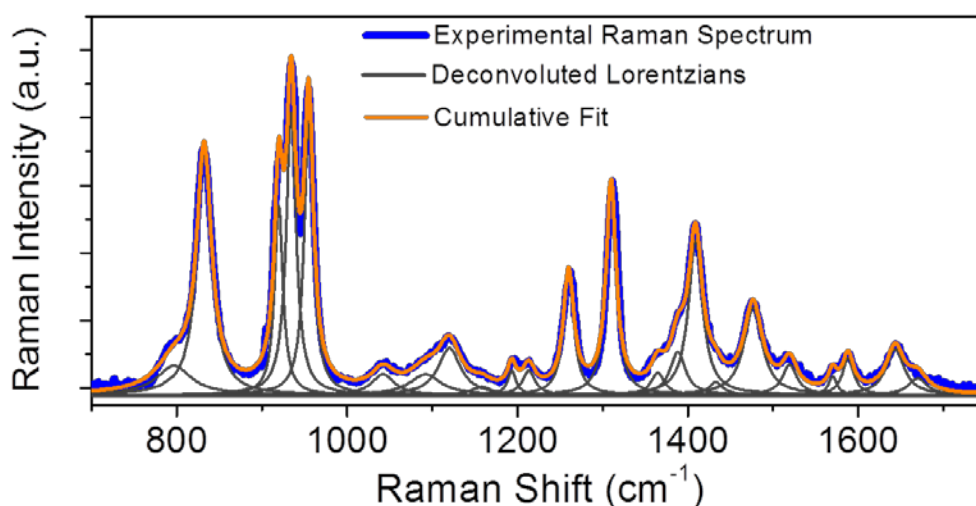

Fig. A.I.2. Experimental (blue), and Lorentzian deconvolved (grey) and cumulative (orange) fit to the Raman spectrum of 6-ClG at 215 nm excitation wavelength.

Raman lineshape depends on wo key factors the excited molecule; (i) relaxation time or amplitude correlation time (τ_a), which is typically ~ ps (10^{-12} s) for molecular vibrations and (ii) coherence lifetime (τ_c) that results in vibrational dephasing. In solids where the environment of a molecule is relatively rigid, $\tau_a \ll \tau_c$, different molecules experiences distinct but the static environment. The vibrational line-shape takes Gaussian profile. In other extreme situation, when $\tau_c \ll \tau_a$, *i.e.* in the gaseous system, the line-shape becomes Lorentzian. In a liquid, intermolecular interactions (such as hydrogen bonding) prevent very rapid motion, but the molecules are also not static in one place. In this case, the lineshape may become complex, and can be presented as Voigt function where Gaussian and Lorentzian lineshapes are convoluted with a relative weight.

In this thesis, all Raman spectra are deconvoluted with Lorentzian functions. For the validity of this choice, unconstrained fitting of Raman band was carried out using all three line-shape functions. Fig. AI.3 shows that Gaussian function is unable to describe the wings of the Raman band, and both Voigt and Lorentzian shapes work equally well. The deconvolution with Voigt function has maximal (> 90 %) weight of Lorentzian linewidth compared to that of Gaussian. Thus, Lorentzian functions are used to get widths and intensities of Raman bands for all samples described in this thesis. Data acquisition and processing were done using SynerJY software. (Jobin-Yvon). This fact is demonstrated for a band of a standard solvent, cyclohexane (Fig. A.I.3, left panel) and for a band of the sample, Guanosine monophosphate or GMP. (Fig. A.I.3, right panel)
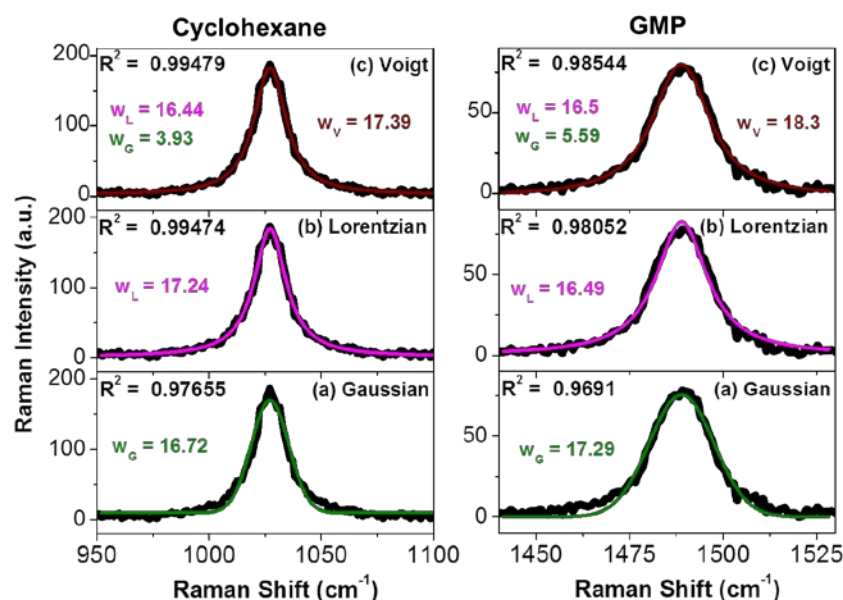
Fig. A.I.3. Fit to the experimental Raman band at 1027 cm^{-1} of cyclohexane (on left) and at 1689 cm^{-1} of GMP (on right) with (a) Gaussian, (b) Lorentzian and (c) Voigt line-shape functions. The width of Voigt profile (w_V) is determined using the relation: $w_V = 0.5346 * w_L + \sqrt{\{(0.2166 * w_L^2) + w_G^2\}}$; where w_L and w_G are the width of the convoluted Lorentzian and Gaussian profiles respectively.

Appendix II

Correction for Spectrometer Response

Procedure of intensity correction for wavelength dependent response of spectrometer and detector

(i)   Take the sample spectrum, I_λ at a particular excitation wavelength, say λ. Note down position of both ends of the spectrum in wavelength, say λ_1 and λ_2 nm.

(ii) NIST calibrated standard D_2O lamp (Ocean Optics Inc, Dunedin, FL, USA) spectrum is recorded at whole wavelength range (208-240 nm) of the spectrometer detection by changing grating position corresponding to each experiment at the different excitation wavelength. Interpolate this spectrum from λ_1 nm to λ_2 nm, in 1024 points to obtain standard lamp response, D_λ.

(iii) Linearly interpolate the true spectrum of the lamp (expressed as irradiance in $\mu w/cm^2/nm$ unit) from λ_1 nm to λ_2 nm, in 1024 points to obtain true lamp output, T_λ.

(iv) Calculate the correction factor at current excitation wavelength, λ as $S_\lambda = D_\lambda/T_\lambda$

(v)   Now, correct the sample spectrum by taking into account spectrometer and detector response as,

$$I_{corrected}(\lambda) = \frac{I(\lambda)}{S(\lambda)}$$

(vi) Repeat this method for spectra recorded at each excitation.

Appendix III

Relations between Einstein's coefficient of absorption, transition dipole moment and experimentally measurable quantities, such as, molar extinction coefficient and absorption cross-section

A.III.1 Einstein's coefficient and transition dipole moment

The relation between Einstein's coefficient for spontaneous absorption (B_{21}) and transition dipole moment, $\vec{\mu}_{fi}$ for a randomly oriented molecule,[1]

$$B_{21} = \frac{\pi|\vec{\mu}_{fi}|^2}{3\eta^2\varepsilon_0\hbar^2} \qquad\qquad (A.\,III.\,i)$$

where, $\vec{\mu}_{fi} = e\vec{M}_{fi}$ is transition electric dipole moment operator. $\vec{M}_{fi}$ is matrix element of the transition length operator $= \langle f|\,\vec{r}\,|i\rangle$. $|i\rangle$ and $|f\rangle$ are initial and final eigenstate of the absorbing molecule, $\vec{r}$ is position operator and $|\vec{\mu}_{fi}|^2$ is the transition probability. Transition dipole moment ($\vec{\mu}_{fi}$) characterizes single photon absorption or emission by a molecule. This vector describes in which direction the charge distribution will move in a molecule with respect to that of ground electronic sate (S_0) following an absorption of photon to reach a particular excited state (S_N).

A.III.2 Absorption cross-section and extinction coefficient

In spectroscopy, strength of an absorption band can be related to experimentally measurable quantities like absorption cross-section, $\sigma(\omega)$.
$\sigma(\omega)$ can be determined from molar absorptivity, ϵ_A, of a molecule via following equation[1],

$$\sigma(\omega) = \frac{2.303 \text{ x } 10^{19}\epsilon_A(\omega)}{N_A} \qquad\qquad (A.\,III.\,ii)$$

Where, if $\epsilon_A(\omega)$, molar extinction coefficient is expressed in L mol^{-1} cm^{-1} and N_A is Avogadro number = 6.023 x 10^{23}, unit of $\sigma(\omega)$ would be Å^2/molecule. Extinction coefficient can easily be determined by fitting measured absorbance of a molecule with their concentrations according to Beer-Lambert's law.

A.III.3 Transition dipole length or dipole strength

Transition dipole moment can be related to measurable integrated $\sigma(\omega)$ using following equation[1],

$$|\vec{\mu}_{fi}|^2 = \frac{3\hbar c\eta\varepsilon_0}{\pi\omega_{fi}} \int \sigma(\omega)d\omega \qquad\qquad (A.\,III.\,iii)$$

Where, $\int \sigma(\omega)d\omega$ = area under the gaussian fitted absorption spectrum in $\mathring{A}^2$ molecule^{-1} cm^{-1}.

$\hbar$ = reduced Planck constant = 1.054 x 10^{-34} J.s

η = refractive index of water = 1.33

ε_0 = permittivity of vacuum = 8.85 x 10^{-12} F.m^{-1}

c = speed of light = 2.99 x 10^8 m.s^{-1}

ω_{fi} = transition frequency or peak of the absorption band in cm^{-1}

$\vec{\mu}_{fi} = e\vec{M}_{fi}$, where e = charge of electron = 1.60 x 10^{-19} C and $\vec{M}_{fi} = \langle i|\vec{r}|f\rangle$ is electric dipole moment operator and $\vec{r} = \{rx, ry, rz\}$, position operator.

Magnitude of $\vec{M}_{fi}$, $|\vec{M}_{fi}|^2 = D_{fi}$ is transition dipole length expressed in $\mathring{A}$.

The transition probability is proportional to the square of the length of the vector. The transition moment vector can be resolved in three cartesian coordinates,

$$\vec{M}_{fi}^2 = M_{fi}^2(x) + M_{fi}^2(xy) + M_{fi}^2(z)$$

where $M_{fi}(x) = \langle i|\mu_x|f\rangle$, μ_x being the x component of dipole moment vector.

A.III.4 Oscillator strength

Another quantity to express the strength of photon absorption by a molecule in state $|i\rangle$ to reach state $|f\rangle$ is oscillator strength, f_{fi}. In classical theory it is the probability of an electronic transition induced by interaction of electrons in a molecule with incident electromagnetic radiation. Oscillator strength is the popular choice to express strength of absorption line in computational chemistry. Classically f_{fi} means, ratio of the intensity of the measured transition (absorption or emission) by a molecule to the

intensity of a 'harmonically oscillating' electron in a three-dimensional harmonic potential well. Such an electron is considered a perfect harmonic oscillator or an oscillating dipole with $f_{fi} = 1$.

This dimensionless quantity is defined in terms of dipole strength (or induced transition dipole moment) of a transition[1] as,

$$f_{fi} = \frac{2m_e\omega_{fi}}{3\hbar e^2}|\vec{\mu}_{fi}|^2 \qquad\qquad (A.\,III.\,iv)$$

where $\vec{\mu}_{fi}$ is transition electric dipole moment, ω_{fi} is the transition frequency. Derivation of this relation is well documented in many text books[3].

Substituting equation A.II.iii in A.II.iv and converting unit of **ω** from Hz to wavenumber, f_{fi} becomes

$$f_{fi} = 1.13 \times 10^{12}\,\eta \int \sigma(\tilde{v})d\tilde{v} \qquad\qquad (A.\,II.\,v)$$

where $\tilde{v}$ is wavenumber in cm^{-1} and $\sigma(\tilde{v})$ is in cm^2/molecule instead of Å^2/molecule (1 Å^2 = 10^{-16} cm^2).

Example:

For B_b state of 6-ClG, $\tilde{v}_{fi}$=45650 cm^{-1}, and $\int \sigma(\tilde{v})d\tilde{v}$ = integrated area under deconvoluted absorption cross-section = 4100 Å^2 molecule cm^{-1} = 4100 x 10^{-16} cm^2 molecule cm^{-1} giving f value of 0.62.

Equation A.II.v can be expressed in terms of molar extinction coefficient also [2],

$$f_{fi} = 4.3 \times 10^{-9} \int \epsilon\,(\tilde{v})d\tilde{v} \qquad\qquad (A.\,III.\,vi)$$

where, $\epsilon\,(\tilde{v})$ is experimental extinction coefficient in L mol^{-1} cm^{-1} and $\tilde{v}$ is frequency of incident light in cm^{-1}. $f_{fi} \approx 1$ for allowed transition and $f_{fi} \ll 1$ for forbidden (*e.g.* n→π*) transition.

Converting **ω** from Hz to wavenumber ($\omega = 2\pi c v$), equation A.II.iv becomes,

$$f_{fi} = \frac{8\pi^2 v_i m_e c}{3he^2}|\vec{\mu}_{fi}|^2 = \frac{8\pi^2 v_i m_e c}{3he^2}D_{fi} \qquad\qquad (A.\,III.\,vii)$$

where ν_i is the corresponding excitation energy in cm^{-1}, e is the charge of electron = 4.8 x 10^{-10} esu, m_e is the mass of electron = 9.1038 x 10^{-28} g, h is Planck constant = 6.63 x 10^{-27} erg.s. and D$_{fi}$ is dipole strength expressed in esu^2 cm^2.

A.III.5 Theoretical determination of transition dipole moment

Configuration interaction singles (CIS) or time dependent (TD) Hatre-Fock (HF)/density functional theoretical (DFT) computation of excited states in Gaussian09 reports this dipole strength (D$_{fi}$) in atomic unit (au) under the heading "**Ground to excited state transition electric dipole moments (Au)".** It can be converted to CGS via the relation, 1 au (1 bohr. electron) = 2.54 x 10^{-18} esu.cm.

Subsequently, transition dipole moment vector ($\vec{\mu}_{fi}$) has three orthogonal components, which are printed for each corresponding states, μ_x, μ_y and μ_z are related to D$_{fi}$ through,

$$D_{fi} = |\vec{\mu}_{fi}|^2 = \left|e\vec{M}_{fi}\right|^2 = e^2 \left|\sqrt{\left(\mu_x^2 + \mu_y^2 + \mu_z^2\right)}\right|^2 \qquad \text{(A. III. viii)}$$

Dot product of $\vec{\mu}_{fi}$ corresponding to different excited states with a fixed reference vector of the molecule, generally the one joining C$_6$ and N$_3$ atom in case of purine system would give their orientation with respect to each other. These vectors can be plotted on molecular geometry using Chemcraft v1.6 software for visualization. Relative orientation of L_a and B_a, and B_a and B_b transitions in GMP are depicted Fig 1. (a) and (b) respectively.
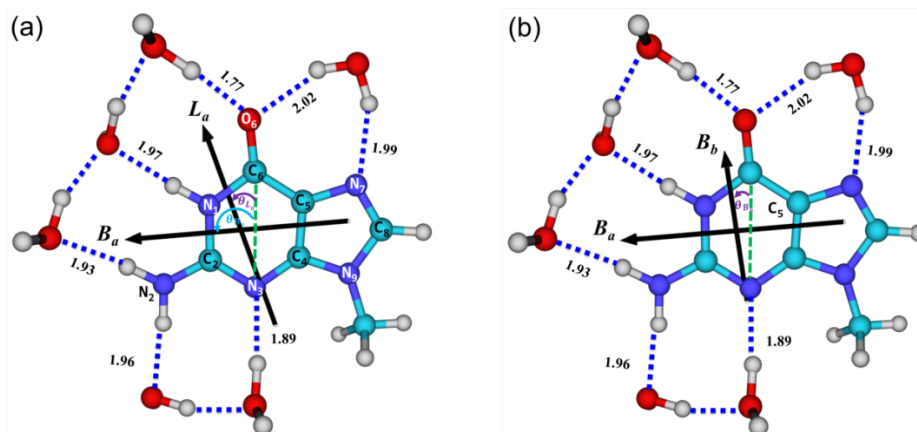
Fig. A.III.1 Transition dipole moments ($\vec{\mu}$) of (a) L_a and B_a and (b) B_a and B_b electronic states of GMP, computed on 9-meG•6H$_2$O model complex at TD-

B3LYP/6-311+G(2d,p) level of DFT with PCM solvation. $\vec{\mu}$ of L_a, B_a and B_b state are oriented at 19.4º (θ_{La}), 86.1º (θ_{Ba}) and 8.4º (θ_{Bb}) with respect to $\overrightarrow{C_6 - N_1}$ and have magnitude of 2.16, 2.38 and 1.07 au respectively.

A.III.6 Absorption spectra from computed oscillator strength

A CIS or TD (HF or DFT) output of G09 prints the oscillator strengths, f_{ij}, for each electronic transition from ground electronic state (j=0) to an excited electronic state (i), related to dipole strength via eqn. A.II.vii.

Conventionally a UV/Vis spectrum for i^{th} transition is expressed as molar extinction coefficient (ε) which is a function of energy of incident photon ($\tilde{\nu}$), with a Gaussian band shape as,

$$\varepsilon_i(\tilde{\nu}) = \varepsilon_i^{max} exp\left[-\left(\frac{\tilde{\nu} - \tilde{\nu}_i}{b}\right)^2\right] \qquad (A.\,III.\,ix)$$

where $\tilde{\nu}$ is excitation frequency in cm-1, $\tilde{\nu}_i$ is the frequency where photo-absorption is maximum, ε_i^{max} and 2b is the full width at half maxima (FWHM) of the simulated absorption band. 2b is the width expressed in cm^{-1} at half of the maximum absorption ($\varepsilon^{max}/2$). This molar extinction coefficient can be expressed in terms of oscillator strength (*f*) and dipole strength (D) using A.III.iv–A.III.vii according to,[4]

$$\varepsilon(\tilde{\nu}) = \sum_{i=1}^{n} \varepsilon_i(\tilde{\nu}) = \sum_{i=0}^{n} \left(1.3062974 \times 10^8 . \frac{f_i}{b} exp\left[-\left(\frac{\tilde{\nu} - \tilde{\nu}_i}{b}\right)^2\right]\right) \qquad (A.\,III.\,x)$$

f_{ij} is termed as simply f_i for i^{th} excited state and the summation runs over all excited states of the molecule.

References

1. Kelly, A. M. (2013). *Condensed-Phase Molecular Spectroscopy and Photophysics*. Hoboken, New Jersey, John Wiley & Sons, Inc. http://dx.doi.org/10.1002/9781118493052

2. Turro, N. J., Ramamurthy, V., & Scaiano, J. C. (2009). *Principles of molecular photochemistry: An introduction*. Sausalito, California, University Science Books.

3. Klessinger, M., Michl, J. (1995). *Excited States and Photochemistry of Organic molecules*. New York, New York, VCH Publishers, Inc.

4. Plotting UV/Vis spectra form oscillator and dipole strengths, Gaussian technical note, http://www.gaussian.com/g_whitepap/tn_uvvisplot.htm

Appendix IV

Resonance Raman intensities from excited state gradients

In the short time approximation (STA), resonance Raman intensity of kth fundamental vibrational mode of a molecule is proportional to the square of the magnitude of force exerted on associate excited state (ES), E^e surface along the kth normal mode Q_k and inversely proportional to the vibrational frequency (ω_k)[1].

$$I_k \propto \frac{1}{\omega_k \mu_k} \left(\frac{\partial E_e^P}{\partial Q_k} \right)_{FC}^2 \qquad \text{(A. IV. i)}$$

where $(\partial E_e^P / \partial Q_k)_0$ is mass–weighted instantaneous gradient evaluated on P^{th} electronic excited state surface along k^{th} normal mode following photoexcitation. The subscript 'FC' stands for the gradient is evaluated at ground state equilibrium geometry, *i.e.,* case of Frank-Condon (FC) excitation. ω_k and μ_k is the frequency and reduced mass of kth normal mode in the electronic ground state. With the efficient implementation of an algorithm for analytic gradient within TD-DFT formalism, evaluation of cartesian forces on potential energy surface (PES) of a particular excited state has become available. These non-mass weighted cartesian forces, $(\partial E_e^P / \partial x)_0$ can easily be converted to normal coordinate space by coordinate transformation to obtain mass weighted gradients,

$$\left(\frac{\partial E_e^P}{\partial Q_k} \right)_{FC} = L^T \left(\frac{\partial E_e^P}{\partial x} \right)_{FC} \qquad \text{(A. IV. ii)}$$

where the L is the orthogonal matrix obtained as the solution of the ground state normal mode eigenvalue problem. Transpose of L, L^T perform the basis change from cartesian coordinate to normal mode coordinate. For a molecule having N atoms both $(\partial E_e^P / \partial Q_k)$ and $(\partial E_e^P / \partial x)$ are column vector of (3N–6) x 1 and 3N x 1 dimension respectively. L is of 3N x (3N–6) dimension.

The assumption behind this description of RR intensity are, photoexcitation (i) does not induce any *duschinsky rotation between normal modes of excited state and those of ground state,* (ii) does not cause any change in frequency of vibrational modes

on the excited state from those in the ground state and (iii) PES of ground and excited states are harmonic. (See Chapter 2 and cited references there in)

Step-by-Step Computational Strategies

Method of computing excited state gradient along normal coordinate for simulation of RR intensities using G09 software suite.

(i) Step 1: Locate stationary point on electronic ground states (GS) potential energy surface (PES) to obtain normal modes

It is done by a GS geometry optimization followed by checking the sign of second derivative of energy with respect to mass weighted cartesian nuclear coordinate, i.e. appearance of all real harmonic frequencies. The keyword for a calculation run with G09 suite is,

#P B3LYP/6-311+G(2d,p) Opt Freq=HPModes Pop=full

Freq=HPModes prints the eigenvalues of the mass-weighted Hessian in Cartesian coordinate with more significant digits than in the normal frequency output. These eigenvalues are the vibrational frequencies and eigenvectors are mass-weighted normal coordinates. They constitute the 3N x (3N−6) matrix L who's each column represents a normal coordinate vector corresponding to a normal mode of vibration. This is the transformation matrix (L) which does the change of basis to project gradients in cartesian coordinate onto normal mode coordinate.

Note: Locate the string "**mass-weighted force constant matrix**" in output file to get mass-weighted normal coordinates.

(ii) **Step 2**: Computation of Frank-Condon (Vertical) excitation employing linear response time dependent DFT (TDDFT) method.

On that geometry (GS minima) do a TDDFT calculation with a bigger basis set (do not forget to include diffuse function for excited state (ES) properties calculation) to get the excitation energies. To compute first 15 singlet states the input will looks like,

#P td=(nstates=15) B3LYP/6-311+G(2d,p) pop=full

(iii) Step 3: Evaluation of cartesian gradient on PES of electronic ES.

Visualize the involved orbital (in Chemcraft 1.6 or GaussView or any other visualization software) in transition associated to a particular ES state you are interested in. Look for state with high oscillator strength (f > 0.1) because they correspond to strongly allowed $\pi\pi^*$ transition in general aromatic molecules. Use the

checkpoint file from previous calculation to compute gradient on excited state PES at ground state geometry with respect to nuclear coordinate.

Suppose, N^{th} state is the ES corresponding to the laser excitation used in experiment, then the input will look like:

```
#P td=(Read,Root=N) B3LYP/6-311+G(2d,p) Guess=Read geom=check
Force IOp(7/33=1)
```

'Guess=Read' reads the GS orbital and 'TD=Read' reads the TD results from previous calculation stored in the checkpoint file. 'N' is the electronic ES of your interest. 'Force' keyword request computation of cartesian force exerted on each atom on the Nth excited state surface at GS geometry (Frank-Condon excitation). 'IOp(7/33=1)' prints the forces on atoms in standard orientation otherwise printed in input coordinate frame. Eigenvectors of the mass-weighted Hessian (the matrix, L) are also printed in the standard orientation. Arrange x, y and z components of gradients on each atom in a single column vector, say Q which will be of (3N x 1) dimension.

Note: Locate the gradients by the string, '**Forces in standard orientation'** in G09 output file.

(iv) Step 4: Project the gradient along normal mode coordinate.

Cartesian forces are converted to gradient along normal modes, matrix A of (3N-6) x 1 dimension, via following linear transformation

$$A = L^T . Q \hspace{3cm} (A. IV. iii)$$

Where L^T = Transpose of matrix L of (3N-6) x 3N dimension. Now, **A** will be of (3N-6) x 1 dimension representing gradient in mass-weighted normal coordinate space. Each element of **A** is gradient along an individual normal mode.

Example

Computation of RR spectra of O-Nitrophenol in cyclohexane with excitation of 355 nm

See "Assessment of TD-DFT and CC2 Methods for the Calculation of Resonance Raman Intensities: Application to o-Nitrophenol, Guthmuller, J. J. Chem. Theory Comput. 2011, 7, 1082–1089" for details

Job 1: Geometry optimization of o-nitrophenol with PCM solvation using cyclohexane as solvent. (**Step 1**)

```
#P B3LYP/6-311++g(2df,p) opt scrf=(iefpcm,solvent=cyclohexane)
freq=hpmodes pop=full gfinput
```

To Do: Extract normal mode vectors, L and store them in **Matrrix_L.txt** as described in **Step 1**. Optimized geometry is shown in Fig. A.IV.1.

Job 2: TD-DFT on optimized geometry – Read checkpoint file of **Job 1** (**Step 2**)

```
#p td=(singlets,nstates=30) B3LYP/6-311++g(2df,p) guess=read
geom=checkpoint scrf=(iefpcm,solvent=cyclohexane) gfinput pop=full
```

To Do: Visualize the lowest singlet state, S_1 as a pure H→L transition at 3.38 eV (366.18 nm) with an oscillator strength of 0.0763 (same as in the mentioned paper, 9th row in Table 2.) corresponding to 355 nm excitation wavelength. So, we are interested in $^1\pi\pi^*$ singlet excited state (Root=1).

Job 3: Computation of gradient on S_1 surface – Use the checkpoint file of Job 2 (**Step 3**)

```
# TD=(read,Root=1) B3LYP/6-311++G(2df,p) FORCE guess=read
geom=check scrf=(iefpcm,solvent=cyclohexane) IOp(7/33=1)
```

To Do: Extract cartesian gradient vector, **Q** as described in **Step 3** and write them in **Cartesian_Gradient_Root_1.txt**

Job 4: Projection of the cartesian gradient along normal coordinate

Transpose the matrix L (Matrrix_L.txt) and evaluate the matrix multiplication according to eqn. A.IV.3 tcompute gradient along mass-weighted normal mode coordinate. Then compute RR intensities according to eqn. A.IV.1.
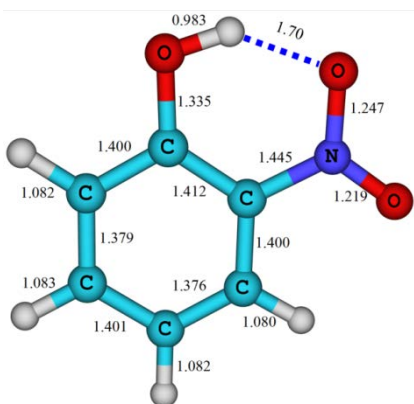
Fig. A.IV.1 Energy optimized structure of o-Nitrophenol at B3LYP/6-311++G(2df,p) level of DFT with continuum solvation according to self-consistent reaction field PCM and cyclohexane as solvent.

.
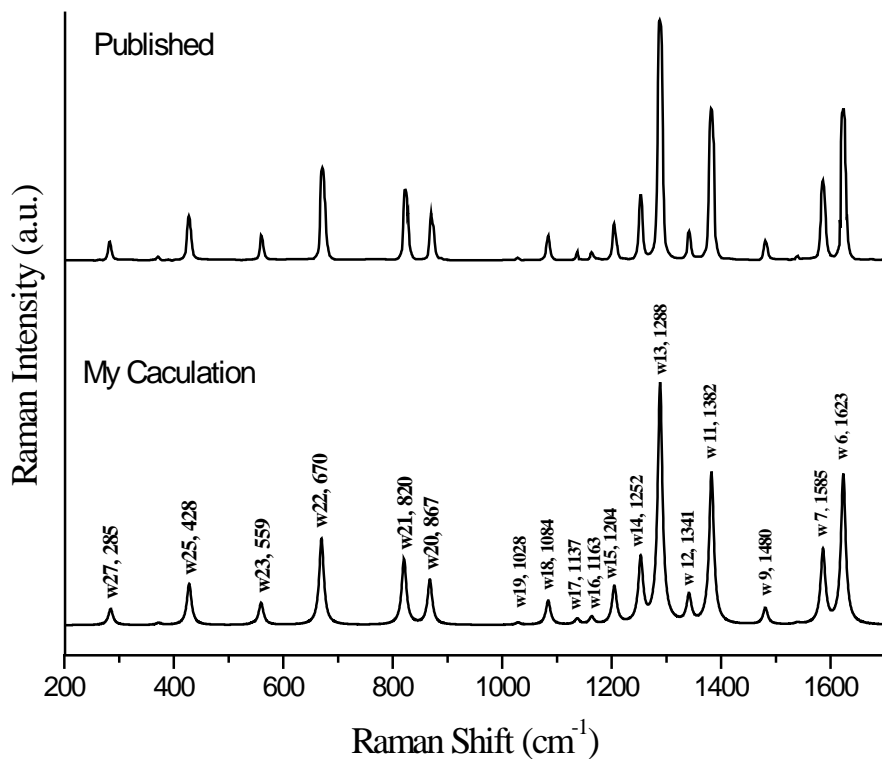
Fig. A.IV.2 Computed RR spectra of o-Nitrophenol in cyclohexane at B3LYP/6-311++G(2df,p) level within short time approximation. The spectrum shown at the top is adapted with permission from Ref 2 (Fig. 3, panel b). Copyright (2011) American Chemical Society.

Reference

1. Heller, E. J.; Sundberg, R.; Tannor, D. *J. Phys. Chem.* 1982, 86, 1822–1833.
2. Guthmuller, J. *J. Chem. Theory Comput.* 2011, 7, 1082–1089.

Appendix V

Raman spectroscopic characterization of human and mouse skin cells*†

A.V.1 Introduction

Melanin pigmentation displays high variability among individual humans as well as among different tissues within the same individual. Phenotype of human and other animal skin exhibits a wide variety of coloration and gradations, ranging from white to brown to black, primarily due to production and distribution of melanin containing melanosomes. The underlying molecular mechanisms that bring about this variability are manifold including environmental, genetic and endocrine factors.[1–6] It is established that the variation of concentration alone does not account for the observed differences in skin coloration. To understand pigmentation of skin and the regulating factors including environmental and therapeutic agents, one must characterize the melanin containing cells. Important applications of characterizing skin cells are (i) to develop *in vitro* model systems that can be used as an alternative for experiments on live animal in cosmetic industry and for developing artificial skin model. and (ii) to assess different molecular biological manipulations of skin cells in order to regulate pigmentation, reducing phototoxicity of ingredients of sun screen etc.[7]

The majority of traditional methods that have been developed to obtain qualitative information about concentration of cellular components are invasive in nature. All these methods require sample processing, including fixation, sectioning, and fluorescent antibody staining. These procedures not only result in destruction of tissue samples, but alter the original system under investigation by physical disruption at times. Vibrational spectroscopy, a laser based technique provides with a non-invasive alternative to monitor cells and intact tissue samples.[8–11] Every molecule (proteins, lipids or nucleic acids) present inside cell has a unique set of vibrational modes, that can used for quantitative analysis.

Typical choice of excitation wavelengths for micro Raman characterization of different cell types are 632 and 785 nm[12–16] and other visible and near IR excitations.[17–20] Other recently developed and comparatively expensive method

for noninvasive diagnosis of live cells are multiphoton-induced autofluorescence, second harmonic generation imaging and multi-spectral optical imaging.[21–23] Raman spectroscopic methods have successfully been used for tissue characterization and pathologic tissue classification.[12,24–32] Among various cell types, *in vivo* human skin and *in vitro* models of different skin cells are routinely noninvasively investigated employing confocal vibrational microspectroscopy.[14,18,33–39] Most recently Pudlas *et al* have demonstrated that Raman imaging in combination with multivariate analysis is able to noninvasively distinguish different skin cells in cell suspensions of *in vitro* model.[12]

Being optically dark, it has been difficult to detect vibrational signature of melanin in synthetic system, and *in vivo* studies as well. Both natural (from ink sack of *sepia officinalis and liver of Rana esculenta*) and synthetic (made from oxidation of tyrosine and Dopa) melanin have board (full width at half maxima > 100 cm^{-1}) Raman signature dominated by two bands at ~ 1400 cm^{-1} and 1600 cm^{-1}.[35,40,41] Both these bands are interpreted as in-plane aromatic stretching and C=C stretching based on vibrational spectral analysis of monomer.[42]Though many studies have investigated human skin *in vivo* and skin cells *in vitro* using vibrational microspectroscopy, only one report by Schenke-Layland and coworkers have obtained a feeble band at ~ 1380 cm^{-1} which was assigned to melanin pigment.[12]

The main difficulties in obtaining vibrational signature from melanin that is confined in intact melanosomes inside melanocyte are simultaneous presence of bands at ~ 1400-1420 cm^{-1} originating from lipids (CH_2 and CH_3 deformations) and ~1550-1650 cm^{-1} from protein backbone (Amide I and Amide II), aromatic amino acids (Tyr, Phe and Trp) and water. Moreover, typically these mentioned components have much higher cross-section than melanin. Nevertheless, there can be spectral differences arising from changes in concentrations of specific cellular component as results of melanin production. This difference can be significant between melanin containing cells from different species, and between pigmented and depigmented cell types from same animal. In this part of the thesis, efforts have been made to discriminate human skin cells (Primary melanocyte and keratinocyte) and mouse cancerous cells (B16 melanoma) based on their average vibrational spectral behavior.

A.V.2 Material and Methods

A.V.2.1 Sample Preparation for Raman microscopy

In the current study three cell types, B-16 pigmented (pigmented B16) and depigmented (depigmented B16) mouse cells (derived from a melanoma tumor from the skin of a C57BL/6 strain mouse producing melanin), human *in vitro* modified keratinocytes, HaCaT cells, primary epidermal human keratinocytes (PHK) and primary human melanocytes (PHM), that are obtained from foreskins of human individual and cultured in growth medium, were analyzed using microRaman spectroscopy. To perform imaging experiments a few thousand cells were seeded on 0.01 % poly-lysine coated quartz slides and were kept inside incubator at 37°C overnight with growth medium. After 12 to 18 hours when the cells were adhered to the slide, the growth medium was taken out and the slide was washed twice with phosphate buffer saline (PBS, 20 mM). Then the cells were fixed on the slide by addition of chilled methanol and kept at -20°C for 5-10 min. After the methanol is evaporated, these slides were stored at -20°C to be imaged at later time. Before recording Raman image one such slide was rehydrated with 1 mL of 10 mM PBS buffer for 30 min. During course of the experiment 200-300 µl of miliQ water was added every 45 min to keep the cells hydrated and to prevent precipitation of phosphate salts. Raman signal from every cell that is to be imaged was monitored continuously with 20 s exposure time while varying z-values gradually. Spectral recording was performed at the z-value where signal is optimal. The cell types used where primary human keratinocytes, primary human melanocytes, primary human melanocytes treated with tyrosine and polythiouracil and HaCaT cells.

A.V.2.2 Confocal Raman microscopy

Raman spectra from individual cells were recorded using a LabRAM HR800 Confocal Microscope (HORIBA Jobin Yvon SAS, rue de Lille, France) A Helium-neon diode laser operating at 785 nm and with a power at the sample surface of around 30-40 mW was used as the Raman excitation source. A water immersion achromatic objective of 60x magnification and numerical aperture of 1.33 was employed for excitation and maximal collection of Raman scattered photons in a 180° back scattering geometry. (Chapter 2) Raman spectrum was recorded on a liquid nitrogen cooled CCD chip after dispersing through an 800 mm focal length spectrograph equipped with an 1800 grooves/mm grating.

After locating a cell in bright field image, Raman signal was monitored with 20-30 s exposure while sample stage was continually scanned (along Z direction) to find the focal plane. To obtain a spectrum from a single point inside cell, a minimum of 2 scans each of 60-120 seconds exposure time at 0.65 cm^{-1}/pixel spectral resolution were collected. A Raman map of the cell was then obtained by using the X-Y scanner (spatial resolution ~ 0.1 µm) of the sample stage across the focal plane. Confocal

pinhole is normally kept at 200 or 300 µm for thin optical sectioning and spectrometer slit was set at 200 µm for good spectral resolution. No coverslip was used on cells that are adhered to quartz slide. On an average total signal collection time for a Raman map consisting 64-100 spectra (8 by 8 to 10 by 10 spectral arrays) from a cell was 3-4.5 hr. All recorded Raman spectra are within fingerprint region of 1100-1800 cm^{-1}. The Raman spectra were calibrated against 520.7 cm^{-1} peak of silicon (Si).

A.V.2.3 Data processing

Hyper spectral Raman image and individual spectrum were acquired through LabSpec 5.5 (HORIBA Jobin Yvon SAS, rue de Lille, France) that also controls the microscope. Background spectrum (signal from outside cell) that is primarily broad water band at ~ 1650 cm^{-1} is recorded during each Raman map. This signal is subtracted from all spectra recorded from inside cell. Afterwards 10-15 spectra from each cell are averaged to obtain mean behavior of each cell type. All spectral processing is performed with LabSpec 5.5. Quartz does not have any Raman band (Figure A.V.1a) that can interfere with spectral signature from within cells. While recording spectra from a cell that is fixed on quartz slide, size of confocal pinhole was optimized (200 µm) to avoid interference from two bands of poly-lysine. (Fig. A.V.1b)
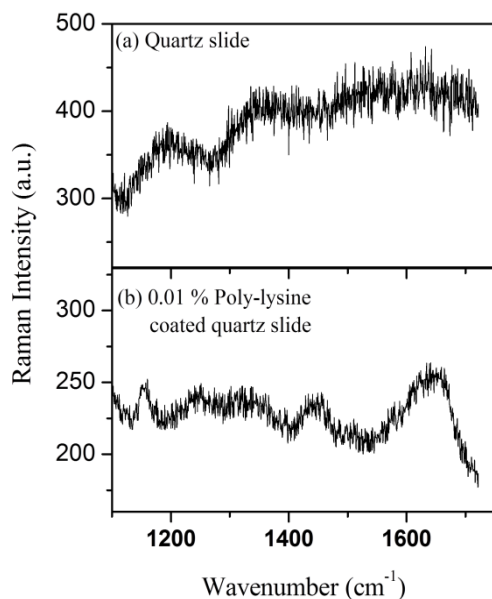

Fig. A.V.1. 785 nm excited microRaman spectra of (a) dry quartz slide with 20x objective and (b) poly-lysine coated (0.01%) quartz slide with 60x water immersion objective. Each of these spectra is accumulated for 60 sec and obtained with 40 mW power on sample. Poly-lysine has to characteristic band at ~ 1150 cm^{-1} and at ~ 1445 cm^{-1}. The broad band ~ 1650 cm^{-1} is from water. While imaging cells a confocal pinhole of 200 µm in size ensures thin enough optical sectioning to exclude poly-lysine coating from the recording plane.

A.V.3 Results and Discussions

## A.V.3.1 Raman spectral characteristics of skin cells

Bright field micrographs six different cell types (Fig. A.V.2) and corresponding average Raman spectra from cytoplasm of these cells are shown in Fig. A.V.2. Spectral assignments of observed Raman bands within 1100-1800 cm^{-1} region are described in Table A.V.1. Mean band positions corresponding to various cellular ingredients agree with previously published Raman spectral assignment of different animal cell types.[43–47] When the cells are immobilized on slide, they are not completely flat specifically along the edge. Thus while obtaining hyperspectral map at a fixed z value, autofluorescence background of Raman signal varies across whole mapping area.
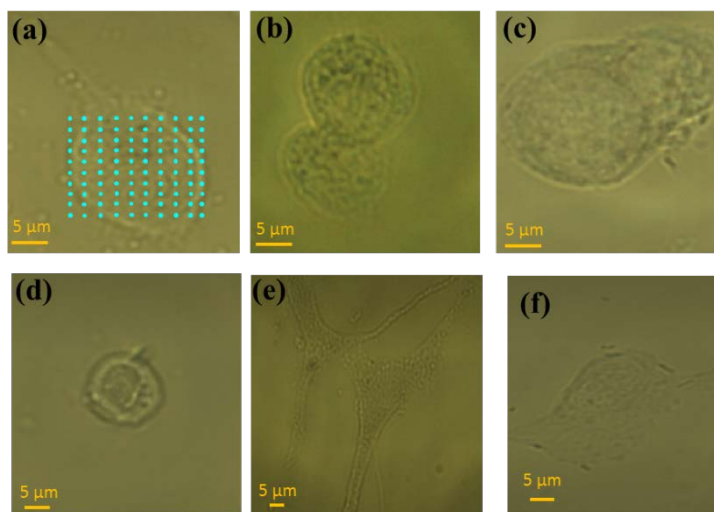
Fig A.V.2. Bright field micrographs of (a) pigmented and (b) unpigmented B16 melanocyte, (c) HaCaT, primary human (d) keratinocyte and (e) melanocyte, and (f) PTU treated human melanocyte cells with 60x water immersion objective. All cells are fixed on 0.01 % poly-lysine coated quartz slide with chilled (-20 degree C) methanol and stored at -20 degree C. Cells were rehydrated with 10 mM phosphate buffer for one hour before used for Raman imaging. A typical 10 x10 =100 points grid, from whose each point a spectrum is recorded is shown in (a).

Though all these are common vibrational modes present, the relative intensity of the peaks vary with the cell type. The most distinct spectra are of PHK and that of untreated PHM. While Amide III mode (1246 cm^{-1}) is mostly broad and of less intensity in all other cell types, in PHK it is narrow, well defined and of considerably higher intensity than amide II (1630 cm^{-1}) and tryptophan (Trp) signal (1588 cm^{-1}). Most notably, the intensities of CH$_3$ bend and deformation modes within 1300 cm^{-1} to 1420 cm^{-1}, those originate form lipids are the dominating contributor in PHK cell when compared to other call types. These results suggest increased amount of lipids

that are key building blocks of plasma membrane and other cellular components, including nuclear membrane, vesicles such as endosomes and lysosomes and others.
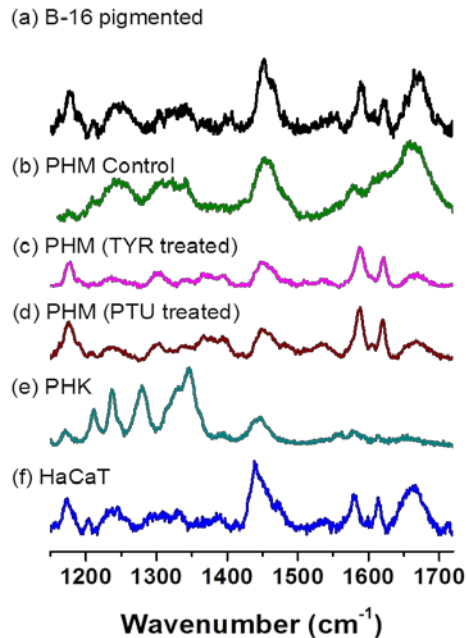
Fig. A.V.3 Averaged Raman spectra from cytoplasm of different cell types. (a) pigmented mouse B16 melanoma; (b) untreated or control primary human melanocyte (PHM); (c) tyrosine treated PHM; (d) PTU treated PHM; (e) primary human keratinocyte (PHK); and (f) immortal keratinocyte HaCaT cell. All spectra are recorded with 785 nm excitation and 30-40 mW power on sample and using water immersion achromatic objective of 60x magnification. These spectra are obtained by averaging spectra recorded from 5 to 8 cells of each types.

The pigmented B16 and immortal keratinocyte HaCaT have a strong band at ~ 1665 cm^{-1} unlike other cell types studied here. This band is generally associated to amide I (C=O str. Coupled with NH$_2$ be.) of protein and specifically also from α-helical protein secondary structure. The CH$_2$ deformation indicating lipid contribution at ~ 1450 cm^{-1} is present in all cell types. However, under broad envelope of this band, distinct shoulders are present in only B16 and HaCaT cells, probably indicating presence of more heterogeneous population of lipid molecules. The lipid composition of different cell types, and tissues might vary significantly, because different lipids are required for performing different functions.[48]

The pigmented primary human melanocyte has bands at similar positions as in pigmented B16 cells. However, the shape of a few bands, particularly that centered around amide I vibration (~ 1660 cm^{-1}). Treatment of these melanocytes with 1-phenyl 2-thiourea (PTU) is reported to inhibit the production of melanin by blocking all tyrosinase dependent steps in melanin biosynthesis, while melanin production increases with the supply of precursor tyrosine.[49,50] However, in the current study, hardly any Raman spectral difference was observed between the two cell types.(Fig.

A.V.3, c and d) The general characteristic features in the spectra of PTU and tyrosine treated cells with those of HaCaT and pigmented B-16 cells are many: 1176 cm^{-1} (C=O stretch and C-OH bend), broad 1246 cm^{-1} (amide III), 1403 cm^{-1} (CH$_3$ bend from lipid), 1450 cm^{-1} (CH$_2$ deformation from lipid), 1543 cm^{-1} (amide II) and 1630 cm^{-1} (amide I and the broad C=C indole stretching).

A.V.3.2 In vitro spectral signature of melanin

Melanosomes, the organelles that encapsulate melanin are localized along the periphery of cells. To capture melanosome signature a thin optical sectioning of z-map is performed along periphery of pigmented primary human melanocyte. Such a z-scan map is shown in Fig. A.V.3 where a weak band ~ 1391 cm^{-1} is observed to appear and eventually disappear while different layers of a cell is focused and defocussed. We observe that from z= 16 μm to z=20 μm, the melanin band is not observed. But from z=20 μm to z= 26 μm, we see a systematic change in the intensity of the 1391 cm^{-1} melanin band, which peaks at z= 24 μm. Beyond z= 26 μm, the 1391 cm^{-1} band vanishes.
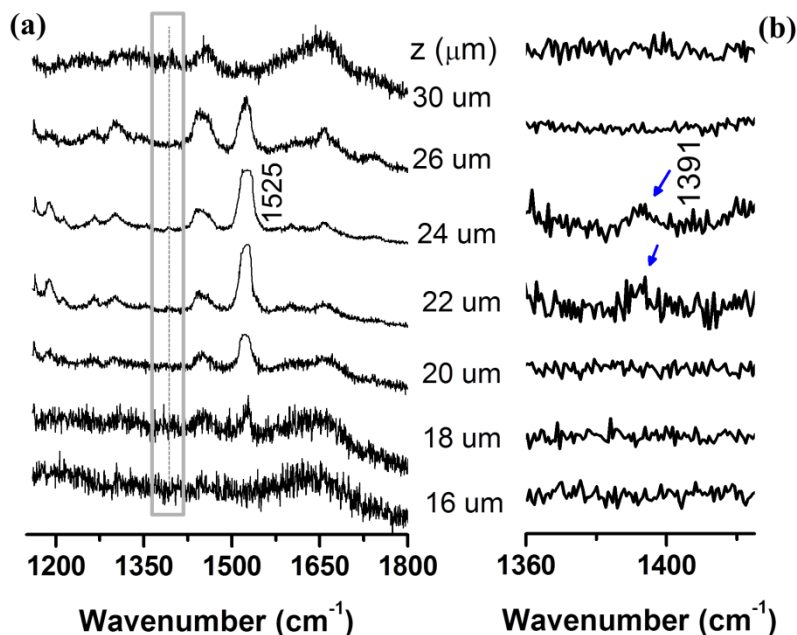
Fig. A.V.4. (a) Consecutively recorded Raman spectra from different layers of a pigmented primary human melanocyte (PHM) cell by varying the sample stage along z axis with respect to fixed position of microscope objective, (b) magnified version of region marked in rectangle in (a) within 1360- 1425 cm^{-1} . Spectra are recorded with 90 sec exposure, 60x objective, ~40 mW incident power from a 785 nm diode laser and confocal pinhole of 200 um.

A band of similarly weak intensity at 1380 cm^{-1} was reported in human melanocyte and was ascribed to melanin.[12] Two characteristic broad vibrational bands at around 1360-1400 cm^{-1} and around 1570-1595 cm^{-1} are reported for melanin from various sources, such as, synthetic melanin and natural melanins from *Sepia officinalis,* mushroom and liver of *Rana esculenta*, black human hair, human skin and neuromelanin from substantia nigra of human brain.[41,42,51–55] In Raman spectra the second band is stronger than the first one[41,55] and in IR absorption spectra the ~ 1580 cm^{-1} band is much weaker than the first one.[42,51–54] The positions of these two bands are known to vary with sources and might as well on purification and preparations procedures. Thus the observed 1391 cm^{-1} band in human melanocyte is expected to be a characteristic vibrational signature of melanin observed in all mentioned studies. However the other band ~ 1580 cm^{-1} is masked under strong protein amide I contribution in cells. It is worth to note that with resonance excitation at 260 nm, this band of synthetic dopa melanin and tyrosinase oxidized melanin is observed at ~ 1615 cm^{-1}.(see Chapter 7)

A unique Raman signature in untreated primary human melanocyte (PHM) is observed ~ 1525 cm^{-1} during collecting signal from different layers of the cell through optical sectioning. (Fig. A.V.4) This band is not seen in any other cell types studied here. Human epidermis contains two major endogenously absorbed vitamin A as retinoids (retinol and retinyl esters) and carotenoids (mostly β-carotene) from diets of animal origins and fruits.[56,57] β-carotene has as very strong band at 1157 cm^{-1} and 1525 cm^{-1} and low intensity band at ~1442 cm^{-1} that overlap with CH$_2$ scissoring mode of lipid in same region.[58] β-carotene is detected in several algal cells through Raman microspectroscopy.[58] Comparison of intensities of C=C str. and amide I band at ~ 1660 cm^{-1} with that of 1525 cm^{-1} (Fig. A.V.4, a) indicates presence of a significant amount of carotenoids in pigmented and untreated human melanocytes.

A.V.4 Conclusions

In summary, pigmented primary human melanocyte and mouse B16 cells, and keratinocytes (primary human and immortal HaCaT) can be differentiated through Raman microspectroscopy. Primary human keratinocyte and primary human melanocytes have distinguishing marker bands indicating high concentration of β-carotene and lipids respectively. Major spectral changes are not observed in average spectral response of PTU and Tyrosine treated primary human melanocytes. To differentiate among these cells, multivariate analysis, such as, principal component analysis of densely recorded hyperspectral Raman image is necessary.

References

[1] G.-E. Costin, V. J. Hearing, *FASEB J.* **2007**, *21*, 976.

[2] J. Y. Lin, D. E. Fisher, *Nature* **2007**, *445*, 843.

[3] Y. Yamaguchi, V. J. Hearing, *BioFactors* **2009**, *35*, 193.

[4] P. Sulem, D. F. Gudbjartsson, S. N. Stacey, A. Helgason, T. Rafnar, K. P. Magnusson, A. Manolescu, A. Karason, A. Palsson, G. Thorleifsson, M. Jakobsdottir, S. Steinberg, S. Pálsson, F. Jonasson, B. Sigurgeirsson, K. Thorisdottir, R. Ragnarsson, K. R. Benediktsdottir, K. K. Aben, L. A. Kiemeney, J. H. Olafsson, J. Gulcher, A. Kong, U. Thorsteinsdottir, K. Stefansson, *Nat. Genet.* **2007**, *39*, 1443.

[5] N. F. Box, T. Terzian, *Pigment Cell Melanoma Res.* **2008**, *21*, 525.

[6] T. Hoshino, M. Matsuda, Y. Yamashita, M. Takehara, M. Fukuya, K. Mineda, D. Maji, H. Ihn, H. Adachi, G. Sobue, Y. Funasaka, T. Mizushima, *J. Biol. Chem.* **2010**, *285*, 13254.

[7] C. A. Brohem, L. B. da Silva Cardeal, M. Tiago, M. S. Soengas, S. B. de Moraes Barros, S. S. Maria-Engler, *Pigment Cell Melanoma Res.* **2011**, *24*, 35.

[8] H. Sato, Y. Maeda, M. Ishigaki, B. B. Andriana, in *Encycl. Anal. Chem.*, John Wiley & Sons, Ltd, Chichester, UK, **2000**, pp. 1–12.

[9] F. Siebert, P. Hildebrandt, *Vibrational Spectroscopy in Life Science*, Wiley-VCH Verlag GmbH & Co. KGaA, Weinheim, Germany, **2007**.

[10] M. Ghomi, Ed. , *Applications of Raman Spectroscopy to Biology: From Basic Studies to Disease Diagnosis*, IOS Press, Inc., Virginia, USA, **2012**.

[11] A. T. Tu, *Raman Spectroscopy in Biology: Principles and Applications*, John Wiley & Sons, Ltd, New York, USA, **1982**.

[12] M. Pudlas, S. Koch, C. Bolwien, S. Thude, N. Jenne, T. Hirth, H. Walles, K. Schenke-Layland, *Tissue Eng. Part C Methods* **2011**, *17*, 1027.

[13] C. Yu, E. Gestl, K. Eckert, D. Allara, J. Irudayaraj, *Cancer Detect. Prev.* **2006**, *30*, 515.

[14] G. Zhang, D. J. Moore, C. R. Flach, R. Mendelsohn, *Anal. Bioanal. Chem.* **2007**, *387*, 1591.

[15] N. D. Magee, J. S. Villaumie, E. T. Marple, M. Ennis, J. S. Elborn, J. J. McGarvey, *J. Phys. Chem. B* **2009**, *113*, 8137.

[16] A. V. Feofanov, A. I. Grichine, L. A. Shitova, T. A. Karmakova, R. I. Yakubovskaya, M. Egret-Charlier, P. Vigny, *Biophys. J.* **2000**, *78*, 499.

[17] N. M. Sijtsema, C. Otto, G. M. J. Segers-Nolten, A. J. Verhoeven, J. Greve, *Biophys. J.* **1998**, *74*, 3250.

[18] P. J. Caspers, G. W. Lucassen, G. J. Puppels, *Biophys. J.* **2003**, *85*, 572.

[19] E. Zuser, T. Chernenko, J. Newmark, M. Miljković, M. Diem, *Analyst* **2010**, *135*, 3030.

[20] N. M. Sijtsema, A. G. J. Tibbe, I. G. M. J. Segers-Nolten, A. J. Verhoeven, R. S. Weening, J. Greve, C. Otto, *Biophys. J.* **2000**, *78*, 2606.

[21] G. R. Holtom, B. D. Thrall, B.-Y. Chin, H. S. Wiley, S. D. Colson, *Traffic* **2001**, *2*, 781.

[22] T. Binzoni, A. Vogel, A. H. Gandjbakhche, R. Marchesini, *Phys. Med. Biol.* **2008**, *53*, 617.

[23] E. A. Gibson, O. Masihzadeh, T. C. Lei, D. A. Ammar, M. Y. Kahook, *J. Ophthalmol.* **2011**, *2011*, 1.

[24] M. Diem, M. Romeo, S. Boydston-White, M. Miljkovi?, C. Matthaus, *Analyst* **2004**, *129*, 880.

[25] P. Lasch, J. Kneipp, Eds. , *Biomedical Vibrational Spectroscopy*, John Wiley & Sons, Inc., Hoboken, NJ, USA, **2008**.

[26] R. Salzer, H. W. Siesler, Eds. , *Infrared and Raman Spectroscopic Imaging*, Wiley-VCH Verlag GmbH & Co. KGaA, Weinheim, Germany, **2009**.

[27] U. Zelig, J. Kapelushnik, R. Moreh, S. Mordechai, I. Nathan, *Biophys. J.* **2009**, *97*, 2107.

[28] R. J. Erckens, F. H. M. Jongsma, J. P. Wicksted, F. Hendrikse, W. F. March, M. Motamedi, *Lasers Med. Sci.* **2001**, *16*, 236.

[29] M. M. Mariani, P. J. R. Day, V. Deckert, *Integr. Biol.* **2010**, *2*, 94.

[30] J. Chan, S. Fore, S. Wachsmann-Hogiu, T. Huser, *Laser Photonics Rev.* **2008**, *2*, 325.

[31] J. Zhu, J. Zhou, J. Guo, W. Cai, B. Liu, Z. Wang, Z. Sun, *Chem. Cent. J.* **2013**, *7*, 37.

[32] A. C. S. Talari, Z. Movasaghi, S. Rehman, I. ur Rehman, *Appl. Spectrosc. Rev.* **2015**, *50*, 46.

[33] P. J. Caspers, G. W. Lucassen, R. Wolthuis, H. A. Bruining, G. J. Puppels, *Biospectroscopy* **1998**, *4*, S31.

[34] P. J. Caspers, H. A. Bruining, G. J. Puppels, G. W. Lucassen, E. A. Carter, *J. Invest. Dermatol.* **2001**, *116*, 434.

[35] L. Knudsen, C. K. Johansson, P. A. Philipsen, M. Gniadecka, H. C. Wulf, *J. Raman Spectrosc.* **2002**, *33*, 574.

[36] L. Smith, S. MacNeil, *Ski. Res. Technol.* **2011**, *17*, 257.

[37] M. Foerster, M.-A. Bolzinger, G. Montagnac, S. Briancon, *Eur. J. Dermatology* **2012**, *21*, 851.

[38] A. P. Rangel, J. L. Raniero, L. J. Tosato, M. G. Fávero, P. P. Martin, A. Abrahão, *Rev. Bras. Eng. Biomédica* **2014**, *30*, 11.

[39] C. Danciu, A. Falamas, C. Dehelean, C. Soica, H. Radeke, L. Barbu-Tudoran, F. Bojin, S. Pînzaru, M. F. Munteanu, *Cancer Cell Int.* **2013**, *13*, 75.

[40] Z. Huang, H. Lui, X. K. Chen, A. Alajlan, D. I. McLean, H. Zeng, *J. Biomed. Opt.* **2004**, *9*, 1198.

[41] V. Capozzi, G. Perna, A. Gallone, P. F. Biagi, P. Carmone, A. Fratello, G. Guida, P. Zanna, R. Cicero, *J. Mol. Struct.* **2005**, *744-747*, 717.

[42] S. A. Centeno, J. Shamir, *J. Mol. Struct.* **2008**, *873*, 149.

[43] G. J. Puppels, H. S. Garritsen, G. M. Segers-Nolten, F. F. de Mul, J. Greve, *Biophys. J.* **1991**, *60*, 1046.

[44] T. C. Bakker Schut, P. J. Caspers, G. J. Puppels, A. Nijssen, F. Heule, M. H. A. Neumann, D. P. Hayes, *J. Invest. Dermatol.* **2002**, *119*, 64.

[45] A. Synytsya, P. Alexa, J. Besserer, J. De Boer, S. Froschauer, R. Gerlach, M. Loewe, M. Moosburger, I. Obstová, P. Quicken, B. Sosna, K. Volka, M. Würkner, *Int. J. Radiat. Biol.* **2004**, *80*, 581.

[46] C. Murali Krishna, G. Kegelaer, I. Adt, S. Rubin, V. B. Kartha, M. Manfait, G. D. Sockalingum, *Biochim. Biophys. Acta* **2005**, *1726*, 160.

[47] C. Aksoy, F. Severcan, *Spectrosc. An Int. J.* **2012**, *27*, 167.

[48] C. Klose, M. A. Surma, K. Simons, *Curr. Opin. Cell Biol.* **2013**, *25*, 406.

[49] J. R. Whittaker, *Dev. Biol.* **1966**, *14*, 1.

[50] J. J. Eppig, *Zeitschrift für Zellforsch. und Mikroskopische Anat.* **1970**, *103*, 238.

[51] J. A. Pierce, D. M. Rast, *Phytochemistry* **1995**, *39*, 49.

[52] E. Harki, T. Talou, R. Dargent, *Food Chem.* **1997**, *58*, 69.

[53] M. G. Bridelli, D. Tampellini, L. Zecca, *FEBS Lett.* **1999**, *457*, 18.

[54] B. Bilińska, *Spectrochim. Acta Part A Mol. Biomol. Spectrosc.* **2001**, *57*, 2525.

[55] A. Samokhvalov, Y. Liu, J. D. Simon, *Photochem. Photobiol.* **2007**, *80*, 84.

[56] A. Vahlquist, *J. Invest. Dermatol.* **1982**, *79*, 89.

[57] A. Vahlquist, J. B. Lee, G. Michaëlsson, O. Rollman, *J. Invest. Dermatol.* **1982**, *79*, 94.

[58] O. Samek, A. Jonáš, Z. Pilát, P. Zemánek, L. Nedbal, J. Tříska, P. Kotas, M. Trtílek, *Sensors* **2010**, *10*, 8635.

Appendix VI

Computing X-ray structure factor and radial distribution function of melanin protomolecules

A.VI.1 Structure Factor

Reciprocal space patterns in X-ray or neutron scattering is known as static structure factor $S(q)$, given by Debye's equation,[1–3]

$$S(q) = \frac{1}{N} \sum_{j,k} b_j b_k \frac{\sin(q|r_j - r_k|)}{q|r_j - r_k|}$$

A. VI. i

where

    a. N is the total number of atoms in the system.

    b. q is the scattering vector which is also known as momentum transfer vector, with

       $|q| = 4\pi\sin\theta/\lambda$, θ is diffraction half-angle and λ is wavelength of the experiment.

    c. $|r_j - r_k|$ is the distance between j^{th} and k^{th} atoms.

    d. b_j is atomic scattering length of jth atom and depends on q.

A.VI.2 Radial Distribution Function (RDF)

Contribution of a pair of atoms towards total scattering intensity is not straightforwardly interpreted using eqn. A.VI.i. For this purpose, it is more convenient to use the formalism of Radial Distribution Function (RDF), denoted by g(r). It is also known as pair distribution function or pair correlation function.

RDF is the probability of finding an atom within a shell of thickness *dr* at the distance *r* of another atom chosen as a reference point. Now, if the material under study is compose of more than one chemical species, say α and β, then RDF is expressed as partial radial distribution function, $g_{\alpha\beta}(r)$.

The probability density of being an atom of α species at a distance r from an atom of β species is given by,

$$g_{\alpha\beta}(r) = \frac{dn_{\alpha\beta}(r)}{4\pi r^2 dr \rho_\alpha}$$

A. VI. ii

where $\rho_\alpha = \dfrac{V}{N_\alpha} = \dfrac{V}{N \times C_\alpha}$; with

    a. c_α and ρ_α is concentration and density of atomic species, α.

    b. N and V is total number of atoms and model volume respectively.

    c. $4\pi r^2 dr \approx \left[\dfrac{4}{3}\pi(r + dr)^3 - \dfrac{4}{3}\pi r^3\right]$ = the volume of shell of thickness dr

The total RDF of any system would be a weighted sum of all the respective partial RDFs, and the weights would depend on the relative concentration and intrinsic x-ray scattering amplitudes of the chemical species the material is made off.

Alternate to eqn. A.VI.i, structure factor can be expressed as Fourier transform of partial RDF,

$$S(q) = 1 + 4\pi\rho \int_0^\infty r^2 \frac{Sin\,(qr)}{qr}(g(r) - 1)dr \qquad\qquad \text{A.\,IV.\,iii}$$

where, g(r) is radial distribution function, defined in terms of $g_{\alpha\beta}(r)$ (see Eqn. A.VI.ii),

$$g(r) = \frac{\sum_{j,k} c_\alpha b_\alpha\, c_\beta b_\beta\, g_{\alpha\beta}(r)}{\langle b^2 \rangle} \qquad\qquad \text{A.\,VI.\,iv}$$

with, $c_\alpha = N_\alpha/N$ = concentration of species α; b_α is X-ray scattering length of species α and $\langle b^2 \rangle = \left(\sum_\alpha c_\alpha b_\alpha\right)^2$

X-ray scattering properties of melanin protomolecules are computed using these equations implemented in the program, Interactive Structure Analysis of Amorphous and Crystalline Systems (I.S.A.A.C.S) v 2.8.[4,5]

References

[1]   B. J. Thijsse, *J. Appl. Crystallogr.* **1984**, *17*, 61.
[2]   M. T. Dove, M. G. Tucker, D. A. Keen, *Eur. J. Mineral.* **2002**, *14*, 331.
[3]   M. T. Dove, *Eur. J. Mineral.* **2002**, *14*, 203.
[4]   S. Le Roux, V. Petkov, *J. Appl. Crystallogr.* **2010**, *43*, 181.
[5]   I.S.A.A.C.S v2.8; http://isaacs.sourceforge.net/index.html

Published, communicated and in-preparation papers those are included in the thesis

1. Mondal, S. and Puranik, M. *U l t r a f a s t excited state dynamics of 6-chloroguanine upon deep ultraviolet excitation,* 2016. **Phys. Chem. Chem. Phys.**, 2016,**18**, 13874-13887; **DOI:** 10.1039/C6CP01746K

2. Mondal, S., Thampi, A. and Puranik, M. *Kinetics of melanin polymerization during enzymatic and non‑enzymatic oxidation* (communicated)

3. Mondal, S. and Puranik, M. *Ultrafast nuclear dynamics of photoexcited guanosine monophosphate,* (communicated)

4. Mondal, S., Puranik M. and Patil S. *Aggregation Dynamics and Structural Hierarchy in dopa-eumelanin* (in preparation)

5. Mondal, S. and Puranik, M. *Ultrafast femtosecond structural dynamics of photoexcited adenine* (in preparation)

6. Mondal, S. and Puranik, M. *Structural model of eumelanin protomolecule* (in preparation)

7. Mondal, S. and Puranik, M. *Substitution induced electronic and vibrational reorganizations in Purines* (in preparation)

Not included in thesis

1. Milán-Garcés, Erix A.; Mondal, S.; Udgaonkar, J. B. and Puranik, M. *Intricate packing in the hydrophobic core of barstar through a CH‑π interaction*, **J Raman Spec**. 2014, 45, 814-821. DOI: 10.1002/jrs.4558